A

Acceleration Wave Propagation in Inhomogeneous Heat-Conducting Rods

Nigel H. Scott
School of Mathematics, University of East Anglia, Norwich, UK

Overview

An acceleration wave is a singular surface propagating through a material body across which the particle acceleration experiences a finite discontinuity, or jump, but the particle velocity and deformation gradient are continuous. Acceleration waves may propagate in 1-, 2-, or 3-dimensional material bodies. For purely elastic materials and for heat-conducting elastic materials, and for many other materials, it is possible to deduce an explicit expression for the squared speed of acceleration waves. It is also possible to deduce an explicit nonlinear equation (of Bernoulli type) for the growth of acceleration wave amplitude, for which exact solutions may be written down. Acceleration wave theory is of great interest in mechanics generally because it furnishes some of the few exact solutions that are available in nonlinear mechanics. Chen [1] has given a full account of most aspects of acceleration wave theory. Straughan [2, Chap. 4] also has given an excellent account of acceleration wave theory, concentrating largely on various nonclassical theories of heat conduction rather than on the classical theory considered here.

We model acceleration wave propagation in an inhomogeneous heat-conducting rod as a problem in one-dimensional wave propagation (see [1]). As a further source of inhomogeneity, we allow the rod to have a slowly varying cross-sectional area which requires modification of the original model (see [3]). The speed of acceleration wave propagation is found to depend on the material inhomogeneity but to be independent of the changing cross-sectional area. However, the growth of wave amplitude is certainly influenced by the changing cross-sectional area. Increasing cross-sectional area renders the acceleration wave less likely to build up into a shock wave after a finite distance of propagation, while decreasing cross-sectional area renders the acceleration wave more likely to build up into a shock.

Introduction

In this entry, we consider the propagation and growth of acceleration waves in a materially inhomogeneous, heat-conducting, nonlinearly elastic rod. We also allow the rod to have slowly varying cross-sectional area. The region ahead of the wave may be prestrained and is not assumed to be in either mechanical or thermal equilibrium. The rod is modeled as a one-dimensional continuum with modifications to allow for the slowly varying cross section. The wave then turns out to

R.B. Hetnarski (ed.), *Encyclopedia of Thermal Stresses*, DOI 10.1007/978-94-007-2739-7,

be a longitudinal plane wave whose speed of propagation is unaffected by the varying cross section but whose amplitude growth is so affected.

In the next section, the third, we give the basic equations and kinematic jump conditions, and in the fourth section, we make the usual constitutive assumptions concerning the Helmholtz free energy and heat flux and derive some associated jump conditions. In the fifth section, we introduce the equations of momentum and energy balance and are able to deduce an expression for the squared wave speed.

In the sixth section, "The Growth Equation," we derive an equation for the growth of wave amplitude which is of Bernoulli type as is commonly the case for acceleration waves. There follows a detailed discussion of the precise role of each of the eight terms appearing in the coefficients (26) and (25) of the growth equation (24).

In the seventh and final section, we consider the behavior of the solution of the growth equation as the distance of propagation increases.

Basic Equations and Kinematic Jump Conditions

The rod occupies the material region $X \geqslant 0$ and has slowly varying cross-sectional area $A(X)$, so that the motion is essentially one-dimensional. An acceleration wave is a singular surface propagating with positive speed U such that the motion $x(X,t)$ and its first derivatives, namely, the velocity $\dot{x}$ and the deformation gradient $F = \partial x/\partial X$, are continuous but some of the second derivatives are discontinuous, for example, the acceleration $\ddot{x}$. The superposed dot denotes the material time derivative. We shall assume that the wave is initiated at the end $X = 0$ of the rod at time $t = 0$. The temperature $\theta(X,t)$ is taken to be continuous, and we shall prove that $\dot{\theta}$ and the temperature gradient $G = \partial\theta/\partial X$ are also continuous. The jump in any quantity $\phi(X,t)$ across the wave front is defined to be

$$[\phi] = \phi^- - \phi^+ \tag{1}$$

where the superscript $^+$ signifies evaluation just ahead of the wave and the superscript $^-$ signifies evaluation just behind the wave. The wave front derivative $\delta/\delta X$ denotes the space derivative moving with the wave front, and we have

$$\begin{aligned} \frac{\delta\phi}{\delta X} &= \frac{\partial\phi}{\partial X} + \frac{1}{U}\dot{\phi} \\ \frac{\delta}{\delta X}[\phi] &= \left[\frac{\partial\phi}{\partial X}\right] + \frac{1}{U}\left[\dot{\phi}\right] \end{aligned} \tag{2}$$

where we have used the fact that the wave front derivative $\delta/\delta X$ and the jump operator $[\,]$ commute:

$$\frac{\delta}{\delta X}[\phi] = \left[\frac{\delta\phi}{\delta X}\right]$$

for any function $\phi(X,t)$.

Across an acceleration wave front, we have

$$[\dot{x}] = 0 \quad [F] = 0 \quad [\theta] = 0 \tag{3}$$

and we denote the nonzero jump in acceleration by a:

$$[\ddot{x}] = a \tag{4}$$

Using (1)–(4), it is possible to deduce the following kinematic jump conditions which are independent of any constitutive assumptions and the equations of momentum and energy balance:

$$\begin{aligned} [\dot{F}] &= -\frac{a}{U} \\ \left[\frac{\partial F}{\partial X}\right] &= \frac{a}{U^2} \\ \left[\frac{\partial \dot{F}}{\partial X}\right] &= \frac{1}{U^2}[\ddot{x}] - \frac{2}{U}\frac{\delta a}{\delta X} + \frac{1}{U^2}\frac{\delta U}{\delta X}a \end{aligned} \tag{5}$$

and

$$\begin{aligned} \left[\dot{\theta}\right] &= -U[G] \\ \left[\frac{\partial\dot{\theta}}{\partial X}\right] &= -U\left[\frac{\partial^2\theta}{\partial X^2}\right] + U\frac{\delta}{\delta X}[G] \end{aligned} \tag{6}$$

Equation $(5)_1$ is obtained by putting $\phi = \dot{x}$ in $(2)_2$ and using $(3)_1$, the fact that $\partial\dot{x}/\partial X = \dot{F}$, and (4). Equation $(5)_2$ is obtained by putting $\phi = F$ in $(2)_2$ and using $(3)_2$, $(5)_1$, and (4). Equation $(5)_3$ is obtained by successively putting $\phi = \ddot{x}$ and $\phi = \dot{F}$ in $(2)_2$ and eliminating $[\ddot{F}]$ between the resulting two equations. Equation (6) is derived similarly.

Constitutive Equations and Associated Jump Conditions

We make the usual constitutive assumptions concerning the specific Helmholtz free energy ψ and the referential heat flux Q:

$$\psi = \psi(F, \theta, \overline{X}) \quad Q = Q(F, \theta, G, \overline{X}) \qquad \overline{X} = X \tag{7}$$

which are both taken to be continuously differentiable as many times as required. In addition, Q vanishes identically in F, θ, and $\overline{X}$ if $G = 0$:

$$Q(F, \theta, 0, \overline{X}) \equiv 0 \tag{8}$$

expressing the fact that heat flux vanishes in the absence of temperature gradient. $\overline{X}$ denotes the explicit dependence of quantities on X, that is, the X-dependence due to material inhomogeneity.

The energy balance equation, see (20) below, forces

$$[Q] = 0 \tag{9}$$

The second law of thermodynamics requires the thermal conductivity to be nonnegative, but we shall require it to be strictly positive, that is, the material is a *definite conductor*:

$$\kappa = -\frac{\partial Q}{\partial G} > 0 \tag{10}$$

This requirement, together with (9) and (6), yields

$$[G] = 0 \quad \left[\dot{\theta}\right] = 0 \quad \left[\frac{\partial \dot{\theta}}{\partial X}\right] = -U\left[\frac{\partial^2 \theta}{\partial X^2}\right] \tag{11}$$

Thus, θ and its first derivatives are continuous across an acceleration wave front in a definite elastic conductor (see [4]). Such a wave is said to be *isothermal*.

The Piola-Kirchhoff stress T and the specific entropy η are given by

$$T = \rho_0 \frac{\partial \psi}{\partial F} \quad \eta = -\frac{\partial \psi}{\partial \theta} \tag{12}$$

where $\rho_0(X)$ is the mass per unit volume of the rod in the reference configuration. Since ψ is a continuously differentiable function of its continuous arguments, taking jumps of (12) gives

$$[T] = 0 \quad [\eta] = 0 \tag{13}$$

We now take jumps of the material time derivative of (12) and use the jump conditions $(5)_1$ and $(11)_2$ to obtain

$$\left[\dot{T}\right] = -\frac{E}{U}a \quad [\dot{\eta}] = -\frac{\beta}{\rho_0 U}a \tag{14}$$

in which the elastic modulus E and the temperature coefficient of stress β are defined by

$$E = \frac{\partial T}{\partial F} \quad \beta = -\frac{\partial T}{\partial \theta} \tag{15}$$

It is a universal requirement of elasticity that E be strictly positive, and for most materials, β is observed to be strictly positive. In the subsequent analysis, we insist that $E > 0$ but β is unrestricted.

Momentum and Energy Balance and the Wave Speed

The integral form of the equation of momentum balance appropriate to a one-dimensional continuum with varying cross section is

$$\frac{d}{dt}\int_{X_1}^{X_2}\rho_0\dot{x}A\,dX=\int_{X_1}^{X_2}\rho_0 bA\,dX+T(X_2)A(X_2)-T(X_1)A(X_1) \tag{16}$$

in which X_1 and X_2 are any two positions and $b(X,t)$ is the body force per unit mass (acting along the rod in the direction of X increasing). The point form of this equation is

$$\rho_0 A\ddot{x}=\frac{\partial(TA)}{\partial X}+\rho_0 Ab \tag{17}$$

or equivalently

$$\rho_0\ddot{x}=\frac{\partial T}{\partial X}+\rho_0 b+T\frac{d}{dX}\ln A \tag{18}$$

After writing $\partial T/\partial X=E\partial F/\partial X-\beta G+\partial T/\partial\overline{X}$; taking jumps of (18); assuming that b is continuous; using (4), $(5)_2$, and $(11)_1$; and assuming that the acceleration wave amplitude a is not identically zero, we finally obtain an expression for the wave speed:

$$\rho_0 U^2=E \tag{19}$$

which has been obtained by all authors on acceleration waves. The condition $E>0$ ensures that U is real. Equation (19) gives the wave speed in terms of quantities which may be assumed known on the wave front. It has the same form as when thermal effects are neglected (except that here E is temperature dependent). The wave speed is unaffected by the varying cross section.

The appropriate integral version of the reduced energy equation is

$$\int_{X_1}^{X_2}\rho_0\theta\dot{\eta}A\,dX=\int_{X_1}^{X_2}\rho_0 rA\,dX-Q(X_2)A(X_2)+Q(X_1)A(X_1) \tag{20}$$

with corresponding point form

$$\rho_0\theta\dot{\eta}=-\frac{\partial Q}{\partial X}+\rho_0 r-Q\frac{d}{dX}\ln A \tag{21}$$

where $r(X,t)$ is the heat supply per unit mass of the rod. The heat supply is assumed continuous across the wave front. Taking jumps of (21) and using $(14)_2$, $(5)_2$, $(11)_1$, (10), $(11)_3$, and (9) finally yield

$$\left[\frac{\partial\dot{\theta}}{\partial X}\right]=\left(\theta\beta-U^{-1}Q_F\right)\frac{a}{\kappa} \tag{22}$$

It can be seen from (8) that if the material is in thermal equilibrium ahead of the wave, then $Q_F\equiv\partial Q/\partial F$ vanishes identically in F, θ, and $\overline{X}$.

The Growth Equation

We now derive an equation governing the growth of the wave amplitude a of a plane acceleration wave propagating along the rod. Take the material time derivative of (18) and use $(2)_1$ to obtain

$$\rho_0\ddot{\dot{x}}=\frac{\partial T}{\partial F}\frac{\partial\dot{F}}{\partial X}+\frac{\partial T}{\partial\theta}\frac{\partial\dot{\theta}}{\partial X}+\frac{\delta}{\delta X}\left(\frac{\partial T}{\partial F}\right)\dot{F}+\frac{\delta}{\delta X}\left(\frac{\partial T}{\partial\theta}\right)\dot{\theta}-\frac{1}{U}\left\{\frac{\partial^2 T}{\partial F^2}\dot{F}^2+2\frac{\partial^2 T}{\partial F\partial\theta}\dot{F}\dot{\theta}+\frac{\partial^2 T}{\partial\theta^2}\dot{\theta}^2\right\}+\rho_0\dot{b}+\left\{\frac{\partial T}{\partial F}\dot{F}+\frac{\partial T}{\partial\theta}\dot{\theta}\right\}\frac{d}{dX}\ln A \tag{23}$$

The modulus $\partial T/\partial F$ occurring in the first and third terms of (23) is replaced by $\rho_0 U^2$ from $(15)_1$ and (19). Jumps are then taken of (23) assuming that $\dot{b}$ is continuous and remembering that $\dot{\theta}$ is. On rewriting all the jumps in terms of a using (5) and (22) and noting that $[\ddot{x}]$ no longer appears, on account of (19), we eventually arrive at an ordinary differential equation for the acceleration wave amplitude. It is a Bernoulli equation of the form usually encountered in acceleration wave theory:

$$\frac{\delta a}{\delta X}+\mu a+\gamma a^2=0 \tag{24}$$

where

$$\mu(X)=\frac{1}{2}\frac{\delta}{\delta X}\ln\rho_0+\frac{1}{2}\frac{\delta}{\delta X}\ln U+\frac{1}{2}\frac{\delta}{\delta X}\ln A+\frac{\theta\beta^2}{2\rho_0 U\kappa}-\frac{\beta Q_F}{2\rho_0 U^2\kappa}-\frac{E_F}{\rho_0 U^3}\dot{F}^+-\frac{E_\theta}{\rho_0 U^3}\dot{\theta}^+ \tag{25}$$

and

$$\gamma(X) = \frac{E_F}{2\rho_0 U^4} = \frac{\rho_0 E_F}{2E^2} \tag{26}$$

The second-order moduli occurring are defined by

$$E_F = \frac{\partial E}{\partial F} \quad E_\theta = \frac{\partial E}{\partial \theta} \tag{27}$$

The coefficients $\mu(X)$ and $\gamma(X)$ may be assumed known on the wave front.

Equation (24) is the growth equation for acceleration waves propagating into a materially inhomogeneous nonlinearly elastic heat-conducting rod of slowly varying cross section which may be prestrained and need not be in either mechanical or thermal equilibrium ahead of the wave.

For the remainder of this section, we discuss the coefficients $\gamma(X)$ and $\mu(X)$ defined by (26) and (25), respectively. The coefficient γ depends only on the material density and the elasticities and not on the varying cross section or on thermal effects (except that the elasticities are temperature dependent). In the special case of linear elasticity, the second-order modulus E_F vanishes and so, therefore, does γ. If γ vanishes then, of course, (24) reduces to a linear equation.

Turning now to the coefficient μ, we see that the sixth and seventh terms are absent if either the material is linearly elastic (since then E_F and E_θ vanish) or the material ahead of the wave is quiescent. The fifth term vanishes if the material ahead of the wave is in a state of thermal equilibrium. The fourth term may be thought of as the most important explicit effect of thermal conductivity since terms five and seven are absent if the material ahead of the wave is in thermal equilibrium. The fourth term is intrinsically positive, vanishing only if β does, since $\theta > 0$ and $0<\kappa<\infty$. If β vanishes identically in F at a particular temperature, then the result $E_\theta = -\partial\beta/\partial F$ shows that thermal effects are entirely absent from the equation of growth at that temperature since then the fourth, fifth, and last terms of (25) vanish. We recall that the vanishing of β is also the condition for the uncoupling of mechanical and thermal effects in the propagation of sinusoidal waves through a prestrained thermoelastic solid [5].

We continue our discussion of the thermal terms of (25) by considering the role of the thermal conductivity κ. For a nearly perfect conductor (κ large), the fourth and fifth terms are negligible, and any spatial temperature variations may be expected to equalize out rapidly. However, $\dot{\theta}$ need not be small (though it must be spatially uniform), and so the last term of (25) need not be negligible. In the limit $\kappa \to \infty$, the fourth and fifth terms of (25) vanish, and the spatially uniform temperature $\theta(t)$ acts merely as a parameter. If θ is constant, we are left with the growth equation of purely mechanical elasticity, which is well known to be synonymous with isothermal elasticity. On the other hand, for a nearly perfect insulator (κ small), we may expect the heat flux Q and all its partial derivatives to be in some sense small so that, in particular, Q_F is small and, unless β vanishes, the fourth term of (25) becomes large and positive, predominating over all the others. Therefore, in the limit $\kappa \to 0$, we find that $\mu(X) \to \infty$ unless β vanishes. The growth equation (24) retains meaning in this limit only if we insist that $a(X) \to 0$ as $\mu(X) \to \infty$. We must therefore take $a(X) = 0$ in the limit, that is, there can be no isothermal acceleration wave in a one-dimensional elastic nonconductor ($\kappa = 0$) unless β vanishes. However, in general, an acceleration wave in a nonconductor is *isentropic* but not isothermal (see [4]) (an acceleration wave is said to be isentropic if the entropy and its first derivatives are continuous across the wave front). It is clear from [6, Eq. (2.4)] that a one-dimensional isentropic acceleration wave cannot also be isothermal unless β vanishes, as is consistent with our conclusion above that there can be no isothermal acceleration wave in a one-dimensional elastic nonconductor unless β vanishes. We return briefly to the isentropic acceleration wave which propagates in a nonconductor when we discuss growth estimates for $a(X)$ in the final section.

The only effect of the varying cross section on the growth equation (24) is through the third term in (25) which we may interpret in terms of three-dimensional acceleration wave propagation. In his investigation of three-dimensional acceleration wave propagation in elastic materials, Wright [7, Eq. (3.12)] introduced a quantity $a^{1/2}$ (in his notation) defined on the wave front and equal to the area of a ray tube (which varies due to geometric spreading). The coefficient of the linear term in Wright's equation of growth [7, Eq. (4.13)] contains the term

$$\frac{1}{2}\frac{\delta}{\delta X}\ln(a^{1/2})$$

which we claim to be analogous to our term

$$\frac{1}{2}\frac{\delta}{\delta X}\ln A$$

in the growth equation for one-dimensional rods with slowly varying cross section.

It remains to interpret the first two terms of (25). The first clearly arises from any inhomogeneities in density, and the second contributes only if the wave speed varies as the wave front moves. This could happen because of varying F and θ ahead of the wave and because of material inhomogeneities. To make more explicit the effects of material inhomogeneities, we use (19) to eliminate the second term of (25) in favor of $\delta(\ln E)/\delta X$, which is evaluated ahead of the wave using $(2)_1$. The resulting alternative expression for $\mu(X)$ is given by

$$\begin{aligned}\mu(X) = &\frac{1}{4}\frac{\delta}{\delta X}\ln\rho_0 + \frac{1}{4}\frac{\partial}{\partial \overline{X}}\ln E + \frac{1}{2}\frac{\delta}{\delta X}\ln A \\ &+ \frac{\theta\beta^2}{2\rho_0 U\kappa} - \frac{\beta Q_F}{2\rho_0 U^2\kappa} + \frac{E_F}{4\rho_0 U^2}\left(\frac{\partial F^+}{\partial X} - \frac{3}{U}\dot{F}^+\right) \\ &+ \frac{E_\theta}{4\rho_0 U^2}\left(\frac{\partial \theta^+}{\partial X} - \frac{3}{U}\dot{\theta}^+\right)\end{aligned} \tag{28}$$

the first two terms of which now exhibit explicitly the dependence of $\mu(X)$ on material inhomogeneity. Because E does not depend explicitly on time, we may write $\delta(\ln E)\delta\overline{X}$ in place of $\partial(\ln E)\partial\overline{X}$.

Solutions of the Growth Equation

On substituting $b = a^{-1}$ in the growth equation (24), we obtain the first-order linear equation

$$\frac{\delta b}{\delta X} - \mu b = \gamma$$

which may be solved using the integrating factor $exp\{-\int \mu(X')\,dX'\}$ to obtain

$$b(X) = \frac{\frac{1}{b_0} + \int_0^X \gamma(X') exp\left(-\int_0^{X'} \mu(X'')\,dX''\right) dX'}{exp\left(-\int_0^X \mu(X')\,dX'\right)}$$

where $b_0 = b(0)$. On inverting this fraction, we obtain the solution to the growth equation (24)

$$a(X) = \frac{a_0 exp\left(-\int_0^X \mu(X')\,dX'\right)}{1 + a_0\int_0^X \gamma(X') exp\left(-\int_0^{X'} \mu(X'')\,dX''\right) dX'} \tag{29}$$

in which $a_0\ (= 1/b_0)$ is the initial amplitude $a(0)$ of the acceleration wave when it begins propagating from the end $X = 0$ of the rod.

We return briefly to our discussion of the limiting case of low thermal conductivity (κ small) to recall that the coefficient $\mu(X)$ is dominated by the large positive thermal term now denoted by

$$\zeta = \frac{\theta\beta^2}{2\rho_0 U\kappa} \tag{30}$$

On substituting this into (29) and assuming $\gamma(X)$ to be integrable for small X, we find that

$$a(X) = a_0 e^{-\zeta X}\{1 + O(\zeta^{-1})\} \quad \text{as} \quad \zeta \to \infty \tag{31}$$

Any isothermal acceleration wave that is initiated in a nearly perfect insulator is therefore very rapidly damped out over the very short length scale ζ^{-1}. This bears out our conclusions in the previous section on the nonexistence of isothermal acceleration waves in one-dimensional nonconductors.

If thermal effects are absent and the region ahead of the wave is quiescent, then the coefficient $\mu(X)$ may be integrated exactly so that (29) reduces to

$$a(X) = \frac{a_0 \left\{ \frac{\rho_0(X)A(X)U(X)}{\rho_0(0)A(0)U(0)} \right\}^{-1/2}}{1 + a_0 \int_0^X \gamma(X') \left\{ \frac{\rho_0(X')A(X')U(X')}{\rho_0(0)A(0)U(0)} \right\}^{-1/2} dX'} \tag{32}$$

The quantity $\rho_0 AU$ is the rate of mass transport across the wave front. If, in addition, the quantities ρ_0, U, and γ are constant, then (32) further simplifies to give the wave amplitude in terms only of the varying cross section $A(X)$:

$$a(X) = \frac{a_0 \sqrt{A(0)}}{\sqrt{A(X)} \left\{ 1 + a_0 \sqrt{A(0)}\, \gamma \int_0^X \frac{dX'}{\sqrt{A(X')}} \right\}} \tag{33}$$

Chen [1, Sect. 13] gives many asymptotic results for (29) with $\mu(X)$ and $\gamma(X)$ varying, but, for simplicity, here we consider only μ and γ constant.

We now investigate conditions under which both μ and γ are constant. The acceleration wave is assumed to be propagating into a rod of uniform density, but slowly varying cross section, in a state of thermal and mechanical equilibrium, so that the first term and last three terms of (25) vanish. If body forces are absent, we may further conclude, from (17), that

$$T(X)A(X) = T(0)A(0) \tag{34}$$

It follows that a rod of varying cross section cannot be in both a state of homogeneous stress and homogeneous strain (except for the state of zero stress and strain). In fact, (17) also yields an explicit formula for the change in deformation gradient at the wave front:

$$\frac{\partial F^+}{\partial X} = -\frac{T^+}{E} \frac{d}{dX} \ln A \tag{35}$$

We therefore insist that the material ahead of the wave be unstressed and unstrained so that the wave speed U is constant and, consequently, the second term of (25) vanishes, while the fourth is constant. We shall specify the cross-sectional area of the rod in the form

$$A = A(0)\mathrm{e}^{2\varepsilon X} \tag{36}$$

where ε is a positive or negative constant, so that μ defined by (25) reduces to the constant

$$\mu = \varepsilon + \zeta \tag{37}$$

with ζ defined by (30). The conditions imposed in this paragraph are sufficient to force γ also to be constant.

In the case of constant μ and γ, the solution (29) reduces to

$$a(X) = \begin{cases} \dfrac{a_0 \mathrm{e}^{-\mu X}}{1 + a_0 \gamma (1 - \mathrm{e}^{-\mu X})/\mu} & \mu \neq 0 \\ \dfrac{a_0}{1 + a_0 \gamma X} & \mu = 0 \end{cases} \tag{38}$$

The behavior of this solution has been discussed in [8] in terms of varying the initial wave amplitude a_0 for fixed material constants μ and γ. However, our present objective is to focus attention on the effects of varying cross section on a wave with fixed initial amplitude a_0 and fixed material constants μ and γ. Thus, μ varies only as the parameter ε in (36) varies. From (36) and (37), we see that a rod with a smaller value of μ may be regarded as being more rapidly narrowing (or less rapidly broadening) than a rod with a larger value of μ.

We now analyze the behavior of the solution (38) for fixed a_0, γ, and $\zeta > 0$ with μ varying. First, we note that if $\gamma = 0$, then $a(X) = a_0 \mathrm{e}^{-\mu X}$ and if $a_0\gamma = -\mu$, then $a(X) = a_0$. For a nearly perfect insulator (κ small), we have ζ large so that $\mu \to \infty$, and $(38)_1$ gives $a(X) \to 0$, as before. All other possibilities are included in the three cases set out below. In case 1, $a(X)$ becomes infinite at a finite, positive value of X, and in the remaining two cases, $a(X)$ remains finite for all X, and asymptotic expansions are given for large X.

- *Case 1*: $\mu > 0$, $a_0\gamma < -\mu$ or $\mu < 0$, $a_0\gamma > -\mu$

The solution $a(X)/a_0$ increases monotonically in X becoming infinite at the finite, positive value of X given by

$$X_\infty(\mu) = -\frac{1}{\mu}\ln\left(1+\frac{\mu}{a_0\gamma}\right) \qquad (39)$$

We may interpret this blowup as the formation of a shock at $X = X_\infty$.

If $\mu = 0$, then from $(38)_2$ blowup occurs at $X_\infty = -1/a_0\gamma$, positive for $a_0\gamma<0$. This may also be obtained by taking the limit $\mu \to 0$ in (39).

- *Case 2*: $\mu > 0,\ a_0\gamma > -\mu$

$$a(X) \sim \frac{a_0 e^{-\mu X}}{1+a_0\gamma/\mu}\{1+O(e^{-\mu X})\} \quad \text{as } X \to \infty$$

- *Case 3*: $\mu<0,\ a_0\gamma< -\mu$

$$a(X) \sim -\frac{\mu}{\gamma}\{1+O(e^{\mu X})\} \quad \text{as } X \to \infty$$

We are now in a position to discuss the effects of varying cross section on acceleration wave propagation. In case 1, we can show that $X_\infty(\mu)$ is monotonically increasing so that a shock forms quicker in the more rapidly narrowing (less rapidly broadening) rod. In case 2, we see that the amplitude decay is faster in the more rapidly broadening rod. In case 3, the wave amplitude approaches a finite limit for large X which is larger in magnitude for a more rapidly narrowing rod. In summary, a broadening rod tends to dampen out the wave, while a narrowing rod tends to concentrate it.

References

1. Chen PJ (1973) Growth and decay of waves in solids. In: Truesdell C (ed) Mechanics of Solids, vol III. Springer, Berlin, pp 203–402
2. Straughan B (2011) Heat waves. Springer, Berlin
3. Fu YB, Scott NH (1988) Acceleration wave propagation in an inhomogeneous heat-conducting elastic rod of slowly varying cross section. J Thermal Stress 11:127–140
4. Coleman BD, Gurtin ME (1965) Waves in materials with memory IV. Thermodynamics and the velocity of general acceleration waves. Arch Ration Mech Anal 19:317–338
5. Chadwick P (1979) Basic properties of plane harmonic waves in a pre-stressed heat-conducting elastic material. J Thermal Stresses 2:193–214
6. Chadwick P, Currie PK (1974) Intrinsically characterized acceleration waves in heat-conducting elastic materials. Proc Camb Phil Soc 76:481–491
7. Wright TW (1973) Acceleration waves in simple elastic materials. Arch Ration Mech Anal 50:237–277
8. Chadwick P, Currie PK (1972) The propagation and growth of acceleration waves in heat-conducting elastic materials. Arch Ration Mech Anal 49:137–158

Acceleration Waves

▶ Acceleration Waves in Layers of Isotropic Solids at Finite Temperatures
▶ Acceleration Waves in Nonlinear Thermoelastic Micropolar Media
▶ Acceleration Waves in Thermoelastic Materials with Voids
▶ Ellipticity Condition and Acceleration Waves in Nonlinear Thermoelastic Solids

Acceleration Waves in Layers of Isotropic Solids at Finite Temperatures

Carmela Currò and Giovanna Valenti
Department of Mathematics and Informatics, University of Messina, Messina, Italy

Synonyms

Acceleration waves

Overview

Nonlinear wave propagation is a topic of great interest in continuum mechanics. In fact, from a qualitative viewpoint, the evolution models described by quasilinear first-order hyperbolic systems can be validated through wave processes. The mathematical theory of quasilinear hyperbolic systems is dominated by the concept of characteristic hypersurface across which

a continuous solution may exhibit jump discontinuities in its first-order normal derivatives. Such a solution is called acceleration wave or weak discontinuity and the characteristic hypersurface, which acts as transporter of these discontinuities, may be interpreted as a propagating wave front.

Wave propagation phenomena in solids are interesting both theoretically and practically. Since solid materials are currently employed in engineering applications at high temperatures, even near the melting temperature T_{M}, it is here considered the continuum model proposed by Sugiyama [1], which incorporates explicitly the microscopic thermal vibration of constituent atoms. In fact, this model, derived statistically mechanically from a three-dimensional anharmonic crystal lattice by adopting the continuum approximation, is valid in a wide temperature range up to T_{M}, and it is confined within isotropic solids. For such a model, both linear and nonlinear wave propagations have been investigated at high temperature even near the phase transition point [2–4].

The propagation of an acceleration wave in a stratified medium consisting of different isotropic solids is here investigated. Such a medium is one of the simplest examples of a composite material and it covers a broad range of applications, including sandwich panels in aircrafts, submarine coatings, electrical devices with sandwich structure, etc.

The coefficients of the transmitted and reflected waves through each interface are explicitly derived and the critical time is discussed. As an illustrative example, a semi-infinite solid embedded with a thin layer of another kind is considered and two possible control methods for the formation of a shock are presented.

Basic Methodology

Layers of Isotropic Solids: Model Assumption

We consider a half-space $X \geq 0$ which consists of an arbitrary number of region S_i defined as

$$S_i = \{(X,t) : X_i \leq X \leq X_{i+1}, t \geq 0\} \quad i = 0, 1, 2, \ldots$$

and we denote by $\mathcal{D}_{i+1}$ the straight line separating S_i and S_{i+1} in the $(X,t)-$ plane. Each region S_i is occupied by a different isotropic solid in contact with one another. The basic equations, describing the three-dimensional isotropic solid at a finite temperature in plane symmetry, are obtained from the general system proposed in [1] by assuming that all the field variables depend only on the position X and time t, as follows:

$$\begin{aligned}
&\rho_{i\kappa}\frac{\partial \mathbf{v}_i}{\partial t} - \frac{\partial}{\partial X}(\mathbf{T}_{i\kappa 1}) = 0\\
&\rho_{i\kappa}\frac{\partial}{\partial t}\left(\phi_{i\kappa} + \frac{1}{2}\mathbf{v}_i^2\right) - \frac{\partial}{\partial X}(\mathbf{v}_i \cdot \mathbf{T}_{i\kappa 1}) = 0\\
&\frac{\partial \mathbf{F}_{i1}}{\partial t} - \frac{\partial \mathbf{v}_i}{\partial X} = 0
\end{aligned} \tag{1}$$

where the subscript i refers to the particular isotropic solid occupying the region S_i. Furthermore, we also have the following:

- $\mathbf{v}$ is the velocity.
- ρ_κ, $\mathbf{T}_{\kappa 1}$, ϕ_κ are, respectively, the mass density, the Piola-Kirchhoff stress tensor, and the internal energy density in the reference configuration.
- $\mathbf{F}_1 = \left(\frac{\partial \mathbf{x}}{\partial X}\right)$ is the first column vector in the deformation gradient tensor $\mathbf{F}$ with $\mathbf{x}$ the position vector in the current configuration.

All quantities are expressed in terms of the dimensionless velocity $\mathbf{q}$, the potential energy density σ, and the deviation of the dimensionless temperature r from a reference equilibrium state

$$\begin{aligned}
&\mathbf{v} = \frac{\Omega}{\alpha}\mathbf{q}, \quad \mathbf{T}_{\kappa 1} = \frac{\Omega^2}{\alpha^2}\rho_\kappa(\nabla_{\mathbf{F}_1}\sigma)\\
&\phi_\kappa = \frac{\Omega^2}{\alpha^2}\left(\frac{3}{2}\left(\frac{k_{\mathrm{B}}T}{D} + r\right) + \sigma\right)
\end{aligned} \tag{2}$$

In (2), $\nabla_{\mathbf{w}} f = \frac{\partial f}{\partial \mathbf{w}}$, Ω and α^{-1} are, respectively, the microscopic frequency and microscopic length characteristic of the solid occupying S_i, while D is the depth of the atomic pair potential between the constituent atoms in the solid, k_{B} is the Boltzmann constant and T is the absolute temperature at a reference equilibrium state which we assume as a reference configuration. The model under consideration explicitly takes

into account microscopic thermal vibrations of the constituent atoms through a symmetric tensor $\mathbf{g}(\mathbf{F}, r)$, which describes the deviation of the atomic thermal vibration from a reference equilibrium state, and it is related to $\mathbf{F}$ and r by the following state equation:

$$(\lambda \mathbf{1} + \mathbf{g})\nabla_{\mathbf{g}}\sigma = \frac{k_B T}{2D}\left(1 + \frac{D}{k_B T} r\right)\mathbf{1} \tag{3}$$

with λ the dimensionless mean square displacement of the thermal vibration of the constituent atom at a reference equilibrium state, $\mathbf{1}$ is the identity matrix.

In what follows, we adopt for $\sigma(\mathbf{F}, \mathbf{g})$ the following expansion form:

$$\begin{aligned}\sigma(\mathbf{F},\mathbf{g}) = {} & \beta_0 + \beta_1 I_1 + \beta_2 I_1^2 + \beta_3 I_2 + \beta_4 I_1 I_4 + \beta_5 I_7 + \beta_6 I_4^2 \\ & + \beta_7 I_5 + \beta_8 I_1^3 + \beta_9 I_3 + \beta_{10} I_6 + \beta_{11} I_8 + \beta_{12} I_9 \\ & + \beta_{13} I_1 I_2 + \beta_{14} I_1 I_5 + \beta_{15} I_1 I_7 + \beta_{16} I_2 I_4 + \beta_{17} I_4^3 \\ & + \beta_{18} I_4 I_5 + \beta_{19} I_4 I_7 + \beta_{20} I_1^2 I_4 + \beta_{21} I_1 I_4^2\end{aligned} \tag{4}$$

where the basic invariants are defined by

$$\begin{aligned}& I_1 \equiv g_{ii}, \quad I_2 \equiv g_{ik} g_{ki}, \quad I_3 \equiv g_{ik} g_{kj} g_{ji} \\ & I_4 \equiv B_{ss} - 3, \quad I_5 \equiv (B_{st} - \delta_{st})(B_{st} - \delta_{st}) \\ & I_6 \equiv (B_{st} - \delta_{st})\left(B_{tp} - \delta_{tp}\right)\left(B_{ps} - \delta_{ps}\right), I_7 \equiv g_{st}(B_{ts} - \delta_{ts}) \\ & I_8 \equiv g_{ps}(B_{st} - \delta_{st})\left(B_{tp} - \delta_{tp}\right), \quad I_9 \equiv g_{tp} g_{ps}(B_{st} - \delta_{st})\end{aligned} \tag{5}$$

being $\mathbf{B} = \mathbf{F}\mathbf{F}^T$ the left Cauchy-Green tensor. The explicit expressions of the expansion coefficients $\beta' s$, which depend on the temperature T and on the material under investigation, have been estimated in terms of the Morse-type atomic pair potential [3].

Outline of the Wave Propagation Theory

Since we are interested to study the propagation of acceleration waves in layers of isotropic solids, we briefly summarize the main results concerning the one-dimensional wave propagation theory for hyperbolic system. In continuum theory, the physical conservation laws are usually expressed as

$$\frac{\partial \mathbf{G}^0(\mathbf{U})}{\partial t} + \frac{\partial \mathbf{G}(\mathbf{U})}{\partial X} = 0 \tag{6}$$

where $\mathbf{G}^0$ and $\mathbf{G}$ are N-components column vectors depending on the field vector $\mathbf{U} \in R^N$. We suppose the system (6) to be hyperbolic in the time-direction, namely, the eigenvalue problem

$$(\nabla_{\mathbf{U}}\mathbf{G} - V\nabla_{\mathbf{U}}\mathbf{G}^0)\mathbf{d} = 0, \quad \mathbf{l}(\nabla_{\mathbf{U}}\mathbf{G} - V\nabla_{\mathbf{U}}\mathbf{G}^0) = 0 \tag{7}$$

has only N real eigenvalues (characteristic speeds) $V = V(\mathbf{U})$ and a complete set of linearly independent right $\mathbf{d}$ and left $\mathbf{l}$ eigenvectors. If all the eigenvalues are distinct, then the system (6) is said to be strictly hyperbolic, whereas if $V^{(j)}$ has multiplicity m^j, then m^j linearly independent eigenvectors $\mathbf{d}_j$ and $\mathbf{l}_j$, must correspond to $V^{(j)}$. For such a system, it is possible to consider a particular class of continuous solutions, usually known as weak discontinuities or (in continuum mechanics) acceleration waves, having a jump in the normal derivative across a moving front $\Sigma(t)$ of Cartesian equation $\varphi(X, t) = 0$:

$$[\![\mathbf{U}]\!] = \mathbf{U}_1 - \mathbf{U}_0 = 0, \qquad \left[\!\left[\frac{\partial \mathbf{U}}{\partial \varphi}\right]\!\right] = \Pi \neq 0,$$
$$[\![\cdot]\!] = \lim_{\varphi \to 0^+}(\cdot) - \lim_{\varphi \to 0^-}(\cdot)$$

where the square brackets indicate the jump, $\mathbf{U}_0$ and $\mathbf{U}_1$ denote the known unperturbed field ahead $\Sigma(t)$ and the unknown perturbed field behind $\Sigma(t)$, respectively. In the one-dimensional wave propagation, the following results hold [5]:

- The normal velocity is equal to a characteristic speed evaluated at $\mathbf{U}_0$, $V(\mathbf{U}_0) = -\frac{\varphi_t}{\varphi_X}$, $C^{(V)} : \frac{dX}{dt} = V(\mathbf{U}_0)$, is the associated characteristic curve.
- The jump vector Π belongs to the subspace of the right eigenvectors corresponding to $V(\mathbf{U}_0)$:
- $$\Pi = \sum_{j=1}^{m^j} \pi^j \mathbf{d}_j(\mathbf{U}_0) \tag{8}$$

- The amplitude coefficients π^j satisfies a system of m^j Bernoulli equations [5] which, if $m^j = 1$, reduces to only one equation for $\pi^1 = \pi$:

$$\begin{aligned} &\frac{d\pi}{dt} + \varphi_X \left(\nabla_{\mathbf{U}} V \cdot \mathbf{d}\right)_0 \pi^2 + b(t)\pi = 0 \\ &b(t) = \left\{ \mathbf{d}^T \left((\nabla_{\mathbf{U}} \mathbf{l})^T - (\nabla_{\mathbf{U}} \mathbf{l}) \right) \cdot \frac{d\mathbf{U}}{dt} \right. \\ &\qquad \left. + \left(\nabla_{\mathbf{U}} V \cdot \mathbf{d}\right) \left(\mathbf{l} \cdot \frac{\partial \mathbf{U}}{\partial X} \right) \right\}_0 \end{aligned} \tag{9}$$

where $\frac{d}{dt} = \frac{\partial}{\partial t} + V(\mathbf{U}_0)\frac{\partial}{\partial X}$ stands for the time derivative along the characteristic lines $C^{(V)}$ and the subscript "0" indicates the quantity evaluated in the unperturbed field $\mathbf{U}_0$. If the wave satisfies the genuine nonlinearity condition, that is, $(\nabla_{\mathbf{U}} V \cdot \mathbf{d}) \neq 0$, the discontinuity becomes unbounded in a finite time t_c (critical time) when the weak discontinuity evolves into a shock wave.

Wave Propagation Through a Stratified Medium

Acceleration Wave Through a Layer

In order to study the propagation of an acceleration wave through the stratified medium herein considered, firstly we focus our attention on a fixed layer S_i, which, without loss of generality, we suppose to be the first layer S_0. The model under consideration (1), bearing in mind (2), admits the hyperbolic conservative form (6) with the field vector $\mathbf{U} = \left(\mathbf{q}, \mathbf{F}_1, r\right)^T$ and

$$\begin{aligned} \mathbf{G}^0(\mathbf{U}) &= \left(\rho_\kappa \alpha^{-1} \Omega \mathbf{q};\ \rho_\kappa \alpha^{-2} \Omega^2 \left(\tfrac{1}{2} q^2 + \tfrac{3}{2}\left(\tfrac{k_B T}{D} + r\right) + \sigma\right); \mathbf{F}_1\right)^T \\ \mathbf{G}(\mathbf{U}) &= -\left(\rho_\kappa \alpha^{-2} \Omega^2 \nabla_{\mathbf{F}_1} \sigma;\ \rho_\kappa \alpha^{-3} \Omega^3 \mathbf{q} \cdot \nabla_{\mathbf{F}_1} \sigma;\ \alpha^{-1} \Omega \mathbf{q}\right)^T \end{aligned} \tag{10}$$

Therefore, the characteristic equation (7) gives rise to three different kind of waves whose dimensionless characteristic velocities $\widetilde{V}_0 \equiv \left(\frac{\alpha}{\Omega} V\right)_{S_0}$, evaluated at the thermal equilibrium state $\overline{\mathbf{U}} = (0,0,0,1,0,0,0)^T$, are given by [3]

$$\begin{aligned} \widetilde{V}_{0L}^2 &= 4\left(2(\beta_6 + \beta_7) - \frac{\lambda \beta_4 (3\beta_4 + 2\beta_5)}{(a+2b)} \right. \\ &\quad \left. - \frac{\lambda \beta_5^2 (a+b)}{(a-b)(a+2b)} \right)_{S_0} \text{ longitudinal waves} \\ \widetilde{V}_{0S} &= 0 \quad \text{standing waves} \\ \widetilde{V}_{0T}^2 &= \left(4\beta_7 - \frac{2\lambda \beta_5^2}{a-b} \right)_{S_0} \text{ double transverse waves} \\ a &\equiv \frac{4}{3}\beta_1 + 2\lambda\beta_2 + 2\lambda\beta_3, \quad b \equiv \frac{1}{3}\beta_1 + 2\lambda\beta_2 \end{aligned}$$

It turns out that

$$\widetilde{V}_{0L}^{(-)} < \widetilde{V}_{0T}^{(-)} < 0 < \widetilde{V}_{0T}^{(+)} < \widetilde{V}_{0L}^{(+)} \tag{11}$$

where $^{(+)}$ and $^{(-)}$ indicate that the corresponding wave propagates in the positive and negative $X-$ directions, respectively. In particular, we focus our attention on the fastest acceleration wave, that is, a longitudinal acceleration wave propagating with velocity $\widetilde{V}_{0L}^{(+)}$ in S_0. Since the unperturbed field $\overline{\mathbf{U}}$ is constant the coefficient $b(t)$ occurring in (9) vanishes and the amplitude $\pi_0(t)$ is given by [3]

$$\pi_0(t) = \frac{\overline{\pi}_0}{1 - \frac{A_0 \Omega_0}{\widetilde{V}_{0L}^2} \overline{\pi}_0 t} \tag{12}$$

where $\overline{\pi}_0$ is the initial amplitude and $A_0 \equiv -\widetilde{V}_{0L}^2 \left(\nabla_{\mathbf{U}} \tilde{V}_{0L}^+ \cdot \mathbf{d}_{0L}^+ \right)_{\overline{\mathbf{U}}}$. From (12) it is easy to ascertain that if $\left(\nabla_{\mathbf{U}} \tilde{V}_{0L}^+ \cdot \mathbf{d}_{0L}^+ \right)_{\overline{\mathbf{U}}} \overline{\pi}_0 < 0$ holds, the critical time $t_c^{(0)}$ is

$$t_c^{(0)} = -\frac{1}{\left(\nabla_{\mathbf{U}} \tilde{V}_{0L}^+ \cdot \mathbf{d}_{0L}^+ \right)_{\overline{\mathbf{U}}} \overline{\pi}_0 \Omega_0} \tag{13}$$

Associated to (13), we have the critical distance $X_c^{(0)}$, namely, the distance passed by the acceleration wave before the shock formation,

$$X_c^{(0)} = \alpha_0^{-1} \Omega_0 \widetilde{V}_{0L}^{(+)} t_c^{(0)} \tag{14}$$

so that the interaction between the longitudinal wave and the straight line $\mathcal{D}_1$ (separating S_0

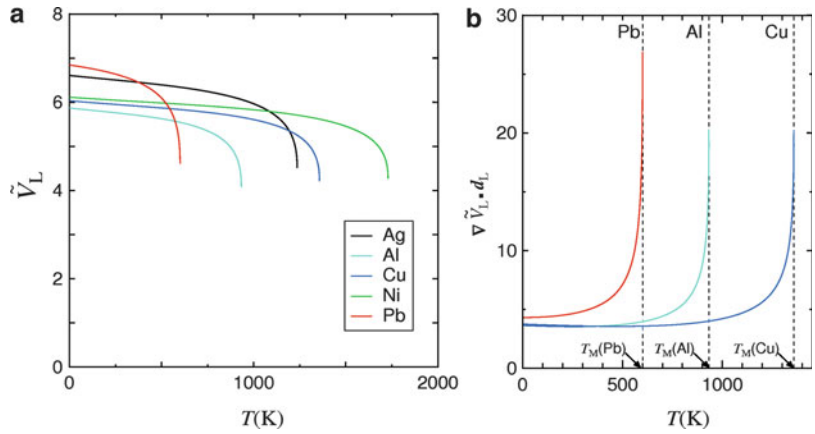

Acceleration Waves in Layers of Isotropic Solids at Finite Temperatures, Fig. 1 Temperature dependence up to the melting point of: (**a**) dimensionless propagation speed $\tilde{V}_L$ in Ag, Al, Cu, Ni, and Pb; (**b**) $\nabla_{\mathbf{U}} \tilde{V}_L \cdot \boldsymbol{d}_L$ for Al, Cu, Pb. T_M is the melting temperature [6]

from S_1) occurs if and only if the impact time t_1 is less than $t_c^{(0)}$, that is, the thickness L_0 of S_0 must satisfy the following condition:

$$L_0 < -\frac{\tilde{V}_{0L}^{(+)}}{\left(\nabla_{\mathbf{U}} \tilde{V}_{0L}^{(+)} \cdot \mathbf{d}_{0L}^{(+)}\right)_{\overline{\mathbf{U}}} \overline{\pi}_0 \, \alpha_0}$$

From (13), (14) it follows that the behavior of the critical time as well as the critical distance is influenced by the term $\left(\nabla_{\mathbf{U}} \tilde{V}_{0L}^{(+)} \cdot \mathbf{d}_{0L}^{(+)}\right)_{\overline{\mathbf{U}}}$. In Fig. 1, the temperature dependence of both the dimensionless propagation speed $\tilde{V}_L$ and $\nabla_{\mathbf{U}} \tilde{V}_L \cdot \mathbf{d}_L$ evaluated at $\overline{\mathbf{U}}$ are shown, for different metals, up to the melting point. The numerical results are consistent with the experimental data, although the data available are those observed at temperatures that are much lower than T_M. In the temperature range near the melting point the present theory predicts that, as T tends to T_M from the low-temperature side, the propagation speeds decrease rapidly but their values are, however, finite.

Reflected and Transmitted Waves at an Interface

Now we investigate the propagation of the fastest longitudinal acceleration wave generated at P_0 through the next layers. Therefore we suppose that in each region S_i, the field variables are continuous while its first derivatives suffer jumps across the characteristic of the system (1) and we assume that the impact time of the acceleration wave propagating in S_i with the line $\mathcal{D}_{i+1}$ is less than the critical time in S_i. This last assumption means that the considered acceleration wave does not evolve into a shock wave before reaching the line $\mathcal{D}_{i+1}$, separating two adjacent regions S_i and S_{i+1}. Such a situation can be described by assuming that the coefficients of the field equations are piecewise continuous functions with discontinuities occurring across $\mathcal{D}_{i+1}$. A general theory of quasilinear hyperbolic equations with discontinuous coefficients was first developed in [7–9] and later, more systematically, in [10].

Since the interface line $\mathcal{D}_{i+1}$ acts as a strong discontinuity (shock line) for $\mathbf{U}$, that is, it suffers a jump across $\mathcal{D}_{i+1}$, the field variables are connected by the Rankine-Hugoniot jump relations, which, for a general conservation system (6), are as follows:

$$\left(s\mathbf{G}^0 + \mathbf{G}\right)_{\mathcal{D}_{i+1}^-} = \left(s\mathbf{G}^0 + \mathbf{G}\right)_{\mathcal{D}_{i+1}^+} \qquad (15)$$

being s the shock speed.

Therefore, when the longitudinal wave propagating in S_0 meets the interface $\mathcal{D}_1$, it splits into reflected and transmitted waves that, owing to the hyperbolicity of the governing system, propagate along the characteristics. Since the shock velocity is equal to the characteristic velocity

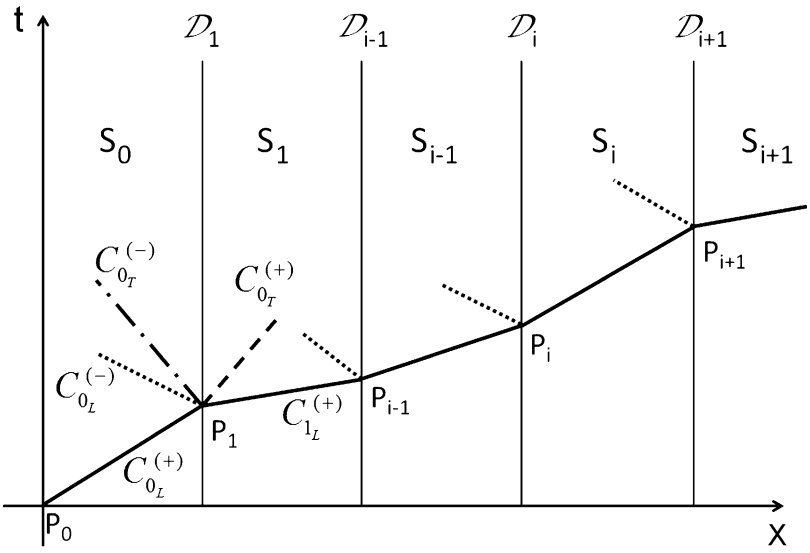

Acceleration Waves in Layers of Isotropic Solids at Finite Temperatures, Fig. 2 Propagation of an acceleration wave through a stratified medium. C_{i_L}, C_{i_T} are the characteristic curves associated, respectively, to the longitudinal and transversal waves propagating in the layer S_i

$s = \widetilde{V}_0 = \widetilde{V}_1 = 0$, it follows from (11) that the evolutionary Lax conditions [11] are satisfied so that the solution is physically meaningful. Therefore we have two reflected waves along the characteristic propagating with the velocities $\widetilde{V}_{0L}^{(-)}$, $\widetilde{V}_{0T}^{(-)}$ and two transmitted ones propagating with the velocities $\widetilde{V}_{1L}^{(+)}$, $\widetilde{V}_{1T}^{(+)}$ (see Fig. 2).

The amplitudes of the reflected and transmitted waves in terms of the incident one can be determined by following the procedure given in [10]. We denote by $\mathbf{U}_0^{(R)}$ and $\mathbf{U}_1^{(T)}$ the reflected (in S_0) and transmitted (in S_1) field vectors, respectively, so that we have

$$\begin{aligned}\mathbf{U}_0^{(R)} &= \overline{\mathbf{U}} + \Pi_0\varphi_0 + \Pi_{0L}^{(R)}\varphi_{0L} + \Pi_{0T}^{(R)}\varphi_{0T}\\ \mathbf{U}_1^{(T)} &= \overline{\mathbf{U}} + \Pi_{1L}^{(T)}\varphi_{1L} + \Pi_{1T}^{(T)}\varphi_{1T}\end{aligned} \tag{16}$$

In (16), Π_0, $\Pi_{0L}^{(R)}$, $\Pi_{0T}^{(R)}$ are the incident and reflected discontinuity vectors transported along the characteristics φ_0, φ_{0L}, φ_{0T} propagating with velocities $\widetilde{V}_{0L}^{(+)}$, $\widetilde{V}_{0L}^{(-)}$, $\widetilde{V}_{0T}^{(-)}$, whereas $\Pi_{1L}^{(T)}$, $\Pi_{1T}^{(T)}$ are the transmitted discontinuity vectors along the characteristics φ_{1L}, φ_{1T} with velocities $\widetilde{V}_{1L}^{(+)}$, $\widetilde{V}_{1T}^{(+)}$. According to (8), the discontinuity vectors are expressed as follows:

$$\begin{aligned}\Pi_0 &= \mu\mathbf{d}_{0L}^{(+)}, \qquad \Pi_{0L}^{(R)} = \mu_{1L}\mathbf{d}_{0L}^{(-)}\\ \Pi_{0T}^{(R)} &= \mu_{1T}^{(1)}\mathbf{d}_{0T}^{(1)(-)} + \mu_{1T}^{(2)}\mathbf{d}_{0T}^{(2)(-)}\\ \Pi_{1L}^{(T)} &= \nu_{1L}\mathbf{d}_{1L}^{(+)}\\ \Pi_{1T}^{(T)} &= \nu_{1T}^{(1)}\mathbf{d}_{1T}^{(1)(+)} + \nu_{1T}^{(2)}\mathbf{d}_{1T}^{(2)(+)}\end{aligned} \tag{17}$$

where the coefficient $\mu = \pi_0(t_1)$ represents the amplitude of the known incident discontinuity and its expression is obtained from (12). After differentiating (16) with respect to X and taking into account (17), we obtain the following:

$$\begin{aligned}\alpha_0^{-1}\mathbf{U}_{0X}^{(R)} &= \mu\mathbf{d}_{0L}^{(+)} + \mu_{1L}\mathbf{d}_{0L}^{(-)} + \mu_{1T}^{(1)}\mathbf{d}_{0T}^{(1)(+)} + \mu_{1T}^{(2)}\mathbf{d}_{0T}^{(2)(+)}\\ \alpha_1^{-1}\mathbf{U}_{1X}^{(T)} &= \nu_{1L}\mathbf{d}_{1L}^{(+)} + \nu_{1T}^{(1)}\mathbf{d}_{1T}^{(1)(+)} + \nu_{1T}^{(2)}\mathbf{d}_{1T}^{(2)(+)}\end{aligned} \tag{18}$$

provided we choose, without loss of generality, $\frac{\partial\varphi_0}{\partial X} = \frac{\partial\varphi_{0L}}{\partial X} = \frac{\partial\varphi_{0T}}{\partial X} = \frac{\partial\varphi_{1L}}{\partial X} = \frac{\partial\varphi_{1T}}{\partial X} = 1$

In order to characterize completely the transmitted and reflected discontinuities, we need to determine the amplitude coefficients involved in (17). These, together with the acceleration of the shock, are uniquely determined as solutions of the algebraic system obtained by differentiating the Rankine-Hugoniot relations (15) along the shock line and by using (18) as follows:

$$
\begin{aligned}
&\dot{s} = \mu_{1T}^{(1)} = \mu_{1T}^{(2)} = v_{1T}^{(1)} = v_{1T}^{(2)} = 0\\
&\mu_{1L} = \mu\frac{\Psi_0\,\widetilde{V}_{1L}^{(+)} - \Phi_0\,\widetilde{V}_{0L}^{(+)}}{\Psi_0\,\widetilde{V}_{1L}^{(+)} + \Phi_0\,\widetilde{V}_{0L}^{(+)}}\\
&v_{1L} = 2\mu\frac{\Psi_0\Phi_0\,\widetilde{V}_{0L}^{2}}{\widetilde{V}_{1L}^{(+)}\left(\Psi_0\,\widetilde{V}_{1L}^{(+)} + \Phi_0\,\widetilde{V}_{0L}^{(+)}\right)}\\
&\mu = \pi_0(t_1) = \frac{\overline{\pi}_0\,\widetilde{V}_{0L}^{(+)}}{\widetilde{V}_{0L}^{(+)} + \left(\nabla_{\mathbf{U}}\,\tilde{V}_{0L}^{(+)}\cdot\mathbf{d}_{0L}^{(+)}\right)_{\overline{\mathbf{U}}}\,\alpha_0\,\overline{\pi}_0\,L_0}\\
&\Phi_0 = \frac{\left(\rho_\kappa\alpha^{-2}\Omega^3\right)_0}{\left(\rho_\kappa\alpha^{-2}\Omega^3\right)_1}, \qquad \Psi_0 = \frac{\left(\alpha^{-1}\Omega^2\right)_0}{\left(\alpha^{-1}\Omega^2\right)_1}
\end{aligned}
\tag{19}
$$

As a consequence of $(19)_1$, we notice that neither transmission nor reflection is possible along the characteristics corresponding to transverse waves. Therefore, after interaction, we can observe only one reflected as well as one transmitted acceleration wave propagating with the speed $\widetilde{V}_L$ so that, in what follows, we will drop the subscript "L" in the coefficients of the reflected and transmitted waves. The $(19)_1$ points out also that there is no acceleration of the shock, as it is expected, being the interface at rest.

Now, by means of an iterative approach, we are able to investigate the reflection and transmission of the incident wave across each layer.

Let us consider the region S_i and we specialize the coefficients of the reflected and transmitted waves at $P_{i+1} = (X_{i+1}, t_{i+1})$. Actually, the amplitude π_i of the acceleration wave propagating in S_i and the corresponding critical time $t_c^{(i)}$ are as follows:

$$
\begin{aligned}
&\pi_i(t) = \frac{\pi_i(t_i)}{1 + \left(\nabla_{\mathbf{U}}\,\tilde{V}_{iL}^{(+)}\cdot\mathbf{d}_{iL}^{(+)}\right)_{\overline{\mathbf{U}}}\,\Omega_i\pi_i(t_i)(t - t_i)}\\
&t_c^{(i)} = t_i - \frac{1}{\left(\nabla_{\mathbf{U}}\,\tilde{V}_{iL}^{(+)}\cdot\mathbf{d}_{iL}^{(+)}\right)_{\overline{\mathbf{U}}}\,\pi_i(t_i)\Omega_i}\\
&t_{i+1} = t_i + \frac{\alpha_i L_i}{\Omega_i\,\widetilde{V}_{iL}^{(+)}}, \qquad t_0 = 0, \quad L_i = X_{i+1} - X_i,\\
&\quad i = 0, 1, \ldots
\end{aligned}
\tag{20}
$$

with $\pi_i(t_i) \equiv v_i$ the coefficient of the transmitted wave at $\mathcal{D}_i$. Therefore in order to have a critical time greater than it would be in absence of interaction, we must require that the weak discontinuity of the incident wave velocity decreases through each layer, that is, $\left[\nabla_{\mathbf{U}}\,\tilde{V}_{iL}^{(+)}\cdot\mathbf{d}_{iL}^{(+)}\right] > 0$ (see [12]). The interaction between the acceleration wave propagating in S_i and the interface $\mathcal{D}_{i+1}$ is possible if the following condition holds:

$$
L_i < -\frac{\widetilde{V}_{iL}^{(+)}}{\left(\nabla_{\mathbf{U}}\,\tilde{V}_{iL}^{(+)}\cdot\mathbf{d}_{iL}^{(+)}\right)_{\overline{\mathbf{U}}}\,\pi_i(t_i)\alpha_i} \tag{21}
$$

so that under assumption (21), the acceleration wave never evolves into a shock wave in the region S_i.

After a simple algebra, the reflection and transmission coefficients, in each layer S_i, are determined in terms of the initial amplitude $\overline{\pi}_0$ of the incident acceleration wave in S_0 as follows [6]:

$$
\begin{aligned}
&\mu_{i+1} = \frac{\overline{\pi}_0\,\chi_i(\Psi_i - \Phi_i\delta_i)}{\left(1 - \overline{\pi}_0\sum_{k=0}^{i}\omega_k\chi_k\right)(\Psi_i + \Phi_i\delta_i)}\\
&v_{i+1} = \frac{\overline{\pi}_0\,\chi_{i+1}}{\left(1 - \overline{\pi}_0\sum_{k=0}^{i}\omega_k\chi_k\right)}
\end{aligned}
$$

where

$$
\begin{aligned}
&\Phi_i = \frac{\left(\rho_\kappa\alpha^{-2}\Omega^3\right)_i}{\left(\rho_\kappa\alpha^{-2}\Omega^3\right)_{i+1}}, \qquad \Psi_i = \frac{\left(\alpha^{-1}\Omega^2\right)_i}{\left(\alpha^{-1}\Omega^2\right)_{i+1}},\\
&\delta_i = \frac{\widetilde{V}_{iL}^{(+)}}{\widetilde{V}_{i+1L}^{(+)}}, \omega_i = -\frac{\left(\nabla_{\mathbf{U}}\,\tilde{V}_{iL}^{(+)}\cdot\mathbf{d}_{iL}^{(+)}\right)_{\overline{\mathbf{U}}}\,\alpha_i L_i}{\widetilde{V}_{iL}^{(+)}},\\
&\chi_k = 2^k\prod_{j=0}^{k-1}\frac{\delta_j^2\Phi_j\Psi_j}{\Psi_j + \Phi_j\delta_j}, \qquad \chi_0 = 1
\end{aligned}
$$

An Illustrative Example

In order to show characteristic features of the propagation of an acceleration wave in a stratified medium, especially its peculiar temperature

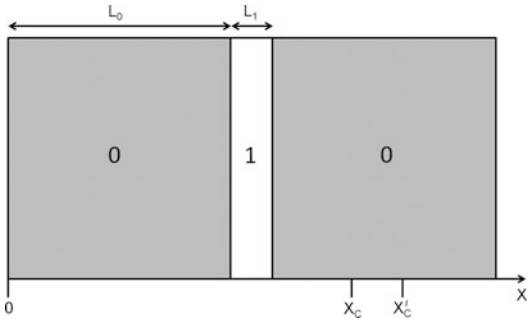

Acceleration Waves in Layers of Isotropic Solids at Finite Temperatures, Fig. 3 A thin layer "1" of thickness L_1 embedded at distance L_0 in a semi-infinite solid "0." X_c' and X_c are the critical distances in the solid "0" with and without the thin layer "1," respectively

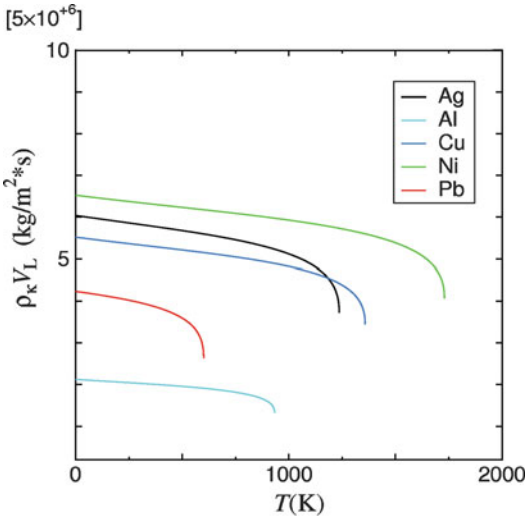

Acceleration Waves in Layers of Isotropic Solids at Finite Temperatures, Fig. 4 Temperature dependence of the characteristic impedance $\rho_\kappa V_L$ for Ag, Al, Cu, Ni, and Pb up to the melting point [6]

dependence, we consider a semi-infinite solid (denoted by "0") in which a thin layer of another kind of solid (indicated by "1") is embedded at a distance L_0 as shown in Fig. 3. Furthermore, we assume that the thin layer of thickness L_1 is perpendicular to the $X-$ axis and that the longitudinal acceleration wave (excited at $X = 0$) propagates through the layered solid in the positive $X-$ direction.

The subsequent analysis will be devoted to investigate the effects of the embedded thin layer on the shock formation arising at the critical time and consequently at the critical distance. Actually, the critical distance X_c' is related to X_c, critical distance in the absence of the thin layer, as follows:

$$X_c' = X_c + \Gamma(X_c - L_0) + \Lambda L_1 \qquad (22)$$

where the dimensionless quantities Γ and Λ are given, respectively, by the following:

$$\Gamma = \frac{\left((\rho_\kappa V_L)_0 - (\rho_\kappa V_L)_1\right)^2}{4\,(\rho_\kappa V_L)_0\,(\rho_\kappa V_L)_1} \geq 0$$
$$\Lambda = 1 - \frac{\alpha_1 \tilde{V}_{0L}^2 \left(\Phi_0 \tilde{V}_{0L} + \Psi_0 \tilde{V}_{1L}\right)\left(\nabla \tilde{V}_{1L} \cdot \mathbf{d}_{1L}\right)}{2\alpha_0 \tilde{V}_{1L}^3 \left(\nabla \tilde{V}_{0L} \cdot \mathbf{d}_{0L}\right)} \qquad (23)$$

The quantity $\rho_\kappa V_L$ is well known as the characteristic impedance of the medium, whose temperature dependence is shown in Fig. 4 for different metals. From (22) it is straightforward to see that there are two dimensionless characteristic quantities Γ and Λ which play an important role in the determination of the critical distance X_c'. Therefore, we show explicitly the temperature dependencies of Γ and Λ up to the melting point for three representative pairs of metals "Pb-Al," "Pb-Ag," and "Ag-Cu." Furthermore, we assume that the temperatures of the two metals "0" and "1" are equal to each other, so that from (23) it follows that temperature dependence of Γ, for a fixed pair of metals, does not vary interchanging the position of the materials.

Case Pb-Al. Temperature dependence of the characteristic quantities Γ and Λ is shown in Fig. 5 (solid line) up to the melting temperature of Pb, which is lower than that of Al. We notice the following:

1. Γ decreases monotonously with the increase of the temperature and changes drastically as the temperature approaches the melting point of Pb (Fig. 5a).

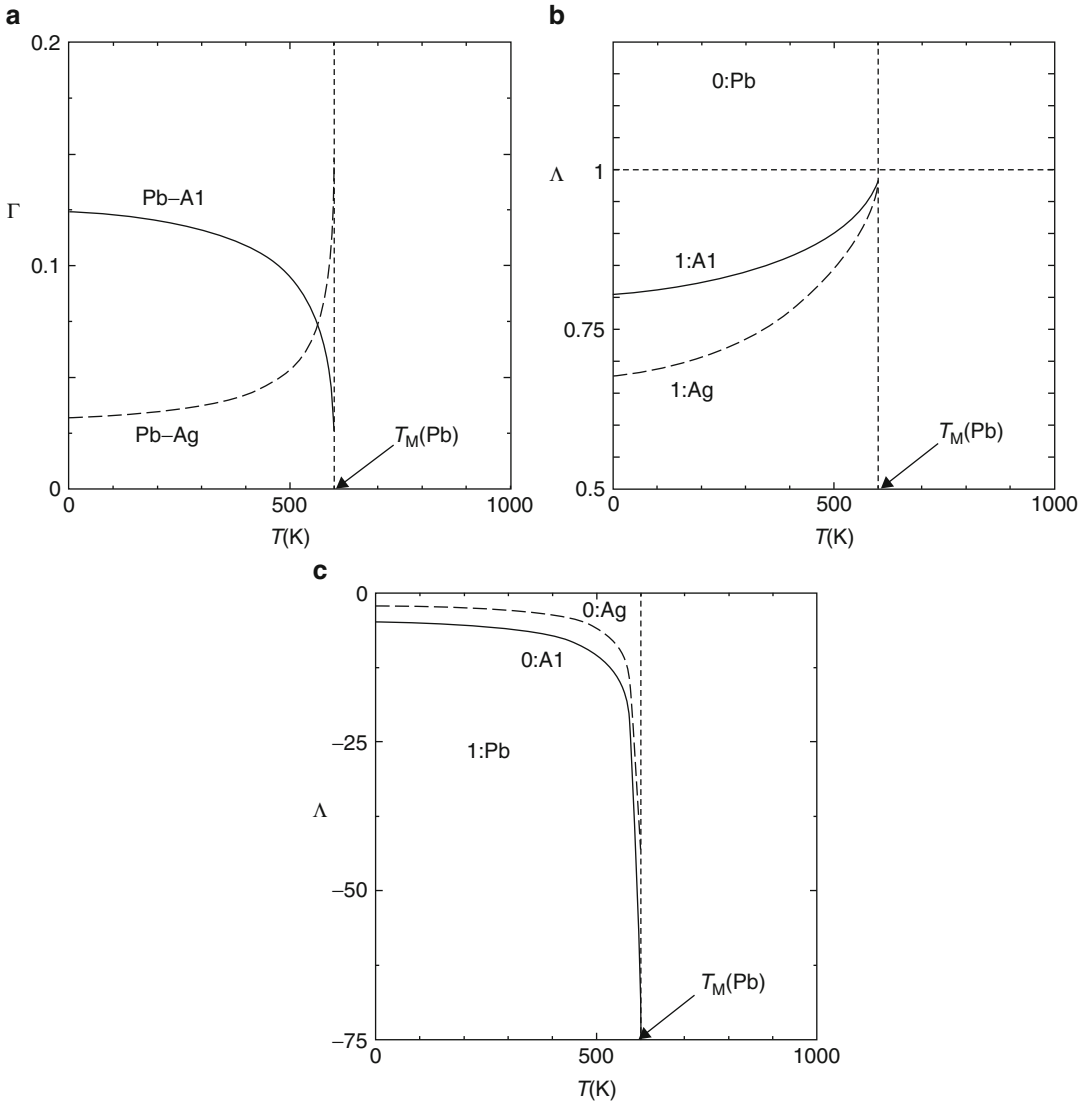

Acceleration Waves in Layers of Isotropic Solids at Finite Temperatures, Fig. 5 Temperature dependence of the characteristic quantities Γ and Λ for the pair of metals Pb-Al (*solid line*) and Pb-Ag (*dashed line*)

2. *Metal Pb with thin layer of Al*. Λ increases monotonously with the increase of the temperature, it is always positive and its value is much larger than that of Γ in the whole range of the temperature up to the melting point of Pb (Fig. 5b).
3. *Metal Al with thin layer of Pb*. Λ is always negative, it decreases monotonously with the increase of the temperature and changes drastically as the temperature approaches the melting point of Pb. The absolute value of Λ is much larger than the value of Γ in the whole range of the temperature up to the melting point of Pb (Fig. 5c).

Case Pb-Ag. Temperature dependence of the characteristic quantities Γ and Λ is shown in Fig. 5 (dashed line) up to the melting temperature

of Pb which is lower than that of Ag. We observe the following:

1. Γ increases monotonously with the increase of the temperature and it changes drastically as the temperature approaches the melting point of Pb (Fig. 5a).
2. *Metal Pb with thin layer of Ag*. Λ is always positive, it increases monotonously with the increase of the temperature and its value is larger than that of Γ in the whole range of the temperature up to the melting point of Pb (Fig. 5b).
3. *Metal Ag with thin layer of Pb*. Λ is always negative, it decreases monotonously with the increase of the temperature and changes drastically as the temperature approaches the melting point of Pb. The absolute value of Λ is much larger than the value of Γ in the whole range of the temperature up to the melting point of Pb (Fig. 5c).

Case Ag-Cu. Temperature dependence of the characteristic quantities Γ and Λ is shown in Fig. 6 up to the melting temperature of Ag which is lower than that of Cu. We notice the following:

1. Γ is not a monotonous function of the temperature and it vanishes at the critical temperature $T_c = 1{,}184\,\mathrm{K}$, and it changes drastically as the temperature approaches the melting point of Ag (Fig. 6a).
2. *Metal Ag with thin layer of Cu*. Λ increases monotonously with the increase of the temperature, it is always positive and its value is larger than that of Γ in the whole range of the temperature up to the melting point of Ag. In the temperature region near the critical temperature T_c, if $L_1 \ll X_c$, taking into account (22) and the behavior of Γ, we have $X_c' \approx X_c$ (Fig. 6b).
3. *Metal Cu with thin layer of Ag*. Λ decreases monotonously with the increase of the temperature, it is always negative and changes drastically as the temperature approaches the melting point of Ag. The absolute value of Λ is much larger than the value of Γ in the whole range of the temperature up to the melting point of Ag (Fig. 5c).

Control of Critical Distance

The position at which a shock wave emerges from an acceleration wave may be checked by using the relation (22). In what follows, for the sake of simplicity, we focus our attention on a thickness L_1 negligibly small ($L_1 \ll X_c$) so that, for finite values of Λ, by using the dimensionless length in the unit X_c, the relation (22) becomes

$$\tilde{X}_c' = 1 + \Gamma(1 - \tilde{L}_0), \qquad (0 < \tilde{L}_0 < 1) \tag{24}$$

where $\tilde{X}_c' \equiv X_c'/X_c$ and $\tilde{L}_0 \equiv L_0/X_c$. Therefore, even when the thickness L_1 is negligibly small, the critical distance X_c' is, in general, greater than the critical distance X_c. As seen clearly from (24), the critical distance may be controlled through the dimensionless position $\tilde{L}_0$ (**Method**-α) or through the characteristic quantity Γ (**Method**-β).

Method-α. The temperature of the metal "1" is assumed to be the same as that of metal "0" and the critical distance X_c' is controlled by changing the position L_0 of the thin layer. As illustrative cases, we consider the pair of metals Pb-Al and Pb-Ag, for which the characteristic quantity Γ is shown in Fig. 5. The linear relationship between the critical distance $\tilde{X}_c'$ and the position $\tilde{L}_0$ of the thin layer at several temperatures is shown in Fig. 7a and b. In both cases, the relative change of the critical distance $\tilde{X}_c' - 1$ by the change of the position $\tilde{L}_0$ is at most $\sim 15\,\%$ [6].

Method-β. The temperature of the metal "0" is fixed at a certain temperature, say at the room temperature $T = 300\,\mathrm{K}$ and the position L_0 of the thin layer is fixed too. Therefore, the critical distance is controlled through Γ by changing the temperature of the thin layer. The three representative pairs of metals previously considered (Al-Pb, Ag-Pb, Ag-Cu) are analyzed.

Metal Pb with thin layer of Al and vice versa. When the thin layers corresponds to aluminum, the temperature dependence of Γ, shown in Fig. 8a, is weak and the relative change of the

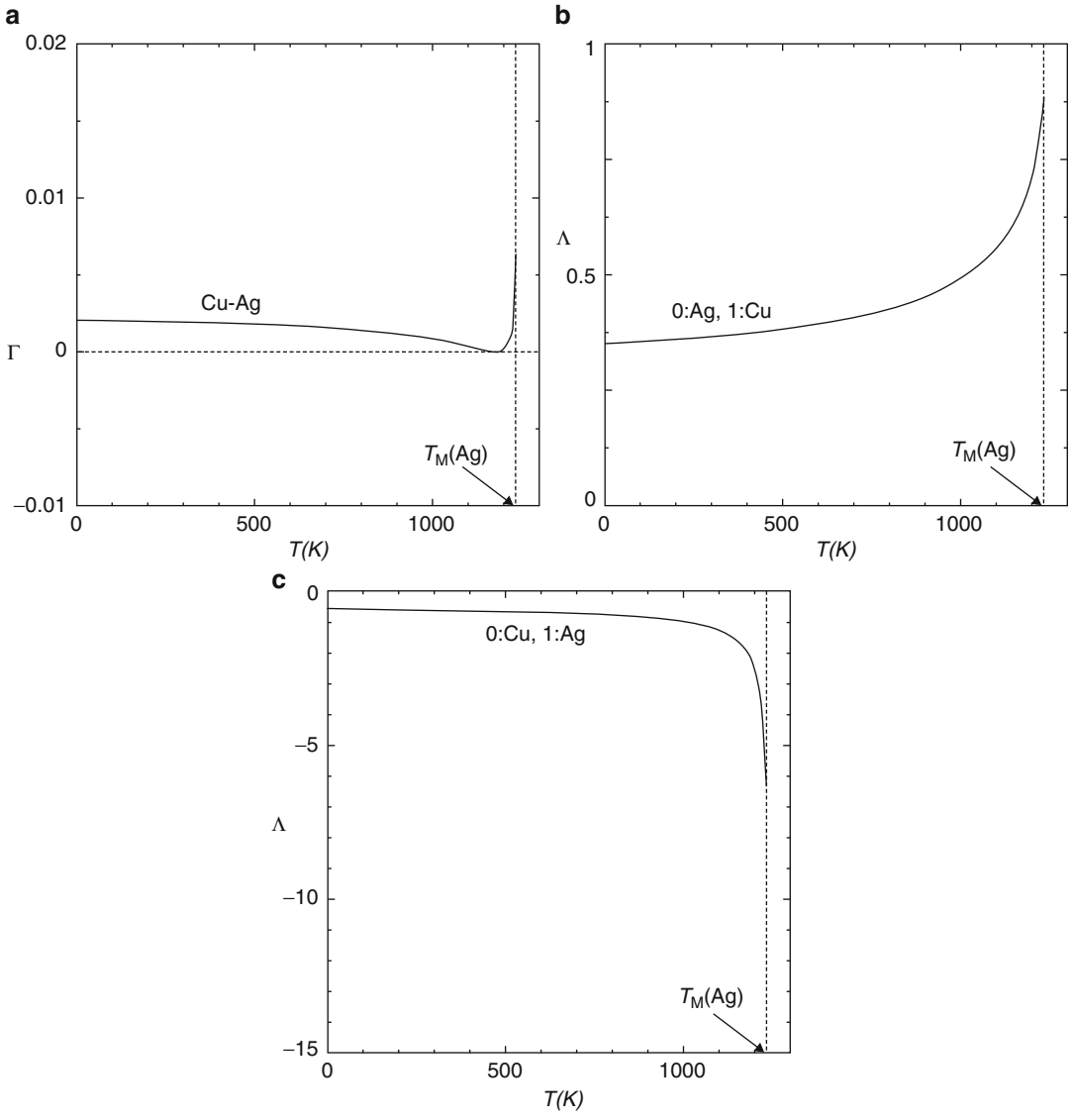

Acceleration Waves in Layers of Isotropic Solids at Finite Temperatures, Fig. 6 Temperature dependence of the characteristic quantities Γ and Λ for the pair of metals Cu-Ag [6]

critical distance $\tilde{X}_c' - 1$ is around 10% so that X_c' cannot be changed much by the temperature change of aluminum. In the opposite case (Fig. 8b), the temperature dependence of Γ is more strong than that in the previous case and the relative change of the critical distance $\tilde{X}_c' - 1$ is less than 14 %. However, the critical distance X_c' can be changed more drastically with respect to the previous case by the temperature change of Pb.

Metal Pb with thin layer of Ag and vice versa. As it is to see from Fig. 9, the dependence of Γ on the temperature of the metal "1" is weak if the thin layer is Ag, whereas it is stronger in the opposite situation. Therefore, the critical distance X_c' can be changed more drastically by the temperature change of Pb rather than Ag.

Metal Ag with thin layer of Cu and vice versa. Figure 10 shows that Γ increases monotonously

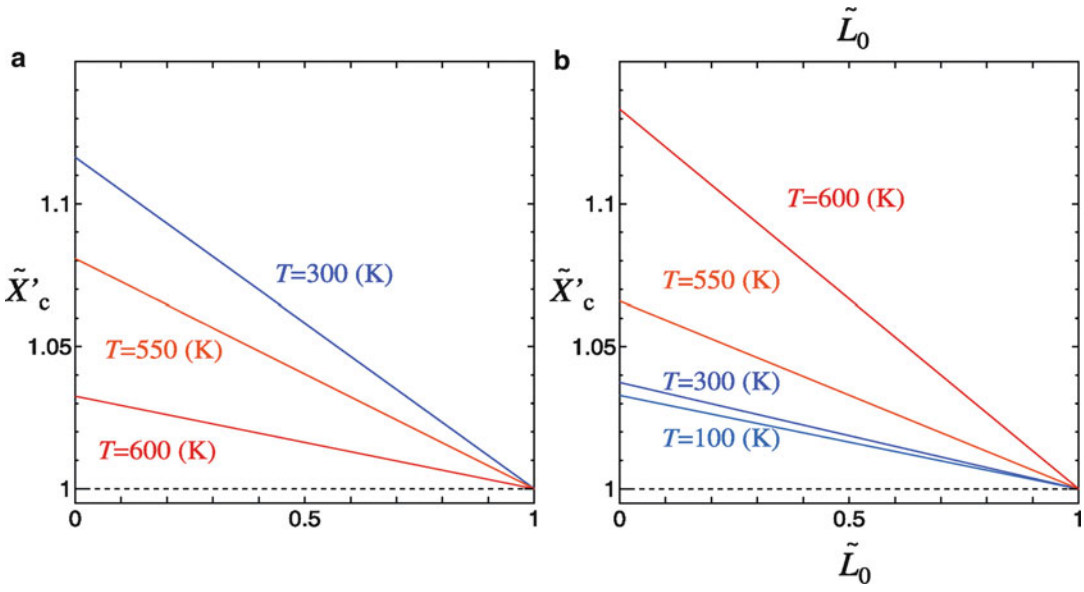

Acceleration Waves in Layers of Isotropic Solids at Finite Temperatures, Fig. 7 Linear relationship between the critical distance $\tilde{X}'_c$ and the position $\tilde{L}_0$ of the thin layer at several temperatures for: (**a**) Pb-Al, (**b**) Pb-Ag [6]

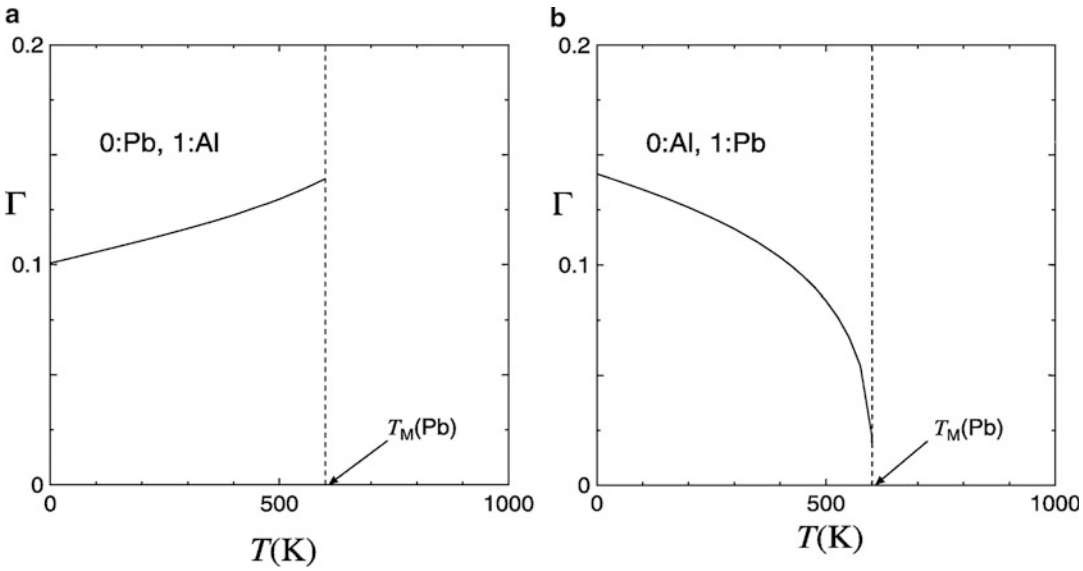

Acceleration Waves in Layers of Isotropic Solids at Finite Temperatures, Fig. 8 Dependence of the characteristic quantity Γ on the temperature of the thin layer for the pair of metals Pb-Al: (**a**) thin layer of Al; (**b**) thin layer of Pb [6]

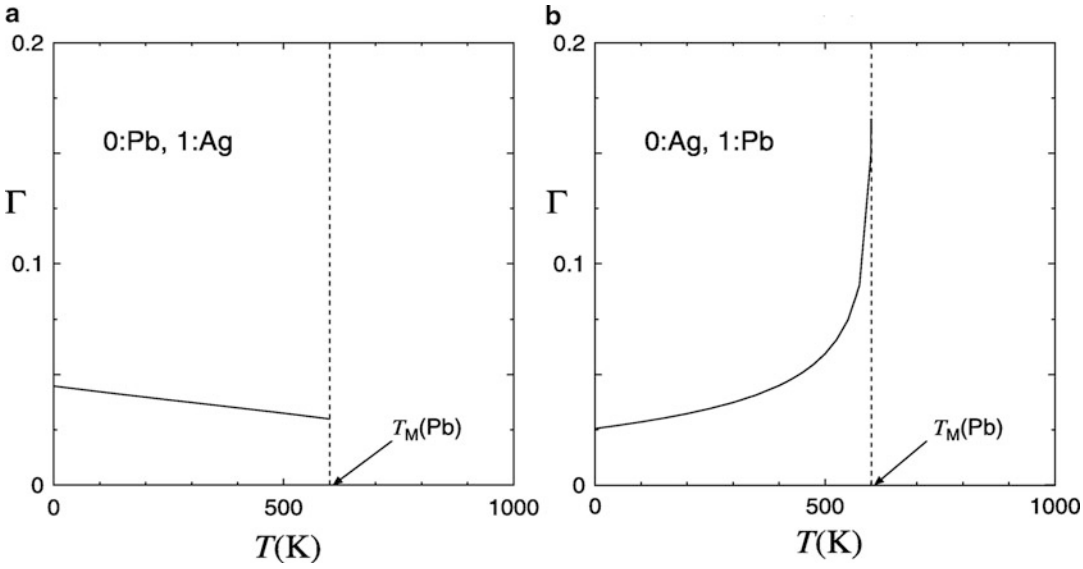

Acceleration Waves in Layers of Isotropic Solids at Finite Temperatures, Fig. 9 Dependence of the characteristic quantity Γ on the temperature of the thin layer for the pair of metals Pb-Ag: (**a**) thin layer of Ag; (**b**) thin layer of Pb [6]

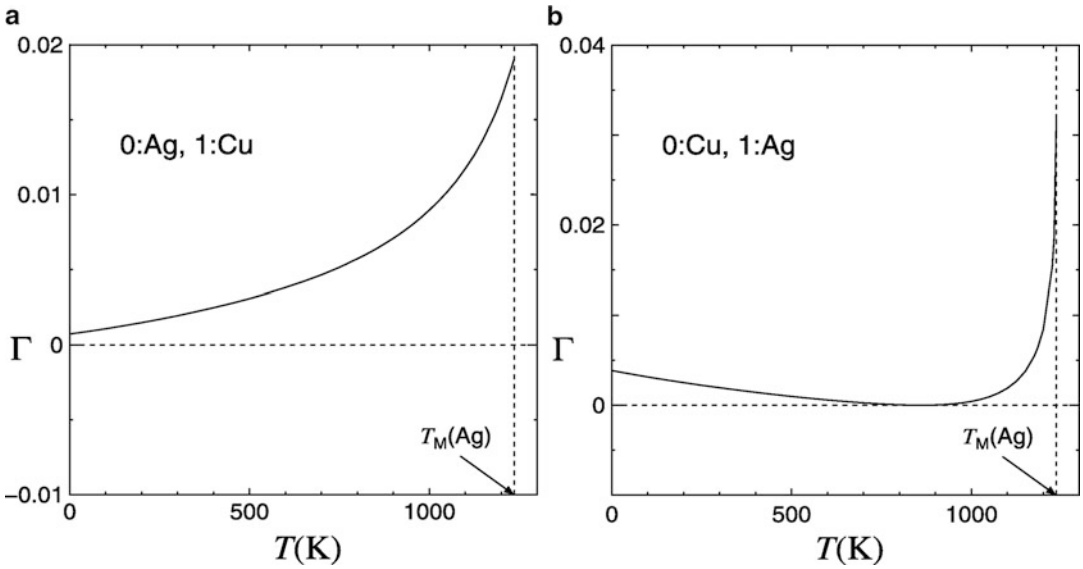

Acceleration Waves in Layers of Isotropic Solids at Finite Temperatures, Fig. 10 Dependence of the characteristic quantity Γ on the temperature of the thin layer for the pair of metals Ag-Cu: (**a**) thin layer of Ag; (**b**) thin layer of Cu [6]

with the increase of the temperature of Cu, whereas, if the thin layer is Ag, then Γ is not a monotonous function. In both cases, the value of Γ is small, but in the second one, it vanishes for a critical value of the temperature.

It is remarkable that, even in such a simple situation studied here, nonlinear wave propagation phenomena exhibit the wide variety of their interesting aspects depending on the temperatures of solids as well as on the geometrical of a stratified medium.

Acknowledgments The Figs. 1, 4, 6–10 are reprinted from [6] with permission from Elsevier.

References

1. Sugiyama M (2003) Statistical-thermodynamic study of nonequilibrium phenomena in three-dimensional anharmonic crystal lattices. II. Continuum approximation of the basic equations. J Phys Soc Jpn 72:1989–1994
2. Sugiyama M, Goto K, Takada K, Valenti G, Currò C (2003) Statistical-thermodynamic study of nonequilibrium phenomena in three-dimensional anharmonic crystal lattices. III. Linear waves. J Phys Soc Jpn 72:3132–3141
3. Valenti G, Currò C, Sugiyama M (2004) Acceleration waves analyzed by a new continuum model of solids incorporating microscopic thermal vibrations. Continuum Mech Thermodyn 16:185–198
4. Currò C, Sugiyama M, Suzumura H, Valenti G (2007) Weak shock waves in isotropic solids at finite temperatures up to the melting point. Continuum Mech Thermodyn 18:395–409
5. Boillat G (1975) La propagation des ondes. Gauthier Villars, Paris
6. Currò C, Valenti G, Sugiyama M, Taniguchi S (2009) Propagation of an acceleration wave in layers of isotropic solids at finite temperatures. Wave Motion 46(4):108–121
7. Jeffrey A (1976) Quasilinear hyperbolic systems and waves. Pitman Research Note, 5, London
8. Donato A (1978) The propagation of weak discontinuities in quasilinear hyperbolic systems when a characteristic shock occurs. Proc R Soc Edinb 78A:285–290
9. Brun L (1975) Ondes de choc finites dans les solides élastiques. In: Mandel J, Brun L (eds) Mechanical waves in solids. Springer, Vienna
10. Boillat G, Ruggeri T (1979) Reflection and transmission of discontinuity waves through a shock wave. General theory including also the case of characteristic shock. Proc R Soc Edinb 83A:17–24
11. Lax PD (1957) Hyperbolic systems of conservation laws II. Commun Pure Appl Math 10:537–566
12. Ruggeri T (1980) Interaction between a discontinuity wave and a shock wave: critical time for the fastest transmitted wave, example of the polytropic fluid. Appl Anal 11:103–122

Acceleration Waves in Nonlinear Thermoelastic Micropolar Media

Victor A. Eremeyev
Otto–von–Guericke University Magdeburg, Magdeburg, Germany
South Scientific Center of RASci and South Federal University, Rostov on Don, Russia

Synonyms

Acceleration waves; Micropolar continuum; Thermoelasticity

Definition

By the term "acceleration wave", we mean an isolated geometric surface that moves relative to the material points, across which the acceleration is discontinuous but the displacement and velocity are continuous. More generally, we call an acceleration wave a propagating surface across which second derivatives of some fields undergo discontinuity jump. In the theory of the nonlinear thermoelastic micropolar continuum (called also Cosserat continuum), acceleration waves relate with some jumps of linear and angular accelerations as well as second derivatives of temperature. Acceleration waves are similar to sound waves in solids; they also relate with the localization of deformations in solids.

Overview

Analytic solutions in the theory of the propagation of nonlinear waves are exceptional, and

acceleration waves present one of the exceptions. An *acceleration wave* (or a *wave of weak discontinuity of order 2*) is a solution to the motion equations of continuum that possesses discontinuities in the second derivatives on some surfaces that will be called *singular*. It means that the acceleration wave is represented by a traveling surface which is a carrier of discontinuity jumps of the second derivatives of a solution with respect to the spacial coordinates and time, whereas the solution and its first derivatives are continuous in some surface neighborhood. From the mathematical point of view, existence of acceleration waves closely relates with *hyperbolicity* of the dynamic equations or their *ellipticity* for the equilibrium equations. Existence of acceleration waves in any direction is equivalent to the fact that all eigenvalues of an algebraic spectral problem for the acoustic tensor are positive for any direction of wave propagation.

From the physical point of view, the hyperbolicity of the equations of motion is a natural property of dynamics of elastic media as well as ellipticity is a natural property of its statics. The violation of hyperbolicity (or elipticity) means that discontinuous solutions may appear. Such solutions may model shear-bands, phase transitions, interfaces, fracture, defects, slip surfaces, and other phenomena. So, the algebraic criterion for such phenomena is important in mechanics of materials.

The investigations of acceleration waves in nonlinear elastic and thermoelastic media are performed in many works, see [1, 2]. Acceleration waves in elastic micropolar media are considered in [3]. In a micropolar continuum, each material particle has six degrees of freedom; they are three translational and three rotational degrees of freedom. Besides ordinary stresses there are introduced couple stresses. This gives a possibility to describe micro-inhomogeneous media, for example, foams, cellular solids, lattices, masonries, particle assemblies, magnetic rheological fluids, and liquid crystals. A generalization for elastic and viscoelastic micropolar media is presented in [4]. The relation between the existence of acceleration waves and the condition of strong ellipticity of the equilibrium equations was established in [5–7]. The relation of the ellipticity to localization phenomena in micropolar elastoplasticity is done in [8].

In what follows we use the tensor notations as in [7, 9].

Motion and Thermoconductivity Equations

The motion of a micropolar media is described by two kinematic variables:

$$\mathbf{x} = \mathbf{x}(\mathbf{X}, t), \quad \mathbf{d}_K = \mathbf{d}_K(\mathbf{X}, t), \quad K = 1, 2, 3 \tag{1}$$

The vector $\mathbf{x}$ describes the position of a material point in the actual configuration at instant t, while $\mathbf{X}$ describes the position of the material point in the reference configuration. $\mathbf{d}_K$ are called directors; they are attached to each material point. $\mathbf{d}_K$ describe the orientation of the material particles in the actual configuration. For micropolar media, $\mathbf{d}_K$ constitute orthonormal frame, and so $\mathbf{d}_k \cdot \mathbf{d}_m = \delta_{km}$, where δ_{km} is the Kronecker symbol.

We introduce three orthonormal directors $\mathbf{D}_i$ in the reference configuration. For the sake of simplicity, we choose $\mathbf{D}_i(\mathbf{X}) \equiv \mathbf{d}_i(\mathbf{X}, 0)$. Next, we introduce the proper orthogonal tensor $\mathbf{H} \equiv \mathbf{d}_K \otimes \mathbf{D}_K$, $\det\mathbf{H} = 1$, called microrotation tensor, where $\otimes$ is the tensor product. $\mathbf{H}$ describes relative microrotation of a particle of the micropolar media. Kinematics of a micropolar medium is depicted in Fig. 1. Here $\mathbf{N}$ is the unit normal to the boundary of the body in the reference configuration.

The linear velocity is given by the standard relation $\mathbf{v} = \dot{\mathbf{x}}$ where the overdot denotes the material derivative with respect to t. The angular velocity vector, called microgyration vector, is given by

$$\boldsymbol{\omega} = -\frac{1}{2}\left(\mathbf{H}^T \cdot \dot{\mathbf{H}}\right)_\times \tag{2}$$

where the dot denotes the dot (inner) product and $(\ldots)^T$ – transposed. Symbol $(\ldots)_\times$ stands for the vector invariant of a second-order tensor, [7, 9].

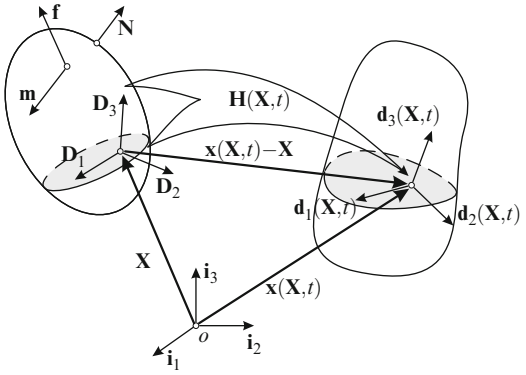

Acceleration Waves in Nonlinear Thermoelastic Micropolar Media, Fig. 1 Deformation of a micropolar body

In particular, for a dyad $\mathbf{a} \otimes \mathbf{b}$ we have $(\mathbf{a} \otimes \mathbf{b})_{\times} = \mathbf{a} \times \mathbf{b}$, where $\times$ is the vector (cross) product. Relation (2) means that $\boldsymbol{\omega}$ is the axial vector associated with the skew-symmetric tensor $\mathbf{H}^T \cdot \dot{\mathbf{H}}$, see [7, 9].

The equations of motion, which represent the local balance of momentum and of moment of momentum (the balance of angular momentum) for an arbitrary part of the micropolar body in the reference configurations, are [1, 7, 10],

$$\begin{aligned} &\mathrm{Div}\, \mathbf{T}_\kappa + \rho \mathbf{f} = \rho \dot{\mathbf{v}} \\ &\mathrm{Div}\, \mathbf{M}_\kappa + (\mathbf{F} \cdot \mathbf{T}_\kappa^T)_{\times} + \rho \mathbf{m} = \rho \gamma \dot{\boldsymbol{\omega}} \end{aligned} \tag{3}$$

Here $\mathbf{T}_\kappa$ and $\mathbf{M}_\kappa$ are the first Piola–Kirchhoff stress and couple-stress tensors; $\mathbf{F} = \mathrm{Grad}\, \mathbf{x}$ is the deformation gradient; Grad and Div are the gradient and divergence operators in Lagrangian coordinates, respectively; ρ is the mass density in the reference configuration; $\mathbf{f}$ and $\mathbf{m}$ are the vectors of mass forces and mass couples, respectively; and $\rho\gamma$ is the scalar measure of the rotational inertia of a particle.

In heat conductive media (3) are supplemented with the Lagrangian heat thermoconductivity equation [10]:

$$\rho \theta \dot{\eta} = -\mathrm{Div}\ \mathbf{q} + \rho h \tag{4}$$

where θ is the temperature, η the specific entropy, $\mathbf{q}$ the heat flux in the reference configuration, and h the density of external heat source.

The constitutive equations of a Cosserat thermoelastic continuum can be derived with the use of the specific free energy $\psi = \psi(\mathbf{E}, \mathbf{K}, \theta)$ as follows:

$$\begin{aligned} &\mathbf{T}_\kappa = \rho \mathbf{H} \cdot \psi_{,\mathbf{E}}, \quad \mathbf{M}_\kappa = \rho \mathbf{H} \cdot \psi_{,\mathbf{K}} \\ &\eta = -\psi_{,\theta}, \quad \mathbf{q} = \mathbf{q}(\mathbf{E}, \mathbf{K}, \theta, \mathrm{Grad}\ \theta) \\ &\mathbf{E} = \mathbf{H}^T \cdot \mathbf{F} - \mathbf{I} \\ &\mathbf{K} = -\frac{1}{2} \boldsymbol{\varepsilon} : (\mathbf{H}^T \cdot \mathrm{Grad}\ \mathbf{H}) \end{aligned} \tag{5}$$

where $\mathbf{E}$ and $\mathbf{K}$ are the strain tensor and wryness tensor, respectively, $\mathbf{I}$ is the identity tensor, and $\boldsymbol{\varepsilon} \equiv -\mathbf{I} \times \mathbf{I}$ the permutation tensor, and the double dot product : of two 3rd-order tensors $\mathbf{A}$, $\mathbf{B}$ represented in the Cartesian base $\mathbf{i}_a$ is defined as $\mathbf{A} : \mathbf{B} = A_{amn} B_{mnb} \mathbf{i}_a \otimes \mathbf{i}_b$. Detailed discussion on strain measures in the micropolar continuum is given in [11].

In what follows we use the referential *Fourier law* for $\mathbf{q}$:

$$\mathbf{q} = -\mathbf{k}(\theta) \cdot \mathrm{Grad}\theta, \quad \mathbf{h} \cdot \mathbf{k}(\theta) \cdot \mathbf{h} > 0, \quad \forall \mathbf{h} \neq \mathbf{0} \tag{6}$$

where $\mathbf{k}$ is the positive definite thermoconductivity tensor.

We assume ψ to be a twice continuously differentiable function and vector function $\mathbf{q}$ to be continuously differentiable. We use the following notation:

$$\psi_{,\mathbf{E}} = \frac{\partial \psi}{\partial \mathbf{E}}, \quad \psi_{,\mathbf{K}} = \frac{\partial \psi}{\partial \mathbf{K}}, \quad \psi_{,\theta} = \frac{\partial \psi}{\partial \theta}, \quad \ldots$$

Acceleration Waves

We consider motions of the continuum when discontinuities of kinematic and dynamic quantities appear at a smooth surface $S(t)$ that is called singular (Fig. 2). For the quantities describing the motion at $S(t)$, we suppose existence of unilateral limit values. For the second derivatives of the motion, the limits from each of both sides from $S(t)$ can differ, in general. A jump for a quantity

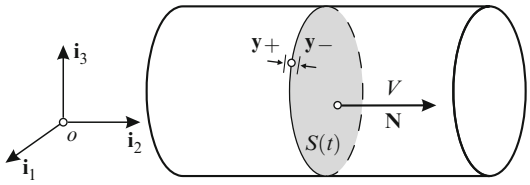

Acceleration Waves in Nonlinear Thermoelastic Micropolar Media, Fig. 2 Singular surface

at $S(t)$ is denoted by the double square brackets, for example, $[\![\mathbf{y}]\!] = \mathbf{y}^+ - \mathbf{y}^-$.

On the singular surface the following balance equations must be valid:

$$\begin{aligned} \rho V[\![\mathbf{v}]\!] &= -[\![\mathbf{T}_\kappa]\!]\cdot\mathbf{N} \\ \rho\gamma V[\![\boldsymbol{\omega}]\!] &= -[\![\mathbf{M}_\kappa]\!]\cdot\mathbf{N} \\ \rho\theta V[\![\eta]\!] &= [\![\mathbf{q}]\!]\cdot\mathbf{N} \end{aligned} \tag{7}$$

where V is the intrinsic speed of propagation of $S(t)$ in the direction $\mathbf{N}$ and $\mathbf{N}$ is the unit normal to S, see [10].

An acceleration wave (or *weak discontinuity wave* or *singular surface of the second order*) is a traveling singular surface $S(t)$ at which the second spatial and time derivatives of the position vector $\mathbf{r}$ and of the microrotation tensor $\mathbf{H}$ have jumps, while $\mathbf{r}$ and $\mathbf{H}$ together with all their first derivatives are continuous. So on $S(t)$ we have

$$[\![\mathbf{F}]\!] = \mathbf{0}, \quad [\![\mathrm{Grad}\,\mathbf{H}]\!] = \mathbf{0}, \quad [\![\mathbf{v}]\!] = \mathbf{0}, \quad [\![\boldsymbol{\omega}]\!] = \mathbf{0} \tag{8}$$

From (7) and (8) it follows $[\![\mathbf{T}_\kappa]\!]\cdot\mathbf{N} = \mathbf{0}$, $[\![\mathbf{M}_\kappa]\!]\cdot\mathbf{N} = \mathbf{0}$.

Regarding the thermoelastic behavior there are two types of acceleration waves. The first one is the *homothermal* acceleration wave when *the temperature field and its first derivatives are continuous at* $S(t)$:

$$[\![\theta]\!] = 0, \quad [\![\mathrm{Grad}\,\theta]\!] = \mathbf{0}, \quad \left[\!\left[\dot{\theta}\right]\!\right] = 0 \tag{9}$$

The second type is the *homentropic* (or *homocaloric*) acceleration wave when *the entropy field and its first derivatives are continuous at* $S(t)$:

$$[\![\eta]\!] = 0, \quad [\![\mathrm{Grad}\,\eta]\!] = \mathbf{0}, \quad [\![\dot{\eta}]\!] = 0 \tag{10}$$

For the homentropic acceleration wave, the Fourier condition holds: $[\![\mathbf{q}]\!]\cdot\mathbf{N} = 0$.

Homothermal Acceleration Waves

Equations (8) and (9) imply continuity of the strain measures $\mathbf{E}$ and $\mathbf{K}$ at $S(t)$: $[\![\mathbf{E}]\!] = \mathbf{0}$, $[\![\mathbf{K}]\!] = \mathbf{0}$. Hence, in view of the constitutive equations (5), it follows the continuity of the tensors $\mathbf{T}_\kappa$ and $\mathbf{M}_\kappa$, of the entropy density, and of the heat flux vector:

$$[\![\mathbf{T}_\kappa]\!] = \mathbf{0}, \quad [\![\mathbf{M}_\kappa]\!] = \mathbf{0}, \quad [\![\eta]\!] = 0, \quad [\![\mathbf{q}]\!] = \mathbf{0}$$

Obviously the balance equations (7) are valid on $S(t)$.

In what follows we use *Maxwell's theorem* which states that, see [1, 2],

Theorem (Maxwell). For a continuously differentiable field $\mathbf{Y}$ such that $[\![\mathbf{Y}]\!] = \mathbf{0}$, the following relations hold:

$$\left[\!\left[\dot{\mathbf{Y}}\right]\!\right] = -V\boldsymbol{\phi}, \quad [\![\mathrm{Grad}\,\mathbf{Y}]\!] = \boldsymbol{\phi}\otimes\mathbf{N} \tag{11}$$

where $\boldsymbol{\phi}$ is the tensor amplitude of the jump of the first gradient of $\mathbf{Y}$; the tensor amplitude is a tensor of the order equal to the order of $\mathbf{Y}$.

Straightforward application of Maxwell's theorem to the continuous fields of $\mathbf{v}$, $\boldsymbol{\omega}$, $\mathbf{T}_\kappa$, and $\mathbf{M}_\kappa$ results in the system of equations at $S(t)$:

$$\begin{aligned} &[\![\dot{\mathbf{v}}]\!] = -V\mathbf{a}, \quad [\![\mathrm{Grad}\,\mathbf{v}]\!] = \mathbf{a}\otimes\mathbf{N}, \quad [\![\dot{\boldsymbol{\omega}}]\!] = -V\mathbf{b}, \\ &[\![\mathrm{Grad}\,\boldsymbol{\omega}]\!] = \mathbf{b}\otimes\mathbf{N}, \quad V[\![\mathrm{Div}\,\mathbf{T}_\kappa]\!] = -\left[\!\left[\dot{\mathbf{T}}_\kappa\right]\!\right]\cdot\mathbf{N}, \\ &V[\![\mathrm{Div}\,\mathbf{M}_\kappa]\!] = -\left[\!\left[\dot{\mathbf{M}}_\kappa\right]\!\right]\cdot\mathbf{N} \end{aligned}$$

where $\mathbf{a}$ and $\mathbf{b}$ are the vectorial amplitudes of the jumps in the linear and angular accelerations.

Using the motion and constitutive equations, one can derive the following relations for $\mathbf{a}$ and $\mathbf{b}$:

$$\begin{aligned} &\left(\psi_{,\mathbf{EE}}\cdot\cdot\left(\mathbf{N}\otimes\mathbf{H}^T\cdot\mathbf{a}\right)\right)\cdot\mathbf{N} \\ &+\left(\psi_{,\mathbf{EK}}\cdot\cdot\left(\mathbf{N}\otimes\mathbf{H}^T\cdot\mathbf{b}\right)\right)\cdot\mathbf{N} = V^2\mathbf{H}^T\cdot\mathbf{a}, \\ &\left(\psi_{,\mathbf{KE}}\cdot\cdot\left(\mathbf{N}\otimes\mathbf{H}^{\mathbf{T}}\cdot\mathbf{a}\right)\right)\cdot\mathbf{N} \\ &+\left(\psi_{,\mathbf{KK}}\cdot\cdot\left(\mathbf{N}\otimes\mathbf{H}^T\cdot\mathbf{b}\right)\right)\cdot\mathbf{N} = \gamma V^2\mathbf{H}^T\cdot\mathbf{b} \end{aligned}$$

With matrix notation, we rewrite these in a more compact form:

$$\mathbb{Q}(\mathbf{N})\cdot\boldsymbol{\xi} = V^2\mathbb{B}\cdot\boldsymbol{\xi} \tag{12}$$

where
$\boldsymbol{\xi} = (\mathbf{a}', \mathbf{b}') \in \mathrm{IR}^6, \mathbf{a}' = \mathbf{H}^T\cdot\mathbf{a}, \mathbf{b}' = \mathbf{H}^{\mathbf{T}}\cdot\mathbf{b}$, and

$$\mathbb{Q}(\mathbf{N}) \equiv \begin{bmatrix} \psi_{,\mathbf{EE}}\{\mathbf{N}\} & \psi_{,\mathbf{EK}}\{\mathbf{N}\} \\ \psi_{,\mathbf{KE}}\{\mathbf{N}\} & \psi_{,\mathbf{KK}}\{\mathbf{N}\} \end{bmatrix}, \quad \mathbb{B} \equiv \begin{bmatrix} \mathbf{I} & \mathbf{0} \\ \mathbf{0} & \gamma\mathbf{I} \end{bmatrix}$$

For arbitrary fourth-order tensor $\mathbf{G}$ and vector $\mathbf{N}$ that are represented in a Cartesian basis $\mathbf{i}_k$ $(k = 1, 2, 3)$, we have used here the notation $\mathbf{G}\{\mathbf{N}\} \equiv G_{klmn}N_lN_n\mathbf{i}_k \otimes \mathbf{i}_m$.

$\mathbb{Q}(\mathbf{N})$ is the *homothermal acoustic tensor* in the micropolar continuum. From the existence of the free energy function ψ, it follows that $\mathbb{Q}(\mathbf{N})$ is symmetric. This provides that the squared velocity of propagation for an acceleration wave in an elastic micropolar continuum is real-valued. The requirement that $\mathbb{Q}(\mathbf{N})$ has to be positive definite is necessary for existence of an acceleration wave

$$\boldsymbol{\xi}\cdot\mathbb{Q}(\mathbf{N})\cdot\boldsymbol{\xi} > 0, \quad \forall\boldsymbol{\xi}\neq\mathbf{0}, \quad \forall|\mathbf{N}| = 1 \tag{13}$$

The inequality (13) coincides with the condition of strong ellipticity of the equilibrium equations for an elastic micropolar continuum [5]. The condition can be represented in an equivalent form

$$\frac{\mathrm{d}^2}{\mathrm{d}\tau^2}\psi(\mathbf{E}+\tau\mathbf{a}'\otimes\mathbf{N}, \mathbf{K}+\tau\mathbf{b}'\otimes\mathbf{N})|_{\tau=0} > 0, \quad \forall\mathbf{N}{:}|\mathbf{N}| = 1, \quad \mathbf{a}'\neq\mathbf{0}, \quad \mathbf{b}'\neq\mathbf{0}$$

Applying Maxwell's theorem to $\mathbf{q}$ and to Grad θ, we get

$$V[\![\mathrm{Div}\ \mathbf{q}]\!] = -[\![\dot{\mathbf{q}}]\!]\cdot\mathbf{N}, \quad [\![\mathrm{Grad\ Grad}\ \theta]\!] = \mathbf{g}\otimes\mathbf{N}, \quad [\![(\mathrm{Grad}\ \theta)]\!] = -V\mathbf{g}$$

where $\mathbf{g} = \mathrm{g}\mathbf{N}$ is the vector amplitude of the jump in the second gradient of the temperature which satisfies the equation

$$\mathrm{g}\mathbf{N}\cdot\mathbf{k}(\theta)\cdot\mathbf{N} = \rho_0\theta\left(\mathbf{a}'\cdot\psi_{,\theta\mathbf{E}}\cdot\mathbf{N} + \mathbf{b}'\cdot\psi_{,\theta\mathbf{K}}\cdot\mathbf{N}\right) \tag{14}$$

Now, using again the matrix notation, we can rewrite (12) and (14):

$$\mathbb{Q}_\theta(\mathbf{N})\cdot\boldsymbol{\zeta} = V^2\mathbb{B}_\theta\cdot\boldsymbol{\zeta} \tag{15}$$

where $\boldsymbol{\zeta} = (\mathbf{a}', \mathbf{b}', \mathrm{g}) \in \mathrm{IR}^7$, $\mathbb{Q}_\theta$, and $\mathbb{B}_\theta$ are matrices with tensor components

$$\mathbb{Q}_\theta(\mathbf{N}) \equiv \begin{bmatrix} \psi_{,\mathbf{EE}}\{\mathbf{N}\} & \psi_{,\mathbf{EK}}\{\mathbf{N}\} & \mathbf{0} \\ \psi_{,\mathbf{KE}}\{\mathbf{N}\} & \psi_{,\mathbf{KK}}\{\mathbf{N}\} & \mathbf{0} \\ -\rho_0\theta\mathbf{N}\cdot\psi_{,\theta\mathbf{E}} & -\rho_0\theta\mathbf{N}\cdot\psi_{,\theta\mathbf{E}} & \mathbf{N}\cdot\mathbf{k}(\theta)\cdot\mathbf{N} \end{bmatrix}$$

$$\mathbb{B}_\theta \equiv \begin{bmatrix} \mathbf{I} & \mathbf{0} & \mathbf{0} \\ \mathbf{0} & \gamma\mathbf{I} & \mathbf{0} \\ \mathbf{0} & \mathbf{0} & 0 \end{bmatrix}$$

Thus, an homothermal acceleration wave exists only if (15) has nontrivial solutions and the eigenvalues for the problem (15) are real and positive.

Homocaloric (Homentropic) Acceleration Waves

By the definition of an homentropic acceleration wave, we have $[\![\eta]\!] = 0$. From this it follows that $[\![\theta]\!] = 0$. Applying again Maxwell's theorem, we introduce a scalar thermal amplitude Θ such that

$$\left[\!\left[\dot{\theta}\right]\!\right] = -V\Theta, \quad [\![\mathrm{Grad}\ \theta]\!] = \Theta\mathbf{N} \tag{16}$$

If $\mathbf{k}$ is a positive definite, the thermal amplitude is zero. This means that for a heat conductive media, the acceleration wave is homothermal one. For heat nonconductors, $\mathbf{k} = \mathbf{0}$. This assumption can be used if one neglects the heat conductivity or considers very fast deformation processes. In heat nonconductive media a homocaloric acoustic tensor differs from $\mathbb{Q}$, in general.

In what follows, we will treat a heat conductive media only.

Existence of Acceleration Waves

Acoustic tensor $\mathbb{Q}_\theta$ is not symmetric, and $\mathbb{B}_\theta$ is not positive definite, in general. However, the spectral problem (15) has only real solutions. This statement is analogues to *Fresnel–Hadamard–Duhem theorem* in the nonlinear elasticity. But this theorem does not guarantee existence of an acceleration wave as problem (15) may have zero or negative eigenvalues. For existence of acceleration waves, all the eigenvalues of (15) must be positive for any **N**. Thus, we should impose the additional restriction on the constitutive equations

$$\boldsymbol{\zeta} \cdot \mathbb{Q}_\theta(\mathbf{N}) \cdot \boldsymbol{\zeta} > 0, \quad \forall \boldsymbol{\zeta} \neq \mathbf{0}, \quad \forall |\mathbf{N}| = 1 \quad (17)$$

Inequality (17) constitutes the *strong ellipticity* condition for the thermoelastic micropolar continuum.

Thus, the following theorem holds true.

Theorem. The condition for existence of a homothermal acceleration wave for all directions of propagations in a micropolar thermoelastic continuum is equivalent to the condition of strong ellipticity of the equilibrium equations of the continuum.

Existence of acceleration waves in all the directions and the condition of strong ellipticity are local as they are defined at each point of the continuum. In case of nonhomogeneous deformation, this means that the conditions can violate or be valid in different parts of the medium.

As an example, we consider the physically linear material which free energy has the form of a quadratic function:

$$\begin{aligned} \rho\psi &= W_1(\mathbf{E}) + W_2(\mathbf{K}) \\ 2W_1(\mathbf{E}) &= \alpha_1 \operatorname{tr}\left(\mathbf{E} \cdot \mathbf{E}^T\right) + \alpha_2 \operatorname{tr}\mathbf{E}^2 + \alpha_3 \operatorname{tr}{}^2\mathbf{E} \\ &\quad + \alpha_0(\theta - \theta_0)\operatorname{tr}\mathbf{E} + \mathrm{c}(\theta - \theta_0)^2 \\ 2W_2(\mathbf{K}) &= \beta_1 \operatorname{tr}\left(\mathbf{K} \cdot \mathbf{K}^T\right) + \beta_2 \operatorname{tr}\mathbf{K}^2 + \beta_3 \operatorname{tr}{}^2\mathbf{K} \end{aligned} \quad (18)$$

where α_k, β_k $(k = 1, 2, 3)$ are elastic constants, α_0 corresponds to the thermal expansion coefficient, c is the specific heat capacity, and θ_0 is the reference temperature.

The acoustic tensor $\mathbb{Q}(\mathbf{N})$ is given by

$$\mathbb{Q}(\mathbf{N}) \equiv \begin{bmatrix} \mathbf{Q}_1(\mathbf{N}) & \mathbf{0} \\ \mathbf{0} & \mathbf{Q_2}(\mathbf{N}) \end{bmatrix}$$
$$\rho\mathbf{Q}_1(\mathbf{N}) = W_{1\,\mathbf{EE}}\{\mathbf{N}\}$$
$$\rho\mathbf{Q}_2(\mathbf{N}) = W_{2,\mathbf{KK}}\{\mathbf{N}\}$$

For constitutive equation (18), inequality (13) implies

$$\begin{aligned} &\alpha_1 > 0, \quad \alpha_1 + \alpha_2 + \alpha_3 > 0, \quad \beta_1 > 0, \\ &\beta_1 + \beta_2 + \beta_3 > 0 \end{aligned} \quad (19)$$

If (19) are valid then the system of equations for a physically linear material defined by relation (19) is strongly elliptic for any deformations. Then the solutions of (12) are given by

$$\begin{aligned} V_{1,2} &= \sqrt{\frac{\alpha_1}{\rho}}, \ \boldsymbol{\xi}_{1,2} = (\mathbf{e}_{1,2}, \mathbf{0}) \\ V_3 &= \sqrt{\frac{\alpha_1 + \alpha_2 + \alpha_3}{\rho}}, \ \boldsymbol{\xi}_3 = (\mathbf{0}, \mathbf{N}) \\ V_{4,5} &= \sqrt{\frac{\beta_1}{\gamma\rho}}, \ \boldsymbol{\xi}_{4,5} = (\mathbf{e}_{4,5}, \mathbf{0}) \\ V_6 &= \sqrt{\frac{\beta_1 + \beta_2 + \beta_3}{\gamma\rho}}, \ \boldsymbol{\xi}_6 = (\mathbf{0}, \mathbf{N}) \end{aligned} \quad (20)$$

where $\mathbf{e}_1, \mathbf{e}_2, \mathbf{e}_4, \mathbf{e}_5$ are arbitrary unit vectors in the tangential plane to $S(t)$ such that $\mathbf{e}_1 \cdot \mathbf{e}_2 = \mathbf{e}_1 \cdot \mathbf{N} = \mathbf{e}_2 \cdot \mathbf{N} = 0, \mathbf{e}_4 \cdot \mathbf{e}_5 = \mathbf{e}_4 \cdot \mathbf{N} = \mathbf{e}_5 \cdot \mathbf{N} = 0$.

Solutions $(20)_{1,2}$ describe *transverse and longitudinal acceleration waves*, respectively, while $(20)_{4,5}$ describe *transverse and longitudinal acceleration waves of microrotation*. V_k in (20) coincide with the limits of the phase velocities of plane harmonic waves (acoustic waves) in linear micropolar elasticity when the frequency of the waves tends to infinity, see [10, 12].

References

1. Truesdell C, Noll W (1965) The nonlinear field theories of mechanics. In: Flügge S (ed) Handbuch der Physik, vol III/3. Springer, Berlin, pp 1–602

2. Truesdell C (1984) Rational thermodynamics, 2nd edn. Springer, New York
3. Kafadar CB, Eringen AC (1971) Micropolar media – I. The classical theory. Int J Eng Sci 9:271–305
4. Maugin GA (1974) Acceleration waves in simple and linear viscoelastic micropolar materials. Int J Eng Sci 12:143–157
5. Eremeyev VA (2005) Acceleration waves in micropolar elastic media. Doklady Phys 50:204–206
6. Altenbach H, Eremeyev VA, Lebedev LP, Rendón LA (2010) Acceleration waves and ellipticity in thermoelastic micropolar media. Arch Appl Mech 80:217–227
7. Eremeyev VA, Lebedev LP, Altenbach H (2012) Foundations of microplar mechanics. Springer, Heidelberg
8. Dietsche A, Steinmann P, Willam K (1993) Micropolar elastoplasticity and its role in localization. Int J Plast 9:813–831
9. Lebedev LP, Cloud MJ, Eremeyev VA (2010) Tensor analysis with applications in mechanics. World Scientific, Hackensack
10. Eringen AC (1999) Microcontinuum field theory. I. Foundations and solids. Springer, New York
11. Pietraszkiewicz W, Eremeyev VA (2009) On natural strain measures of the non-linear micropolar continuum. Int J Solid Struct 46:774–787
12. Nowacki W (1986) Theory of asymmetric elasticity. Pergamon Press, Oxford

Acceleration Waves in Thermoelastic Materials with Voids

Brian Straughan
Department of Mathematical Sciences, Science Laboratories, Durham University, Durham, UK

Synonyms

Acceleration waves

Overview

The theory of voids in nonlinear elastic materials is outlined. This is a theory capable of describing certain classes of porous media and is particularly suitable for dealing with the motion of nonlinear waves. This entry concentrates on the motion of nonlinear acceleration waves in elastic materials containing voids. A thermodynamic description is given of the theory of nonlinear elastic materials with voids, and then acceleration waves are defined and it is outlined how to obtain the wavespeeds and amplitudes. After this, more involved theories of elastic materials with voids are introduced which also allow propagation of a temperature wave in addition to the usual elastic and void waves.

Introduction

The object of this entry is to examine a class of theory which is believed capable of describing certain motions in porous media. This is the theory of elastic materials containing voids developed by Nunziato and Cowin [1]. This theory is particularly useful to describe nonlinear wave motion and accounts well for the elastic behavior of the matrix, being a generalization of nonlinear elasticity theory. There are many studies involving the linearized theory of elastic materials with voids; see, for example, the accounts in Ciarletta and Iesan [2] or Iesan [3], but this entry concentrates on wave motion in the fully nonlinear theory.

The basic idea of including voids in a continuous body is due to Goodman and Cowin [4], although they developed constitutive theory appropriate to a fluid. This they claim is more appropriate to flow of a granular medium. General descriptions of the theory of elastic materials with voids and various applications are given in the books of Ciarletta and Iesan [2] and Iesan [3]. The topic of acceleration waves in thermoelastic materials with voids is covered in some detail in Chapter 7 of the book by Straughan [5], pp. 291–330, and hence, this entry provides an introductory account. Complete details may be found in Straughan [5].

The potential application area for the theory of elastic materials with voids is huge. In particular, wave motion in elastic materials with voids has many applications. Straughan [5], pp. 301, 302, describes several application areas of immediate interest including acoustic microscopy, production of ceramics, and noise transmission through buildings.

Bodies and Their Configurations

Consider a body B deformed from a *reference configuration* at time $t = 0$ to a *current configuration* at time t.

Points in the reference configuration are labeled by boldface notation $\mathbf{X}$ or indicial notation X_A. In the current configuration $\mathbf{X} \to \mathbf{x}$. The mapping is thus

$$\mathbf{x} = \mathbf{x}(\mathbf{X}, t) \tag{1}$$

or

$$x_i = x_i(X_A, t) \tag{2}$$

The coordinates X_A are *material* (or *Lagrangian*) coordinates, whereas x_i are *spatial coordinates* (*Eulerian coordinates*).

In elasticity, one needs the displacement vector $\mathbf{u}$ of a typical particle from $\mathbf{X}$ in the reference configuration to $\mathbf{x}$ at time t, so

$$u_i(X_A, t) = x_i(X_A, t) - X_i \tag{3}$$

The velocity of a particle v_i is

$$v_i(X_A, t) = \frac{\partial x_i}{\partial t}|_{\mathbf{X}\ \text{constant}}$$

The deformation gradient tensor F_{iA} is defined by

$$F_{iA} = \frac{\partial x_i}{\partial X_A}$$

From expression (3), one finds the displacement gradient to be determined as

$$u_{i,A} = \frac{\partial u_i}{\partial X_A} = \frac{\partial x_i}{\partial X_A} - \delta_{iA} = F_{iA} - \delta_{iA}$$

Continuum Theory of Elastic Materials with Voids

The balance equations for a continuous body containing voids are given by Goodman and Cowin [4]. In this entry, use is made of the equations as given by Nunziato and Cowin [1] since these are appropriate for an elastic body.

The idea is to assume that there is a distribution of voids throughout the body B. If $\gamma(\mathbf{X}, t)$ denotes the density of the elastic matrix, then the mass density $\rho(\mathbf{X}, t)$ of B has the form

$$\rho = v\gamma \tag{4}$$

where $0 < v \leq 1$ is a volume distribution function with $v = v(\mathbf{X}, t)$. Since the density or void distribution in the reference configuration can be different, we also have

$$\rho_0 = v_0\gamma_0$$

where ρ_0, γ_0, v_0 are the equivalent functions to ρ, γ, v, but defined in the reference configuration.

The thermomechanics of a body containing a distribution of voids is governed by a system of conservation laws. These are now outlined. The balance of mass equation is

$$\rho|\det \mathbf{F}| = \rho_0$$

Letting π_{Ai} denote the Piola-Kirchoff stress tensor, the balance of angular momentum equation is

$$\pi\mathbf{F}^T = \mathbf{F}\pi^T$$

The balance of linear momentum equation may be written as

$$\rho_0 \ddot{x}_i = \pi_{Ai,A} + \rho_0 f_i \tag{5}$$

where f_i is an external body force. A balance law is required for the void distribution and this is taken to be

$$\rho_0 k\ddot{v} = h_{A,A} + g + \rho_0 \ell \tag{6}$$

where k is a constant inertia coefficient, h_A is a stress vector, g is an intrinsic body force (giving rise to void creation/extinction inside the body), and ℓ is an externally supplied void

body force. Finally, the energy balance equation may be written as

$$\rho_0 \dot{\varepsilon} = \pi_{Ai} \dot{F}_{iA} + h_A \dot{v}_{,A} - g\dot{v} - q_{A,A} + \rho_0 r \quad (7)$$

where ε, q_A and r are, respectively, the internal energy function, the heat flux vector, and the externally supplied heat supply function.

A physical interpretation of equation (7) is provided by Straughan [5], p. 303. One also requires an entropy inequality. The Clausius-Duhem inequality is employed, namely,

$$\rho_0 \dot{\eta} \geq -\left(\frac{q_A}{\theta}\right)_{,A} + \frac{\rho_0 r}{\theta} \quad (8)$$

where η is the specific entropy function and θ is the adiabatic temperature in the body.

An elastic body containing voids is defined in Straughan [5] to be one which has as constitutive variables the set

$$\Sigma = \{v_0, v, F_{iA}, \theta, \theta_{,A}, v_{,A}\} \quad (9)$$

supplemented with $\dot{v}$. Thus, the constitutive theory assumes

$$\begin{aligned} &\varepsilon = \varepsilon(\Sigma, \dot{v}), \quad \pi_{Ai} = \pi_{Ai}(\Sigma, \dot{v}), \quad q_A = q_A(\Sigma, \dot{v}) \\ &\eta = \eta(\Sigma, \dot{v}), \quad h_A = h_A(\Sigma, \dot{v}), \quad g = g(\Sigma, \dot{v}) \end{aligned} \quad (10)$$

This is different from Nunziato and Cowin [1] who regard η as the independent variable rather than θ, and they also assume $q_A = 0$. The Helmholtz free energy function ψ is introduced as normal by the relation

$$\varepsilon = \psi + \eta\theta \quad (11)$$

Straughan [5] describes how the entropy inequality (8) may be exploited using (9)–(11) to deduce the relations

$$\psi \neq \psi(\dot{v}, \theta_{,A}) \quad (12)$$

$$h_A = \rho_0 \frac{\partial \psi}{\partial v_{,A}} \quad \Rightarrow \quad h_A \neq h_A(\dot{v}, \theta_{,A}) \quad (13)$$

$$\pi_{Ai} = \rho_0 \frac{\partial \psi}{\partial F_{iA}} \quad \Rightarrow \quad \pi_{Ai} \neq \pi_{Ai}(\dot{v}, \theta_{,A}) \quad (14)$$

$$\eta = -\frac{\partial \psi}{\partial \theta} \quad \Rightarrow \quad \eta \neq \eta(\dot{v}, \theta_{,A})$$

and then

$$\varepsilon \neq \varepsilon(\dot{v}, \theta_{,A})$$

To specify a material for an elastic body containing voids, one needs to postulate a suitable functional form for $\psi = \psi(v_0, v, F_{iA}, \theta, v_{,A})$. Such a form is usually constructed with the aid of experiments. The functions g and q_A still involve $\dot{v}$ and this can lead to almost viscoelastic-like behavior, cf. Nunziato and Cowin [1]. Other writers, for example, Iesan [3] and Ciarletta and Iesan [2], omit $\dot{v}$ from the constitutive list at the outset. In this way, one deduces that g follows as a derivative of the Helmholtz free energy, Iesan [3], p. 7. However, it may be that some of the desirable features of viscoelasticity are lost. The wavespeeds of acceleration waves in this case are derived in Iesan [3] and Ciarletta and Iesan [2].

The system of equations which arises via the above procedure results in what is effectively a hyperbolic system for the displacement and void fraction; however, the temperature equation is essentially parabolic. Hyperbolic systems are discussed in great depth in the book of Dafermos [6]; see also the book by Whitham [7]. Therefore, in the interests of clarity the first consideration is of an acceleration wave in the isothermal case, and in so doing one is able to see explicitly the void influence.

Acceleration Waves

Assume now the temperature $\theta =$ constant, then from (11) and (12)

$$\psi = \psi(v_0, v, F_{iA}, v_{,A}) \quad (15)$$

Furthermore, to consider the propagation of an acceleration wave in an elastic body with voids, it

is sufficient to consider the momentum equations (5) and (6) with $f_i = 0$ and $\ell = 0$. These equations are thus

$$\rho_0 \ddot{x}_i = \pi_{Ai,A} \tag{16}$$

$$\rho_0 k\ddot{v} = h_{A,A} + g \tag{17}$$

Definitions and properties of acceleration waves in full generality may be found in the books of Truesdell and Toupin [8], Truesdell and Noll [9], Truesdell and Rajagopal [10], Fabrizio and Morro [11], Chen [12], McCarthy [13], and Straughan [5, 14]. A short but highly illuminating article dealing with acceleration waves is that of Varley and Cumberbatch [15]. This entry concentrates on an acceleration wave in an elastic body containing voids. An acceleration wave in an elastic body with voids in three dimensions is defined as follows. The functions, u_i and v, are C^1 everywhere, but the second and higher derivatives of u_i and v are allowed to have finite discontinuities across a surface $\mathcal{S}$. Thus, an *acceleration wave* is a surface $\mathcal{S}$ across which $u_{i,tt}, u_{i,tA}, u_{i,AB}$, $u_{i,ttt}, u_{i,ttA}, u_{i,tAB}, u_{i,ABC}$ suffer at most finite discontinuities, with the functions and first derivatives $u_i, u_{i,t}, u_{i,A}$ continuous *everywhere*. The same continuity requirements hold for v.

For a function $h(\mathbf{x}, t)$ which may be discontinuous across $\mathcal{S}$, the values h^+ and h^- are defined as follows:

$$h^+(\mathbf{x}, t) = \lim_{\mathbf{x}\to\mathcal{S}} h(\mathbf{x}, t) \text{ from the right}$$
$$h^-(\mathbf{x}, t) = \lim_{\mathbf{x}\to\mathcal{S}} h(\mathbf{x}, t) \text{ from the left}$$

In particular, for a right moving wave, h^+ is the value of h at $\mathcal{S}$ approaching from the region which $\mathcal{S}$ is about to enter. The jump of h at $\mathcal{S}$, written as $[h]$, is

$$[h] = h^- - h^+ \tag{18}$$

To proceed with an acceleration wave analysis, general compatibility relations for a function $\psi(\mathbf{X}, t)$ are needed across $\mathcal{S}$. These may be found in detail in Truesdell and Toupin [8], or in Chen [12]. Those required are now quoted. If ψ is continuous in $\mathbb{R}^3$ but its derivative is discontinuous across $\mathcal{S}$, then

$$[\psi_{,A}] = N_A B, \qquad \text{where } B = [N^R \psi_{,R}] \tag{19}$$

When $\psi \in C^1(\mathbb{R}^3)$, then

$$[\psi_{,AB}] = N_A N_B C, \qquad \text{where } C = [N^R N^S \psi_{,RS}] \tag{20}$$

In (19) and (20), N_A refers to the unit normal to $\mathcal{S}$ but referred back to the reference configuration. The relation corresponding to the Hadamard formula in three dimensions is, cf. Chen [12] (4.15),

$$\frac{\delta}{\delta t}[\psi] = [\dot{\psi}] + U_N B \tag{21}$$

where $\dot{\psi} = \partial\psi/\partial t|_{\mathbf{X}}$, U_N is the speed at the point on $\mathcal{S}$ with unit normal N_A and B is defined in (19).

Upon expanding $\pi_{Ai,A}$ and $h_{A,A}$ as functions of their constitutive variables in equations (16), (17), and taking the jumps across $\mathcal{S}$, one finds from equations (16) and (17)

$$\rho_0[\ddot{x}_i] = \frac{\partial \pi_{Ai}}{\partial F_{rK}}[x_{r,KA}] + \frac{\partial \pi_{Ai}}{\partial v_{,K}}[v_{,KA}] \tag{22}$$

$$\rho_0 k[\ddot{v}] = \frac{\partial h_A}{\partial F_{iK}}[x_{i,KA}] + \frac{\partial h_A}{\partial v_{,K}}[v_{,KA}] \tag{23}$$

Use of the Hadamard relation (21) leads to the following relations between the jumps of the second derivatives

$$[x_{r,KA}] = \frac{N_K N_A}{U_N^2}[\ddot{x}_r], \qquad [v_{,KA}] = \frac{N_K N_A}{U_N^2}[\ddot{v}]$$

Using these expressions in (22) and (23) and defining the wave amplitudes a_i and b by

$$a_i(t) = [\ddot{x}_i], \qquad b(t) = [\ddot{v}]$$

one derives from (22) and (23)

$$\rho_0 U_N^2 a_i = Q_{ir} a_r + \frac{\partial \pi_{Ai}}{\partial v_{,K}} N_K N_A b \tag{24}$$

$$\rho_0 k U_N^2 b = \frac{\partial h_A}{\partial F_{iK}} N_K N_A a_i + Q_c b \tag{25}$$

where Q_{ir} is the (elastic) acoustic tensor given by

$$Q_{ir} = N_K N_A \frac{\partial \pi_{Ai}}{\partial F_{rK}} \tag{26}$$

and Q_c is an "acoustic variable" associated with the voids given by

$$Q_c = N_K N_A \frac{\partial h_A}{\partial v_{,K}}$$

Straughan [5], p. 307, shows that if $J_i = -\rho_0 N_A N_K \, \partial^2 \psi / \partial v_{,K} \, \partial F_{iA}$, then (24) and (25) lead to the propagation conditions:

$$(\rho_0 U_N^2 \delta_{ij} - Q_{ij}) a_j = J_i b \tag{27}$$

$$(\rho_0 k U_N^2 - Q_c) b = J_i a_i \tag{28}$$

As Straughan [5], p. 307, remarks, there are various avenues to explore. For example, he considers:

(a) $a_i = a(t) n_i$, a longitudinal wave.
(b) $a_i = \hat{a}(t) s_i$, s_i is a tangential vector to $\mathcal{S}$, a transverse wave.
(c) Body has a center of symmetry, then $J_i = 0$.

In particular, in case (a), one deduces the wavespeed equation as

$$(\rho_0 U_N^2 - Q_{ij} n_i n_j)(\rho_0 k U_N^2 - Q_c) - (J_i n_i)^2 = 0 \tag{29}$$

This is a fourth-order equation for U_N. It shows there are two waves: a fast wave and a slow wave, each of which moves in the positive and negative n_i directions. Thus, there is essentially an elastic wave and a wave associated with the void distribution. This is seen clearly in case (c) where the body has a center of symmetry for then $J_i = 0$, and equation (29) shows there are two waves with speeds $U_N = \sqrt{Q_{ij} n_i n_j / \rho_0}$ and $U_N = \sqrt{Q_c / \rho_0 k}$. The first of these is the elastic wave whose speed is governed by the acoustic tensor Q_{ir}, whereas the second is a void wave whose speed is dictated by the void acoustic variable Q_c. In the general case, one may show from (29) that there are two waves with wavespeeds $U_N = U_1$, $U_N = U_2$, and $U_1 < U_2$, with U_1 and U_2 greater than or less than those of the purely elastic or void cases which arise when $J_i = 0$.

By returning to equations (16) and (17) and differentiating these with respect to time or with respect to the variable X_A, one may now proceed to actually derive a Bernoulli equation for the wave amplitudes a and b and solve this explicitly. In certain cases, one finds $a(t)$ and $b(t)$ blow up in a finite time, a phenomenon associated with shock wave formation, cf. Dafermos [6], McCarthy [13], and Chen [12].

While one may consider the propagation of acceleration waves in the non-isothermal case, the above equations are not sufficiently general to allow also propagation of a thermal wave. Straughan [5] concentrates on three classes of thermoelastic waves with voids, namely, those corresponding to a Green-Laws-Lindsay theory and those corresponding to Green-Naghdi theories of type II and type III. A general introduction to thermoelastic bodies in these three theories and in other situations capable of allowing the propagation of a temperature wave may be found in the book by Straughan [14]; see also the review article by Hetnarski and Ignaczak [16].

Thermoelastic Waves with Voids

The object now is to consider a theory of voids as developed by Nunziato and Cowin [1] but to also allow for the possibility of propagation of a temperature wave. Straughan [5] considers three such possibilities based on thermodynamics of Green-Laws-Lindsay and of Green-Naghdi type II and type III. The first approach develops a thermo-poroacoustic theory which allows for nonlinear elastic effects and for the presence of voids, by using the thermodynamics which utilizes a generalized temperature $\phi(\theta, \dot{\theta})$ rather than just the

standard absolute temperature θ, $\dot{\theta}$ being the material derivative of θ.

The basic equations are those of balance of linear momentum, void balance, and balance of energy, and are, balance of linear momentum,

$$\rho\,\ddot{x}_i = \pi_{Ai,A} + \rho F_i \tag{30}$$

void balance,

$$\rho k\ddot{v} = h_{A,A} + g + \rho\ell \tag{31}$$

and balance of energy,

$$\rho\dot{\varepsilon} = -q_{A,A} + \pi_{Ai}\,\dot{x}_{i,A} + h_A\,\dot{v}_{,A} - g\dot{v} + \rho r \tag{32}$$

The thermodynamic development uses the entropy inequality

$$\rho\dot{\eta} - \frac{\rho r}{\phi} + \left(\frac{q_A}{\phi}\right)_{,A} \geq 0 \tag{33}$$

where η is the specific entropy and $\phi = \phi(\theta, \dot{\theta})\,(> 0)$ is a generalized temperature function which reduces to θ in the equilibrium state. The Helmholtz free energy function ψ is now defined by $\psi = \varepsilon - \eta\phi$.

Assuming the constitutive theory that

$$\psi, \phi, \eta, \pi_{Ai}, q_A, h_A, g \tag{34}$$

depend on the variables

$$x_{i,A}, v, v_{,A}, \theta, \dot{\theta}, \theta_{,A} \tag{35}$$

the entropy inequality may be used to deduce the relations

$$\begin{aligned} &\phi = \phi(\theta, \dot{\theta}, v), \pi_{Ai} = \rho\frac{\partial\psi}{\partial x_{i,A}}, q_A = -\rho\frac{\partial\psi}{\partial\theta_{,A}} \Big/ \frac{1}{\phi}\frac{\partial\phi}{\partial\dot{\theta}} \\ &h_A = \rho\frac{\partial\psi}{\partial v_{,A}}, \quad g = -\rho\left(\frac{\partial\psi}{\partial v} + \eta\frac{\partial\phi}{\partial v}\right) \end{aligned} \tag{36}$$

with the entropy given by

$$\eta = -\frac{\partial\psi}{\partial\dot{\theta}} \Big/ \frac{\partial\phi}{\partial\dot{\theta}} \tag{37}$$

Let, as in definition (18), $[\cdot]$ denote the jump of a function across the singular surface $\mathcal{S}$. A void-temperature acceleration wave is defined for equations (30)–(32) to be a singular surface $\mathcal{S}$ across which x_i, v and θ together with their first derivatives are continuous, but the second and higher derivatives suffer a finite discontinuity. If a_i, B, C denote the wave amplitudes,

$$a_i = [\ddot{x}_i], \qquad B = [\ddot{v}], \qquad C = [\ddot{\theta}] \tag{38}$$

then, expanding $\pi_{Ai,A}$, $h_{A,A}$, and $q_{A,A}$, using the constitutive theory (34), (35), after some calculation, one shows from (30) to (32) that the amplitudes satisfy the equations

$$(Q_{ij} - \rho U_N^2\delta_{ij})a_j = U_N N_A\frac{\partial\pi_{Ai}}{\partial\dot{\theta}}\,C \tag{39}$$

$$\left(\rho k U_N^2 - N_A N_B\frac{\partial h_A}{\partial v_{,B}}\right)B = N_A N_B\frac{\partial h_A}{\partial\theta_{,B}}\,C \tag{40}$$

$$\begin{aligned} \left(\rho\frac{\partial\varepsilon}{\partial\dot{\theta}}\,U_N^2 + N_A N_B\frac{\partial q_A}{\partial\theta_{,B}}\right)C = &-\frac{\partial q_A}{\partial v_{,B}}\,N_A N_B B \\ &+ \rho U_N N_A\phi\,\frac{\partial\eta}{\partial F_{iA}}\,a_i \end{aligned} \tag{41}$$

where Q_{ij} is the acoustic tensor, cf. (26), given by

$$Q_{ij} = N_A N_B\frac{\partial\pi_{Ai}}{\partial F_{jB}} \tag{42}$$

After some calculation, cf. Straughan [5], p. 313, it may then be deduced that there is a plane wave whose wavespeed U_N satisfies the sixth-order equation

$$\begin{aligned} &(U_N^2 - U_M^2)(U_N^2 - U_P^2)(U_N^2 - U_T^2) \\ &\quad -(U_N^2 - U_P^2)U_N^2 K_1 - (U_N^2 - U_M^2)K_2 = 0 \end{aligned} \tag{43}$$

In this equation the coefficients U_M^2, U_P^2, U_T^2, K_1 and K_2 are given by

$$U_M^2 = N_A N_B v_i v_j \frac{\partial^2 \psi}{\partial F_{iA} \partial F_{jB}} \tag{44}$$

$$U_P^2 = \frac{N_A N_B}{k} \frac{\partial^2 \psi}{\partial v_{,A} v_{,B}} \tag{45}$$

$$U_T^2 = \frac{N_A N_B}{\phi_{\dot\theta} \eta_{\dot\theta}} \frac{\partial^2 \psi}{\partial \theta_{,A} \theta_{,B}} \tag{46}$$

$$K_1 = \frac{N_A N_K v_i v_j}{\phi_{\dot\theta} \eta_{\dot\theta}} \frac{\partial^2 \psi}{\partial \dot\theta \partial F_{iA}} \frac{\partial^2 \psi}{\partial \dot\theta \partial F_{jK}} \tag{47}$$

$$K_2 = \frac{N_A N_B N_R N_S}{k \phi_{\dot\theta} \eta_{\dot\theta}} \frac{\partial^2 \psi}{\partial v_{,A} \partial \theta_{,B}} \frac{\partial^2 \psi}{\partial v_{,S} \partial \theta_{,R}} \tag{48}$$

Straughan [5] interprets U_M, U_P and U_T as follows. Firstly, U_M is the wavespeed of an elastic wave in the absence of other effects. Next, U_P is the wavespeed of a wave associated with the void fraction, while U_T is the wavespeed of a thermal wave. One may then deduce that equation (43) has three distinct real solutions U_N^2 and three distinct waves propagate.

A complete account of the amplitude behavior is included in Straughan [5].

Straughan [5] also describes thermoelastic void acceleration waves when one replaces $\theta, \dot\theta$ by θ and α, where α is a thermal displacement variable

$$\alpha = \int_{t_0}^{t} \theta(\mathbf{X}, s) ds + \alpha_0 \tag{49}$$

where $\mathbf{X}$ is the spatial coordinate in the reference configuration of the body with θ being the absolute temperature. In some ways, this is introducing the history of the temperature field into the situation. This theory breaks down into two categories known as type II and type III depending on whether $\dot\alpha_{,A}$ is included in the list of constitutive variables or not. If $\dot\alpha_{,A}$ is not included, one arrives at a type II theory, whereas inclusion of $\dot\alpha_{,A}$ leads to a type III theory. In the case of type II theory, one finds the possibility of three waves: one due to the elastic displacement, one due to the voids, and also one due to a temperature wave. One can completely determine the wavespeeds and amplitudes. For type III theory, the situation is more complex and in some ways resembles classical thermoelastic voids theory where the temperature equation is effectively parabolic.

Straughan [5] further describes a generalization of the thermoelastic voids theory where a microrotation vector is included, allowing for rotation effects on the microstructure level. Here, an acceleration wave analysis is possible, but the analysis is surprisingly complex. Yet further intricate features which may be necessary to describe the intriguing effects being found in nanomaterials are studied by Paoletti [17]. He develops a comprehensive nonlinear acceleration wave analysis. Further recent articles which are worthy of consideration dealing with thermoelasticity and voids, and more exotic theories based on these, are those of Aouadi [18], Chirita and Ghiba [19], and Iesan and Scalia [20]. These articles deal with various aspects of wave motion, and well posedness, including in the now important situation where the elastic tensor might not be positive definite. The last mentioned area is very important in the study of auxetic materials.

Acknowledgments This research was supported by the Leverhulme Research grant "Tipping Points, Mathematics, Metaphors and Meanings."

References

1. Nunziato JW, Cowin SC (1979) A nonlinear theory of elastic materials with voids. Arch Ration Mech Anal 72:175–201
2. Ciarletta M, Iesan D (1993) Non-classical elastic solids. Longman, New York
3. Iesan D (2004) Thermoelastic models of continua. Kluwer, Dordrecht
4. Goodman MA, Cowin SC (1972) A continuum theory for granular materials. Arch Ration Mech Anal 44:249–266
5. Straughan B (2008) Stability, and wave motion in porous media, vol 165, Applied mathematical sciences. Springer, New York
6. Dafermos CM (2010) Hyperbolic conservation laws in continuum physics, vol 325, 3rd edn, Grundleheren der mathematischen Wissenschaften. Springer, Heidelberg/New York
7. Whitham GB (1974) Linear and nonlinear waves. Wiley, New York

8. Truesdell C, Toupin RA (1960) The classical field theories. In: Flügge S (ed) Handbuch der physik, vol III/1. Springer, 226–793
9. Truesdell C, Noll W (1992) The non-linear field theories of mechanics, 2nd edn. Springer, Berlin
10. Truesdell C, Rajagopal KR (1999) An introduction to the mechanics of fluids. Birkhäuser, Basel
11. Fabrizio M, Morro A (2003) Electromagnetism of continuous media. Oxford University Press, Oxford
12. Chen PJ (1973) Growth and decay of waves in solids. In: Flügge S, Truesdell C (eds) Handbuch der physik, VIa/3. Springer, Berlin, pp 303–402
13. McCarthy MF (1975) Singular surfaces and waves. In: Eringen AC (ed) Continuum mechanics of single-substance bodies, II. Academic, New York, pp 449–521
14. Straughan B (2011) Heat waves, vol 177, Applied mathematical sciences. Springer, New York
15. Varley E, Cumberbatch E (1965) Non-linear theory of wave-front propagation. J Inst Math Appl 1:101–112
16. Hetnarski RB, Ignaczak J (1999) Generalized thermoelasticity. J Therm Stress 22:451–461
17. Paoletti P (2012) Acceleration waves in complex materials. Discret Contin Dyn Syst B 17:637–659
18. Aouadi M (2012) Uniqueness and existence theorems in thermoelasticity with voids without energy dissipation. J Frankl Inst 349:128–139
19. Chirita S, Ghiba ID (2010) Strong ellipticity and progressive waves in elastic materials with voids. Proc R Soc Lond A 466:439–458
20. Iesan D, Scalia A (2006) Propagation of singular surfaces in thermo-microstretch continua with memory. Int J Eng Sci 44:845–858

Actuator

▶ Piezoelectric Smart Structures for Control of Thermoelastic Response

Adaptive Control

▶ Piezoelectric Smart Structures for Control of Thermoelastic Response

Advanced Composite Materials

▶ Functionally Graded Structures: Aerothermoelastic Interactions

Advanced/Mixed Two-Dimensional Models

▶ Refined and Advanced Governing Equations for the Thermomechanical Analysis of Shells

Aeroelasticity

▶ Linear Aero-Thermo-Servo-Viscoelasticity, Part II: Dynamic Considerations: Lifting Surface and Panel Flutter and Aerodynamic Noise

Aerothermoelastic Behavior of Flat and Curved Panels

Laith K. Abbas[1], Rui Xiaoting[1] and Piergiovanni Marzocca[2]
[1]Institute of Launch Dynamics, Nanjing University of Sciences and Technology, Nanjing, People's Republic of China
[2]Department of Mechanical and Aeronautical Engineering, Clarkson University, The Wallace H. Coulter School of Engineering, Potsdam, NY, USA

Synonyms

Aerothermoelasticity; Edge movability; Hypersonic speed; Lyapunov first quantity; Nonlinear aerothermoelastic analysis; Piston aerodynamic theory; Stable/unstable LCO; Thermal loading and degradation

Definitions

Aeroelasticity (*AE*) is the science which studies the mutual interactions among inertial, elastic, and aerodynamic forces acting on structural members exposed to an airstream, and the influence of this study on design.

Aerothermoelasticity (*ATE*) is the science that studies the mutual interactions among inertial,

elastic, and aerodynamic forces acting on structural members under the combined effect of aerodynamic heating and loading.

Overview

The panel flutter is a form of dynamic aeroelastic instability resulting from the interaction between the motion of a high-speed aerospace vehicle's skin panel, typical of spacecrafts and missiles, and the aerodynamic loads exerted on that panel by air flowing past one side at supersonic or hypersonic speed and to still air on the other side. Often a skin panel encounters flutter and then a limit cycle oscillation (LCO), which is an oscillation bounded in amplitude. There have been many incidents reported in the literature dating back to the V-2 rocket of World War II, the X-15, the Saturn launch vehicle of the Apollo program, and continuing on to the present day [1–3].

One essential limitation of the linearized panel flutter analysis is that it gives information only up to the point of instability. Furthermore, the linearized analysis is restricted to cases where the aeroelastic response is small. Often this assumption is violated before the onset of instability. Thus, to study the behavior of aeroelastic systems in the proximity of the instability boundary including the postinstability region, the inherent nonlinearities of structural and aerodynamic nature must be accounted for. By using the Von Kármán large deflection plate theory combined with the linear piston theory aerodynamics (PTA), one of the most popular unsteady aerodynamic theories, it was recognized that geometrical nonlinearities due to moderate plate deflection, mainly creating mid-plane stretching forces, can play an important role in panel flutter [4]. The nonlinear panel dynamic response, due to large deformations and mutual interaction between the aerodynamic loading and high order panel modes, despite the deterministic nature of the panel equation, can be oscillatory, quasiperiodic, limit cycle, or random-like irregular chaotic [5]. Various nonlinearities can influence differently the character of the panel flutter boundary; these nonlinearities could be of several origins, including structural or geometric, thermodynamic, aerodynamic arising from flow characteristics, and material nonlinearities. Furthermore, in the presence of thermal effects, aerothermoelastic considerations have to be considered in the design of space reentry vehicles and high-speed aircraft, since theses effects may produce deformations, stresses, and changes in material properties that can dramatically affect their aeroelastic behavior. In this sense, the structural panels of supersonic/hypersonic flight vehicles can experience, among others, the thermal flutter instability generated by the combined influence of the thermal field, unsteady aerodynamic loads, elasticity of structures, and the dynamic effects.

The effect of panel heating is twofold. First, there is reduction in stiffness due to softening of the panel material; second, thermal stresses are generated due to mismatch in thermal expansion coefficients of the panel and support structure. These effects, in turn, affect the static and dynamic behaviors of the panel [6]. The bulk of literature dealing with flat and curved panels flutter is based on the stress-strain equations including shear wall and thermal effects [6–16]. In these works, quasi-steady first-order or nonlinear piston theories and Euler equations for unsteady aerodynamic have been considered. Other aerodynamic models, perhaps less computationally efficient, are also available and have been explored. In recent years, viscoelastic materials, such as some composite materials, have been widely used in the aerospace industry partly due to their inherent properties to reduce undesired vibrations.

Stability and vibration studies of plates and shells with initial geometric imperfections are of a significant importance in modern solid mechanics. These structures are rather sensitive to small deviations from their design shape. Experimental and numerical studies conducted so far have shown unambiguously that the basic cause of the discrepancy between theory and experiment is the initial deflections of the structure [7, 17, 18]. This means that generally, the influence of initial deflections has to be studied within the framework of large deflection theory, meaning primarily dynamic instability (including flutter) where imperfections play a vital part [18].

Small deviations of the shell's surface from its idealized shape were also shown to drastically reduce its resistance to panel flutter, a dynamic instability of the shell, even though the deviations were only on the order of one shell thickness or less. Even the best manufacturing methods admit this magnitude of imperfection in the fabricated shell geometry [19]. Previous investigations have suggested that detailed studies are needed to better understand and explore the complex motions that can be encountered in the presence of various coupled nonlinearities. These studies are also needed when it comes to system identification and damage detection, since the vibration behavior of the system needs to be clearly understood.

Aerothermoelastic Analysis Methodology

Structural Modeling

To derive the aerothermoelastic governing equations of a curved panel, the geometrically nonlinear theory of infinitely long two-dimensional panels with some small initial curvature is usually considered. The classical von Kármán nonlinear strain-displacement relation for a general plate undergoing both extension and bending in conjunction with the Kirchhoff plate-hypothesis is adopted. The effects of thermal degradation and Kelvin's model of structural damping can also be considered.

Let us consider an isotropic curved panel model (Fig. 1) with a width a, infinity long length b, thickness h, maximum rise height H, and constant radii curvature $\Re_x$ [20]. The thickness h is small compared to the length a. In addition, b is infinitely long as compared to a. The panel is supported on the sides $x = 0$ and $x = a$. These sides are fixed with respect to the longitudinal displacements.

The displacements from the unstressed state of the panel's mid-plane surface in the x and z directions are denoted by u and w, and the total transverse displacement of a given mid-plane surface point after deformation is given by:

$$w_{total}(x,t) = \hat{w}(x) + w(x,t) \tag{1}$$

Herein $\hat{w}(x)$ indicates the initial undeformed shape (initial geometric imperfection) of the mid-plane surface, while $w(x,t)$ corresponds to the transverse displacement of the mid-plane surface relative to its undeformed configuration. The strain ε_x of the mid-plane surface in the x-direction and based on the von Kármán assumption is given by [4]:

$$\varepsilon_x = u_{,x} + \frac{1}{2}(w_{,x})^2 + w_{,x}\hat{w}_{,x} - w/\Re_x \tag{2}$$

The subscript $(\cdot)_{,x}$ denotes the differentiation with respect to x. The bending equation of motion is given by [4, 21, 22]:

$$M_{,xx} + N_x(w_{,xx} + 1/\Re_x) + P_z = 0 \tag{3}$$

where N_x represent the axial stress resultant, M is the bending moment; furthermore, $M \equiv D\aleph$ where D is the panel stiffness $\equiv Eh^3/12\ (1-\upsilon^2)$, E is the modulus of elasticity, υ is Poisson's ratio, and $\aleph$ is the curvature change of the mid-plane surface $(\equiv -w_{,xx})$. The bending moment can be recast as:

$$M = -Dw_{,xx} \tag{4}$$

In (3), P_z is the distributed load on the panel and can be expressed as follows:

$$P_z = -\rho_m h w_{,tt} + P_z^A(x,t) + P_z^{stat}(x) + \Delta B^T \tag{5a}$$

The first term in the (5a) corresponds to the transverse inertial load, while the superscript $(\cdot)^A$ indicates an unsteady aerodynamic load and the superscript $(\cdot)^{stat}$ indicates an initial static load. B^T is the thermal load defined as [8]:

$$B^T = \frac{E\alpha}{(1-\upsilon)} \int_{-h/2}^{h/2} T(x,z)\, z\, dz \tag{5b}$$

where α is the linear thermal expansion coefficient, $T(x,z)$ is the temperature increment from a free-stress temperature T_0, and Δ in (5a) is the Laplace operator. The material properties of the panel, E and α, are influenced by the thermal field as follows [7]:

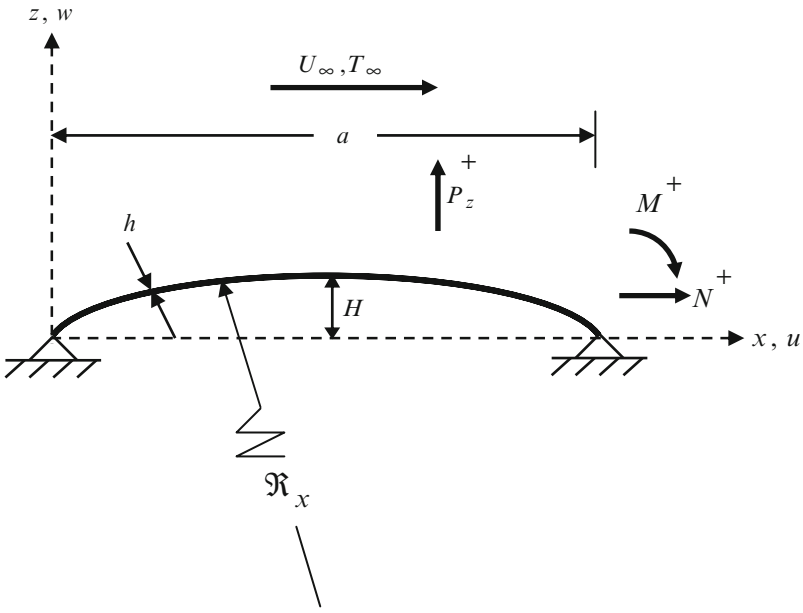

Aerothermoelastic Behavior of Flat and Curved Panels, Fig. 1 Two-dimensional panel with initial curvature

$$E = E_0 + E_1 T = E_0(1 + e_T T), \quad \alpha = \alpha_0 + \alpha_1 T = \alpha_0(1 + \alpha_T T) \tag{6a}$$

where

$$e_T = E_1/E_0 < 0, \quad \alpha_T = \alpha_1/\alpha_0 > 0 \tag{6b}$$

In (6b), e_T and α_T are the coefficients associated with the thermal degradation. As a result of the temperature dependence of the thermoelastic material properties and of the spatially distributed temperature field, the thermoelastic coefficients of the material become functions of the space variables, for example, $E \Rightarrow E(x)$ and $\alpha \Rightarrow \alpha(x)$. This implies that the structural panel presents a certain level of nonhomogeneity [4]. Typical aerospace panel, such as a fuselage section, wing and empennage panels, is usually solidly connected to structural members of the airframe. For this reason, it has been assumed that $\sigma_x \to \sigma$, that is, the tangential stresses act only in the x -direction. Physically, this stress is generated by the constraint of the panel with the members of the airframe. This condition yields:

$$\sigma_x = N_x/h = (E(x)/(1 - \upsilon^2))(\varepsilon_x + \upsilon\varepsilon_y) = \sigma \tag{7}$$

Moreover, when the flight vehicle travels at high flight speeds regimes, due to aerodynamic heating, the skin panel temperature could potentially reach the high values of several hundred degrees. This effect can result in a lower value of the flutter instability boundary or in larger limit cycle amplitude at the same dynamic pressure. This implies that also the effect of the temperature should be carefully considered for more accurate results. This can be done including an in-plane tension σ_x^T, acting in the x -direction, due to the temperature [23]:

$$\sigma_x^T = -(E(x)/(1 - \upsilon))\alpha(x)\, T \tag{8}$$

This implies that the total in-plane stress, in the x -direction, can be expresses as:

$$\sigma_{x\_total} = \sigma_x + \sigma_x^T \tag{9a}$$

By substituting (2) in (7), assuming $\varepsilon_y = 0$, and making use of (8) in (9a), the total in-plane thermomechanical stress is obtained as:

$$\sigma_{x\_total} = (E(x)/(1 - \upsilon^2))\left[\left(u_{,x} + \frac{1}{2}(w_{,x})^2 + w_{,x}\hat{w}_{,x} - w/\Re_x\right) - \alpha(x)(1 + \upsilon)T\right] \tag{9b}$$

Therefore, (3) becomes:

$$(D/h)w_{,xxxx} - \sigma_{x\_total}(w_{,xx} + 1/\Re_x) - P_z/h = 0 \tag{10}$$

To evaluate the tangential stress component σ_{x_total}, one expresses the average end-shortening Δ_x as [4, 7]:

$$\Delta_x = \frac{1}{a}\int_0^a u(x,t)_{,x}\,dx \tag{11}$$

Solving (9b) for $u_{,x}$, one obtains:

$$u_{,x} = (1-\upsilon^2)(\sigma_{x\_total}/E(x)) - \frac{1}{2}(w_{,x})^2 - w_{,x}\hat{w}_{,x} + w/\Re_x + \alpha(x)(1+\upsilon)T \tag{12}$$

In particular, the operator $\frac{1}{a}\int_0^a(\cdot)dx$ that appears in (11) is applied to (12) for the particular case of immovable edges $x = (0, a)$, that is, $\Delta_x = 0$, then the tangential stress σ_{x_total} yields:

$$\sigma_{x\_total} = \left[\frac{1}{(1-\upsilon^2)\int_0^a E(x)^{-1}dx}\right]\left[\begin{array}{l}\frac{1}{2}\int_0^a (w_{,x})^2 dx \\ +\int_0^a w_{,x}\hat{w}_{,x}dx \\ -\int_0^a \frac{w}{\Re_x}dx \\ -\int_0^a \alpha(x)(1+\upsilon)Tdx\end{array}\right] \tag{13}$$

Structural Damping Independent of Time and Temperature

Structural damping for panels consists of both material damping and frictional damping acting at the panel supports. Support damping has not been considered here, and therefore, conservative results are likely to be obtained, that is, a lower value of the flutter speed and larger LCOs than the one would occur if this additional damping component would be accounted for [24]. The most widely used material-damping models are the linear viscous and hysteresis models. It has been proved that these damping models can significantly influence the flutter boundaries and it's extremely dependent on the type of model employed. If only linear damping is considered, the work by Ellen [25] provides a useful classification of structural damping and showed which classes are always stabilizing using spatial derivatives arguments. The structural damping plays an important role in the flutter stability with low aerodynamic damping but would not affect significantly the flutter boundary with high aerodynamic damping. Fazelzadeh [22] showed that the structural damping reduced the panel domain of stability in linear analysis, whereas in nonlinear simulation, damping can have a stabilizing or destabilizing contribution.

From the mathematical point of view, structural damping independent of time and temperature can be introduced into the system by adding a term of the form $(g_{sb}\partial^{j+1}w/\partial t\partial x^j)$ to the bending terms of (10) and $(g_{sm}\partial^{j+1}w/\partial t\partial x^j)$ to the membrane terms of the (13). Herein, g_s is structural damping coefficient and it is constant for viscous damping. g_{sb} and g_{sm} are bending and membrane damping coefficients, respectively. In the following, it will be assumed that these three damping coefficients are time and temperature independent. Based on the Kelvin's model on elastic materials, $E(x)$ is replaced with the operator $E(x)(1 + g_s\partial/\partial t)$ [26, 27]. By substituting (13) in (10), the aerothermoelastic bending governing equations becomes:

$$D\left(1+g_{sb}\frac{\partial}{\partial t}\right)w_{,xxxx} - \left(1+g_{sm}\frac{\partial}{\partial t}\right) \times \left[\frac{h}{(1-\upsilon^2)\int_0^a E(x)^{-1}dx}\right] \times \left[\begin{array}{c}\frac{1}{2}\int_0^a (w_{,x})^2 dx + \int_0^a w_{,x}\hat{w}_{,x}dx \int_0^a \frac{w}{\Re_x}dx \\ -(1+\upsilon)\int_0^a \alpha(x)Tdx\end{array}\right] \times (w_{,xx} + 1/\Re_x) + \rho_m h w_{,tt} - P_z^A(x,t) = P_z^{stat}(x) \tag{14a}$$

To improve accuracy and retain additional physics into the model, one could consider a

thermoviscoelastic problem. Hilton [28] described the viscoelastic creep or relaxation functions and how this should be used in the case of thermal problems. Following Hilton one could recast the thermoviscoelastic problem using the following, general, constitutive equation:

$$\sigma_{kl}(x,t) = \int_{-\infty}^{t} E^{*}_{klmn}[x,t,t',T(x,t')]\ \varepsilon_{mn}(x,t')\ \mathrm{d}t' - \int_{-\infty}^{t} E^{T^{*}}_{kl}[x,t,t',T(x,t')]\ \alpha T(x,t')\ \mathrm{d}t' \tag{14b}$$

where E^{*} is the viscoelastic moduli, T is the temperature function, and α is the thermal expansion coefficient. The viscoelastic moduli can be described by a Prony series [28]. The first integral is the contribution of the stress from ordinary strains, while the second integral is due to the thermal stresses. Both integrals are hereditary integrals meaning that a viscoelastic material has memory. Following the development, one could include this constitutive equation into the model by re-deriving the panel stiffness, D.

Aerodynamic Modeling

The fluid-structure interaction model used here is based on the nonlinear piston theory [29]. According to this theory, the radial aerodynamic pressure p applied to the surface of the shell can be obtained by analogy with the instantaneous isentropic pressure on the face of a piston moving with velocity v_z into a perfect gas which is confined in a one-dimensional channel; this pressure is given by:

$$p^{+}(x,t)/p_{\infty} = \{1 + (\gamma-1)[(\gamma-1)/2](v_z/c_{\infty})\}^{2\gamma/(\gamma-1)} \tag{15}$$

In the analogy, the local transverse piston velocity (downwash velocity) v_z normal to the panel and the undisturbed speed of sound c_{∞} may be expressed in terms of the panel transverse displacement $w(x,t)$ in order to obtain the radial aerodynamic pressure applied to the surface of the shell as a consequence of the external supersonic flow:

$$v_z = w_{,t} + U_{\infty}[\hat{w} + w]_{,x};\quad c^2_{\infty} = \gamma p_{\infty}/\rho_{\infty} \tag{16}$$

Herein $p_{\infty}, \rho_{\infty}, U_{\infty}$,and γ are the pressure, air density, and air speed of the undisturbed flow and the isentropic gas coefficient ($\gamma = 1.4$ for dry air), respectively. To study the nonlinear panel flutter, in addition to the inclusion of geometrical nonlinearities, a nonlinear piston theory aerodynamics (PTA) model is used. PTA is a popular modeling technique for supersonic and hypersonic aeroelastic analyses [4]. Retaining, in the binomial expansions of (15), the terms up to and including $(v_z/c_{\infty})^3$ yields the pressure formula for the PTA in the third-order approximation [7]:

$$p^{+}(x,t)/p_{\infty} = 1 + \gamma(v_z/c_{\infty})\eta + [\gamma(\gamma+1)/4][(v_z/c_{\infty})\eta]^2 + [\gamma(\gamma+1)/12][(v_z/c_{\infty})\eta]^3 \tag{17}$$

The linear term of this expression corresponds to Ackeret's formula for the quasi-steady pressure on a thin profile in a supersonic flow field, whereas the quadratic term is from Busemann's formula for $M_{\infty} >> 1$. In (17), the aerodynamic correction factor $\eta = M_{\infty}/\sqrt{M^2_{\infty} - 1}$ enables one to extend the validity of the PTA to the entire low supersonic/hypersonic flight speed regime. Note that PTA provides results in excellent agreement with those based on the Euler solution and the CFL3D codes and with the exact unsteady supersonic aerodynamics theory [7]. Consider the flow only on the upper surface of the panel $U^{+}_{\infty} \equiv U_{\infty}$ and $M_{\infty} = U_{\infty}/c_{\infty}$, that is, consider $U^{-}_{\infty} = 0$ and $p^{-} = p_{\infty}$; from (15) and (17), the aerodynamic pressure difference can be expressed as:

$$\begin{aligned} P^{A}_{z}(x.t) = p^{+} - p_{\infty} = \delta p|_{PTA} = \\ -(2q_{\infty}/M_{\infty})\eta\Big\{(1/U_{\infty})w_{,t} \\ + (\hat{w}+w)_{,x} + [(1+\gamma)/4]\eta M_{\infty} \\ \times [(1/U_{\infty})w_{,t} + (\hat{w}+w)_{,x}]^2 \\ + [(1+\gamma)/12]\eta^2 M^2_{\infty} \\ \times [(1/U_{\infty})w_{,t} + (\hat{w}+w)_{,x}]^3\Big\} \end{aligned} \tag{18}$$

where the undisturbed dynamic pressure $q_{\infty} = \rho_{\infty}U^2_{\infty}/2$.

Thermal Loading

A linear temperature distribution T throughout the panel thickness is considered:

$$T(x,z) = \overset{0}{T}(x) + z\ \overset{1}{T}(x) \tag{19a}$$

Note that this temperature distribution was obtained via an exact analysis by Bolotin [21]. Using (5b) yields the thermal moment given by $E\alpha h^3\, \overset{1}{T}_{,xx}/12(1-\upsilon)$. A membrane temperature distribution $\overset{0}{T}(x)$, implying $\overset{1}{T}(x) = 0$, will be considered. This temperature distribution can correspond to the steady-state flight regime of a high-speed aerospace vehicle. Such a representation of the temperature field is adopted here to reduce the problem to an eigenvalue one [8]. Specifically, $\overset{0}{T}(x)$ is expressed as:

$$\overset{0}{T}(x) = \overset{*}{T}\cos(\pi\, x/a) \tag{19b}$$

where $\overset{*}{T}$ is the temperature amplitude.

Aeroelastic Governing Equations

Substitution of (18) and (19) into (14a) and using the nondimensional parameters, which are presented in Appendix A, one can obtain the geometrically nonlinear aerothermoelastic governing equations of infinitely long curved panels in the form of $Q\{\hat{\overline{W}}, \overline{W}(\xi,\bar{t})\} = 0$, where

$$\begin{aligned}
Q\left\{\hat{\overline{W}}, \overline{W}(\xi,\bar{t})\right\} \equiv\ & \underbrace{\left(1 + g_{sb}\Omega_0\frac{\partial}{\partial\bar{t}}\right)\left(1 + \delta_e e\overset{*}{\bar{\mathrm{T}}}T_{cr}\right)\overline{W}_{,\xi\xi\xi\xi\xi}}_{\text{bending resistance with thermal degradation effect}} - \underbrace{P_{\bar{z}}^{stat}}_{\text{pressure on plate}} - \delta_{em}\left(1 + g_{sm}\Omega_0\frac{\partial}{\partial\bar{t}}\right) \\
& \times\left[1/\int_0^1 \frac{1}{(1+\delta_e e\overset{*}{\bar{\mathrm{T}}}T_{cr})}d\xi\right]\frac{12}{\bar{h}^2}\underbrace{\left[\frac{1}{2}\int_0^1(\overline{W}_{,\xi})^2 d\xi + \int_0^1 \overline{W}_{,\xi}\hat{\overline{W}}_{,\xi}d\xi - \frac{\hat{h}}{\bar{h}}\int_0^1 \overline{W}d\xi\right]}_{\text{in-plane force due to length change}}\left(\overline{W}_{,\xi\xi} + \frac{\hat{h}}{\bar{h}}\right) \\
& + \delta_{em}\left(1 + g_{sm}\Omega_0\frac{\partial}{\partial\bar{t}}\right)\times\left[1/\int_0^1 \frac{1}{(1+\delta_e e\overset{*}{\bar{\mathrm{T}}}T_{cr})}d\xi\right]\times\underbrace{\frac{1}{(1-\upsilon)}\left[\int_0^1(1+\delta_\alpha\alpha\overset{*}{\bar{\mathrm{T}}}T_{cr})\overset{*}{\bar{\mathrm{T}}}d\xi\right]}_{\text{thermal degradation effect}} \\
& \times\left(\overline{W}_{,\xi\xi} + \frac{\hat{h}}{\bar{h}}\right) + \underbrace{\pi^4\overline{W}_{,\bar{t}\bar{t}}}_{\text{inertia effect}} + \underbrace{\frac{M_\infty\pi^4}{\bar{h}\bar{\rho}\bar{\Omega}^2}\eta\left[\begin{array}{l}\delta_{a1\bar{t}}\dfrac{\bar{\Omega}}{M_\infty}\overline{W}_{,\bar{t}} + \delta_{a1\xi}(\hat{\overline{W}}_{,\xi} + \overline{W}_{,\xi}) + \\ \dfrac{1+\gamma}{4}\eta M_\infty\left(\delta_{a2\bar{t}}\dfrac{\bar{\Omega}}{M_\infty}\overline{W}_{,\bar{t}} + \delta_{a2\xi}(\hat{\overline{W}}_{,\xi} + \overline{W}_{,\xi})\right)^2 + \\ \dfrac{1+\gamma}{12}\eta^2 M_\infty^2\left(\delta_{a3\bar{t}}\dfrac{\bar{\Omega}}{M_\infty}\overline{W}_{,\bar{t}} + \delta_{a3\xi}(\hat{\overline{W}}_{,\xi} + \overline{W}_{,\xi})\right)^3\end{array}\right]}_{\text{aerodynamic loads (3rd PTA)}} = 0
\end{aligned} \tag{20a}$$

A quick look at (20a) may suggest that only the explicit terms in $\hat{w}$ have to be included in order to obtain the equation of motion which takes into account the effects of imperfection [30]. Panels with sinusoidal curvature, in nondimensional form, may also be approximated by a sinusoidal function, in this case:

$$\hat{\overline{W}} = \hat{w}/h = \hat{\delta}\left\{\sum_{p=1}^{n} q_p \sin(p\pi\xi)\right\} \tag{20b}$$

Herein, q_p is the amplitude of geometric imperfection. To identify the effects of geometrical imperfection, edge movability, aerodynamic and thermal terms, various tracers have been adopted in the (20a) and (20b). The tracers δ_e

and δ_α identify the terms associated with the thermal degradation of the elastic modulus and the coefficient of thermal expansion, respectively. $\delta_{em} \in [0,1]$ identifies the degree of edge movability, where $\delta_{em} = 1$ indicates immovable edges. Movable edges can be simulated by assuming the panel is supported at the edges $\xi = 0$ and $\xi = 1$ by springs. In a later section of this entry, discussion of dynamic degree of movability simulation, a progressive damage, will be considered. The tracer $\hat{\delta} \in [0,1]$ indicates the implication of geometrical imperfection. The tracer δ_{ajk} has three indices: The first index (a) identifies aerodynamic contribution, the second index (j) identifies the degrees of linearity, $(1 \equiv \text{linear}, \quad 2 \equiv \text{quadratic}, \quad \text{and} \quad 3 \equiv \text{cubic})$, while the third index (k) represents the derivatives of the $\overline{W}$ with respect to $\bar{t}$ or ξ.

Solution Methodology

In the present work, Galerkin's method and direct numerical integration DNIT will be considered to solve the integro-differential equation (18) to evaluate the structural response and the character of the curved panel flutter boundary with thermoelastic-elastic properties. For the simply supported panels on $\xi = 0,\ 1$, it is required that $\overline{W} = \overline{W}_{,\xi\xi} = 0$. For these conditions, a solution can be found in the form:

$$\overline{W}(\xi,\bar{t}) = \sum_{j=1}^{n} \psi_j(\bar{t})\bar{\phi}_j(\xi) \tag{21}$$

where n number of harmonic modes, $n \leq \infty$; $\bar{\phi}_j(\xi)$ are assumed orthogonal shape functions and $\psi_j(\bar{t})$ are unknown generalized coordinates that depend on time. The assumed functions $\bar{\phi}_j(\xi)$ are chosen to satisfy the boundary conditions. To fulfill such conditions, the mode shape functions $\bar{\phi}_j(\xi) = \sin(\lambda_j \xi)$ and $\lambda_j = j\pi,\ j = 1, 2, \cdots$ are considered. Cleary, the assumed approximate solution is not exactly the same as the unknown exact solution. Consequently, (21) will not satisfy the partial differential equations (PDE) (20a), that is,

$$Q(\xi,\bar{t}) = Q\left\{\hat{\overline{W}}, \sum_{j=1}^{n} \psi_j(\bar{t})\bar{\phi}_j(\xi)\right\} = R_e(\xi,\bar{t}) \neq 0,$$

where $R_e(\xi,\bar{t})$ is the residual function that results from the use of the approximate solution. Multiplying the residual by the basic function $\bar{\phi}_r(\xi) = \sin(r\pi\xi)$ with $r = 1, 2, \ldots, n \leq \infty$ and integrating over the panel length, ξ from 0 to 1, and imposing the result to be 0, one obtains:

$$\int_0^1 R_e(\xi,\bar{t})\bar{\phi}_r(\xi)\mathrm{d}\xi = 0 \tag{22}$$

As a result of (22), a set of nonlinear, simultaneous ordinary differential equations with respect to the series in (21), and function of geometrical imperfection (20b) can be obtained:

$$\frac{\mathrm{d}^2\psi_r}{\mathrm{d}\bar{t}^2} + g\frac{\mathrm{d}\psi_r}{\mathrm{d}\bar{t}} + F_r(\psi_j, M_\infty, \overset{*}{\mathrm{T}}) = 0, \quad j,r = 1,2,3,\ldots \tag{23}$$

The $F_r(\psi_j, M_\infty, \overset{*}{\mathrm{T}})$ functions can be represented as:

$$F_r(\psi_j, M_\infty, \overset{*}{\mathrm{T}}) = F_r^{(l)}(\psi_j, M_\infty, \overset{*}{\mathrm{T}}) + F_r^{(a)}(\psi_j, M_\infty) + F_r^{(th)}(\psi_j, M_\infty, \overset{*}{\mathrm{T}}) + F_r^{(s)}(\psi_j, M_\infty) \tag{24}$$

where $F_r^{(l)}(\psi_j, M_\infty, \overset{*}{\mathrm{T}})$ are linear functions and $F_r^{(a)}(\psi_j, M_\infty)$, $F_r^{(th)}(\psi_j, M_\infty)$ and $F_r^{(s)}(\psi_j, M_\infty)$ are functions including the *a*erodynamic, *th*ermal, and *s*tructural nonlinearities, respectively.

Panel Stability in the Vicinity of the Flutter Boundary via Lyapunov First Quantity

From the mathematical point of view, the benign or catastrophic character of the flutter boundary can be revealed via determination of the nature of the supercritical or subcritical Hopf-Bifurcation, as featured by the nonlinear aeroelastic system [31, 32]. The system of governing equations obtained from (22) is converted to a system of four differential equations in state-space form expressed generically as:

$$\frac{dx_j}{dt} = \sum_{m=1}^{n} a_m^{(j)} x_m + P_j(x_1, x_2, x_3, x_4);\ j = \overline{1,4} \tag{25}$$

For the present case, the functions $P_j(x_1, x_2, x_3, x_4)$ include both the structural and aerodynamic nonlinear terms as well as the thermal damage terms. Equation (25) can be presented in a form that can then be used toward the evaluation of the Lyapunov first quantity (LFQ), that is, $L(M_F)$. Considering the solution of the linearized counterpart of (25) under the form $x_j = A_j e^{\omega t}$, one obtains the characteristic equation:

$$\omega^4 + p\omega^3 + q\omega^2 + r\omega + s = 0 \tag{26}$$

As a reminder, for steady motion, the equilibrium is stable in Lyapunov's sense if the real parts of all the roots of the characteristic equation are negative. Such an analysis can be done by applying Routh-Hurwitz's criterion. For sufficiently small values of the speed, all the roots of the characteristic equation are in the left half-plane of the complex variable, and the zero solution of the system is asymptotically stable. On the same boundary, the two roots of the characteristic equation are purely imaginary and the remaining two are complex conjugate and remain also in the

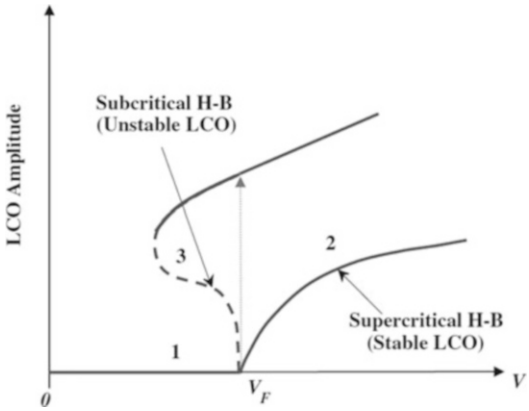

Aerothermoelastic Behavior of Flat and Curved Panels, Fig. 2 Character of the flutter boundary in the terms of LCOs amplitudes; *H-B* Hopf-Bifurcation

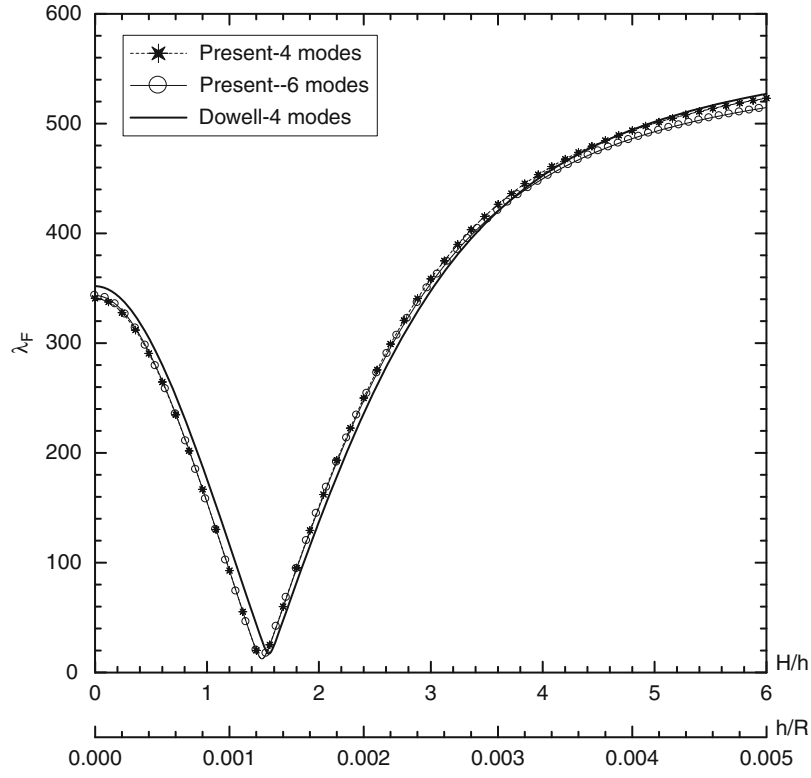

Aerothermoelastic Behavior of Flat and Curved Panels, Fig. 3 Comparison of flutter dynamic pressure versus the curvature ratio (Case #1)

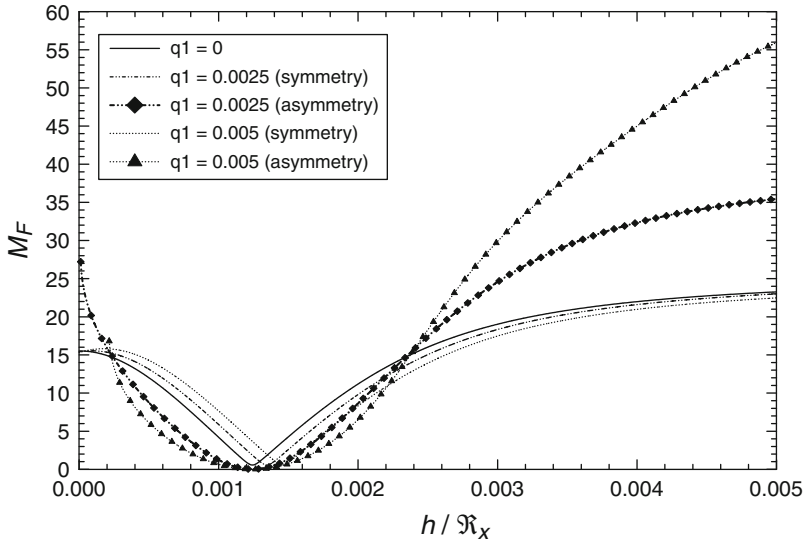

Aerothermoelastic Behavior of Flat and Curved Panels, Fig. 4 Effect of the imperfections on the flutter speed versus the curvature ratio (Case #1)

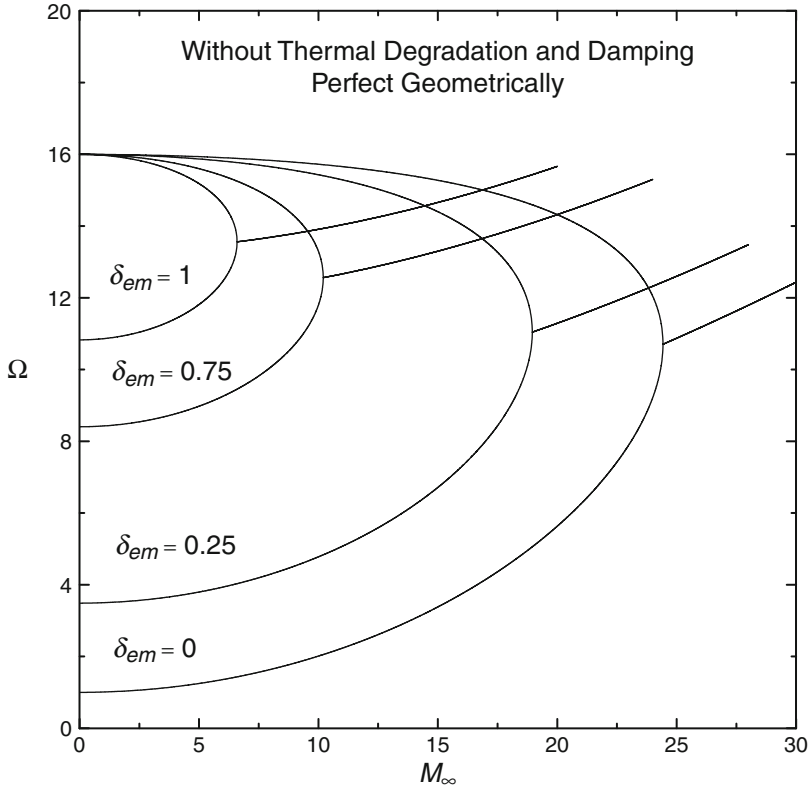

Aerothermoelastic Behavior of Flat and Curved Panels, Fig. 5 Frequency coalescence for different values of δ_{em}

left half-plane of the complex variable (Hopf-Bifurcation conditions). The nature of the LCO that provides important information on the behavior of the aeroelastic system in the vicinity of the flutter boundary can be examined by the nature of the Hopf-Bifurcation of the associated nonlinear aeroelastic system. Figure 2 presents several pertinent scenarios; $V = V_F$ defines the

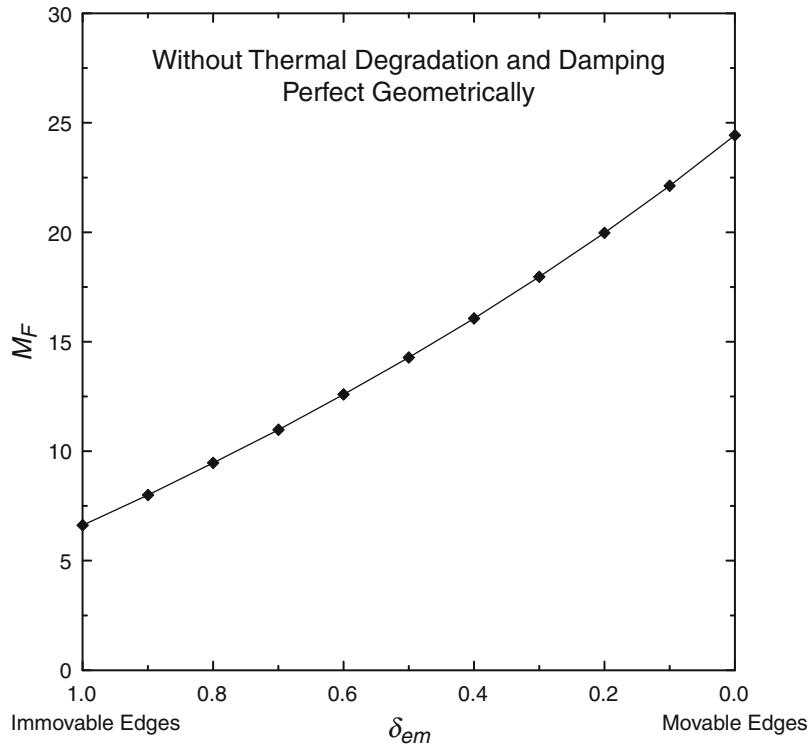

Aerothermoelastic Behavior of Flat and Curved Panels, Fig. 6 Flutter speed versus δ_{em}

flutter boundary that can be determined via a linearized analysis. The nonlinear approach to the problem enables one to determine the aeroelastic behavior in the vicinity of the flutter boundary. As a result of the nonlinear analysis, one can determine the aeroelastic behavior of the structure for a flight speed in the vicinity of the flutter speed V_F. In this sense, curve 2 corresponds to a stable LCO (supercritical Hopf-Bifurcation (H-B)) and curve 3 to an unstable LCO (subcritical Hopf-Bifurcation). In order to identify the benign and catastrophic portions of the stability boundary, it is necessary to solve the problem of stability for the system of equations in the state-space form in the critical case of a pair of pure imaginary roots and to determine the sign of the LFQ [32].

The flutter critical boundary is benign (i.e., yields stable LCO), or is catastrophic, yielding unstable LCO, if the following inequalities,

$$L(M_F) < 0, \text{ and } L(M_F) > 0 \qquad (27)$$

are fulfilled, respectively. The combination of effects from the structural and aerodynamic nonlinearities, the thermal load and thermal damage, significantly affects the character of the flutter boundary. In the region of the benign flutter boundary, one can slightly exceed the flutter critical speed M_F without catastrophic failure of the panel, and as a result, the amplitude of the transverse deflection remains limited. Conversely, in the region of catastrophic flutter boundary, an explosive type of flutter can occur.

Aerothermoelastic Behaviors of Panel

A number of numerical simulations are presented in this section. A linear analysis is performed first. The numerical simulation considers as a test case study #1, an aluminum cylindrical panel whose mechanical properties and geometric parameters are: $E = 7 \times 10^{10}$ Pa,

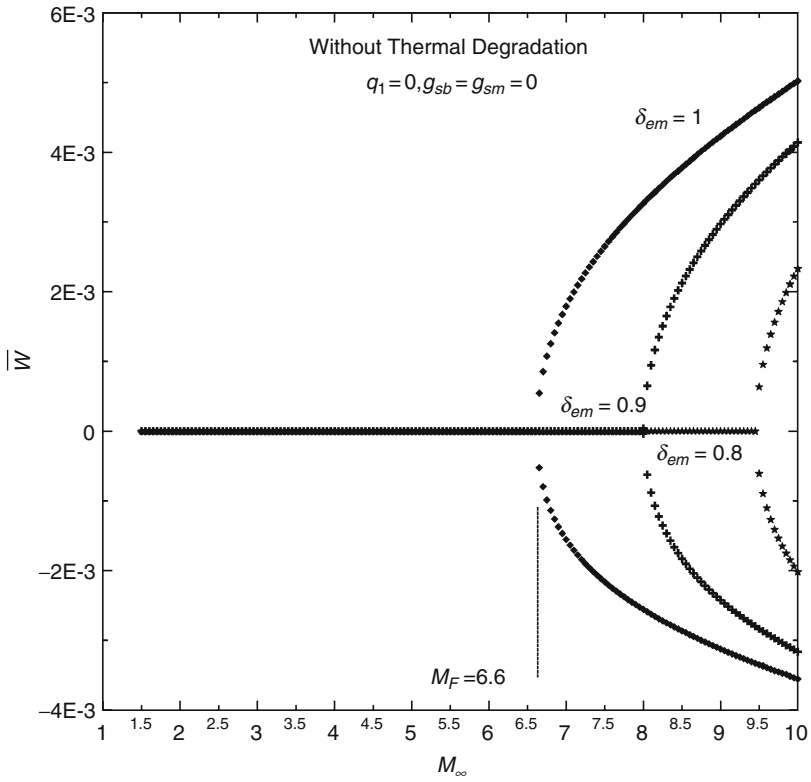

Aerothermoelastic Behavior of Flat and Curved Panels, Fig. 7 Bifurcation diagram of the aerothermoelastic curved panel (Case #2) with respect to the variation of flight Mach number and static edge degree movability (without thermal degradation and damping)

$\upsilon = 0.3$, $\rho_m = 3{,}000\,\mathrm{kg/m^3}$, $a = 1\,\mathrm{m}$, $R = 10\,\mathrm{m}$, $R/h = 1{,}000$, $\rho_\infty = 1.225\,\mathrm{kg/m^3}$, $c_\infty = 340.4\,\mathrm{m/s}$, $\gamma = 1.4$, $\eta = 1$, $P_z^{stat} = 0$, $\delta_{em} = 1$ and $q_1 = 0$. As a result, considering four modes, and without thermal degradation, the Mach flutter is $M_F = 4.2$, and the flutter frequency is $\omega_F = 3.7\,\mathrm{rad/s}$. Figure 3 reveals the implications of the curvature ratio on the normalized flutter dynamic pressure of the infinitely long cylindrical panel and compares it with that of its finite length counterpart, $\lambda_F \equiv 2q_\infty a^3/D$. The results obtained from the present analysis using four and six modes are compared with the four mode solution of Dowell [33, 34] and very good agreements are reached.

In Fig. 4, the effects of the geometric imperfection on the flutter boundary are highlighted along with the variation of curvature ratio. The results reveal that the effect of the imperfections, represented in terms of q_1, depends on the curvature ratio and the symmetric or asymmetric shape of the imperfection.

To have a clear and accurate view of the complex behavior of the aerothermoelastic system, the nonlinear dynamic behavior has been numerically simulated as a case study #2 for a monolithic titanium (Ti-6Al-4V) panel. A cylindrical panel whose mechanical properties [35] ($T = 294.15$ K) and geometric parameters are $E_0 = 110.352 \times 10^9\,\mathrm{Pa}$, $\upsilon = 0.31$, $\alpha_0 = 4.85\,{}^*10^{-5}/\mathrm{c^o}$, $\rho_m = 4,430\,\mathrm{kg/m^3}$, $a = 1\,\mathrm{m}$, $\Re_x = 10\,\mathrm{m}$, $h = 0.01\,\mathrm{m}$, $\rho_\infty = 1.225\,\mathrm{kg/m^3}$, $c_\infty = 340.4\,\mathrm{m/s}$, $\gamma = 1.4$, $\eta = 1$, $P_z^{stat} = 0$, $\delta_{em} = 1$, $e_T = -6.5764 \times 10^{-4}/\mathrm{K}$, $\alpha_T = 3.07085 \times 10^{-4}/\mathrm{K}$, $q_1 = 0$, $g_{sb} = g_{sm} = 0$ and the initial conditions are $\overline{W}_1 = 0.1$, $\overline{W}_r = \dot{\overline{W}}_r = 0$ has been considered. From these data, the following parameters are obtained: $\bar{h} = 0.01, \hat{h} = 0.001, H = a^2/(8\Re_x) = 0.0125\,\mathrm{m}$, $H/h = 1.25$, $\Omega_0 \approx 150\ (1/s)$, $t = 5\,s$, $\bar{\rho} \approx 3616$, and $T_{cr} = 1.90$ K. To investigate the effect of degree of edge movability on the linear flutter Mach number for a system

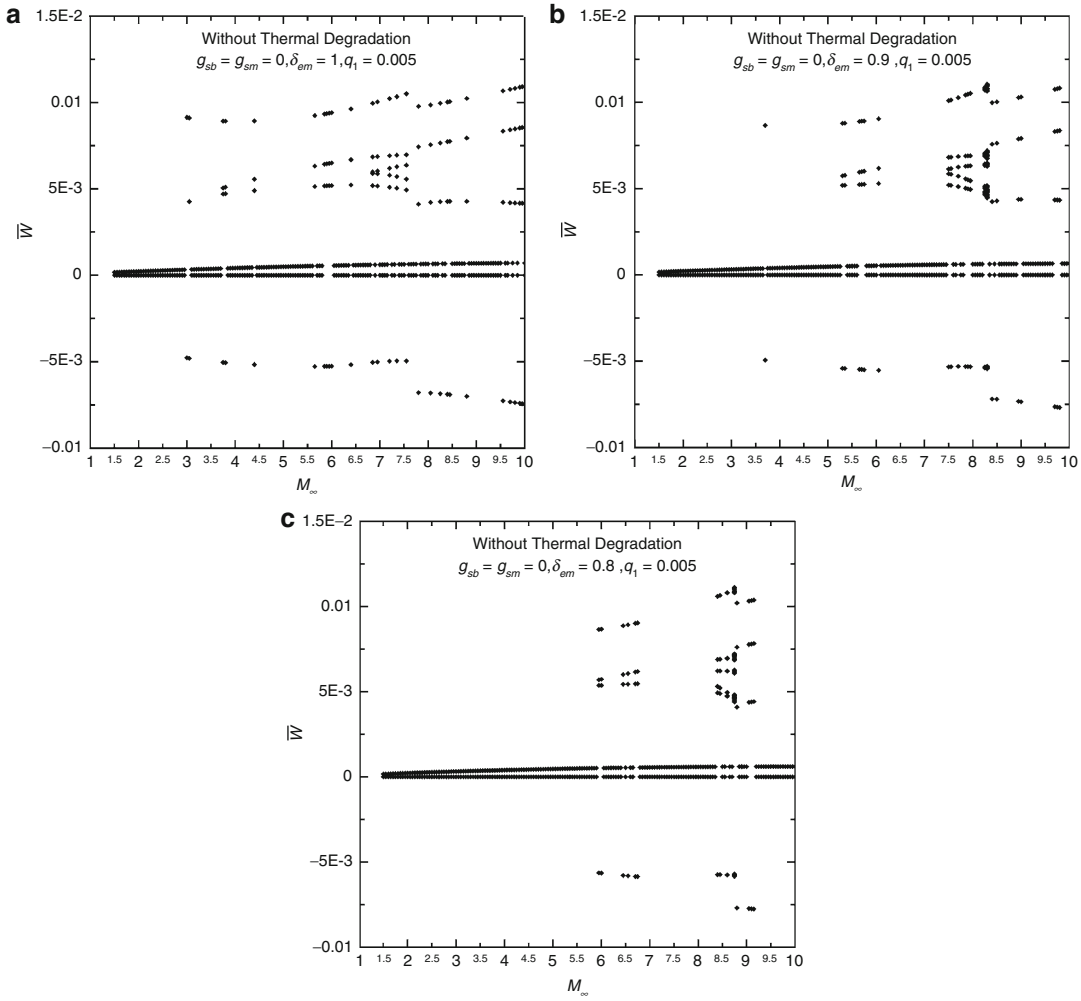

Aerothermoelastic Behavior of Flat and Curved Panels, Fig. 8 Bifurcation diagram of the aerothermoelastic curved panel (Case #2) with respect to the variation of flight Mach number and static edge degree movability (without thermal degradation and damping) under the effect of imperfections

without thermal degradation, damping, and geometrically perfect, Figs. 5 and 6 show the frequency coalescence, and the flutter speed for selected δ_{em}, respectively. It appears that the flutter speed is obtained from the coalescence of the two consecutive eigen-frequencies and this speed increases when the degree of edges movability increases, implying lower values of δ_{em}. The edge constraint effect can induce earlier flutter. This is due to the reduction in the in-plane forces, and to the panel curvature effect.

For the dynamic analysis, the nondimensional time integration was carried out from $\bar{t} = 0$ to $\bar{t} \approx 750$ time units and only the last 50 units have been retained for the bifurcation representation. The analysis was performed with no damping on the system. The linear Mach flutter (without thermal degradation) is $M_F = 6.6$, as shown in Fig. 7. It is also shown that for static partial degree of edge movability, for example, $\delta_{em} = 1; 0.9; 0.8;$ and 0.75, the flutter speed increases, meaning that the system will exhibit LCO at higher Mach numbers.

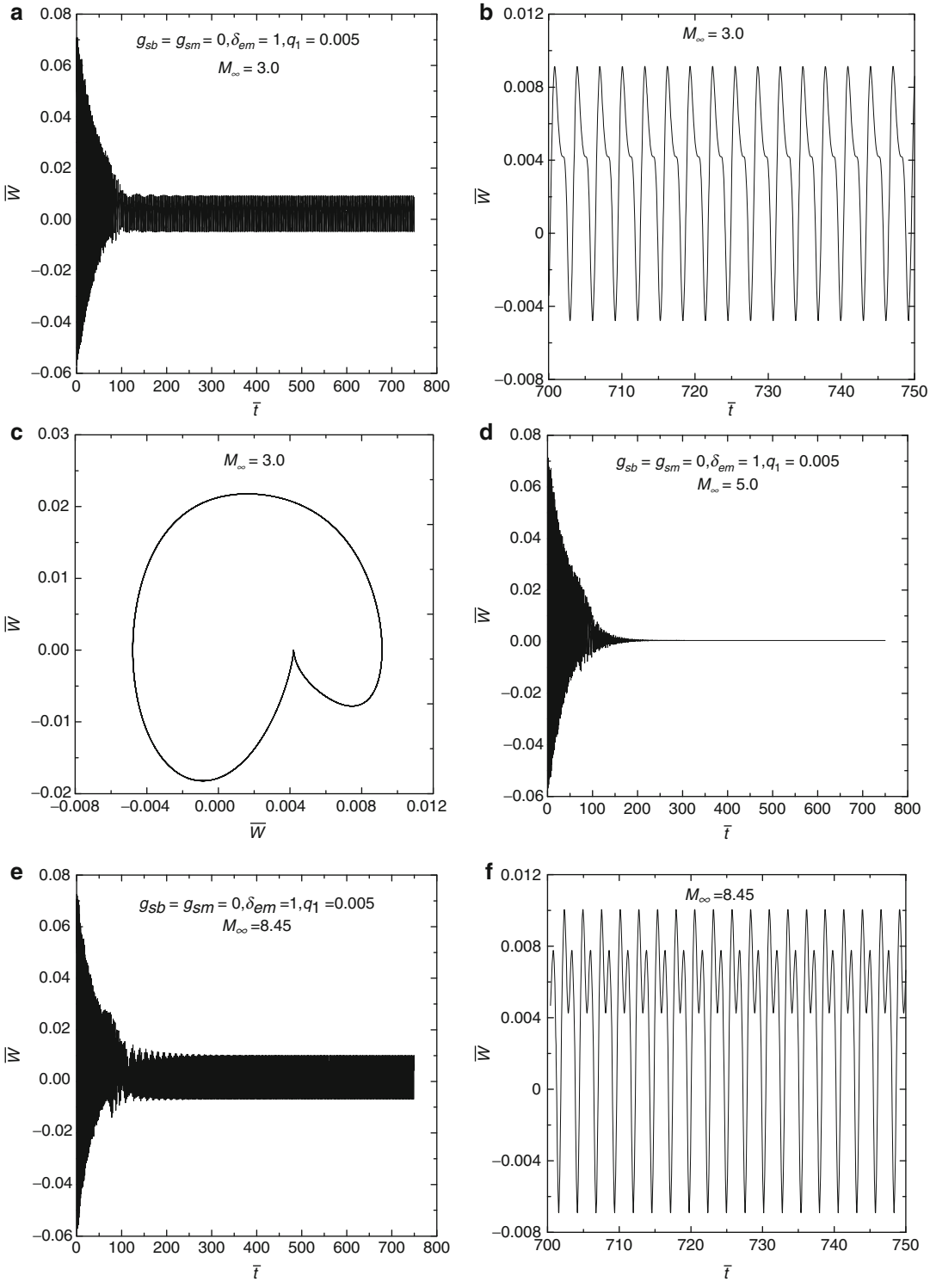

Aerothermoelastic Behavior of Flat and Curved Panels, Fig. 9 (continued)

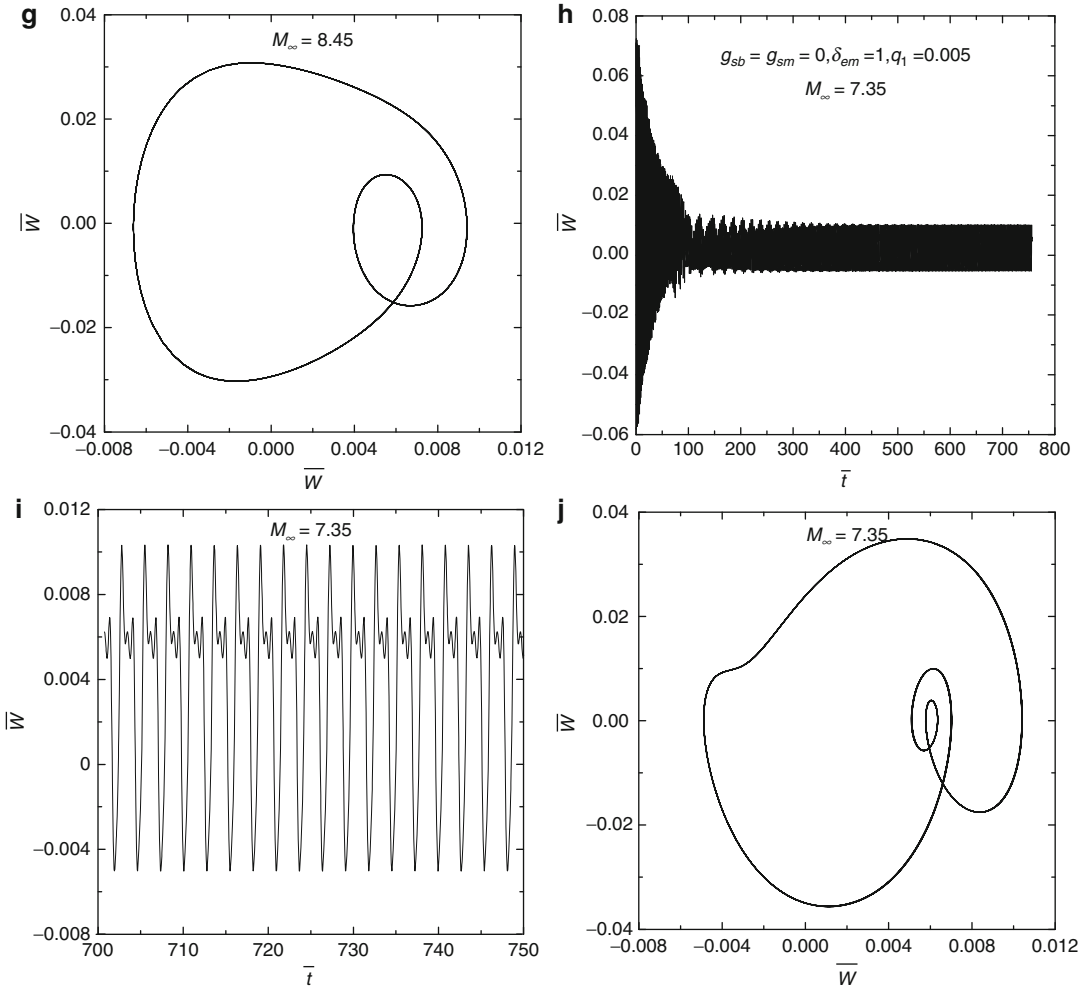

Aerothermoelastic Behavior of Flat and Curved Panels, Fig. 9 Time histories and phase portraits of the aerothermoelastic curved skin panel (Case #2) for different flight Mach number $(g_{sb} = g_{sm} = 0, \delta_{em} = 1, q_1 = 0.005)$

In the absence of structural damping and thermal degradation, the nonlinear dynamic simulation of the system exposed to geometrically imperfect $q_1 = 0.005$ has been determined as shown in Fig. 8 for different values of δ_{em} (1; 0.9 and 0.8).

Figure 9 shows the time histories (a, b, d, e, f, h, and i) and phase portraits (c, g, and j) of the considered system without damping for different flight Mach number. Imperfection can increase the LCO amplitude of the nonlinear oscillatory skin panel motion as shown in Fig. 9c, j, g or damp out as shown in Fig. 9d depending on the fluid-structure interaction behavior and on δ_{em}.

To consider the effect of heated panel, a wall temperature has been computed as follows: $\overset{*}{T} = T_w = T_\infty + R_f[(1-\gamma)/2]M_\infty^2$ where $R_f = \sqrt{\text{Pr}} \approx 0.3$ [16]. The maximum material temperature was limited to $\overset{*}{T} = T_w \approx 810$ K [35] to prevent thermal buckling. Within this constrain, in the case of heated panels, the time simulation was interrupted at $M_\infty = 5.4$. Figure 10 shows the bifurcation diagram when

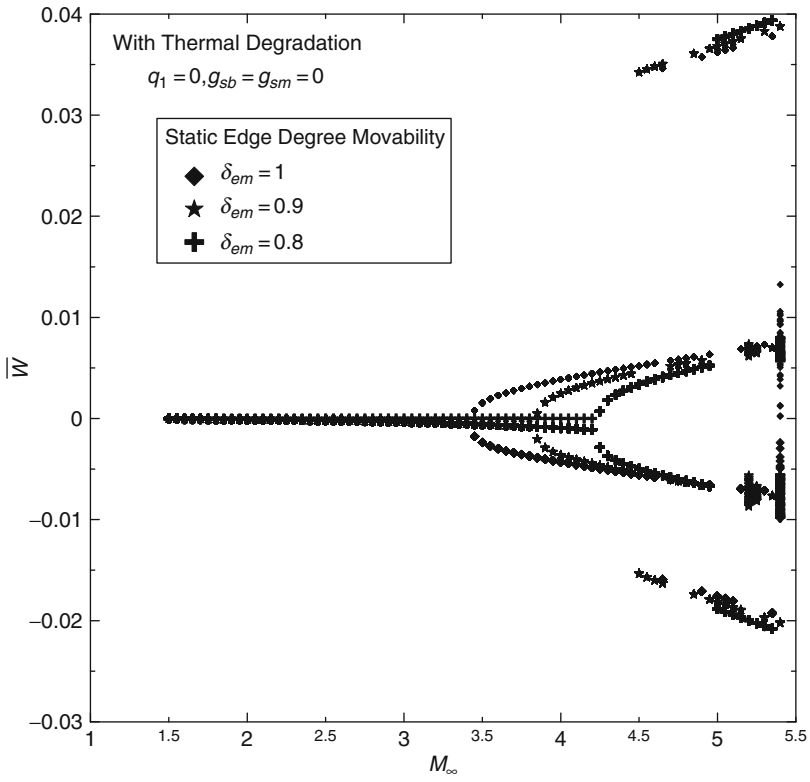

Aerothermoelastic Behavior of Flat and Curved Panels, Fig. 10 Bifurcation diagram of the aerothermoelastic curved panel (Case #2) with respect to the variation of flight Mach number and static edge degree movability (with thermal degradation and no damping)

the thermal degradation has been considered. It clearly appears that the thermal degradation reduces the flutter speed. Furthermore, limit cycles appear at speeds as low as $M_\infty \approx 3.5$ due to the temperature-dependent material degradation effect, while unheated panel will exhibit LCOs at $M_\infty > 6.6$ (linear flutter Mach number). In addition, in the case of heated panels, LCOs with large amplitude are present, as compared to the case of unheated panel, and are growing at faster rate with jumps in amplitudes above $M_\infty > 4.5$. Decreasing the static partial edge movable from immovable $\delta_{em} = 1$ toward $\delta_{em} = 0$ has a significant effect on the shifting of the nonlinear flutter boundaries and the LCO behavior.

Effect of dynamic partial edge degree movability on the behavior of the nonlinear aerothermoelastic system (Case #2) is highlighted in Fig. 11. Herein δ_{em} has been considered for linear, quadratic, and cubic variations with the time simulation, that its $\delta_{em} = a + bt$, $a + bt^2$, and $a + bt^3$, or in dimensionless form $\delta_{em} = a + b\bar{t}/\Omega_0, a + b(\bar{t}/\Omega_0)^2$, and $a + b(\bar{t}/\Omega_0)^3$, where a and b are constants. The analysis also considers that the edge might start moving at a predefined t_0 during the time simulation of the nonlinear dynamic system. This simulates the dynamic change in edge movability occurring while the system has already exhibited an LCO. The bifurcation diagrams with respect to the variation of flight Mach number, assuming $q_1 = 0$, $g_{sb} = g_{sm} = 0$, $t_0 = 0\,s$, are presented in the subsequent figures. The values $a = 1$, $b = -0.04(\text{linear})$, $b = -0.008(\text{quadratic})$, $b = -0.0016(\text{cubic})$ have been selected to represent the edge condition from immovable, $\delta_{em} = 1$, to partially movable, $\delta_{em} = 0.8$, in finite time. In addition, the edge condition from partial movable, $\delta_{em} = 0.8$, to immovable $\delta_{em}(\text{linear}) = 0.8 + 0.04t$ to reach $\delta_{em} = 1$ in finite time has been considered as well, along with the conditions $t_0 = 2.5$ and $4.5\,s$. All these

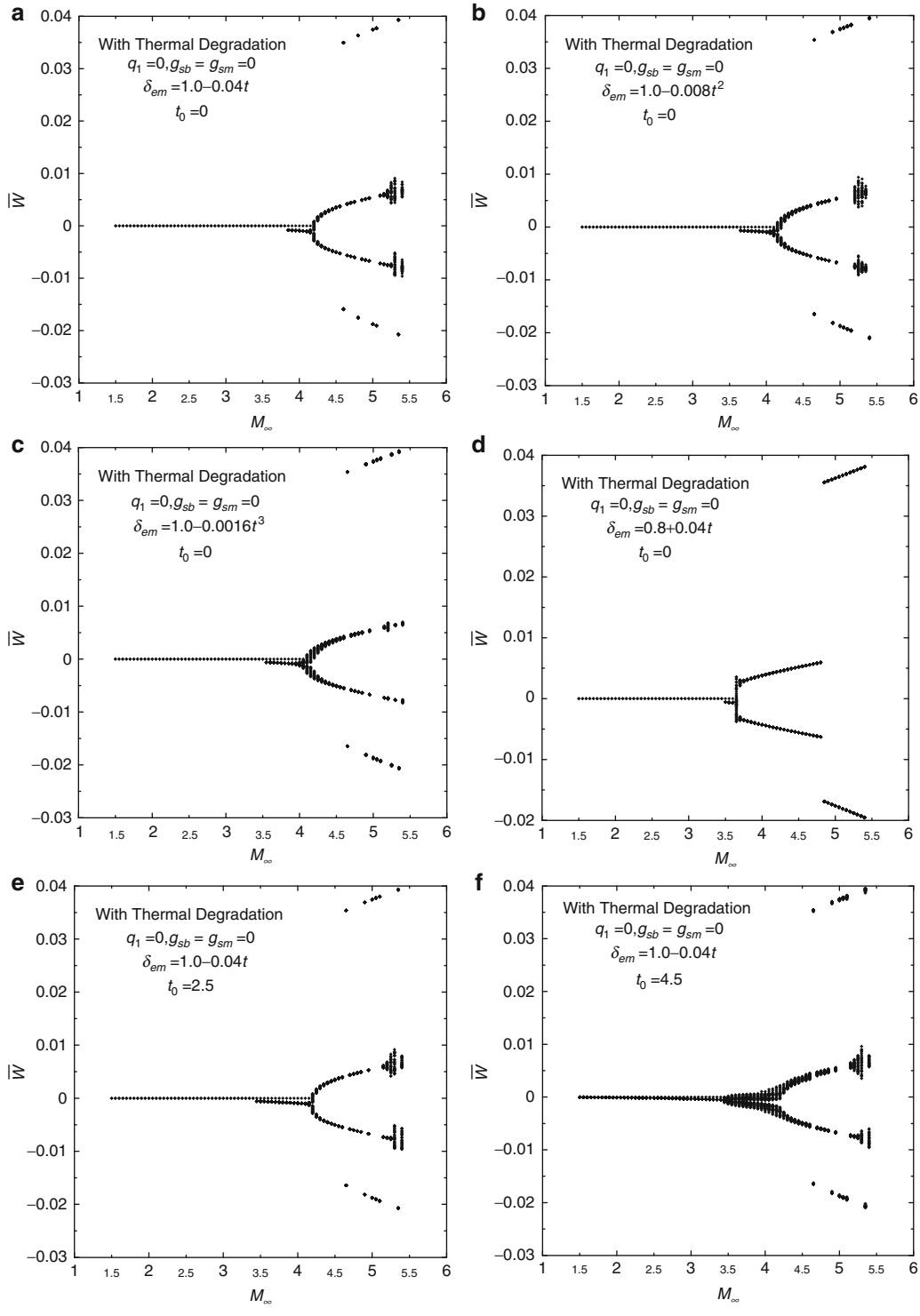

Aerothermoelastic Behavior of Flat and Curved Panels, Fig. 11 Bifurcation diagram of the aerothermoelastic curved panel (Case #2) with respect to the variation of flight Mach number, degrees of movability, and its starting time

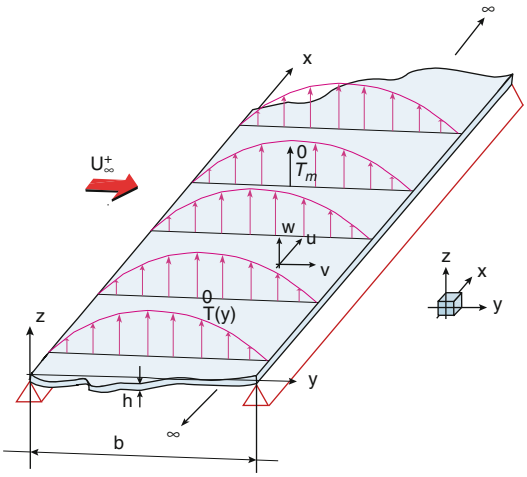

Aerothermoelastic Behavior of Flat and Curved Panels, Fig. 12 Spacecraft on reentry mission. The panels are exposed to high temperature field

selected conditions have been presented in Fig. 11a–f), respectively. Comparing these results with the one in Fig. 9 (case when $\delta_{em} = 0.8$), no significant change has been revealed from Fig. 11a–c in the behavior of the system or the amplitude of LCO when different models of δ_{em} are implemented in the simulation. In Fig. 11d, when the condition of linear variation is from partially movable to immovable, the nonlinear flutter boundary decreases with time, up to $M_\infty \approx 3.6$, significantly smaller in comparison with $M_\infty \approx 4.3$ obtained for the case of static edge movability $\delta_{em} = 0.8$. In addition, different LCO behavior is obtained and it is evident from comparing Fig. 11a with Fig. 11d. For the case when $t_0 = 2.5\,s$ (half of the simulation time), the system exhibits an LCO behavior, Fig. 11e, similar to the one shown in Fig. 11a. However, as t_0 increases, there are changes in the LCO behavior. When $t_0 = 4.5\,s$ (near the end of the time simulation), the nonlinear flutter boundary is significantly affected, evident from comparing results displayed in Fig. 11a, e, f. These simulations show that the degree of edge mobility is an important effect to consider in the flutter and post-flutter behavior of high-speed panels, and the amplitude of oscillations of the panel at the time this structural change is triggered will promote a different post-flutter behavior.

Additional numerical simulations are presented for a Ti-8 Mn [6] infinitely long thin-flat panel (see Fig. 12).

Figures 13 and 14 depict the LFQ and in this context, the benign and catastrophic post-flutter scenarios are highlighted. In these plots, the effects of the structural and aerodynamic nonlinearities considered in conjunction with that of the temperature and the thermal damage on stable/unstable LCO are emphasized. With the increase of the thermal field, the transition from benign boundary ($L(M_F) < 0$) toward catastrophic flutter boundary ($L(M_F) > 0$) occurs at lower values of the flight speed (Fig. 13). This reveals that the temperature exerts a detrimental effect not only on the flutter boundary but on the character of the flutter boundary as well. It also clearly appears that the aerodynamic nonlinearities are, in general, destabilizing. In addition, the effect of the damage on the elastic modulus is prevalent (Fig. 14), and, as a result, the occurrence of the catastrophic flutter boundary is shifted toward lower values of the flight speed.

Consideration About the Aerothermoelastic Behavior of Panel

A number of results related to the dynamic simulation of infinitely long thin-walled circular cylindrical panels featuring initial geometric imperfections and taking into consideration the thermal field and degradation due to its operation at supersonic/hypersonic speed have been presented. In this context, the implications of structural and aerodynamic nonlinearities, on the LCOs and on the character, benign or catastrophic of the panel flutter critical boundary, have been examined. The static and dynamic edge movability conditions simulating the propagation of supports degradation have been considered to explore the effect produced on the aerothermoelastic system responses. The dynamic response is either suppressed or evolves into an LCO, depending on the thermal degradation, imperfection, static or dynamic condition of edge movability, as well as the time when the edge constrain change is triggered. With the

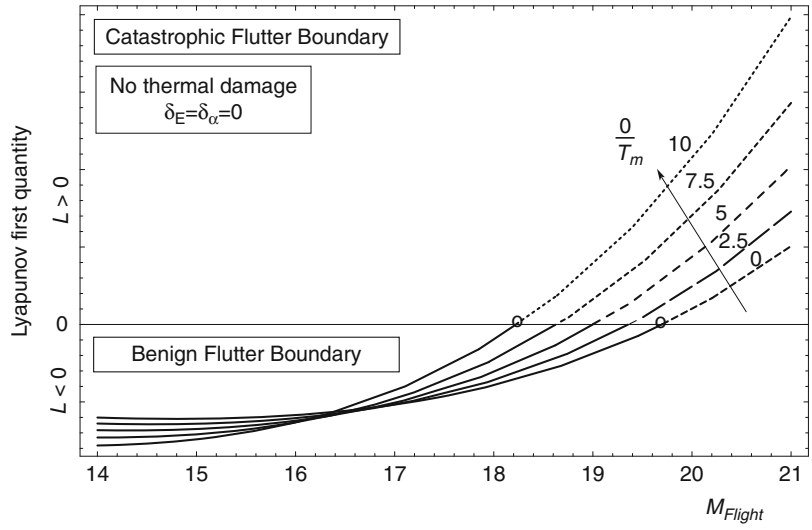

Aerothermoelastic Behavior of Flat and Curved Panels, Fig. 13 Benign and catastrophic flutter boundary. No thermal damage

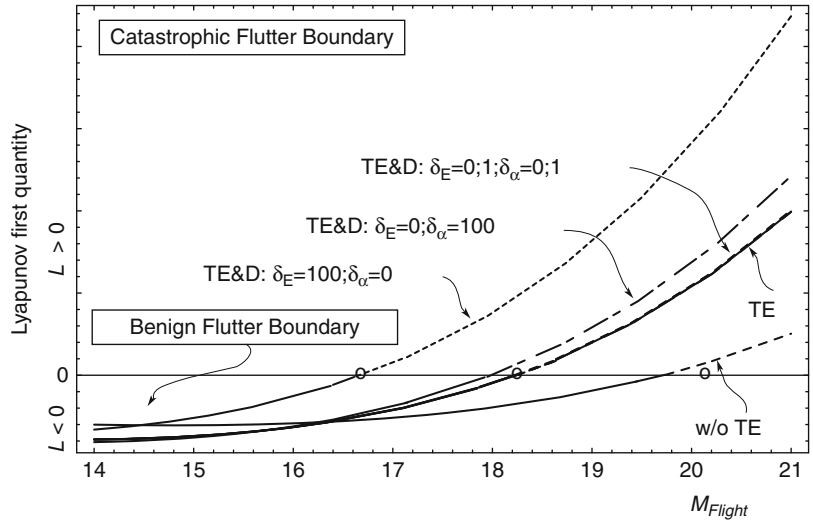

Aerothermoelastic Behavior of Flat and Curved Panels, Fig. 14 Benign and catastrophic flutter boundary. Thermal damage included

increase of the supersonic/hypersonic flight speed, when the aerodynamic nonlinearities become prevalent, the flutter boundary becomes catastrophic, irrespective of the presence of structural nonlinearities. It was also shown that the effect of temperature and thermal degradation are invariably detrimental in the sense of reducing the flutter speed and of rendering the flutter boundary a catastrophic one. In addition, as a by-product of this analysis, conclusions on the effects of the temperature field coupled with those of the thermal degradation on the eigen-frequency and flutter boundary have been outlined.

Appendix A: Dimensionless Parameters

$\overline{W} = w/a$
$\hat{\overline{W}} = \hat{w}/a$
$\bar{\xi} = x/a$
$\bar{t} = t\Omega_0$
$\Omega_0 = (\pi/a)^2\sqrt{D/\rho_m h}$
$\bar{\Omega} = \Omega_0 a/c_\infty$
$\bar{h} = h/a$
$\hat{h} = h/\Re_x$
$P_z^{stat} = \Delta P_z^{stat}(x)a^4/D_0 h$

(*continued*)

$T_{cr} = D_0/Eha^2\alpha_0$

$\bar{\rho} = (\rho_m/\rho_\infty)$

$H \approx a^2/(8\Re_x)$

$\overset{*}{\tau} = \overset{*}{T}/T_{cr}$

$\overset{*}{\mathrm{T}} = \overset{*}{\tau}\cos(\pi\xi)$

References

1. Dowell EH, Edwards J, Strganac TW (2003) Non-linear aeroelasticity. J Aircr 5(40):857–874
2. Dowell EH (1974) Aeroelasticity of plates and shells. Kluwer, Dordrecht, pp 35–49
3. Dowell EH (1972) Panel flutter. NASA SP-8004
4. Librescu L, Marzocca P, Silva WA (2002) Supersonic/hypersonic flutter and postflutter of geometrically imperfect circular cylindrical panels. J Spacecr Rocket 39(5):802–812
5. Moon FC (1992) Chaotic and fractal dynamics. Wiley, New York
6. Gee DJ, Sipcic SR (1999) Coupled thermal model for non-linear panel flutter. AIAA J 37(5):624–649
7. Librescu L, Marzocca P, Silva WA (2004) Linear/non-linear supersonic panel flutter in a high-temperature field. J Aircr 41(4):918–924
8. Fung YC (1954) The static stability of a two dimensional curved panel in a supersonic flow with an application to panel flutter. J Aeronaut Sci 21:556–565
9. Houbolt JC (1965) A study of several aerothermoelastic problems of aircraft structures in high-speed flight, vol 5, Mitteilungen Aus Dem Institute fur Flugzeugstatik und Leichtbau. Verlag Leeman, Zurich
10. Schaeffer HG, Heard WL Jr (1965) Flutter of a flat panel subjected to a non-linear temperature distribution. AIAA J 8:1918–1923
11. Ventres CS, Dowell EH (1970) Comparison of theory and experiment for non-linear flutter of loaded plates. AIAA J 8:2022–2030
12. Yang TY, Han AD (1976) Flutter of thermally buckled finite element panels. AIAA J 14:975–977
13. Xue DY, Mei C (1993) Finite element non-linear panel flutter with arbitrary temperatures in supersonic flow. AIAA J 31(1):154–162
14. Zhou RC, Xue DY, Mei C (1994) Finite element time domain modal formulation for non-linear flutter of composite panels. AIAA J 32(10):2044–2052
15. Pourtakdoust SH, Fazelzadeh SA (2005) Non-linear aerothermoelastic behavior of skin panel with wall shear stress effect. J Therm Stresses 28:147–169
16. Bein T, Friedmann PP, Zhong X, Nydick I (1993) Hypersonic flutter of a curved shallow panel with aerodynamic heating. AIAA Paper 93-1318
17. Amabili M, Pellicano F (2001) Non-linear supersonic flutter of circular cylindrical shells. AIAA J 39(4):564–573
18. Kubenko VD, Koval'chuk PS (2004) Influence of initial geometric imperfections on the vibration and dynamic stability of elastic shells. Int Appl Mech 40(88):47–877
19. Walter JH, Gerald WB, Ronald OS (1971) The influence of a high velocity fluid environment on the static and dynamic stability of thin cylindrical shell structures. In: International association for shell structures, Pacific symposium on hydromechanically loaded shells: part I, Honolulu, 10–15 October 1971
20. Bolotin VV, Grishko AA, Kounadis AN, Gantes CJ (1998) Non-linear panel flutter in remote post-critical domains. Int J Nonlinear Mech 33(5):753–764
21. Bolotin VV (1963) Stability of elastic bodies in a gas flow. In: Herrmann G (ed) Nonconservative problems of the theory of elastic stability, 1st edn. Corrected and Authorized edn. Pergamon, New York, pp 199–306 (translated from Russian)
22. Fazelzadeh SA (2004) Chaotic analysis of non-linear curved-panel flutter under supersonic flow. In: Seventh international symposium transport noise and vibration, Petersburg, 8–10 June 2004
23. Nowacki W (1986) Thermo-elasticity. Pergamon, New York
24. Bolotin VV, Grishko AA, Panov MY (2002) Effect of damping on the postcritical behaviour of autonomous non-conservative systems. Int J Nonlinear Mech 37(7):1163–1179
25. Ellen CH (1968) Influence of structural damping on panel flutter. AIAA J 6:2169–2174
26. Drozdov A (1998) Viscoelastic structures: mechanics of growth and aging. Academic, New York
27. Lottati I (1985) The role of damping on supersonic panel flutter. AIAA J 23:1640–1642
28. Hilton HH (2001) Implications and constraints of time-independent poisson ratios in linear isotropic and anisotropic viscoelasticity. J Elast 63(3):221–251
29. Ashley H, Zartarian G (1956) Piston theory – a new aerodynamic tool for the aeroelastician. J Aerosp Sci 23(10):1109–1118
30. Resende HB (1993) Hypersonic panel flutter in a rarefied atmosphere. NASA Contractor Report 4514, Grant NGL-05-020-243, May 1993
31. Librescu L (1965/1967) Aeroelastic stability of orthotropic heterogeneous thin panels in the vicinity of the flutter critical boundary. J Méc Pt I 4(1):51; Pt II 6(1):133
32. Librescu L, Marzocca P, Silva WA (2002) Post-flutter instability of a shell type structures in hypersonic flow field. J Spacecr Rockets 39(5):802
33. Dowell EH (1969) Non-linear flutter of curved plates, Part 1. AIAA J 7(3):424–431
34. Dowell EH (1970) Non-linear flutter of curved plates, Part 2. AIAA J 8(2):259–261
35. William LK (1996) Analysis of hypersonic aircraft hat-stiffened panels with varying face sheet geometry and fiber orientation. NASA Technical Memorandum 4770, December 1996

Aerothermoelastic Behavior of Lifting Surfaces

Laith K. Abbas[1], Rui Xiaoting[1] and Piergiovanni Marzocca[2]
[1]Institute of Launch Dynamics, Nanjing University of Sciences and Technology, Nanjing, People's Republic of China
[2]Department of Mechanical and Aeronautical Engineering, Clarkson University, The Wallace H. Coulter School of Engineering, Potsdam, NY, USA

Synonyms

Aerothermoelasticity; Freeplay; Hypersonic speed; Nonlinear 2D wing models; Nonlinear aerothermoelastic analysis; Piston aerodynamic theory; Thermal loading

Definitions

Aeroelasticity (*AE*) is the science which studies the mutual interactions among inertial, elastic, and aerodynamic forces acting on structural members exposed to an airstream, and the influence of this study on design.

Aerothermoelasticity (*ATE*) is the science that studies the mutual interactions among inertial, elastic, and aerodynamic forces acting on structural members under the combined effect of aerodynamic heating and loading. The design of the reentry space vehicles and high-speed aircraft structures requires special attention to the thermoelastic and aerodynamic instabilities that might occur if the mutual interaction of these forces is not properly accounted for. The combined extreme aerodynamic heating and loading that are present during high supersonic/hypersonic flights, and acting on the vehicle airframe, produces complex interactions between the flow, dynamics, structure, propulsion systems, and also control. Aerothermoelasticity considers the effect of aerodynamic heating in the framework of aeroelasticity. Similarly, the science considering the coupling of aerodynamic force, elastic deformation of the host structure, and control force is called aeroservoelasticity.

Overview

Strong interaction can occur between the flow about an aerospace vehicle and its structural components, resulting in several important aeroelastic phenomena. These aeroelastic phenomena can significantly influence the performance of the vehicle. Moreover, the tendency to reduce weight, increase structural flexibility and operating speed certainly increase the likelihood of the flutter occurrence within the vehicle operational envelope [1–7]. Aerospace systems inherently contain complex interaction of structural and aerodynamic nonlinearities [8]. These complex aeroelastic interactions can be hazardous and limit the performance of the flight vehicle because an aeroelastic system may exhibit a variety of responses that are typically associated with nonlinear regimes of response, including flutter, limit cycle oscillations (LCOs), and even chaotic vibrations [9]. Aerodynamic nonlinearities such as complex nonlinear flows with shock waves, vortices, flow separation at high angle-of-attack, and aerodynamic heating. Structural nonlinearities are subdivided into distributed nonlinearities and concentrated ones. Distributed nonlinearities are spread over the entire structure-like material and geometric nonlinearity, but concentrated nonlinearities have a local effect in a control mechanism or an attachment of external stores. Most flight vehicles (including generic missile, space shuttle, and high-performance combat aircraft) may have inherently concentrated structural nonlinearities such as freeplay, friction, hysteresis, and preload in the hinge part of their control surfaces and folded sections, etc. Concentrated structural nonlinearities may be generated from a worn or loose hinge connection of control surface, joint slippage, and manufacturing tolerance. Multipurpose military missile fin with folded mechanism may have two-axial nonlinearities at both the folding fin axis and pitch control axis. Concentrated structural

nonlinearities are generally known to cause significant instabilities in the aeroelastic responses of aero-surfaces. Among all these several nonlinearities, the freeplay usually gives the most critical flutter condition [10]. Aerothermoelastic loads have a critical role in the design of the aero-surfaces of the supersonic/hypersonic aerospace vehicles and reentry vehicles since kinetic heating at high Mach numbers can produce large reduction in structural stiffness. Depending on the temperature and initial conditions, the nonlinearities can be hardening or softening spring type. The strength of the metal is reduced after it has been in a high-temperature environment for a period of time.

Aerothermoelastic Analysis Methodology

Structural Modeling

The structural model considered is of a double-wedge two degrees-of-freedom (2-DOF) plunging-pitching lifting surface. The model is free to rotate in the xOz plane and free to translate in the vertical direction as shown in Fig. 1. While a linear model can be obtained considering linear flexural and torsional stiffnesses, herein the nonlinear restoring force and moment from bending and torsional springs accounting for freeplay in both degrees-of-freedom have been considered. The nonlinear aeroelastic governing equations can be written as:

$$m\ddot{h} + S_\alpha \ddot{\alpha} + c_h \dot{h} + F(h) = -L(t) \tag{1}$$

$$S_\alpha \ddot{h} + I_\alpha \ddot{\alpha} + c_\alpha \dot{\alpha} + G(\alpha) = M_{EA}(t) \tag{2}$$

where m is the airfoil mass per unit wing span, h is the plunging displacement at the elastic axis (EA), positive in the downward direction, S_α is the static unbalance moment about the elastic axis per unit wing span, α is the pitch angle, positive rotation nose up, c_h and c_α are the linear viscous damping coefficients in plunging and pitching, respectively, L is the unsteady lift per unit wing span, t is the physical time variable, I_α is the cross-section mass moment of inertia about its elastic axis per unit span, M_{EA} is the unsteady aerodynamic moment about the elastic axis per unit wing span, and $\dot{(\,)}$, $\ddot{(\,)}$ are first and second time derivatives. The cubic stiffness functions (restoring force $F(h)$ and moment $G(\alpha)$) [10–12] (as illustrated in Fig. 2) and can be written as follows:

$$F(h) = F_a + F_b + F_c;\; G(\alpha) = G_a + G_b + G_c \tag{3}$$

$$F_a(h) = \begin{cases} K_h h\ , \\ 0\ , \\ K_h h\ , \end{cases} \quad F_b(h) = \begin{cases} -K_h h_s\ , \\ 0\ , \\ K_h h_s\ , \end{cases}$$
$$F_c(h) = \begin{cases} \hat{K}_h (h - h_s)^3\ , & h > h_s \\ 0\ , & -h_s \le h \le h_s \\ \hat{K}_h (h + h_s)^3\ , & h < -h_s \end{cases} \tag{4}$$

where K_h, K_α are linear stiffness coefficients in plunging and pitching, respectively, $\hat{K}_h$, $\hat{K}_\alpha$ are the nonlinear cubic stiffness coefficients in plunge and pitch, respectively, and h_s is the plunging freeplay magnitude. Similar expressions for G_a, G_b and G_c can be expressed replacing the plunging variable h with the pitching variable α.

Aerodynamic Modeling

To study the behavior of the nonlinear aeroelastic system in supersonic/hypersonic aeroelastic analyses, a third-order expansion form of the piston theory aerodynamics (PTA) [3] model is used:

$$p(x,t) - p_\infty = p_\infty \left[\underbrace{\gamma (v_z/c_\infty)\eta}_{\text{Linear terms of PTA}} + \underbrace{[\gamma(\gamma+1)/4][(v_z/c_\infty)\eta]^2}_{\text{Quadratic terms of PTA}} + \underbrace{[\gamma(\gamma+1)/12][(v_z/c_\infty)\eta]^3}_{\text{Cubic terms of PTA}} \right] \tag{5}$$

where ∞ is the free stream, p is the pressure, c_∞ is the speed of sound, and η is the correction factor. Equation (5) can be used for low supersonic/hypersonic speed ($Ma_\infty \ge 1.3$) and for moderate angles-of-attack ($\alpha \le \pm 20°$). In (5) the local transverse velocity (downwash velocity) v_z normal to the airfoil surface may be expressed for upper and lower airfoil surface as follows [13, 14]:

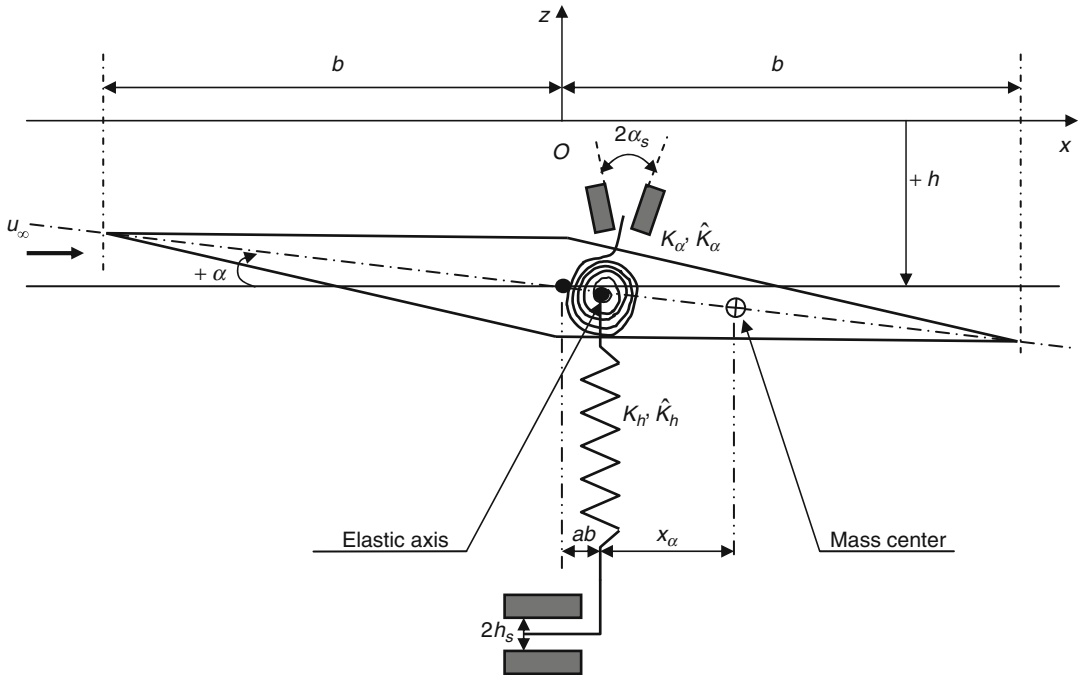

Aerothermoelastic Behavior of Lifting Surfaces, Fig. 1 Two degrees-of-freedom double-wedge airfoil geometry

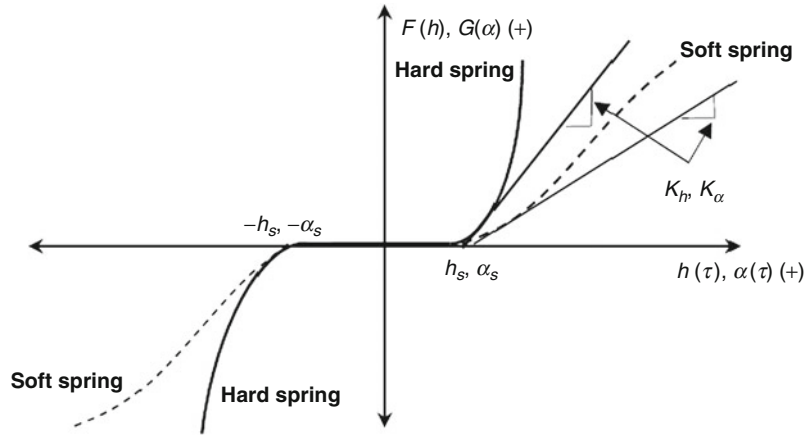

Aerothermoelastic Behavior of Lifting Surfaces, Fig. 2 Freeplay nonlinear plunge and pitch stiffness

$$v_{z,u} = -\{\dot{h} + (x - ba)\dot{\alpha}\} + u_\infty\{-\alpha + \partial f_u(x)/\partial x\};$$
$$v_{z,l} = \{\dot{h} + (x - ba)\dot{\alpha}\} - u_\infty\{-\alpha + \partial f_l(x)/\partial x\} \quad (6)$$

where $\partial f_u(x)/\partial x = \hat{\tau}$ for $-b < x < 0$; $\partial f_u(x)/\partial x = -\hat{\tau}$ for $0 < x < b$ $\partial f_l(x)/\partial x = -\hat{\tau}$ for $-b < x < 0$; $\partial f_l(x)/\partial x = \hat{\tau}$ for $0 < x < b$

In (6) a is the dimensionless offset between the elastic axis and the midchord, b is the airfoil semi-chord, $f(x)$ is the function describing airfoil surface, x being the coordinate in the chordwise direction, x is the spatial coordinate and $()_u$, $()_l$ are the airfoil upper and lower surface, respectively.

Aerodynamic Heating

The minimum value of the effective torsional rigidity stiffness (loss in the torsional rigidity) of instantaneously accelerated, double-wedge solid wings of constant chord and finite span subjected to axial stresses induced by aerodynamic heating is [15]:

$$\left(S_{eff}/S\right)_{\min} = 1 - 0.0456(E\alpha_{th}/G)\left\{\left[T_{aw}^{(f)} - T_{aw}^{(0)}\right]/\hat{\tau}^2\right\} \tag{7}$$

where S and S_{eff} are the torsional rigidity at the room temperature and the effective (apparent) torsional rigidity accounting also for the additional torsional rigidity due to aerodynamic heating, respectively. In (7), E and G are the modulus of elasticity and torsional rigidity, respectively; $\hat{\tau}$ is the airfoil thickness ratio, $T_{aw}^{(0)}$ is the initial airfoil temperature at $t = 0$ (initial flight Mach number $Ma_{\infty}^{(0)}$), $T_{aw}^{(f)}$ is the final temperature for $t>0$ (final flight Mach number $Ma_{\infty}^{(f)}$) and α_{th} is the linear coefficient of thermal expansion. In general, the adiabatic wall temperature (the concept of adiabatic wall temperature is used in the field of high velocity aerodynamics) is given by:

$$T_{aw} = T_{\infty}\left\{1 + \left[r(\gamma - 1)Ma_{\infty}^2/2\right]\right\} \tag{8}$$

where γ is the isentropic gas coefficient, ($\gamma = 1.4$ for dry air), T_{∞} is the free stream temperature at flight altitude and r is the temperature-recovery factor and in case of a turbulent boundary layer on a plate, $r = \sqrt[3]{Pr}$ for Prandtl numbers Pr close to 1. Substituting (8) into (7) with $r \approx 0.9$ and $\gamma = 1.4$, the minimum torsional rigidity is:

$$\begin{aligned}\left(S_{eff}/S_{\min}\right) &= 1 - (0.00821)(E\alpha_{th}/G)\\ &\quad T_{\infty}\left\{\left[Ma_{\infty}^{2(f)} - Ma_{\infty}^{2(0)}\right]/\hat{\tau}^2\right\}\end{aligned} \tag{9}$$

implying that the maximum reduction (in per cent) in torsional stiffness depend on: (1) material $(E\alpha_{th}/G)$; (2) geometry $(\hat{\tau})$; (3) altitude (T_{∞}); and (4) velocity $(Ma_{\infty}^{2(f)} - Ma_{\infty}^{2(0)})$. Notice that the minimum torsional rigidity is not dependent on the magnitude of the heat-transfer coefficient. The torsional frequency ω_{α} of cantilevered beam can be written, including the loss in the effective torsional stiffness, as follows:

$$\omega_{\alpha} = (\pi/2L_{\text{beam}})\sqrt{\frac{\left(S_{eff}/S\right)_{\min} * S}{I_{\alpha}}} \tag{10}$$

where L_{beam} represents the beam length.

Aeroelastic Governing Equations

Using the following dimensionless form:

$$\begin{aligned}\xi &= h/b,\ \tau = U_{\infty}t/b\\ \chi_{\alpha} &= S_{\alpha}/(mb),\ r_{\alpha}^2 = I_{\alpha}/\left(mb^2\right)\\ \omega_{\xi} &= \sqrt{K_h/m},\ \omega_{\alpha} = \sqrt{K_{\alpha}/I_{\alpha}}\\ \zeta_h &= c_h/2(K_h m)^{1/2},\ \zeta_{\alpha} = c_{\alpha}/2(K_{\alpha}I_{\alpha})^{1/2}\\ u^* &= u/(b\omega_{\alpha}),\ \bar{\omega} = \omega_{\xi}/\omega_{\alpha}\\ \hat{\eta}_h &= \hat{K}_h/K_h,\ \hat{\eta}_{\alpha} = \hat{K}_{\alpha}/K_{\alpha},\ \mu = m/\left(4\rho_{\infty}b^2\right)\\ \hat{\tau} &= t_h/b, \xi_s = h_s/b\end{aligned}$$

the system of governing equations of a supersonic/hypersonic double-wedge airfoil featuring plunging-pitching coupled motion can be described as:

$$\begin{aligned}&\xi''(\tau) + \chi_{\alpha}\alpha''(\tau) + 2\zeta_h(\bar{\omega}/u^*)\xi'(\tau)\\ &+ (\bar{\omega}/u^*)^2\bar{F}_a(\xi)\xi(\tau) + (\bar{\omega}/u^*)^2\bar{F}_b(\xi_s)\\ &+ (\bar{\omega}/U^*)^2\bar{F}_c(\xi)\left[\xi^3(\tau) + 3(-1)^n\xi_s\xi^2(\tau)\right.\\ &\left.+ 3\xi_s^2\xi(\tau) + (-1)^n\xi_s^3\right] = \bar{L}(\tau)\end{aligned} \tag{11a}$$

$$\begin{aligned}&\left(\chi_{\alpha}/r_{\alpha}^2\right)\xi''(\tau) + \alpha''(\tau) + (2\zeta_{\alpha}/u^*)\alpha'(\tau)\\ &+ \left(1/u^{*2}\right)\bar{G}_a(\alpha)\alpha(\tau) + \left(1/u^{*2}\right)\bar{G}_b(\alpha_s)\\ &+ \left(1/u^{*2}\right)\bar{G}_c(\alpha)\left[\alpha^3(\tau) + 3(-1)^n\alpha_s\alpha^2(\tau)\right.\\ &\left.+ 3\alpha_s^2\alpha(\tau) + (-1)^n\alpha_s^3\right] = \bar{M}_{EA}(\tau)\end{aligned} \tag{11b}$$

where ξ is the dimensionless plunging displacement at the elastic axis location, τ is the dimensionless time, x_{α} is the dimensionless distance between the mass center of the airfoil section and the elastic axis, ζ_h, ζ_{α} are the damping ratios in plunging and pitching respectively, $\bar{\omega}$ is the dimensionless frequency ratio, u, u^* velocity and its dimensionless counterpart (reduced velocity) respectively, ξ_s is the dimensionless plunging freeplay magnitude, r_{α} is the dimensionless radius of gyration about elastic axis, α_s is the pitching freeplay magnitude, $\hat{\eta}_h$, $\hat{\eta}_{\alpha}$ are the normalized nonlinear stiffness coefficients in plunging and pitching, respectively, μ is the reduced mass ratio, ρ_{∞} is the air stream density, t_h is the airfoil half thickness, $()'$, $()''$ are the first and second time derivatives with respect to τ and

$$\bar{F}_a(\xi)=\begin{Bmatrix}1,\\0,\\1,\end{Bmatrix}\quad \bar{F}_b(\xi)=\begin{Bmatrix}-\xi_s,\\0\ ,\\\xi_s\ ,\end{Bmatrix}$$

$$\bar{F}_c(\xi)=\begin{cases}\hat{\eta}_h\,, & \xi(\tau)>\xi_s & ,n=1\\ 0\ , & -\xi_s\le\xi(\tau)\le\xi_s & \\ \hat{\eta}_h\ , & \xi(\tau)<-\xi_s & ,n=2\end{cases} \tag{12}$$

Similar expression for $\bar{G}'s$ by replacing $\xi(\tau)\Leftrightarrow\alpha(\tau)$. The unsteady aerodynamic lift and moment appearing in (11a and 11b) can be expressed as:

$$\bar{L}(\tau)=-\frac{\eta}{12M_\infty\mu}\begin{bmatrix}12(\xi'-a\alpha'+\alpha)\\-3(\gamma+1)\hat{\tau}\eta M_\infty(\alpha')\\+M_\infty^2(\gamma+1)\eta^2\{(\xi'-a\alpha'+\alpha)\\\times[(\xi'-a\alpha'+\alpha)^2+3\hat{\tau}^2+(\alpha')^2]\}\end{bmatrix} \tag{13a}$$

$$\bar{M}_{EA}(\tau)=\frac{\eta}{12\mu M_\infty r_\alpha^2}\begin{bmatrix}12\left[a\xi'-\left(\frac{1}{3}+a^2\right)\alpha'+a\alpha\right]\\+3(\gamma+1)\hat{\tau}\eta M_\infty(\xi'-2a\alpha'+\alpha)\\-M_\infty^2(\gamma+1)\eta^2\left\{\frac{1}{5}(\alpha')^3\right.\\-a(\xi'-a\alpha'+\alpha)\\\times\left[(\xi'-a\alpha'+\alpha)^2+3\hat{\tau}^2\right]\\+\alpha'\left[(\xi'-a\alpha'+\alpha)^2\right.\\\left.\left.+\hat{\tau}^2-a\alpha'(\xi'-a\alpha'+\alpha)\right]\right\}\end{bmatrix} \tag{13b}$$

Solution Methodology

To perform the nonlinear aerothermoelastic analysis in time domain, (12) are transformed into a state-space matrix form:

$$\dot{\mathbf{y}}(\tau)=\begin{bmatrix}\boldsymbol{0} & \boldsymbol{I}\\ \boldsymbol{M}^{-1}(\boldsymbol{Q_{L2}}+\boldsymbol{Q_{NL2}}-\boldsymbol{K_L}-\boldsymbol{K_{NL}}) & \boldsymbol{M}^{-1}(\boldsymbol{Q_{L1}}+\boldsymbol{Q_{NL1}}-\boldsymbol{C})\end{bmatrix}y(\tau)-\begin{bmatrix}\boldsymbol{0} & \boldsymbol{0}\\ \boldsymbol{0} & \boldsymbol{M}^{-1}\end{bmatrix}\boldsymbol{R}(\xi_s,\alpha_s) \tag{14}$$

where $y(\tau)=\begin{Bmatrix}\xi(\tau)\\ \alpha(\tau)\\ \dot{\xi}(\tau)\\ \dot{\alpha}(\tau)\end{Bmatrix}$, $\boldsymbol{R}(\xi_{s,\alpha s})=\begin{Bmatrix}0\\0\\Q_f(1,1)\\Q_f(2,1)\end{Bmatrix}$

Herein $\boldsymbol{y}$ is the state vector and $\boldsymbol{M}$ is the mass matrix. $\boldsymbol{K_L}$ and $\boldsymbol{K_{NL}}$ in (14) represents the linear and nonlinear stiffness matrices, while the aerodynamic damping and stiffness matrices $\boldsymbol{Q_{NL1}}$ and $\boldsymbol{Q_{NL2}}$ contain both uncoupling and coupling nonlinear quadratic and cubic terms, respectively. The matrices $\boldsymbol{Q_{NL1}}$ and $\boldsymbol{Q_{NL2}}$ include the damping and stiffness aerodynamic linear terms, respectively, $\boldsymbol{R}$ and $\boldsymbol{Q_f}$ are the freeplay force/moment vectors. Reference [16] gives the matrices of (14) in detail. A numerical simulation using the fifth to sixth Runge-Kutta Fehlberg time integration scheme with step size control is carried out for the system in (14). This numerical integration technique provides both transient and steady-state responses for prescribed initial conditions.

Aerothermoelastic Behaviors of Lifting Surfaces

To emphasize the importance of aerodynamic heating on the nonlinear aerothermoelastic behavior of the examined aeroelastic system in the presence of an initial structural freeplay, the influence of the loss in effective torsional stiffness of a solid thin double-wedge wing has been analyzed. Selected bifurcation diagrams are presented from the response amplitude as a function of the flight Mach number, see Fig. 3.

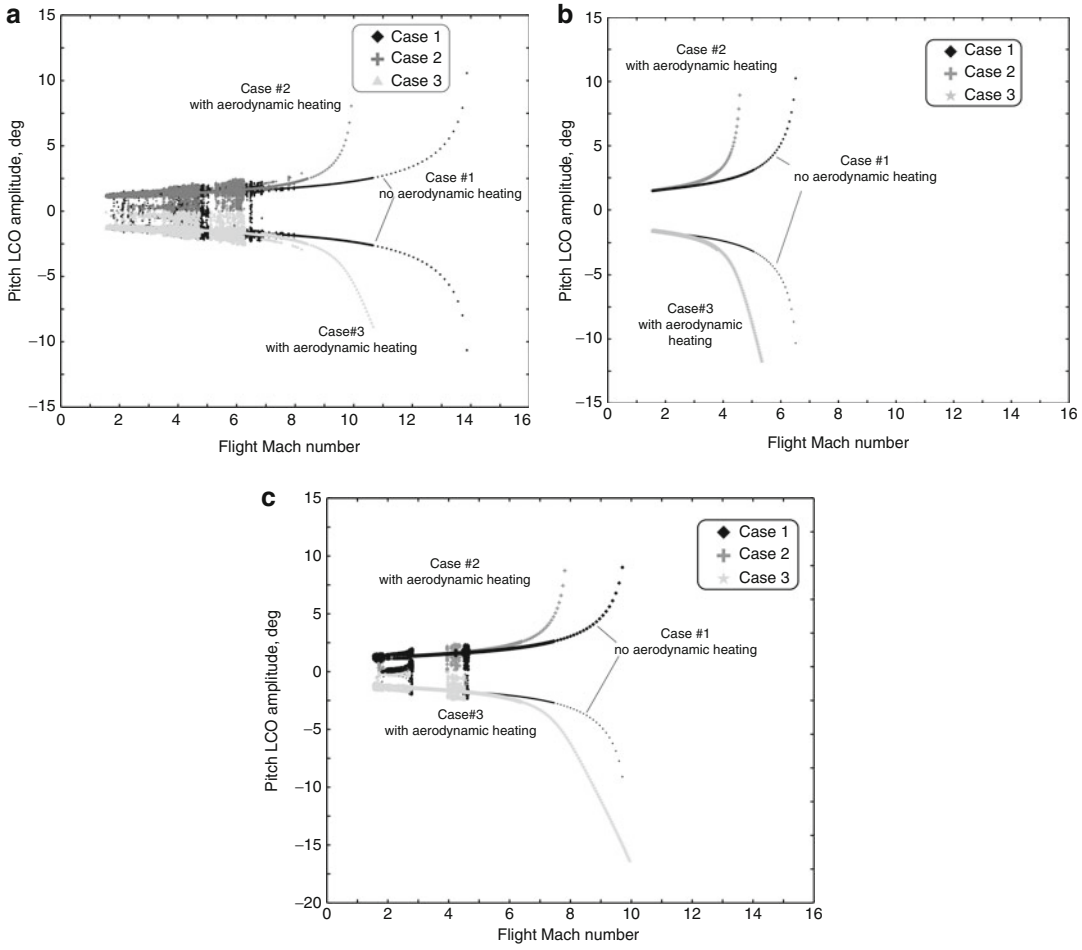

Aerothermoelastic Behavior of Lifting Surfaces, Fig. 3 Bifurcation pitch diagrams

The baseline parameters of 2DOF plunging-pitching airfoil are presented as follows:

1. Mechanical properties: titanium (Ti-6%Al-4%V), mass density $\rho = 4{,}420$ kg/m^3, TEC (0–100 C^0) 8.8×10^{-6}/K, TEC (0–300 C^0) 9.2×10^{-6}/K, modulus of elasticity $E = 114 \times 10^9$ N/m^2, modulus of rigidity $G = 43.51 \times 10^9$ N/m^2, Poisons' ratio $\vartheta = 0.31$.
2. Flight condition: height $H = 5$, 10 km, $\rho_\infty = 0.736$, 0.4135 kg/m^3, $c_\infty = 317.07$, 299.53 m/s, $T_\infty = 255.7$, 223.26 K, $\eta = 1.0$, $\gamma = 1.4$.
3. Airfoil geometry parameters: rectangular shape, wing aspect ratio $A_R = 4.5$, $b = 0.25$ m, $\hat{\tau} = 0.05, 0.1$, m $= 55.2$ kg/m.
4. Airfoil physical parameters: $\chi_\alpha = 0.25$, $r_\alpha = 0.5$, $\zeta_h, \zeta_\alpha = 0$, $a = -0.25$.
5. Cubic stiffening: $\hat{\eta}_h, \hat{\eta}_\alpha = 0, 20$.
6. Initial condition: $\xi(\tau = 0) = \dot{\xi}(\tau = 0) = \dot{\alpha}(\tau = 0) = 0$, $\alpha(\tau = 0) = 5^\circ$.
7. Initial freeplay: $\alpha_s = 1.0^\circ$, $\xi_s = 0.01$.

Three cases were performed to demonstrate the complex nonlinear behaviors of the system. Case #1 is for a system with no aerodynamic heating and ($\hat{\eta}_h = \hat{\eta}_\alpha = 0$), such that linear flutter Mach number $Ma_{\mathrm{LF}} = 15.2$. Case # 2 is for the system with aerodynamic heating and $\hat{\eta}_h = \hat{\eta}_\alpha = 0$ yielding $Ma_{\mathrm{LF}} = 10.4$. Because of the symmetry in the pitch LCO amplitude only, the positive side of the LCO curve is presented

Aerothermoelastic Behavior of Lifting Surfaces,

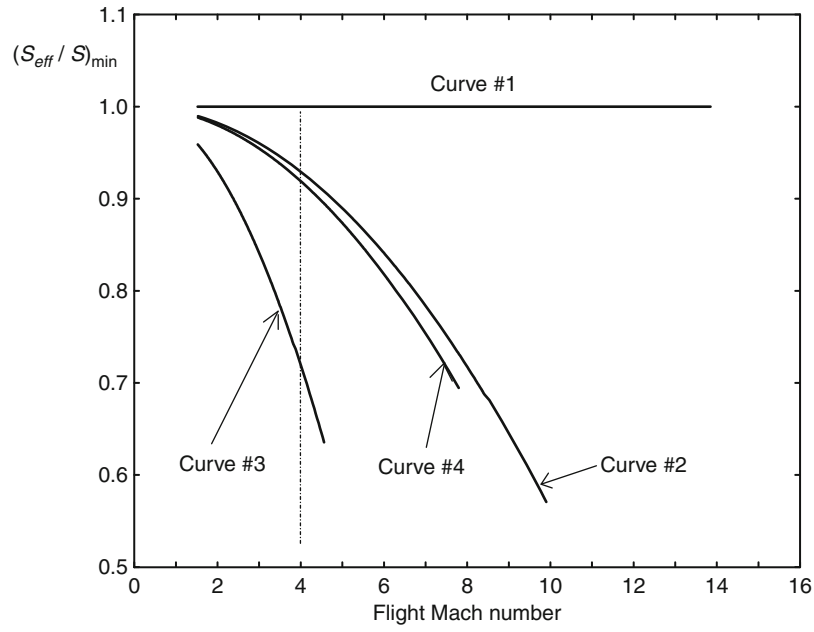

Fig. 4 Reduction in torsional stiffness for solid double-wedge wing due to aerodynamic heating. Effect of thickness ratio and altitude

for Case #2. Case # 3 is for a system with aerodynamic heating and ($\hat{\eta}_h = 0, \hat{\eta}_\alpha = 20$) and the flutter speed is the same as Case #2. For this case, for the sake of clarity, the negative side of the pitch LCO is displayed. Note that the simulations are restricted to cases where the pitching displacement is within $\pm 20°$ to remain within the limits of validity of the proposed model and approach. In Fig. 3a, where the altitude is 10,000 m and $\hat{\tau} = 0.1$, the aeroelastic system exhibits a bifurcation behavior for all three cases at $Ma_\infty \approx 1.5$ due to the presence of coupling freeplays (in both plunge and pitch). For the speed range ($1.5 < Ma_\infty \leq 7$), different types of response behavior (periodic, quasiperiodic, or chaotic) will occur. Within the speed ranges ($7 < Ma_\infty \leq 14$) for Case #1, ($7 < Ma_\infty \leq 10$) for Case #2, and ($7 < Ma_\infty \leq 11$) for Case #3, a stable LCO is experienced; its amplitude increases with the increase of the flight Mach number. From Fig. 3a, it appears that pitch LCO amplitude for Case #1 is less than 12 deg for speed less than the linear flutter speed. When considering Case #2, the pitch amplitude is about 10° at $Ma_\infty \approx 10$, while if the pitching stiffness nonlinearity is considered, Case #3, the pitch amplitude reaches 10° at $Ma_\infty \approx 11$. This result reveals that the flutter speed, as well as the LCO behavior, is affected by the loss of the torsional stiffness. The effect of varying the thickness ratio is indicated in Fig. 3b. Herein, the altitude is 10,000 m and $\hat{\tau} = 0.05$. A stable LCO is experienced for all three cases. Although the system accounts for freeplays, no chaotic behavior is encountered. Decreasing the thickness ratio has a significant effect on the linear flutter value. This fact is evident in Fig. 3b where $Ma_{\mathrm{LF}} = 7.2$ for the same Case #1 of Fig. 3a but with a smaller thickness ratio. In addition, the linear flutter for Cases #2 and #3 decreases to $Ma_{\mathrm{LF}} = 4.8$. Although in Case #3 the pitching stiffness nonlinearity is considered and contributes to decrease the amplitude of the LCO as compared to Case # 2 (compare the value of the pitching LCO amplitude at $Ma_\infty \approx 5.5$), there is certainly a detrimental reduction in flutter speed as well as the amplitude of the LCO as compared to the corresponding Cases #2 and #3 of Fig. 3a. Results for a flight altitude of 5,000 m and $\hat{\tau} = 0.1$ are also presented in Fig. 3c. The three cases present a different behavior: $1.5 < Ma_\infty \leq 3$ (periodic LCO), $3 < Ma_\infty \leq 4$ (stable LCO), $4 < Ma_\infty \leq 5$ (chaotic behavior)

for all three cases. For $Ma_\infty > 5$: Case #1, $5 < Ma_\infty \leq 10$ (stable LCO, $Ma_{LF} = 10.6$); Case #2 which accounts for the influence of aerodynamic heating, $5 < Ma_\infty \leq 8$ (stable LCO, $Ma_{LF} = 8.3$); Case #3 which accounts for both aerodynamic heating and pitch stiffening nonlinearity, $5 < Ma_\infty \leq 10$ (stable LCO, $Ma_{LF} = 8.3$). In Fig. 4, the curves show how susceptible this system is to loss of torsional stiffness when aerodynamic heating is considered in conjunction with altitude, thickness ratios. Case #1 (5,000 and 10,000 m) does not include the aerodynamic heating; therefore, there is no reduction in the effective torsional stiffness. For flight Mach number $Ma_\infty \approx 4$, Case #2 (10,000 m and $\hat{\tau} = 0.1$), and #4 (5,000 m and $\hat{\tau} = 0.1$) and Case #3 (10,000 m and $\hat{\tau} = 0.05$), which also included the aerodynamic heating, present a reduction in torsional stiffness of 5 %, 7 %, and 25 % of the original value, respectively. Clearly, the thickness ratio has a more detrimental role in the loss in torsional stiffness and consequently in the flutter speed and the LCO behavior of the examined aeroelastic lifting surface.

Consideration About the Aerothermoelastic Behavior of Lifting Surfaces

Aerodynamic heating significantly influences the nonlinear aerothermoelastic behavior of lifting surfaces. A solid thin double-wedge airfoil encountered all nonlinearities (structural-freeplay and cubic stiffness, aerodynamic-third order piston theory) in the supersonic/hypersonic flight speed regime is considered in the selected results reported under this section. The results show how susceptible flutter speed, as well as the LCO behavior, is to loss of torsional stiffness when aerodynamic heating is considered in conjunction with altitude and thickness ratios. The thickness ratio has a more detrimental role in the loss in torsional stiffness and consequently in the flutter speed and the LCO behavior of the examined aeroelastic lifting surface.

References

1. Marzocca P, Librescu L, Chiocchia G (2002) Aeroelastic response of 2-D lifting surfaces to gust and arbitrary explosive loading signatures. Int J Impact Eng 25(1):41–65
2. Marzocca P, Librescu L, Silva WA (2002) Aeroelastic response of nonlinear wing section by functional series technique. AIAA J 40(5): 813–824
3. Marzocca P, Librescu L, Silva WA (2002) Flutter, post-flutter and control of a supersonic 2-D lifting surface. J Guid Control Dynam 25(5):962–970
4. Librescu L, Marzocca P, Silva WA (2002) Post-flutter instability of a shell type structures in hypersonic flow field. J Spacecr Rocket 39(5):802–812
5. Librescu L, Chiocchia G, Marzocca P (2003) Implications of cubic physical/aerodynamic nonlinearities on the character of the flutter instability boundary. Int J Nonlinear Mech 38(3):173–199
6. Librescu L, Na S, Marzocca P et al (2003) Active aeroelastic control of 2-D wing-flap systems in an incompressible flow field. 44th AIAA/ASME/ASCE/AHS structures, structural dynamics, and materials conferences. AIAA, Norfolk, pp 1414–1425
7. Qin Z, Marzocca P, Librescu L (2002) Aeroelastic instability and response of advanced aircraft wings at subsonic flight speeds. Aerosp Sci Technol 6(3):195–208
8. Dowell EH (1978) A modern course in aeroelasticity. Sijthoff and Noordhoff, Rockville
9. Dowell EH, Edwars J, Strganac T (2003) Nonlinear aeroelasticity. J Aircr 40(5):857–874
10. Hyun DH, Lee I (2000) Transonic and low-supersonic aeroelastic analysis of a two-degree-of-freedom airfoil with a freeplay non-linearity. J Sound Vib 234(5):859–880
11. Lee BHK, Price SJ, Wong YS (1999) Nonlinear aeroelastic analysis of airfoils: bifurcation and chaos. Prog Aerosp Sci 35(3):205–334
12. Zhao YH, HU HY (2004) Aeroelastic analysis of a non-linear airfoil based on unsteady vortex lattice model. J Sound Vib 276(3–5):491–510
13. Ashley H, Zartarian G (1956) Piston theory – a new aerodynamic tool for the aeroelastician. J Aerosp Sci 23(10):1109–1118
14. Thuruthimattam B, Friedmann P, Mcnamara J et al (2002) Modeling approaches to hypersonic aeroelasticity. In Proceedings of IMECE'02. American Society of Mechanical Engineers, New Orleans, pp 32943–32955
15. Budiansky BMJ (1956) Influence of aerodynamic heating on the effective torsional stiffness of thin wings. J Aeronaut Sci 23(12):1081–1093, 1108
16. Laith K, Abbas CQ, Marzocca P et al (2007) Numerical studies of a nonlinear aeroelastic system with plunging and pitching freeplays in supersonic/hypersonic regimes. Aerosp Sci Technol 11(5): 405–418

Aerothermoelastic Behaviors of Functionally Graded Panel Structures

Piergiovanni Marzocca[1], Seyyed Ahmad Fazelzadeh[2] and Mohammad Hosseini[3]
[1]Department of Mechanical and Aeronautical Engineering, Clarkson University, The Wallace H. Coulter School of Engineering, Potsdam, NY, USA
[2]Department of Mechanical Engineering, Shiraz University, Shiraz, Iran
[3]Department of Mechanical Engineering, Sirjan University of Technology, Sirjan, Iran

Synonyms

Aerothermoelasticity

Overview

The static and dynamic behavior of FGM panels depends on their material, geometrical, and structural properties. In this section, examples for a wide range of nondimensional aerodynamic pressure and panel curvature in conjunction with selected values of temperature fields through the thickness and several panel volume fraction indexes are presented. The transient solutions are discarded in calculations and steady-state data are used to distinguish panel dynamic behavior. The variation of volume fraction index makes different types of motions including divergence, limit cycle oscillation (LCO), and periodic and chaotic motions possible.

Static Behavior of FGM Panels: Thermal Divergence

The effect of the aspect ratio, the relative thickness, in conjunction with the steady aerodynamic pressure and the volume fraction index of FGMs on thermal divergence of supersonic panels is presented in [1]. A few characteristic results are presented here. For such analysis, a mathematical formulation based on the first-order shear deformation theory was developed. The Galerkin approach is used to reduce the system of PDE into a set of ODEs which are then solved by standard eigenvalue algorithm to determine the critical temperature difference and divergence boundary. The FGM used is composed of alumina and aluminum. Young's modulus, Poisson's ratio, and coefficient of thermal expansion for aluminum are $E_m = 70\,GPa$, $v = 0.3$, $\alpha_m = 23 \times 10^{-6}\,(1/^{\circ}\mathrm{C})$ and for alumina $E_c = 380\,GPa$, $v = 0.3$, and $\alpha_m = 7.4 \times 10^{-6}\,(1/^{\circ}\mathrm{C})$, respectively. The plate is assumed to be simply supported on all of its four edges. The critical temperature difference for functionally graded plates and the influence of aerodynamic pressure and temperature distribution are presented in Figs. 1 and 2 which demonstrate the divergence boundaries, $\lambda - \Delta T_{cr}$, for several design parameters. For all of the parameters, left and right sides of these boundaries show the stable and divergence regions, respectively. In particular, the effect of the aspect ratio and volume fraction index on the divergence boundaries is investigated in Fig. 2. A lower value of a/b reduces the critical buckling temperature. Therefore, stable regions are extended to the right for a higher aspect ratio at the fixed volume fraction index. The divergence boundaries of the square plate, for several volume fraction indexes with uniform and linear temperature distributions, are shown in Fig. 3. Results indicate that the stable regions are extended for the linear temperature model. This is because the bending moments generated by thermal loads in the linear temperature distribution model tend to cause the plate to remain flat before buckling.

One of the interesting results obtained in the static instability regime is some snap-through behavior that is due to small changes in the nondimensional aerodynamic pressure. This is due to the fact that in some physical parameter intervals, there are two possible steady-state motions coexisting, which one will occur depends on the physical parameter or the initial conditions [2, 3]. For the considered problem, the panel can

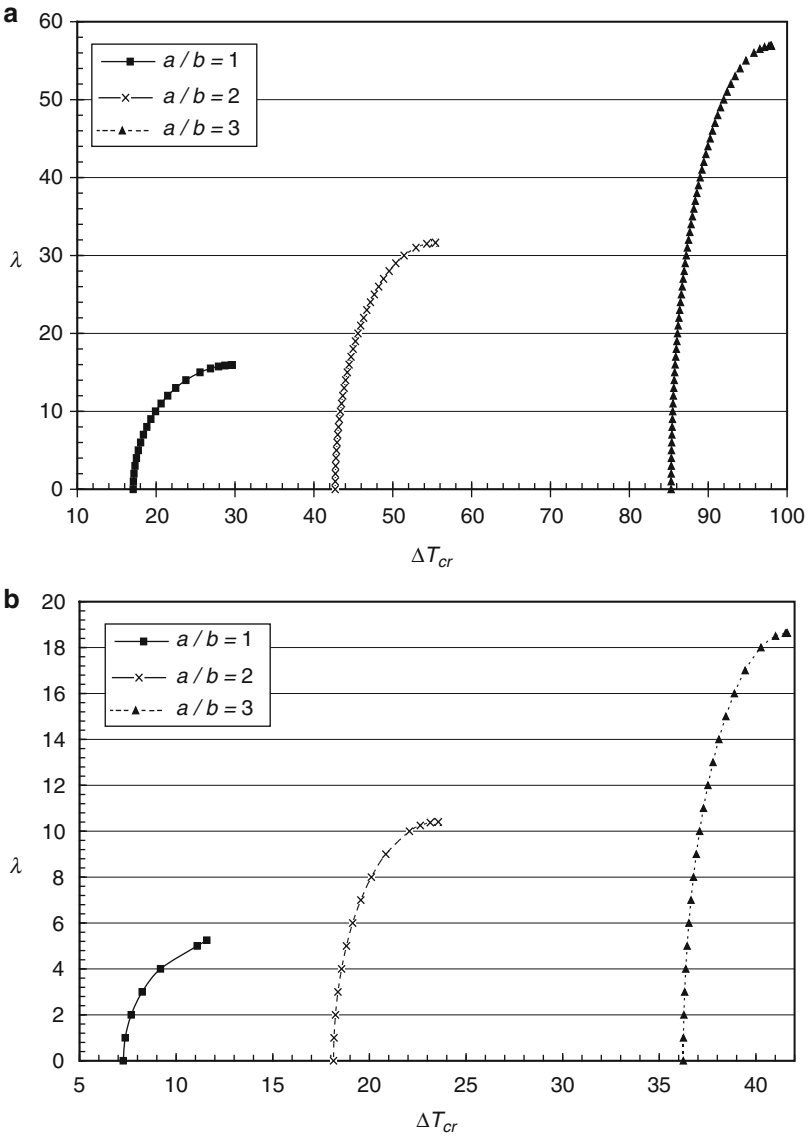

Aerothermoelastic Behaviors of Functionally Graded Panel Structures, Fig. 1 Effect of aspect ratios a/b and critical temperature on non-dimensional aerodynamic pressure λ for $h/a = 0.01$ and various volume fraction parameter: (**a**) $k = 0$; (**b**) $k = 5$

buckle upward or downward and the numerical simulation follows either one of the two, depending on the initial conditions, as shown in Fig. 4.

Dynamic Behavior of FGM Panels: Limit Cycle and Chaotic Analysis of Flat Panels

A functionally graded flat panel with infinite length in y-direction, an $h/a = 0.01$, and with immovable simply supported boundary along the y-direction is investigated [4]. A few characteristic results are presented here. Different values of volume fraction indexes are considered to investigate the effect on panel dynamic behavior. The numerical study is carried out to supply information on the nonlinear bending of the plates with different combinations of loading conditions. To this end, silicon nitride and stainless steel are chosen to be the constituent materials of the FGM plate, referred to as Si3N4/SUS304. Their material properties such as Young's modulus and thermal expansion coefficient are assumed to be

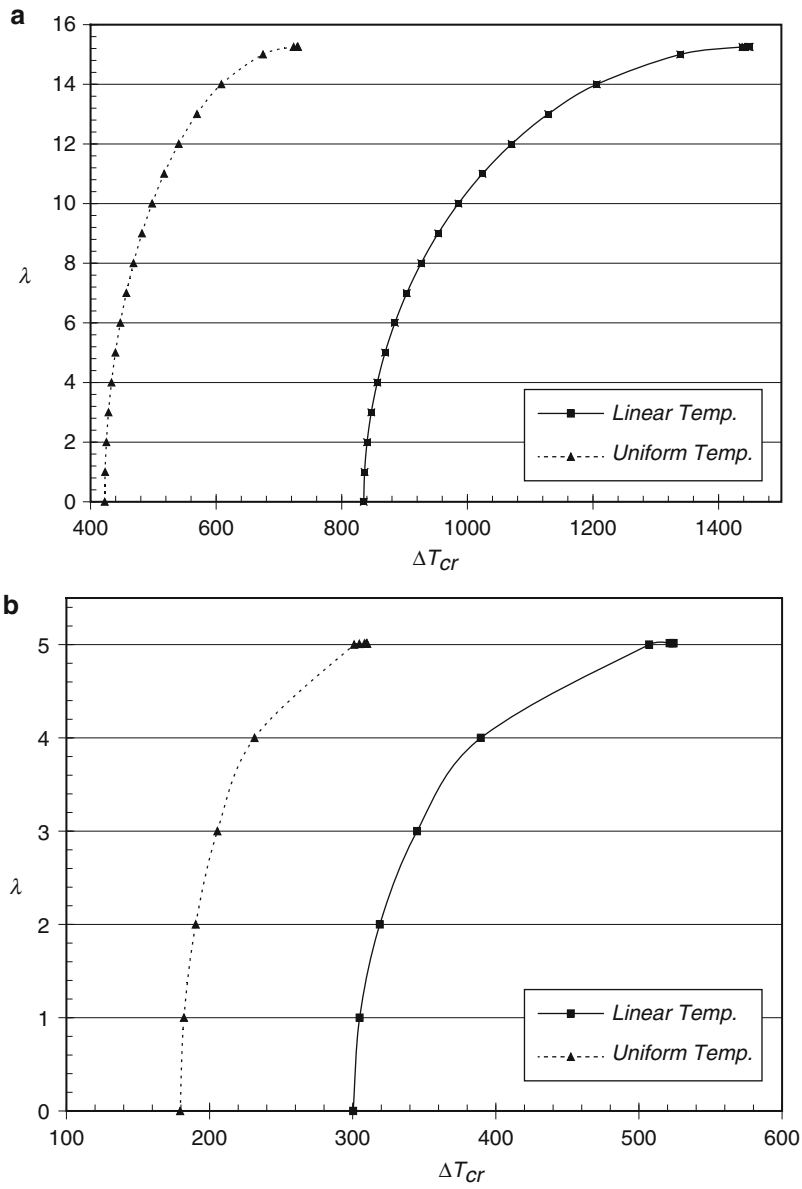

Aerothermoelastic Behaviors of Functionally Graded Panel Structures, Fig. 2 The divergence boundaries for uniform and linear temperature cases $h/a = 0.05$, $a/b = 1$; (**a**) $k = 0$; (**b**) $k = 5$

temperature dependent and listed in [5]. The mass density is: $\rho_c = 2370\ \mathrm{kg/m^3}$ for Si3N4; and $\rho_m = 8166\ \mathrm{kg/m^3}$ for SUS304. Also, Poisson's ratio is assumed to be equal for both materials, $v = 0.28$. Furthermore, in the numerical simulation, the reference temperature, T_o, is taken as 300 K and $\mu/M_\infty = 0.1$. All the results, being represented subsequently, are associated with the dimensionless displacement (or velocity) of a point located at $\xi = 0.75$. This particular location was selected because the maximum panel displacement is approximately in this point, Dowell [6]. The magnitude of the maximum plate deflection for various volume fraction indexes with respect to nondimensional dynamic pressure is shown in Fig. 4. Herein bifurcation diagrams of maximum panel deflection against the dimensionless aerodynamic pressure for different values of the volume fraction at $\Delta T = 10$ are provided. Because of plate response

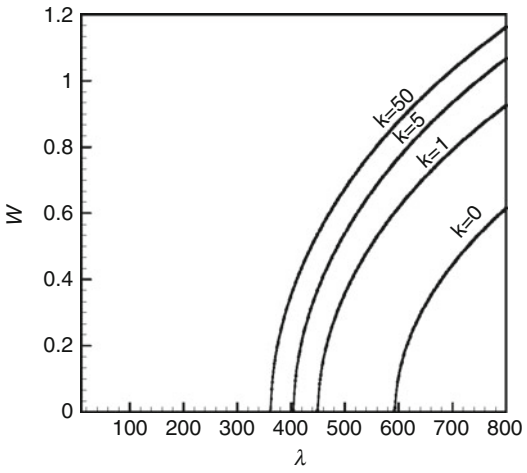

Aerothermoelastic Behaviors of Functionally Graded Panel Structures, Fig. 3 Behavior of the post-critical limit cycle amplitude of FGM panels verses the non-dimensional dynamic pressure

symmetry, whenever $\Delta T = 0$, only the positive displacement values are presented. Increasing the ceramic constituent of the FG plate increases the critical dynamic pressures. In addition, limit cycle amplitudes of maximum plate deflection decrease. This improves the panel dynamic behavior due to expanding the stability domain. Under the compression caused by thermal loading, and the low values of dynamic pressure, the panel first experiences static buckling (divergence). Due to stabilizing effect of aerodynamic damping, after the divergence region, a stable region is observed as the dynamic pressure increases until the dynamic pressure reaches the critical value at which LCO begins. Finally, the system loses dynamic stability because of high flow velocity. The size of the stable region is wider as the ceramic constituent increases. On the other hand, an increase in the volume faction of the metal reduces the bending stiffness of the whole plate. Therefore, the maximum displacement of the plate increases as the metal volume fraction increases. This results in moving the bifurcation point to lower values of dynamic pressure. The panel dynamic behavior in terms of the bifurcation diagram, maximum Lyapunov exponent, and Lyapunov dimension of maximum panel deflection is shown in Fig. 5. For computing the maximum Lyapunov exponent and Lyapunov dimension, 200,000 data points are taken directly from the deflection of the plate. Both maximum Lyapunov exponents and Lyapunov dimensions are employed to characterize the onset conditions of chaotic motion for a large deflection plate. In this sense, one can see that for divergence and stable region, all Lyapunov exponents are negative as shown in these figures. When the largest Lyapunov exponent is zero, the panel experiences limit cycles and a positive Lyapunov exponent indicates chaotic motion. It is worth remarking that the Lyapunov dimension is equal to zero for divergence and stable state, integer value for regular motion such as LCOs and quasi-periodic oscillations, and a positive noninteger value for chaotic flutter.

Dynamic Behavior of FGM Panels: Flutter and Post-flutter of Curved Panels

Numerical study to supply information about the nonlinear bending deformation of the curved plates with different combinations of loading and height-rise geometric conditions are provided in [7]. A few characteristic results are presented here. Selected values of volume fraction indexes of the FGM constituents are considered to investigate panel dynamic behavior. The functionally graded materials consist of silicon nitride and stainless steel, Si3N4/SUS304. The mass density for Si3N4 is $\rho_c = 2370\ \mathrm{kg/m^3}$ and for SUS304 is $\rho_m = 8166\ \mathrm{kg/m^3}$. Poisson's ratio is assumed to be equal for both materials, $v = 0.28$. The other material properties are assumed temperature dependent as per Reddy and Chin [5]. In the numerical simulation, the reference temperature is assumed to be 300 K. Four bending modes are considered in the solution procedure. All the results, being represented subsequently, are also associated with the dimensionless displacement (or velocity) of a point located at $\xi = 0.75$. For a fully metal case with isotropic property ($k = 50$), the accuracy of the method for the nonlinear analysis is verified against the results reported in [8] and good agreement is obtained as shown in Fig. 6. Figure 7

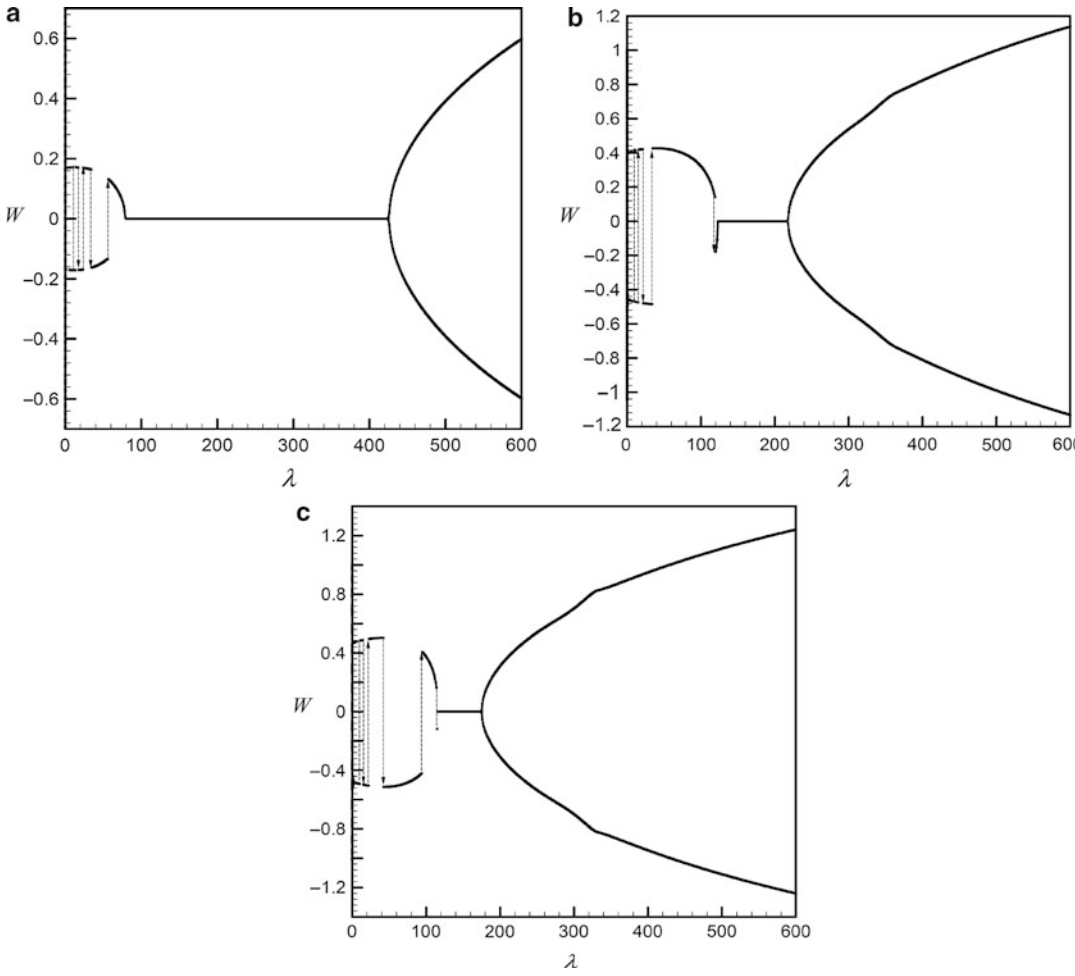

Aerothermoelastic Behaviors of Functionally Graded Panel Structures, Fig. 4 Bifurcation diagram of Poincaré maps of maximum panel deflection under increasing non-dimensional aerodynamic pressure with $\Delta T = 10$: (**a**) k = 0, (**b**) k = 5, (**c**) k = 50

shows the maximum panel deflection in divergence situation against panel height-rise values and for a selected values of nondimensional aerodynamic pressure when a panel made only by a ceramic constituent is considered. As expected, by increasing the temperature value, the maximum panel deflection increases. It is also shown that for lower values of nondimensional aerodynamic pressure, higher displacements are obtained for small curvature. The temperature has certainly a dominant effect on the maximum plate displacement with respect to the nondimensional aerodynamic pressure especially when the plate has low height-rise values. Panels with higher curvature are less sensitive to the effect of temperature. The figure also shows the presence of a snap-through typical of flat plates $(H/h = 0, R \to \infty)$ which occurs for the nondimensional aerodynamic pressure $\lambda = 120$ and temperature differential $\Delta T = 15$ K. The effect of panel curvature as well as volume fraction indexes can be seen clearly. Different types of motion are observed through variation of curvature value. It should be noted that, in contrast to fully ceramic constituent where the panel experiences only divergence situation, for other volume

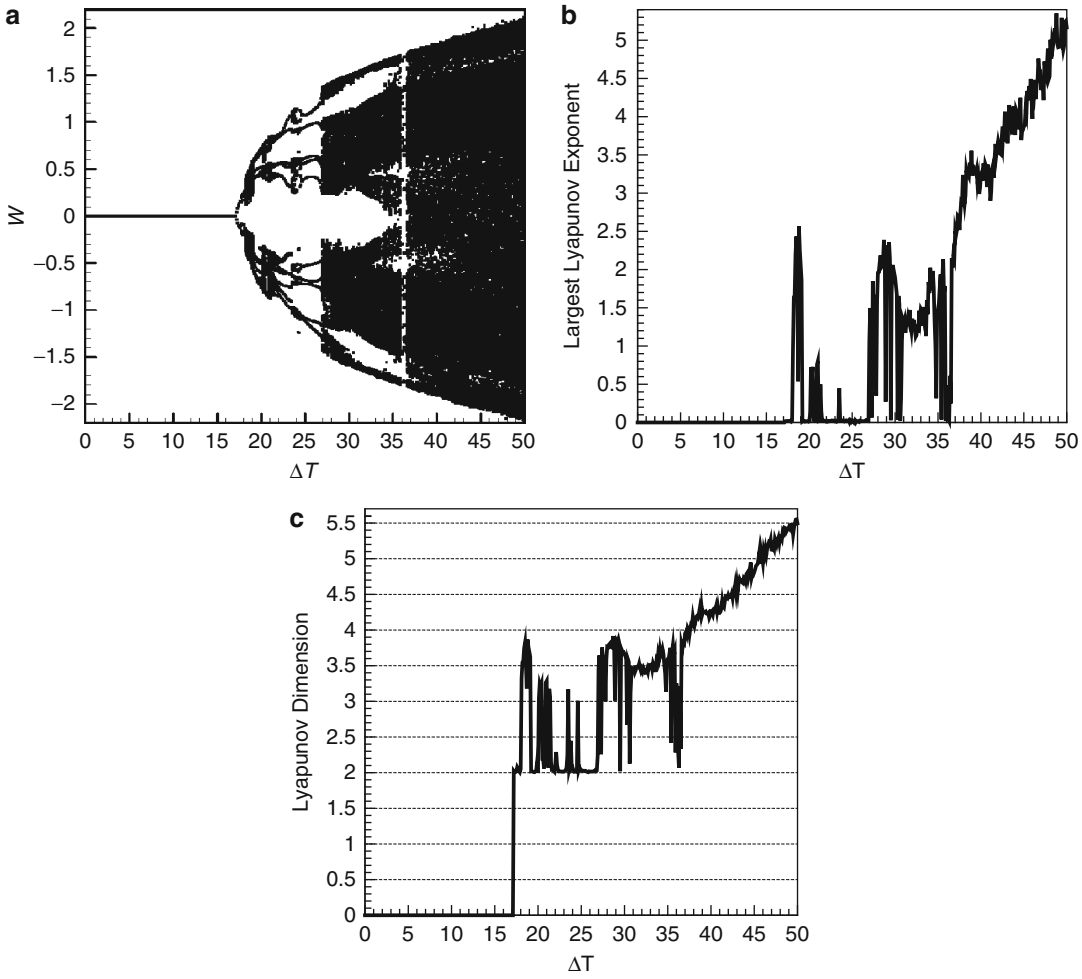

Aerothermoelastic Behaviors of Functionally Graded Panel Structures, Fig. 5 (**a**) Bifurcation diagram of Poincaré maps, (**b**) Largest Lyapunov exponent (**c**) Lyapunov dimension of maximum panel deflection under increasing temperature gradient through thickness direction with $k = 1$, $\lambda = 150$

fraction indexes distinct behavior is observed for different curvature values. A number of switching occurs between divergence and periodic motion. It is also evident that there are some jumps in amplitude of limit cycle oscillation for higher values of curvature as observed in the figure. The effect of thermal loads due to temperature changes along the curved panel thickness is also studied in this figure. As was previously mentioned, the influence of temperature on the system dynamic behavior is more accentuated for low curvature value. Results show that a dynamic transition occurs from a divergence state to a regular or irregular motion with increasing the temperature. Qualitatively, different behaviors are observed by gradual change of curvature parameter, going from periodic motion, to a sequence of double periodic motions, to quasi-periodic motions, and to a divergence state. The panel dynamic behavior in terms of the bifurcation diagram, maximum Lyapunov exponent, and Lyapunov dimension of maximum panel deflection is shown in Fig. 8. The panel curvature parameter is the control parameter and varies between $H/h = 0$ and $H/h = 5$. The volume fraction index, $k = 1$, is considered.

Two temperature values, $\Delta T = 0$ K and $\Delta T = 20$ K, are investigated for each figure and the aerodynamic pressure is assumed to be $\lambda = 500$. There are two instances when the largest exponent sign becomes positive. These intervals correspond to bifurcation of transition to chaotic motion. Before going into the chaotic region, the curved panel undergoes quasi-periodic motions. After the first region of chaotic motions, there is a region of quasi-periodic motions. As H/h increases, a second chaotic regime occurs, and then a periodic motion is observed. Maximum Lyapunov exponent is zero for periodic motion while for a divergence state it becomes negative. As shown in this figure, the Lyapunov dimensions for divergence, periodic, and chaotic motions are zero, integer, and noninteger positive values, respectively. The same dynamical behaviors are observed when thermal loadings are applied to the panel. However, the temperature load triggers a chaotic behavior at lower curvature values. Before going into the chaotic region, multi-periodic and quasi-periodic motion usually occur. It may be noticed that for volume fraction indexes other than zero value, there are some limit cycle switching in higher curvature values. Although not displayed here, when considering the case of fully ceramic constituent, no switching in dynamical system behaviors takes place. The effect of aerodynamic pressure as a control parameter for bifurcation diagram was also investigated in [7]. From results reported in [7], the panel first experiences static buckling (divergence) followed by a dynamic instability (flutter) and either regular or chaotic behaviors are observed. The ceramic

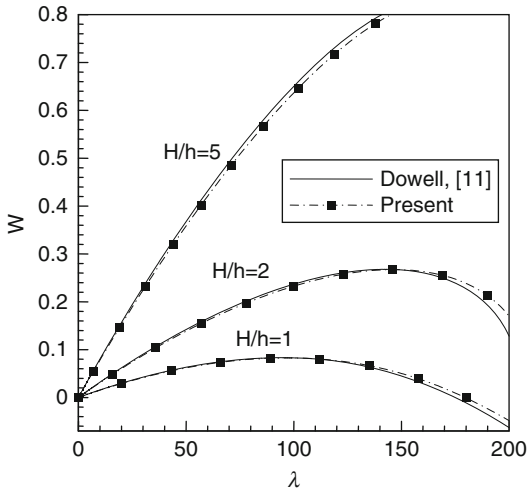

Aerothermoelastic Behaviors of Functionally Graded Panel Structures, Fig. 6 SUS304 curved panel ($k = 50$) amplitude as a function of the nondimensional aerodynamic pressure and for selected raise-to-thickness ratios

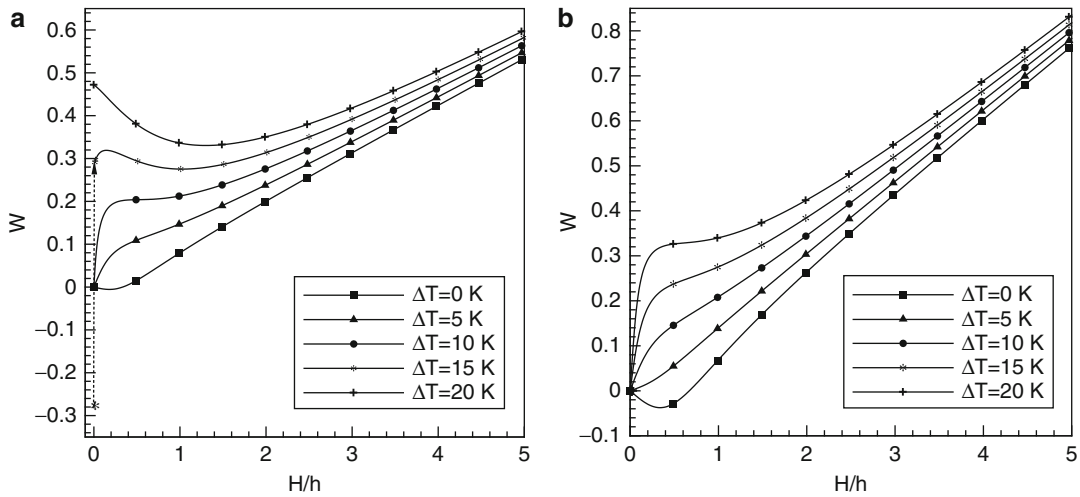

Aerothermoelastic Behaviors of Functionally Graded Panel Structures, Fig. 7 Maximum plate deflection in divergence situation under curvature gradient for $k = 0$, (**a**) $\lambda = 120$ while (**b**) $\lambda = 200$

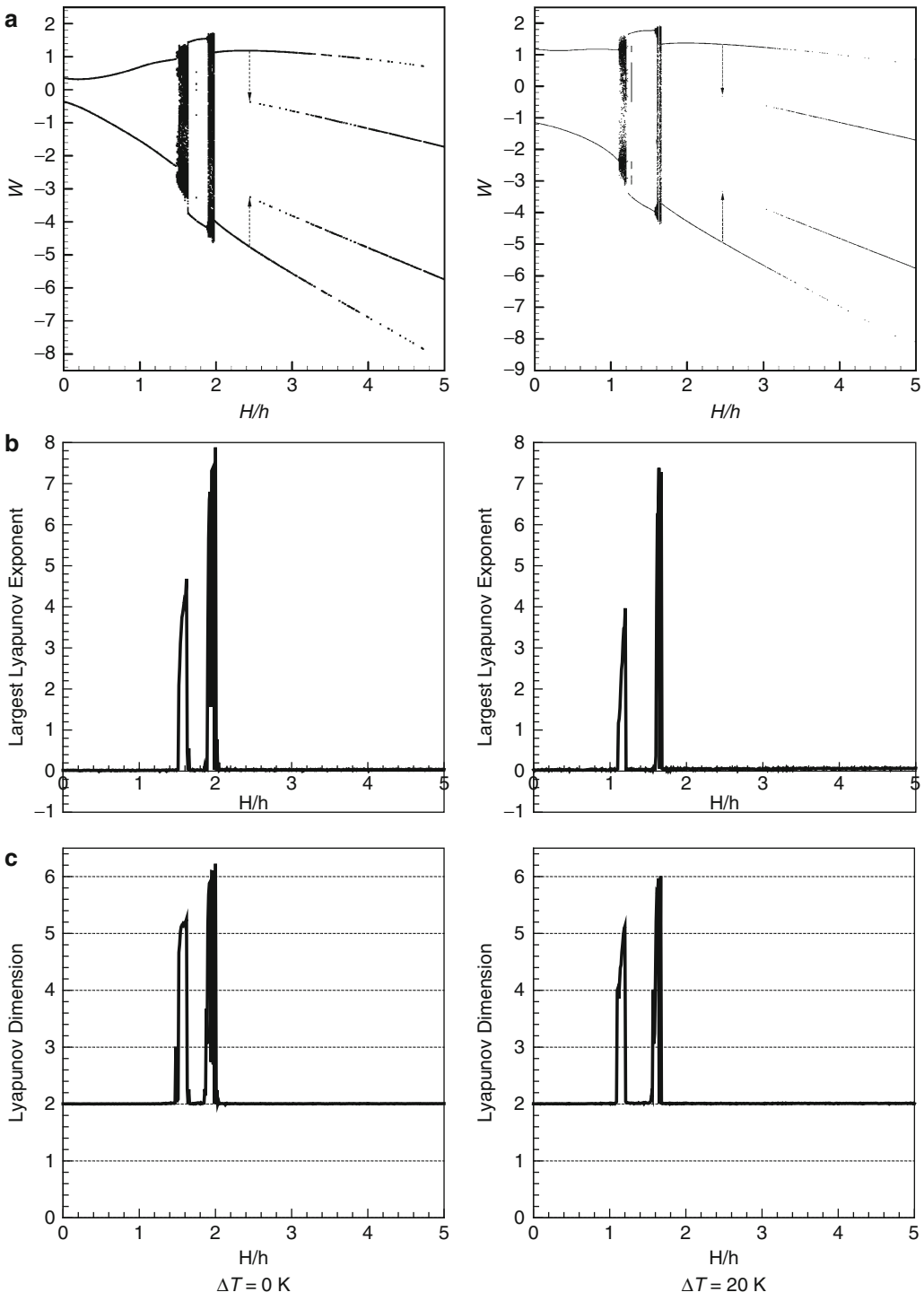

Aerothermoelastic Behaviors of Functionally Graded Panel Structures, Fig. 8 (**a**) Bifurcation diagram of Poincaré maps, (**b**) Largest Lyapunov exponent, and (**c**) Lyapunov dimension of maximum plate deflection under increasing height-raise values with $k = 1$, $\lambda = 500$

constituent delays the appearance of the bifurcation on the panels. The maximum deflection of the FGM curved panel decreases when considering a case with larger ceramic phase constituent. This is because of the stiffness of the ceramic which is higher than the stiffness of the metal. When the temperature value increases, the bifurcation point moves to lower values of dynamic pressure and maximum deflection value increases in both divergence and flutter behaviors. Chaotic regime may be detected in the dynamical behavior of the curved panel due to thermal loading.

Consideration About the Static and Dynamic Behavior of FGM Shells Under Aerothermoelastic Loading Conditions

The critical thermal load and divergence of panels are affected by the temperature distribution across the panel thickness. Numerical results show that the stability regions decrease for selected temperature distributions with the increase in volume fraction index. The stable region can be extended by increasing the aspect ratio and/or the relative thickness. The influence of nondimensional aerodynamic pressure on the critical temperature difference is more significant for lower aspect ratio a/b, thicker plate, and higher volume fraction index k. The extent of the stable region in the case of linear temperature distribution is greater than for the case of uniform temperature distribution, independent of other design parameters. The stable region increases as the FGM is richer in its ceramic constituent. Snap-through is observed in the divergence region by increasing thermal loading and aerodynamic pressure. Increasing the ceramic constituent in the FG plate causes flutter to appear at higher dynamic pressures, while decreases the panel's limit cycle amplitude. This is a natural result as the metal is more ductile than the ceramic, and the stiffness changes based on the percent of each constituent; therefore, increasing the % of ceramic constituent increases the panel structural stiffness. Curved plates with different volume fraction indexes present distinct dynamical behavior. Under the same specific defined parameters, divergence behavior is observed for a single constituent ceramic panel, while chaotic motion is observed in a single constituent metallic panel. Temperature clearly affects the plate dynamical behaviors, especially for low height-rise panels. As the temperature increases, chaotic dynamic phenomena might occur as the height-rise values increase. Different dynamical behaviors are observed by slowly changing the aerodynamic pressure and bifurcations may occur at specific values of the aerodynamic pressure. These bifurcations can be delayed by increasing the percentage of ceramic constituent. Increasing the metal constituent will lead to a chaotic motion at lower values of temperature. Chaotic behaviors are also observed at higher values of temperature accompanied by increasing aerodynamic pressure. Changes from divergence or stable state regime to periodic or aperiodic regimes can be identified by the Lyapunov dimension jumping from zero to an integer or to noninteger values, respectively. Maximum Lyapunov exponent and Lyapunov dimension are compatible with the bifurcation diagrams.

References

1. Fazelzadeh SA, Hosseini M, Madani H (2011) Thermal divergence of supersonic functionally graded plates. J Therm Stress 34:759–777
2. Hao YX, Chen LH, Zhang W, Lei JG (2008) Nonlinear oscillations, bifurcations and chaos of functionally graded materials plate. J Sound Vib 312:862–892
3. Prakash T, Ganapathi M (2006) Supersonic flutter characteristics of functionally graded flat panels including thermal effects. Compos Struct 72(1):10–18
4. Hosseini M, Fazelzadeh SA (2010) Aero-thermo-elastic post-critical and vibration analysis of temperature-dependent functionally graded panels. J Therm Stress 33(12):1188–1212
5. Reddy JN, Chin CD (1998) Thermo-mechanical analysis of functionally graded cylinders and plates. J Therm Stress 21:593–629
6. Dowell EH (1975) Aeroelasticity of plates and shells. Noordhoff International, Leyden
7. Hosseini M, Fazelzadeh SA, Marzocca P (2011) Chaotic and bifurcation dynamic behavior of functionally graded curved panels under aero-thermal loads. Int J Bifurc Chaos 21(3):931–954
8. Dowell EH (1969) Non-linear flutter of curved panels. AIAA J 7:424–431

Aerothermoelastic Control of Lifting Surfaces

Laith K. Abbas[1], Chen Qian[2] and Piergiovanni Marzocca[3]
[1]Institute of Launch Dynamics, Nanjing University of Sciences and Technology, Nanjing, People's Republic of China
[2]College of Aerospace Engineering, Institute of Vibration Engineering Research, Nanjing University of Aeronautics and Astronautics, Nanjing, People's Republic of China
[3]Department of Mechanical and Aeronautical Engineering, Clarkson University, The Wallace H. Coulter School of Engineering, Potsdam, NY, USA

Synonyms

Aerothermoelasticity; Freeplay; Hypersonic speed; Nonlinear 2D wing models; Nonlinear aerothermoelastic control analysis; Piston theory aerodynamics; Thermal loading

Overview

The interest toward the development and implementation of active control technology was prompted by the new and sometimes contradictory requirements imposed on the design of the new generation of the flight vehicle that mandated increasing structural flexibilities, high maneuverability, and at the same time, the ability to operate safely in severe environmental conditions. Designing reentry space vehicles and high-speed aircraft requires special attention to the nonlinear thermoelastic and aerodynamic instability of their structural components. The aerodynamic heating effects are usually estimated from the adiabatic wall temperature due to high-speed airstreams. The thermal effects are important since temperature environment critically influences the static and dynamic behaviors of flight structures in supersonic/hypersonic regimes and is likely to cause instability, catastrophic failure, and oscillations, resulting in structural failure due to fatigue.

Active aerothermoelastic control strategies provide solutions to a large number of problems involving aerospace flight vehicle structures. To prevent damaging phenomena produced by thermal effects on both flutter boundary and post-flutter behavior, linear/nonlinear active control methods should be implemented. A serious loss of torsional stiffness may induce the dynamic instability; consequently, in the design process, the loss of torsional stiffness that may be incurred by lifting surfaces subject to axial stresses induced by aerodynamic heating should be considered.

Active control can be used to expand the flutter boundary and convert unstable limit cycle oscillations (LCO) into the stable LCO and/or to shift the transition between these two states toward higher flight Mach numbers. The advances of active control technology have rendered the applications of active flutter suppression and active vibrations control systems feasible in the last two decades [1, 2]. A great deal of research activity devoted to the aeroelastic active control and flutter suppression of flight vehicles has been accomplished. The state-of-the-art advances in these areas are presented in [3, 4]. The reader is also referred to a sequence of articles [5, 6] where a number of recent contributions related to the active control of aircraft wing are discussed at length. In the next sections, the nonlinear aerothermoelastic governing equations for the control of lifting surfaces are presented [7, 8] along with the solution methodology adopted and the analysis of selected example cases.

Nonlinear Aerothermoelastic Control Equations

The structural model considered is of a double-wedge two degrees-of-freedom (2-DOF) plunging/pitching lifting surface. The model is free to rotate in the xOz plane and free to translate in the vertical direction as shown in Fig. 1. While a linear model can be obtained considering linear flexural and torsional stiffnesses, herein the nonlinear restoring force and moment from

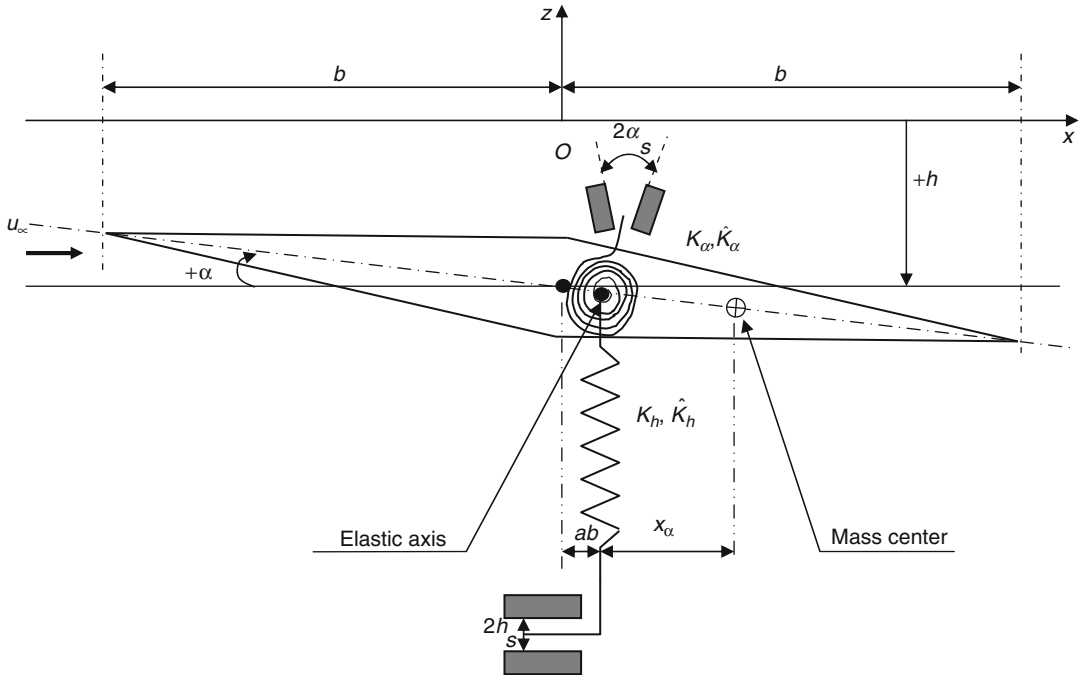

Aerothermoelastic Control of Lifting Surfaces, Fig. 1 Two degrees-of-freedom double-wedge airfoil geometry

bending and torsional springs accounting for freeplay in both degrees-of-freedom have been considered. The nonlinear aeroelastic governing equations can be written as:

$$m\ddot{h} + S_\alpha \ddot{\alpha} + c_h \dot{h} + F(h) = -L(t) \tag{1}$$

$$S_\alpha \ddot{h} + I_\alpha \ddot{\alpha} + c_\alpha \dot{\alpha} + G(\alpha) = M_{EA}(t) \tag{2}$$

Herein m is the airfoil mass per unit wing span, h is the plunging displacement at the elastic axis (EA), positive in the downward direction, S_α is the static unbalance moment about the elastic axis per unit wing span, α is the pitch angle, positive rotation nose up, c_h and c_α are the linear viscous damping coefficients in plunging and pitching, respectively, L is the unsteady lift per unit wing span, t is the physical time variable, I_α is the cross-section mass moment of inertia about its elastic axis per unit span, M_{EA} is the unsteady aerodynamic moment about the elastic axis per unit wing span, and $\dot{(\,)}$, $\ddot{(\,)}$ are first and second time derivatives. The active nonlinear control can be represented in terms of the moment M_C in (1) as [7, 8]:

$$M_C = f_1 \alpha(t) + f_2 \alpha^3(t) \tag{3}$$

where f_1, f_2 are the linear and nonlinear control gains, respectively. A third-order expansion form of the PTA is used to study the behavior of the nonlinear aerothermoelastic system in supersonic/hypersonic aeroelastic analyses. The system of governing equations of a supersonic/hypersonic double-wedge controlled airfoil featuring plunging/pitching coupled motion can be cast as [7]:

$$\begin{aligned}
&\xi''(\tau) + \chi_\alpha \alpha''(\tau) + 2\zeta_h(\bar{\omega}/U^*)\xi'(\tau) \\
&\quad + (\bar{\omega}/U^*)^2 \bar{F}_a(\xi)\xi(\tau) + (\bar{\omega}/U^*)^2 \bar{F}_b(\xi_s) \\
&\quad + (\bar{\omega}/U^*)^2 \bar{F}_c(\xi)[\xi^3(\tau) + 3(-1)^n \xi_s \xi^2(\tau) \\
&\quad + 3\xi_s^2 \xi(\tau) + (-1)^n \xi_s^3] = \bar{L}(\tau)
\end{aligned} \tag{4a}$$

$$\begin{aligned}
&(\chi_\alpha / r_\alpha^2)\xi''(\tau) + \alpha''(\tau) + (2\zeta_\alpha/U^*)\alpha'(\tau) \\
&\quad + (1/U^{*2})\bar{G}_a(\alpha)\alpha(\tau) + (1/U^{*2})\bar{G}_b(\alpha_s) \\
&\quad + (1/U^{*2})\bar{G}_c(\alpha)[\alpha^3(\tau) + 3(-1)^n \alpha_s \alpha^2(\tau) \\
&\quad + 3\alpha_s^2 \alpha(\tau) + (-1)^n \alpha_s^3] = \bar{M}_{EA}(\tau) \\
&\quad - (1/U^{*2})(\varphi_1 \alpha(\tau) + \varphi_2 \alpha^3(\tau))
\end{aligned} \tag{4b}$$

where ξ is the dimensionless plunging displacement at the elastic axis location, τ is the

dimensionless time, x_α is the dimensionless distance between the mass center of the airfoil section and the elastic axis, ζ_h, ζ_α are the damping ratios in plunging and pitching, respectively, $\bar{\omega}$ is the dimensionless frequency ratio, u, u^* velocity and its dimensionless counterpart (reduced velocity), respectively, ξ_s is the dimensionless plunging freeplay magnitude, r_α is the dimensionless radius of gyration about elastic axis, α_s is the pitching freeplay magnitude, $\hat{\eta}_h$, $\hat{\eta}_\alpha$ are the normalized nonlinear stiffness coefficients in plunging and pitching, respectively, μ is the reduced mass ratio, ρ_∞ is the air stream density, t_h is the airfoil half thickness, $()'$, $()''$ are the first and second time derivatives with respect to τ and

$$\bar{F}_a(\xi)=\begin{Bmatrix}1\,,\\0\,,\\1\,,\end{Bmatrix}\;\bar{F}_b(\xi)=\begin{Bmatrix}-\xi_s\,,\\0\;\;,\\\xi_s\;\;,\end{Bmatrix}\qquad \bar{F}_c(\xi)=\begin{cases}\hat{\eta}_h\,, & \xi(\tau)>\xi_s \quad ,n=1\\ 0\;\;, & -\xi_s\le\xi(\tau)\le\xi_s\\ \hat{\eta}_h\,, & \xi(\tau)<-\xi_s \quad ,n=2\end{cases} \tag{5}$$

Similar expression for $\bar{G}'s$ by replacing $\xi(\tau)\Leftrightarrow\alpha(\tau)$. The unsteady aerodynamic lift and moment appearing in (4a and 4b) can be expressed as:

$$\bar{L}(\tau)=-\frac{\eta}{12M_\infty\mu}\Bigg[12(\xi'-a\alpha'+\alpha)-3(\gamma+1)\hat{\tau}\eta M_\infty(\alpha')+M_\infty^2(\gamma+1)\eta^2\Big\{(\xi'-a\alpha'+\alpha)\Big[(\xi'-a\alpha'+\alpha)^2+3\hat{\tau}^2+(\alpha')^2\Big]\Big\}\Bigg] \tag{6a}$$

$$\bar{M}_{EA}(\tau)=\frac{\eta}{12\mu M_\infty r_\alpha^2}\Bigg[12[a\xi'-\left(\frac{1}{3}+a^2\right)\alpha'+a\alpha]+3(\gamma+1)\hat{\tau}\eta M_\infty(\xi'-2a\alpha'+\alpha).-M_\infty^2(\gamma+1)\eta^2\Big\{\frac{1}{5}(\alpha')^3-a(\xi'-a\alpha'+\alpha)\Big[(\xi'-a\alpha'+\alpha)^2+3\hat{\tau}^2\Big]+\alpha'\Big[(\xi'-a\alpha'+\alpha)^2+\hat{\tau}^2-a\alpha'(\xi'-a\alpha'+\alpha)\Big]\Big\}\Bigg] \tag{6b}$$

The two normalized linear and nonlinear control gain parameters φ_1,φ_2 are defined as $\varphi_1=f_1/K_\alpha,\varphi_2=f_2/K_\alpha$, respectively.

Solution Methodology

To perform the nonlinear aerothermoelastic analysis in the time domain, (4a, 4b) is transformed into state-space matrix form:

$$\dot{\mathbf{y}}(\tau)=\begin{bmatrix}\mathbf{0} & \mathbf{I}\\ \mathbf{M}^{-1}(\mathbf{QL2_{ext}}+\mathbf{QNL2_{ext}}-\mathbf{KL}-\mathbf{KNL}-\mathbf{M_{control}}) & \mathbf{M}^{-1}(\mathbf{QL1_{ext}}+\mathbf{QNL1_{ext}}-\mathbf{C})\end{bmatrix}\mathbf{y}(\tau)-\begin{bmatrix}\mathbf{0} & \mathbf{0}\\ \mathbf{0} & \mathbf{M}^{-1}\end{bmatrix}\mathbf{R}(\xi_s,\alpha_s)$$

$$\text{where }\mathbf{y}(\tau)=\begin{Bmatrix}\xi(\tau)\\ \alpha(\tau)\\ \dot{\xi}(\tau)\\ \dot{\alpha}(\tau)\end{Bmatrix},\mathbf{R}(\xi_s,\alpha_s)=\begin{Bmatrix}0\\0\\ \mathrm{Q_f}(1,1)\\ \mathrm{Q_f}(2,1)\end{Bmatrix},\mathbf{M_{control}}=\begin{bmatrix}0 & 0\\ 0 & (1/U^{*2})(\varphi_1+\varphi_2\alpha^2(\tau))\end{bmatrix} \tag{7}$$

Aerothermoelastic Control of Lifting Surfaces, Table 1 Baseline parameters of 2-DOF plunging/pitching airfoil

Material used: Titanium (Ti-6%Al-4%V)		
Mechanical properties $\rho = 4{,}420\ \mathrm{kg/m^3}$; TEC (0–100 C^0) $8.8*10^{-6}$/K; TEC (0–300 C^0) $9.2*10^{-6}$/K; $E = 114*10^9\ \mathrm{N/m^2}$; $G = 43.51*10^9\ \mathrm{N/m^2}$; $\vartheta = 0.31$		
Flight condition: $h = 10{,}000$ m; $\rho_\infty = 0.4135\ \mathrm{kg/m^3}$; $c_\infty = 299.53$ m/s; $T_\infty = 223.26$ K; $\eta = 1$; $\gamma = 1.4$		
Airfoil geometry parameters: Section of rectangular wing, aspect ratio = 3; $b = 0.5$ m; $\hat{\tau} = 0.15$; $m = 331.5\ \mathrm{kg/m}$		
Airfoil physical parameters: $\chi_\alpha = 0.25$; $r_\alpha = 0.5$; $\zeta_h, \zeta_\alpha = 0$; $a = -0.25$; $\bar{\omega} = 0.2135$		
Cubic stiffness nonlinearities $\hat{\eta}_h = 0$; $\hat{\eta}_\alpha = 10$	Initial condition $\xi(\tau = 0) = \dot{\xi}(\tau = 0) = \dot{\alpha}(\tau = 0) = 0$; $\alpha(\tau = 0) = 5^\circ$	Initial freeplay $\alpha_s = 1^\circ$; $\xi_s = 0$

where **y** is the state vector and **M** is the mass matrix. **KL** and **KNL** in (7) represents the linear and nonlinear stiffness matrices, while the aerodynamic damping and stiffness matrices $\mathbf{QNL1}_{ext}$ and $\mathbf{QNL2}_{ext}$ contain both uncoupling and coupling nonlinear quadratic and cubic terms, respectively. The matrices **QL1** and **QL2** include the damping and stiffness aerodynamic linear terms, respectively, **R** and $\mathbf{Q}_f$ are the freeplay force/moment vectors. $\mathbf{M}_{\mathbf{control}}$ represents the active linear and nonlinear control moment matrix. A numerical simulation using the fifth to sixth Runge-Kutta Fehlberg time integration scheme with step size control is carried out for the system in (7).

Aerothermoelastic Control of Lifting Surfaces: Analysis

Before we apply any control and to emphasize the importance of aerodynamic heating on the nonlinear aerothermoelastic behavior of the examined aerothermoelastic system, the influence of the loss in effective torsional stiffness of a solid thin double-wedge wing under various parameters such as flight condition, thickness ratio, pitch freeplay, and pitching stiffness nonlinearity has been analyzed. Unless otherwise stated, the numerical simulations consider the baseline parameters which are listed in Table 1.

A number of bifurcation diagrams were constructed from the amplitude of the pitch LCO as a function of the flight Mach number for a plunging/pitching airfoil with a freeplay structural nonlinearity in pitch, cubic pitch structural nonlinearities subjected to supersonic/hypersonic flow which induced also aerodynamic heating are presented in Fig. 2. Because of symmetric pitch LCO amplitude and to have a better graphical representation, some of the plots in Fig. 2 have been presented in positive or in negative side of the LCO curve as shown later. In Fig. 2a case #1 (positive side of LCO curve) is for the system with no aerodynamic heating and $\hat{\eta}_h = \hat{\eta}_\alpha = 0$, such that $M_{LF} = 17.4$. Case #2 (negative side) is for the system with no aerodynamic heating also, but $\hat{\eta}_h = 0$, $\hat{\eta}_\alpha = 10$ (hard structural nonlinearities) and the flutter speed is the same as case #1. Note that the simulations are restricted to cases where the pitching displacement is within $\pm 20^\circ$ to remain within the limits of validity of the proposed model and approach. The aerothermoelastic system exhibits a bifurcation behavior for these two cases at $M_\infty \approx 1.7$ due to the presence of freeplay in pitch direction. For the speed range $(1.7 < M_\infty \leq 7)$, different types of response behavior (periodic, quasiperiodic, or chaotic) will occur. Within the speed ranges $(7 < M_\infty \leq 17)$ for case #1, $(7 < M_\infty \leq 21)$ for case #2, a stable LCO is experienced; its amplitude increases with the increase of the flight Mach number. At $M_\infty \approx 16$, the case #1 exhibits a pitch LCO with amplitude of about 9.9°, while the case #2, the LCO has a pitching amplitude about 6.6°. It appears that cubic structural nonlinearities significantly decrease the LCO amplitude, while the linear flutter speed remains constant, besides case #1 has maximum amplitude of ($\approx$13°) at $M_\infty \approx 16.2$ compared with ($\approx$17°) at $M_\infty \approx 21$ for case #2. Figure 2b shows the effect of aerodynamic heating. Case #1 in Fig. 2b is the same as

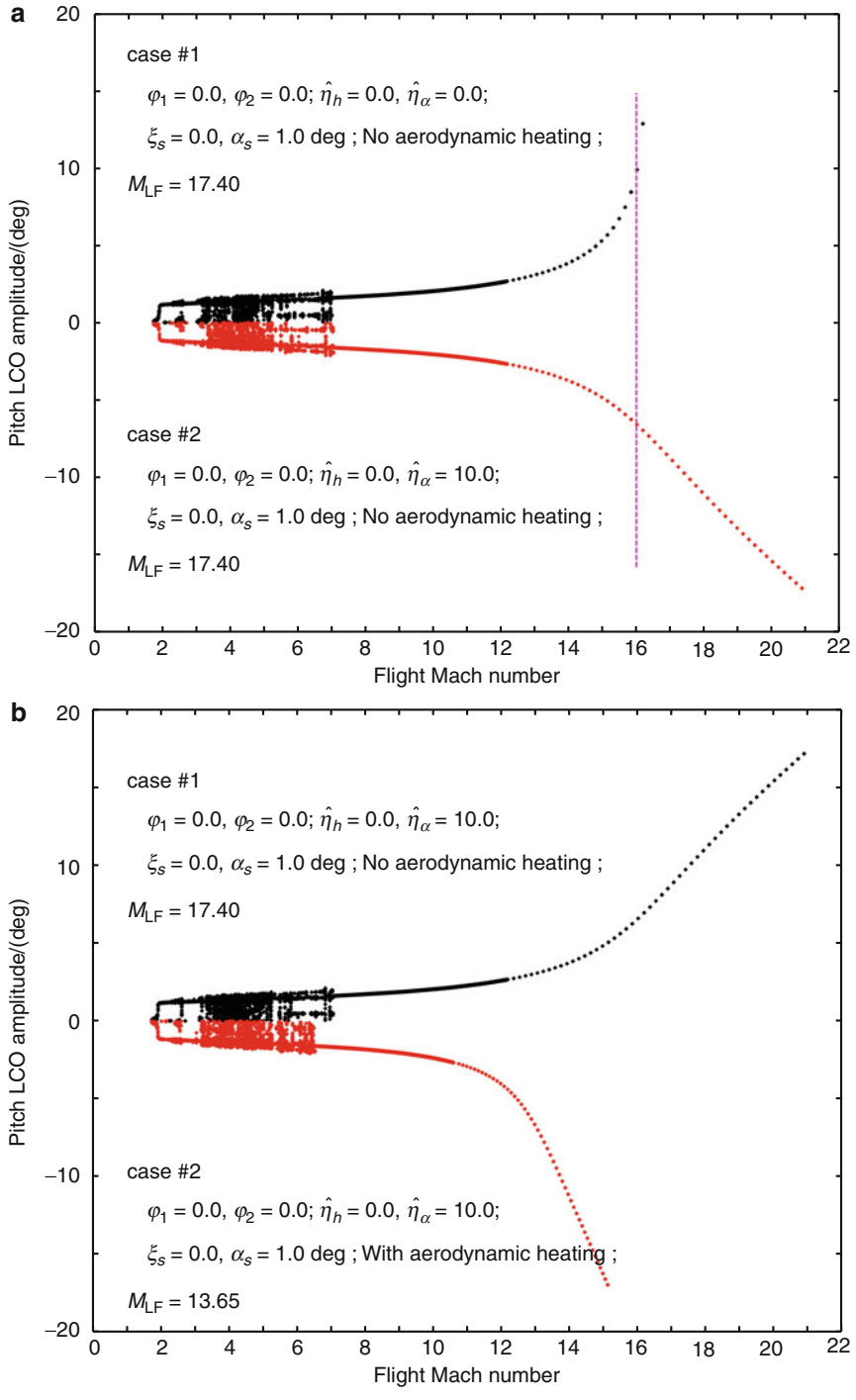

Aerothermoelastic Control of Lifting Surfaces, Fig. 2 Bifurcation pitch diagrams for the double-wedge airfoil with nonlinearities

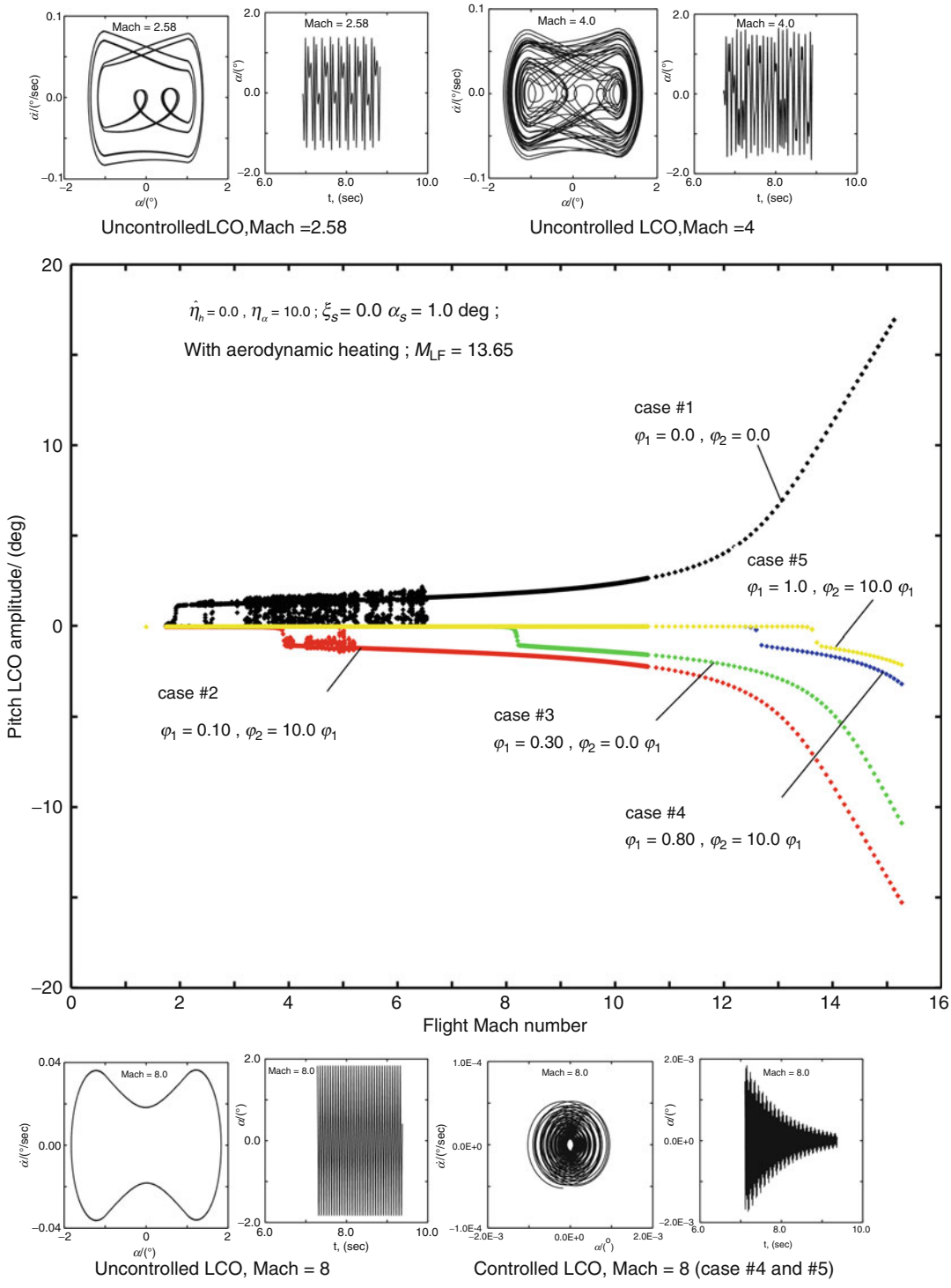

Aerothermoelastic Control of Lifting Surfaces, Fig. 3 Pitch LCO amplitude versus flight Mach number for a 2-DOF system with all nonlinearities. Time histories and phase portraits represent the uncontrolled and controlled system, respectively

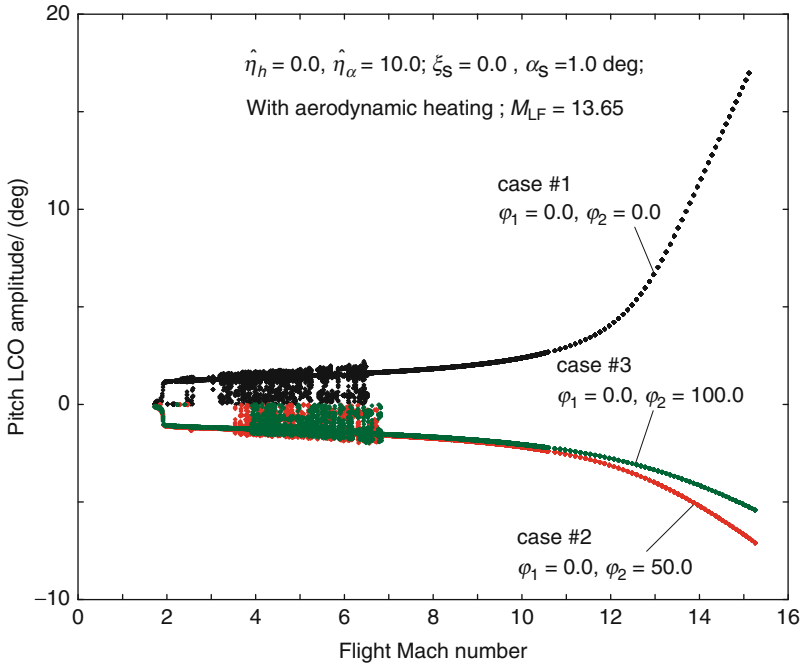

Aerothermoelastic Control of Lifting Surfaces, Fig. 4 Effect of nonlinear active control for system encompassing all nonlinearities

case #2 in Fig. 2a but in positive side. The result of case #2 reveals that the flutter speed ($M_{LF} = 13.65$), as well as the LCO behavior, is affected by the loss of the torsional stiffness. In both cases, the pitching structural nonlinearities are considered ($\hat{\eta}_h = 0$, $\hat{\eta}_\alpha = 10$). Under pitch active control, a considerable change in the amplitude of the LCO is significantly observed in Fig. 3. Case #1 is the same as case #2 in Fig. 2b but in positive side and does not include any active control ($\varphi_1 = \varphi_2 = 0$). Case #2 ($\varphi_1 = 0.1$, $\varphi_2 = 10\varphi_1$), #3 ($\varphi_1 = 0.3, \varphi_2 = 10\varphi_1$), #4 ($\varphi_1 = 0.8$, $\varphi_2 = 10\varphi_1$), and #5 ($\varphi_1 = 1$, $\varphi_2 = 10\varphi_1$) present a shift of the bifurcation behavior to $M_\infty \approx 3.8$, 8.0, 12.5, and 13.5, respectively. The unstable LCO including the chaotic region in case #1 (until $M_\infty \approx 7$) has been suppressed as shown in case #3. Figure 3 also shows the phase portraits and time histories for various flight Mach numbers which represent the uncontrolled (case #1) and controlled system (such as case #4 and #5), respectively. Clearly, increasing the linear pitch gain can extend the flutter boundary and convert the unstable LCO into stable LCO and/or shift the transition between these two states toward higher flight Mach numbers with suppression of LCO.

Figure 4 shows the effect of nonlinear active control gain with zero linear gain ($\varphi_1 = 0, \varphi_2 \neq 0$). It shows that increasing φ_2 alone (for case #2, $\varphi_2 = 50$ and for case #3, $\varphi_2 = 100$) is less effective in stabilizing the aerothermoelastic system than for the linear one. This leads to a practical application of the control mechanism on actual and future generation aerospace vehicle lifting surfaces.

Consideration About the Aerothermoelastic Control Behavior of Lifting Surfaces

The influence of aerodynamic heating on the nonlinear aerothermoelastic behavior of a solid thin double-wedge airfoil encountered all nonlinearities (structural freeplay and cubic stiffness, aerodynamic third-order piston theory) in supersonic/hypersonic flight speed regime is highlighted in the preceding sections. The nonlinear aerothermoelastic analysis of aerosurfaces is an important aspect of design. Linear and nonlinear active control can extend the flutter boundary and convert the unstable aerothermoelastic behavior into stable one and/or shift

the transition between these two states toward higher flight Mach numbers with suppression of LCO. Moreover, the analysis presented can serve as a guideline for selecting appropriate control gains to maximize performance. Active control can be produced via a device behaving similarly to a linear/nonlinear spring. The issue of the design of the controller is not addressed here. Only a theoretical analysis of the nonlinear active control of aerothermoelastic phenomena of a lifting surface at supersonic/hypersonic flight speed regimes is presented. The application of various controllers using different linear/nonlinear control theories such as optimal control (LQR and others) for more robust control strategy is an active area of current research.

Acknowledgment The authors express their indebtedness to the editor of the *Chinese Journal of Aeronautics* for their kind permission.

References

1. Marzocca P, Librescu L, Chiocchia G (2002) Aeroelastic response of 2-D lifting surfaces to gust and arbitrary explosive loading signatures. Int J Impact Eng 25(1):41–65
2. Mukhopadhyay V (2003) Historical perspective on analysis and control of aeroelastic responses. J Guid Control Dynam 26:673–684
3. Horikawa H, Dowell EH (1979) An elementary explanation of the flutter mechanism with active feedback controls. J Aircr 16(4):225–232
4. Vipperman JS, Clark RL, Conner MD, Dowell EH (1998) Investigation of the experimental active control of a typical section airfoil using trailing edge flap. J Aircr 35:224–229
5. Mukhopadhyay V (2000) Benchmark active control technology. J Guid Control Dyn 24:146–192, Part I 23:913–960, Part II 23:1093–1139, 2001, Part III
6. Na S, Librescu L, Kim M-H, Jeong I-J, Marzocca P (2006) Robust aeroelastic control of flapped wing systems using a sliding mode observer. Aerosp Sci Technol 10(2):120–126
7. Laith K, Abbas CQ, Marzocca P, Zafer G, Mostafa A (2008) Active aerothermoelastic control of hypersonic double-wedge lifting surface. Chin J Aeronaut 21:8–18
8. Marzocca P, Librescu L, Chiocchia G (2002) Aeroelastic response of 2-D lifting surfaces to gust and arbitrary explosive loading signatures. Int J Impact Eng 25(1):41–65

Aerothermoelastic Stability

▶ Thermoelastic Stability of Panels in High-Speed Flows: Linear Analysis
▶ Thermoelastic Stability of Panels in High-Speed Flows: Nonlinear Analysis

Aerothermoelasticity

▶ Aerothermoelastic Behavior of Flat and Curved Panels
▶ Aerothermoelastic Behavior of Lifting Surfaces
▶ Aerothermoelastic Behaviors of Functionally Graded Panel Structures
▶ Aerothermoelastic Control of Lifting Surfaces
▶ Functionally Graded Structures: Aerothermoelastic Interactions

Aerothermoviscoelasticity

▶ Linear Aero-Thermo-Servo-Viscoelasticity, Part I: General Theory

Aeroviscoelasticity Designer FGMs: Passive Control Through Tailored Functionally Graded Materials

Harry H. Hilton
Aerospace Engineering Department, College of Engineering and Private Sector Program Division, National Center for Supercomputing Applications (NCSA), University of Illinois at Urbana-Champaign (UIUC), Urbana, IL, USA

Overview

This entry covers four distinct areas, namely, the interaction in a closed loop system of designer aerodynamics, of viscoelastic materials and structures, and of controls. The presence of

varying temperatures not only induces thermal stresses but also strongly affects material properties. The effects of temperature on viscoelastic material properties as well as on flutter velocities and times to reach flutter conditions are discussed. It is shown that optimized FGM distribution can increase flutter velocities and lengthen the time to when flutter will occur.

Introduction

The confluence of designer aerodynamics, of viscoelastic materials and structures, and of controls in a closed loop dynamical system introduces several distinct problems in each of the four contributing areas as well as in their ensemble.

All functionally graded materials, or FGMs for short, are from a fundamental mechanics point of view nonhomogeneous materials where the property distributions are prescribed during the manufacturing phase. Such distributions may follow continuous and/or piecewise continuous functions. Other possible sources of inhomogeneities are dissimilar materials, composites, and temperature distributions. A striking example of artificially created dissimilar material FGMs is illustrated in Fig. 1 where thin layers of distinct materials are deposited in a prescribed fashion on a plate [1]. A comprehensive formulation (space limitations necessitate citing publications where expanded bibliographies can be found) of viscoelastic FGMs may be found in [2] and of aero-thermo-servo-elasticity with FGMs in [3]. A treatment of the differences and similarities between thermo-elasticity and thermo-viscoelasticity is given in [4].

Linear viscoelasticity has become a mature though not closed field [5]. However, much research remains to be undertaken in nonlinear viscoelasticity [6]. For a list of additional references, see [7].

Tailored aerodynamics have been introduced in publications on airfoil design such as [8–10], where airfoil surfaces are analytically generated to deliver prescribed performance characteristics of low drag, high L/D ratios, etc. Modern airfoil morphing reminiscent of the Wright brothers' original plane also offers control possibilities as seen in [11–14].

Aeroelasticity is a mature field and is covered by a significant number of textbook starting with the everlasting classic [15] and including but not limited to [16–25]. Aero-viscoelasticity on the other hand is still an emerging field starting with [26] and [27] and at this time with no text books. A comprehensive bibliography of the subject as well as an analytical treatment of aero-servo-viscoelasticity may be found in [28].

Elastic designer materials are first described in [29] and viscoelastic ones in [30]. The formal analytical formulation based on calculus of variations is presented in [31].

Analysis

Consider a Cartesian coordinate system $x = \{x_1, x_2, x_3\} = \{x_i\}$, an FGM function $\mathcal{F}(x)$, and a temperature distribution $T(x,t)$. The linear anisotropic viscoelastic constitutive relations can be expressed as [4–6, 32]

$$\sigma_{ij}(x,t) = \int_{-\infty}^{t} E_{ijkl}[x,t,t',\mathcal{F}(x),T(x,t')]\frac{\partial \epsilon_{kl}(x,t')}{\partial t'}dt' - \int_{-\infty}^{t} E^{T}_{ij}[x,t,t',\mathcal{F}(x),T(x,t')]\frac{\partial[\alpha T(x,t')]}{\partial t'}dt' \tag{1}$$

or

$$\epsilon_{ij}(x,t) = \int_{-\infty}^{t} C_{ijkl}[x,t,t',\mathcal{F}(x),T(x,t')]\frac{\partial \sigma_{kl}(x,t')}{\partial t'}dt' + \int_{-\infty}^{t} C^{T}_{ij}[x,t,t',\mathcal{F}(x),T(x,t')]\frac{\partial[\alpha T(x,t')]}{\partial t'}dt' \tag{2}$$

The fundamental difference between elastic and viscoelastic constitutive relations is the fact that the elastic ones are algebraic, while the viscoelastic relations belong to the integral-differential species. Additionally, there remains the most significant matter of the temperature

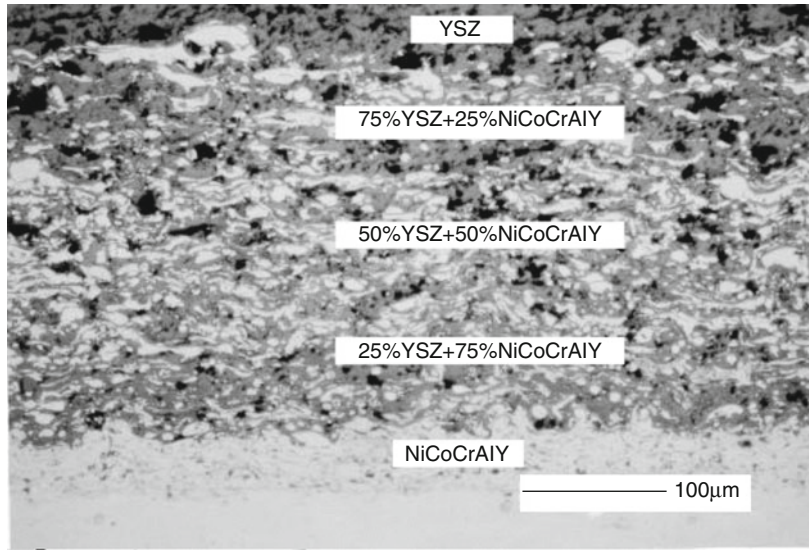

Aeroviscoelasticity Designer FGMs: Passive Control Through Tailored Functionally Graded Materials, Fig. 1 Five-layer functionally graded ZrO_2/NiCoCrAlYcoating [1]

dependence of relaxation moduli E_{ijkl} and creep compliances C_{ijkl}. When one eliminates all relaxation/creep influences at elevated temperatures from Young's modulus experimental measurements, the remainder shows little variations of elastic moduli with temperature [33–35]. Viscoelastic metal and polymer matrix relaxation moduli, on the other hand, show extreme sensitivity to temperature due to real material variations in viscosity coefficients of approximately one order of magnitude per 20 °C – see Fig. 2. The additional most significant effect of this temperature dependence is to change the kernel functions in the hereditary integrals from $E(x, t-t')$ to $E(x,t,t') = E[x,t,t',\mathcal{F}(x),T(x,t')]$ thus destroying the convenient properties of the convolution integrals.

A large class of viscoelastic materials, known as thermo-rheologically simple materials (TSMs), has behavioral responses that admit the presence of the WLF (also known as the Williams-Landel-Ferry shift factor/function) material property shift function a_T [36] empirically defined as

$$\log_e[a_T(t)] = \frac{C_1(T-T_0)}{C_2+T-T_0} \tag{3}$$

with T_0 a conveniently chosen constant reference temperature. It may, but need not, be equated to the rest temperature at which the thermal expansions T vanish. In this entry, the same T_0 is used.

An empirical well-working model for TSMs defines an associated reduced time $\xi(x,t)$ as [37]$\mathcal{F}$

$$\begin{aligned}\xi(x,t) &= \int_0^t a_T[T(x,s)]ds \\ &= \int_0^t \exp\left(\frac{C_1[T(x,s)-T_0]}{C_2+T(x,s)-T_0}\right)ds \\ \xi &\in [0,\infty]\end{aligned} \tag{4}$$

and reduces all relaxation moduli curves at many diverse temperatures to a single master relaxation curve for each TSM with $\hat{E}(x,\xi) = E[x,t,t',\ \mathcal{F}(x),T(x,t')]$ versus ξ. By the above definition, it follows that at $T = T_0$, $a_T = 1$ and $\xi(T_0) \equiv t$.

Further, examinations reveal that

$$\begin{aligned}&\int_{-\infty}^{t} E_{ijkl}[x,t,t',\ \mathcal{F}(x),T(x,t')]\frac{\partial\sigma_{kl}(x,t')}{\partial t'}dt' \\ &\equiv \int_{-\infty}^{\xi(x,t)} \widehat{E}_{ijkl}[x,\xi(x,t)-\xi']\frac{\partial\hat{\sigma}_{kl}(x,\xi')}{\partial\xi'}d\xi'\end{aligned} \tag{5}$$

and thus the convolution integrals are restored in the ξ-space. However, any success at recapturing an elastic-viscoelastic correspondence principle

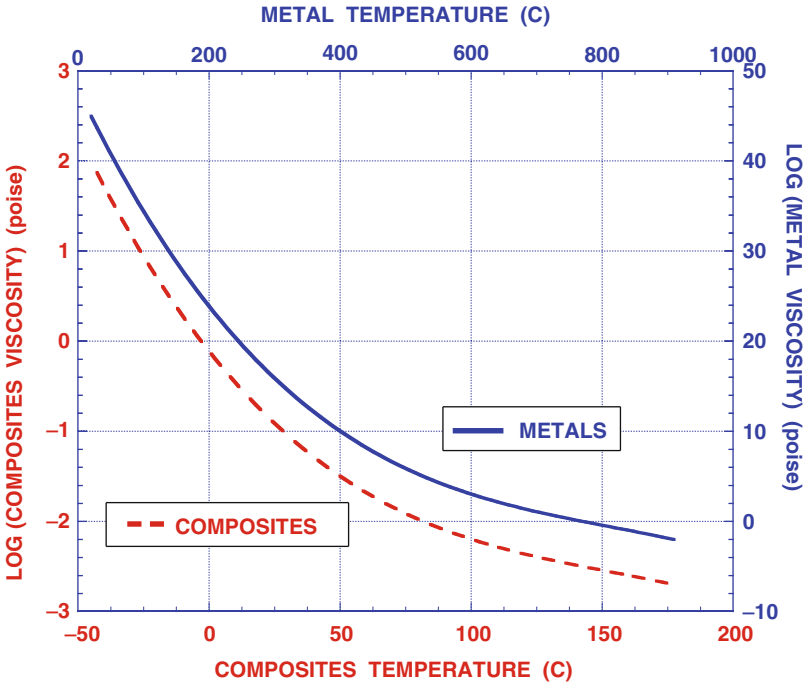

Aeroviscoelasticity Designer FGMs: Passive Control Through Tailored Functionally Graded Materials, Fig. 2 Viscoelastic viscosity temperature dependence

in the ξ-space is thwarted by the fact that the x_i derivatives acquire variable coefficients due to the ξ transformations, to whit

$$\frac{\partial}{\partial x_i} = \underbrace{\frac{\partial \xi(x,t)}{\partial x_i}}_{\substack{=Z_i(x,t) \\ =\hat{Z}_i(x,\xi)}} \frac{\partial}{\partial \xi} \tag{6}$$

The transformation into the ξ-space mandates that

$$\begin{aligned} E_{ijkl}(x,t) &\equiv \hat{E}_{ijkl}(x,\xi) \\ &= E^{\infty}_{ijkl}(x) + \sum_{n=1}^{N_{ijkl}} E_{\underline{ijkl}n}(x) \\ &\quad \times \exp\left(-\frac{\xi(x,t)}{\tau^0_{\underline{ijkl}}(x)}\right) \end{aligned} \tag{7}$$

Equation (5) should be preferentially used in the governing relations as they simplify the "bookkeeping" and numerical solutions when used.

While the convolution integrals are restored in the ξ-space, the variable coefficients generated by the x derivatives negate any possibility of applying the elastic-viscoelastic correspondence principle (EVCP) in either real time t or in reduced time ξ. Table 1 summarizes these phenomena.

The FGM function can be expressed as a series in the finite x domain, such as for instance

$$\mathcal{F}(x) = \sum_{m=0}^{\mathcal{M}} \sum_{n=0}^{\mathcal{N}} \sum_{k=0}^{\mathcal{K}} A_{mnk}\, x_1^m\, x_2^n\, x_3^k \tag{8}$$

Then let

$$\begin{aligned} \mathcal{S} &= \{\mathcal{S}_1, \mathcal{S}_2, \cdots, \mathcal{S}_{\mathcal{S}_s}\} = \{\mathcal{S}_\ell\} \\ \ell &= 1, 2, \cdots, \mathcal{S}_s \end{aligned} \tag{9}$$

be the set of parameters (constants) representing $E_{ijkln}, \tau^0_{ijkln}, A_{mnk}$, geometry, sizing, weight, cost, etc., and in the case of composites fiber orientation, number of plies, volume ratios, stacking sequences, etc., to be optimized.

Further, let $u(x,t)$ be generalized displacements representing rigid body motion, spanwise and chordwise bending, torsion, etc., which leads to sets of governing relations of motion in the generating form

Aeroviscoelasticity Designer FGMs: Passive Control Through Tailored Functionally Graded Materials, Table 1 Elastic and viscoelastic thermal coupling

Material	Temperature	Modulus	Convolution in t/ξ-spaces	EVCP
Elastic	$T(x)$	$E_0[x,\ \mathcal{F}(x)]$	no/no	n/a
Elastic	$T(x,t)$	$E_0[x,\ \mathcal{F}(x)]$	no/no	n/a
Viscoelastic	$T(x)$	$E[x,t-t',\ \mathcal{F}(x),T(x)]$	yes/yes	yes
Viscoelastic	$T(x,t)$	$E[x,t,t',\ \mathcal{F}(x),T(x,t')]$	no/yes	no

$$
\begin{aligned}
\mathcal{L}_u(x,t,S) = {} & \underbrace{m\frac{\partial^2 u(x,t)}{\partial t^2}}_{=\text{inertia }(T_1)} \\
& + \underbrace{c\frac{\partial u(x,t)}{\partial t}}_{=\text{external mechanical damping }(T_2)} \\
& + \underbrace{\int_{-\infty}^{t} \hat{D}_{kl}[x,\xi(x,t)-\xi',\ \mathcal{F}(x)]\frac{\partial \hat{\varepsilon}_{kl}(x,\xi')}{\partial \xi'}d\xi'}_{=\text{internal viscoelastic restoring force }(T_3)} \\
& - \underbrace{\int_{-\infty}^{t} \hat{D}^T[x,\xi(x,t)-\xi',\mathcal{F}(x)]\frac{\partial\left[\widehat{\alpha T}(x,\xi')\right]}{\partial \xi'}d\xi'}_{=\text{internal thermal expansion force }(T_4)} \\
= {} & \underbrace{F_V(x,t)}_{=\text{vibratory force }(T_5)} \\
& + \underbrace{F_{SC}\left(x,t,u(x,t),\frac{\partial(u(x,t)]}{\partial t},\frac{\partial^2(u(x,t)]}{\partial t^2},\int^t u(x,t')dt'\right)}_{=\text{differential and integral servo control force }(T_6)} \\
& + \underbrace{F_A\left(x,t,u(x,t),\frac{\partial(u(x,t)]}{\partial t},\frac{\partial^2[u(x,t)]}{\partial t^2}\right)}_{=\text{aerodynamic forces }(T_7)}
\end{aligned}
\tag{10}
$$

where the $\hat{D}_{kl}$ and $\hat{D}^T$ are differential spatial operators specific to the appropriate u component for beam and plate bending, torsion, etc. For instance, for Euler-Bernoulli beam bending, it is

$$
D_{1111}(x) = \frac{\partial^2}{\partial x_1^2}\left\{E[x,t,\mathcal{F}(x),T(x,t)]\frac{\partial^2}{\partial x_1^2}\right\} \tag{11}
$$

In order to examine the stability behavior of (10), it is advantageous to proceed in the following manner:

- Express the solution functions in terms of series

$$
u(x,t) = \sum_{m=1}^{M^u} A_m(t) f_m^u(x) \tag{12}
$$

  where each term $f_m^u(x)$ satisfies the BCs.
- Apply Galerkin's method and eliminate the x dependence resulting in integral ordinary differential equations of the type

$$
\begin{aligned}
& C_3\frac{d^3U(t)}{dt^3} + \underbrace{(S_2+A_2+C_2)}_{=B_2}\frac{d^2U(t)}{dt^2} \\
& + \underbrace{(S_1+A_1+C_1)}_{=B_1}\frac{dU(t)}{dt} \\
& + \underbrace{\left(\underbrace{S_0}_{\text{elastic}}+A_0+C_0\right)}_{=B_0}U(t) \\
& + \underbrace{\int_{-\infty}^{t}\hat{S}_I[\xi(t)-\xi']\frac{d\hat{U}(\xi')}{d\xi'}d\xi'}_{\text{viscoelastic including temperature dependence}} \\
& + \underbrace{C_I\int^t U(t')dt' = 0}_{\text{integral controller}}
\end{aligned}
\tag{13}
$$

where

$$
\begin{aligned}
S_n, S_I &= \text{structural coefficients,} \\
S_2 &= \text{mass coefficient} \\
A_n(V) &= \text{aerodynamic coefficients} \\
C_n &= \text{servo} - \text{control coefficients for} \\
&\quad \text{differential controllers} \\
C_I &= \text{integral controller coefficient}
\end{aligned}
$$

Aeroviscoelasticity Designer FGMs: Passive Control Through Tailored Functionally Graded Materials, Fig. 3 Viscoelastic flutter velocity

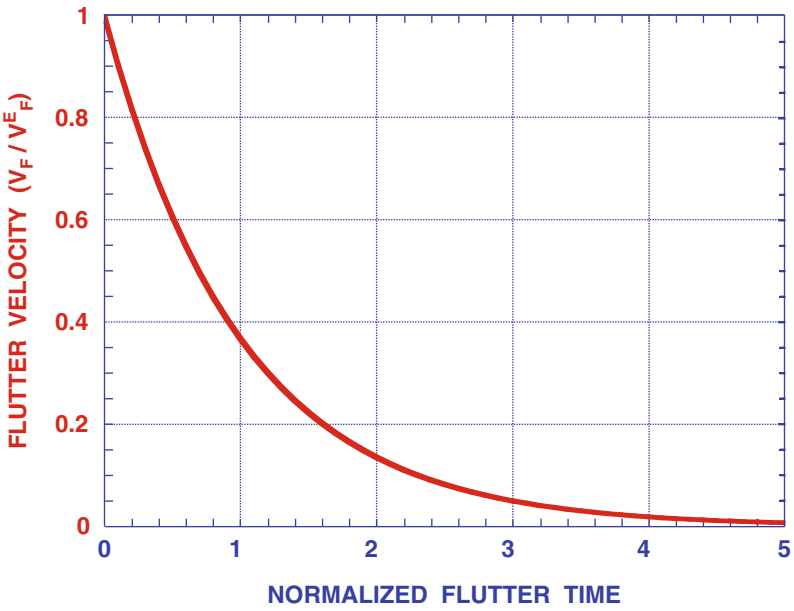

The presence of temperature functions $T(x,t)$ or $T(t)$, but not $T(x)$, in the $\hat{S}_I[\xi(t)]$ functions precludes the possibility of solutions $U(t) \sim \exp[(d + \imath\omega)t]$. Consequently, the customary flutter criterion of simple harmonic motion (SHM) when $d(V_F, \omega_F) = 0$ no longer represents an attainable flutter criterion. Instead an alternate viscoelastic one must be enforced, such that

$$\text{viscoelastic} \Rightarrow \begin{cases} \lim\limits_{\substack{t\to t_F \\ V\to V_F}} \{u(x,t,V)\} \to \infty \\ \text{or} \\ \lim\limits_{\substack{t\to t_F \\ V\to V_F}} \left\{\dfrac{\partial u[x,t,V]}{\partial t}\right\} \to \infty \end{cases} \tag{14}$$

These instability conditions can be determined from the solution's non-converging series or from a single unbounded amplitude in the solution series or through limit cycle analyses when applicable. In any case, (14) points to the fact that under variable temperatures viscoelastic flutter conditions are dictated by a combination of velocity (V_F) and critical time or time to flutter (t_F).

Figure 3 describes typical conditions according to the stability prescription (14). The ultimate viscoelastic velocity that can be reached is in this case the viscoelastic flutter velocity, and the graph depicts its reduced value compared to the equivalent elastic one. For a given lifting surface, both of these values will, of course, vary with altitude, trim angle, $T(t)$, etc. The time t_F is the time at which the viscoelastic flutter velocity occurs, and it is paired with a flutter velocity V_F, which in these cases are not eigenvalues. For a constant T, Fig. 3 would have roughly the same shape but different values. In general an increase in temperature decreases both V_F and t_F shifting the curve toward the origin. Conversely, a decrease in temperature has an opposite delaying effect.

The designer material formulation is basically that of an inverse problem solved through the calculus of variations [31]. The optimization is subject to prescribed constraints based on cost, weight, t_F, V_F, and some of the parameters S enumerated after (9). Formally the constraints can be stated as

$$\mathcal{C}(\mathcal{S}) = 0 \tag{15}$$

where S is a subset of the entire ensemble S. After (13) are solved for the $U(t)$, the temporal influence is eliminated by specifying t_F and hence $U(t_F)$, or any other convenient time, or an average U_{ave} value, such as

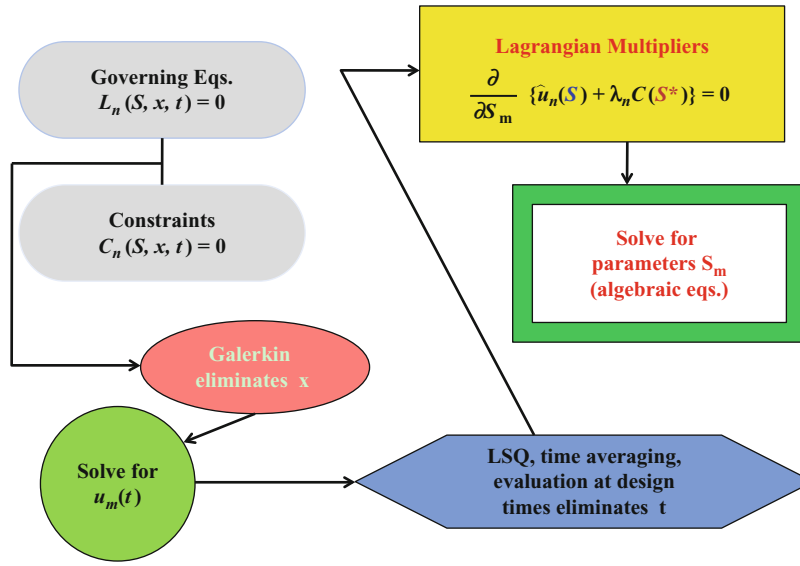

Aeroviscoelasticity Designer FGMs: Passive Control Through Tailored Functionally Graded Materials, Fig. 4 Designer flow chart

$$U_{ave}(S) = \int_0^{t_F} \frac{U(t)}{t_F} dt \qquad (16)$$

The next step is to solve the now remaining algebraic relations for each S_m from

$$\frac{\partial}{\partial S_m}\{\mathcal{L}_u(S) + \lambda \mathcal{C}(S)\} = 0 \qquad (17)$$

where λ is a Lagrangian multiplier [38]. The protocol is summarized in the flow chart of Fig. 4.

Discussion and Conclusions

Figure 5 depicts in a normalized fashion the effects of constant temperatures on V_F and t_F. As can be expected, an increase in temperature brings with it higher relaxation and creep rates and, therefore, both decrease in value as the temperature is elevated. The converse is seen as cooling effects take place.

The control that can be exercised on flutter and times to flutter at one constant temperature can be seen in Fig. 6. From left to right, the first curve representing a lifting surface with optimized homogeneous viscoelastic properties yields the shortest t_F and the lowest flutter velocities. When designer FGMs are applied to the same geometric surface, V_F s and t_F s are increased and flutter conditions are improved.

The use of FGM passive control principles is extremely attractive for UAVs and MAVs, where the lifting surfaces are light weight and more importantly highly flexible. Their limited mission scope compared to a more complex fighter or transport flight vehicle makes them ideally suited for a priori built in FGM distributions.

Of course these designer material studies create materials with hypothetical elastic or viscoelastic optimize properties. The next step, not part of these studies, is to develop manufacturing techniques to produce such materials to designer/tailored properties specifications. In [39], analyses are presented which relate material chemical structure to polymer properties. It offers a partial path to the inverse manufacturing quandary.

Finally, in [7], case analyses are developed to extend the designer material concepts to the entire vehicle. The possibility of carrying out the solution of possibly some 800,000,000 simultaneous algebraic equations for an estimated set of necessary parameters will materialize when the University of Illinois at Urbana-Champaign NSF/NCSA Blue Waters™ sustained petascale supercomputer comes online in late 2012 [40, 41].

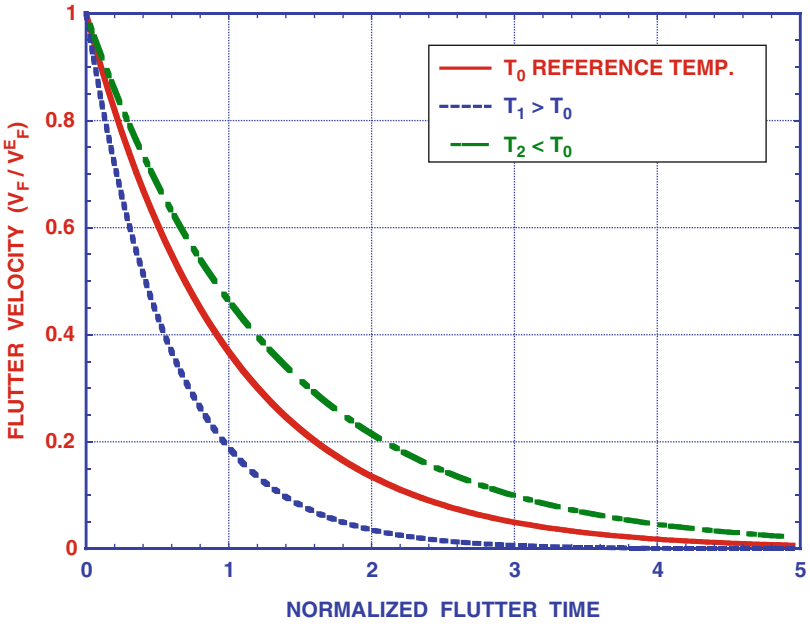

Aeroviscoelasticity Designer FGMs: Passive Control Through Tailored Functionally Graded Materials, Fig. 5 Temperature effects on viscoelastic flutter velocity

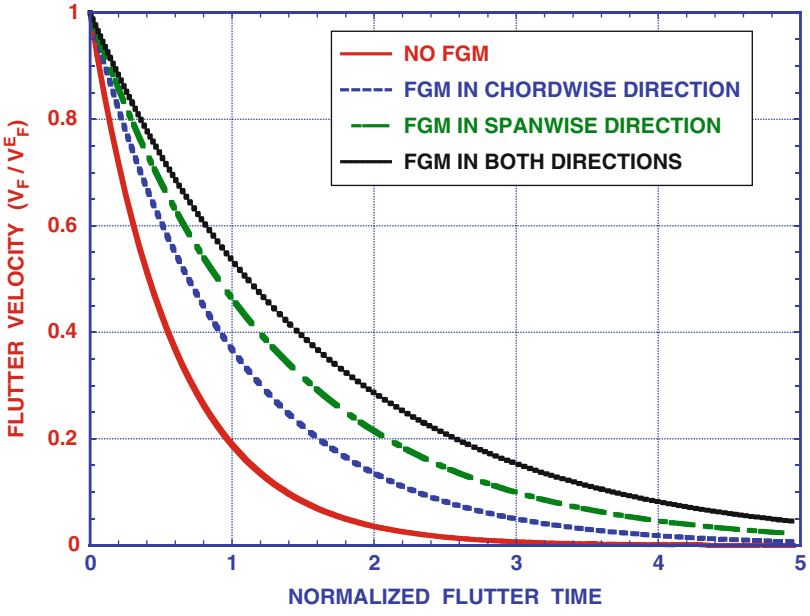

Aeroviscoelasticity Designer FGMs: Passive Control Through Tailored Functionally Graded Materials, Fig. 6 FGM influence on viscoelastic flutter velocity

References

1. Aik KK (2003) Plasma sprayed functionally graded ZrO_2/NiCoCrAlY thermal barrier coating. http://www.ntu.edu.sg/mae/research/programmes/adv_materials/FGM.htm
2. Buttlar WG, Eshan VD, Harry HH,Glaucio HP (2012) Viscoelastic functionally graded materials: theory and applications. Appl Mech Rev, in press
3. Marzocca P, Fazelzaded SA, Hosseini M (2011) A review of nonlinear aero-thermo-elasticity of functionally graded panels. J Therm Stresses 34:536–568
4. Hilton HH (2011) Equivalences and contrasts between thermo-elasticity and thermo-viscoelasticity: a comprehensive critique. J Therm Stresses 34:488–535. doi:10.1080/01495739.2011.564010
5. Brinson HF, Catherine Brinson L (2008) Polymer engineering science and viscoelasticity: an introduction. Springer, New York
6. Drozdov AD (1998) Mechanics of viscoelastic solids. Wiley, New York
7. Hilton HH (2012) A rational integrated approach to designer systems of systems: tailored aerodynamics, aeroelasticity, stability and control, geometry, materials, structures, propulsion, performance, sizing, weight, cost. In: Proceedings AIAA complex aerospace system exchange event (CASE), AIAA Paper 2012-XXXX, Pasadena, CA, 2012
8. Liebeck RH (1973) A class of airfoils designed for high lift in incompressible flow. J Aircr 10:610–617
9. Anonymous (2000) Eppler airfoil design and analysis code. http://www.airfoils.com/eppler.htm
10. Selig MS (2011) PROFOIL-WWW: Airfoil design software for the web. http://www.profoil.org
11. Cagle CM, Robin WS (2007) Composite elastic skins for shape changing structures. *NASA Tech Briefs LAR–16599–1*. http://www.techbriefs.com/content/view/1113/34/
12. Bloomfield MW, Herencia JE, Paul MW (2008) Optimization of anisotropic composite plates using an increased design envelope of ply orientations. In: Proceedings 49þAIAA/ASCE/ASME/AHS SDM conference, Schaumburg
13. Friswell MI, Herencia JE, Baker D, Paul MW (2008) The optimization of hierarchical structures with applications to morphing aircraft. In: Proceedings 2nd international conference on multidisciplinary design optimization and applications, www.asmdo.com/conference2008/
14. Brinkmeyer AWM, Santer AP, Paul MW (2012) Morphing composite panel with pseudo-bistable viscoelastic behavior. In: SEM XII international congress & exposition on experimental and applied mechanics, SEM Paper 404
15. Bisplinghoff RL, Holt A, Robert LH (1955) Aeroelasticity. Addison-Wesley, Cambridge, MA, (1980) Dover Publications, New York
16. Scanlan RH, Rosenbaum R (1951) Introduction to the theory of aircraft vibration and flutter. Macmillan, New York
17. Fung YC (1955) An introduction to the theory of aeroelasticity. Wiley, New York
18. Bisplinghoff RL, Holt A (1962) Principles of aeroelasticity. Wiley, New York
19. Dowell EH (1975) Aeroelasticity of plates and shells. Noordhoff International, Leyden
20. Dowell EH, Ilganov M (1988) Studies in nonlinear aeroelasticity. Springer, New York
21. Hodges DH, Alvin Pierce G (2002) Introduction to structural dynamics and aeroelasticity. Cambridge University Press, New York
22. Dowell EH, Tang D (2003) Dynamics of very high dimensional systems. World Scientific, River Edge
23. Dowell EH, Robert C, David C, Howard CC Jr, John WE, Kenneth CH, David AP, Robert HS, Emil S, Fernado S, Thomas WS (2004) A modern course in aeroelasticity. Kluwer, Boston
24. Donaldson BK (2006) Introduction to structural dynamics. Cambridge University Press, New York
25. Wright JR, Cooper JE (2007) Introduction to aircraft aeroelasticity and loads. Wiley, Hoboken
26. Hilton H (1957) Pitching instability of rigid lifting surfaces on viscoelastic sup-ports in subsonic or supersonic potential flow. In: Advances in solid mechanics. Edwards Bros, Ann Arbor, pp 1–19
27. Hilton HH (1960) The divergence of supersonic, linear viscoelastic lifting surfaces, including chord-wise bending. J Aerosp Sci 27:926–934
28. Merrett CG, Harry HH (2012) Generalized linear aero-servo-viscoelasticity: theory and applications. AIAA J, in press
29. Weaver PM, Ashby MF (1996) The optimal selection of material and section shape. J Eng Des 7:129–150
30. Hilton HH, Yi S (1992) Analytical formulation of optimum material properties for viscoelastic damping. J Smart Mater Struct 1:113–122
31. Hilton HH, Lee DH, Abdul RA, Fouly E (2008) General analysis of viscoelastic designer functionally graded auxetic materials engineered/tailored for specific task performances. Mech Time Dep Mater 12:151–178
32. Merrett CG, Harry HH (2012) Linear aero-thermo-servo-viscoelasticity: parts I & II. In: Hetnarski RB (ed) Encyclopedia of thermal stresses, viscoelasticity section. Springer, Berlin
33. Beldica CE, Harry HH, Cyrille G (2001) The relation of experimentally generated wave shapes to viscoelastic material characterizations: analytical and computational simulations. In: Proceedings of the sixteenth annual technical conference of the American society for composites CD-ROM Vol. pp 1–11
34. Beldica CE, Hilton HH (1999) Analytical simulations of optimum anisotropic linear viscoelastic damping properties. J Reinf Plast Comp 18:1658–1676
35. Beldica CE, Harry HH (2011) Analytical and computational simulations of experimental determinations

of deterministic and random linear viscoelastic constitutive relations. Accepted for publication. J Sandwich Struct Mater
36. Williams ML, Landel RF, Ferry JD (1955) The temperature dependence of relaxation mechanism in amorphous polymers and other glass-liquids. J Am Chem Soc 77:3701–3707
37. Schwarzl F, Staverman AJ (1952) Time-temperature dependence of linear viscoelastic behavior. J Appl Phys 23:838–843
38. Lagrange JL (1762) Essai d'une nouvelle methode pour déterminer les maxima et les minima des formules integrales indéfinies. Mélanges de philosophie et de mathématique de la Société Royale de Turin
39. Van Krevelen DW (1990) Properties of polymers: their correlation with chemical structure; their numerical estimation and prediction from additive group contributions, 3rd edn. Elsevier, Amsterdam
40. Anonymous (2009) http://www.ncsa.illinois.edu/News/Stories/Kramer/
41. Anonymous (2011) http://www.ncsa.uiuc.edu/BlueWaters/

Air Gap Nucleation

▶ Thermomechanical Growth Instability in Solidification

Allowable Temperature Rates for Pressure Components Using European Standards

Bohdan Węglowski
Institute of Thermal Power Engineering, Faculty of Mechanical Engineering, Cracow University of Technology, Cracow, Poland

Overview

The process of converting chemical energy, contained in fuel, into thermal energy takes place as a result of fuel combustion in power boilers, which ensures the production of steam of given parameters, mainly pressure and temperature, with the required large expense. Despite the relatively simple manufacturing process technology (Clausius-Rankine cycle) carried out in steam power plants, the equipment used in this process is of a highly complex, sophisticated design, with complex functional relationships between elements [1, 2]. The high temperature can contribute to premature failures of power units and, as a consequence, exclusion from the operation. The analysis of power units' operation [3] reveals that most loaded power unit elements are the boiler and turbine. The share of boiler failures requiring power block shutdown is caused, in most cases, by damage to the boiler pressure parts, that is, the evaporator and superheater.

During operation of the boiler, the high flame temperature in the combustion chamber, and the exhaust gas boiler superheater, can cause an overheating condition of steel, of which tube exchangers are made.

In contrast to steady-state boiler operation, completely different thermal and flow conditions prevail in transient conditions, that is, during start-up, shutdown, and rapid changes in boiler load. In transient conditions, there are large fluctuations in temperature, pressure, and mass flow rate of coolant. This affects the rate of heating and cooling criteria of thick boiler pressure parts. Uneven and too rapid changes in temperature of the wall give rise to thermal stresses, large enough to cause damage in the form of cracks. These cracks are visible, for example, in cylindrical pressure vessel boiler tubes in areas of precipitation. Therefore, boiler manufacturers put temperature rate limits, defining the acceptable rate of heating and cooling of boiler components. These elements are called "critical" and determine the duration of the start-up and shutdown processes.

Therefore, the correct start-up [2, 4–6], and the stable ability of the boiler to produce steam for a rating, is an essential element of operating boilers. The optimization of start-up allows the reduction in operation time of oil burners, so that they only work for the necessary period to achieve stable operation of the boiler at the beginning of the boiler start-up. The rate of the initial stages of boiler start-up is to provide a uniform process of heating the boiler, because of the possibility of deformation of the structure, from

uneven elongation under the influence of changes in temperature. Starting procedures also depend on the technical condition of the power boiler. Owing to pressure and temperature, there are five basic states of the boiler:

1. Cold state: (low-pressure boiler) the lack of steam pressure in the drum, temperature of below 80 °C, the open vent and drain valves in the boiler superheater.
2. Hot boiler state: steam drum pressure about 0.5 MPa, the temperature above 80 °C, closed drainage and venting.
3. Hot boiler margin: a state of the boiler equipment at the ready movement by allowing a planned power unit and the parameters of saturated steam in the drum, with a value of temperature 200 °C, pressure of 1.5 MPa.
4. Cold boiler margin: a state of the boiler equipment at the ready movement for reaching the planned power plant unit when starting from cold.
5. Emergency shutdown of the boiler: it is switched off owing to damage to the boiler, or it is impossible to maintain the boiler equipment in service in accordance with the instructions and rules of operation. This also includes unscheduled boiler shutdowns.

Commissioning of the boiler being on and off are processes that significantly determine the consumption of boiler pressure parts and their residual life [6–9]. During start-up and shutdown, parts with complex shapes are subjected to excessive stresses.

Proper design of the boiler pressure parts, material selection, and properly carried out calculations provide a low failure rate of the boiler. This is important in the period in which improving the performance of power units is associated with the construction of large units with supercritical parameters, owing to the use of new grades of steel with high strength, at high temperatures.

The proper design of boiler components subjected to thermomechanical loads is possible by using the European standard EN 12952-3:2001. This standard was adopted July 25, 2001, by CEN (Comité Européen de Normalisation/European Committee for Standardization) and was introduced, without any changes, in all member countries of CEN, as a national standard.

Fatigue Loads and Their Evaluation According to EN 12952-3

It is assumed that the boiler components are subjected to cyclic loads, when the boiler is designed for more than 500 starts from a cold state.

If you are given the size of the load, to which boiler pressure parts are subjected – that is, the number and types of transients, such as during start-up or shutdown, and the load changes adopted during the life of the calculation – the calculation of fatigue damage is determined by the hypothesis of linear accumulation Palmgren-Miner damage. This summation can be represented by the formula

$$\sum_{1}^{k} \frac{n_K}{N_k} = \left(\frac{n_1}{N_1} + \frac{n_2}{N_2} + \ldots + \frac{n_k}{N_k} \right) \qquad (1)$$

where n_1 is the number of cycles with the same alternating stress $2f_{vak}$, medium stress variable $\bar{f}_{vak}$, and the reference temperature t_k^* and N_k is the number of allowable cycles of load changes for given load conditions. This sum, which is a degree of exhaustion of the material, must not exceed 1.0.

In the case of pressure elements working in creep conditions, that is, at temperatures above 400 °C, calculating the total damage should also consider the contribution coming from the creep damage.

When they are not known to the boiler load, then the calculations shall be 2,000 starts from cold, with an increased margin of damage. Then, the degree of exhaustion of the material shall be less than, or equal to, 0.4:

$$\sum_{1}^{k} \frac{n_K}{N_k} \leq \begin{cases} 1,0 \;\; \text{for known load} \\ \\ 0,4 \;\; \text{for the adopted} \\ 2000 \text{ stats form cold} \end{cases} \qquad (2)$$

The determination of the number of load cycles and stresses is necessary to calculate the total damage from the low cycle load, according to (1). For this purpose, a stress analysis is performed to calculate the damage derived from thermal fatigue.

Stress Analysis

During operation, stresses arise on the thick-walled pressure parts of boilers, as a result of local changes in temperature and pressure. The greatest stresses occur at the edges of the inner surface, between the intersecting surfaces. Usually, these are the edges of the holes created by the surfaces of two cylinders, or a sphere and a cylinder. Owing to the dynamic operation of the boiler – that is, variations in temperature and pressure – the stresses occurring in thick-walled boiler components change over time.

Analyzing the simplest case of uniaxial load (Fig. 1), the range of stresses in the cycle (3) can be defined as the difference between the maximum and minimum value of the stress, and the mean stress as the arithmetic mean (4):

$$2f_{va} = \hat{f} - \check{f} \tag{3}$$

$$f_v = \frac{1}{2}(\hat{f} - \check{f}) \tag{4}$$

In fact, for complex shapes in place of the highest stress concentration – for example, on the edge of the hole – there is a multiaxial stress state described by equations

$$f_1 = f_{\text{tang}} = f_{\text{tang,p}} + f_{\text{tang,t}} \tag{5}$$

$$f_2 = f_{\text{rad}} = -p \tag{6}$$

$$f_3 = f_{ax} = -p \tag{7}$$

where

f_1 is shear stress on the base body and tangential to the hole, caused by pressure ($f_{\text{tang.p}}$ – component of the pressure, N/mm^2) and the temperature difference in the wall ($f_{\text{tang.t}}$ – component temperature, N/mm^2), N/mm^2;

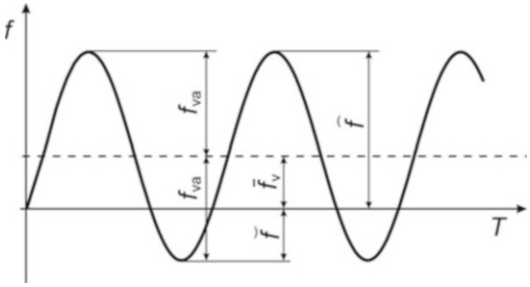

Allowable Temperature Rates for Pressure Components Using European Standards, Fig. 1 Schematic course of changes in stress during the uniaxial stress state [1]

f_2 is radial stress on the body of basic compensation of fluid pressure (p) on the inner surface of the hole in the main body, N/mm^2;

f_3 is axial stress to compensate for the fluid pressure (p) on the outer surface of the hole or branching, N/mm^2.

Using the hypothesis of maximum shear stress can save time differences of principal stresses:

$$\Delta f_{12} = f_1 - f_2 = f_{\text{tang}} + p \tag{8}$$

$$\Delta f_{23} = f_2 - f_3 = 0 \tag{9}$$

$$\Delta f_{31} = f_3 - f_1 = -(f_{\text{tang}} + p) \tag{10}$$

In this case, the extent of the stress cycle is determined by the largest value from the strain differences (11),

$$2f_{va} = \max \begin{Bmatrix} \Delta\hat{f}_{12} - \Delta\check{f}_{12} \\ \Delta\hat{f}_{23} - \Delta\check{f}_{23} \\ \Delta\hat{f}_{31} - \Delta\check{f}_{31} \end{Bmatrix} \tag{11}$$

while the corresponding average stress range is the average of the differences of principal stresses (12):

$$\bar{f}_v = \frac{1}{2}(\Delta\hat{f} - \Delta\check{f}) \tag{12}$$

This means that during boiler cycling (temperature and pressure change over time), the stresses in the weakened hole pressure elements can be defined as maximum stress $\Delta\hat{f}_{12}$ minus minimum

stress $\Delta\breve{f}_{12}$. If $\Delta\hat{f}_{12}$ and $\Delta\breve{f}_{12}$ are above stresses, the range of stress variation is

$$2f_v = \Delta f_v = \Delta\hat{f}_{12} - \Delta\breve{f}_{12} \tag{13}$$

For the calculation of minimum and maximum stress, the finite element method can be used, or a simplified calculation with the relevant coefficients of stress concentration factors or notch.

For purposes of computing, the considered load cycle was introduced in the reference temperature cycle

$$t^* = 0,75 \cdot \hat{t} + 0,25 \cdot \breve{t} \tag{14}$$

where

$\hat{t} = \max\{t_{\hat{\sigma}}, t_{\breve{\sigma}}\}$ is the maximum temperature at which the greatest stress occurs in the cycle,

$\breve{t} = \min\{t_{\hat{\sigma}}, t_{\breve{\sigma}}\}$ is the minimum temperature at which there is least stress in the cycle.

The reference temperature t^* is also the temperature at which all known temperature-dependent material properties are determined.

Calculation of Minimum and Maximum Stress

To determine the allowable range of stresses for all the pressure components, fatigue diagrams of steel are used.

By knowing the number of cycles at which there is destruction of the item, or the projected number of cycles, the difference between the maximum and minimum stress $2f_a$ during one cycle can be determined from the graph of fatigue. An example of the fatigue curve described by (15), for different ferritic steels (R_m), is shown in Fig. 2:

$$2f_a = 0.8 \cdot R_m + (173150 - 0.8 \cdot R_m) \cdot N_A^{-0.547} \tag{15}$$

In the case of calculations for an infinite number of cycles, (15) takes a simpler form:

$$2f_a = 0.8 \cdot R_m \tag{16}$$

Since the fatigue curves described by (15) have been developed, based on experimental data, they do not include safety factors. These should be taken into account by applying a safety factor to determine the acceptable range of strain $S_S = 1.5$, and the load cycles $S_L = 10$. After taking safety factors into account, and the adoption of the design number of cycles $N_A = N$ in (15),

$$2f_{as} = 0.8 \cdot R_m + (173150 - 0.8 \cdot R_m) \cdot N^{-0.547} \tag{17}$$

$$2f_{al} = 0.8 \cdot R_m + (173150 - 0.8 \cdot R_m) \cdot (N \cdot S_L)_A^{-0.547} \tag{18}$$

can calculate the allowable range of stress (19):

$$2f_{at^*}^* = \min\left\{\begin{matrix} \dfrac{2f_{as}}{S_S} \\ 2f_{al} \end{matrix}\right\} \tag{19}$$

The thick-walled pressure parts of boilers are designed to work in fixed thermal conditions and under specified pressure. The work of the same elements in transient states, which occur during the start-up and shutdown of the boiler, characterizes variable pressure and temperature on the large differences in wall thickness. There are also large differences in temperature at the periphery of the pressurized parts, especially where there is a two-phase factor. This is not only the boiler drum, where, by definition, there is a gas phase and liquid, but this situation can also occur in the elements, in which liquid is derived from the condensation of steam during the boiler shutdown or start-up. The steam condenses on the inner walls of the cooler parts of the boiler [10–12]. Therefore, further calculations, relating to the proper determination of the range of permissible stresses, are related to the properties of the material of which the pressure elements are made of. On the basis of the yield R_{et^*} at the reference temperature, (14) works whereby the fatigue work pressure and an element of the standard EN 12952-3:2001 make further calculations by introducing the concept of an authoritative range of stresses $2f_a^*$:

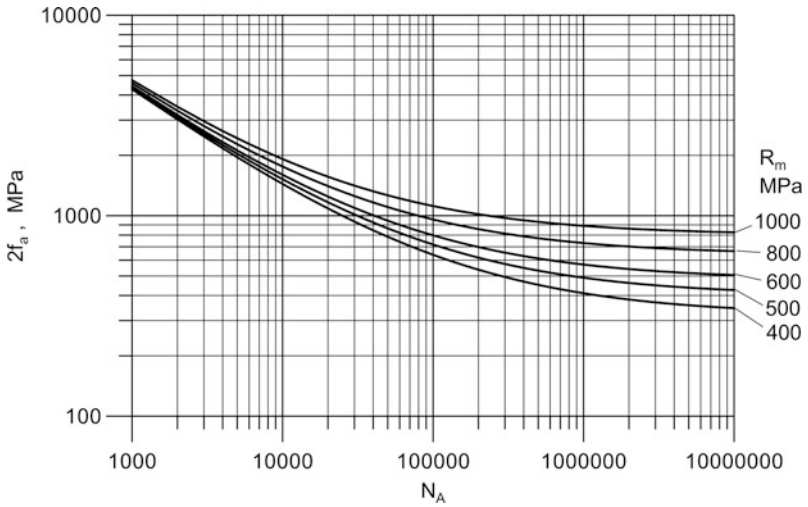

Allowable Temperature Rates for Pressure Components Using European Standards, Fig. 2 Fatigue diagram for creep of ferritic steels. N_A, number of load cycles, $2f_a$, the stress range of ferritic steels, R_m, minimum tensile strength at room temperature [1, 2]

$$\left|f_v^*\right| + \frac{2f_{va}^*}{2} \le R_{p0.2/t^*} \tag{20}$$

If fatigue occurs in the spring, which is a reliable range of stresses $2f_a^*$ as a function of the corrected stress range $2f_{va}^*$, the corrected average value of equivalent stress range f_v^* can be expressed by the formula

$$2f_a^* = \frac{2f_{va}^*}{1 - \left(\frac{f_v^*}{R_m}\right)^2} \tag{21}$$

In terms of elastic plastic, for which the inequalities are satisfied in (22) and (23),

$$\left|f_v^*\right| + \frac{2f_{va}^*}{2} > R_{p0.2/t^*} \tag{22}$$

and

$$2f_{va}^* \le R_{p0.2/t^*} \tag{23}$$

maximum stress f_v^* is

$$f_v^* = C_k \times \max(|\Delta f_{12}|, |\Delta f_{23}|, |\Delta f_{31}|) \tag{24}$$

where C_k is the correction factor that takes into account the effect of surface finish and welded joints.

A meaningful range of stresses in the elastic–plastic range is calculated as the elastic range using formula (21), except that the reduced value will be the average of the maximum stress f_{vR}^*:

$$f_{vR}^* = R_{p0.2/t^*} - \frac{2f_{va}^*}{2} \tag{25}$$

The corrected range of stresses $2f_a^*$ is

$$2f_a^* = \frac{2f_{va}^*}{1 - \left(\frac{f_{vR}^*}{R_m}\right)^2} \tag{26}$$

In terms of art, when corrected stress range

$$2f_{va}^* > 2R_{p0.2t^*} \tag{27}$$

a meaningful range of stresses $2f_a^*$ as a function of yield strength is

$$2f_a^* = \frac{(2f_{va}^*)^2}{2R_{p0.2/t^*}} \tag{28}$$

In this case, the average equivalent stress range f_v^* can be assumed to be equal to zero.

The above relationships allow the calculation of the corrected equivalent stress range $2f_{va}^*$ depending on yield strength. They are:

For an elastic range,

$$2f_{va}^* = 2f_a^* \tag{29}$$

For an elastic–plastic range,

$$2f_{va}^{*} = 2 \cdot R_m \cdot \left(\frac{R_{p0.2t^*}}{R_m} - \frac{R_m}{2f_a^*} + \sqrt{1 - 2 \cdot \frac{R_m}{2 \cdot f_a^*} \cdot \frac{R_{p0.2t^*}}{R_m} + \left(\frac{R_m}{2f_a^*} \right)^2} \right) \tag{30}$$

For a plastic range,

$$2f_{va}^{*} = \sqrt{2 \cdot R_{p0.2t^*} \cdot 2f_a^*} \tag{31}$$

Since all elements of the boiler, which are essential for the conduct of unrest, and for which we calculate operating at temperatures above 100 °C, can then be calculated according to formulas (29), (30), or (31), and adjusted for equivalent $2f_{va}^{*}$, stress takes into account the reduction in fatigue stress at temperatures above 100 °C, using a correction coefficient C_{t^*}.

Depending on the steel used for the element, a pressure correction factor C_{t^*} is calculated from formulas (31) or (33):

$$\text{For ferritic steel, } C_{t^*} = 1.03 - 1.5 \cdot t^* - 1.5 \cdot 10^{-6} \cdot t^{*2} \tag{32}$$

$$\text{For austenitic steels, } C_{t^*} = 1.043 - 4.3 \cdot 10^{-4} \cdot t^* \tag{33}$$

The dependence of C_{t^*} computes the temperature t^* in the temperature range 100–600 °C, as presented in Fig. 3.

Stress Concentration Factors and Notch

The simplification, by using the hypothesis of maximum shear stress in the stress analysis, which leads to the multi-axis stress state of the main courses, requires the use of stress concentration factors α_m for cylindrical surfaces and α_{sp} for spherical shells. In the case of the boiler drum, it will be a factor α_m for the cylindrical shells. If the maximum stress in the cycle $f_{\max}$ is known, then the operating pressure can be calculated from formula (34),

$$\alpha_m = \frac{f_{\max}}{\frac{p_0 \cdot d_{ms}}{2 \cdot e_{ms}}} \tag{34}$$

where d_{ms} is the mean diameter of the drum and e_{ms} the average thickness of the nozzle wall (Fig. 4). If the load element is unknown, α_m can be seen from the graph (Fig. 4), depending on the concentration ratio α_m of the geometrical parameters.

The stress concentration factor α_m, shown in Fig. 6, is a function of the geometrical parameter ξ for various wall thickness ratios, of the average branching e_{mb} to the average thickness of the main body e_{ms}, and is described by equation

$$\alpha_m = 2,2 + e^A \cdot \xi^B \tag{35}$$

where

$$\xi = \frac{d_{mb}}{d_{ms}} \sqrt{\frac{d_{ms}}{2 \cdot e_{ms}}},$$

$$A = -1.14 \left(\frac{e_{mb}}{e_{ms}} \right)^2 - 0.89 \cdot \frac{e_{mb}}{e_{ms}} + 1.43$$

$$B = 0,326 \left(\frac{e_{mb}}{e_{ms}} \right)^2 - 0.59 \cdot \frac{e_{mb}}{e_{ms}} + 1.08 \tag{36}$$

Similarly, the stress concentration factor for spherical shells α_{sp} is used in the calculation of steam piping components, such as tees and ball valves for steam valve body. Stress concentration factors α_m and α_{sp} allow for proper calculation of circumferential stress components, owing to pressure. It should be noted, however, that they relate to the equivalent stress in the middle of the wall.

The values Δf_{12} in (13) can be calculated using the finite volume method (FEM). In both cases, one can assume that the corrected stress extent $2f_{va}^{*}$ is

$$2f_{va}^{*} = 2f_{va} \tag{37}$$

In case that the values of Δf_{12} are calculated taking account the stress concentration factors α_m

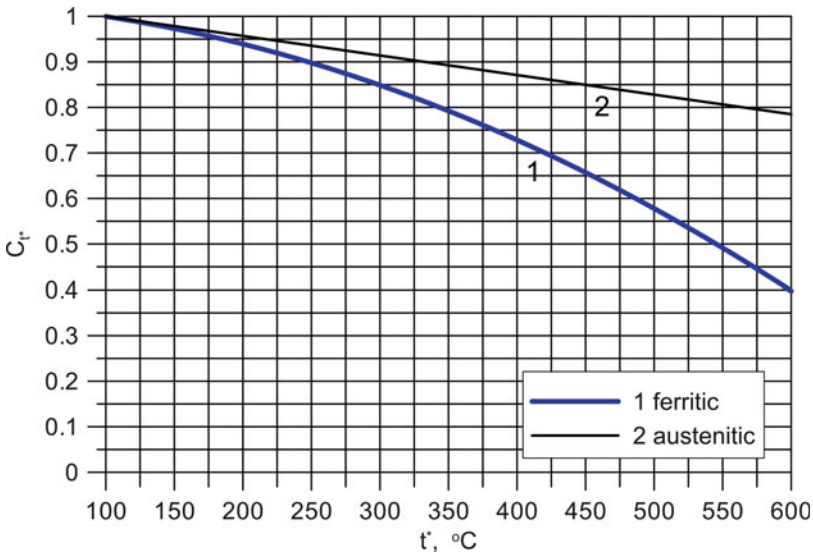

Allowable Temperature Rates for Pressure Components Using European Standards, Fig. 3 Correction factor C_{t^*} for taking account of the temperature influence [1]

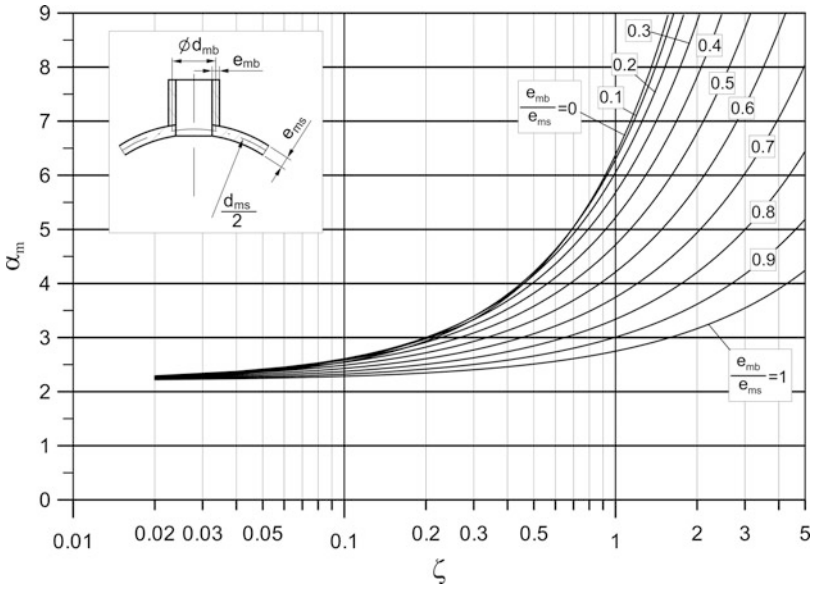

Allowable Temperature Rates for Pressure Components Using European Standards, Fig. 4 Stress concentration factor α_m for cylindrical shells as a function of geometrical parameters [1]

and α_{sp}, the impact of micro-notches and the structure of the surface and welded joints should also be considered. Then, the corrected stress extent of $2f^*_{va}$ is

$$2f^*_{va} = 2f_{va} \cdot C_k \tag{38}$$

EN 12952-3 shows the correction factors C_{k0}, taking into account the effect of notches on the surface, caused by the mill scale and correction factors, as well as taking into account the effect of notches for welded joints, which, owing to notch effects, have been divided into three classes. Considering it can calculate the adjusted extent of stresses (38) and corrected mean stress cycle:

$$\bar{f}^*_v = \bar{f}_v \cdot C_k \tag{39}$$

In the calculations of the second component that comes from changes in temperature, the

stress concentration factor is used and takes into account the stresses arising in the areas of stress concentration α_t for cylindrical and spherical shells weakened by holes for pipes, the temperature change agent.

In the calculations, it is convenient to use (40), describing the change of thermal stress concentration coefficient α_t, depending on the ratio of the average diameter of the connector pipe to the average radius of the cylindrical and spherical vessel,

$$\alpha_t = \left\{ \left[2 - \frac{h+2700}{h+1700} + \frac{h}{h+1700} \cdot \left(e^{-7z} - 1 \right) \right]^2 + 0,81 \cdot z^2 \right\}^{\frac{1}{2}} \tag{40}$$

where

$$z = \frac{d_{mb}}{d_{ms}}$$

h – heat transfer coefficient, W/m^{2}K.

Heat transfer coefficient h is taken depending on the medium-pressure element:

h = 1,000 W/m^{2}K for steam

h = 3,000 W/m^{2}K for water

The temperature coefficient of stress concentration α_t, depending on the ratio of the average diameter of the spigot to the average radius of the cylindrical and spherical body, for water and steam inner surface, is shown in Fig. 5.

Permissible Stress Ranges

The range of stress Δf_v changes, calculated using (13), should be less than the allowable range of stress in the cycle $2f_{va}$, which can be written in the form of inequalities:

$$\Delta f_v \leq 2f_{va} \tag{41}$$

The total stress extent Δf_{tang} is calculated by the hypothesis of the largest shear stress, the stress intensity range as peripheral variables from minimum $p_{\min}$ to maximum $p_{\max}$ pressure in the cycle, and as for principal stresses,

$$\Delta f_{\text{tang}} = 2f_{va} - (p_{\min} - p_{\max}) \tag{42}$$

and for the second principal stress,

$$\Delta f_{\text{tang}} = 2f_{va} - (-p_{\min} + p_{\max}) \tag{43}$$

The total range of stress on the peripheral edge of the hole is a combination of stresses on the main directions of the load from the pressure and thermal stresses, resulting from the temperature difference between the thickness of the weakened wall of the pressure ring (44),

$$\Delta f_{\text{tang}} = \Delta f_{\text{tang,p}} + \Delta f_{\text{tang,t}} \tag{44}$$

where $\Delta f_{\text{tang,p}}$ is the component of the pressure, $\Delta f_{\text{tang,t}}$ is the temperature component.

In special cases, when combined with connection, there is additional stress and influence of stress on the inner surface, and the entire range of admissible stress can diminish the value of these stresses $\Delta f_{\text{tang,f}}$.

During start-up and shutdown, large temperature differences occur in the cross wall of the pressure elements. These temperature differences are caused by different heat transfer coefficients in water and steam regions.

The formation of a protective layer of magnetite Fe_3O_4 is important for the operation of pressure equipment and is a phenomenon that occurs on the inner surface. Since the magnetite layer is generated during operation of the boiler, which is the period when the wall elements have a high temperature, then during the cooling of the boiler, stresses will occur in the layers close to the inner surface compressive. In order to prevent degradation of the protective magnetite layer on the inner surface, the range of admissible stress f_{tang} is narrowed by raising the lower limit of 200 MPa, and the top is lowered by 600 MPa:

$$f_{\text{tang,po}} - 600\text{MPa} \leq f_{\text{tang}} \leq f_{\text{tang,po}} + 200\text{MPa} \tag{45}$$

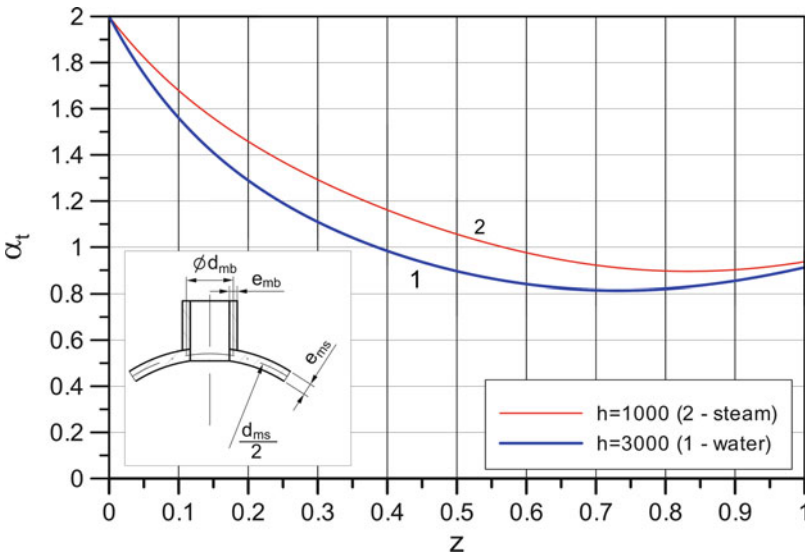

Allowable Temperature Rates for Pressure Components Using European Standards, Fig. 5 Stress concentration factor due to thermal stresses α_t for cylindrical and spherical shells [1]

This prevents damage to the protective inner layer of magnetite, penetrating cracks and subsequent oxidation of the batch.

Circumferential Stresses on the Pressure

The pressure component $\Delta f_{\text{tang,p}}$, as part of the allowable range of stress in the weakened peripheral element hole laden EU standard pressure p, is defined (because of the large ratio of diameter to wall thickness) as for thin-walled vessels:

$$\Delta f_{\text{tang, p}} = \frac{\alpha_m \cdot d_{ms}}{2 \cdot e_{ms}} \cdot p \text{ for cylindrical shells} \tag{46}$$

$$\Delta f_{\text{tang,p}} = \frac{\alpha_{sp} \cdot d_{ms}}{4 \cdot e_{ms}} \cdot p \text{ for spherical shells} \tag{47}$$

Signs in (46) and (47) are as in the previous sections.

Thermal Stresses

The second component of the stresses inside the hole, on the surface peripheral stresses $\Delta f_{\text{tang,t}}$, are derived from the temperature difference between the wall thickness,

$$\Delta f_{\text{tang,t}} = \frac{\alpha_t \cdot \beta_{Lt^*} \cdot E_{t^*}}{1 - v} \cdot \Delta t \tag{48}$$

where

β_{Lt^*} is the coefficient of linear expansion at the calculation temperature t^*, K^{-1};

E_{t^*} is the module of elasticity at the calculation temperature t^*, MPa;

v is the number of Poisson;

α_t is the coefficient of stress concentration on the temperature difference.

The temperature difference Δt is defined as the difference between the mean integral temperature in the wall t_m and inner wall surface temperature t_i:

$$\Delta t = t_m - t_i \tag{49}$$

For the same range of pressure changes, for which the stresses were calculated from pressure $\Delta f_{\text{tang,p}}$, the extent of thermal stress can be calculated

$$\Delta f_{\text{tang,t}} = \frac{\alpha_t \cdot \beta_{Lt^*} \cdot E_{t^*}}{1 - v} \cdot (\Delta t_2 - \Delta t_1) \tag{50}$$

When the refrigerant temperature rises and heats the inner surface of the pressure elements, as follows from (49), the temperature difference Δt_1 in the wall is reduced by adopting a

negative sign. When an item is cooled, then the difference Δt_2 is positive. In this way, the calculated thermal stress is the second component of the acceptable range of peripheral stress variables Δf_{tang}.

Determination of the Stress Boundary

The calculated total allowable extent of peripheral stress Δf_{tang} (45) takes into account the stress from the pressure, the change of temperature and stress condition, limiting the amount owing to the behavior of the oxide layer on the inner surface. The determination of the yield strength helps to identify thermal stress, because stress from the pressure is easy to calculate.

For components made of austenitic materials, in contact with steam or water, and for components made from other materials, in contact only with water vapor, the maximum circumferential stress on the inner surface of the hole is determined by (51), while the minimum allowable circumferential stress on the inner surface hole, according to (52), is

$$f_{\text{tang,max}} = f_{\text{tang,pmax}} + g_s \cdot \Delta f_{\text{tang,t}} \tag{51}$$

$$f_{\text{tang,min}} = f_{\text{tang,pmax}} - g_s \cdot \Delta f_{\text{tang,t}} \tag{52}$$

In the case of components made of ferritic or martensitic steel, in contact with water, the maximum allowable stress on the circumferential inner surface of the hole is determined by formula (53) and the minimum by (54):

$$f_{\text{tang. max}} = \min \left\{ \begin{array}{l} f_{\text{tang,pmax}} + g_s \cdot \Delta f_{\text{tang,t}} \\ f_{\text{tang,po}} + 200 \dfrac{\text{N}}{\text{mm}^2} \end{array} \right\} \tag{53}$$

$$f_{\text{tang. min}} = \max \left\{ \begin{array}{l} f_{\text{tang,pmax}} - g_s \cdot \Delta f_{\text{tang,t}} \\ f_{\text{tang,po}} - 600 \dfrac{\text{N}}{\text{mm}^2} \end{array} \right\} \tag{54}$$

In (53) and (54), the symbol g_s is the ratio determining the share of thermal stresses within the allowable stress on the surface of the inner peripheral opening, at the beginning of withdrawal, that is, when the pressure is highest and is $p_{\max}$. g_s factor can take values from 0 to 1 ($0 \le g_s \le 1$). If $g_s = 0$ then it is used by the entire range of thermal stresses $f_{\text{tang},t}$ caused by temperature changes at the pressure minimum $p_{\min}$. In practice, the majority of boiler pressure parts shall be a factor $g_s = 0.5$. The result is that the distribution of thermal stresses $f_{\text{tang,t}}$ is symmetrical between $f_{\text{tang,p max}}$ and $f_{\text{tang,p min}}$ for the heating and cooling of the pressure element.

Permissible Heating Rate and Temperature Differences in the Wall

The permissible rate of temperature changes in boiler pressure parts can be calculated assuming quasi-stationary state changes in temperature. As defined by formulas (49) and (50), it allows the use of the allowable temperature difference for calculating the rate of temperature changes in the wall (55),

$$v_t = \Delta t \cdot \frac{D_{th}}{\gamma_{ec} \cdot e_{ms}^2} \tag{55}$$

where

$D_{th} = \frac{k}{\rho_m c_p}$ is the metal temperature compensation coefficient, m^2/s;

e_{ms} is the average wall thickness of the body, m;

γ_{ec} is the ratio for an element of pressure.

The form factor for the ratio of outer diameter d_o to inner diameter d_i of $u_o = \frac{d_o}{d_i}$ is equal to:

For tubular forms,

$$\gamma_{ec} = \gamma_{cyl} = \frac{\left(u_o^2 - 1\right) \cdot \left(3u_o^2 - 1\right) - 4u_o^2 \ln u_o}{8\left(u_o^2 - 1\right) \cdot \left(u_o - 1\right)^2} \tag{56}$$

For spherical shells,

$$\gamma_{ec} = \gamma_{sp} = \frac{1}{3} \cdot \left[u_o + \frac{\left(u_o - 1\right)^3}{5 \cdot \left(u_o^3 - 1\right)} \right] \tag{57}$$

The calculation of temperature differences in the boundary wall of the pressure elements, during heating and cooling processes to be carried out, assume a total not to exceed the

permissible range of stresses. Using (51), (52), and (50) limits for temperature differences can be determined

$$\frac{f_{\text{tang,min}} - f_{\text{tang,p}}}{W} \leq \Delta t \leq \frac{f_{\text{tang,max}} - f_{\text{tang,p}}}{W} \quad (58)$$

where

$$W = \frac{\alpha_t \cdot \beta_{Lt^*} \cdot E_{t^*}}{1 - \nu} \quad (59)$$

Using formulas (55) and (58), the limit values can be calculated: the difference in temperature and heating rate, taking the pressure $p = p_{\min}$ for the beginning of start-up and $p = p_{\max}$ for the end of start-up. In the case of shutdown, the beginning is assumed for $p = p_{\max}$ and the end for $p = p_{\min}$.

At the beginning of the start-up ($p = p_{\min}$), the limit values are:

Allowable temperature difference,

$$\Delta t_1 \geq \frac{f_{\text{tang,min}} - \Delta f_{\text{tang,pmin}}}{W} \quad (60)$$

Allowable heating rate,

$$v_{t1} = \Delta t_1 \cdot v_t \quad (61)$$

At the end of the run ($p = p_{\max}$), the limit values are:

Allowable temperature difference,

$$\Delta t_1' \geq \frac{f_{\text{tang,min}} - \Delta f_{\text{tang,pmax}}}{W} \quad (62)$$

Allowable heating rate,

$$v_{t1} = \Delta t_1' \cdot v_t \quad (63)$$

Similarly, sets of limit values for cooling ($p = p_{\max}$) are:

Allowable temperature difference,

$$\Delta t_2 \geq \frac{f_{\text{tang,max}} - \Delta f_{\text{tang,pmax}}}{W} \quad (64)$$

Allowable heating rate,

$$v_{t1} = \Delta t_2 \cdot v_t \quad (65)$$

At the end of shutdown ($p = p_{\min}$), the limit values are:

Allowable temperature difference,

$$\Delta t_2' \geq \frac{f_{\text{tang,max}} - \Delta f_{\text{tang,pmin}}}{W} \quad (66)$$

Allowable heating rate,

$$v_{t1} = \Delta t_2' \cdot v_t \quad (67)$$

Calculated in this way, the heating rate and the permissible limit temperature differences in thick-walled pressure parts of boilers are allowed to run riot and are exempt from service, so as to not exceed the allowable stress. This contributes to improving the life of boiler pressure parts.

The Calculation of the Temperature Difference, Heating Rate and Maximum Stress on the Example of Drum Boiler OP-230

In order to illustrate the methods of determining the basic parameters during transient operation using EN 12952-3, calculations were made for the drum of the steam boiler OP-230. The OP-230 boiler is a natural circulation boiler with two passes and is fuelled by pulverized coal. The burners are located at the corners of the combustion chamber.

Basic data on the efficiency of the boiler and pressure and temperature of superheated steam are listed in Table 1.

To perform the calculations necessary to determine the geometrical dimensions adequately (Table 2), the parameters of the pressure element are analyzed (Table 3), as well as the properties of the material of which the pressure is part (Table 4).

Properties of the material, from which boiler OP-230's drum is made, are given for calculating the temperature determined from (14).

Allowable Temperature Rates for Pressure Components Using European Standards, Table 1 Basic data for boiler OP-230

Sn	The parameter name	Value	Unit
1.	Maximum live steam output (feed water temperature 205 °C)	230	t/h
2.	Maximum sustainable yield steam (feed water temperature 150 °C)	212	t/h
3.	Maximum live steam output (feed water temperature 205 °C)	253	t/h
4.	Minimum live steam output	115	t/h
5.	Steam pressure at the outlet from the boiler	13,5	MPa
6.	Superheated steam temperature	540	°C
7.	Feed water temperature	205/150	°C

Allowable Temperature Rates for Pressure Components Using European Standards, Table 2 Geometrical parameters of the drum boiler OP-230

Sn	The parameter name	Symbol	Value	Unit
1.	Outer diameter of the element	d_0	1.884	m
2.	Average wall thickness of the element	e_{ms}	0.90	m
3.	Average diameter	d_{ms}	1.792	m
4.	Outer diameter of the branch	d_{ob}	0.415	m
5.	Average wall thickness of the branch	e_{mb}	0.064	m
6.	Average diameter of the branch	d_{mb}	0.351	m

The Results of Calculations Allowable Parameters for Heating and Cooling of the Pressure Element

For drum boiler OP-230, allowable temperature differences were calculated, such as the rate of heating and cooling and permissible stresses during start-up and shutdown of the boiler of the movement. For the calculation of the drum geometric dimensions given in Table 2, and the operating parameters and material properties for start-ups from cold state, as well as after 2 and 8 h of stopping, respectively, from Tables 3 and 4, the calculations assume that the degree of exhaustion of the material of the drum should not exceed 0.4 at 2,000 actuations from a cold state. Safety factors were $S_S = 1.5$ for the stresses and $S_L = 10$ for cycles. A summary of the results is shown in Table 5.

A graphical presentation of the results given in Table 5 is shown in Figs. 6 and 7.

The calculated limit of the drum wall temperature difference for heating and cooling, as a function of pressure (Fig. 6), shows that during the start-up, with the increase of pressure, the temperature difference in the wall can be increased. The value of allowable temperature difference is dependent on the state, which initiated the process to run the boiler. For elements with a higher initial temperature (less downtime), the allowable temperature difference is smaller in the wall.

Similar relationships are observed by analyzing the allowable heating rate of thick, pressurized boiler components (Fig. 7). With the increasing pressure, the pressure element may be heated at a faster rate. The rate of heating depends on the initial wall temperature of the pressure element, which is how long the boiler standstill is triggered.

The calculated degree of wear of the drum (the states of cold) for $N = 2{,}000$ cycles is 0.0872, the states after 8 h. standstill is 0.0321, and the states after 2 h. standstill is 0.0222.

Analysis of Thermal Strength Conditions of the Drum Boiler OP-230 During Heating

The results of calculations of the heating rate, and the maximum allowable temperature differences, were compared with measurements performed on a real drum boiler OP-230, working in one of the Polish conventional power plants. Metal temperatures were measured on the outer surface of the drum in the positions shown in Fig. 8 (points 1–7).

The transient temperature distribution, in the cross section of the boiler drum, was calculated as the solution of the inverse heat conduction problem, with the cross section divided into the control volumes. The calculated temperature histories on the inner surface of the boiler drum are presented in Fig. 9 and the temperature differences over the wall thickness in Fig. 10.

Allowable Temperature Rates for Pressure Components Using European Standards, Table 3 Parameters of drum boiler OP-230

Sn	The parameter name	Symbol	Value (from cold)	Value (after 8 h)	Value (after 2 h)	Unit
1.	Design pressure	p_c	14.9	14.9	14.9	MPa
2.	Design temperature	t_c	343	343	343	°C
3.	Operation pressure	p_o	14.9	14.9	14.9	MPa
4.	Minimum pressure cycle	$p_{\min}$	0.0	7.5	10.3	MPa
5.	The maximum pressure cycle	$p_{\max}$	14.9	14.9	14.9	MPa
6.	Minimum temperature cycle	$t_{\min}$	20	290	313	°C
7.	Maximum temperature cycle	$t_{\max}$	353	353	353	°C
8.	Reference temperature	t^*	269.7	337.2	335.5	°C

Allowable Temperature Rates for Pressure Components Using European Standards, Table 4 Material properties of the drum (15NiCuMoNb5-6-4) at room temperature t and computing t^*

Sn	Parameter	Symbol	Value (from cold)	Value (after 8 h)	Value (after 2 h)	Unit
1.	Tensile strength at room temperature $T = 20\ ^\circ C$	R_m	627	627	627	MPa
2.	Yield strength at temperature t^*	$Re(t^*)$	362	346	343	MPa
3.	Coefficient of linear expansion at temperature t^*	$\beta_{L(t^*)}$	1.47E-5	1.54E-5	1.54E-5	$\frac{1}{K}$
4.	Young's modulus at temperature t^*	E_t	1.958E5	1.896E5	1.891E-5	MPa
5.	Metal diffusivity at temperature t*	D_{th}	1.63E-7	1.509E-7	1.498E-7	$\frac{m^2}{s}$
6.	Poisson's ratio in t^*	ν	0.291	0.294	0.294	–

Allowable Temperature Rates for Pressure Components Using European Standards, Table 5 Summary of allowable parameters of values for the drum of the boiler OP-230

Parameter	Beginning of start-up	End of start-up	Beginning of shutdown	End of shutdown
Starting from cold				
Maximum temperature difference, K	−32.2	−116.5	32.2	116.5
Maximum rate of temperature change, K/s	6.3	23.0	−6.3	−23.0
Starting at 8 h standstill				
Maximum temperature difference, K	−47.8	−88.9	34.4	75.5
Maximum rate of temperature change, K/s	8.7	16.2	−6.3	−13.8
Starting at 2 h standstill				
Maximum temperature difference, K	−29.05	−127.47	34.5	60.1
Maximum rate of temperature change, K/s	10.0	14.7	−6.3	−10.9

The temperature differences are observed between upper and lower part of the drum. The reason is that at the bottom of the drum there is water, which heats up more slowly. The non-uniform heating of the boiler drum over its circumference during start-up is caused by the condensation of steam on the inner surface of the drum in its steam space. The upper part of

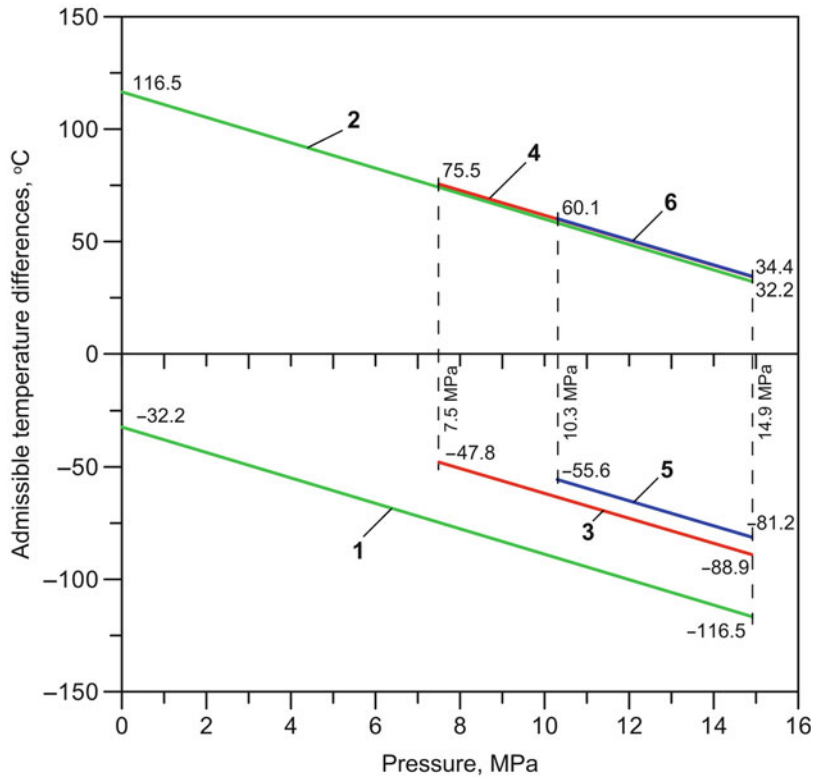

Allowable Temperature Rates for Pressure Components Using European Standards, Fig. 6 The allowable temperature differences in the wall of the boiler drum OP-230 during start-up (*1*,*3*,*5*) and shutdown (*2*,*4*,*6*), from a cold state (*1*,*2*), after 8 h standstill (*3*,*4*), after 2 h standstill (*5*,*6*)

the drum is heated faster because of the high value of the heat transfer coefficient resulting from steam condensation. High differences in temperatures between the upper and lower parts of the drum leads to the high thermal stresses. The result is not only a large temperature difference between points on the circumference of 7 and 1 but also generates large temperature gradients in the thickness of the drum.

An analysis of temperature changes on the drum wall thickness shows (Fig. 10) that, during the start-up, the wall is heated ununiformly. Periods of heating and cooling the inner wall surface can be observed.

Calculated according to EN 12952-3 (Fig. 6), the permissible temperature differences in the wall were compared with values obtained during the actual start-up of power plant (Fig. 9). This comparison, as a percentage of the two characteristic points (up and down the cross section of the drum), is presented in Fig. 11. Stocking z_T permissible temperature difference was calculated from formula (68),

$$z_T = 100\% - \frac{\Delta t_m(p)}{\Delta t_d(p)} \cdot 100\% \qquad (68)$$

where $\Delta t_m(p)$ is the actual wall temperature difference for the pressure p, $\Delta t_d(p)$ is the allowable wall temperature difference for the pressure p, calculated from the equation of the characteristic points of a straight start and end of heating and cooling.

The periods for which the wall temperature rises, the temperature difference *r(T1-T1')* and *r(T7-T7')* were negative. The values were referenced to an acceptable temperature difference for heating (curve 2, Fig. 6), while the wall was cooled, and the temperature difference *r(T1-T1')* and *r(T7-T7')* were positive for the heating curve (curve 1, Fig. 6). The typical temperature difference between supply

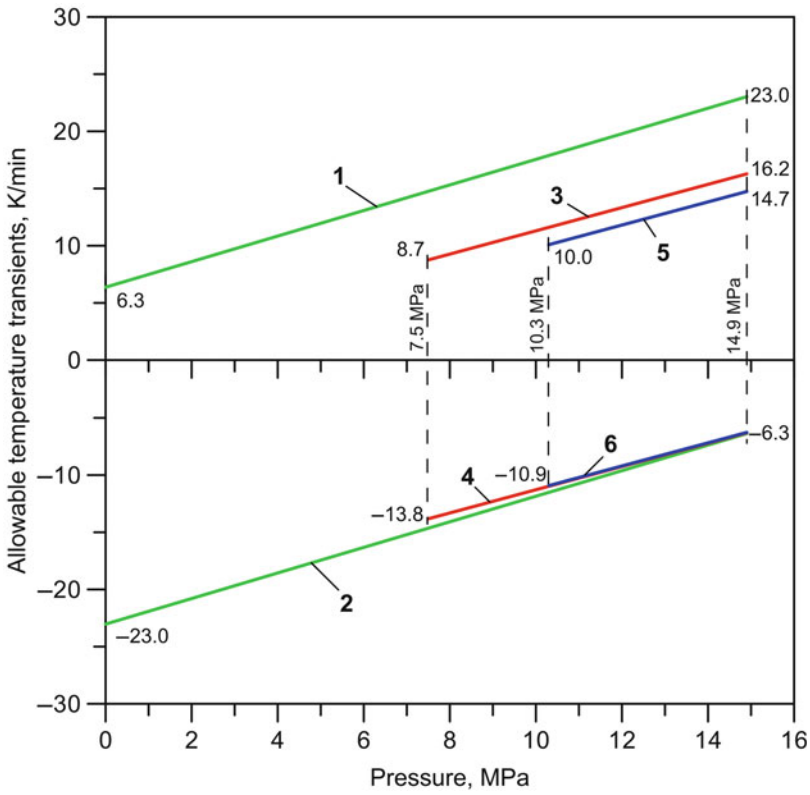

Allowable Temperature Rates for Pressure Components Using European Standards, Fig. 7 The admissible rate of change of temperature in the wall of the boiler drum OP-230 during start-up (*1*,*3*,*5*) and the shutdown (*2*,*4*,*6*), from a cold state (*1*,*2*), after 8 h standstill (*3*,*4*), after 2 h standstill (*5*,*6*)

disturbances in relation to permissible value is large, usually greater than 40 %.

The heating or cooling rate of temperature changes in pressure elements can be v_T, calculated using the moving average filter [6, 13]

$$v_T = \left.\frac{df}{dt}\right|_{t=t_i} = \frac{1}{693\Delta t}(-63f_{i-4} + 42f_{i-3} + 117f_{i-2} + 162f_{i-1} + 177f_0 + 162f_{i+1} + 117f_{i+2} + 42f_{i+3} - 63f_{i+4}) \quad (69)$$

where f_i are medium or wall temperatures at nine successive time points, with time step Δt.

Calculated by (69), heating rate at points located on the inner surface of the drum (1 and 7, Fig. 8) are shown in Fig. 12 and are in the range from −3 to 3 K/min.

A comparison of the heating rate with the allowable values allows the assessment of

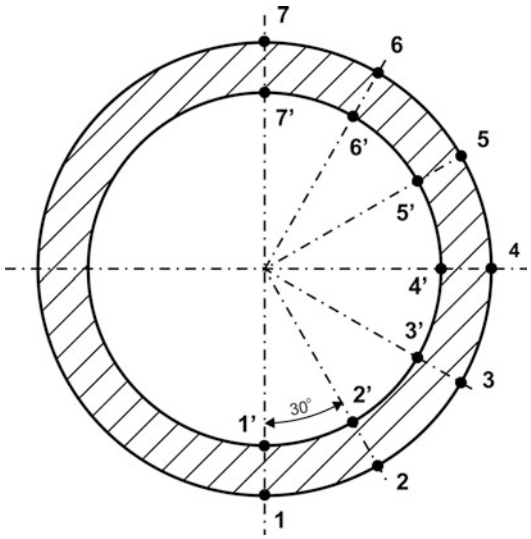

Allowable Temperature Rates for Pressure Components Using European Standards, Fig. 8 Temperature measurement location: *1–7* on the outer cylindrical surface of the pressure element, and the corresponding points on the inner surface *1–7*

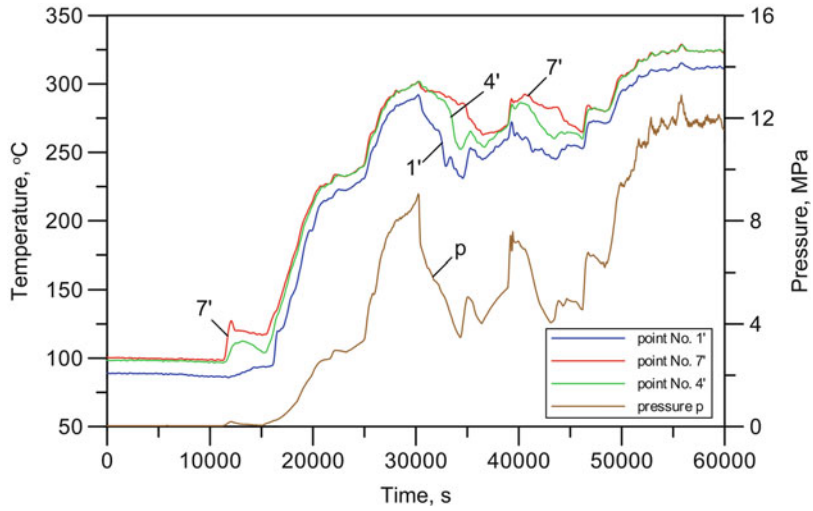

Allowable Temperature Rates for Pressure Components Using European Standards, Fig. 9 Pressure and calculated temperatures at points at the inner surface of the drum

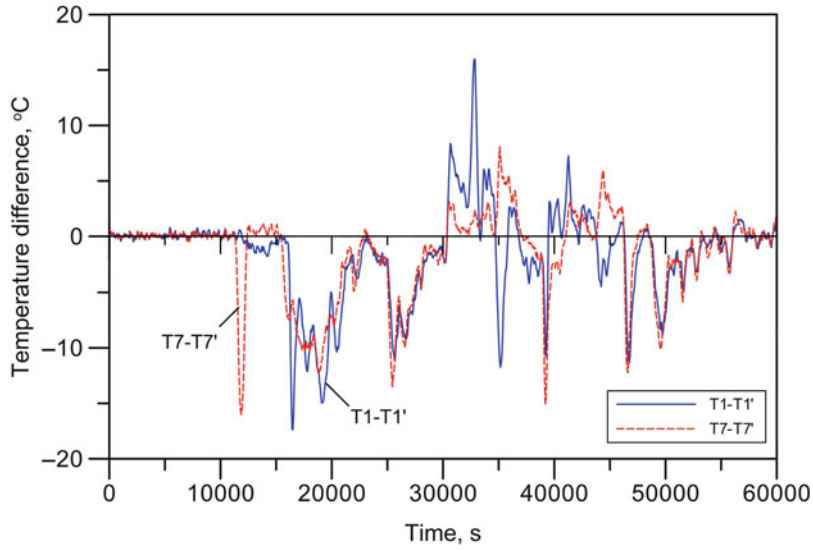

Allowable Temperature Rates for Pressure Components Using European Standards, Fig. 10 Temperature differences *T7–T7* and *T1–T1* calculated using inverse methods

whether the boiler drum was heated properly. Just like stocks temperature difference, inventories of heating rate can also be calculated (Fig. 13). As shown, the supply is large, because in comparison to the limit, the value was bigger than 60 %. It should be noted that the manufacturers of boilers for such thick drum parts, as presented, recommend a very low heating rate of 1.5–2.5 K/min, usually constant over the entire range of pressures, for heating and cooling. In a few cases, they permit cooling at a little more steady rate after the pressure drops below 60 % of the nominal pressure. In this case, even those measured on the real object of heating rate would exceed limit values.

Temperature distribution and stresses in the boiler drum were determined based on the solution of the inverse heat conduction problem. The calculated stresses are shown in Figs. 14, 15, and 16. Presented figures show the history of circumferential (Fig. 14), longitudinal (Fig. 15), and reduced (Fig. 16) stresses at the points

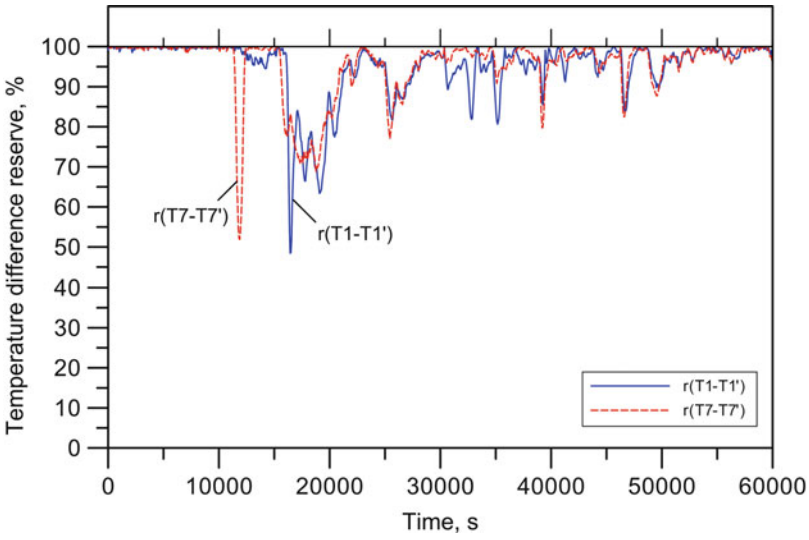

Allowable Temperature Rates for Pressure Components Using European Standards, Fig. 11 Temperature difference reserve between points at the outer and inner surface of the drum on top of *r(T7–T7')* and a lower *r(T1–T1')* part of the drum

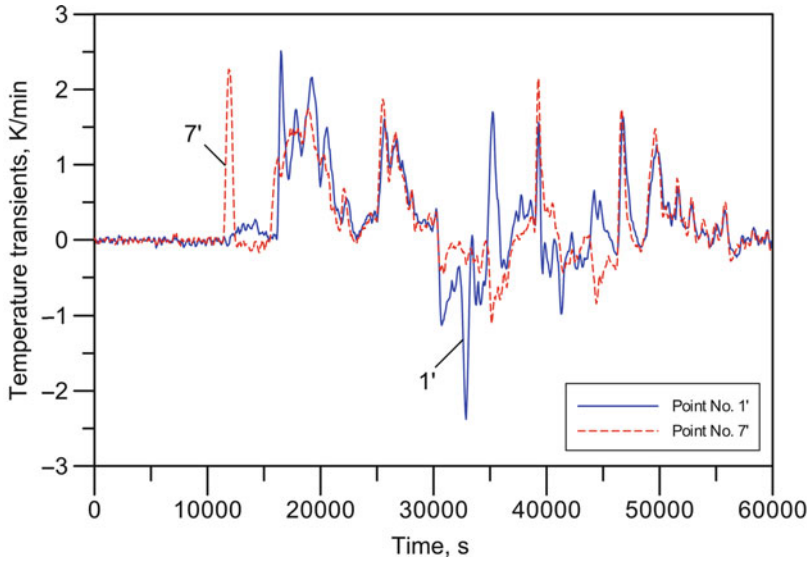

Allowable Temperature Rates for Pressure Components Using European Standards, Fig. 12 Rate of change of temperature at points *1* and *7'* located at the inner surface of the drum

(1 and 7), on the inner surface at boiler drum, during boiler operation. In addition, stress has been shown in point No. 4 (Fig. 8), located in the middle of the cross section of the drum.

Summary

High thermal stresses occur during the power boiler operation in its thick-walled components, especially during boiler start-up and shutdown. The nonuniform heating of the boiler drum over its circumference during start-up is caused by the condensation of steam on the inner surface of the drum in its steam space. Also filling the installation with freshwater in between the periods of boiler operation causes the significant increase in the thermal stress in the boiler drum, especially over its circumference and in the region of the boiler drum; downcomer intersection. Very high thermal stress can occur during the injection of cool water into the thick-walled component, as in case of the attemperator. In some cases, the thick-walled boiler components are subjected to the

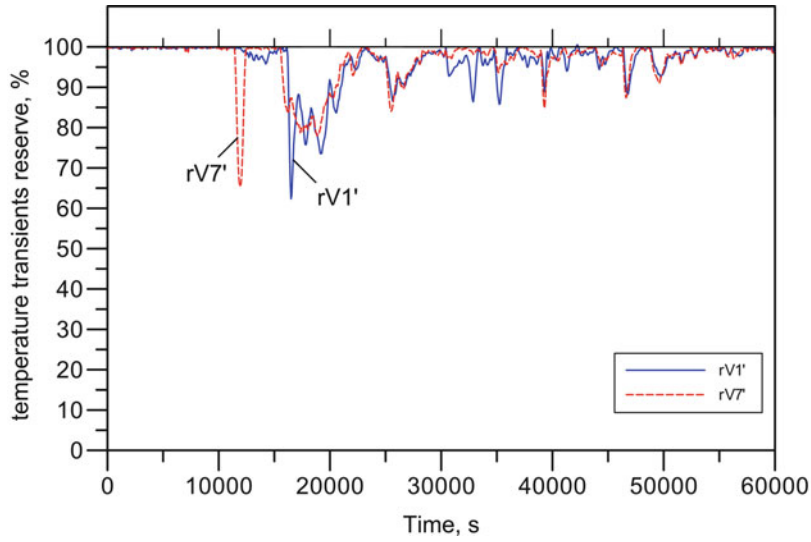

Allowable Temperature Rates for Pressure Components Using European Standards, Fig. 13 Temperature transient reserve at the points *1* and *7* located at the inner surface of the drum

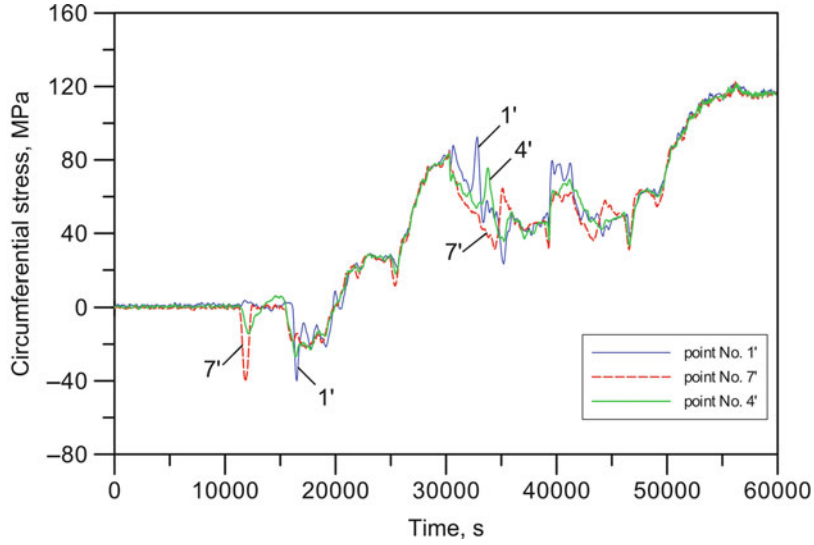

Allowable Temperature Rates for Pressure Components Using European Standards, Fig. 14 The circumferential stresses at the points *1*, *4*, and *7* at the inner surface of the boiler drum

thermal shock, especially when the steam condensation occurs on their inner surface or freshwater of lower temperature is filled into the installation [14].

Processes of conducting thick-walled boiler components, as occurs in the start-up and shutdown of boilers, are difficult processes and require special supervision. Because the thick-walled boiler components are subjected to the irregular and fast temperature changes, it is necessary to monitor the operation of the thick-walled pressure components. For this reason, criterial boiler components, such as boiler drums, superheater chambers, and attemperator chambers, or steam piping fittings, ought to be monitored continuously. For proper monitoring operation systems, there must be acceptable rates for safeguarding the boiler pressure parts from large thermal loads.

EU standard EN 12952-3 Water-tube boilers and auxiliary installation, Part 3: *Design and calculation of pressure parts*, is commonly used to determine the allowable parameters, not only in European countries.

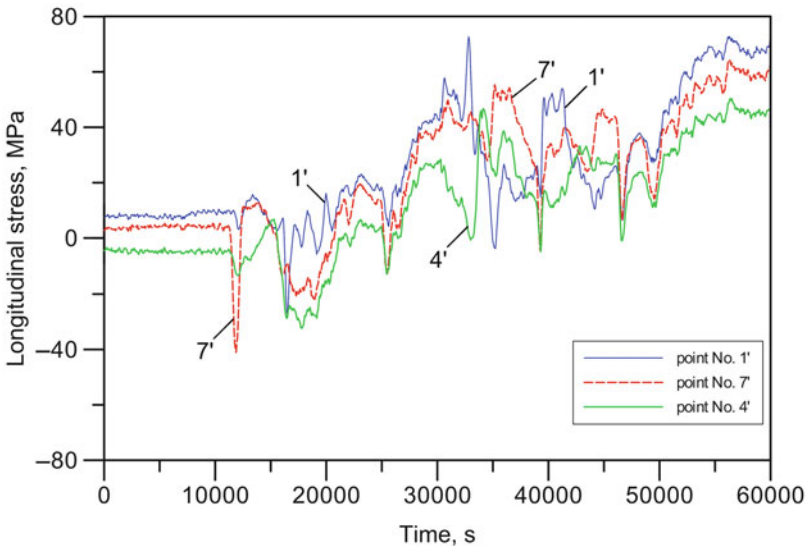

Allowable Temperature Rates for Pressure Components Using European Standards, Fig. 15 The longitudinal stress in the points *1*, *4*, and *7* at the inner surface of the steam boiler drum

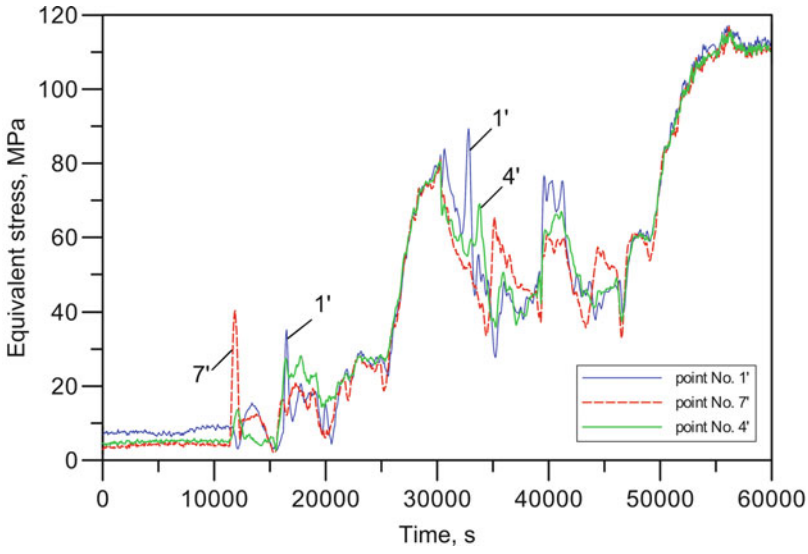

Allowable Temperature Rates for Pressure Components Using European Standards, Fig. 16 The equivalent stress in the points *1*, *4*, and *7* at the inner surface of the steam boiler drum

The presented calculations are based on the cited norm, allowing the determination of permitted variations in the walls of the pressure elements: the heating and cooling rate limits, the ranges of allowable stresses, and the degree of wear. Usually, it is used for determining allowable limits in on-line monitoring systems of pressure components. However, it should be noted that other procedures for determining allowable temperature changes during start-up and shutdown of the boiler, which can be used for designing and operating large power boilers, allow a step change in the temperature at the beginning of the heating and cooling of the pressure element, which is weakened by holes [9, 12]. This is an advantage because it allows the reduction of the boiler start time, without degrading the pressure parts of boilers, enabling faster connection of the power units to electric systems.

References

1. European Standard, EN 12952-3, Water-tube boilers and auxiliary installations, Part 2: Design and calculation for pressure parts. CEN (European Committee for Standarization), rue de Stassart 36, B-1050 Brussels, 25 July 2001
2. TRD 301 Anlage 1: Technische Regeln für Dampfkessel: Berechnung auf Wechselbeanspruchung durch schwellenden Innendruck bzw. durch kombinierte Innendruck- und Temperaturänderungen. Carl Heymans, Köln, and Beuth-Verlag, Berlin, Ausgabe 1986
3. Taler J, Węglowski B, Zima W, Grądziel S, Zborowski M (1999) Analysis of thermal stresses in a boiler drum during start-up. Tran ASME J Pressure Vessel Technol 121:84–93
4. Tonti A (2010) Cyclic capability of steam generators, EN12952-4, other codes and experimental results. Int J Pressure Vessel Piping 87:650–655
5. Osocha P, Węglowski B (2010) Optimization of loads and geometry of thick-walled pipeline elements operating in creep conditions. In: EngOpt 2010 - International Conference on Engineering Optimization, Lisbon, Portugal, 05–10 June 2010
6. Taler J (1997) Analytical solution of the overdetermined inverse heat conduction problem with an application to monitoring thermal stresses. Heat Mass Transfer 33:209–218
7. Taler J, Zima W (1999) Solution of inverse heat conduction problems using control volume approach. Int J Heat Mass Transfer 42:1123–1140
8. Taler J, Duda P (1999) A space marching method for multidimensional transient inverse heat conduction problems. Heat Mass Transfer 34:349–356
9. Taler J, Lubecki S (2011) Optimization of steam pipeline and T-pipe heating. J Thermal Stress 34:1021–1034
10. Węglowski B,Taler J, Zima W, Grądziel S, Zborowski M (2000) Development and implementation of a computer based system for thermal stress monitoring in thick walled boilers. In: Ninth international conference on pressure vessel technology, Sydney, Australia, 9–14 April 2000, Proceedings, vol 1, pp 875–882
11. Taler J, Duda P, Węglowski B (2008) Thermal-strength monitoring and remnant lifetime assessment of pressure components of power steam boilers. In: Diagnostics of new-generation thermal power plant. PAN, Gdańsk, pp 252–338 (Chapter 6)
12. Taler J, Dzierwa P (2011) A new method for optimum heating of steam boiler pressure components. Int J Energy Res 35:897–908
13. Taler J, Węglowski B, Sobota T, Jaremkiewicz M, Taler D (2011) Inverse space marching method for determining temperature and stress distributions in pressure components. Developments in Heat Transfer, InTech, September 2011, pp 273–292
14. Węglowski B, Taler J, Zima W, Zborowski M (2000) Development and implementation of a computer based system for thermal stress monitoring in thick walled boilers. In: Ninth international conference on pressure vessel technology – 9, vol 1, Sydney Australia 9-14 April 2000, pp 875–882

Alternative Formulations

▶ Alternative Formulations: Reciprocal Relations

Alternative Formulations: Reciprocal Relations

Stan Chiriţă
Department of Mathematics, Alexandru Ioan Cuza University of Iaşi, Iaşi, Romania
Octav Mayer Institute of Mathematics, Romanian Academy, Iaşi, Romania

Synonyms

Alternative formulations; Linear theory; Reciprocal relations; Thermoelasticity

Overview

We give an alternative characterization of the solution to the mixed boundary–initial value problem of linear thermoelasticity in which the initial conditions are incorporated into the field equations. In the classical elasticity, such characterization was established by Ignaczak [8] (see also Gurtin [2, 3]).

We will use the alternative formulation of the mixed boundary–initial value problem in order to establish some reciprocal relations within the framework of linear theory of thermoelasticity for anisotropic and inhomogeneous materials. The reciprocal relation is derived for a body of volume region B and surface ∂B and represents an integral relation over B and ∂B between body supplies, surface traction and surface flux, and displacements and temperature variations of two solutions

of the mixed problem of the linear thermoelasticity, namely, a solution of an actual problem and a solution of an auxiliary or virtual problem.

The first reciprocal theorem in the classical thermoelastodynamics is due to Ionescu–Cazimir [9]. The proof is based on the assumption of null initial data and systematic use of the Laplace transform. Ieşan [5] has established a reciprocal theorem without using the Laplace transform. The method of proof is based on a characterization of the boundary–initial value problem in which the initial conditions are incorporated into the basic equations of motion. Later, Ieşan [6, 7] has established a new reciprocal theorem where the proof avoids both the use of the Laplace transform and the incorporation of the initial conditions into the basic equations of motion.

Despite its long existence, the reciprocal theorem was, until recently, not used extensively to actually solve problems. A recent book by Achenbach [1] presents, however, novel uses of reciprocity relations for the actual determination of elastodynamics fields. Various other applications of the reciprocal theorems have been presented in Ionescu–Cazimir [9] and Nowacki [10, 11].

Basic Formulation

We consider a body made by a thermoelastic material, which at the time $t = 0$ occupies the region B of the three-dimensional Euclidian space E^3 whose boundary surface is ∂B. The fundamental system of field equations consists of the equation of motion

$$\sigma_{ji,j} + \varrho_0 b_i = \varrho_0 \ddot{u}_i \tag{1}$$

the energy equation

$$\varrho_0 T_0 \dot{S} = -q_{i,i} + \varrho_0 r \tag{2}$$

the constitutive equations

$$\begin{aligned} \sigma_{ij} &= C_{ijkl} e_{kl} - M_{ij}\theta \\ \rho_0 S &= M_{ij} e_{ij} + a\theta \\ q_i &= -k_{ij}\theta_{,j} \end{aligned} \tag{3}$$

and the geometrical equations

$$e_{ij} = \frac{1}{2}(u_{i,j} + u_{j,i}) \tag{4}$$

We assume here that the elasticity tensor C_{ijkl}, the stress–temperature tensor M_{ij}, the conductivity tensor k_{ij}, the specific heat $c = T_0 a$, and the density ϱ_0 are prescribed and that C_{ijkl}, M_{ij}, and k_{ij} are smooth on $\overline{B}$ while a and ϱ_0 are continuous on $\overline{B}$. Moreover, we assume that C_{ijkl}, M_{ij}, and k_{ij} are symmetric.

The mixed problem $\mathcal{P}$ of the dynamic thermoelasticity consists to find a thermoelastic process $[u_i, e_{ij}, \sigma_{ij}, \theta, S, q_i]$ corresponding to the body force b_i and the heat supply r that satisfies the initial conditions

$$\begin{aligned} u_i(\mathbf{x}, 0) &= u_{0i}(\mathbf{x}) \\ \dot{u}_i(\mathbf{x}, 0) &= \dot{u}_{0i}(\mathbf{x}) \quad \text{on} \quad \overline{B} \\ S(\mathbf{x}, 0) &= S_0(\mathbf{x}) \end{aligned} \tag{5}$$

the displacement condition

$$u_i = \hat{u}_i \quad \text{on} \quad \Sigma_1 \times [0, t_0) \tag{6}$$

the traction condition

$$\sigma_{ji} n_j = \hat{s}_i \quad \text{on} \quad \Sigma_2 \times [0, t_0) \tag{7}$$

the temperature condition

$$\theta = \hat{\theta} \quad \text{on} \quad \Sigma_3 \times [0, t_0) \tag{8}$$

and the heat flux condition

$$q_i n_i = \hat{q} \quad \text{on} \quad \Sigma_4 \times [0, t_0) \tag{9}$$

where Σ_1, Σ_2, Σ_3, and Σ_4 are subsets of the boundary ∂B such that $\Sigma_1 \cup \overline{\Sigma}_2 = \Sigma_3 \cup \overline{\Sigma}_4 = \partial B$, $\Sigma_1 \cap \Sigma_2 = \Sigma_3 \cap \Sigma_4 = \emptyset$, and $\mathbf{u}_0$, $\dot{\mathbf{u}}_0$, and S_0 and $\hat{\mathbf{u}}$, $\hat{\mathbf{s}}$, $\hat{\theta}$, and $\hat{q}$ are prescribed functions. If such a thermoelastic process exists, it is called a solution of the mixed problem $\mathcal{P}$.

Alternative Formulations

In this section, we give another formulation of the mixed problem $\mathcal{P}$ in which the initial conditions are incorporated into the field equations. Such alternative formulation was obtained in linear thermoelastodynamics by Ieşan [4] and constitutes a generalization of a result established by Ignaczak [8] for the classical linear elastodynamics.

The operation of convolution between any two functions u and $v \in C(B \times [0, t_0))$ is defined by

$$u * v(\mathbf{x}, t) = \int_0^t u(\mathbf{x}, t-\tau) v(\mathbf{x}, \tau) d\tau, \quad (\mathbf{x}, t) \in B \times [0, t_0) \tag{10}$$

For convenience, we recall the following properties of the operation of convolution:

1. $u * v = v * u$ for all $u, v \in C(B \times [0, t_0))$.
2. $u * (v * w) = (u * v) * w$ for all $u, v, w \in C(B \times [0, t_0))$.
3. $u * (v + w) = u * v + u * w$ for all $u, v, w \in C(B \times [0, t_0))$.
4. $u * v = 0$ implies $u = 0$ or $v = 0$.

We further introduce the functions:

$$\begin{aligned} \ell(t) &= 1 \\ i(t) &= t, \quad t \in [0, t_0) \end{aligned} \tag{11}$$

and note that

$$\ell * u(\mathbf{x}, t) = \int_0^t u(\mathbf{x}, \tau) d\tau \tag{12}$$

and

$$\begin{aligned} i * u(\mathbf{x}, t) &= \ell * (\ell * u)(\mathbf{x}, t) \\ &= \int_0^t \int_0^s u(\mathbf{x}, \tau) d\tau ds \end{aligned} \tag{13}$$

for all $u \in C(B \times [0, t_0))$.

Let $[u_i, e_{ij}, \sigma_{ij}, \theta, S, q_i]$ be a solution of the mixed problem $\mathcal{P}$ corresponding to the external force system $[b_i, s_i]$ and external thermal system $[r, q]$. We introduce the pseudo-body force field f_i and the pseudo-heat supply field R defined on $\overline{B} \times [0, t_0)$ by

$$\begin{aligned} f_i(\mathbf{x}, t) &= \varrho_0(\mathbf{x}) i * b_i(\mathbf{x}, t) + \varrho_0(\mathbf{x})[t\dot{u}_{0i}(\mathbf{x}) + u_{0i}(\mathbf{x})] \\ R(\mathbf{x}, t) &= \frac{\varrho_0(\mathbf{x})}{T_0} \ell * r(\mathbf{x}, t) + \varrho_0(\mathbf{x}) S_0(\mathbf{x}) \end{aligned} \tag{14}$$

Theorem 1. *The thermoelastic process* $[u_i, e_{ij}, \sigma_{ij}, \theta, S, q_i]$ *satisfies the Equations* (1) *and* (2) *and the initial conditions* (5) *if and only if it satisfies*

$$\begin{aligned} \varrho_0 \ddot{u}_i &= i * \sigma_{ji,j} + f_i \\ \varrho_0 \dot{S} &= -\frac{1}{T_0} \ell * q_{i,i} + R \end{aligned} \tag{15}$$

in $B \times [0, t_0)$.

Proof. First of all, we observe that

$$\begin{aligned} i * \ddot{u}_i(\mathbf{x}, t) &= \int_0^t \int_0^s \ddot{u}_i(\mathbf{x}, \tau) d\tau ds \\ &= u_i(\mathbf{x}, t) - [t\dot{u}_i(\mathbf{x}, 0) + \mathbf{u_i}(\mathbf{x}, 0)] \end{aligned} \tag{16}$$

and

$$\ell * \dot{S}(\mathbf{x}, t) = \int_0^t \dot{S}(\mathbf{x}, \tau) d\tau = S(\mathbf{x}, t) - S(\mathbf{x}, 0) \tag{17}$$

Let us first suppose that the thermoelastic process $[u_i, e_{ij}, \sigma_{ij}, \theta, S, q_i]$ satisfies the Equations (1) and (2) and the initial conditions (5). Then, by using (16) and (17), we have

$$\begin{aligned} &i * \left[\sigma_{ji,j}(\mathbf{x}, t) + \varrho_0(\mathbf{x}) b_i(\mathbf{x}, t)\right] \\ &= \varrho_0(\mathbf{x})[u_i(\mathbf{x}, t) - (t\dot{u}_{0i}(\mathbf{x}) + u_{0i}(\mathbf{x}))] \end{aligned} \tag{18}$$

and

$$\begin{aligned} &-\frac{1}{T_0} \ell * q_{i,i}(\mathbf{x}, t) + \frac{\varrho_0(\mathbf{x})}{T_0} \ell * r(\mathbf{x}, t) \\ &= \varrho_0(\mathbf{x})[S(\mathbf{x}, t) - S_0(\mathbf{x})] \end{aligned} \tag{19}$$

Thus, the relation (15) follows from the relations (18) and (19).

Let us now consider that the thermoelastic process $[u_i, e_{ij}, \sigma_{ij}, \theta, S, q_i]$ satisfies the Equation (15). Then, by substituting (14) into (15) and by using the relations (16) and (17), we can write

$$\begin{aligned} & i * \left[\sigma_{ji,j}(\mathbf{x},t) + \varrho_0(\mathbf{x}) b_i(\mathbf{x},t)\right] \\ & + \varrho_0(\mathbf{x})[t\dot{u}_{0i}(\mathbf{x}) + u_{0i}(\mathbf{x})] = i * \varrho_0(\mathbf{x})\ddot{u}_i(\mathbf{x},t) \\ & + \varrho_0(\mathbf{x})[t\dot{u}_i(\mathbf{x},0) + u_i(\mathbf{x},0)] \end{aligned} \tag{20}$$

and

$$\begin{aligned} & -\frac{1}{T_0}\ell * q_{i,i}(\mathbf{x},t) + \frac{\varrho_0(\mathbf{x})}{T_0}\ell * r(\mathbf{x},t) + \varrho_0(\mathbf{x}) S_0(\mathbf{x}) \\ & = \varrho_0(\mathbf{x})\ell * \dot{S}(\mathbf{x},t) + \varrho_0(\mathbf{x}) S(\mathbf{x},0) \end{aligned} \tag{21}$$

Further, we set $t = 0$ into relation (20) to obtain

$$u_{0i}(\mathbf{x}) = u_i(\mathbf{x},0) \tag{22}$$

and then we derive (20) and we set $t = 0$ into the result in order to deduce

$$\dot{u}_{0i}(\mathbf{x}) = \dot{u}_i(\mathbf{x},0) \tag{23}$$

Herewith, we set $t = 0$ into relation (21) to obtain

$$S_0(\mathbf{x}) = S(\mathbf{x},0) \tag{24}$$

Moreover, if we use these results into relations (20) and (21), then we obtain

$$\begin{aligned} & i * \left[\sigma_{ji,j}(\mathbf{x},t) + \varrho_0(\mathbf{x}) b_i(\mathbf{x},t) - \varrho_0(\mathbf{x})\ddot{u}_i(\mathbf{x},t)\right] = 0 \\ & \frac{1}{T_0}\ell * \left[-q_{i,i}(\mathbf{x},t) + \varrho_0(\mathbf{x}) r(\mathbf{x},t) - \varrho_0(\mathbf{x}) T_0 \dot{S}(\mathbf{x},t)\right] = 0 \end{aligned} \tag{25}$$

In view of the properties of the operation of convolution, from (25), we see that the thermoelastic process $[u_i, e_{ij}, \sigma_{ij}, \theta, S, q_i]$ satisfies the Equations (1) and (2) and the proof is complete.

A direct consequence of the Theorem 1 is the following result.

Theorem 2. *A thermoelastic process* $[u_i, e_{ij}, \sigma_{ij}, \theta, S, q_i]$ *is solution of the mixed problem* $\mathcal{P}$ *if and only if it satisfies the Equation* (15) *and the boundary conditions* (6)–(9).

Remark 1. Let us denote by $\mathcal{P}_0$ the problem $\mathcal{P}$ when $\Sigma_2 = \partial B$. Then we can obtain an alternative formulation of the problem $\mathcal{P}_0$ in terms of the components of the stress tensor and the temperature variation by substituting u_i from (15) into geometrical relation (4) and then the result into the Saint–Venant compatibility conditions:

$$\begin{aligned} & e_{ii,jj} + e_{jj,ii} = 2e_{ij,ij}, \quad (i \neq j, \text{ not summed}) \\ & e_{rr,ij} + e_{ij,rr} = e_{jr,ir} + e_{ir,jr}, \quad (i \neq j \neq r \neq i, \\ & \text{not summed}) \end{aligned} \tag{26}$$

Such a formulation can be found in [4].

Reciprocal Relations

In what follows, we use the alternative formulation described in the above section in order to establish a counterpart of Graffi's reciprocal theorem in the isothermal theory (see, e.g., Gurtin [3]). To this end, we consider two thermoelastic processes $p^{(\alpha)} = \left[u_i^{(\alpha)}, e_{ij}^{(\alpha)}, \sigma_{ij}^{(\alpha)}, \theta^{(\alpha)}, S^{(\alpha)}, q_i^{(\alpha)}\right]$ and $\alpha = 1, 2$, corresponding to the two systems of given data:

$$\mathcal{D}^{(\alpha)} = \left\{b_i^{(\alpha)}, r^{(\alpha)}; \hat{u}_i^{(\alpha)}, \hat{s}_i^{(\alpha)}, \hat{\theta}^{(\alpha)}, \hat{q}^{(\alpha)}; u_{0i}^{(\alpha)}, \dot{u}_{0i}^{(\alpha)}, S_0^{(\alpha)}\right\} \tag{27}$$

$\alpha = 1, 2$, and introduce the notations:

$$\begin{aligned} & f_i^{(\alpha)}(\mathbf{x},t) = \varrho_0(\mathbf{x}) i * b_i^{(\alpha)}(\mathbf{x},t) + \varrho_0(\mathbf{x})\left[t\dot{u}_{0i}^{(\alpha)}(\mathbf{x}) + u_{0i}^{(\alpha)}(\mathbf{x})\right] \\ & R^{(\alpha)}(\mathbf{x},t) = \frac{\varrho_0(\mathbf{x})}{T_0}\ell * r^{(\alpha)}(\mathbf{x},t) + \varrho_0(\mathbf{x}) S_0^{(\alpha)}(\mathbf{x}) \end{aligned} \tag{28}$$

and

$$\begin{aligned} & s_i^{(\alpha)}(\mathbf{x},t) = \sigma_{ji}^{(\alpha)}(\mathbf{x},t) n_j \\ & q^{(\alpha)}(\mathbf{x},t) = q_i^{(\alpha)}(\mathbf{x},t) n_i \end{aligned} \tag{29}$$

Theorem 3 (Reciprocal theorem). *Suppose that the conductivity tensor k_{ij} is symmetric. Let* $p^{(\alpha)} = [u_i^{(\alpha)}, e_{ij}^{(\alpha)}, \sigma_{ij}^{(\alpha)}, \theta^{(\alpha)}, S^{(\alpha)}, q_i^{(\alpha)}]$ *be thermoelastic processes corresponding to the given data* $\mathcal{D}^{(\alpha)} = \left\{ b_i^{(\alpha)}, r^{(\alpha)}; \hat{u}_i^{(\alpha)}, \hat{s}_i^{(\alpha)}, \hat{\theta}^{(\alpha)}, \hat{q}^{(\alpha)}; u_{0i}^{(\alpha)}, \dot{u}_{0i}^{(\alpha)}, S_0^{(\alpha)} \right\}$; *and* $\alpha = 1, 2$. *Then*

$$\begin{aligned}
&\int_B \left(f_i^{(1)} * u_i^{(2)} - i * R^{(1)} * \theta^{(2)} \right) dv \\
&+ \int_{\partial B} i * \left(s_i^{(1)} * u_i^{(2)} + \frac{1}{T_0} \ell * q^{(1)} * \theta^{(2)} \right) da \\
&= \int_B \left(f_i^{(2)} * u_i^{(1)} - i * R^{(2)} * \theta^{(1)} \right) dv \\
&+ \int_{\partial B} i * \left(s_i^{(2)} * u_i^{(1)} + \frac{1}{T_0} \ell * q^{(2)} * \theta^{(1)} \right) da
\end{aligned} \tag{30}$$

and

$$\begin{aligned}
&\int_B \varrho_0 \left(b_i^{(1)} * u_i^{(2)} - \frac{1}{T_0} \ell * r^{(1)} * \theta^{(2)} \right) dv \\
&+ \int_{\partial B} \left(s_i^{(1)} * u_i^{(2)} + \frac{1}{T_0} \ell * q^{(1)} * \theta^{(2)} \right) da \\
&+ \int_B \varrho_0 \left(u_{0i}^{(1)} \dot{u}_i^{(2)} + \dot{u}_{0i}^{(1)} u_i^{(2)} - S_0^{(1)} \theta^{(2)} \right) dv \\
&= \int_B \varrho_0 \left(b_i^{(2)} * u_i^{(1)} - \frac{1}{T_0} \ell * r^{(2)} * \theta^{(1)} \right) dv \\
&+ \int_{\partial B} \left(s_i^{(2)} * u_i^{(1)} + \frac{1}{T_0} \ell * q^{(2)} * \theta^{(1)} \right) da \\
&+ \int_B \varrho_0 \left(u_{0i}^{(2)} \dot{u}_i^{(1)} + \dot{u}_{0i}^{(2)} u_i^{(1)} - S_0^{(2)} \theta^{(1)} \right) dv
\end{aligned} \tag{31}$$

In particular, when both thermoelastic processes correspond to null initial data, then

$$\begin{aligned}
&\int_B \varrho_0 \left(b_i^{(1)} * u_i^{(2)} - \frac{1}{T_0} \ell * r^{(1)} * \theta^{(2)} \right) dv \\
&+ \int_{\partial B} \left(s_i^{(1)} * u_i^{(2)} + \frac{1}{T_0} \ell * q^{(1)} * \theta^{(2)} \right) da \\
&= \int_B \varrho_0 \left(b_i^{(2)} * u_i^{(1)} - \frac{1}{T_0} \ell * r^{(2)} * \theta^{(1)} \right) dv \\
&+ \int_{\partial B} \left(s_i^{(2)} * u_i^{(1)} + \frac{1}{T_0} \ell * q^{(2)} * \theta^{(1)} \right) da
\end{aligned} \tag{32}$$

Proof. From the symmetry of C_{ijkl} and by using the definition and the properties of convolution, we have

$$C_{ijkl} e_{ij}^{(1)} * e_{kl}^{(2)} = C_{ijkl} e_{ij}^{(2)} * e_{kl}^{(1)} \tag{33}$$

and

$$a\theta^{(1)} * \theta^{(2)} = a\theta^{(2)} * \theta^{(1)} \tag{34}$$

Then, by means of the constitutive equations (3), we obtain

$$\begin{aligned}
\left[\sigma_{ij}^{(1)} + M_{ij} \theta^{(1)} \right] * e_{ij}^{(2)} &= \left[\sigma_{ij}^{(2)} + M_{ij} \theta^{(2)} \right] * e_{ij}^{(1)} \\
\left[\varrho_0 S^{(1)} - M_{ij} e_{ij}^{(1)} \right] * \theta^{(2)} &= \left[\varrho_0 S^{(2)} - M_{ij} e_{ij}^{(2)} \right] * \theta^{(1)}
\end{aligned} \tag{35}$$

which further give

$$\sigma_{ij}^{(1)} * e_{ij}^{(2)} - \varrho_0 S^{(1)} * \theta^{(2)} = \sigma_{ij}^{(2)} * e_{ij}^{(1)} - \varrho_0 S^{(2)} * \theta^{(1)} \tag{36}$$

If we set

$$I_{\alpha\beta} = \int_B i * \left[\sigma_{ij}^{(\alpha)} * e_{ij}^{(\beta)} - \varrho_0 S^{(\alpha)} * \theta^{(\beta)} \right] dv \tag{37}$$

then (36) implies

$$I_{12} = I_{21} \tag{38}$$

On the other hand, by taking into account the constitutive equations (3), the geometric equations (4), and the Equation (15) and the symmetries of the thermoelastic coefficients, we obtain

$$\begin{aligned}
I_{\alpha\beta} &= \int_B i * \sigma_{ij}^{(\alpha)} * u_{i,j}^{(\beta)} dv \\
&- \int_B i * \left(-\frac{1}{T_0} \ell * q_{i,i}^{(\alpha)} + R^{(\alpha)} \right) * \theta^{(\beta)} dv \\
&= \int_{\partial B} i * \left(s_i^{(\alpha)} * u_i^{(\beta)} + \frac{1}{T_0} \ell * q^{(\alpha)} * \theta^{(\beta)} \right) da \\
&+ \int_B \left(f_i^{(\alpha)} * u_i^{(\beta)} - i * R^{(\alpha)} * \theta^{(\beta)} \right) dv \\
&+ \int_B \frac{1}{T_0} i * \ell * k_{ij} \theta_{,j}^{(\alpha)} * \theta_{,i}^{(\beta)} dv \\
&- \int_B \varrho_0 u_i^{(\alpha)} * u_i^{(\beta)} dv
\end{aligned} \tag{39}$$

Finally, if we substitute (39) into (38), we are led to the reciprocal relation (30).

Note that the reciprocal relation (31) is a direct consequence of the relations (30) and (15) and the properties of the convolution and the identity:

$$\ell * \dot{u}_i(\mathbf{x},t) = u_i(\mathbf{x},t) - u_i(\mathbf{x},0) \tag{40}$$

Obviously, when the two thermoelastic processes correspond the null initial data, the relation (31) takes the form (32) and the proof is complete.

Remark 2. Suppose both thermoelastic processes correspond the null initial data. Then the relation (40) implies

$$u_i^{(\alpha)}(\mathbf{x},t) = \ell * \dot{u}_i^{(\alpha)}(\mathbf{x},t) \tag{41}$$

and the reciprocal relation (32) takes the following form:

$$\begin{aligned}
&\int_B \left[b_i^{(1)} * \dot{u}_i^{(2)} - \frac{1}{T_0} r^{(1)} * \theta^{(2)} \right] dv \\
&+ \int_{\partial B} \left[s_i^{(1)} * \dot{u}_i^{(2)} + \frac{1}{T_0} q^{(1)} * \theta^{(2)} \right] da \\
&= \int_B \left[b_i^{(2)} * \dot{u}_i^{(1)} - \frac{1}{T_0} r^{(2)} * \theta^{(1)} \right] dv \\
&+ \int_{\partial B} \left[s_i^{(2)} * \dot{u}_i^{(1)} + \frac{1}{T_0} q^{(2)} * \theta^{(1)} \right] da
\end{aligned} \tag{42}$$

The reciprocal relation (42) was established by Ionescu–Cazimir [9] by using the method of Laplace transform.

Remark 3. We recall that the theory of thermoelasticity based on the hypothesis that the term $M_{ij}\dot{e}_{ij}$ can be neglected in the energy equation is known as the uncoupled theory of linear thermoelasticity. By contrast, the general linear theory is known as the linear theory of coupled thermoelasticity. Let us suppose that $p^{(1)}$ is a thermoelastic process corresponding to the mixed problem associated with the linear coupled thermoelasticity, while the thermoelastic process $p^{(2)}$ corresponds to the mixed problem associated with the linear uncoupled thermoelasticity. That means we have

$$\varrho_0 S^{(2)} = a\theta^{(2)} \tag{43}$$

Then we have the following reciprocal relation:

$$\begin{aligned}
&\int_B \left(f_i^{(1)} * u_i^{(2)} - i * R^{(1)} * \theta^{(2)} \right) dv \\
&+ \int_{\partial B} i * \left(s_i^{(1)} * u_i^{(2)} + \frac{1}{T_0} \ell * q^{(1)} * \theta^{(2)} \right) da \\
&= \int_B \left(f_i^{(2)} * u_i^{(1)} - i * R^{(2)} * \theta^{(1)} \right) dv \\
&+ \int_{\partial B} i * \left(s_i^{(2)} * u_i^{(1)} + \frac{1}{T_0} \ell * q^{(2)} * \theta^{(1)} \right) da \\
&- \int_B M_{ij} i * \theta^{(1)} * e_{ij}^{(2)} dv
\end{aligned} \tag{44}$$

In the case when the both thermoelastic processes correspond to null initial data, the reciprocal relation becomes

$$\begin{aligned}
&\int_B \left(b_i^{(1)} * u_i^{(2)} - \frac{1}{T_0} \ell * r^{(1)} * \theta^{(2)} \right) dv \\
&+ \int_{\partial B} \left(s_i^{(1)} * u_i^{(2)} + \frac{1}{T_0} \ell * q^{(1)} * \theta^{(2)} \right) da \\
&= \int_B \left(b_i^{(2)} * u_i^{(1)} - \frac{1}{T_0} \ell * r^{(2)} * \theta^{(1)} \right) dv \\
&+ \int_{\partial B} \left(s_i^{(2)} * u_i^{(1)} + \frac{1}{T_0} \ell * q^{(2)} * \theta^{(1)} \right) da \\
&- \int_B M_{ij} \theta^{(1)} * e_{ij}^{(2)} dv
\end{aligned} \tag{45}$$

Further, if we use the relation (41), then we can write (45) in the following form:

$$\begin{aligned}
&\int_B \left(b_i^{(1)} * \dot{u}_i^{(2)} - \frac{1}{T_0} r^{(1)} * \theta^{(2)} \right) dv \\
&+ \int_{\partial B} \left(s_i^{(1)} * \dot{u}_i^{(2)} + \frac{1}{T_0} q^{(1)} * \theta^{(2)} \right) da \\
&= \int_B \left(b_i^{(2)} * \dot{u}_i^{(1)} - \frac{1}{T_0} r^{(2)} * \theta^{(1)} \right) dv \\
&+ \int_{\partial B} \left(s_i^{(2)} * \dot{u}_i^{(1)} + \frac{1}{T_0} q^{(2)} * \theta^{(1)} \right) da \\
&- \int_B M_{ij} \theta^{(1)} * \dot{e}_{ij}^{(2)} dv
\end{aligned} \tag{46}$$

a relation found by Ionescu–Cazimir [9] by using the Laplace transform.

References

1. Achenbach JD (2003) Reciprocity in elastodynamics. Cambridge University Press, Cambridge

2. Gurtin ME (1964) Variational principles for linear elastodynamics. Arch Ration Mech Anal 16:34–50
3. Gurtin ME (1972) The linear theory of elasticity. In: Truesdell C (ed) Handbuch der Physik VI a/2. Springer, Berlin/Heidelberg/New York, pp 1–296
4. Ieşan D (1966) Principes variationnels dans la théorie de la thérmoélasticité couplée. Analele St Univ "Al I Cuza" Iaşi, Sect I Matematică 12:439–456
5. Ieşan D (1974) On some reciprocity theorems and variational theorems in linear dynamic theories of continuum mechanics. Memorie dell'Accad Sci Torino Cl Sci Fis Mat Nat Ser 4:17
6. Ieşan D (1989) On some theorems in thermoelastodynamics. Rev Roum Sci Techniques – Méc Appl 34:101–111
7. Ieşan D (2004) Thermoelastic models of continua. Kluwer, Boston/Dordrecht/London
8. Ignaczak J (1963) A completeness problem for stress equations of motion in the linear elasticity theory. Arch Mech Stosow 15:225–235
9. Ionescu-Cazimir V (1964) Problem of linear coupled thermoelasticity. Theorems on reciprocity for the dynamic problem of coupled thermoelasticity. I. Bull Acad Polon Sci, Ser Sci Technol 12:473–480
10. Nowacki W (1962) Thermoelasticity. Pergamon Press, Oxford/London/New York/Paris
11. Nowacki W (1986) Theory of asymmetric elasticity. Polish Scientific/Warszawa and Pergamon Press, Oxford/New York/Paris/Frankfurt

Alumina

► Effect of Thermal Stresses on Crack-Tip Toughness of Polycrystalline Ceramics

Amorphous Polymers

► Coupled and Generalized Thermoviscoelasticity

Analysis of a Prestressed Bi-Material Accelerated-Life-Test (ALT) Specimen

Ephraim Suhir
Department of Electrical Engineering, University of California, Santa Cruz, CA, USA

Overview

Application of mechanical prestressing could be an effective means for achieving a failure-mode-shift-free "destructive ALT effect" in electronic and photonic devices and micro-electro-mechanical systems (MEMS). A simple, physically meaningful, and easy-to-use analytical ("mathematical") predictive model has been developed to assess the stresses in a bi-material assembly subjected to the combined action of thermal stresses and external ("mechanical") prestressing. The compressive prestressing is applied to the assembly component that is expected to experience thermal compression. The model is an extension and a modification of the author's 1986 and 1989 "bi-metal thermostat" models suggested as a generalization of the 1925 Timoshenko's theory.

Introduction

The objective of the analysis is to indicate the feasibility of using mechanically prestressed test specimens, when there is a need to avoid the "shift" in the modes and mechanisms of failure in electronic, photonic, or MEMS assemblies subjected to thermal loading during ALT. When planning and conducting ALT, there is always a temptation to broaden (enhance) the temperature range to achieve the maximum "destructive ALT effect" in a shortest period of time. There exists, however, one major pitfall – a possible shift in the modes and mechanisms of failure as a result of broadening the temperature range. Enhanced ALT conditions may hasten failure mechanisms that are quite different from those that could possibly occur in actual service. The likely pitfalls include, but might not be limited to, the change in material properties at high or low temperatures; time-dependent strain due to diffusion; enhanced creep at elevated temperatures; brittle fracture at low temperatures; generation and movement of dislocations caused by an elevated thermal stress; occurrence of a bi-modal distribution of failures, etc. Because of the possibility of such pitfalls, it is necessary to establish the appropriate narrow enough temperature limits in order to prevent the distortion of the actual dominant

failure mechanism(s). There is an obvious incentive, therefore, for trying to find ways of increasing the induced stresses without broadening the ALT temperature range.

One way to enhance the "destructive ALT effect" without compromising the acceptable temperature limits is to mechanically prestress the test specimens prior to conducting thermal ALT. For instance, a low expansion silicon chip attached to a high-expansion polymeric substrate will experience thermally induced compression, when the chip-substrate assembly manufactured at an elevated temperature is subsequently cooled down to a low (say, room) temperature. This compression can be enhanced, and the interfacial stresses will be increased, if the chip is mechanically prestressed in compression.

The objective of this entry is to present a simple, easy-to-use, and physically meaningful predictive model for the evaluation of the thermo-mechanical stresses in a mechanically prestressed bi-material specimen. The problem of stress concentration and fracture in bi- and multi-material assemblies has been addressed for a long time and by numerous investigators. The number of published work dealing with this problem is enormous (see, e.g., the recent review [1]). Let us indicate just some major publications, which address prediction of thermal stress in assemblies comprised of dissimilar materials: general monographs (e.g., [2–6]); pioneering work by Timoshenko [7] (who used a strength-of-materials approach), and by Aleck [8] (who used the theory-of-elasticity concept that was later on extended in many researchers (see, e.g., [9, 10]); numerous publications in the electronics, photonics, and MEMS systems [11–38], including fracture mechanics-based analyses [15–18], thermal fatigue in ductile metals [19–24], that is particularly important when there is a need to assess the life-time of solder joint interconnections in electronics and photonics [23–32]); thermal stress in thin films fabricated on thick substrates [33–38], etc.

Our model is an extension of the models developed earlier [11, 12] as generalizations of the classical Timoshenko's theory of bi-metal thermostats [7]. The model predicts the magnitude and the distribution of the interfacial shearing and peeling stresses in a bi-material assembly subjected to the combined action thermal and mechanical stresses.

Basic Equations

Let an elongated bi-material adhesively bonded or soldered assembly be manufactured at an elevated temperature, then cooled down to a low (say, room) temperature, and then, prior to ALT testing, subjected to mechanical compression applied to the assembly component with the lower coefficient of thermal expansion (contraction), as schematically shown in Fig. 1. It is this component that will experience compressive thermal stress in actual operating conditions.

The longitudinal interfacial displacements $u_1(x)$ and $u_2(x)$ in the assembly components #1 and #2 can be evaluated, in an approximate analysis, by the formulas of the type suggested in [14]:

$$\left.\begin{aligned} u_1(x) &= -\alpha_1 \Delta t x + \lambda_1 \int_0^x [\hat{T} - T(\xi)]d\xi + \kappa_1 \tau(x) - \frac{h_1}{2} w_1'(x) \\ u_2(x) &= -\alpha_2 \Delta t x + \lambda_2 \int_0^x T(\xi)d\xi - \kappa_2 \tau(x) + \frac{h_2}{2} w_2'(x) \end{aligned}\right\} \quad (1)$$

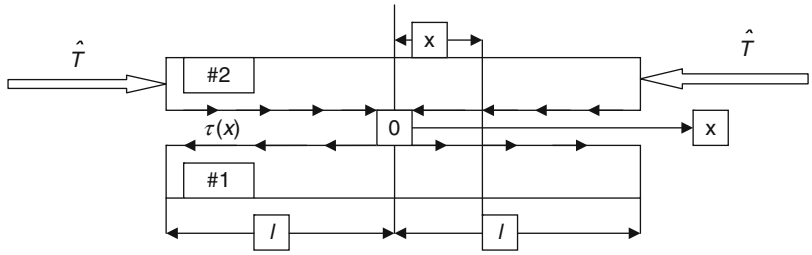

Analysis of a Prestressed Bi-Material Accelerated-Life-Test (ALT) Specimen, Fig. 1 Bi-material assembly subjected to the combined action of thermally induced and compressive external forces applied to one of the assembly components

where α_1 and α_2 are the coefficients of thermal expansion (CTE) of the component materials, Δt is the change in temperature,

$$\lambda_1 = \frac{1 - \nu_1}{E_1 h_1},\ \lambda_2 = \frac{1 - \nu_2}{E_2 h_2} \tag{2}$$

are the axial compliances of the components, E_1 and E_2 are Young's moduli of the materials, ν_1 and ν_2 are their Poisson's ratios, h_1 and h_2 are the thicknesses of the components, $\hat{T}$ are the external "mechanical" compressive forces (per unit assembly width) acting on the low expansion component #1,

$$T(x) = \int_{-l}^{x} \tau(\xi) d\xi \tag{3}$$

is the force acting in the cross-section x of the component #2, l is half the assembly length, $\tau(x)$ is the interfacial shearing stress,

$$\kappa_1 = \frac{h_1}{3G_1},\ \kappa_2 = \frac{h_2}{3G_2} \tag{4}$$

are the longitudinal interfacial compliances of the assembly components in the case of a long enough and/or stiff enough assembly [11],

$$G_1 = \frac{E_1}{2(1 + \nu_1)},\ G_2 = \frac{E_2}{2(1 + \nu_2)} \tag{5}$$

are the shear moduli of the materials, and $w_1(x)$ and $w_2(x)$ are the component deflections. The origin of the coordinate x is in the mid-cross-section of the assembly at the interface. The first terms in (1) are stress-free thermal contractions. The second terms are evaluated based on the Hooke's law assuming that the longitudinal displacements are the same for all the points of the given cross-section. The third terms are "corrections" to this assumption and account for the fact that the interfacial longitudinal displacements are somewhat larger than the displacements of the inner points of the cross-section. The fourth terms are due to bending.

The condition of the compatibility of the displacements (1) can be written as

$$u_1(x) = u_2(x) - \kappa_0 \tau(x) \tag{6}$$

where

$$\kappa_0 = \frac{h_0}{G_0} \tag{7}$$

is the longitudinal interfacial compliance of the bonding layer, h_0 is its thickness,

$$G_0 = \frac{E_0}{2(1 + \nu_0)} \tag{8}$$

is the shear modulus of the bonding material, and E_0 and ν_0 are its elastic constants. Introducing the formulas (1) into the condition (6) we obtain the following integral equation for the shearing stress function, $\tau(x)$:

$$\kappa\tau(x) - (\lambda_1 + \lambda_2)\int_0^x T(\xi)d\xi - \frac{h_1}{2}w_1'(x) - \frac{h_2}{2}w_2'(x) = -(\Delta\alpha\Delta t + \lambda_1\hat{T})x \tag{9}$$

where $\Delta\alpha = \alpha_2 - \alpha_1$ is the difference in the CTE of the component materials, and

$$\kappa = \kappa_0 + \kappa_1 + \kappa_2 \tag{10}$$

is the total longitudinal interfacial compliance of the assembly. As evident from the (9), the "external" thermal strain $\Delta\alpha\Delta t$ can be enhanced, without broadening the temperature range, by mechanically prestressing one of the assembly components. The (9) indicates also that such an enhancement increases with an increase in the axial compliance of the compressed component. From (9) we find by differentiation:

$$\kappa\tau'(x) - (\lambda_1 + \lambda_2)T(x) - \frac{h_1}{2}w_1''(x) - \frac{h_2}{2}w_2''(x) = -(\Delta\alpha\Delta t + \lambda_1\hat{T}) \tag{11}$$

$$\kappa\tau''(x) - (\lambda_1 + \lambda_2)\tau(x) - \frac{h_1}{2}w_1'''(x) - \frac{h_2}{2}w_2'''(x) = 0 \tag{12}$$

$$\kappa\tau'''(x) - (\lambda_1 + \lambda_2)\tau'(x) - \frac{h_1}{2}w_1^{IV}(x) - \frac{h_2}{2}w_2^{IV}(x) = 0 \tag{13}$$

Treating the assembly components as elongated rectangular plates we proceed from the following equations of bending (equilibrium):

$$\int_{-l}^{x}\int_{-l}^{x} p(\xi)d\xi d\xi_1 = -D_1 w_1''(x) + \frac{h_1}{2}T(x) = D_2 w_2''(x) - \frac{h_2}{2}T(x) \tag{14}$$

where $p(x)$ is the interfacial peeling stress (i.e., normal interfacial stress acting in the through-thickness direction of the assembly), and

$$D_1 = \frac{E_1 h_1^3}{12(1-\nu_1^2)},\ D_2 = \frac{E_2 h_2^3}{12(1-\nu_2^2)} \tag{15}$$

are the flexural rigidities of the components. From (14) we find by differentiation:

$$\int_{-l}^{x} p(\xi)d\xi = -D_1 w_1'''(x) + \frac{h_1}{2}\tau(x) = D_2 w_2'''(x) - \frac{h_2}{2}\tau(x) \tag{16}$$

$$p(x) = -D_1 w_1^{IV}(x) + \frac{h_1}{2}\tau'(x) = D_2 w_2^{IV}(x) - \frac{h_2}{2}\tau'(x) \tag{17}$$

Solving the (17) for the fourth derivatives of the deflection functions and substituting the obtained expressions into the (13) we obtain the following equation

$$\kappa\tau'''(x) - \lambda\tau'(x) = -\mu p(x) \tag{18}$$

that couples the interfacial shearing stress $\tau(x)$ and the interfacial peeling stress $p(x)$. In the obtained equation,

$$\lambda = \lambda_1 + \lambda_2 + \frac{h_1^2}{4D_1} + \frac{h_2^2}{4D_2} \tag{19}$$

is the total axial compliance of the assembly (with consideration of the effect of bending), and

$$\mu = \frac{h_1}{2D_1} - \frac{h_2}{2D_2} \tag{20}$$

is the factor of the peeling stress. As evident from the formula (19), the total axial compliance of the assembly increases with a decrease in the flexural rigidities of its components. As to the factor (20), it is the lowest for adherends with close flexural rigidities and is the highest in the case of considerably different rigidities.

It is assumed that the peeling stress is related to the deflections $w_1(x)$ and $w_2(x)$ as

$$p(x) = K[w_1(x) - w_2(x)] \tag{21}$$

where K is the through-thickness stiffness of the assembly. The formula (21) reflects an assumption that no peeling stress could possibly occur in the given cross-section, if the deflections $w_1(x)$ and $w_2(x)$ are the same in this cross-section. In an approximate analysis, by analogy with the longitudinal interfacial stiffness (compliance), one could assume:

$$K = \frac{1}{\frac{(1-\nu_1)h_1}{3E_1} + \frac{(1-\nu_2)h_2}{3E_2} + \frac{(1-\nu_0)h_0}{E_0}} \tag{22}$$

This formula indicates that while the entire bonding layer experiences stresses acting in the through-thickness direction of the assembly, only the inner portions of the assembly components, that is, the regions adjacent to the interface, are in the state of appreciable stress. From (21) follows

$$p^{IV}(x) = K[w_1^{IV}(x) - w_2^{IV}(x)] \tag{23}$$

Solving the (17) for the fourth derivatives of the deflection functions and substituting the obtained expressions into the (23) we obtain an equation that couples the interfacial shearing, $\tau(x)$, and the interfacial peeling, $p(x)$, stresses:

$$p^{IV}(x) + 4\beta^4 p(x) = \mu K \tau'(x) \tag{24}$$

where

$$\beta = \sqrt[4]{K\frac{D_1 + D_2}{4D_1D_2}} \tag{25}$$

is the parameter of the interfacial peeling stress. The (24) indicates that the longitudinal gradient of the interfacial shearing stress plays the role of the external loading for the peeling stress. It is noteworthy that the (24) has the form of the equation of bending of a beam lying on a continuous elastic foundation. In the engineering theory of such beams, this equation is being written, however, for the deflection function, and not for the peeling stress.

The (18) and (24) are the two basic equations in the problem in question. These equations indicate that the two types of the interfacial stresses are coupled. Separating the functions $\tau(x)$ and $p(x)$ in the (18) and (24), it is found that these two functions could be determined, in effect, from the same equation:

$$\tau^{VI}(x) - k^2\tau^{IV}(x) + 4\beta^4\left[\tau''(x) - k^2\tau(x) + \frac{\mu^2}{\kappa}\frac{D_1D_2}{D_1 + D_2}\tau(x)\right] = 0 \tag{26}$$

or

$$p^{VI}(x) - k^2 p^{IV}(x) + 4\beta^4\left[p''(x) - k^2 p(x) + \frac{\mu^2}{\kappa}\frac{D_1D_2}{D_1 + D_2}p(x)\right] = 0 \tag{27}$$

Here

$$k = \sqrt{\frac{\lambda}{\kappa}} \tag{28}$$

is the parameter of the interfacial shearing stress. The solution to the (26) should be sought, however, in an anti-symmetric form and should contain only odd functions, while the solution to the (27) should be symmetric with respect to the mid-cross-section of the assembly and should contain, therefore, only even functions. This circumstance is reflected by the appropriate boundary conditions.

Boundary Conditions

Since there are no external forces acting at the ends of the component #2, the force $T(x)$ must be zero at the end $x = l$ of this component:

$$T(l) = 0 \tag{29}$$

Since no concentrated bending moments act at the assembly ends, the curvatures $w_1''(x)$ and $w_2''(x)$ must be zero at these ends:

$$w_1''(l) = w_2''(l) = 0 \tag{30}$$

As to the lateral forces, the following boundary conditions have to be fulfilled:

$$D_1 w_1'''(l) + \hat{T} w'(l) = 0,\ w_2'''(l) = 0 \tag{31}$$

The first condition in (31) indicates that the lateral projection of the external force $\hat{T}$ should be equilibrated by the elastic force. Considering, however, that a typical electronic or photonic assembly is stiff enough, so that the angle of rotation $w'(l)$ is small, and, in addition, that the external force $\hat{T}$ should be sufficiently low (actually, well below its critical value), one could assume, in an approximate analysis, that the third derivative $w_1'''(l)$ of the deflection function for the component #1 can also be put equal to zero. Then the conditions (31) can be substituted, with following conditions:

$$w_1'''(l) \approx w_2'''(l) = 0 \tag{32}$$

The peeling stress *p(x)* must be self-equilibrated. This means that the following equilibrium conditions are to be fulfilled:

$$\int_{-l}^{l} p(\xi) d\xi = 0,\ \int_{-l}^{l} \int_{-l}^{x} p(\xi) d\xi d\xi_1 = 0 \tag{33}$$

The (11), considering the conditions (29) and (30), results in the following boundary condition for the shearing stress function:

$$\tau'(l) = -\frac{\Delta\alpha\Delta t + \lambda_1 \hat{T}}{\kappa} \tag{34}$$

The (12), considering (32), yields:

$$\kappa\tau''(l) - (\lambda_1 + \lambda_2)\tau(l) = 0 \tag{35}$$

Note that the (14), considering the boundary conditions (30), (32) and the second condition in (33), is always fulfilled at the assembly ends.

Equation (16), taking into account the conditions (32) and the first condition in (33), yields:

$$\tau(l) = 0 \tag{36}$$

Then the formula (35) results in a zero boundary condition for the second derivative of the shearing stress function as well:

$$\tau''(l) = 0 \tag{37}$$

As to the peeling stress, there follow from (21), considering (30) and (32), the conditions:

$$p''(l) = 0,\ p'''(l) = 0 \tag{38}$$

Solutions to the Basic Equations

The interfacial shearing stress function $\tau(x)$ is sought in the form:

$$\tau(x) = C_1 \sinh\gamma_1 x \cos\gamma_2 x + C_3 \cosh\gamma_1 x \sin\gamma_2 x + C_5 \sinh\gamma x \tag{39}$$

The differentiation leads to:

$$\tau'(x) = (\gamma_1 C_1 + \gamma_2 C_3)\cosh\gamma_1 x\cos\gamma_2 x + (-\gamma_2 C_1 + \gamma_1 C_3)\sinh\gamma_1 x\sin\gamma_2 x + \gamma C_5 \cosh\gamma x \tag{40}$$

$$\tau''(x) = [(\gamma_1^2 - \gamma_2^2)C_1 + 2\gamma_1\gamma_2 C_3]\sinh\gamma_1 x\cos\gamma_2 x + [(\gamma_1^2 - \gamma_2^2)C_3 - 2\gamma_1\gamma_2 C_1]\cosh\gamma_1 x\sin\gamma_2 x + \gamma^2 C_5 \sinh\gamma x \tag{41}$$

$$\tau'''(x) = [\gamma_1(\gamma_1^2 - 3\gamma_2^2)C_1 - \gamma_2(\gamma_2^2 - 3\gamma_1^2)C_3]\cosh\gamma_1 x\cos\gamma_2 x + [\gamma_2(\gamma_2^2 - 3\gamma_1^2)C_1 + \gamma_1(\gamma_1^2 - 3\gamma_2^2)C_3]\sinh\gamma_1 x\sin\gamma_2 x + \gamma^3 C_5\cosh\gamma x \tag{42}$$

$$\tau^{IV}(x) = [(\gamma_1^4 - 6\gamma_1^2\gamma_2^2 + \gamma_2^4)C_1 + 4\gamma_1\gamma_2(\gamma_1^2 - \gamma_2^2)C_3]\sinh\gamma_1 x\cos\gamma_2 x + [(\gamma_1^4 - 6\gamma_1^2\gamma_2^2 + \gamma_2^4)C_3 - 4\gamma_1\gamma_2(\gamma_1^2 - \gamma_2^2)C_1]\cosh\gamma_1 x\sin\gamma_2 x + \gamma^4 C_5 \sinh\gamma x \tag{43}$$

$$\tau^{V}(x) = [\gamma_1(\gamma_1^4 - 10\gamma_1^2\gamma_2^2 + 5\gamma_2^4)C_1 + \gamma_2(\gamma_2^4 - 10\gamma_1^2\gamma_2^2 + 5\gamma_1^4)C_3]\cosh\gamma_1 x\cos\gamma_2 x + [-\gamma_2(\gamma_2^4 - 10\gamma_1^2\gamma_2^2 + 5\gamma_1^4)C_1 + \gamma_1(\gamma_1^4 - 10\gamma_1^2\gamma_2^2 + 5\gamma_2^4)C_3]\sinh\gamma_1 x\sin\gamma_2 x + \gamma^5 C_5\cosh\gamma x \tag{44}$$

$$\tau^{VI}(x) = [(\gamma_1^6 - \gamma_2^6 + 15\gamma_1^2\gamma_2^4 - 15\gamma_1^4\gamma_2^2)C_1 + 2\gamma_1\gamma_2(3\gamma_1^4 + 3\gamma_2^4 - 10\gamma_1^2\gamma_2^2)C_3] \sinh\gamma_1 x\cos\gamma_2 x + [2\gamma_1\gamma_2(-3\gamma_1^4 - 3\gamma_2^4 + 10\gamma_1^2\gamma_2^2)C_1 + (\gamma_1^6 - \gamma_2^6 + 15\gamma_1^2\gamma_2^4 - 15\gamma_1^4\gamma_2^2)C_3] \cosh\gamma_1 x\sin\gamma_2 x + \gamma^6 C_5 \sinh\gamma x \tag{45}$$

Then the (26) results in the following three equations for the factors γ_1, γ_2 and γ:

$$\gamma_1^6 - \gamma_2^6 + 15\gamma_1^2\gamma_2^4 - 15\gamma_1^4\gamma_2^2 - k^2(\gamma_1^4 - 6\gamma_1^2\gamma_2^2 + \gamma_2^4) + 4\beta^4[\gamma_1^2 - \gamma_2^2 - k^2(1-\delta)] = 0 \tag{46}$$

$$3\gamma_1^4 + 3\gamma_2^4 - 10\gamma_1^2\gamma_2^2 - 2k^2(\gamma_1^2 - \gamma_2^2) + 4\beta^4 = 0 \tag{47}$$

$$\gamma^6 - k^2\gamma^4 - 4\beta^4\gamma^2 + 4\beta^4 k^2(1-\delta) = 0 \tag{48}$$

where

$$\delta = \frac{\mu^2}{\lambda}\frac{D_1 D_2}{D_1 + D_2} \tag{49}$$

is the parameter of coupling of the interfacial stresses. This parameter, as follows from the formula (20), is very small if the assembly components have close flexural rigidities.

Introducing new unknowns, ξ and η, as

$$\xi = \gamma_1^2 - \gamma_2^2,\ \eta = 2\gamma_1\gamma_2 \tag{50}$$

the (46) and (47) assume the form:

$$\xi^3 - k^2\xi^2 - 3\eta^2\xi + 4\beta^4\xi + k^2\eta^2 - 4\beta^4 k^2(1-\delta) = 0 \tag{51}$$

$$\eta^2 = 3\xi^2 - 2k^2\xi + 4\beta^4 \tag{52}$$

Introducing the η^2 value from the (52) into the (51), the following cubic equation is obtained for the unknown ξ:

$$\xi^3 - k^2\xi^2 + \frac{1}{4}(k^4 + 4\beta^4)\xi - \frac{1}{2}k^2\beta^4\delta = 0 \tag{53}$$

After the ξ value is found, the η value can be determined from the (52), and then the γ_1 and γ_2 values could be evaluated as

$$\gamma_{1,2} = \sqrt{\frac{\xi}{2}\left(\pm 1 + \sqrt{1 + \frac{\eta^2}{\xi^2}}\right)} \tag{54}$$

These values are close to each other, if the ξ value is small, and the η value is large. In such a case, as one could see from the (52), $\eta = 2\beta^2$. Note that the result (54) could be obtained, if the (27) and the particular solution

$$p(x) = C_0\cosh\gamma_1 x\cos\gamma_2 x + C_2\sinh\gamma_1 x\sin\gamma_2 x + C_4\cosh\gamma x \tag{55}$$

for the peeling stress $p(x)$ were considered.

Constants of Integration

The constants C_1, C_3, and C_5 of integration in the expression (39) for the interfacial shearing stress can be found, based on the boundary conditions (34), (36), and (37), from the following system of equations:

$$\left.\begin{aligned}
&(\sinh u_1\cos u_2)C_1 + (\cosh u_1\sin u_2)C_3 + (\sinh u)C_5 = 0\\
&(u_1\cosh u_1\cos u_2 - u_2\sinh u_1\sin u_2)C_1 + (u_2\cosh u_1\cos u_2 + u_1\sinh u_1\sin u_2)C_3\\
&\quad + (u\cosh u)C_5 = -l\frac{\Delta\alpha\Delta t + \lambda_1\hat{T}}{\kappa}\\
&[(u_1^2 - u_2^2)\sinh u_1\cos u_2 - 2u_1u_2\sinh u_1\sin u_2]C_1\\
&\quad + [(u_1^2 - u_2^2)\cosh u_1\sin u_2 + 2u_1u_2\sinh u_1\cos u_2]C_3 + (u^2\sinh u)C_5 = 0
\end{aligned}\right\} \tag{56}$$

Here the following notation is used:

$$u_1 = \gamma_1 l,\ u_2 = \gamma_2 l,\ u = \gamma l \tag{57}$$

As to the constants C_0, C_2, and C_4 in the expression (55) for the interfacial peeling stress, $p(x)$, they can be determined after substituting the solutions (39) and (55) into the (18) or into the (24) and comparing the expressions at the left and the right parts of the obtained relationships. This leads to the following formulas for the constants C_0, C_2, and C_4 of integration:

$$\left.\begin{aligned} C_0 &= -\frac{\kappa}{\mu}\left[\gamma_1(\gamma_1^2 - 3\gamma_2^2 - k^2)C_1 - \gamma_2(\gamma_2^2 - 3\gamma_1^2 + k^2)C_3\right] \\ C_2 &= -\frac{\kappa}{\mu}\left[\gamma_1(\gamma_1^2 - 3\gamma_2^2 - k^2)C_3 + \gamma_2(\gamma_2^2 - 3\gamma_1^2 + k^2)C_1\right] \\ C_4 &= -\frac{\kappa}{\mu}\gamma(\gamma^2 - k^2)C_5 \end{aligned}\right\} \tag{58}$$

Numerical Example

Input Data

Component #1: Young's modulus: $E_1 = 12{,}300\ \mathrm{kg/mm^2}$; Poisson's ratio: $\nu_1 = 0.24$; CTE: $\alpha_1 = 2.2 \times 10^{-6} 1/^\circ\mathrm{C}$; Thickness: $h_1 = 0.5\ \mathrm{mm}$; External force: $\hat{T} = 8.0\ \mathrm{kg/mm}$;

Component #2: Young's modulus: $E_2 = 2{,}000\ \mathrm{kg/mm^2}$; Poisson's ratio: $\nu_2 = 0.30$; CTE: $\alpha_2 = 13.2 \times 10^{-6} 1/^\circ\mathrm{C}$; Thickness: $h_2 = 1.5\ \mathrm{mm}$;

Bonding layer: Young's modulus: $E_0 = 200\ \mathrm{kg/mm^2}$; Poisson's ratio: $\nu_0 = 0.40$; Thickness: $h_0 = 0.05\ \mathrm{mm}$;

Change in temperature: $\Delta t = 100\ ^\circ\mathrm{C}$; Assembly length: $2l = 20\ \mathrm{mm}$

Computed Data

Thermal strain: $\Delta\alpha\Delta t = (\alpha_2 - \alpha_1)\Delta t = 11 \times 10^{-6} \times 100 = 0.0011$.

Axial compliances, as predicted by the formulae (2):

$$\lambda_1 = \frac{1-\nu_1}{E_1 h_1} = \frac{1 - 0.24}{12300 \times 0.5} = 1.2358 \times 10^{-4}\mathrm{mm/kg}$$
$$\lambda_2 = \frac{1-\nu_2}{E_2 h_2} = \frac{1 - 0.30}{2000 \times 1.5} = 2.3333 \times 10^{-4}\mathrm{mm/kg}$$

Shear moduli, as predicted by the formulae (8) and (5):

$$G_0 = \frac{E_0}{2(1+\nu_0)} = \frac{200}{2 \times 1.4} = 71.4\,\mathrm{kg/mm^2}$$
$$G_1 = \frac{E_1}{2(1+\nu_1)} = \frac{12{,}300}{2 \times 1.24} = 4{,}960\,\mathrm{kg/mm^2}$$
$$G_2 = \frac{E_2}{2(1+\nu_2)} = \frac{2000}{2 \times 1.30} = 769\,\mathrm{kg/mm^2}$$

Interfacial shearing compliances, as predicted by the formulae (7), (4) and (10):

$$\kappa_0 = \frac{h_0}{G_0} = \frac{0.05}{71.4} = 7.00 \times 10^{-4}\mathrm{mm^3/kg}$$
$$\kappa_1 = \frac{h_1}{3G_1} = \frac{0.5}{3 \times 4960} = 0.3360 \times 10^{-4}\mathrm{mm^3/kg}$$
$$\kappa_2 = \frac{h_2}{3G_2} = \frac{1.5}{3 \times 769} = 6.5020 \times 10^{-4}\mathrm{mm^3/kg}$$
$$\kappa = \kappa_0 + \kappa_1 + \kappa_2 = 7.00 \times 10^{-4} + 0.3360 \times 10^{-4} + 6.5020 \times 10^{-4} = 13.838 \times 10^{-4}\mathrm{mm^3/kg}$$

Boundary condition for the interfacial shearing stress, as given by the formula (34):

$$\tau'(l) = -\frac{\Delta\alpha\Delta t + \lambda_1 \hat{T}}{\kappa} = -\frac{0.0011 + 0.0009886}{13.838 \times 10^{-4}} = -1.5093\,\mathrm{kg/mm^3}$$

Note that because of the prestressing of the low expansion component of the assembly, the interfacial stresses in the assembly increase by a factor of 1.9. Flexural rigidities of the assembly components (treated as elongated rectangular plates) are evaluated on the basis of the formulae (15):

$$D_1 = \frac{E_1 h_1^3}{12(1-\nu_1^2)} = \frac{12{,}300 \times 0.5^3}{12 \times 0.9424} = 136.0\,\mathrm{kg/mm}$$
$$D_2 = \frac{E_2 h_2^3}{12(1-\nu_2^2)} = \frac{2{,}000 \times 1.5^3}{12 \times 0.9100} = 618.1\,\mathrm{kg/mm}$$

Total axial compliance of the assembly, as predicted by the formula (19):

$$\lambda = \lambda_1 + \lambda_2 + \frac{h_1^2}{4D_1} + \frac{h_2^2}{4D_2} = 1.2358 \times 10^{-4} + 2.3333 \times 10^{-4} + 4.5956 \times 10^{-4} + 9.1005 \times 10^{-4} = 17.2652 \times 10^{-4}\mathrm{mm/kg}$$

Parameter of the interfacial shearing stress, as given by the formula (28):

$$k = \sqrt{\frac{\lambda}{\kappa}} = \sqrt{\frac{17.2652 \times 10^{-4}}{13.838 \times 10^{-4}}} = 1.117\,\mathrm{mm}^{-1}$$

Factor of the peeling stress, as given by the formula (20):

$$\begin{aligned}\mu &= \frac{h_1}{2D_1} - \frac{h_2}{2D_2} = \frac{0.5}{272} - \frac{1.5}{618.1} \\ &= 18.382 \times 10^{-4} - 24.268 \times 10^{-4} \\ &= -5.886 \times 10^{-4}\mathrm{kg}^{-1}\end{aligned}$$

Through-thickness stiffness, as predicted by the formula (22):

$$\begin{aligned}K &= \frac{1}{\frac{(1-\nu_1)h_1}{3E_1} + \frac{(1-\nu_2)h_2}{3E_2} + \frac{(1-\nu_0)h_0}{E_0}} \\ &= \frac{1}{0.103 \times 10^{-4} + 1.750 \times 10^{-4} + 1.500 \times 10^{-4}} \\ &= 2{,}982\ \mathrm{kg/mm}^3\end{aligned}$$

Parameter of the peeling stress, as predicted by the formula (25):

$$\begin{aligned}\beta &= \sqrt[4]{K\frac{D_1 + D_2}{4D_1D_2}} = \sqrt[4]{2982\frac{754.1}{336246.4}} \\ &= 0.7441\,\mathrm{mm}^{-1}\end{aligned}$$

Parameter of coupling of the interfacial stresses, as predicted by the formula (49):

$$\begin{aligned}\delta &= \frac{\mu^2}{\lambda}\frac{D_1D_2}{D_1 + D_2} = \frac{34.6450 \times 10^{-8}}{17.2652 \times 10^{-4}}\frac{84061.6}{754.1} \\ &= 0.02237\end{aligned}$$

Equation (53) for the unknown ξ value yields

$$\xi^3 - 1.2477\xi^2 + 0.6957\xi - 0.004278 = 0$$

and has the following root: $\xi = 0.00615$. Then the (52) yields: $\eta = 1.10047$. From the formula (54) follows:

$$\gamma_1 = 0.74385\,\mathrm{mm}^{-1};\ \gamma_2 = 0.73970\,\mathrm{mm}^{-1}$$

Note that the obtained two values are very close to each other and to the β value. This is because the η value turned out to be, in this example, substantially larger than the ξ value, which is the case for adherends with not-very-much-different flexural rigidities. The (48) for the γ value yields:

$$\gamma^6 - 1.2477\gamma^4 - 1.22627\gamma^2 + 1.495788 = 0$$

Its root is $\gamma = 1.0165\,\mathrm{mm}^{-1}$ and is not very much different from the k value.

The parameters $u_1 = \gamma_1 l$, $u_2 = \gamma_2 l$, and $u = \gamma l$, expressed by the formulae (57), are as follows:

$$\begin{aligned}u_1 &= \gamma_1 l = 0.74385 \times 10 = 7.4385 \\ u_2 &= \gamma_2 l = 0.73970 \times 10 = 7.3970 \\ u &= \gamma l = 1.0165 \times 10 = 10.165\end{aligned}$$

These parameters are large enough, so that the assembly can be treated as an elongated one. The (56) for the constants C_1, C_3, and C_5 of integration yield:

$$\begin{aligned}&0.028876C_1 + 0.058733C_3 + C_5 = 0 \\ &0.021609C_1 - 0.063992C_3 - C_5 = 0.00011431 \\ &0.062380C_1 - 0.03110C_3 - C_5 = 0\end{aligned}$$

These equations have the following solutions:

$$\begin{aligned}C_1 &= 0.0003488\,\mathrm{kg/mm}^2 \\ C_3 &= -0.0011520\,\mathrm{kg/mm}^2 \\ C_5 &= 0.00005759\,\mathrm{mm}^2\end{aligned}$$

The shearing stress in the region close to the assembly ends can be computed by the formula: $\tau(x) = e^{-0.7438x}[0.0001744(\cos 0.7397x) - 0.0005770(\sin 0.7397x)] + 0.000028795e^{-1.0165x}$, which can be obtained from the solution (39). The calculated stresses are shown in Table 1. At the bottom line the stresses calculated using the simplified formula [14]

$$\tau_1(x) = k\frac{\Delta\alpha\Delta t + \lambda_1\hat{T}}{\lambda}$$

Analysis of a Prestressed Bi-Material Accelerated-Life-Test (ALT) Specimen, Table 1 Calculated interfacial shearing stresses

x,mm	8.0	8.4	8.5	8.75	9.0	9.5	9.7	9.9	10
$\tau(x)$, kg/mm^2	0.0813	0.2164	0.2584	0.2518	0.2313	0.1422	0.0894	0.0297	0
$\tau_1(x)$, kg/mm^2	0.1441	0.2262	0.2530	0.3345	0.4422	0.7730	0.9665	1.2085	1.351

Analysis of a Prestressed Bi-Material Accelerated-Life-Test (ALT) Specimen, Table 2 Calculated peeling stresses

x, mm	4.0	5.0	6.0	6.5	7.0	7.5
$p(x)$, kg/mm^2	0.0285	−0.0910	−0.1650	−0.3032	−0.4744	−0.6502
x, mm	8.0	8.25	8.5	9.0	9.5	10.0
$p(x)$, kg/mm^2	−0.7670	−0.7719	−0.7179	−0.3467	0.5419	2.1439

are indicated. The calculated data indicate that this formula can be used for conservative engineering assessments. The interfacial peeling stress, on the basis of the solution (55), is given by:

$$p(x) = e^{-0.7438x}(-0.001150\cos 0.7397x + 0.002221\sin 0.7397x) - 0.000014750e^{-1.0165x}$$

The computed peeling stress is shown in Table 2. These data indicate that this stress is indeed self-equilibrated.

References

1. Suhir E (2009) Analytical thermal stress modeling in electronic and photonic systems. ASME Appl Mech Rev 62(4):1–20
2. Boley BA, Weiner JH (1974) Theory of thermal stresses. Quantum Publishers, New York
3. Noda N, Hetnarski RB, Tanigawa Y (2004) Thermal stresses, 2nd edn. Taylor and Francis, New York
4. Ceniga L (2008) Analytical models of thermal stresses in composite materials. Nova, New York
5. Lanin A, Fedik I (2008) Thermal stress resistance of materials. Springer, Berlin
6. Lau JH (ed) (1993) Thermal stress and strain in microelectronics packaging. New York, Van-Nostrand Reinhold
7. Timoshenko SP (1925) Analysis of bi-metal thermostats. J Opt Soc Am 11:233–255
8. Aleck BJ (1949) Thermal stresses in a rectangular plate clamped along an edge. ASME J Appl Mech 16:118–122
9. Kuo AY (1989) Thermal stresses at the edge of a bimetallic thermostat. ASME J Appl Mech 56:585–589
10. Eischen JW, Chung C, Kim JH (1990) Realistic modeling of the edge effect stresses in bimaterial elements. ASME J Electron Packag 112(1):143–148
11. Suhir E (1986) Stresses in bi-metal thermostats. ASME J Appl Mech 53(3):657–660
12. Suhir E (1989) Interfacial stresses in bi-metal thermostats. ASME J Appl Mech 56(3):595–600
13. Zhao J-H, Dai X, Ho PS (1998) Analysis and modelling verification for thermal-mechanical deformation in flip-chip packages. In: Proceeding of 48th Electronic Components & Technology Conference, Seattle, 25–28, May 1998, pp 336–344
14. Suhir E (2001) Analysis of interfacial thermal stresses in a tri-material assembly. J Appl Phys 89(7):3685–3694
15. Gillanders JT, Riddle RA, Streit RD, Finnie I (1990) Methods for determining the mode I and mode II fracture toughness of glass using thermal stresses. ASME J Eng Mater Technol 112:151–156
16. John R, Hartman GA, Gallagher JP (1992) Crack growth induced by thermal-mechanical loading. Exp Mech 32(2):102–108
17. Bae J-S, Krishnaswamy S (2001) Subinterfacial cracks in bimaterial systems subjected to mechanical and thermal loading. Eng Fract Mech 68(9):1–2
18. Tee TY, Zhong Z (2004) Integrated vapor pressure, hygroswelling, and thermo-mechanical stress modelling of QFN package during reflow with interfacial fracture mechanics analysis. Microelectron Reliab 44:105–114
19. Coffin LF (1959) Internal stress and fatigue of metals. Elsevier, New York
20. Garofalo F (1965) Fundamentals of creep and creep fracture of metals. McMillan, New York
21. Brown SB, Kim KH, Anand L (1989) An internal variable constitutive model for hot working of metals. Int J Plast 5(2):95–130

22. Nelson W (1990) Accelerated testing: statistical models, test plans and data analyses. Wiley, New York
23. Solomon HD, (1986) Fatigue of 60/40 Solder. In: IEEE CPMT Transactions, vol. CHMT-9, No. 4, pp 423–431
24. Morgan HS (1991) Thermal stresses in layered electrical assemblies bonded with solder. ASME J Electron Packag 113(4):42
25. Suhir E (1991) Stress relief in solder joints due to the application of a flex circuit. ASME J Electron Packag 113(3):16–20
26. Suhir E (1994) Thermally induced stresses in an optical glass fiber soldered into a ferrule. IEEE/OSA J Lightwave Technol 12(10):1766–1770
27. Lau J (ed) (1995) Ball grid array technology. McGraw-Hill, New York
28. Hwang JS (1996) Modern solder technology for competitive electronics manufacturing. McGraw-Hill, New York
29. Cheng ZN, Wang GZ, Chen L, Wilde J, Becker K (2000) Viscoplastic anand model for solder alloys and its application. Solder Surf Mt Technol 12(2):31–36
30. Ghaffarian R (2003) Qualification approaches and thermal cycle test results for CSP/BGA/FCBGA. Microelectron Reliab 43(5):695–706
31. Shangguan D (ed) (2005) Lead-free solder interconnect reliability. ASM, Materials Park
32. Suhir E (2006) Interfacial thermal stresses in a bimaterial assembly with a low-yield-stress bonding layer. Model Simul Mater Sci Eng 14:1421–1432
33. Roll K (1976) Analysis of stress and strain distribution in thin films and substrates. J Appl Phys 47(7):3224
34. Suhir E (1988) An approximate analysis of stresses in multilayer elastic thin films. ASME J Appl Mech 55(3):657–660
35. Suhir E (1994) Approximate evaluation of the elastic thermal stresses in a thin film fabricated on a very thick circular substrate. ASME J Electron Packag 116(3):171–176
36. Pecht M, Wu X, Paik KW, Bhandarkar SN (1995) To cut or not to cut: a thermomechanical stress analysis of polyimide thin-film on ceramics structures. In: IEEE transactions on components and packaging technologies-Part B, vol. 18(1), pp 491–495
37. Suhir E (2000) Predicted thermally induced stresses in, and the bow of, a circular substrate/thin-film structure. J Appl Phys 88(5)
38. Noor K, Malik M (2000) An assessment of five modelling approaches for thermo-mechanical stress analysis of laminated composite panels. Comput Mech 25:43–58

Analytic Continuation

► Orthotropic Rectangular Plate with a Rigid Ribbonlike Inclusion, Thermal Stress
► Thermal Stresses of Thin Films on Flexible Substrates

Analytical Method

► Analytical Method of FGM
► Thermoelastic Wave Propagation Analysis in Thick Hollow Cylinder Based on Green-Naghdi Theory of Coupled Thermoelasticity Using Analytical Method

Analytical Method of FGM

Yoshinobu Tanigawa[1] and Ryuusuke Kawamura[2]
[1]Osaka Prefecture University, Osaka, Japan
[2]Institute of Education and Research for Engineering, University of Miyazaki, Miyazaki, Japan

Synonyms

Analytical method

Overview

Functionally graded materials (FGMs) are the composite materials to express the desired functions by the continuous or discontinuous changes in the composition of the constituent materials. FGMs are therefore the nonhomogeneous materials. The importance for FGMs is how to design the material so as to express the desired functions, how to fabricate the designed FGMs, and how to evaluate the fabricated FGMs.

Material properties of FGMs are dependent on position and temperature, since FGMs are the nonhomogeneous materials. The governing equations for the temperature field and the associate thermoelastic field of FGMs become of nonlinear form in general. Then, analytical treatment is difficult. There are mainly five kinds of analytical methods to solve the governing equations of FGMs: (a) direct method, (b) stress function method, (c) potential function method, (d) laminated composite methods, and (e) Green function

method. The direct method is that the governing equations expressed by displacements are solved directly. The laminated composite methods are explained by Guo, and Green function method is explained by Watanabe in the ETS. Then, stress function method and potential method are discussed in this entry.

Fundamental Equations for FGMs

The equations of motion of FGMs are

$$\sigma_{ji,j} + F_i = \rho \ddot{u}_i \tag{1}$$

where σ_{ij} are stresses, ρ is density, F_i are body forces, u_i are displacements, and the superscript dot denotes the partial differentiation with respect to the time. The density in FGMs is defined as a function of the position, namely, $\rho(x_1, x_2, x_3)$ because FGMs are nonhomogeneous materials.

The constitutive equations for a nonhomogeneous, isotropic body in consideration of temperature change are

$$\varepsilon_{ij} = \frac{1}{2G}\left(\sigma_{ij} - \frac{v}{1+v}\sigma_{kk}\delta_{ij}\right) + \alpha T \delta_{ij} \tag{2}$$

or

$$\sigma_{ij} = 2\mu\varepsilon_{ij} + \lambda\varepsilon_{kk}\delta_{ij} - \beta T \delta_{ij} \tag{3}$$

where ε_{ij} are strains, T is temperature change from a reference temperature, G is shear modulus of elasticity, v is Poisson ratio, α is coefficient of linear thermal expansion, δ_{ij} is Kronecker delta, μ and λ are Lamé elastic constants, and β is thermoelastic constant. The material properties in a nonhomogeneous body are defined as functions of the position, namely, $G(x_1, x_2, x_3)$, $v(x_1, x_2, x_3)$, and $\alpha(x_1, x_2, x_3)$. The relationship among the material properties holds as follows:

$$\begin{aligned} 2G &= \frac{E}{1+v}, \lambda = \frac{vE}{(1+v)(1-2v)} = \frac{2vG}{1-2v}, \\ \mu &= G, \beta = \frac{\alpha E}{1-2v} = \alpha(3\lambda + 2\mu) \end{aligned} \tag{4}$$

where E is Young's modulus which is defined as a function of the position $E(x_1, x_2, x_3)$.

The strains ε_{ij} are defined by displacements u_i:

$$\varepsilon_{ij} = \frac{1}{2}(u_{i,j} + u_{j,i}) \tag{5}$$

Substituting (3) into (1) gives the equations of motion in terms of displacements:

$$\begin{aligned} &\mu u_{i,kk} + (\lambda + \mu) u_{k,ki} - \beta T_{,i} + F_i \\ &\quad + \left[\mu_{,k}(u_{i,k} + u_{k,i}) + \lambda_{,i} u_{k,k} - \beta_{,i} T\right] = \rho \ddot{u}_i \end{aligned} \tag{6}$$

Comparing with the equations of motion for a homogeneous, isotropic body, it is apparent that the terms of the partial differentiation of the material properties with respect to the position are added to those for a homogeneous, isotropic one in those for FGMs.

Basic Equations of Plane Problem

Let us consider a plane strain problem in which the deformation in the long body is given by

$$u_x = u_x(x, y),\ u_y = u_y(x, y),\ u_z = \varepsilon_0 z + \varepsilon_1 \tag{7}$$

and a plane stress one in which a state of stress in a thin plate is characterized by

$$\begin{aligned} &\sigma_{xx} = \sigma_{xx}(x, y),\ \sigma_{yy} = \sigma_{yy}(x, y) \\ &\sigma_{xy} = \sigma_{xy}(x, y),\ \sigma_{zz} = \sigma_{zx} = \sigma_{zy} = 0 \end{aligned} \tag{8}$$

The constitutive equations are common to both problems, which are defined as

$$\begin{aligned} \varepsilon_{xx} &= \frac{1}{E^*}(\sigma_{xx} - v^* \sigma_{yy}) + \alpha T - \varepsilon_0^* \\ \varepsilon_{yy} &= \frac{1}{E^*}(\sigma_{yy} - v^* \sigma_{xx}) + \alpha T - \varepsilon_0^* \\ \varepsilon_{xy} &= \frac{1}{2G}\sigma_{xy} \\ \sigma_{xx} &= (\lambda^* + 2\mu)\varepsilon_{xx} + \lambda^* \varepsilon_{yy} - \beta^* T \\ \sigma_{yy} &= (\lambda^* + 2\mu)\varepsilon_{yy} + \lambda^* \varepsilon_{xx} - \beta^* T \\ \sigma_{xy} &= 2\mu\varepsilon_{xy} \end{aligned} \tag{9}$$

where

$$E^* = \frac{E}{1-\nu^2},\ \nu^* = \frac{\nu}{1-\nu},\ \alpha^* = (1+\nu)\alpha,$$
$$\lambda^* = \lambda,\ \beta^* = \beta,\ \varepsilon_0^* = \nu\varepsilon_0 \tag{10}$$

for the plane strain problem,

$$E^* = E,\ \nu^* = \nu,\ \alpha^* = \alpha,$$
$$\lambda^* = \frac{2\mu\lambda}{\lambda+2\mu},\ \beta^* = \frac{2\mu\beta}{\lambda+2\mu},\ \varepsilon_0^* = 0 \tag{11}$$

for the plane stress problem.

The equations of motion of plane problems are given by

$$\frac{\partial\sigma_{xx}}{\partial x} + \frac{\partial\sigma_{yx}}{\partial y} + F_x = \rho\ddot{u}_x$$
$$\frac{\partial\sigma_{xy}}{\partial x} + \frac{\partial\sigma_{yy}}{\partial y} + F_y = \rho\ddot{u}_y \tag{12}$$

The compatibility equation is

$$\frac{\partial^2\varepsilon_{xx}}{\partial y^2} + \frac{\partial^2\varepsilon_{yy}}{\partial x^2} = 2\frac{\partial^2\varepsilon_{xy}}{\partial x\partial y} \tag{13}$$

The equations of motion of plane problems (12) can be expressed in terms of displacements.

$$\begin{aligned}
&\mu\nabla^2 u_x + (\lambda^*+\mu)\frac{\partial}{\partial x}\left(\frac{\partial u_x}{\partial x} + \frac{\partial u_y}{\partial y}\right) - \beta^*\frac{\partial T}{\partial x} + F_x \\
&\quad + \frac{\partial\lambda^*}{\partial x}\left(\frac{\partial u_x}{\partial x} + \frac{\partial u_y}{\partial y}\right) + 2\frac{\partial\mu}{\partial x}\frac{\partial u_x}{\partial x} \\
&\quad + \frac{\partial\mu}{\partial y}\left(\frac{\partial u_x}{\partial y} + \frac{\partial u_y}{\partial x}\right) - \frac{\partial\beta^*}{\partial x}T = \rho\ddot{u}_x \\
&\mu\nabla^2 u_y + (\lambda^*+\mu)\frac{\partial}{\partial y}\left(\frac{\partial u_x}{\partial x} + \frac{\partial u_y}{\partial y}\right) - \beta^*\frac{\partial T}{\partial y} + F_y \\
&\quad + \frac{\partial\lambda^*}{\partial y}\left(\frac{\partial u_x}{\partial x} + \frac{\partial u_y}{\partial y}\right) + 2\frac{\partial\mu}{\partial y}\frac{\partial u_y}{\partial y} \\
&\quad + \frac{\partial\mu}{\partial x}\left(\frac{\partial u_y}{\partial x} + \frac{\partial u_x}{\partial y}\right) - \frac{\partial\beta^*}{\partial y}T = \rho\ddot{u}_y
\end{aligned} \tag{14}$$

The plane problems for FGMs are how to solve (14) with respect to displacements u_x and u_y.

Analytical Method for Plane Problems of FGMs

Stress Function Method

We consider quasi-static problems without body forces. Equations (12) reduce to

$$\frac{\partial\sigma_{xx}}{\partial x} + \frac{\partial\sigma_{yx}}{\partial y} = 0$$
$$\frac{\partial\sigma_{xy}}{\partial x} + \frac{\partial\sigma_{yy}}{\partial y} = 0 \tag{15}$$

We introduce the thermal stress function χ that automatically satisfies the equilibrium equations (15) and is related to stresses as follows:

$$\sigma_{xx} = \frac{\partial^2\chi}{\partial y^2},\ \sigma_{yy} = \frac{\partial^2\chi}{\partial x^2},\ \sigma_{xy} = -\frac{\partial^2\chi}{\partial x\partial y} \tag{16}$$

Substituting (16) into the compatibility (13) yields the basic equation of stress function χ for FGMs:

$$\begin{aligned}
&\nabla^2\left(\frac{1}{E^*}\nabla^2\chi\right) - \frac{\partial^2}{\partial y^2}\left(\frac{1+\nu^*}{E^*}\right)\frac{\partial^2\chi}{\partial x^2} \\
&\quad - \frac{\partial^2}{\partial x^2}\left(\frac{1+\nu^*}{E^*}\right)\frac{\partial^2\chi}{\partial y^2} \\
&\quad + 2\frac{\partial^2}{\partial x\partial y}\left(\frac{1+\nu^*}{E^*}\right)\frac{\partial^2\chi}{\partial x\partial y} \\
&\quad + \nabla^2(\alpha^* T) = 0
\end{aligned} \tag{17}$$

where

$$\begin{aligned}
\nabla^4 &= \nabla^2\nabla^2 \\
&= \left(\frac{\partial^2}{\partial x^2} + \frac{\partial^2}{\partial y^2}\right)\left(\frac{\partial^2}{\partial x^2} + \frac{\partial^2}{\partial y^2}\right) \\
&= \frac{\partial^4}{\partial x^4} + 2\frac{\partial^4}{\partial x^2\partial y^2} + \frac{\partial^4}{\partial y^4}
\end{aligned}$$

For homogeneous materials, (17) reduces to

$$\nabla^2\nabla^2\chi + \alpha^* E^*\nabla^2 T = 0 \tag{18}$$

It is difficult to solve (17) directly, since material properties are dependent on the position. As material properties of FGMs mainly change in one direction, we assume material properties are dependent on the position y:

$$E^* = E^*(y),\ v^* = v^*(y),\ \alpha^* = \alpha^*(y) \tag{19}$$

The governing (17) reduces to

$$\begin{aligned}\frac{1}{E^*(y)}\nabla^2\nabla^2\chi + \frac{\partial^2}{\partial y^2}\left[\frac{1}{E^*(y)}\right]\nabla^2\chi \\ + 2\frac{\partial}{\partial y}\left[\frac{1}{E^*(y)}\right]\frac{\partial}{\partial y}(\nabla^2\chi) \\ - \frac{\partial^2}{\partial y^2}\left[\frac{1+v^*(y)}{E^*(y)}\right]\frac{\partial^2\chi}{\partial x^2} \\ + \nabla^2[\alpha^*(y)T] = 0\end{aligned} \tag{20}$$

It is necessary to assume material properties as function of the position to solve (20).

Noda and Jin [1–3] gave solutions of (20) when material properties are expressed by exponential functions of the position.

[Case 1] Young's modulus is expressed by an exponential function of the position.

When Young's modulus is expressed by an exponential function of the position, Poisson ratio is constant and the linear thermal expansion is arbitrary function of the position

$$\begin{aligned}&E^* = E_0^*\exp(\delta y),\ v^* = v_0^*(1+\varepsilon y)\exp(\delta y),\\ &\alpha^* = \alpha^*(y)\end{aligned} \tag{21}$$

The governing equation (20) reduces to

$$\begin{aligned}\nabla^2\nabla^2\chi + \delta^2\nabla^2\chi - 2\delta\frac{\partial}{\partial y}(\nabla^2\chi) - (1+v_0^*)\delta^2\frac{\partial^2\chi}{\partial x^2} \\ = -E_0^*\exp(\delta y)\nabla^2[\alpha^*(y)T]\end{aligned} \tag{22}$$

The general solution of (22) can be expressed by

$$\chi = \chi_c + \chi_p \tag{23}$$

where χ_c and χ_p are complementary solution and particular solution, respectively,

$$\begin{aligned}\nabla^2\nabla^2\chi_c + \delta^2\nabla^2\chi_c - 2\delta\frac{\partial}{\partial y}(\nabla^2\chi_c) \\ - (1+v_0^*)\delta^2\frac{\partial^2\chi_c}{\partial x^2} = 0\end{aligned} \tag{24}$$

$$\begin{aligned}\nabla^2\nabla^2\chi_p + \delta^2\nabla^2\chi_p - 2\delta\frac{\partial}{\partial y}(\nabla^2\chi_p) \\ - (1+v_0^*)\delta^2\frac{\partial^2\chi_p}{\partial x^2} = -E_0^*\exp(\delta y)\nabla^2[\alpha^*(y)T]\end{aligned} \tag{25}$$

By use of the separation of variables, the general solution of (24) can be expressed by

$$\chi_c = \begin{pmatrix}\cos(sx)\\ \sin(sx)\end{pmatrix}\exp(p_i y)\ (i = 1,2,3,4) \tag{26}$$

where p_i $(i = 1,2,3,4)$ are eigenvalues of an eigenfunction:

$$\begin{aligned}p^4 - 2\delta p^3 + (\delta^2 - 2s^2)p^2 + 2s^2\delta p \\ + s^2(s^2 + v_0^*\delta^2) = 0\end{aligned} \tag{27}$$

[Case 2] Young's modulus and Poisson ratio are expressed by exponential functions of the position.

When Young's modulus and Poisson ratio can be expressed by exponential functions of the position and the linear thermal expansion is arbitrary function of the position,

$$\begin{aligned}&E^* = E_0^*\exp(\delta y),\ v^* = v_0^*(1+\varepsilon y)\exp(\delta y),\\ &\alpha^* = \alpha^*(y)\end{aligned} \tag{28}$$

The governing equation (20) reduces to

$$\begin{aligned}\nabla^2\nabla^2\chi - 2\delta\frac{\partial}{\partial y}(\nabla^2\chi) + \delta^2\frac{\partial^2\chi}{\partial y^2} \\ = -E_0^*\exp(\delta y)\nabla^2[\alpha^*(y)T]\end{aligned} \tag{29}$$

The complementary solution χ_c of (29) is

$$\chi_c = \begin{pmatrix} \cos(sx) \\ \sin(sx) \end{pmatrix} \exp(p_i y) \quad (i = 1, 2, 3, 4) \tag{30}$$

where p_i (i = 1,2,3,4) are eigen values of an eigen function:

$$\begin{aligned} &p^4 - 2\delta p^3 + (\delta^2 - 2s^2)p^2 + 2s^2\delta p + s^4 \\ &\quad = (p^2 - \delta p - s^2)^2 = 0 \end{aligned} \tag{31}$$

Equation (31) has double roots, and the eigenvalues are

$$p_1 = \frac{\delta + \sqrt{\delta^2 + 4s^2}}{2}, \; p_2 = \frac{\delta - \sqrt{\delta^2 + 4s^2}}{2} \tag{32}$$

Then, the complementary solution χ_c of (29) can be expressed by

$$\chi_c = \begin{pmatrix} \cos(sx) \\ \sin(sx) \end{pmatrix} \begin{pmatrix} \exp(p_i y) \\ y \exp(p_i y) \end{pmatrix} \quad (i = 1, 2) \tag{33}$$

Thermal Stresses in an Infinite Plate by Stress Function Method

Let us consider steady thermal stresses in an infinite plate with thickness a, when material properties are expressed by

$$\begin{aligned} &k = k_0 \exp(\varepsilon y), \; E^* = E_0^* \exp(\delta y) \\ &\nu^* = \nu_0^*(1 + \omega y) \exp(\delta y), \; \alpha^* = \alpha_0^* \exp(\gamma y) \end{aligned} \tag{34}$$

where k denotes thermal conductivity.

The steady heat conduction equation is

$$\frac{\partial}{\partial x}\left(k\frac{\partial T}{\partial x}\right) + \frac{\partial}{\partial y}\left(k\frac{\partial T}{\partial y}\right) = 0 \tag{35}$$

When material properties are given by (34), the heat conduction equation (35) reduces to

$$\nabla^2 T + \varepsilon \frac{\partial T}{\partial y} = 0 \tag{36}$$

The boundary conditions are

$$\begin{aligned} &T = 0 \;\; \text{on} \;\; y = 0 \\ &T = T_a g(x) \;\; \text{on} \;\; y = a \end{aligned} \tag{37}$$

The second boundary condition in (37) is assumed to be $g(-x) = g(x)$ for the sake of brevity. Introducing Fourier cosine integral, $g(x)$ can be expressed by

$$\begin{aligned} g(x) &= \int_0^\infty C(s) \cos(sx) \mathrm{d}s \\ C(s) &= \frac{2}{\pi} \int_0^\infty g(x) \cos(sx) \mathrm{d}x \end{aligned} \tag{38}$$

The general solution of (36) can be expressed by

$$\begin{aligned} T(x, y) = \int_0^\infty &[A(s) \exp(q_1 y) + B(s) \exp(q_2 y)]. \\ &\times \cos(sx) \mathrm{d}s \end{aligned} \tag{39}$$

where $A(s)$ and $B(s)$ are unknown constants, and

$$q_1 = \frac{-\varepsilon + \sqrt{\varepsilon^2 + 4s^2}}{2}, \; q_2 = -\frac{\varepsilon + \sqrt{\varepsilon^2 + 4s^2}}{2} \tag{40}$$

The unknown constants $A(s)$ and $B(s)$ can be determined by (37) as

$$A(s) = -B(s) = T_a \frac{C(s)}{\exp(q_1 a) - \exp(q_2 a)} \tag{41}$$

Then, the temperature is determined as

$$T(x,y) = T_a \int_0^\infty \frac{C(s)}{\exp(q_1 a) - \exp(q_2 a)} \times [\exp(q_1 y) - \exp(q_2 y)] \cos(sx) \mathrm{d}s \tag{42}$$

Next, we consider thermal stresses in the plate. Taking into consideration of (34), the governing (29) reduces to

$$\nabla^2\nabla^2\chi - 2\delta\frac{\partial}{\partial y}(\nabla^2\chi) + \delta^2\frac{\partial^2\chi}{\partial y^2} = -E_0^*\alpha_0^*\exp[(\delta+\gamma)y]\left(\nabla^2 T + 2\gamma\frac{\partial T}{\partial y} + \gamma^2 T\right) \tag{43}$$

The boundary conditions are

$$\begin{aligned} \sigma_{yy} = \sigma_{xy} = 0 \quad \text{on} \quad y = 0 \\ \sigma_{yy} = \sigma_{xy} = 0 \quad \text{on} \quad y = a \end{aligned} \tag{44}$$

The general solution of (43) can be expressed by

$$\begin{aligned} \chi = \int_0^\infty \Big[& (D_1 + yE_1)\exp(p_1 y) \\ & + (D_2 + yE_2)\exp(p_2 y)\Big]\cos(sx)\,\mathrm{d}s \\ & + E_0^*\alpha_0^* T_a \int_0^\infty \{F_1 \exp[(\delta+\gamma+q_1)y] \\ & + F_2 \exp[(\delta+\gamma+q_2)y]\}\cos(sx)\mathrm{d}s \end{aligned} \tag{45}$$

where D_1, D_2, E_1, and E_2 are unknown constants, p_1 and p_2 are given by (32), and F_1 and F_2 are

$$\begin{aligned} F_1 &= -\frac{C(s)}{\exp(q_1 a) - \exp(q_2 a)} \times \frac{q_1^2 - s^2 + 2\gamma q_1 + \gamma^2}{\left[(\delta+\gamma+q_1)^2 - s^2 - \delta(\delta+\gamma+q_1)\right]^2} \\ F_2 &= \frac{C(s)}{\exp(q_1 a) - \exp(q_2 a)} \times \frac{q_2^2 - s^2 + 2\gamma q_2 + \gamma^2}{\left[(\delta+\gamma+q_2)^2 - s^2 - \delta(\delta+\gamma+q_2)\right]^2} \end{aligned} \tag{46}$$

The thermal stresses are obtained as

$$\begin{aligned} \sigma_{xx} = \frac{\partial^2\chi}{\partial y^2} = & \int_0^\infty \Big\{\left[D_1 p_1^2 + E_1(2p_1 + p_1^2 y)\right]\exp(p_1 y) \\ & + \left[D_2 p_2^2 + E_2(2p_2 + p_2^2 y)\right]\exp(p_2 y)\Big\}\cos(sx)\mathrm{d}s \\ & + E_0^*\alpha_0^* T_a \int_0^\infty \Big\{F_1(\delta+\gamma+q_1)^2 \exp[(\delta+\gamma+q_1)y] \\ & + F_2(\delta+\gamma+q_2)^2 \exp[(\delta+\gamma+q_2)y]\Big\}\cos(sx)\mathrm{d}s \\ \sigma_{yy} = \frac{\partial^2\chi}{\partial x^2} = & -\int_0^\infty \Big[(D_1 + yE_1)\exp(p_1 y) \\ & + (D_2 + yE_2)\exp(p_2 y)\Big]s^2\cos(sx)\,\mathrm{d}s \\ & - E_0^*\alpha_0^* T_a \int_0^\infty \Big\{F_1 \exp[(\delta+\gamma+q_1)y] \\ & + F_2 \exp[(\delta+\gamma+q_2)y]\Big\}s^2\cos(sx)\,\mathrm{d}s \\ \sigma_{xy} = -\frac{\partial^2\chi}{\partial x\partial y} = & \int_0^\infty \Big\{\left[D_1 p_1 + E_1(1+p_1 y)\right]\exp(p_1 y) \\ & + \left[D_2 p_2 + E_2(1+p_2 y)\right]\exp(p_2 y)\Big\}s\sin(sx)\mathrm{d}s \\ & + E_0^*\alpha_0^* T_a \int_0^\infty \Big\{F_1(\delta+\gamma+q_1)\exp[(\delta+\gamma+q_1)y] \\ & + F_2(\delta+\gamma+q_2)\exp[(\delta+\gamma+q_2)y]\Big\}s\sin(sx)\mathrm{d}s \end{aligned} \tag{47}$$

Substituting (47) into the boundary conditions (44) gives

$$\begin{aligned} & D_1 + D_2 = -E_0^*\alpha_0^* T_a(F_1 + F_2) \\ & p_1 D_1 + E_1 + p_2 D_2 + E_2 \\ & \quad = -E_0^*\alpha_0^* T_a\Big[F_1(\delta+\gamma+q_1) \\ & \qquad + F_2(\delta+\gamma+q_2)\Big] \\ & \exp(p_1 a)D_1 + a\exp(p_1 a)E_1 \\ & \qquad + \exp(p_2 a)D_2 + a\exp(p_2 a)E_2 \\ & \quad = -E_0^*\alpha_0^* T_a\{F_1 \exp[(\delta+\gamma+q_1)a] \\ & \qquad + F_2 \exp[(\delta+\gamma+q_2)a]\} \\ & p_1\exp(p_1 a)D_1 + (1+p_1 a)\exp(p_1 a)E_1 \\ & \qquad + p_2\exp(p_2 a)D_2 + (1+p_2 a) \\ & \qquad \exp(p_2 a)E_2 \\ & \quad = -E_0^*\alpha_0^* T_a\Big\{F_1(\delta+\gamma+q_1) \\ & \qquad \exp[(\delta+\gamma+q_1)a]. \\ & \qquad + F_2(\delta+\gamma+q_2) \\ & \qquad \exp[(\delta+\gamma+q_2)a]\Big\} \end{aligned} \tag{48}$$

The unknown constants can be determined by solving algebraic equations (48).

Potential Function Method

Tanigawa et al. [4–7] proposed new potential function method. When body forces are absent, inertia terms are negligible, and material properties are defined as functions of one variable, (14) reduce to

$$\begin{aligned}
&\mu\nabla^2 u_x + (\lambda^* + \mu)\frac{\partial}{\partial x}\left(\frac{\partial u_x}{\partial x} + \frac{\partial u_y}{\partial y}\right) \\
&\quad + \frac{\partial \mu}{\partial y}\left(\frac{\partial u_x}{\partial y} + \frac{\partial u_y}{\partial x}\right) - \beta^*\frac{\partial T}{\partial x} = 0 \\
&\mu\nabla^2 u_y + (\lambda^* + \mu)\frac{\partial}{\partial y}\left(\frac{\partial u_x}{\partial x} + \frac{\partial u_y}{\partial y}\right) \\
&\quad + \frac{\partial \lambda^*}{\partial y}\left(\frac{\partial u_x}{\partial x} + \frac{\partial u_y}{\partial y}\right) + 2\frac{\partial \mu}{\partial y}\frac{\partial u_y}{\partial y} \\
&\quad - \frac{\partial}{\partial y}(\beta^* T) = 0
\end{aligned} \tag{49}$$

We consider that shear modulus of elasticity G, Láme constant λ^*, thermoelastic constant β^*, Poisson ratio ν, and coefficient of linear thermal expansion α^* are given by

$$\begin{aligned}
&\mu(y) \equiv G(y) = G_0\left(1 + \frac{y}{a}\right)^m = \mu_0\left(1 + \frac{y}{a}\right)^m \\
&\lambda^* = \lambda_0^*\left(1 + \frac{y}{a}\right)^m, \quad \beta^* = \beta_0^* f(y)\left(1 + \frac{y}{a}\right)^m \\
&\nu = \text{const.}, \quad \alpha^* = \alpha_0^* f(y)
\end{aligned} \tag{50}$$

where a is a reference value of length, m is an arbitrary parameter representing nonhomogeneity of material, and subscript 0 means a reference value of material properties at $y = 0$. The constants λ_0^*, β_0^*, and α_0^* are defined as

$$\begin{aligned}
&\lambda_0^* = \frac{2\nu G_0}{1 - 2\nu}, \quad \beta_0^* = \frac{2(1+\nu)\alpha_0 G_0}{1 - 2\nu} \\
&\alpha_0^* = (1 + \nu)\alpha_0
\end{aligned} \tag{51}$$

for the plane strain problem,

$$\lambda_0^* = \frac{2\nu G_0}{1 - \nu}, \quad \beta_0^* = \frac{2(1+\nu)\alpha_0 G_0}{1 - \nu}, \quad \alpha_0^* = \alpha_0 \tag{52}$$

for the plane stress problem.

The dimensionless quantities are introduced by using the reference length a as follows:

$$\bar{x} = \frac{x}{a}, \quad \bar{y} = 1 + \frac{y}{a}, \quad \bar{u}_x = \frac{u_x}{a}, \quad \bar{u}_y = \frac{u_y}{a} \tag{53}$$

Making use of the dimensionless quantities (53), (49) reduce to

$$\begin{aligned}
&\mu_0\bar{\nabla}^2\bar{u}_x + (\lambda_0^* + \mu_0)\frac{\partial}{\partial \bar{x}}\left(\frac{\partial \bar{u}_x}{\partial \bar{x}} + \frac{\partial \bar{u}_y}{\partial \bar{y}}\right) \\
&\quad + \mu_0\frac{m}{\bar{y}}\left(\frac{\partial \bar{u}_x}{\partial \bar{y}} + \frac{\partial \bar{u}_y}{\partial \bar{x}}\right) - \beta_0^* f(\bar{y})\frac{\partial T}{\partial \bar{x}} = 0 \\
&\mu_0\bar{\nabla}^2\bar{u}_y + (\lambda_0^* + \mu_0)\frac{\partial}{\partial \bar{y}}\left(\frac{\partial \bar{u}_x}{\partial \bar{x}} + \frac{\partial \bar{u}_y}{\partial \bar{y}}\right) \\
&\quad + \lambda_0^*\frac{m}{\bar{y}}\left(\frac{\partial \bar{u}_x}{\partial \bar{x}} + \frac{\partial \bar{u}_y}{\partial \bar{y}}\right) + 2\mu_0\frac{m}{\bar{y}}\frac{\partial \bar{u}_y}{\partial \bar{y}} \\
&\quad - \bar{y}^{-m}\frac{\partial}{\partial \bar{y}}\left[\beta_0^* f(\bar{y})\bar{y}^m T\right] = 0
\end{aligned} \tag{54}$$

We introduce two new potential functions ϕ and ψ that are related to the components of displacements $\bar{u}_x$ and $\bar{u}_y$ as follows:

$$\begin{aligned}
\bar{u}_x &= \frac{\partial \phi}{\partial \bar{x}} + \bar{y}\frac{\partial \psi}{\partial \bar{x}} \\
\bar{u}_y &= \frac{\partial \phi}{\partial \bar{y}} + \bar{y}\frac{\partial \psi}{\partial \bar{y}} - \psi
\end{aligned} \tag{55}$$

Substituting (54) into (55), the fundamental equations for ϕ and ψ are obtained:

$$\begin{aligned}
&\bar{\nabla}^2\phi + \frac{m}{\bar{y}}\frac{\partial \phi}{\partial \bar{y}} = \alpha_0^*(m+3)f(\bar{y})T \\
&\bar{\nabla}^2\psi + \frac{m}{\bar{y}}\frac{\partial \psi}{\partial \bar{y}} = \frac{m}{m+1}\frac{1}{\bar{y}^2}\frac{\partial \phi}{\partial \bar{y}} \\
&\qquad - \alpha_0^*\frac{m(m+3)}{m+1}\frac{1}{\bar{y}}f(\bar{y})T
\end{aligned} \tag{56}$$

where

$$\nu^* = \frac{1}{1+m} \tag{57}$$

The parameter m is bounded for a range $m > 1$ for the plane stress problem because of the physical condition for Poisson ratio ν of $0 \le \nu \le 0.5$. And the parameter m is bounded within a range $m > 0$ for the plane strain problem. Because $\nu^* = \nu/(1-\nu)$ holds for the plane strain problem, the relation $\nu = 1/(2+m)$ is assigned.

The components of strain and stress are expressed by the two kinds of new potential functions ϕ and ψ as follows:

$$\begin{aligned}
\varepsilon_{xx} &= \frac{\partial u_x}{\partial x} = \frac{\partial \bar{u}_x}{\partial \bar{x}} = \frac{\partial^2 \phi}{\partial \bar{x}^2} + \bar{y}\frac{\partial^2 \psi}{\partial \bar{x}^2} \\
\varepsilon_{yy} &= \frac{\partial u_y}{\partial y} = \frac{\partial \bar{u}_y}{\partial \bar{y}} = \frac{\partial^2 \phi}{\partial \bar{y}^2} + \bar{y}\frac{\partial^2 \psi}{\partial \bar{y}^2} \\
\varepsilon_{xy} &= \frac{1}{2}\left(\frac{\partial u_x}{\partial y} + \frac{\partial u_y}{\partial x}\right) = \frac{1}{2}\left(\frac{\partial \bar{u}_x}{\partial \bar{y}} + \frac{\partial \bar{u}_y}{\partial \bar{x}}\right) \\
&= \frac{\partial^2 \phi}{\partial \bar{x}\partial \bar{y}} + \bar{y}\frac{\partial^2 \psi}{\partial \bar{x}\partial \bar{y}}
\end{aligned} \tag{58}$$

$$\begin{aligned}
\sigma_{xx} &= 2G_0\bar{y}^m\left\{\frac{\partial^2 \phi}{\partial \bar{x}^2} - \frac{m}{m+1}\frac{1}{\bar{y}}\frac{\partial \phi}{\partial \bar{y}} + \bar{y}\frac{\partial^2 \psi}{\partial \bar{x}^2} - \frac{\partial \psi}{\partial \bar{y}}\right. \\
&\quad \left. - \left[1 + \frac{m-1}{m(m+1)}\right]\alpha_0^* f(\bar{y})T\right\} \\
\sigma_{yy} &= 2G_0\bar{y}^m\left\{\frac{\partial^2 \phi}{\partial \bar{y}^2} - \frac{m}{m+1}\frac{1}{\bar{y}}\frac{\partial \phi}{\partial \bar{y}} + \bar{y}\frac{\partial^2 \psi}{\partial \bar{y}^2} - \frac{\partial \psi}{\partial \bar{y}}\right. \\
&\quad \left. - \left[1 + \frac{m-1}{m(m+1)}\right]\alpha_0^* f(\bar{y})T\right\} \\
\sigma_{xy} &= 2G_0\bar{y}^m\left(\frac{\partial^2 \phi}{\partial \bar{x}\partial \bar{y}} + \bar{y}\frac{\partial^2 \psi}{\partial \bar{x}\partial \bar{y}}\right)
\end{aligned} \tag{59}$$

Thermal Stresses in an Infinite Plate by Potential Function Method

Let us consider steady thermal stresses in an infinite plate with thickness a, when material properties are expressed by

$$\begin{aligned}
&k(y) = k_0\left(1+\frac{y}{a}\right)^l,\ \mu(y) = G(y) = G_0\left(1+\frac{y}{a}\right)^m, \\
&\nu = \text{const.},\ \alpha^* = \alpha_0^*\left(1+\frac{y}{a}\right)^n
\end{aligned} \tag{60}$$

where k denotes thermal conductivity.

The steady heat conduction equation (29) reduces to

$$\frac{\partial^2 T}{\partial x^2} + \frac{l}{a(1+y/a)}\frac{\partial T}{\partial y} + \frac{\partial^2 T}{\partial y^2} = 0 \tag{61}$$

Equation (61) has an alternative form by use of (53)

$$\frac{\partial^2 T}{\partial \bar{x}^2} + \frac{l}{\bar{y}}\frac{\partial T}{\partial \bar{y}} + \frac{\partial^2 T}{\partial \bar{y}^2} = 0 \tag{62}$$

The general solution of (62) can be expressed as

$$\begin{aligned}
T(\bar{x},\bar{y}) &= \begin{pmatrix}1\\ \bar{x}\end{pmatrix}\begin{pmatrix}1\\ \bar{y}^{1-l}\end{pmatrix},\ \begin{pmatrix}\sin(s\bar{x})\\ \cos(s\bar{x})\end{pmatrix}\begin{pmatrix}\bar{y}^q I_q(s\bar{y})\\ \bar{y}^q K_q(s\bar{y})\end{pmatrix} \\
q &= \frac{1-l}{2}
\end{aligned} \tag{63}$$

where $I_q(s\bar{y})$ and $K_q(s\bar{y})$ denote modified Bessel functions of the first and second kind of order q, respectively.

The boundary conditions are

$$\begin{aligned}
&T = 0 \ \text{ on } \ y = 0 \\
&T = T_a g(x) \ \text{ on } \ y = a
\end{aligned} \tag{64}$$

Alternative form has

$$\begin{aligned}
&T = 0 \ \text{ on } \ \bar{y} = 1 \\
&T = T_a g(\bar{x}) \ \text{ on } \ \bar{y} = 2
\end{aligned} \tag{65}$$

The second boundary condition in (65) is assumed to be $g(\bar{x}) = g(-\bar{x})$ for the sake of brevity. Introducing Fourier cosine integral, $g(\bar{x})$ can be expressed by

$$\begin{aligned}
g(\bar{x}) &= \int_0^\infty C(s)\cos(s\bar{x})\mathrm{d}s \\
C(s) &= \frac{2}{\pi}\int_0^\infty g(\bar{x})\cos(s\bar{x})\mathrm{d}\bar{x}
\end{aligned} \tag{66}$$

The general solution of (62) can be expressed by

$$T(\bar{x},\bar{y}) = \int_0^\infty \left[A(s)\bar{y}^q I_q(s\bar{y}) + B(s)\bar{y}^q K_q(s\bar{y})\right] \times \cos(s\bar{x})\,\mathrm{d}s \tag{67}$$

where $A(s)$ and $B(s)$ are unknown constants.

The unknown constants can be determined by (65) as

$$A(s) = T_\mathrm{a}\frac{K_q(s)C(s)}{2^q\left[I_q(2s)K_q(s) - I_q(s)K_q(2s)\right]}$$
$$B(s) = -T_\mathrm{a}\frac{I_q(s)C(s)}{2^q\left[I_q(2s)K_q(s) - I_q(s)K_q(2s)\right]} \tag{68}$$

Then, the temperature is determined.

$$T(\bar{x},\bar{y}) = T_\mathrm{a}\int_0^\infty \frac{K_q(s)\bar{y}^q I_q(s\bar{y}) - I_q(s)\bar{y}^q K_q(s\bar{y})}{2^q\left[I_q(2s)K_q(s) - I_q(s)K_q(2s)\right]} \times C(s)\cos(s\bar{x})\mathrm{d}s \tag{69}$$

We consider thermal stresses in an infinite plate. The fundamental equations (56) for two potential functions reduce to taking into consideration of (60):

$$\bar{\nabla}^2\phi + \frac{m}{\bar{y}}\frac{\partial\phi}{\partial\bar{y}} = \alpha_0^*(m+3)\bar{y}^n T$$
$$\bar{\nabla}^2\psi + \frac{m}{\bar{y}}\frac{\partial\psi}{\partial\bar{y}} = \frac{m}{m+1}\frac{1}{\bar{y}^2}\frac{\partial\phi}{\partial\bar{y}} - \alpha_0^*\frac{m(m+3)}{m+1}\bar{y}^{n-1}T \tag{70}$$

The displacement and thermal stresses are

$$\bar{u}_x = \frac{\partial\phi}{\partial\bar{x}} + \bar{y}\frac{\partial\psi}{\partial\bar{x}},\quad \bar{u}_y = \frac{\partial\phi}{\partial\bar{y}} + \bar{y}\frac{\partial\psi}{\partial\bar{y}} - \psi \tag{71}$$

$$\sigma_{xx} = 2G_0\bar{y}^m\left\{\frac{\partial^2\phi}{\partial\bar{x}^2} - \frac{m}{m+1}\frac{1}{\bar{y}}\frac{\partial\phi}{\partial\bar{y}} + \bar{y}\frac{\partial^2\psi}{\partial\bar{x}^2} - \frac{\partial\psi}{\partial\bar{y}} - \left[1 + \frac{m-1}{m(m+1)}\right]\alpha_0^*\bar{y}^n T\right\}$$
$$\sigma_{yy} = 2G_0\bar{y}^m\left\{\frac{\partial^2\phi}{\partial\bar{y}^2} - \frac{m}{m+1}\frac{1}{\bar{y}}\frac{\partial\phi}{\partial\bar{y}} + \bar{y}\frac{\partial^2\psi}{\partial\bar{y}^2} - \frac{\partial\psi}{\partial\bar{y}} - \left[1 + \frac{m-1}{m(m+1)}\right]\alpha_0^*\bar{y}^n T\right\}$$
$$\sigma_{xy} = 2G_0\bar{y}^m\left(\frac{\partial^2\phi}{\partial\bar{x}\partial\bar{y}} + \bar{y}\frac{\partial^2\psi}{\partial\bar{x}\partial\bar{y}}\right) \tag{72}$$

The boundary conditions are

$$\sigma_{yy} = \sigma_{xy} = 0 \ \text{ on } \ y = 0$$
$$\sigma_{yy} = \sigma_{xy} = 0 \ \text{ on } \ y = a \tag{73}$$

Alternative form has

$$\sigma_{yy} = \sigma_{xy} = 0 \ \text{ on } \ \bar{y} = 1$$
$$\sigma_{yy} = \sigma_{xy} = 0 \ \text{ on } \ \bar{y} = 2 \tag{74}$$

The general solutions of (70) can be expressed by

$$\phi = \phi_\mathrm{c} + \phi_\mathrm{p},\ \psi = \psi_\mathrm{c} + \psi_\mathrm{p} \tag{75}$$

where ϕ_c, ψ_c and ϕ_p, ψ_p are complementary solutions and particular solutions, respectively.

$$\bar{\nabla}^2\phi_\mathrm{c} + \frac{m}{\bar{y}}\frac{\partial\phi_\mathrm{c}}{\partial\bar{y}} = 0,\ \bar{\nabla}^2\psi_\mathrm{c} + \frac{m}{\bar{y}}\frac{\partial\psi_\mathrm{c}}{\partial\bar{y}} = 0 \tag{76}$$

$$\bar{\nabla}^2\phi_\mathrm{p} + \frac{m}{\bar{y}}\frac{\partial\phi_\mathrm{p}}{\partial\bar{y}} = \alpha_0^*(m+3)\bar{y}^n T$$
$$\bar{\nabla}^2\psi_\mathrm{p} + \frac{m}{\bar{y}}\frac{\partial\psi_\mathrm{p}}{\partial\bar{y}} = \frac{m}{m+1}\frac{1}{\bar{y}^2}\frac{\partial(\phi_\mathrm{c}+\phi_\mathrm{p})}{\partial\bar{y}} - \alpha_0^*\frac{m(m+3)}{m+1}\bar{y}^{n-1}T \tag{77}$$

The general solution of (76) can be expressed as

$$\phi_\mathrm{c}(\bar{x},\bar{y}),$$
$$\psi_\mathrm{c}(\bar{x},\bar{y}) = \begin{pmatrix}1\\ \bar{x}\end{pmatrix}\begin{pmatrix}1\\ \bar{y}^{1-m}\end{pmatrix},\ \begin{pmatrix}\sin(s\bar{x})\\ \cos(s\bar{x})\end{pmatrix}\begin{pmatrix}\bar{y}^p I_p(s\bar{y})\\ \bar{y}^p K_p(s\bar{y})\end{pmatrix}$$
$$p = \frac{1-m}{2} \tag{78}$$

According to the symmetry of the problem, the complementary solutions ϕ_c and ψ_c of (76) are given by

$$\phi_c = \int_0^\infty \left[D_1 \bar{y}^p I_p(s\bar{y}) + D_2 \bar{y}^p K_p(s\bar{y})\right] \cos(s\bar{x}) \mathrm{d}s$$
$$\psi_c = \int_0^\infty \left[E_1 \bar{y}^p I_p(s\bar{y}) + E_2 \bar{y}^p K_p(s\bar{y})\right] \cos(s\bar{x}) \mathrm{d}s \tag{79}$$

where D_1, D_2, E_1 and E_2 are unknown constants.

When

$$l = 2n + m + 4, \ l \neq m \tag{80}$$

the particular solutions ϕ_p, ψ_p can be expressed by

$$\phi_p = \int_0^\infty \left[D_1^p \bar{y}^p I_q(s\bar{y}) + D_2^p \bar{y}^p K_q(s\bar{y})\right] \cos(s\bar{x}) \mathrm{d}s$$
$$\psi_p = \int_0^\infty \Big[E_1^{p1} \bar{y}^p I_{p-1}(s\bar{y}) + F_1^{p2} \bar{y}^p I_{q-1}(s\bar{y}) + F_1^{p3} \bar{y}^p I_{q+1}(s\bar{y}) + E_2^{p1} \bar{y}^p K_{p-1}(s\bar{y}) + F_2^{p2} \bar{y}^p K_{q-1}(s\bar{y}) + F_2^{p3} \bar{y}^p K_{q+1}(s\bar{y})\Big] \cos(s\bar{x}) \mathrm{d}s \tag{81}$$

where

$$F_1^{p2} = F_1^{p2A} + F_1^{p3A}, \ F_1^{p3} = F_1^{p2B} + F_1^{p3B},$$
$$F_2^{p2} = F_2^{p2A} + F_2^{p3A}, \ F_2^{p3} = F_2^{p2B} + F_2^{p3B},$$
$$D_1^p = \frac{4\alpha_0^*(m+3)}{(l-m)(l+m-2)} A(s),$$
$$D_2^p = -\frac{4\alpha_0^*(m+3)}{(l-m)(l+m-2)} B(s),$$
$$E_1^{p1} = \frac{s}{m+1} D_1, \ E_2^{p1} = -\frac{s}{m+1} D_2,$$
$$F_1^{p2A} = -\frac{8\alpha_0^* sm(m+3)A(s)}{(1-l)(m+1)(l+m)(l-m)(l-m+2)},$$
$$F_1^{p2B} = -\frac{8\alpha_0^* sm(m+3)A(s)}{(1-l)(m+1)(l+m-4)(l-m-2)(l+m-2)},$$
$$F_2^{p2A} = \frac{8\alpha_0^* sm(m+3)B(s)}{(1-l)(m+1)(l+m)(l-m)(l-m+2)},$$
$$F_2^{p2B} = \frac{8\alpha_0^* sm(m+3)B(s)}{(1-l)(m+1)(l+m-4)(l-m-2)(l+m-2)},$$
$$F_1^{p3A} = -\frac{4\alpha_0^* sm(m+3)A(s)}{(1-l)(m+1)(l-m+2)(l+m)},$$
$$F_1^{p3B} = -\frac{4\alpha_0^* sm(m+3)A(s)}{(1-l)(m+1)(l-m-2)(l+m-4)},$$
$$F_2^{p3A} = -\frac{4\alpha_0^* sm(m+3)B(s)}{(1-l)(m+1)(l-m+2)(l+m)},$$
$$F_2^{p3B} = -\frac{4\alpha_0^* sm(m+3)B(s)}{(1-l)(m+1)(l-m-2)(l+m-4)} \tag{82}$$

Then, general solutions ϕ and ψ are

$$\phi = \int_0^\infty \left[D_1 \bar{y}^p I_p(s\bar{y}) + D_2 \bar{y}^p K_p(s\bar{y}) + D_1^p \bar{y}^p I_q(s\bar{y}) + D_2^p \bar{y}^p K_q(s\bar{y})\right] \cos(s\bar{x}) \mathrm{d}s$$
$$\psi = \int_0^\infty \Big[E_1 \bar{y}^p I_p(s\bar{y}) + E_2 \bar{y}^p K_p(s\bar{y}) + D_1 \frac{s}{m+1} \bar{y}^p I_{p-1}(s\bar{y}) - D_2 \frac{s}{m+1} \bar{y}^p K_{p-1}(s\bar{y}) + F_1^{p2} \bar{y}^p I_{q-1}(s\bar{y}) + F_2^{p2} \bar{y}^p K_{p-1}(s\bar{y}) + F_2^{p3} \bar{y}^p I_{q+1}(s\bar{y}) + F_2^{p3} \bar{y}^p K_{q+1}(s\bar{y})\Big] \cos(s\bar{x}) \mathrm{d}s \tag{83}$$

Substituting (83) and (67) into (71) and (72) gives displacements and thermal stresses as follows:

$$\bar{u}_x = -\bar{y}^p \int_0^\infty \Big\{ D_1 \frac{1}{m+1} \left[(m+1) I_p(s\bar{y}) + s\bar{y} I_{p-1}(s\bar{y})\right] + D_2 \frac{1}{m+1} \left[(m+1) K_p(s\bar{y}) - s\bar{y} K_{p-1}(s\bar{y})\right] + E_1 \bar{y} I_p(s\bar{y}) + E_2 \bar{y} K_p(s\bar{y}) + D_1^p I_q(s\bar{y}) + D_2^p K_q(s\bar{y}) + F_1^{p2} \bar{y} I_{q-1}(s\bar{y}) + F_2^{p2} \bar{y} K_{q-1}(s\bar{y}) + F_1^{p3} \bar{y} I_{q+1}(s\bar{y}) + F_2^{p3} \bar{y} K_{q+1}(s\bar{y}) \Big\} s \sin(s\bar{x}) \mathrm{d}s \tag{84}$$

$$\bar{u}_y = \bar{y}^p \int_0^\infty \Big\{ D_1 \frac{s}{m+1} s\bar{y} I_p(s\bar{y}) + D_2 \frac{s}{m+1} s\bar{y} K_p(s\bar{y}) + E_1 \left[s\bar{y} I_{p-1}(s\bar{y}) - I_p(s\bar{y})\right] - E_2 \left[s\bar{y} K_{p-1}(s\bar{y}) + K_p(s\bar{y})\right] + D_1^p s \left[(p-q)(s\bar{y})^{-1} I_q(s\bar{y}) + I_{q-1}(s\bar{y})\right] + D_2^p s \left[(p-q)(s\bar{y})^{-1} K_q(s\bar{y}) - K_{q-1}(s\bar{y})\right] + F_1^{p2} \left[(p+q-2) I_{q-1}(s\bar{y}) + s\bar{y} I_q(s\bar{y})\right] + F_2^{p2} \left[(p+q-2) K_{q-1}(s\bar{y}) - s\bar{y} K_q(s\bar{y})\right] + F_1^{p3} \left[(p-q-2) I_{q+1}(s\bar{y}) + s\bar{y} I_q(s\bar{y})\right] + F_2^{p3} \left[(p-q-2) K_{q+1}(s\bar{y}) - s\bar{y} K_q(s\bar{y})\right] \Big\} \cos(s\bar{x}) \mathrm{d}s \tag{85}$$

$$\begin{aligned}\frac{\sigma_{xx}}{2G_0} = -\bar{y}^{1-p}\int_0^{\infty}\Bigg[\Bigg[&D_1\frac{s^2}{m+1}\left[(m+2)I_p(s\bar{y})+s\bar{y}I_{p-1}(s\bar{y})\right]\\&+D_2\frac{s^2}{m+1}\left[(m+2)K_p(s\bar{y})-s\bar{y}K_{p-1}(s\bar{y})\right]\\&+E_1 s\left[s\bar{y}I_p(s\bar{y})+I_{p-1}(s\bar{y})\right]+E_2 s\left[s\bar{y}K_p(s\bar{y})-K_{p-1}(s\bar{y})\right]\\&+D_1^{\mathrm{p}}s^2\left\{I_q(s\bar{y})+\frac{m}{m+1}\left[(p-q)(s\bar{y})^{-2}I_q(s\bar{y})+(s\bar{y})^{-1}I_{q-1}(s\bar{y})\right]\right\}\\&+D_2^{\mathrm{p}}s^2\left\{K_q(s\bar{y})+\frac{m}{m+1}\left[(p-q)(s\bar{y})^{-2}K_q(s\bar{y})-(s\bar{y})^{-1}K_{q-1}(s\bar{y})\right]\right\}\\&+F_1^{\mathrm{p}2}s\left\{s\bar{y}I_{q-1}(s\bar{y})+\left[(p+q-1)(s\bar{y})^{-1}I_{q-1}(s\bar{y})+I_q(s\bar{y})\right]\right\}\\&+F_2^{\mathrm{p}2}s\left\{s\bar{y}K_{q-1}(s\bar{y})+\left[(p+q-1)(s\bar{y})^{-1}K_{q-1}(s\bar{y})-K_q(s\bar{y})\right]\right\}\\&+F_1^{\mathrm{p}3}s\left\{s\bar{y}I_{q+1}(s\bar{y})+\left[(p-q-1)(s\bar{y})^{-1}I_{q+1}(s\bar{y})+I_q(s\bar{y})\right]\right\}\\&+F_2^{\mathrm{p}3}s\left\{s\bar{y}K_{q+1}(s\bar{y})+\left[(p-q-1)(s\bar{y})^{p-1}K_{q+1}(s\bar{y})-K_q(s\bar{y})\right]\right\}\\&+\alpha_0^*\left[1+\frac{m-1}{m(m+1)}\right]\times\left[A(s)\bar{y}^{q+n}I_q(s\bar{y})+B(s)\bar{y}^{q+n}K_q(s\bar{y})\right]\Bigg]\Bigg]\cos(s\bar{x})\mathrm{d}s\end{aligned} \tag{86}$$

$$\begin{aligned}\frac{\sigma_{yy}}{2G_0} = \bar{y}^{1-p}\int_0^{\infty}\Bigg[\Bigg[&D_1\frac{s^3}{m+1}\bar{y}I_{p-1}(s\bar{y})-D_2\frac{s^3}{m+1}\bar{y}K_{p-1}(s\bar{y})\\&+E_1 s\left[-(m+1)I_{p-1}(s\bar{y})+s\bar{y}I_p(s\bar{y})\right]+E_2 s\left[(m+1)K_{p-1}(s\bar{y})+s\bar{y}K_p(s\bar{y})\right]\\&+D_1^{\mathrm{p}}s^2\left\{\left[(p-q)\left(p-q-1-\frac{m}{m+1}\right)(s\bar{y})^{-2}+1\right]I_q(s\bar{y})-\frac{m(m+2)}{m+1}(s\bar{y})^{-1}I_{q-1}(s\bar{y})\right\}\\&+D_2^{\mathrm{p}}s^2\left\{\left[(p-q)\left(p-q-1-\frac{m}{m+1}\right)(s\bar{y})^{-2}+1\right]K_q(s\bar{y})+\frac{m(m+2)}{m+1}(s\bar{y})^{-1}K_{q-1}(s\bar{y})\right\}\\&+F_1^{\mathrm{p}2}s\left\{\left[(p+q-1)(p+q-3)(s\bar{y})^{-1}+s\bar{y}\right]I_{q-1}(s\bar{y})-(m+1)I_q(s\bar{y})\right\}\\&+F_2^{\mathrm{p}2}s\left\{\left[(p+q-1)(p+q-3)(s\bar{y})^{-1}+s\bar{y}\right]K_{q-1}(s\bar{y})+(m+1)K_q(s\bar{y})\right\}\\&+F_1^{\mathrm{p}3}s\left\{\left[(p-q-1)(p-q-3)(s\bar{y})^{-1}+s\bar{y}\right]I_{q+1}(s\bar{y})-(m+1)I_q(s\bar{y})\right\}\\&+F_2^{\mathrm{p}3}s\left\{\left[(p-q-1)(p-q-3)(s\bar{y})^{-1}+s\bar{y}\right]K_{q+1}(s\bar{y})+(m+1)K_q(s\bar{y})\right\}\\&-\alpha_0^*\left[1+\frac{m-1}{m(m+1)}\right]\times\left[A(s)\bar{y}^{q+n}I_q(s\bar{y})+B(s)\bar{y}^{q+n}K_q(s\bar{y})\right]\Bigg]\Bigg]\times\cos(s\bar{x})\mathrm{d}s\end{aligned} \tag{87}$$

$$\frac{\sigma_{xy}}{2G_0} = -\bar{y}^{1-p}\int_0^\infty s\Big\{D_1\frac{s}{m+1}\left[I_{p-1}(s\bar{y}) + s\bar{y}I_p(s\bar{y})\right] - D_2\frac{s}{m+1}\left[K_{p-1}(s\bar{y}) - s\bar{y}K_p(s\bar{y})\right] + E_1 s\bar{y}I_{p-1}(s\bar{y}) - E_2 s\bar{y}K_{p-1}(s\bar{y}) + D_1^{\mathrm{p}} s\Big[(p-q)(s\bar{y})^{-1}I_q(s\bar{y}) + I_{q-1}(s\bar{y})\Big] + D_2^{\mathrm{p}} s\Big[(p-q)(s\bar{y})^{-1}K_q(s\bar{y}) - K_{q-1}(s\bar{y})\Big] + F_1^{\mathrm{p2}}\left[(p+q-1)I_{q-1}(s\bar{y}) + s\bar{y}I_q(s\bar{y})\right] + F_2^{\mathrm{p2}}\left[(p+q-1)K_{q-1}(s\bar{y}) - s\bar{y}K_q(s\bar{y})\right] + F_1^{\mathrm{p3}}\left[(p-q-1)I_{q+1}(s\bar{y}) + s\bar{y}I_q(s\bar{y})\right] + F_2^{\mathrm{p3}}\left[(p-q-1)K_{q+1}(s\bar{y}) - s\bar{y}K_q(s\bar{y})\right]\Big\}\sin(s\bar{x})\,\mathrm{d}s \tag{88}$$

The unknown constants D_1, D_2, E_1, and E_2 can be determined by the boundary conditions (74).

References

1. Noda N, Jin Z (1993) Steady thermal stresses in an infinite non-homogeneous elastic solid containing a crack. J Therm Stress 16–2:181–197
2. Noda N, Jin Z (1993) Thermal stress intensity factors for a crack in a strip of functionally gradient material. Int J Sol Struct 30–8:1039–1056
3. Noda N, Jin Z (1994) Crack-tip singular fields in functionally gradient materials. J Appl Mech 61–3:738–740
4. Tanigawa Y, Jeon S-P, Sone D (1997) Formulation of axisymmetric thermoelastic problem for Kassir's nonhomogeneous medium and its analytical development of thermal stresses for semi-infinite body. Trans Jpn Soc Mech Eng, Part A 63–605: 94–101
5. Jeon S-P, Tanigawa Y, Sone D (1997) Analytical development of axisymmetrical thermoelastic field with Kassir's nonhomogeneous material properties and its adaptation to boundary value problems of slab under steady temperature field. J Therm Stress 20(3–4):325–343
6. Tanigawa Y, Morishita H, Ogaki S (1999) Derivation of systems of fundamental equations for a three-dimensional thermoelastic field with nonhomogeneous material properties and its application to a semi-infinite body. J Therm Stress 22–7:689–711
7. Tanigawa Y, Kawamura R, Ishida S (2002) Derivation of fundamental equations system of plane isothermal and thermoelastic problems for inhomogeneous solids and its applications to semi-infinite body and slab. Theor Appl Mech 51:267–279

Analytical Solution for Two-Dimensional Magneto-thermomechanical Response in FG Hollow Sphere

Mohsen Jabbari[1] and A. H. Mohazzab[2]
[1]Faculty of Engineering, Postgraduate School, South Tehran Branch, Islamic Azad University, Tehran, Iran
[2]Islamic Azad University, Tehran, Iran

Definition

Functionally graded materials (FGMs) are heterogeneous and advanced materials in which the elastic and thermal properties vary gradually and continuously from one surface to another. FGMs decrease the thermal stresses and hence are very useful in nuclear, aircraft, and space engineering applications. The application of this issue is seen in geophysics, seismology, plasma physics, magnetic storage elements, magnetic structural elements, and measurement techniques of magnetoelasticity. This entry presents the effect of the magnetic problem of a functionally graded (FG) hollow sphere subjected to mechanical and thermal loads. An analytical solution for stresses and perturbation of the magnetic field vector were determined using the direct method and the power series method. All of the material properties varied continuously across the thickness direction according to the power-law functions of radial directions. The aim of this work was to understand the effect of the magnetic field on a FG hollow sphere subjected to mechanical and thermal loads.

Overview

Abd-Alla et al. presented an investigation of stress, temperature, and magnetic field in an isotropic, homogeneous, viscoelastic medium with

a spherical cavity in a primary magnetic field, when the curved surface of the spherical cavity was subjected to periodic loading [1]. Chen and Lee worked on magneto-thermoelasticity by introducing two displacement and two stress functions [2]. The governing equations of the linear theory of magneto-electro-thermoelasticity with transverse isotropy were simplified. The material nonhomogeneity along the axis of symmetry was taken into account and an approximate laminate model was employed to facilitate the deriving of analytical solutions. Dai and Fu recently considered the magneto-thermoelastic problem of FG hollow structures subjected to mechanical loads. The material stiffness, the thermal expansion coefficient, and the magnetic permeability were assumed to obey simple power-law variations through the structures' wall thickness. The aim of their research was to understand the effect of composition on magneto-thermoelastic stresses and to design optimum FG hollow cylinders and hollow spheres [3]. Dai and Wang presented an analytical method to solve the problem of the dynamic stress-focusing and centered-effect of perturbation of the magnetic field vector in orthotropic cylinders under thermal and mechanical shock loads. Analytical expressions for the dynamic stresses and the perturbation of the magnetic field vector were obtained by means of finite Hankel transforms and Laplace transforms [4]. Recently, Poultangari et al. studied the nonaxisymmetric thermomechanical loads on functionally graded hollow spheres [5]. Tianhu et al. reported the theory of generalized thermoelasticity, based on the theory of Lord and Shulman with one relaxation time, used to study the electro-magneto-thermoelastic interactions in a semi-infinite, perfectly conducting solid subjected to a thermal shock on its surface when the solid and its adjoining vacuum were subjected to a uniform axial magnetic field [6]. They used Laplace transform in the analysis. Maxwell's equations were formulated and the generalized electro-magneto-thermoelastic coupled governing equations were established. Tianhu et al. reported a generalized electro-magneto-thermoelastic problem for an infinitely long solid cylinder based on the theory of Lord and Shulman with one relaxation time [7]. Eslami et al. presented a general solution for one-dimensional, steady-state thermal and mechanical stresses in a hollow, thick sphere made of FGM [8]. The material properties, except Poisson's ratio, were assumed to vary along the radius r according to a power-law function. Lee recently considered the problem of 3D, axisymmetric, quasistatic coupled magneto-thermoelasticity for laminated circular, conical shells subjected to magnetic and temperature fields [9]. Laplace transform and finite difference methods were used to analyze the problem. He obtained solutions for the temperature and thermal deformation distributions in a transient and steady state. Maruszewski presented nonlinear magneto-thermoelastic equations in soft ferromagnetic and elastic bodies. The symmetry of couplings in these equations was also investigated [10]. Wang and Dink studied the transient responses of a magneto-electro-elastic hollow sphere for the fully coupled spherically symmetric problem [11]. By means of the separation of variables technique and the electric and magnetic boundary conditions, the dynamic problem of a magneto-electro-elastic hollow sphere under spherically symmetric deformation was transformed to two Volterra integral equations of the second kind about two functions of time.

Heat Conduction Problem

Consider a hollow sphere of inner radius a and outer radius b made of FGM. The spherical coordinates (r, θ, ϕ) are considered. The heat conduction equation for two-dimensional transient FG sphere is:

$$T_{,rr} + \left(\frac{k'(r)}{k(r)} + \frac{2}{r}\right) T_{,r} + \frac{1}{r^2} T_{,\theta\theta} + \frac{\cot\theta}{r^2} T_{,\theta} = 0$$

$$a \le r \le b, 0 \le \theta \le \pi \qquad (1)$$

where $k(r)$ is heat conduction coefficient. The general thermal boundary conditions are considered to be:

$$\begin{cases} x_{11}T(a,\theta) + x_{12}T_{,r}(a,\theta) = F_1(\theta) \\ x_{21}T(b,\theta) + x_{22}T_{,r}(b,\theta) = F_2(\theta) \end{cases} \quad (2)$$

By choosing suitable values for parameters $x_{ij}(i,j=1,2)$, different types of thermal boundary conditions including conduction, heat flux, and convection may be considered for the sphere. The material properties of sphere are assumed to be graded along the thickness direction according to the power-law function as [3]:

$$\begin{aligned} E(r) &= E_0\left(\frac{r}{a}\right)^{m_1}, \alpha(r) = \alpha_0\left(\frac{r}{a}\right)^{m_2} \\ k(r) &= k_0\left(\frac{r}{a}\right)^{m_3}, \mu(r) = \mu_0\left(\frac{r}{a}\right)^{m_4} \end{aligned} \quad (3)$$

where $E_0, \alpha_0, k_0, \mu_0$ are, respectively, the modulus of elasticity, thermal expansion coefficient, heat conduction coefficient, and magnetic permeability and m_1, m_2, m_3, m_4 are the power-law indices. Since, most of the literatures are working with power-law function, for comparison purposes, it is decided to consider the power-law function for FGM. Meanwhile, the solutions obtained are simple in engineering problems. The solution of temperature equation can be written in the form of power series as:

$$T(r,\theta) = \sum_{n=0}^{+\infty} (E_{1n}r^{\delta_{1n}} + E_{2n}r^{\delta_{2n}})P_n(\cos\theta) \quad (4)$$

where $P_n(\cos\theta)$ is Legendre series. where

$$\delta_{1n,2n} = -\frac{m_3+1}{2} \pm \sqrt{\frac{(m_3+1)^2}{4} + n(n+1)} \quad (5)$$

Constants E_{1n} and E_{2n} are evaluated as follows by substituting (4) into the thermal boundary conditions.

Stress Analysis

Let u and v, be the displacement components in the radial and circumferential directions. Thus strain–displacement relations are:

$$\begin{aligned} \varepsilon_{rr} &= u_{,r} \\ \varepsilon_{\theta\theta} &= \frac{1}{r}(u + v_{,\theta}) \\ \varepsilon_{\varphi\varphi} &= \frac{1}{r}(u + v\cot\theta) \\ \varepsilon_{r\theta} &= \frac{1}{2}\left(\frac{u_{,\theta}}{r} + v_{,r} - \frac{v}{r}\right) \end{aligned} \quad (6)$$

The Hooke's law for two-dimensional hollow sphere can be written as:

$$\begin{aligned} \sigma_{rr} &= \frac{E(r)}{(1+v)(1-2v)}[(1-v)\varepsilon_{rr} + v\varepsilon_{\theta\theta} + v\varepsilon_{\varphi\varphi}] \\ &\quad - \frac{E(r)\alpha(r)}{(1-2v)}T(r,\theta) \\ \sigma_{\theta\theta} &= \frac{E(r)}{(1+v)(1-2v)}[v\varepsilon_{rr} + (1-v)\varepsilon_{\theta\theta} + v\varepsilon_{\varphi\varphi}] \\ &\quad - \frac{E(r)\alpha(r)}{(1-2v)}T(r,\theta) \\ \sigma_{\varphi\varphi} &= \frac{E(r)}{(1+v)(1-2v)}[v\varepsilon_{rr} + v\varepsilon_{\theta\theta} + (1-v)\varepsilon_{\varphi\varphi}] \\ &\quad - \frac{E(r)\alpha(r)}{(1-2v)}T(r,\theta) \end{aligned}$$

$$\sigma_{r\theta} = \frac{E(r)}{(1+v)}\varepsilon_{r\theta} \quad (7)$$

The variation of magnetic field with time or transient magnetic field results in electrical field and when the magnetic field is uniform, there is no electrical field. When the electrical field vanishes, then the coefficient connecting the temperature gradient and the electrical current as well as the coefficient connecting the current density and the heat flow density like Thompson effect can be ignored. Assuming that the magnetic permeability, μ, of the FG hollow sphere is equal to the magnetic permeability of the medium around it, and also the medium is non-ferromagnetic and non-ferroelectric and ignoring the Thompson effect, the simplified Maxwell's equations of electrodynamics for a perfectly conducting elastic medium are [1, 6, 7]:

$$\vec{h} = \nabla \times (\vec{U} \times \vec{H}), \quad \vec{J} = \nabla \times \vec{h}$$

$$f_i = \mu(r)(\vec{J} \times \vec{H})_i, \quad (i = r, \theta) \tag{8}$$

$\vec{J}$ is electric current density vector, h is perturbation of magnetic field vector and H is magnetic intensity vector (A/m). Cubical dilatation is as follows:

$$e = \varepsilon_{rr} + \varepsilon_{\theta\theta} + \varepsilon_{\phi\phi} = u_{,r} + \frac{2}{r}u + \frac{1}{r}v_{,\theta} + \frac{1}{r}v\cot\theta \tag{9}$$

Applying an initial magnetic field vector $\vec{H} = (0, 0, H_\phi)$ in spherical coordinates (r, θ, ϕ) to (8) yields to:

$$\begin{aligned} \vec{U} &= (u, v, 0), \vec{h_\phi} = -H_\phi(e) \\ J &= \left(-H_\phi \frac{1}{r}\frac{\partial e}{\partial \theta}, H_\phi \frac{\partial e}{\partial r}, 0\right) \\ f &= \left(H_\phi{}^2 \frac{\partial e}{\partial r}, H_\phi{}^2 \frac{1}{r}\frac{\partial e}{\partial \theta}, 0\right) \end{aligned} \tag{10}$$

Thus, Lorentz's force is evaluated as follows:

$$\begin{aligned} f = \mu(r) H_\phi{}^2 \Bigg(& u_{,rr} + \frac{2u_{,r}}{r} - \frac{2u}{r^2} + \frac{v_{,r\theta}}{r} - \frac{v_{,\theta}}{r^2} \\ & + \frac{\cot\theta v_{,r}}{r} - \frac{\cot\theta v}{r^2}, \frac{u_{,r\theta}}{r} + \frac{2u_{,\theta}}{r^2} \\ & + \frac{v_{,\theta\theta}}{r^2} + \frac{\cot\theta v_{,\theta}}{r^2} - \frac{(1+\cot^2\theta)v}{r^2}, 0 \Bigg) \end{aligned} \tag{11}$$

The equilibrium equations of FG hollow sphere, irrespective of the body force and the inertia terms are:

$$\begin{aligned} \sigma_{rr,r} + \frac{1}{r}(\sigma_{r\theta,\theta} + 2\sigma_{rr} - \sigma_{\theta\theta} \\ - \sigma_{\varphi\varphi} + \sigma_{r\theta}\cot\theta) + f_r = 0 \\ \sigma_{r\theta,r} + \frac{1}{r}(\sigma_{\theta\theta,\theta} + (\sigma_{\theta\theta} - \sigma_{\varphi\varphi}) \\ \cot\theta + 3\sigma_{r\theta}) + f_\theta = 0 \end{aligned} \tag{12}$$

Using (6)–(11) and (3), Navier equations in terms of radial and circumferential displacements are as follows:

$$\begin{aligned} & u_{,rr} + (m_1+2)\frac{1}{r}u_{,r} + 2\left(\frac{m_1 v}{1-v} - 1\right)\frac{1}{r^2}u \\ & + \left(\frac{1-2v}{2-2v}\right)\frac{1}{r^2}u_{,\theta\theta} \\ & + \left(\frac{1-2v}{2-2v}\right)\frac{\cot\theta}{r^2}u_{,\theta} + \left(\frac{1}{2-2v}\right)\frac{1}{r}v_{,r\theta} \\ & + \left(\frac{m_1 v}{1-v} - \frac{3-4v}{2-2v}\right)\frac{1}{r^2}v_{,\theta} \\ & + \left(\frac{1}{2-2v}\right)\frac{\cot\theta}{r}v_{,r} + \left(\frac{m_1 v}{1-v} - \frac{3-4v}{2-2v}\right)\frac{\cot\theta}{r^2}v \\ & + \frac{H_\phi{}^2\mu_0(1+v)(1-2v)}{E_0(1-v)} r^{m_4-m_1}\left(u_{,rr} + \frac{2}{r}u_{,r} - \frac{2}{r^2}u \right. \\ & \left. + \frac{1}{r}v_{,r\theta} - \frac{1}{r^2}v_{,\theta} + \frac{\cot\theta}{r}v_{,r} - \frac{\cot\theta}{r^2}v\right) \\ & = \frac{(1+v)\alpha_0 a^{-m_2}}{1-v}[(m_1+m_2)r^{m_2-1}T + r^{m_2}T_{,r}] \end{aligned} \tag{13}$$

$$\begin{aligned} & v_{,rr} + (m_1+2)\frac{1}{r}v_{,r} - \left(m_1 + \left(\frac{2-2v}{1-2v}\right)(1+\cot^2\theta)\right)\frac{1}{r^2}v \\ & + \left(\frac{2-2v}{1-2v}\right)\frac{1}{r^2}v_{,\theta\theta} + \left(\frac{2-2v}{1-2v}\right)\frac{\cot\theta}{r^2}v_{,\theta} \\ & + \left(\frac{1}{1-2v}\right)\frac{1}{r}u_{,r\theta}. \\ & + \left(m_1 + \frac{4-4v}{1-2v}\right)\frac{1}{r^2}u_{,\theta} + \frac{2H_\phi{}^2\mu_0(1+v)}{E_0} r^{m_4-m_1} \\ & \left[\frac{1}{r}u_{,r\theta} + \frac{2}{r^2}u_{,\theta} + \frac{1}{r^2}v_{,\theta\theta} + \frac{\cot\theta}{r^2}v_{,\theta} - \frac{(1+\cot^2\theta)}{r^2}v\right] \\ & = \left(\frac{2+2v}{1-2v}\right)\alpha_0 a^{-m_2} r^{m_2-1} T_{,\theta} \end{aligned}$$

For simplifying the Navier equations, it is assumed that the two power-law indices, m_1 and m_4 are equal. Therefore, the solutions of Navier equations are:

$$\begin{aligned} u(r,\theta) &= \sum_{n=0}^{+\infty} u_n(r) P_n(\cos\theta) \\ v(r,\theta) &= \sum_{n=0}^{+\infty} v_n(r) \sin\theta P_n'(\cos\theta) \end{aligned} \tag{14}$$

where $P_n'(\cos\theta)$ is differentiation of Legendre series with respect to circumferential direction. Using (14) and substituting into the Navier equations yields the following:

$$u_n''(1+A)+(m_1+2+2A)\frac{1}{r}u_n'+\left[2\left(\frac{vm_1}{1-v}-1-A\right)-n(n+1)\left(\frac{1-2v}{2-2v}\right)\right]\frac{1}{r^2}u_n+n(n+1)\left(\frac{1}{2-2v}+A\right)\frac{1}{r}v_n'+n(n+1)\left(\frac{vm_1}{1-v}-\frac{3-4v}{2-2v}-A\right)\frac{1}{r^2}v_n=\frac{(1+v)\alpha_0 a^{-m_2}}{(1-v)}[(m_1+m_2)r^{m_2-1}T_n+r^{m_2}T_n'] \quad (15)$$

$$v_n''+(m_1+2)\frac{1}{r}v_n'-\left[n(n+1)\left(\frac{2-2v}{1-2v}\right)+m_1+Bn(n+1)\right]\frac{1}{r^2}v_n-\left(\frac{1}{1-2v}+B\right)\frac{1}{r}u_n'-\left(m_1+\frac{4-4v}{1-2v}+2B\right)\frac{1}{r^2}u_n=-\frac{(2+2v)\alpha_0 a^{-m_2}}{(1-2v)}r^{m_2-1}T_n$$

where

$$A=\frac{H_\phi{}^2\mu_0(1+v)(1-2v)}{E_0(1-v)},\ B=\frac{2H_\phi{}^2\mu_0(1+v)}{E_0} \quad (16)$$

Symbol $(')$ denotes differentiation with respect to r. The general solutions of (15) are:

$$u_n^g(r)=Cr^\mu, v_n^g(r)=Dr^\mu \quad (17)$$

Substituting (17) into the left side of (15) yields:

$$C\{\mu(\mu-1)(1+A)+(m+2+2A)\mu+\frac{2mv}{1-v}-2-2A.-n(n+1)\left(\frac{1-2v}{1-v}\right)\}+\left\{n(n+1)\left(\frac{1}{2-2v}+A\right)\mu+n(n+1)\left(\frac{mv}{1-v}-\frac{3-4v}{2-2v}-A\right)\right\}D=0$$

$$D\left\{\mu(\mu-1)+(m+2)\mu-n(n+1)\frac{2-2v}{1-2v}-m-Bn(n+1)\right\}+C\left\{-\mu\left(\frac{1}{1-2v}+B\right)-\left(m+\frac{4-4v}{1-2v}+2B\right)\right\}=0 \quad (18)$$

Equations (18) are a system of algebraic equations that for obtaining their nontrivial solution, their determinant should be equal to zero and their four roots are evaluated as follows:

Therefore,

$$u_n^g(r)=\sum_{j=1}^{4}C_{nj}r^{\mu_{nj}}, v_n^g(r)=\sum_{j=1}^{4}N_{nj}C_{nj}r^{\mu_{nj}} \quad (19)$$

where

$$N_{nj}=-\frac{\mu(\mu-1)(1+A)+(m+2+2A)\mu+\frac{2mv}{1-v}-2-2A-n(n+1)\left(\frac{1-2v}{2-2v}\right)}{n(n+1)\left[\mu\left(\frac{1}{2-2v}+A\right)+\frac{mv}{1-v}-\frac{3-4v}{2-2v}-A\right]} \quad (20)$$
$$j=(1,\ldots,4)\ n\neq 0$$

Particular solutions of (15) are assumed to be as follows:

$$u_n^p(r)=F_{1n}r^{m_2+\delta_{1n}+1}+F_{2n}r^{m_2+\delta_{2n}+1}$$
$$v_n^p(r)=F_{3n}r^{m_2+\delta_{1n}+1}+F_{4n}r^{m_2+\delta_{2n}+1} \quad (21)$$

Substituting (21) into (15), the coefficients of particular solution are evaluated from the algebraic system of equations solved by Cramer's method.

Combination of the decoupled case for $n=0$, must be considered:

The general solution in this case is as follows:

$$u_0^g(r)=\sum_{i=1}^{2}a_{0i}r^{\eta_i} \quad (22)$$

$$\eta_{1,2} = \frac{1}{2} \pm \sqrt{\frac{1}{4} + \frac{(1-2\nu)(m_1+2+2A)\left(m_1+\frac{4-4\nu}{1-2\nu}+2B\right)}{(1+A)(1+B(1-2\nu))} - 2\left(\frac{m_1\nu}{(1+A)(1-\nu)}-1\right)} \tag{23}$$

And also particular solution for displacement of decoupled case is:

$$u_0^p(r) = F_{10} r^{m_2-m_3} + F_{20} r^{m_2+1} \tag{24}$$

That the constants F_{10} and F_{20} are evaluated by Cramer's method. Therefore, the solution of Navier equations for two-dimensional hollow sphere is obtained as follows:

$$\begin{aligned} u(r,\theta) = &\sum_{n=1}^{+\infty} \left\{ \sum_{j=1}^{4} C_{nj} r^{\mu_{nj}} + F_{1n} r^{m_2+\delta_{1n}+1} \right. \\ &\left. + F_{2n} r^{m_2+\delta_{2n}+1} \right\} P_n(\cos\theta) \\ &+ \sum_{i=1}^{2} a_{0i} r^{\eta_i} + F_{10} r^{m_2-m_3} + F_{20} r^{m_2+1} \\ v(r,\theta) = &\sum_{n=1}^{+\infty} \left\{ \sum_{j=1}^{4} N_{nj} C_{nj} r^{\mu_{nj}} + F_{3n} r^{m_2+\delta_{1n}+1} \right. \\ &\left. + F_{4n} r^{m_2+\delta_{2n}+1} \right\} \sin\theta P_n'(\cos\theta) \end{aligned} \tag{25}$$

Substitution of (25) in (6) yields to strains and substitution of the results into (7) yields to stresses.

Substitution of (25) into (8), the perturbation of the magnetic field vector is obtained.

The von Mises stress is as follows:

$$\sigma_v = \sqrt{(\sigma_{rr}-\sigma_{\theta\theta})^2 + (\sigma_{\theta\theta}-\sigma_{\phi\phi})^2 + (\sigma_{\phi\phi}-\sigma_{rr})^2 + 6\sigma_{r\theta}{}^2} \Big/ \sqrt{2} \tag{26}$$

To determine the displacements and stresses, four boundary conditions are required to evaluate the four unknown constants C_{n1} to C_{n4} and a_{01}, a_{02}. The four boundary conditions may be selected from the list of boundary conditions given in (27). The procedure is continued by expanding the given boundary conditions into the Legendre series. These constants are calculated by solving the system of algebraic equations formed by four boundary conditions in the following expressions:

$$\begin{aligned} u(a,\theta) &= g_1(\theta),\ u(b,\theta) = g_2(\theta) \\ v(a,\theta) &= g_3(\theta),\ v(b,\theta) = g_4(\theta). \\ \sigma_{rr}(a,\theta) &= g_5(\theta),\ \sigma_{rr}(b,\theta) = g_6(\theta) \\ \sigma_{r\theta}(a,\theta) &= g_7(\theta),\ \sigma_{r\theta}(b,\theta) = g_8(\theta) \end{aligned} \tag{27}$$

where $g_i(\theta), (i = 1, \ldots, 8)$ are known boundary condition functions.

Results and Discussion

The first example consist of considering the magneto-thermoelasticity response in an FG hollow sphere of inner radius (metal constituent) $a = 1$ m and outer radius (ceramic constituent) $b = 1.2$ m with the same material properties as given in the first example. The evaluated power-law indices are given in Table 1.

The temperature at the inner radius is zero and at the outer radius is defined by $T(b,\theta) = 100\cos\theta^2/2$ and the mechanical boundary conditions are considered to be traction free at both sides of the sphere. Figures 1–3 show, respectively, the effect of magnetic field on radial displacement, radial stress, and circumferential stress of the FG hollow sphere, considering the thermal load defined as above and for the evaluated power-law indices indicated in Table and at various θ. The left side figures correspond to the effect without magnetic field and the right side figures correspond to the effect with magnetic field. It is to be noted that the radial displacement due to thermal load with magnetic field is greater in magnitude than the radial displacement due to

Analytical Solution for Two-Dimensional Magneto-thermomechanical Response in FG Hollow Sphere, Table 1 Material properties

Material properties		Power-law index
$E_{in} = 66.2\,\text{GPa}$	$E_{out} = 117\,\text{GPa}$	$m_1 = 3.1236$
$\alpha_{in} = 10.3E-6/^{\circ}\text{C}$	$\alpha_{out} = 7.11E-6/^{\circ}\text{C}$	$m_2 = -2.0329$
$K_{in} = 18.1\,\text{W/mK}$	$K_{out} = 2.036\,\text{W/mK}$	$m_3 = -11.9839$

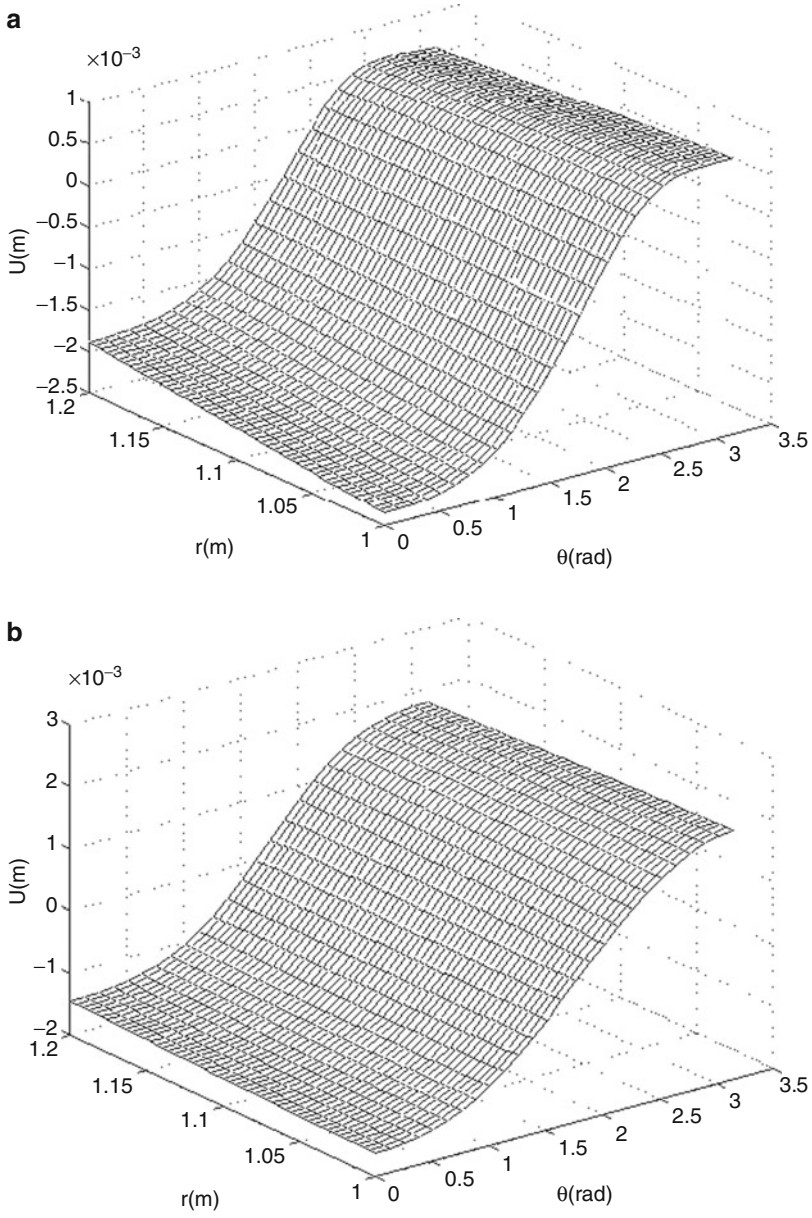

Analytical Solution for Two-Dimensional Magneto-thermomechanical Response in FG Hollow Sphere, Fig. 1 Radial displacement due to thermal load (**a**) without magnetic field (**b**) with magnetic field

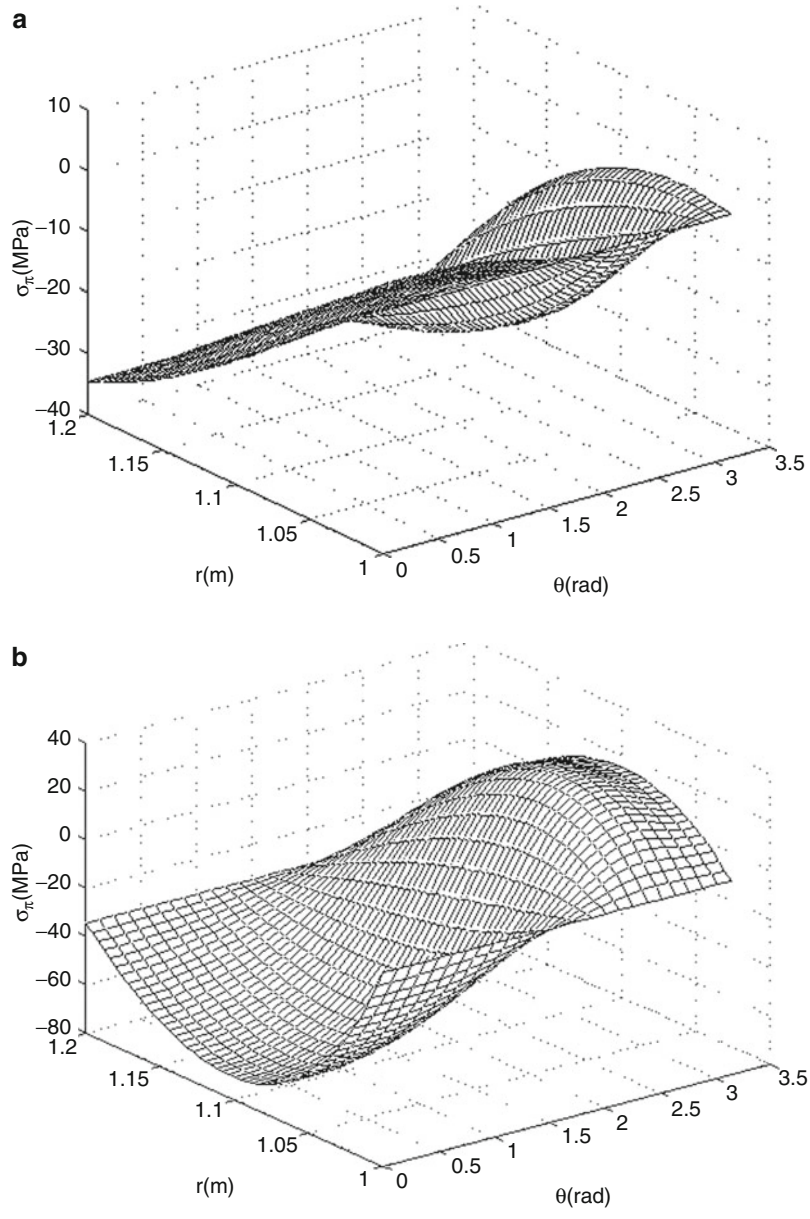

Analytical Solution for Two-Dimensional Magneto-thermomechanical Response in FG Hollow Sphere, Fig. 2 Radial stress due to thermal load (**a**) without magnetic field (**b**) with magnetic field

thermal load without magnetic field. The variations of both cases of displacements are almost the same. The radial stress due to thermal load without magnetic field is smaller in magnitude than the radial stress due to thermal load with magnetic field. The variations of two cases are completely different. At both inner and outer surfaces, the radial stresses are equal in magnitudes. Circumferential stress due to thermal load with magnetic field is greater in magnitude than the circumferential stress due to thermal load without magnetic field. The variations of the curves for the sphere subjected to magnetic field and the one without magnetic field are almost the same.

In order to study the effect of power-law indices on the behavior of the second example FG hollow sphere in Table at the presence of

Analytical Solution for Two-Dimensional Magneto-thermomechanical Response in FG Hollow Sphere,

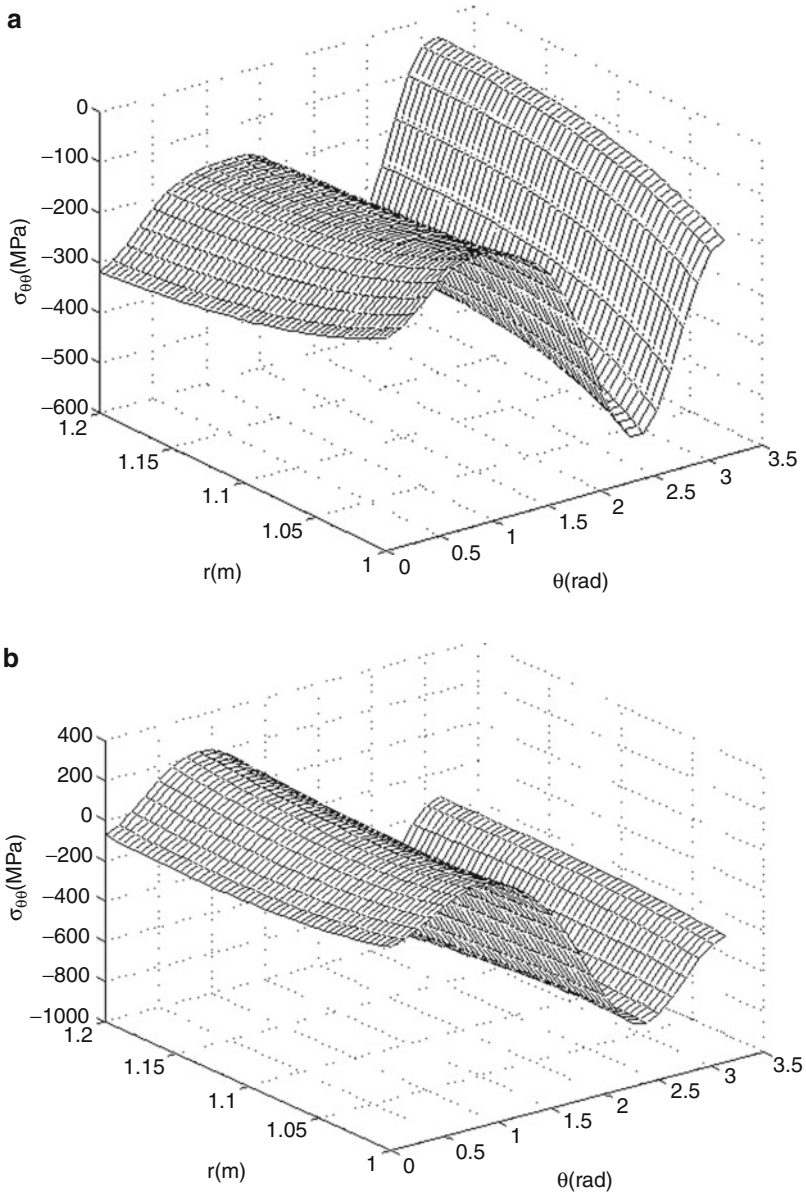

Fig. 3 Circumferential stress due to thermal load (**a**) without magnetic field (**b**) with magnetic field

magnetic field and thermal load, the power indices of material properties are considered to be identical as $m_1 = m_2 = m_3 = m$. For this case, m is considered to be ranging from -1 to $+3$. Figure 4 shows the temperature distribution with various power-law indices. When the power-law index (m) increases, the temperature is decreased, since FG sphere gets cold faster. Figure 5 shows the variation of radial displacement due to thermal load and magnetic field with various power-law indices. Since increasing m, results in higher gravity of the sphere, then, the radial displacement is decreased. Figure 6 shows the variation of radial stress due to thermal load and magnetic field with various power-law indices. As can be observed from the figure, the radial stress becomes zero at the inner radius of the sphere,

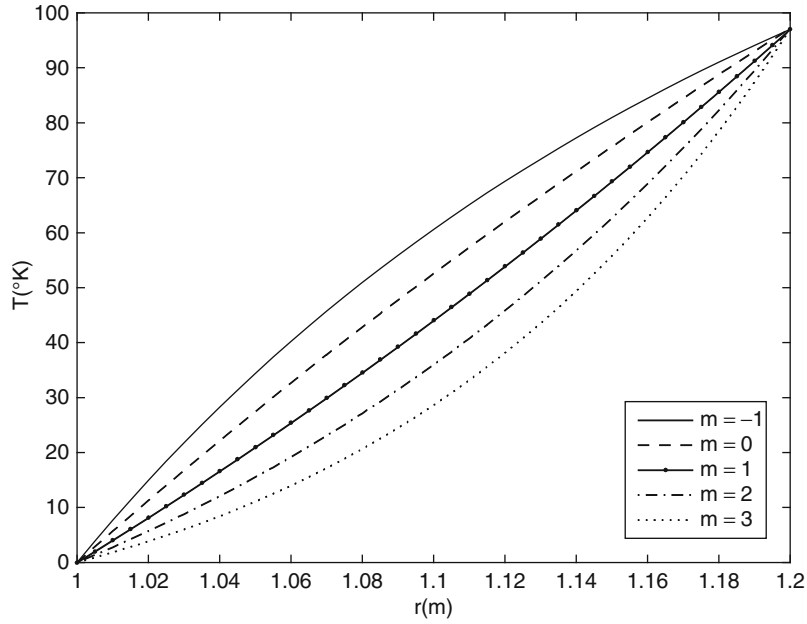

Analytical Solution for Two-Dimensional Magneto-thermomechanical Response in FG Hollow Sphere, Fig. 4 Temperature distribution along the thickness of FG sphere with various power-law indices at $\theta = \pi/4$

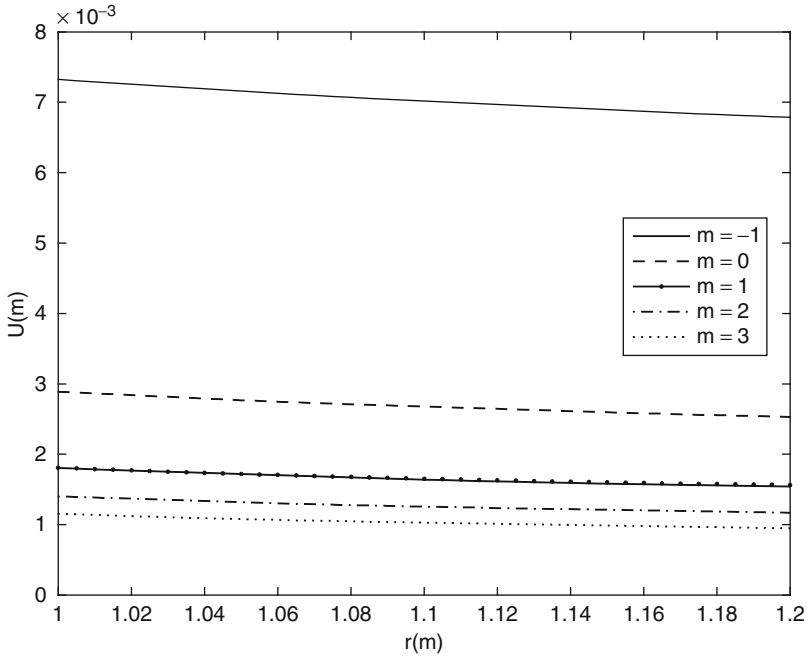

Analytical Solution for Two-Dimensional Magneto-thermomechanical Response in FG Hollow Sphere, Fig. 5 Radial displacement due to thermal load and magnetic field along the thickness of FG sphere with various power-law indices at $\theta = \pi/4$

since there is no constrains at the inner radius. By increasing the power-law index (m), the radial stress is increased. Figure 7 shows the circumferential stress distribution due to thermal load and magnetic field with various power-law indices. In contrary to the effect on radial stress, the circumferential stress is decreased by increasing m. Figure 8 shows the shear stress distribution

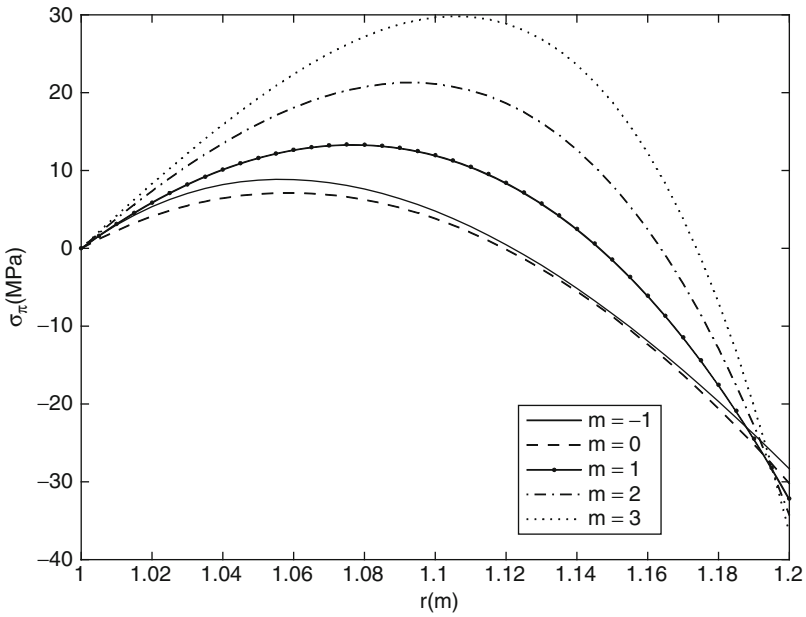

Analytical Solution for Two-Dimensional Magneto-thermomechanical Response in FG Hollow Sphere, Fig. 6 Radial stress due to thermal load and magnetic field along the thickness of FG sphere with various power-law indices at $\theta = \pi/4$

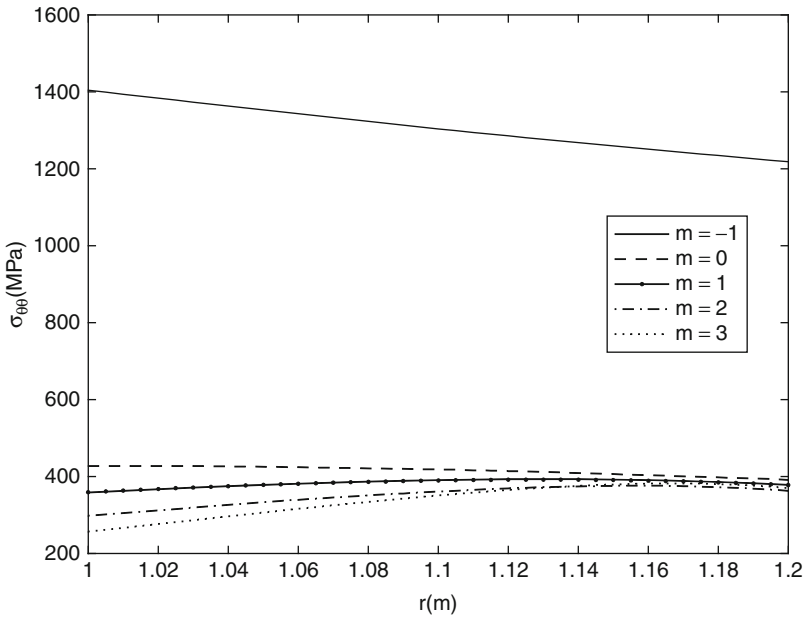

Analytical Solution for Two-Dimensional Magneto-thermomechanical Response in FG Hollow Sphere, Fig. 7 Circumferential stress due to thermal load and magnetic field along the thickness of FG sphere with various power-law indices at $\theta = \pi/4$

due to thermal load and magnetic field with various power-law indices. Similar to the radial stress distribution, as m is increased, the shear stress is also increased. Figure 9 shows the perturbation magnetic field vector due to thermal load with various power-law indices. By increasing m, the perturbation is decreased.

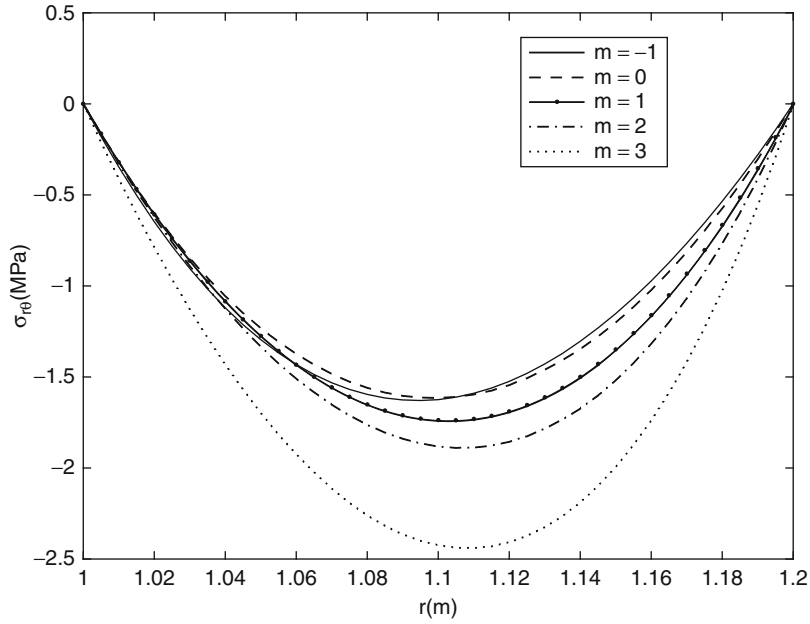

Analytical Solution for Two-Dimensional Magneto-thermomechanical Response in FG Hollow Sphere, Fig. 8 Shear stress due to thermal load and magnetic field along the thickness of FG sphere with various power-law indices at $\theta = \pi/4$

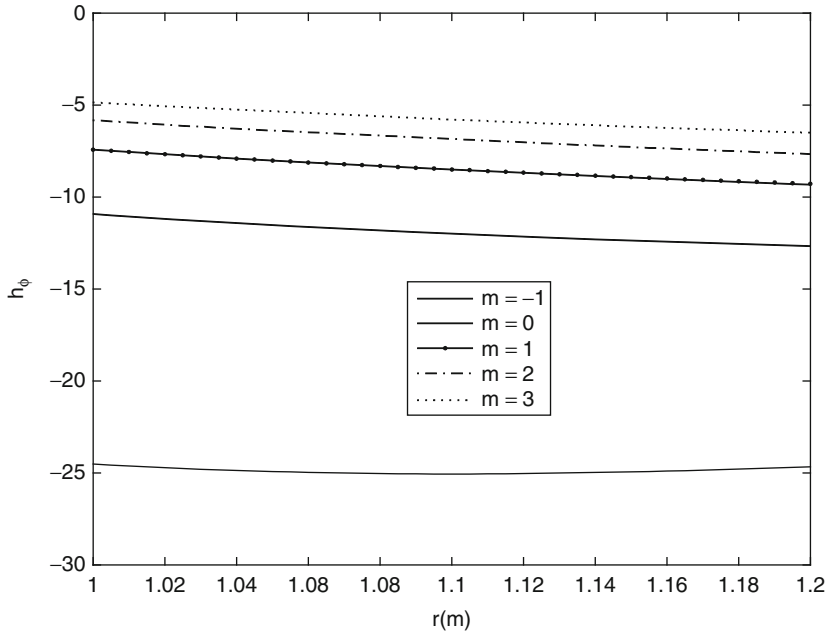

Analytical Solution for Two-Dimensional Magneto-thermomechanical Response in FG Hollow Sphere, Fig. 9 Perturbation of the magnetic field vector due to thermal load along the thickness of FG sphere with various power-law indices at $\theta = \pi/4$

Conclusion

In this entry, the analytical solution for magneto-thermomechanical response for FG hollow sphere is presented. Analytical solution for stresses and perturbation are determined using power series method. The material stiffness, thermal expansion coefficient, heat conduction coefficient, and the magnetic permeability vary continuously across the thickness direction according to the power-law functions of radial direction. Magnetic field results in decreasing the radial displacement and circumferential stress due to mechanical load, and has a negligible effect on mechanical radial stress. Also, the magnetic field results in increasing the radial displacement, radial and circumferential stresses due to thermal load. By increasing power-law index (m), the above-mentioned quantities due to mechanical loads are all decreased. Increasing the power-law indices at the presence of thermal loads, result in increasing radial stress and shear stress values, but has a reverse effect on temperature, radial displacement, circumferential stress, and perturbation of the magnetic field vector distributions. In general, the effect of mechanical loads with magnetic field is more significant when compared to the effect of thermal loads with magnetic field.

Appendix

$$d_1 = (m_2+\delta_{1n}+1)(m_2+\delta_{1n})(1+A) + (m_1+2+2A)\times(m_2+\delta_{1n}+1) + 2\left(\frac{m_1\nu}{1-\nu}-1-A\right) - n(n+1)\left(\frac{1-2\nu}{2-2\nu}\right)$$

$$d_2 = n(n+1)\left[(m_2+\delta_{1n}+1)\left(\frac{1}{2-2\nu}+A\right) + \left(\frac{m_1\nu}{1-\nu}-\frac{3-4\nu}{2-2\nu}-A\right)\right]$$

$$d_3 = -\left[(m_2+\delta_{1n}+1)\left(\frac{1}{1-2\nu}+B\right) + m_1+\frac{4-4\nu}{1-2\nu}+2B\right]$$

$$d_4 = (m_2+\delta_{1n}+1)(m_2+\delta_{1n}) + (m_1+2)\times(m_2+\delta_{1n}+1) - n(n+1)\left(\frac{2-2\nu}{1-2\nu}\right) - m_1 - Bn(n+1)$$

$$d_5 = \frac{(1+\nu)\alpha_0 a^{-m_2}}{(1-\nu)}(m_1+m_2+\delta_{1n})E_{1n}$$

$$d_6 = -\frac{(2+2\nu)\alpha_0 a^{-m_2}}{1-2\nu}E_{1n}$$

$$d_7 = (m_2+\delta_{2n}+1)(m_2+\delta_{2n})(1+A) + (m_1+2+2A)\times(m_2+\delta_{2n}+1) + 2\left(\frac{m_1\nu}{1-\nu}-1-A\right) - n(n+1)\left(\frac{1-2\nu}{2-2\nu}\right)$$

$$d_8 = n(n+1)\left[(m_2+\delta_{2n}+1)\left(\frac{1}{2-2\nu}+A\right) + \left(\frac{m_1\nu}{1-\nu}-\frac{3-4\nu}{2-2\nu}-A\right)\right]$$

$$d_9 = -\left[(m_2+\delta_{2n}+1)\left(\frac{1}{1-2\nu}+B\right) + m_1+\frac{4-4\nu}{1-2\nu}+2B\right]$$

$$d_{10} = (m_2+\delta_{2n}+1)(m_2+\delta_{2n}) + (m_1+2)(m_2+\delta_{2n}+1) - n(n+1)\left(\frac{2-2\nu}{1-2\nu}\right) - m_1 - Bn(n+1)$$

$$d_{11} = \frac{(1+\nu)\alpha_0 a^{-m_2}}{(1-\nu)}(m_1+m_2+\delta_{2n})E_{2n}$$

$$d_{12} = -\frac{(2+2\nu)\alpha_0 a^{-m_2}}{1-2\nu}E_{2n}$$

$$s_1 = \frac{(1-2\nu)(m_1+2+2A)\left(m_1+\frac{4-4\nu}{1-2\nu}+2B\right)}{(1+A)(1+B(1-2\nu))} + 2\left(\frac{m_1\nu}{(1-\nu)(1+A)}-1\right)$$

$$s_2 = \frac{(1+v)\alpha_0 a^{-m_2}(m_1+m_2)}{(1+A)(1-v)} - \frac{(m_1+2+2A)(2+2v)\alpha_0 a^{-m_2}}{(1+A)(1+B(1-v))}$$

$$s_3 = \frac{(1+v)\alpha_0 a^{-m_2}}{(1+A)(1-v)}$$

References

1. Abd-Alla AM, Hammad HAH, Abo-Dahab SM (2004) Magneto-thermo-viscoelastic interactions in an unbounded body with a spherical cavity subjected to a periodic loading. J Appl Math Comp 155:235–248
2. Chen WQ, Lee KY (2003) Alternative state space formulations magnetoelectric thermoelasticity with transverse isotropy and the application to bending analysis of nonhomogeneous plates. J Solids Struct 40:5689–5705
3. Dai HL, Fu YM (2007) Magnetothermoelastic interactions in hollow structures of functionally graded material subjected to mechanical loads. Int J Press Vessel Pip 84(3):132–138
4. Dai HL, Wang X (2006) The dynamic response and perturbation of magnetic field vector of orthotropic cylinders under various shock loads. Int J Press Vessel Pip 83(1):55–62
5. Poultangari R, Jabbari M, Eslami MR (2008) Functionally graded hollow spheres under non-axisymmetric thermo-mechanical loads. Int J Press Vessel Pip 85:295–305
6. Tianhu H, Yapeng S, Xiaogeng T (2004) A two-dimensional generalized thermal shock problem for a half-space in electromagneto-thermoelasticit. Int J Eng Sci 42:809–823
7. Tianhu H, Xiaogeng T, Yapeng S (2005) A generalized electromagneto thermoelastic problem for an infinitely long solid cylinder. Eur J Mech A Solid 24:349–359
8. Eslami MR, Babai MH, Poultangari R (2005) Thermal and mechanical stresses in a functionally graded thick sphere. Int J Press Vessel Pip 82:522–527
9. Lee ZY (2009) Magnetothermoelastic analysis of multilayered conical shells subjected to magnetic and vapor fields. Int J Therm Sci 48(1): 50–72
10. Maruszewsk B (1981) Dynamical magnetothermoelastic problem in cicular cylinders-I: basic equations. Int J Eng Sci 19(9):1233–1240
11. Wang HM, Dink HJ (2006) Transient responses of a magneto-electro-elastic hollow sphere for fully coupled spherically symmetric problem. Eur J Mech A Solid 25:965–980

Anisotropic

▶ Anisotropic Initial Yield and Failure Criteria Including Temperature Effect
▶ Anisotropic Thermoelastic Contact Problems
▶ Axisymmetric Thermal Stresses in an Anisotropic Finite Hollow Cylinder
▶ Thermoelastostatics of Transversely Isotropic Materials: Fundamental Solutions and Green's Functions

Anisotropic Initial Yield and Failure Criteria Including Temperature Effect

Jacek Skrzypek and Artur Ganczarski
Institute of Applied Mechanics, Cracow University of Technology, Cracow, Poland

Synonyms

Anisotropic

Definitions

Termination of pure elastic response to applied loading to anisotropic structural materials, requires formulation and calibration of appropriate limit surfaces, that indicates initiation of yield or failure. Composite materials are typical representatives of novel, anisotropic materials, constituents of which, in general, establish temperature dependent thermo-mechanical properties, both for matrix and fiber/particles phases. The usually applied temperature independent analysis may lead to erroneous estimations of limit surfaces. Mismatch of thermo-mechanical properties, between the composite constituents, results in high magnitude residual stresses, which are built-in during the cool-down from the elevated fabrication temperature, and affect initial limit surfaces. Apart from classical limit analysis at the macro-level (composite), separate analysis of the level of constituents (matrix/fiber), is required.

Overview

General Case for Goldenblat and Kopnov's Initial Yield or Failure Criteria

In the most general case of material anisotropy, both elastic and inelastic, plastic or damage, extension of common isotropic initial yield and failure criteria can be done when single stress invariants are replaced by common invariants of the stress tensor and of the structural tensor of plastic or damage anisotropy, as proposed by Hill [1], Życzkowski [2], Betten [3], Sayir [4]

$$f\left(\Pi, \Pi_{ij}\sigma_{ij}, \Pi_{ijkl}\sigma_{ij}\sigma_{kl}, \Pi_{ijklmn}\sigma_{ij}\sigma_{kl}\sigma_{mn}, \ldots\right) = 0 \tag{1}$$

where Π, Π_{ij}, Π_{ijkl} and Π_{ijklmn} denote structural tensors of plastic/failure anisotropy, and Einstein's summation of tensors holds, whereas $f()$ is an arbitrary scalar function of tensor arguments of common invariants of the stress tensor σ_{ij} and structural anisotropy tensors, e.g., $\Pi_{ij}\sigma_{ij}$, $\Pi_{ijkl}\sigma_{ij}\sigma_{kl}$ and $\Pi_{ijklmn}\sigma_{ij}\sigma_{kl}\sigma_{mn}$. In such cases, initiation of plasticity or failure is governed not only by single material constants k_i (like in the case of isotropy), but also by structural tensors of plastic or failure anisotropy of various orders, $\Pi^{\mathrm{p/f}}$, $\Pi^{\mathrm{p/f}}_{ij}$, $\Pi^{\mathrm{p/f}}_{ijkl}$, $\Pi^{\mathrm{p/f}}_{ijklmn}, \ldots$, different for plasticity (p) or failure (f) initiations. Equation (1) owns a general representation, but practical application of it is strongly limited by a large number of material tests. Additionally, components of all the above structural tensors are temperature dependent, e.g., $\Pi(T)$, $\Pi_{ij}(T)$, $\Pi_{ijkl}(T)$, $\Pi_{ijklmn}(T)$, which makes identification of them much more complicated. In a particular case, when tensorial-polynomial representation was used, Goldenblat and Kopnov [5], and later Sayir [4], proposed the anisotropic plastic flow or failure criterion in a dimensionless form

$$\left(\Pi_{ij}\sigma_{ij}\right)^{\alpha} + \left(\Pi_{ijkl}\sigma_{ij}\sigma_{kl}\right)^{\beta} + \left(\Pi_{ijklmn}\sigma_{ij}\sigma_{kl}\sigma_{mn}\right)^{\gamma} + \ldots - 1 = 0 \tag{2}$$

where all structural anisotropy tensors Π_{ij}, Π_{ijkl}, Π_{ijklmn}, etc., are normalized by the common constant Π, where α, β and γ are arbitrary exponents of a polynomial representation. Assuming $\alpha = 1$, $\beta = 1/2$, $\gamma = 1/3$, (2) is reduced to a simpler form, with the homogeneity of the left-hand side polynomial components assured, namely, cf. Goldenblat and Kopnov [5]

$$\Pi_{ij}\sigma_{ij} + \left(\Pi_{ijkl}\sigma_{ij}\sigma_{kl}\right)^{1/2} + \left(\Pi_{ijklmn}\sigma_{ij}\sigma_{kl}\sigma_{mn}\right)^{1/3} - 1 = 0 \tag{3}$$

Equation (3), when limited to three common invariants of the stress tensor σ_{ij} and structural anisotropy tensors of various orders: Π_{ij} (2nd order), Π_{ijkl} (4th order) and Π_{ijklmn} (6th order), is not the most general one, in the sense of the so-called representation theorems, which determine the most general irreducible forms of the scalar and tensor functions that satisfy the coordinate invariance and material symmetry properties, cf. Spencer [6], Rymarz [7], Rogers [8], etc. However, 2-nd, 4-th and 6-th order structural anisotropy tensors, that appear in (3), are satisfactory to describe basic transformation modes of the limit surfaces due to plastic or damage hardening processes: isotropic change of size, kinematic translation and rotation, as well as distortion (with a curvature change), cf. Kowalsky et al. [9].

Initial Yield/Failure Criteria for Ductile Versus Brittle Materials

Goldenblat and Kopnov's equation (3), with dimensional homogeneity assumed, is quite general too, because of a large number of material tests required for its calibration. Hence, for practical applications, further reduction is frequently recommended. It is governed by a general observation that characterize two basic classes of structural materials behavior, depending on the nature of the dissipative phenomena responsible for termination of pure elastic behavior: ductile or brittle. In general, plastic yield initiation refers to the majority of metallic materials (metals, alloys, intermetallics), for which hydrostatic stress does not influence yield initiation criterion. Additionally, strength differential

effect, that is a different plastic/failure behavior in uniaxial tension and compression, is usually negligible $k_t \approx k_c$, so that initial yield surfaces are considered as cylindrical and convex. On the other hand, failure or damage initiation refers mostly to brittle materials (concrete, ceramic materials, rocks, etc.), for which hydrostatic stress has an essential effect on the initial damage mechanism. Obviously, the strength differential effect is essential in this case $k_t \neq k_c$, but usually the initial damage surfaces remain convex.

As a consequence, when applied to ductile materials, in the general Goldenblat and Kopnov equation one can neglect first terms in (2–3) dependent on the first stress invariant. By contrast, when the initial failure mechanism manifests itself prior to other dissipative phenomena, what happens in a majority of brittle materials, is that the first stress invariant plays an essential role, such that first (linear) terms in (2–3) cannot be omitted. Moreover, third terms in (2–3) which are dependent on the third stress invariant, that basically are responsible for limit surfaces distortion, usually are neglected for the initiation of dissipative phenomena. However, surface distortion often accompanies consecutive hardening phenomena when advanced plasticity and damage response occurs, cf. Kowalsky et al. [9]. As a consequence, dimensional and dimensionless forms of Goldenblat and Kopnov's equations, (2–3), can often be reduced to the forms independent of the third common invariant $\Pi_{ijklmn}\sigma_{ij}\sigma_{kl}\sigma_{mn}$, where the stress components are entered by quadratic and linear terms as follows

$$\left(\Pi_{ij}\sigma_{ij}\right)^{\alpha} + \left(\Pi_{ijkl}\sigma_{ij}\sigma_{kl}\right)^{\beta} - 1 = 0 \qquad (4)$$

and when $\alpha = 1$, $\beta = 1/2$

$$\Pi_{ij}\sigma_{ij} + \sqrt{\Pi_{ijkl}\sigma_{ij}\sigma_{kl}} - 1 = 0 \qquad (5)$$

When exponents $\alpha = \beta = 1$ are assumed in (4), we obtain another reduced, nonhomogeneous form

$$\Pi_{ij}\sigma_{ij} + \Pi_{ijkl}\sigma_{ij}\sigma_{kl} - 1 = 0 \qquad (6)$$

Equation (6) is known as the Tsai–Wu anisotropic initial yield/failure criterion, [10].

Thermal Effects in Composites

In the case of composite materials, one deals at the level of microstructure with an artificial material, composed of two or more components, such that the new improved properties of a composite material are achieved. Usually metal based-, ceramic based-, or polymer based-composites are used. Conventional polycrystalline metals, such as: carbon steels, stainless steels, aluminium-, titanium-, nickel-alloys, exhibit high ductility, high tensile strength, and high damage and fracture resistance. Simultaneously, they suffer from limited high temperature resistance (up to $2{,}000 \div 3{,}000$ K), low creep resistance, relatively low wear surface resistance, high thermal conductivity and thermal expansion coefficients, low corrosion resistance, and relatively high mass density. On the other hand, pure ceramic materials, such as: metal oxides (Al_2O_3, ZrO_2, TiO_2), carbides (SiC, B_4C, TiC, Ti_2C), and nitrides (TiN, CrN, Cr_2N, WN, MoN, ZrN) exhibit properties such as: extremely high hardness, high compressive strength, good surface wear resistance, high temperature resistance, low thermal conductivity, thermal expansion coefficients, good oxidation resistance, and low mass density. Among the disadvantages, the following can be listed: very poor tensile strength $k_t \ll k_c$, high brittleness, low fracture resistance and porosity. A goal of applying a composite material is to achieve improved properties of a material at the macro-level by combining the chosen most advantageous properties of components (matrix and reinforcement properties). Following the basic kinds of composites, with respect to matrix material, are distinguished by such as: metal matrix composites (MMC), ceramic matrix composites (CMC) or polymer matrix composites (PMC). The type and geometry of reinforcement determine properties and group of symmetry of the composite at the macro-level. With respect to reinforcement, two classes of composites can be distinguished: particle reinforced composites (PRC) or fiber reinforced composites (FRC). The PRCs, that

are usually composed of isotropic component materials (matrix and reinforcement), exhibit the property of isotropy at the macro-level, as well. The FRCs, and especially long fiber reinforced composites LFRCs, show anisotropy at the macro-level if geometry and orientation of fibers exhibit a certain specific order. In particular, orthotropy or transverse isotropy assumptions are frequently used for the LFRCs symmetry group. In such cases, the Goldenblat and Kopnov initial yield and failure equation, (3), should be rewritten at the micro-level in a form

$$\Pi_{ij}^{\mathrm{m,f}}\sigma_{ij}^{\mathrm{m,f}} + \left(\Pi_{ijkl}^{\mathrm{m,f}}\sigma_{ij}^{\mathrm{m,f}}\sigma_{kl}^{\mathrm{m,f}}\right)^{1/2} + \left(\Pi_{ijklmn}^{\mathrm{m,f}}\sigma_{ij}^{\mathrm{m,f}}\sigma_{kl}^{\mathrm{m,f}}\sigma_{mn}^{\mathrm{m,f}}\right)^{1/3} - 1 = 0 \tag{7}$$

where all common stress and material anisotropy invariants are defined separately for matrix (m) and fiber (f) materials.

All material anisotropy tensors discussed in this section are, in general, functions of temperature, e.g., $\Pi_{ij}^{\mathrm{m,f}}(T)$, $\Pi_{ijkl}^{\mathrm{m,f}}(T)$, $\Pi_{ijklmn}^{\mathrm{m,f}}(T)$. This temperature effect cannot be ignored in the case of metallic materials that exhibit strong limitations with respect to their use-temperature. The most common metallic materials, used as matrix materials in composites, are aluminum-based or titanium-based alloys. Aluminum matrix composites have a use-temperature upwards to 300 °C, whereas titanium matrix composites can be applied to 800 °C (cf. Herakovich and Aboudi [11]). On the other hand, ceramic matrix materials can resist much higher temperatures, up to 2,000 °C, whereas carbon/carbon composites can withstand temperatures up to 2,200 °C. Two approaches to limit criterions are used: with temperature independent or temperature dependent material properties. In case of metallic materials, temperature dependence of their properties cannot be ignored, especially if either elevated or cryogenic temperatures are considered.

In addition, composites are multi-component materials, usually having essential mismatch of thermo-mechanical properties between the constituents at the micro-level. This mismatch results in strong residual stresses (sometimes up to 2 GPa compressive stress in ultra-fine ceramic films, e.g., used as thermal barrier coatings, for example CrN, Cr_2N etc.). Residual stresses are built-in during the cool-down from the elevated fabrication temperature, and frozen during consecutive mechanical loading conditions. The mismatch effect is typical for both the long-fiber reinforced anisotropic composites and the particle reinforced isotropic composites. However, it manifests itself clearly in case of existence of material anisotropy, independently of material isotropy of constituents at the micro-level, or structural anisotropy of a composite at macro-level.

The above discussed two thermal effects: due to residual stresses, and due to temperature dependent material properties, are in fact coupled, but they are responsible for different transformations of limit surfaces. Temperature dependence of material properties basically results in change of size or shape of limit surface, whereas residual stresses frozen after a fabrication cooling-down process is done control the kinematic effect of the limit surface. These remarks hold for both limit surfaces of constituents (matrix and fibers or particles) and for the resulting common intersection of both surfaces, usually exhibiting corner points.

Basic Methodology

The Pariseau–Tsai–Wu Anisotropic Initial Yield and Failure Criteria: Reduction and Calibration

Equation (6) presented in a previous section defines an anisotropic initial yield/failure criterion, in which material anisotropy is characterized by two anisotropy tensors, the second-order tensor Π_{ij} and the fourth-order tensor Π_{ijkl}. This equation may also be written in matrix notation, when the symmetry conditions for both stress tensors $\sigma_{ij} = \sigma_{ji}$, and structural tensors $\Pi_{ij} = \Pi_{ji}$ and $\Pi_{ijkl} = \Pi_{jikl} = \Pi_{ijlk} = \Pi_{klij}$ hold. Hence, the number of material parameters that define a 6×6 matrix $[\Pi]$ and a 6×1 column

matrix $[\pi]$ is equal to $6+21=27$, when the Voigt vector–matrix notation is applied to the Tsai–Wu equation (6)

$$[\pi]\{\sigma\}+\{\sigma\}^{\mathrm{T}}[\Pi]\{\sigma\}-1=0 \tag{8}$$

Although total number of material anisotropy parameters in (8) is 27, only 24 of them are essentially independent, since tensor Π_{ijkl} must also obey a tensorial transformation rule, involving three Euler angles. Both anisotropy matrices in (8), $[\pi]$ and $[\Pi]$ can explicitly be written as follows

$$[\pi]=[\pi_1,\pi_2,\pi_3,\pi_4,\pi_5,\pi_6]^{\mathrm{T}}$$
$$[\Pi]=\begin{bmatrix}\Pi_{11} & \Pi_{12} & \Pi_{13} & \Pi_{14} & \Pi_{15} & \Pi_{16}\\ & \Pi_{22} & \Pi_{23} & \Pi_{24} & \Pi_{25} & \Pi_{26}\\ & & \Pi_{33} & \Pi_{34} & \Pi_{35} & \Pi_{36}\\ & & & \Pi_{44} & \Pi_{45} & \Pi_{46}\\ & & & & \Pi_{55} & \Pi_{56}\\ & & & & & \Pi_{66}\end{bmatrix} \tag{9}$$

Further reduction of independent material parameters in (9) is possible if the invariance of (8) with respect to change of sign of shear stress components is consistently assumed. This requirement is satisfied if matrix $[\pi]$ is diagonal and matrix $[\Pi]$ is orthotropic

$$[\pi]=[\pi_1,\pi_2,\pi_3,0,0,0]^{\mathrm{T}}$$
$$[\Pi]=\begin{bmatrix}\Pi_{11} & \Pi_{12} & \Pi_{13} & 0 & 0 & 0\\ & \Pi_{22} & \Pi_{23} & 0 & 0 & 0\\ & & \Pi_{33} & 0 & 0 & 0\\ & & & \Pi_{44} & 0 & 0\\ & & & & \Pi_{55} & 0\\ & & & & & \Pi_{66}\end{bmatrix} \tag{10}$$

If $[\pi]$ and $[\Pi]$ have the form (10), then the reduced equation Tsai–Wu (8) is sensitive to a change of sign of normal stress, but insensitive to change of a sign of shear stress components. The reduced form of structural tensors (10) is defined by $3+9=12$ independent material constants. Hence, the complete tensorial form of the Tsai-Wu equation (8), that contains 12 independent material constants (9 for $[\Pi]$ and 3 for $[\pi]$), is furnished as

$$\begin{aligned}&\Pi_{11}\sigma_x^2+\Pi_{22}\sigma_y^2+\Pi_{33}\sigma_z^2\\&\quad+\Pi_{12}\sigma_x\sigma_y+\Pi_{23}\sigma_y\sigma_z+\Pi_{31}\sigma_z\sigma_x\\&\quad+\Pi_{44}\tau_{yz}^2+\Pi_{55}\tau_{zx}^2+\Pi_{66}\tau_{xy}^2\\&\quad+\pi_1\sigma_x+\pi_2\sigma_y+\pi_3\sigma_z-1=0\end{aligned} \tag{11}$$

or

$$\begin{Bmatrix}\sigma_x\\ \sigma_y\\ \sigma_z\\ \tau_{yz}\\ \tau_{zx}\\ \tau_{xy}\end{Bmatrix}\begin{bmatrix}\Pi_{11} & \Pi_{12} & \Pi_{13} & 0 & 0 & 0\\ & \Pi_{22} & \Pi_{23} & 0 & 0 & 0\\ & & \Pi_{33} & 0 & 0 & 0\\ & & & \Pi_{44} & 0 & 0\\ & & & & \Pi_{55} & 0\\ & & & & & \Pi_{66}\end{bmatrix}\times\begin{Bmatrix}\sigma_x\\ \sigma_y\\ \sigma_z\\ \tau_{yz}\\ \tau_{zx}\\ \tau_{xy}\end{Bmatrix}+\begin{Bmatrix}\sigma_x\\ \sigma_y\\ \sigma_z\\ \tau_{yz}\\ \tau_{zx}\\ \tau_{xy}\end{Bmatrix}\begin{bmatrix}\pi_1\\ \pi_2\\ \pi_3\\ 0\\ 0\\ 0\end{bmatrix}-1=0 \tag{12}$$

If the next reduction of the criterion (11) and (12) is done, to the case when only the second order term $\{\sigma\}^{\mathrm{T}}[\Pi]\{\sigma\}$ is independent of hydrostatic pressure, the following 9-parameter Pariseau–Tsai–Wu equation is obtained, in a partly deviatoric form (quadratic terms only), after Chen and Han [13]

$$\begin{aligned}&a_1(\sigma_y-\sigma_z)^2+a_2(\sigma_z-\sigma_x)^2\\&\quad+a_3(\sigma_x-\sigma_y)^2+a_4\tau_{yz}^2+a_5\tau_{zx}^2+a_6\tau_{xy}^2\\&\quad+a_7\sigma_x+a_8\sigma_y+a_9\sigma_z-1=0\end{aligned} \tag{13}$$

where following notation is used $a_1=-\Pi_{23}$, $a_2=-\Pi_{13}$, $a_3=-\Pi_{12}$, $a_4=\Pi_{44}$, $a_5=\Pi_{55}$, $a_6=\Pi_{66}$, and $a_7=\pi_1$, $a_8=\pi_2$, $a_9=\pi_3$. The above equation can alternatively be rewritten as

$$\begin{Bmatrix}\sigma_x\\ \sigma_y\\ \sigma_z\\ \tau_{yz}\\ \tau_{zx}\\ \tau_{xy}\end{Bmatrix}\begin{bmatrix}a_2+a_3 & -a_3 & -a_3 & 0 & 0 & 0\\ & a_3+a_1 & -a_1 & 0 & 0 & 0\\ & & a_1+a_2 & 0 & 0 & 0\\ & & & a_4 & 0 & 0\\ & & & & a_5 & 0\\ & & & & & a_6\end{bmatrix}$$
$$\times\begin{Bmatrix}\sigma_x\\ \sigma_y\\ \sigma_z\\ \tau_{yz}\\ \tau_{zx}\\ \tau_{xy}\end{Bmatrix}+\begin{Bmatrix}\sigma_x\\ \sigma_y\\ \sigma_z\\ \tau_{yz}\\ \tau_{zx}\\ \tau_{xy}\end{Bmatrix}\begin{bmatrix}a_7\\ a_8\\ a_9\\ 0\\ 0\\ 0\end{bmatrix}-1=0 \tag{14}$$

where the matrix–vector notation (14) is used. The above 9-parameter initial yield/failure criterion (13, 14) was first suggested by Pariseau [12] for anisotropic rocks and solids. Later, Tsai and Wu [10] proposed an analogous criterion, but they applied an additional condition of full independence of hydrostatic pressure, $a_9 = -(a_7 + a_8)$, so that the total number of independent parameters was finally reduced to 8.

Assume further (after Chen and Han [13]) that the plane (x, y) in (13), (14) is considered as the transverse isotropy plane. Hence, the coefficients in (13), (14) are not independent, but are subjected to the constraints

$$a_2 = a_1, \quad a_5 = a_4, \quad a_8 = a_7, \quad a_6 = 2(a_1 + 2a_3) \tag{15}$$

Substitution of (15) into (13) and (14), leads to the reduced 5-parameter Pariseau–Tsai–Wu criterion.

$$\begin{aligned}a_1[(\sigma_y-\sigma_z)^2+(\sigma_z-\sigma_x)^2]+a_3(\sigma_x-\sigma_y)^2\\ +a_4(\tau_{yz}^2+\tau_{zx}^2)+2(a_1+2a_3)\tau_{xy}^2\\ +a_7(\sigma_x+\sigma_y)+a_9\sigma_z-1=0\end{aligned} \tag{16}$$

This equation was originaly used by Ralston [14] for an ice crushing failure analysis. In order to calibrate the 5-parameter Pariseau–Tsai–Wu criterion (16), the following tests are to be performed:

– Uniaxial tension and compression in the (x, y) plane of transverse isotropy (e.g., x axis)

$$\begin{aligned}&\sigma_x = k_{tx};\ \sigma_y=\sigma_z=\tau_{xy}=\tau_{zx}=\tau_{zy}=0\\ &a_1k_{tx}^2+a_3k_{tx}^2+a_7k_{tx}=1\\ &\sigma_x=-k_{cx};\ \sigma_y=\sigma_z=\tau_{xy}=\tau_{zx}=\tau_{zy}=0\\ &a_1k_{cx}^2+a_3k_{cx}^2-a_7k_{cx}=1\end{aligned} \tag{17}$$

– Uniaxial tension and compression along the orthotropy axis (z axis)

$$\begin{aligned}&\sigma_z = k_{tz};\ \sigma_x=\sigma_y=\tau_{xy}=\tau_{zx}=\tau_{zy}=0\\ &2a_1k_{tz}^2+a_9k_{tz}=1\\ &\sigma_z=-k_{cz};\ \sigma_x=\sigma_y=\tau_{xy}=\tau_{zx}=\tau_{zy}=0\\ &2a_1k_{cz}^2-a_9k_{cz}=1\end{aligned} \tag{18}$$

– Simple shear in the plane of orthotropy (e.g., zx plane)

$$\begin{aligned}&\tau_{zx}=k_{zx};\ \sigma_x=\sigma_y=\sigma_z=\tau_{xy}=\tau_{zy}=0\\ &a_4k_{zx}^2=1\end{aligned} \tag{19}$$

where k_{ti} and k_{ci} stand for tensile and compressive strengths in corresponding directions $i = x, z$, and k_{zx} is the shear strength in the orthotropy plane. Finally, the following formulae for a_i independent constants $i = 1, 3, 4, 7$ and 9 are achieved

$$\begin{aligned}&a_1=\frac{1}{2k_{tz}k_{cz}},\quad a_3=\frac{1}{k_{tx}k_{cx}}-\frac{1}{2k_{tz}k_{cz}},\\ &a_4=\frac{1}{k_{zx}^2},\\ &a_7=\frac{1}{k_{tx}}-\frac{1}{k_{cx}},\quad a_9=\frac{1}{k_{tz}}-\frac{1}{k_{cz}}\end{aligned} \tag{20}$$

The Hill Versus the Mises–Hu–Marin Initial Yield Conditions: Limitation and Calibration

When only quadratic terms in the Goldenblat–Kopnov criterion (6) are retained, the general 21-parameter Mises yield/failure criterion ($\Pi_{ijkl} = M_{ijkl}$) is obtained

$$M_{ijkl}\sigma_{ij}\sigma_{kl} - 1 = 0 \tag{21}$$

In the case when the form non-sensitive to the change of sign of the normal stress exclusively is saved, (21) is reduced to the 9-parameter equation

$$\begin{aligned} &M_{11}\sigma_x^2 + M_{22}\sigma_y^2 + M_{33}\sigma_z^2 \\ &\quad + 2(M_{12}\sigma_x\sigma_y + M_{23}\sigma_y\sigma_z + M_{31}\sigma_z\sigma_x) \\ &\quad + M_{44}\tau_{yz}^2 + M_{55}\tau_{zx}^2 + M_{66}\tau_{xy}^2 - 1 = 0 \end{aligned} \tag{22}$$

If, additionally, transverse isotropy in the (xy) plane holds, $M_{11} = M_{22}$, $M_{13} = M_{23}$, $M_{44} = M_{55}$, $M_{66} = 2M_{11} - M_{12}$, and the 5-parameter transversely isotropic Mises criterion is obtained

$$\begin{aligned} &M_{11}(\sigma_x^2 + \sigma_y^2) + M_{33}\sigma_z^2 + 2[M_{12}\sigma_x\sigma_y \\ &\quad + M_{13}(\sigma_x\sigma_z + \sigma_z\sigma_y)] + M_{44}(\tau_{yz}^2 + \tau_{zx}^2) \\ &\quad + (2M_{11} - M_{12})\tau_{xy}^2 - 1 = 0 \end{aligned} \tag{23}$$

where M_{11}, M_{33}, M_{12}, M_{13}, M_{44} are 5 independent anisotropy parameters. The 5-parameter Mises criterion (23) is more general than the frequently used deviatoric Hill criterion, also transversely isotropic in the (xy) plane, in which the following holds: $H_{12} = H_{33} - 2H_{11}$ and $H_{13} = H_{33}$. Hence, the Hill criterion is furnished as

$$\begin{aligned} &H_{11}(\sigma_x^2 + \sigma_y^2) + H_{33}\sigma_z^2 \\ &+ (H_{33} - 2H_{11})\sigma_x\sigma_y - H_{33}(\sigma_x\sigma_z + \sigma_z\sigma_y) \\ &+ H_{44}\left(\tau_{yz}^2 + \tau_{zx}^2\right) + (4H_{11} - H_{33})\tau_{xy}^2 - 1 = 0 \end{aligned} \tag{24}$$

where only three parameters are independent, e.g., H_{11}, H_{33} and H_{44}, similarly as in (16), where linear terms are neglected.

In order to calibrate the 3-parameter transversely isotropic Hill criterion (24), two uniaxial tension (or compression) tests along the x and z axes, and one simple shear test in the zx plane have to be performed:

$$\begin{aligned} &\sigma_x = k_x;\ \sigma_y = \sigma_z = \tau_{zx} = \tau_{xy} = \tau_{yz} = 0 \\ &\quad \rightarrow H_{11} = 1/k_x^2 \\ &\sigma_z = k_z;\ \sigma_x = \sigma_y = \tau_{zx} = \tau_{xy} = \tau_{yz} = 0 \\ &\quad \rightarrow H_{33} = 1/k_z^2 \\ &\tau_{zx} = k_{zx};\ \sigma_x = \sigma_y = \sigma_z = \tau_{xy} = \tau_{yz} = 0 \\ &\quad \rightarrow H_{44} = 1/k_{zx}^2 \end{aligned} \tag{25}$$

where k_x, k_z and k_{zx} stand for tensile (or compression) strengths in directions x, z and shear strength in the orthotropy plane zx. Hence, Hill's criterion (24), can be rewritten as

$$\begin{aligned} &\frac{(\sigma_y - \sigma_z)^2 + (\sigma_z - \sigma_x)^2}{2k_z^2} + \left(\frac{1}{k_x^2} - \frac{1}{2k_z^2}\right) \\ &\quad \times (\sigma_x - \sigma_y)^2 + \left(\frac{\tau_{zx}}{k_{zx}}\right)^2 - 1 = 0 \end{aligned} \tag{26}$$

Alternatively, in the case of the 5-parameter, transversely isotropic Mises–Hu–Marin criterion (23), in order to identify five anisotropy modules, the following conditions can be used: four tests, namely, two uniaxial tensions along orthotropy and isotropy axes z and x, a simple shear test in the zx orthotropy plane and one biaxial (bulge) test in the isotropy plane xy. This schematically is shown in Fig. 1a, b

$$\begin{aligned} &\sigma_x = k_x;\ \sigma_y = \sigma_z = \tau_{zx} = \tau_{xy} = \tau_{yz} = 0 \\ &\quad \rightarrow M_{11} = 1/k_x^2 \\ &\sigma_z = k_z;\ \sigma_x = \sigma_y = \tau_{zx} = \tau_{xy} = \tau_{yz} = 0 \\ &\quad \rightarrow M_{33} = 1/k_z^2 \\ &\tau_{zx} = k_{zx};\ \sigma_x = \sigma_y = \sigma_z = \tau_{xy} = \tau_{yz} = 0 \\ &\quad \rightarrow M_{44} = 1/k_{zx}^2 \\ &\left.\begin{matrix}\sigma_x = \sigma_y \\ = k_{(xy)}\end{matrix}\right\};\ \sigma_z = \tau_{zx} = \tau_{xy} = \tau_{yz} = 0 \\ &\quad \rightarrow 2M_{12} = 1/k_{(xy)}^2 - 2/k_x^2 \end{aligned} \tag{27}$$

where, additionally, the biaxial test symbol $k_{(xy)}$ stands for strength measured in the bulge test in the transverse isotropy plane x, y.

Bulge tests were used, e.g., by Jackson et al. [15]. Additionally, one auxiliary condition in the orthotropy plane Fig. 1a, b is postulated:

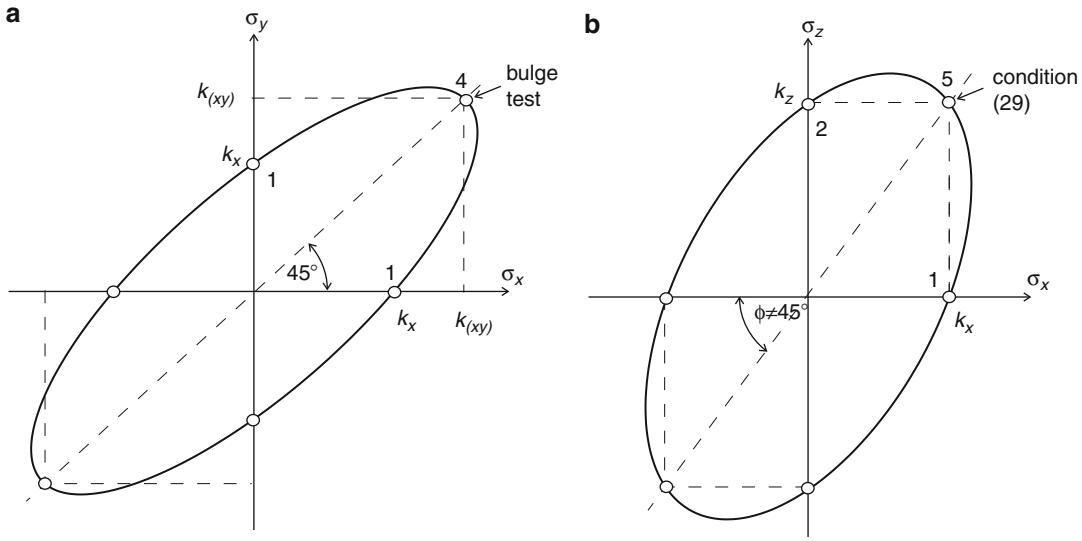

Anisotropic Initial Yield and Failure Criteria Including Temperature Effect, Fig. 1 Auxiliary conditions in biaxial bulge tests: (**a**) plane of transverse isotropy, (**b**) plane of orthotropy

$$\left.\begin{aligned}\sigma_x &= k_x\\ \sigma_z &= k_z\end{aligned}\right\};\sigma_z = \tau_{zx} = \tau_{xy} = \tau_{yz} = 0 \qquad (28)$$
$$\rightarrow 2M_{13} = 1/(k_x k_z)$$

Finally, the non-deviatoric Mises–Hu–Marin criterion (23) is furnished as, cf. Ganczarski and Skrzypek [16], which is a generalization of the plane stress Hu–Marin concept, Hu and Marin [17]

$$\frac{\sigma_x^2+\sigma_y^2}{k_x^2}+\left(\frac{\sigma_z}{k_z}\right)^2+\left(\frac{1}{k_{(xy)}^2}-\frac{2}{k_x^2}\right)\times\sigma_x\sigma_y-\frac{(\sigma_x+\sigma_y)\sigma_z}{k_x k_z}+\left(\frac{\tau_{zx}}{k_{zx}}\right)^2-1=0 \qquad (29)$$

where four independent material parameters k_x, k_z, k_{zx} and $k_{(xy)}$ (biaxial bulge test) have to be measured, with auxiliary condition (28) used. Note that the Mises–Hu-Marin equation (29) appears as a hydrostatic stress dependent one, by contrast to the Hill equation, (26), which satisfies hydrostatic stress independence. The above alternative assumptions: applying the deviatoric 3-parameter Hill's criterion (26), with three classical tests (k_x, k_z, k_{zx}) used, or the 5-parameter non-deviatoric Mises–Hu–Marin criterion (29), with an additional one biaxial bulge test in the isotropy plane xy and one auxiliary condition postulated in the ortho − tropy plane zx, are applied. Hill's criterion (26) holds for orthotropic materials, however, the degree of orthotropy cannot be arbitrarily large. In the case of a high degree of orthotropy, the Hill equation (24), admits the arbitrarily large stress states that do not result in yielding (cf. Ottosen and Ristinmaa [18]). The following inequality limits the range for Hill's criterion

$$\frac{2}{k_x^2k_y^2}+\frac{2}{k_y^2k_z^2}+\frac{2}{k_z^2k_x^2}>\frac{1}{k_x^4}+\frac{1}{k_y^4}+\frac{1}{k_z^4} \qquad (30)$$

In the narrower case of transverse isotropy ($k_x = k_y$), condition (30) reduces to a simpler form

$$\frac{1}{k_z^2}\left(\frac{4}{k_x^2}-\frac{1}{k_z^2}\right)>0 \qquad (31)$$

Substitution of the dimensionless parameter $R = 2(k_z/k_x)^2 - 1$, after Hosford and Backhofen [19], leads to a simplified form of Hill's criterion restriction (31)

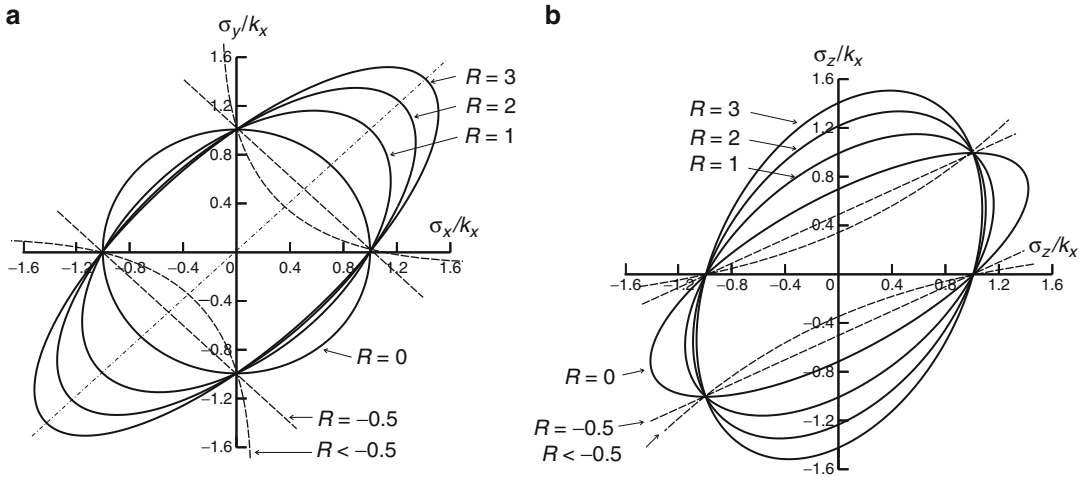

Anisotropic Initial Yield and Failure Criteria Including Temperature Effect, Fig. 2 Transformation of transversely isotropic Hill's limit surface with respect to magnitude of Hosford and Backhofen parameter: (**a**) transverse isotropy plane, (**b**) orthotropy plane

$$R > -0.5 \quad \text{or alternatively} \quad \frac{k_z}{k_x} > 0.5 \qquad (32)$$

However, the key point is that we have assumed the quadratic expression (24) and this expression only allows the yield surface to be a closed surface in the deviatoric stress space when (30) is fulfilled. If the above inequality does not hold, elliptic cross sections degenerate to two hyperbolic branches and the lack of convexity occurs. The yield curves in two planes: the transverse isotropy (σ_x, σ_y) and the orthotropy plane (σ_x, σ_z) for various R -values are sketched in Fig. 2a, b, respectively. It is observed that when R approaches the limit $R = -0.5$, the curves change from closed ellipses to two parallel lines, whereas for $R < -0.5$, concave hyperbolas appear (cf. Ottosen and Ristinmaa [18]). The five parameter Mises–Hu–Marin criterion is free from such restriction and can be used for an arbitrarily large degree of orthotropy.

Effect of Thermal Residual Stresses on the Initial Yield and Failure Surfaces in the Unidirectional Composites

Key Herakovich and Aboudi Findings

The effect of residual stresses in unidirectional composites on initial yield/failure surfaces was studied by Herakovich and Aboudi [11]. The authors considered the unidirectional MMC based on a Ti-15Al-3V matrix reinforced by SCS-6 silicon carbide fibers. Although both constituents behave strictly isotropically, an essential mismatch of thermo-mechanical properties between the constituents at the micro-level introduces strong anisotropy of the composite at the macro-level (representative unit-cell). They investigated initial yield surfaces of unidirectional lamina, composed of any number of layers, but all SCS fibres are in the same direction, the effective properties of which satisfy the transverse isotropy (cf. Table 1).

The plane $x = \mathrm{t}, y = \mathrm{t}$, perpendicular to the fiber direction, is the transverse isotropy plane, whereas the direction of fiber $z = \mathrm{a}$ coincides with the orthotropy axis (cf. Fig. 3). Symbols E_a, $E_\mathrm{t}, G_\mathrm{a}, G_\mathrm{t}, \nu_\mathrm{a}, \nu_\mathrm{t}, Y_\mathrm{a}, Y_\mathrm{t}$ and $\alpha_\mathrm{a}, \alpha_\mathrm{t}$ stand for axial and transverse: Young modulea, Kirchhoff modulae,7 Poisson ratios, yield strengths and thermal expansion coefficients, respectively. Figure 4a, c represents two families of yield surfaces referring to the fabrication temperature $T_\mathrm{i} = 575\ ^\circ\mathrm{C}$ and the operating temperature (after cooling-down) $T_\mathrm{f} = 20\ ^\circ\mathrm{C}$. Following bi-axial states of stress: combined axial and transverse normal (σ_x, σ_z), combined transverse normal (σ_x, σ_y), and combined out-of-plane orthotropic shear and

Anisotropic Initial Yield and Failure Criteria Including Temperature Effect, Table 1 Components and composite's properties, after Herakovich and Aboudi [11]

Property	Constituents			SCS-6/
	Fiber	Ti-15	Ti-6	Ti-15
	SCS-6	Al-3V	Al-4V	Al-3V
E_a (GPa)	414	91	113.7	221
E_t (GPa)	414	91	113.7	145
ν_a	0.25	0.25	0.3	0.27
ν_t	0.25	0.25	0.3	0.40
G_a (GPa)	165.5	3.33	43.73	53.2
G_t (GPa)	165.5	3.33	43.73	51.7
Y_a (MPa)	3,500	758	900	1,517
Y_t (MPa)	3,500	758	900	317
$\alpha_a \cdot 10^{-6}$ (K^{-1})	4.86	9.44	9.44	6.15
$\alpha_t \cdot 10^{-6}$ (K^{-1})	4.86	9.44	9.44	7.90

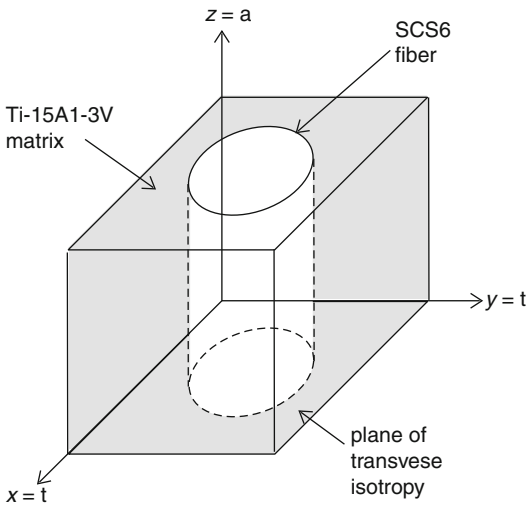

Anisotropic Initial Yield and Failure Criteria Including Temperature Effect, Fig. 3 Transverse isotropy of unidirectional long fiber composite SCS-6/Ti-15Al-3V

transverse normal (τ_{zx}, σ_x), are shown in Fig. 4a, c. At the considered temperature change, no yielding is observed during cooling-down, however, in the case of larger temperature change, yielding during cooling-down may be observed. Both translation and distortion of limit surfaces are noticed. The initial yielding/failure surfaces at the micro-level

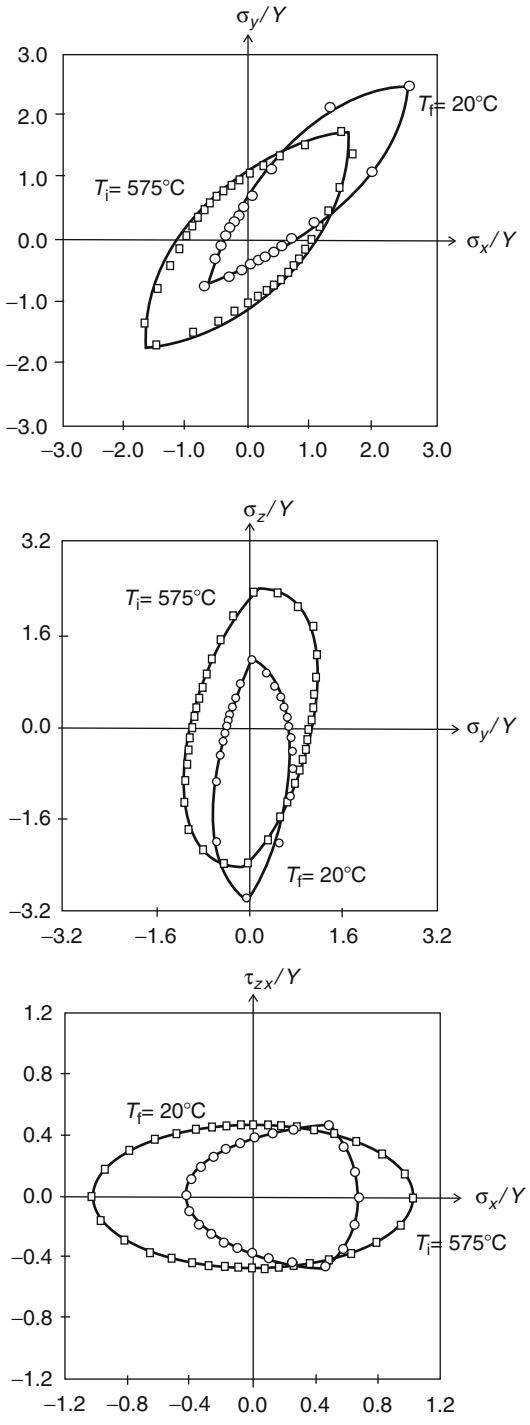

Anisotropic Initial Yield and Failure Criteria Including Temperature Effect, Fig. 4 Initial yield surfaces of transversely isotropic SCS-6/Ti-15Al-3V composite, based on Herakovich and Aboudi [11]

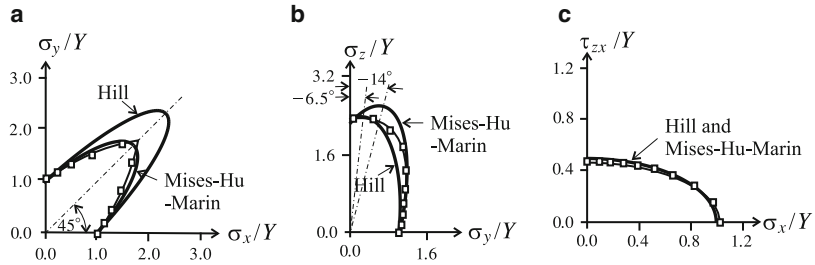

Anisotropic Initial Yield and Failure Criteria Including Temperature Effect, Fig. 5 Approximation of initial failure curves ($T_i = 575\,^\circ$C) of Herakovich and Aboudi experiments [11] by Hill's or Mises–Hu–Marin criterions: (**a**) orthotropy plane, (**b**) isotropy plane, (**c**) shear plane

have to account for the effect of changing residual stresses, which is different in the matrix and the fibres. It is seen that subsequent limit curves are no longer uniform ellipses but represent cross-sections of two limit curves, referring to individual matrix and fiber materials. The corners observed in Fig. 4a, c result from the intersection of different families of individual limit curves.

Modeling Unified Initial Limit Surfaces of SiC/ Ti Composite by Hill's Versus Mises–Hu–Marin's Criterions

Assuming at the beginning that the initial yield surface which corresponds to $T_i = 575\,^\circ$C is free from residual stresses, the classical Hill's approach ((26) for transversely isotropic material) can be tried. Taking the following cross-sections of the limit surface (26), we arrive at:
Isotropy plane ($k_x = Y, k_z = 2.3Y$)

$$\sigma_x^2 - 1.811\sigma_x\sigma_y + \sigma_y^2 = Y^2 \tag{33}$$

Orthotropy plane ($k_y = Y, k_z = 2.3Y$)

$$\sigma_y^2 - 0.189\sigma_y\sigma_z + 0.189\sigma_z^2 = Y^2 \tag{34}$$

Shear plane ($k_{zx} = 0.5Y, k_x = Y$)

$$\sigma_x^2 + 4\tau_{zx}^2 = Y^2 \tag{35}$$

Symbol Y stands for the yield point stress in the plane of transverse isotropy $k_x = k_y = Y$. The above cross-sections are shown in Fig. 5a, c. Hill's approximation fits well to orthotropy (a) and shear (c) planes. However, in the isotropy plane (b), fitting is non-satisfactory.

An assumption is made, therefore, of another approach based on Mises–Hu–Marin equation (29), leading to (cf. Ganczarski and Skrzypek [15]):
Isotropy plane ($k_x = Y, k_{(xy)} = 1.7Y$)

$$\sigma_x^2 - 1.654\sigma_x\sigma_y + \sigma_y^2 = Y^2 \tag{36}$$

Orthotropy plane ($k_y = Y, k_z = 2.3Y$)

$$\sigma_y^2 - 0.434\sigma_y\sigma_z + 0.189\sigma_z^2 = Y^2 \tag{37}$$

Shear plane ($k_{zx} = 0.5Y, k_x = Y$)

$$\sigma_x^2 + 4\tau_{zx}^2 = Y^2 \tag{38}$$

The Mises–Hu–Marin approach (36–38) is compared to Hill's approximation (33–35) in Fig. 5a, c. The Mises–Hu–Marin approach much better fits the Herakovich and Aboudi results in the isotropy plane (Fig. 5a), thanks to an acceptable mis-fitting in the orthotropy plane (Fig. 5b). A worse fitting by Hill's approximation in the isotropy plane (Fig. 3a), when compared to Mises–Hu–Marin approach, results from the influence of the magnitude of axial strength k_z disturbing condition in the isotropy plane (cf. previous discussion referring to applicability of Hill's criterion (31)).

Modeling Temperature Effect During Fabrication on Limit Surfaces by the Pariseau–Tsai–Wu Criterion

As it was mentioned above, temperature change during fabrication (cooling-down) results in both residual stresses, different in

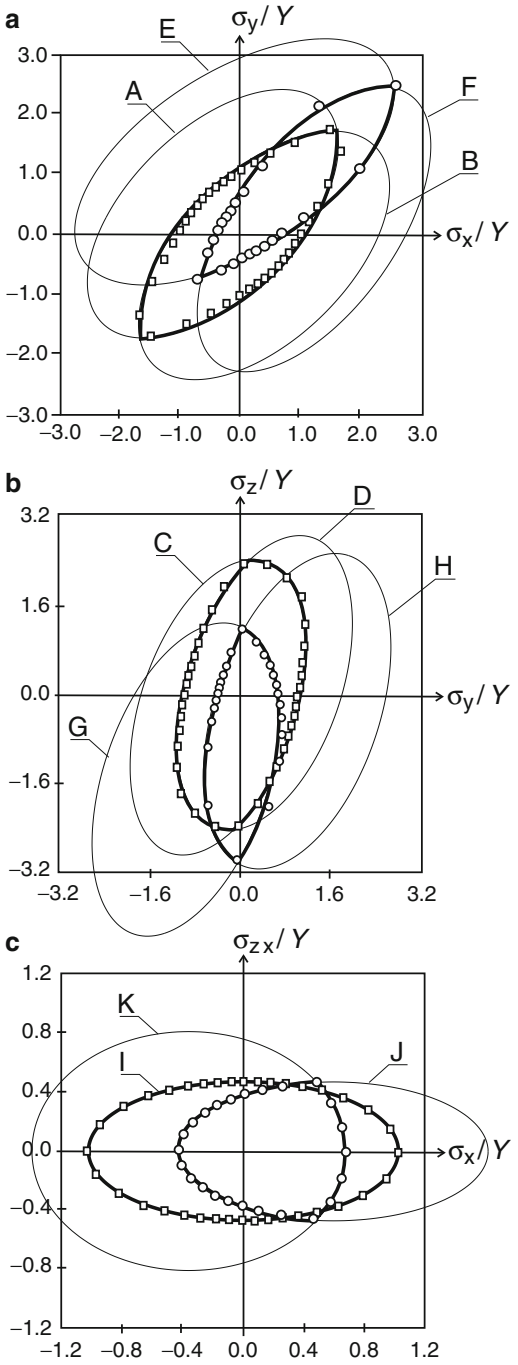

Anisotropic Initial Yield and Failure Criteria Including Temperature Effect, Fig. 6 Cross sections of SCS-6/Ti-15-3 failure surfaces: (**a**) orthotropy plane, (**b**) isotropy plane, (**c**) shear plane, □ – $T_i = 575\,^\circ\mathrm{C}$, ○ – $T_f = 20\,^\circ\mathrm{C}$, experimental results by Herakovich and Aboudi [11] vs. Pariseau–Tsai–Wu approximation

matrix and fiber materials, and a change of material modules of both composite constituents. The appearance of residual stresses manifests itself mainly in translation of limit surfaces for matrix and fiber materials, whereas temperature dependence of anisotropy modules results in a change of size and distortion of limit surfaces. Hence, instead of the unified approach at the level of a representative unit cell, cf. Herakovich and Aboudi [11], the micro-approach should be applied, for matrix and fiber materials separately (7). The Pariseau–Tsai–Wu 5-parameter criterion (16) combined with material constants calibration (20), are used. This approach allows the accurate approximation of two families of limit curves in considered planes, referring to matrix and fiber materials at two temperatures $T_i = 575\,^\circ\mathrm{C}$ and $T_f = 20\,^\circ\mathrm{C}$, where T_i stands for initial fabrication temperature, and T_f for final temperature after cooling-down. At the initial temperature $T_i = 575\,^\circ\mathrm{C}$, this leads to (cf. Ganczarski and Skrzypek [16]):

Isotropy plane $\Sigma_x = \sigma_x/Y, \Sigma_y = \sigma_y/Y$

$$\begin{aligned} \text{(A)}\quad & 0.505\Sigma_x^2 - 0.445\Sigma_x\Sigma_y + 0.404\Sigma_y^2 \\ & + 0.560\Sigma_x = 1 \\ \text{(B)}\quad & 0.376\Sigma_x^2 - 0.414\Sigma_x\Sigma_y + 0.376\Sigma_y^2 \\ & - 0.408\Sigma_x + 0.408\Sigma_y = 1 \end{aligned} \tag{39}$$

Orthotropy plane $(\Sigma_y = \sigma_y/Y, \Sigma_z = \sigma_z/Y)$

$$\begin{aligned} \text{(C)}\quad & 0.530\Sigma_y^2 - 0.251\Sigma_y\Sigma_z + 0.184\Sigma_z^2 \\ & + 0.361\Sigma_y - 8.14\cdot 10^{-3}\Sigma_z = 1 \\ \text{(D)}\quad & 0.541\Sigma_y^2 - 0.256\Sigma_y\Sigma_z + 0.188\Sigma_z^2 \\ & - 0.435\Sigma_y + 3.99\cdot 10^{-3}\Sigma_z = 1 \end{aligned} \tag{40}$$

Shear plane $\Sigma_x = \sigma_x/Y, \Sigma_{zx} = \tau_{zx}/Y$

$$\text{(I)}\quad 0.942\Sigma_x^2 + 4.527\Sigma_{zx}^2 = 1 \tag{41}$$

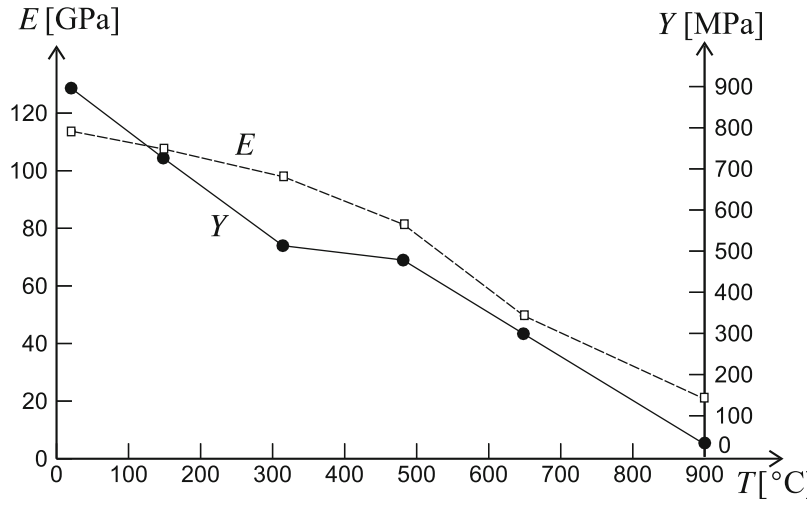

Anisotropic Initial Yield and Failure Criteria Including Temperature Effect,
Fig. 7 Temperature dependent matrix properties of the Ti-6Al-4V system, following Herakovich and Aboudi [11]

And, at final temperature $T_f = 20\,^{\circ}\mathrm{C}$, we arrive at:
Isotropy plane $\Sigma_x = \sigma_x/Y, \Sigma_y = \sigma_y/Y$

$$\begin{aligned} \text{(E)}\quad & 0.500\Sigma_x^2 - 0.725\Sigma_x\Sigma_y + 0.823\Sigma_y^2 \\ & + 1.000\Sigma_x - 2.130\Sigma_y = 1 \\ \text{(F)}\quad & 0.912\Sigma_x^2 - 0.866\Sigma_x\Sigma_y + 0.596\Sigma_y^2 \\ & - 2.102\Sigma_x + 0.921\Sigma_y = 1 \end{aligned} \tag{42}$$

Orthotropy plane $(\Sigma_y = \sigma_y/Y, \Sigma_z = \sigma_z/Y)$

$$\begin{aligned} \text{(G)}\quad & 0.276\Sigma_y^2 - 0.384\Sigma_y\Sigma_z + 0.276\Sigma_z^2 \\ & + 0.935\Sigma_y + 4.92\Sigma_z = 1 \\ \text{(H)}\quad & 0.934\Sigma_y^2 - 0.445\Sigma_y\Sigma_z + 0.320\Sigma_z^2 \\ & - 2.01\Sigma_y + 0.65 \cdot 10^{-3}\Sigma_z = 1 \end{aligned} \tag{43}$$

Shear plane $\Sigma_x = \sigma_x/Y, \Sigma_{zx} = \tau_{zx}/Y$

$$\begin{aligned} \text{(J)}\quad & 1.426\Sigma_x^2 + 6.852\Sigma_{zx}^2 - 1.712\Sigma_x = 1 \\ \text{(K)}\quad & 1.065\Sigma_x^2 + 1.723\Sigma_{zx}^2 + 0.746\Sigma_x = 1 \end{aligned} \tag{44}$$

In the above, the upper case Σ_i stands for dimensionless stress components. The results are shown and compared with Herakovich and Aboudi findings [11] in Fig. 6.

Effect of Temperature Dependent Parameters

In the above simulation, all material properties of composite constituents were considered as temperature independent. On the contrary, in a more accurate analysis, the residual stresses, induced during the cooling-down fabrication process, in constituents result from a mismatch of the temperature dependent properties of both phases: matrix and fiber. Additionally, subsequent yield/failure surfaces have to account for temperature dependent properties: initial yielding of the metal matrix, governed by an actual value of the yield point stress of titanium matrix in the Ti-6Al-4V system, cf. Fig. 7.

This effect can essentially change the predicted initial yield curves of the composite, as shown in Fig. 8, after Herakovich and Aboudi. It is clearly visible, that neglecting temperature dependence of properties, leads to non-acceptable overestimation of a safety region of the system considered at an elevated temperature of 300 °C, when compared to the more accurate temperature-dependent analysis. This error basically results from the fact that the magnitude of the yield point stress is twice as high at the room temperature as at temperature 300 °C.

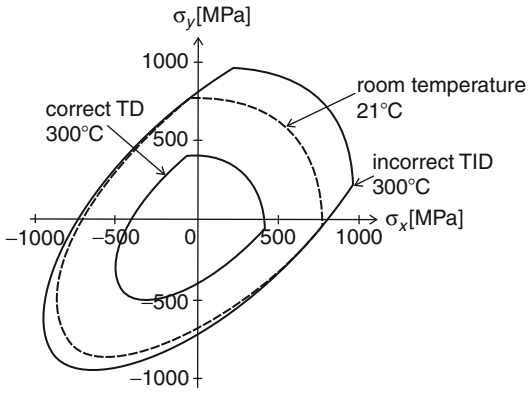

Anisotropic Initial Yield and Failure Criteria Including Temperature Effect, Fig. 8 Temperature independent (TID) vs. temperature dependent (TD) yield surfaces of SiC/Ti composite, following Herakovich and Aboudi [11]

Acknowledgement This work was supported by National Science Centre Poland grant Nr UMO-2011/03/B/ST8/05132.

References

1. Hill R (1948) A theory of the yielding and plastic flow of anisotropic metals. Proc R Soc Lond A193:281–297
2. Życzkowski M (2001) Anisotropic yield conditions. In: Lemaitre J (ed) Handbook of materials behavior models. Academic, San Diego, pp 155–165
3. Betten J (1988) Applications of tensor functions to the formulation of yield criteria for anisotropic materials. Int J Plast 4:29–46
4. Sayir M (1970) Zur Fließbedingungen der Plastizitäts Theorie. Ingenieurarchiv 39:414–432
5. Goldenblat II, Kopnov VA (1966) A generalized theory of plastic flow of anisotropic metals (in Russian), Stroitelnaya Mekhanika, 307–319
6. Spencer AJM (1971) Theory of invariants. In: Eringen C (ed) Continuum physics, Academic Press, New York, pp 239–353
7. Rymarz Cz (1993) Continuum mechanics. PWN, Warszawa (in Polish)
8. Rogers TG (1990) Yield criteria, flow rules, and hardening in anisotropic plasticity. In: Boehler JP (ed) Yielding, damage and failure of anisotropic solids. Mechanical Engineering Publications, London, pp 53–79
9. Kowalsky UK, Ahrens H, Dinkler D (1999) Distorted yield surfaces – modeling by higher order anisotropic hardening tensors. Comput Mater Sci 16:81–88
10. Tsai ST, Wu EM (1971) A general theory of strength for anisotropic materials. Int J Numer Methods Eng 38:2083–2088
11. Herakovich CT, Aboudi J (1999) Thermal effects in composites. In: Hetnarski RB (ed) Thermal stresses V. Lastran Corporation, Rochester, pp 1–142
12. Pariseau WG (1968) Plasticity theory for anisotropic rocks and solids, Chapter 10. In: Proceeding of 10th symposium on rock mechanics, Austin
13. Chen WF, Han DJ (1995) Plasticity for structural engineers. Springer, Berlin/Heidelberg
14. Ralston TD (1977) Yield and plastic deformation in ice crushing failure. In: ICSI.AIDJEX Symposium on sea ice-processes and models, Seattle
15. Jackson LR, Smith KF, Lankford WT (1948) Plastic flow in anisotropic sheet steel. Am Inst Min Metall Eng 2440:1–15
16. Ganczarski A, Skrzypek J (2011) Modeling of limit surfaces for transversely isotropic composite SCS-6/Ti-15-3. Acta Mech Autom 5(3):25–32 (in Polish)
17. Hu ZW, Marin J (1956) Anisotropic loading functions for combined stresses in the plastic range. J Appl Mech 22:1
18. Ottosen NS, Ristinmaa M (2005) The mechanics of constitutive modeling. Elsevier, Amsterdam
19. Hosford WF, Backhofen WA (1964) Strength and plasticity of textured metals. In: Burke J, Coffin L, Reed N, Weisse V, Backhofen WA (eds) Fundamentals of deformation processing. Syracuse University Press, Syracuse, pp 259–298

Anisotropic Materials

▶ Linear Thermoelastic Model

Anisotropic Shells

▶ Temperature Profiles in Composite and Sandwich Shells

Anisotropic Thermoelastic Contact Problems

David L. Clements
School of Mathematics, The University of Adelaide, Adelaide, SA, Australia

Synonyms

Anisotropic

Overview

There exists an extensive literature on thermoelastic contact problems for isotropic materials. For such materials the thermal and elastic constants referred to a Cartesian frame are identical for any orientation of the axes within the material. In contrast for anisotropy the thermal and elastic constants are not identical for all orientations of a coordinate frame within the material. As a result the mathematical equations governing thermoelastic deformations of anisotropic materials are considerably more complex than for isotropic materials. This substantially restricts the classes of problems for which usable analytical solutions to contact problems can be obtained

From the middle of the twentieth century to the present, there has been a substantial increase in the use of composite materials in applications. From a macroscopic viewpoint, composites are often satisfactorily modeled as homogeneous anisotropic materials. Furthermore, in many applications of composite materials thermal effects are significant. This has led to an increased interest in the analysis of anisotropic thermoelastic problems. In the area of contact problems the mathematical difficulties in obtaining analytical solutions result in solutions of such problems being restricted to particular classes of anisotropic materials and/or restricted geometries for the material and the region of contact. Such restrictions may be relaxed if numerical techniques such as the boundary element and finite element methods are used so that a more substantial class of such problems may be solved by employing these techniques.

Here, the linear mathematical model for uncoupled rectilinear thermoelasticity is presented for the wide class of problems which do not involve inertia or coupling effects. The particular classes of anisotropic materials and geometries for which analytical solutions to contact problems within this model may be obtained are identified together with an outline of the analytical techniques which facilitate these solutions. Also, a boundary integral equation formulation of the solution of the equations of the mathematical model is briefly discussed as a possible method for the numerical solution of contact problems for general anisotropy.

Governing Equations

Consider a Cartesian frame $Ox_1x_2x_3$ in a homogeneous rectilinear anisotropic thermoelastic material occupying a region Ω with boundary $\partial\Omega$ in R^3.

We wish to determine the steady state stress induced in the body Ω due to a specified distribution of temperature and displacement or stress over the boundary $\partial\Omega$ resulting from contact with a second body.

Here, attention is largely restricted to the substantial class of contact problems which can be satisfactorily represented by considering the case when the body Ω consists of a half-space bounded by a plane surface [1].

Disregarding body forces and the coupling of the deformation and temperature fields, the steady state temperature distribution $T(x_1, x_2, x_3)$ in an anisotropic material satisfies the heat conduction equation [2]

$$\lambda_{ij}\frac{\partial^2 T}{\partial x_i \partial x_j} = 0 \tag{1}$$

where $\lambda_{ij} = \lambda_{ij}$ are the coefficients of heat conduction and the repeated suffix convention (summing from 1 to 3) is used for Latin suffices only. The flux across a boundary surface of the material with outward pointing normal $\mathbf{n} = (n_1, n_2, n_3)$ is given by $-P$ where

$$P = \lambda_{ij}\frac{\partial T}{\partial x_j}n_i \tag{2}$$

If P is specified over the whole of the boundary $\partial\Omega$ of the material, then it is explicitly required that

$$\int_{\partial\Omega} P\,ds = 0 \tag{3}$$

The equation relating the temperature and elastic displacement u_k to the stress σ_{ij} in the material takes the form

$$\sigma_{ij} = c_{ijkl}\frac{\partial u_k}{\partial x_l} - \beta_{ij}T \tag{4}$$

where c_{ijkl} are the elastic constants and β_{ij} are the stress temperature coefficients. These constants satisfy the symmetry relations

$$c_{ijkl} = c_{klij} = c_{jikl} = c_{ijlk}, \qquad \beta_{ij} = \beta_{ji} \tag{5}$$

The stresses σ_{ij} given by (4) must satisfy the equilibrium equations $\partial\sigma_{ij}/\partial x_j = 0$ and hence,

$$c_{ijkl}\frac{\partial^2 u_k}{\partial x_j \partial x_l} - \beta_{ij}\frac{\partial T}{\partial x_j} = 0 \tag{6}$$

Given a temperature distribution which satisfies (1), the solution to (6) can be written as a sum

$$u_k = u_k^{(1)} + u_k^{(2)} \tag{7}$$

where $u_k^{(1)}$ is a displacement which satisfies the nonhomogeneous system (6) and $u_k^{(2)}$ denotes a solution to the homogeneous system

$$c_{ijkl}\frac{\partial^2 u_k}{\partial x_j \partial x_l} = 0 \tag{8}$$

The stress corresponding to the displacements $u_k^{(1)}$ and $u_k^{(2)}$ may be written as a sum in the form

$$\sigma_{ij} = \sigma_{ij}^{(1)} + \sigma_{ij}^{(2)} \tag{9}$$

where the stress $\sigma_{ij}^{(1)}$ is obtained by substituting $u_k = u_k^{(1)}$ into (4) while $\sigma_{ij}^{(2)}$ is obtained by substituting $u_k = u_k^{(2)}$ into $\sigma_{ij} = c_{ijkl}\partial u_k/\partial x_l$.

Three-Dimensional Problems

For general rectilinear anisotropy, (6) does not readily yield useful analytical solutions to particular contact problems of interest. By restricting attention to a particular class of anisotropic materials, it is possible to obtain solutions to a number of significant contact problems.

In particular for transversely isotropic materials, representations for the displacements u_k satisfying (6) may be obtained in terms of three potential functions. These representations lend themselves to the use of integral transforms to facilitate the solution of contact problems for layers and half-spaces for which the boundary surface(s) are transverse planes of the material.

For a transversely isotropic half-space occupying the region $x_3 \le 0$ with the Ox_3 axis normal to the transverse planes, the nonzero coefficients of heat conduction are $\lambda_{11} = \lambda_{22}$ and λ_{33}, and hence, the equation for the temperature (1) may be written in the form

$$\nabla^2 T + K^2\frac{\partial^2 T}{\partial x_3^2} = 0 \quad \text{where} \quad \nabla^2 = \frac{\partial^2}{\partial x_1^2} + \frac{\partial^2}{\partial x_2^2} \tag{10}$$

and $K^2 = \lambda_{33}/\lambda_{11}$. Also, the stress temperature coefficients are $\beta_{11} = \beta_{22}$ and β_{33}, and the nonzero c_{ijkl} may be expressed in terms of five constants c_{11}, c_{12}, c_{13}, c_{33}, and c_{44} as follows:

$$c_{1111} = c_{2222} = c_{11}, \quad c_{1122} = c_{12}, \quad c_{1133} = c_{2233} = c_{13} \tag{11}$$

$$c_{1313} = c_{2323} = c_{44}, \quad c_{1212} = (c_{11} - c_{12})/2, \quad c_{3333} = c_{33} \tag{12}$$

Use of (11) and (12) in (6) provides

$$c_{11}\frac{\partial^2 u_1}{\partial x_1^2} + \frac{c_{11} - c_{12}}{2}\frac{\partial^2 u_1}{\partial x_2^2} + c_{44}\frac{\partial^2 u_1}{\partial x_3^2} + \frac{\partial}{\partial x_1}\left[\frac{c_{11} + c_{12}}{2}\frac{\partial u_2}{\partial x_2} + (c_{13} + c_{44})\frac{\partial u_3}{\partial x_3}\right] - \beta_{11}\frac{\partial T}{\partial x_1} = 0 \tag{13}$$

$$\frac{c_{11} - c_{12}}{2}\frac{\partial^2 u_2}{\partial x_1^2} + c_{11}\frac{\partial^2 u_2}{\partial x_2^2} + c_{44}\frac{\partial^2 u_2}{\partial x_3^2} + \frac{\partial}{\partial x_2}\left[\frac{c_{11} + c_{12}}{2}\frac{\partial u_1}{\partial x_1} + (c_{13} + c_{44})\frac{\partial u_3}{\partial x_3}\right] - \beta_{11}\frac{\partial T}{\partial x_2} = 0 \tag{14}$$

$$c_{44}\left[\frac{\partial^2 u_3}{\partial x_1^2}+\frac{\partial^2 u_3}{\partial x_2^2}\right]+c_{33}\frac{\partial^2 u_3}{\partial x_3^2} + (c_{13}+c_{44})\frac{\partial}{\partial x_3}\left[\frac{\partial u_1}{\partial x_1}+\frac{\partial u_2}{\partial x_2}\right]-\beta_{33}\frac{\partial T}{\partial x_3}=0 \tag{15}$$

Let the displacements assume the form [3]

$$u_k = u_k^{(1)} + u_k^{(2)} \tag{16}$$

with

$$u_1^{(1)}=\frac{\partial \psi}{\partial x_1},\quad u_2^{(1)}=\frac{\partial \psi}{\partial x_2},\quad u_3^{(1)}=\mu\frac{\partial \psi}{\partial x_3} \tag{17}$$

$$u_1^{(2)}=\frac{\partial \phi}{\partial x_1},\quad u_2^{(2)}=\frac{\partial \phi}{\partial x_2},\quad u_3^{(2)}=k\frac{\partial \phi}{\partial x_3} \tag{18}$$

where k and μ are constants. For a given T the displacements $u_k^{(1)}$ provide a solution to the inhomogeneous system (13)–(15) while the displacements $u_k^{(2)}$ provide a solution to the associated homogeneous system. Substituting (16)–(18) into (13) and (14), it follows that these equations will be satisfied if ϕ and ψ are solutions to the equations

$$c_{11}\nabla^2\phi+[c_{44}+k(c_{13}+c_{44})]\frac{\partial^2\phi}{\partial x_3^2}=0 \tag{19}$$

$$c_{11}\nabla^2\psi+[c_{44}+\mu(c_{13}+c_{44})]\frac{\partial^2\psi}{\partial x_3^2}-\beta_{11}T=0 \tag{20}$$

Also, (15) will be satisfied if ϕ and ψ are solutions to the equations

$$[(c_{13}+c_{44})+kc_{44}]\nabla^2\phi+kc_{33}\frac{\partial^2\phi}{\partial x_3^2}=0 \tag{21}$$

$$[(c_{13}+c_{44})+\mu c_{44}]\nabla^2\psi+\mu c_{33}\frac{\partial^2\psi}{\partial x_3^2}-\beta_{33}T=0 \tag{22}$$

Set

$$\frac{c_{44}+k(c_{13}+c_{44})}{c_{11}}=\frac{kc_{33}}{(c_{13}+c_{44})+kc_{44}}=v \tag{23}$$

Elimination of k from (23) yields the quadratic for v

$$c_{11}c_{44}v^2+[c_{13}(c_{13}+2c_{44})-c_{11}c_{33}]v + c_{33}c_{44}=0 \tag{24}$$

Thus, (19)–(21) will be satisfied if ϕ is given by

$$\left[\nabla^2+v_\alpha\frac{\partial^2}{\partial x_3^2}\right]\phi_\alpha=0 \quad \text{for} \quad \alpha=1,2 \tag{25}$$

where v_1, v_2 are the roots of the quadratic (24). The corresponding values of k obtained from (23) are k_1 and k_2. Equations (16)–(18) thus yield

$$\begin{aligned} u_1&=\frac{\partial}{\partial x_1}(\phi_1+\phi_2+\psi)\\ u_2&=\frac{\partial}{\partial x_2}(\phi_1+\phi_2+\psi)\end{aligned} \tag{26}$$

$$u_3=\left(k_1\frac{\partial\phi_1}{\partial x_3}+k_2\frac{\partial\phi_2}{\partial x_3}+\mu\frac{\partial\psi}{\partial x_3}\right) \tag{27}$$

and the stresses

$$\sigma_{11}=\left[c_{11}\frac{\partial^2}{\partial x_1^2}(\phi_1+\phi_2+\psi)+c_{12}\frac{\partial^2}{\partial x_2^2}(\phi_1+\phi_2+\psi) + c_{13}\left(k_1\frac{\partial^2\phi_1}{\partial x_3^2}+k_2\frac{\partial^2\phi_2}{\partial x_3^2}+\mu\frac{\partial^2\psi}{\partial x_3^2}\right)\right]-\beta_{11}T \tag{28}$$

$$\sigma_{22}=\left[c_{12}\frac{\partial^2}{\partial x_1^2}(\phi_1+\phi_2+\psi)+c_{11}\frac{\partial^2}{\partial x_2^2}(\phi_1+\phi_2+\psi) +c_{13}\left(k_1\frac{\partial^2\phi_1}{\partial x_3^2}+k_2\frac{\partial^2\phi_2}{\partial x_3^2}+\mu\frac{\partial^2\psi}{\partial x_3^2}\right)\right]-\beta_{11}T \tag{29}$$

$$\sigma_{33}=\left[c_{13}\frac{\partial^2}{\partial x_1^2}(\phi_1+\phi_2+\psi)+c_{13}\frac{\partial^2}{\partial x_2^2}(\phi_1+\phi_2+\psi) +c_{33}\left(k_1\frac{\partial^2\phi_1}{\partial x_3^2}+k_2\frac{\partial^2\phi_2}{\partial x_3^2}+\mu\frac{\partial^2\psi}{\partial x_3^2}\right)\right]-\beta_{33}T \tag{30}$$

$$\sigma_{12}=(c_{11}-c_{12})\frac{\partial^2}{\partial x_1\partial x_2}(\phi_1+\phi_2+\psi) \tag{31}$$

$$\sigma_{13} = c_{44}\left[(1+k_1)\frac{\partial^2\phi_1}{\partial x_1\partial x_3} + (1+k_2)\frac{\partial^2\phi_2}{\partial x_1\partial x_3} + (1+\mu)\frac{\partial^2\psi}{\partial x_1\partial x_3}\right] \tag{32}$$

$$\sigma_{23} = c_{44}\left[(1+k_1)\frac{\partial^2\phi_1}{\partial x_2\partial x_3} + (1+k_2)\frac{\partial^2\phi_2}{\partial x_2\partial x_3} + (1+\mu)\frac{\partial^2\psi}{\partial x_2\partial x_3}\right] \tag{33}$$

These representations are particularly useful for the solution of contact problems if attention is restricted to axially symmetric problems so that in terms of cylindrical coordinates (r, θ, z), with the temperature, displacement, and stress independent of θ (25), (20), and (22) can be written as

$$\left[\frac{\partial^2}{\partial r^2} + \frac{1}{r}\frac{\partial}{\partial r} + v_\alpha\frac{\partial^2}{\partial z^2}\right]\phi_\alpha = 0 \quad \text{for} \quad \alpha = 1, 2 \tag{34}$$

$$c_{11}\left[\frac{\partial^2}{\partial r^2} + \frac{1}{r}\frac{\partial}{\partial r}\right]\psi + [c_{44} + \mu(c_{13} + c_{44})]\frac{\partial^2\psi}{\partial z^2} - \beta_{11}T = 0 \tag{35}$$

$$[(c_{13} + c_{44}) + \mu c_{44}]\left[\frac{\partial^2}{\partial r^2} + \frac{1}{r}\frac{\partial}{\partial r}\right]\psi + \mu c_{33}\frac{\partial^2\psi}{\partial z^2} - \beta_{33}T = 0 \tag{36}$$

and the nonzero displacements and stresses are given by

$$u_r = \frac{\partial}{\partial_r}(\phi_1 + \phi_2 + \psi)$$
$$u_z = \frac{\partial}{\partial_z}(k_1\phi_1 + k_2\phi_2 + \mu\psi) \tag{37}$$

$$\sigma_{rr} = \left[c_{11}\frac{\partial^2}{\partial r^2}(\phi_1 + \phi_2 + \psi) + \frac{c_{12}}{r}\frac{\partial}{\partial r}(\phi_1 + \phi_2 + \psi) + c_{13}\left(k_1\frac{\partial^2\phi_1}{\partial z^2} + k_2\frac{\partial^2\phi_2}{\partial z^2} + \mu\frac{\partial^2\psi}{\partial z^2}\right)\right] - \beta_{11}T \tag{38}$$

$$\sigma_{\theta\theta} = \left[c_{12}\frac{\partial^2}{\partial r^2}(\phi_1 + \phi_2 + \psi) + \frac{c_{11}}{r}\frac{\partial}{\partial r}(\phi_1 + \phi_2 + \psi) + c_{13}\left(k_1\frac{\partial^2\phi_1}{\partial z^2} + k_2\frac{\partial^2\phi_2}{\partial z^2} + \mu\frac{\partial^2\psi}{\partial z^2}\right)\right] - \beta_{11}T \tag{39}$$

$$\sigma_{zz} = \left[c_{13}\frac{\partial^2}{\partial r^2}(\phi_1 + \phi_2 + \psi) + \frac{c_{13}}{r}\frac{\partial}{\partial r}(\phi_1 + \phi_2 + \psi) + c_{33}\left(k_1\frac{\partial^2\phi_1}{\partial z^2} + k_2\frac{\partial^2\phi_2}{\partial z^2} + \mu\frac{\partial^2\psi}{\partial z^2}\right)\right] - \beta_{33}T \tag{40}$$

$$\sigma_{rz} = \left[(1+k_1)c_{44}\frac{\partial^2\phi_1}{\partial r\partial z} + (1+k_2)c_{44}\frac{\partial^2\phi_2}{\partial r\partial z} + (1+\mu)c_{44}\frac{\partial^2\psi}{\partial r\partial z}\right] \tag{41}$$

Equations (10) and (34) admit solutions in the form [4]

$$T(r, z) = \int_0^\infty \mathcal{A}(\xi)e^{-\xi z/K}J_0(\xi r)\,d\xi \tag{42}$$

$$\phi_\alpha(r, z) = \int_0^\infty \mathcal{C}_\alpha(\xi)e^{-\xi z_\alpha}J_0(\xi r)\,d\xi, \quad \text{for} \quad \alpha = 1, 2 \tag{43}$$

where $z_\alpha = z/\sqrt{v_\alpha}$ and $\mathcal{A}(\xi)$ and $\mathcal{C}_\alpha(\xi)$ are functions which are determined by the boundary conditions for particular boundary value problems. Also, (35) and (36) admit solutions of the form

$$\psi(r, z) = \int_0^\infty \mathcal{A}(\xi)\mathcal{B}(\xi)e^{-\xi z/K}J_0(\xi r)\,d\xi \tag{44}$$

provided $\mathcal{B}(\xi)$ and μ satisfy the equations

$$\mu = \frac{\beta_{11}K^2(c_{13} + c_{44}) + \beta_{33}(c_{44} - c_{11}K^2)}{\beta_{11}(c_{33} - K^2c_{44}) - \beta_{33}(c_{13} + c_{44})} \tag{45}$$

$$\xi^2\mathcal{B}(\xi) = K^2\frac{\beta_{11}(c_{33} - c_{44}K^2) - \beta_{33}(c_{13} + c_{44})}{(c_{44} - c_{11}K^2)(c_{33} - c_{44}K^2) + K^2(c_{13} + c_{44})^2} \tag{46}$$

The representations (42), (43), and (44) for the solutions to (10), (34), (35), and (36) provide, through the use of standard results for Hankel transforms [4], the solution to a number of axially symmetric contact problems for a transversely isotropic half-space occupying the region $z \leq 0$ [5]. For example, Sharma [3] determines expressions for $\mathcal{A}(\xi), \mathcal{C}_1(\xi)$, and $\mathcal{C}_2(\xi)$ for the case when the boundary $z = 0$ is subjected to a constant temperature over the region $r \leq a$ while the remainder of the surface is at zero temperature. Substitution of these functions in (42), (43), and (44) then provides $T(r, z)$, $\phi_\alpha(r, z)$, and $\psi(r, z)$. Equations (37)–(41) then give the stress and displacement throughout the half-space. Also, Grilitskii and Shelestovskii [6] consider the thermoelastic effects resulting from the indentation of the boundary $z = 0$ of a transversely isotropic half-space by an axially symmetric rigid punch at a constant temperature with both the heat flux and stress zero on $z = 0$ outside the contact region.

Generalized Plane Problems

For generalized plane problems, the temperature, displacement, and stress depend only on two Cartesian coordinates which, without loss of generality, may be taken to be x_1 and x_2. In this case (1) admits a general solution in terms of an arbitrary analytic function $\chi(z)$ in the form

$$T(x_1, x_2) = \chi(z) + \bar{\chi}(\bar{z}) \tag{47}$$

where the bar denotes the complex conjugate and $z = x_1 + \tau x_2$ where τ is the solution with positive imaginary part of the quadratic equation

$$\lambda_{11} + 2\lambda_{12}\tau + \lambda_{22}\tau^2 = 0 \tag{48}$$

Since T is given by (47), we try for a particular solution to (6) in the form [7]

$$u_k^{(1)} = C_k \phi(z) + \bar{C}_k \bar{\phi}(\bar{z}) \tag{49}$$

where the C_k are constants and

$$\phi'(z) = \chi(z) \tag{50}$$

where the prime on the analytic function indicates differentiation with respect to the argument in question. The displacement (49) will be a solution to (6) if

$$D_{ik} C_k = \gamma_i \tag{51}$$

where

$$\begin{aligned} D_{ik} &= c_{i1k1} - c_{i2k2} + \tau(c_{i1k2} + c_{i2k1}) \\ &\quad + \tau^2 c_{i2k2} \quad \text{and} \quad \gamma_i = \beta_{i1} + \tau\beta_{i2} \end{aligned} \tag{52}$$

Equations (51) serve to determine the constants C_k. From (4), the stress field corresponding to the displacement field (49) may be written in the form

$$\sigma_{ij}^{(1)} = (E_{ij} - \beta_{ij})\phi'(z) + (\bar{E}_{ij} - \beta_{ij})\bar{\phi}'(\bar{z}) \tag{53}$$

where

$$E_{ij} = (c_{ijk1} + \tau c_{ijk2}) C_k \tag{54}$$

The solution to (6) consists of the particular solution given by (49) together with any solution of the associated homogeneous system (8) which, for generalized plane problems, has the general solution [8]

$$u_k^{(2)} = 2\Re\left[\sum_{\alpha=1}^{3} A_{k\alpha} f_\alpha(z_\alpha)\right] \tag{55}$$

where $\Re$ denotes the real part of a complex number, $f_\alpha(z_\alpha)$, $\alpha = 1, 2, 3$ are arbitrary analytic functions of the complex variables $z_\alpha = x_1 + \tau_\alpha x_2$, $\alpha = 1, 2, 3$ where τ_α are the three roots with positive imaginary part of the sextic in τ

$$|c_{i1k1} + c_{i2k1}\tau + c_{i1k2}\tau + c_{i2k2}\tau^2| = 0 \tag{56}$$

The $A_{i\alpha}$ occurring in (55) are the solutions of the system

$$(c_{i1k1} + c_{i2k1}\tau_\alpha + c_{i1k2}\tau_\alpha + c_{i2k2}\tau_\alpha^2) A_{k\alpha} = 0 \tag{57}$$

Use of (55) in (4) provides a representation for $\sigma_{ij}^{(2)}$ in terms of the arbitrary functions $f_\alpha(z_\alpha)$ in the form

$$\sigma_{ij}^{(2)} = 2\Re\left[\sum_{\alpha=1}^{3} L_{ij\alpha} f'_\alpha(z_\alpha)\right] \tag{58}$$

where primes denote differentiation with respect to the argument in question and

$$L_{ij\alpha} = (c_{ijk1} + \tau_\alpha c_{ijk2}) A_{k\alpha} \tag{59}$$

Thus, from (49), (53), (55), and (58) the solution to (6) may be written in the form

$$u_k = u_k^{(1)} + u_k^{(2)} = 2\Re\left[\sum_{\alpha=1}^{3} A_{k\alpha} f_\alpha(z_\alpha) + C_k \phi(z)\right] \tag{60}$$

$$\begin{aligned}\sigma_{ij} &= \sigma_{ij}^{(1)} + \sigma_{ij}^{(2)} \\ &= 2\Re\left[\sum_{\alpha=1}^{3} L_{ij\alpha} f'_\alpha(z_\alpha) + (E_{ij} - \beta_{ij})\phi'(z)\right]\end{aligned} \tag{61}$$

For a half-space occupying the region $x_2 \le 0$, the analytic functions $\chi(z)$, $\phi(z)$, and $f_\alpha(z_\alpha)$ in (47), (60), and (61) may be chosen to satisfy given boundary conditions on $x_2 = 0$. In particular, the theory of complex analytic functions can be employed to choose these functions for the solution of various thermoelastic contact problems for the half-space $z \le 0$ while integral transform techniques can be used to choose the functions for the solution of classes of contact problems involving the half-space and also the slab $-h \le x_2 \le 0$.

For example, the integral representations

$$\phi(z) = \int_0^\infty \mathcal{A}(p) p^{-1} \exp(ipz)\, dp \tag{62}$$

$$f_\alpha(z) = \int_0^\infty \mathcal{C}_\alpha(p) \exp(ipz)\, dp \tag{63}$$

may be substituted into (50), (47), (60), and (61) and the mixed boundary conditions on $x_2 = 0$ for the indentation of an anisotropic half-space by a heated rigid punch applied to provide two equations for the unknown functions $\mathcal{A}(p)$ and $\mathcal{C}_\alpha(p)$. The inverse Fourier transform then provides explicit expressions for the functions $\mathcal{A}(p)$ and $\mathcal{C}_\alpha(p)$.

In using complex function theory to solve plane contact problems, it is often advantageous to use an alternative form of the representations (60) and (61).

For example, if the temperature $T(x_1, 0)$ and displacement $u_2(x_1, 0)$ are specified on the segment $-a < x_1 < a$ of the boundary $x_2 = 0$ of the half-space $x_2 < 0$ and the temperature and stresses $\sigma_{i2}(x_1, 0)$ are zero outside this interval, then Cauchy's integral formula yields the function $\chi(z)$

$$\chi(z) = \frac{1}{2\pi i} \int_{-a}^{a} \frac{T(t, 0)}{t - z}\, dt \tag{64}$$

and integrating provides the function $\phi(z)$ in the form

$$\phi(z) = -\frac{1}{2\pi i} \int_{-a}^{a} \log(t - z)\, dt \tag{65}$$

To obtain the displacement and stress, it is useful to define new analytic functions $\theta_i(z)$ for $i = 1, 2, 3$ by

$$f_\alpha(z) = M_{i\alpha} \theta_i(z) \tag{66}$$

where

$$\delta_{ik} = \sum_{\alpha=1}^{3} L_{i2\alpha} M_{\alpha k} \tag{67}$$

Substitution of (66) into (60) and (61) yields

$$u_k = 2\Re\left[\sum_{\alpha=1}^{3} A_{k\alpha} M_{\alpha j} \theta_j(z_\alpha) + C_k \phi(z)\right] \tag{68}$$

$$\sigma_{ij} = 2\Re\left[\sum_{\alpha=1}^{3} L_{ij\alpha} M_{\alpha r} \theta'_r(z_\alpha) + (E_{ij} - \beta_{ij})\phi'(z)\right] \tag{69}$$

In particular, on $x_2 = 0$ for the contact problem under consideration, (68) and (69) provide

$$B_{kj}\theta_j'(x_1) + \overline{B}_{kj}\overline{\theta}_j'(x_1) = g_k'(x_1) \quad \text{for} - a < x_1 < a \tag{70}$$

$$\theta_i'(x_1) + \overline{\theta}_i'(x_1) = -(E_{ix} - \beta_{i2})\phi'(x_1) \quad \text{for} \quad x_1 < -a \quad \text{and} \quad x_1 > a \tag{71}$$

where

$$B_{kr} = \sum_{\alpha=1}^{3} A_{k\alpha}M_{\alpha r} \tag{72}$$

and

$$g_k(x_1) = u_k(x_1, 0) - 2\Re[C_k\phi(x_1)] \tag{73}$$

The problem of determining the analytic function $\theta(z)$ thus reduces to a Hilbert problem for which the solution is well documented [8].

Boundary Integral Equations

The analytical techniques so far outlined are only applicable for restricted materials and/or geometries. More general applicability may be obtained by employing numerical techniques such as the boundary element method. A number of boundary element formulations for uncoupled thermoelastic problems involve a thermal domain integral. A formulation which removes the need to calculate domain integrals and which may be employed for the numerical solution of generalized plane contact problems involves first using the standard boundary integral equation [8] for the temperature field

$$\lambda T(\mathrm{x}_0) + (\lambda_{11})^{-1}\int_{\partial\Omega}[P(\mathrm{x})\Phi(\mathrm{x}, \mathrm{x}_0) - \Gamma(\mathrm{x}, \mathrm{x}_0)T(\mathrm{x})]\,ds(\mathrm{x}) = 0 \tag{74}$$

where $\mathrm{x} = (x_1, x_2)$, $\lambda = 1$ if $\mathrm{x}_0 = (a, b) \in \Omega$, $0 < \lambda < 1$ if $\mathrm{x}_0 \in \partial\Omega$ and Φ and Γ are given by

$$\Phi(x_1, x_2; a, b) = \frac{-1}{2\pi i(\tau - \overline{\tau})}\left(\frac{\lambda_{11}}{\lambda_{22}}\right)\{\log(z - c) + \log(\overline{z} - \overline{c})\} \tag{75}$$

$$\Gamma(x_1, x_2; a, b) = \lambda_{ij}\frac{\partial\Phi}{\partial x_j}n_i = \frac{\mathcal{M}}{z - c} + \frac{\overline{\mathcal{M}}}{\overline{z} - \overline{c}} \tag{76}$$

where $c = a + \tau b$ and

$$\mathcal{M} = \frac{-1}{2\pi i(\tau - \overline{\tau})}\left(\frac{\lambda_{11}}{\lambda_{22}}\right)\{\lambda_{11}n_1 + \lambda_{12}n_2 + (\lambda_{12}n_1 + \lambda_{22}n_2)\tau\}$$

Equation (74) provides a means for calculating numerical values for the real part of the function $\chi(z)$ in (47) and also for calculating values of the function P in (2) on the boundary $\partial\Omega$.

The second step in the boundary element formulation involves using this information to obtain the imaginary part of the function $\chi(z)$, and then, in turn, equations (50) and (49) yield the analytic function $\phi(z)$ and the particular solution to the equilibrium equations (6). Let

$$\chi(z) = (T + iV)/2 \tag{77}$$

The function T is available from (74) and V is an unknown real function. The function V may be determined as follows [9]. From (2), (47), and (48)

$$\begin{aligned} P(x_1, x_2) &= \lambda_{ij}\frac{\partial T}{\partial x_j}n_i \\ &= 2\Re[(\lambda_{11} + \tau\lambda_{12})n_1\chi'(z) \\ &\quad + (\lambda_{21} + \tau\lambda_{22})n_2\chi'(z)] \\ &= 2\Re[(-\tau n_1 + n_2)(\lambda_{21} + \tau\lambda_{22})\chi'(z)] \end{aligned} \tag{78}$$

Integrating (78) along the boundary $\partial\Omega$ yields

$$\begin{aligned} \int_{s_0}^{s} P(q)dq &= 2\Re\int_{s_0}^{s}(\lambda_{21} + \tau\lambda_{22})(-\tau n_1 + n_2)\chi'(z)dq \\ &= -2\Re[(\lambda_{21} + \tau\lambda_{22})\int_{z_0}^{z}\chi'(z)dz \\ &= -2\Re[(\lambda_{21} + \tau\lambda_{22})(\chi(z) - \chi(z_0))] \end{aligned} \tag{79}$$

where s_0 is a fixed and s an arbitrary point corresponding, respectively, to the points z_0 and z on $\partial\Omega$. Let $\tau = \tau' + i\tau''$ where τ' and τ'' are real. Then using (77), it follows from (79)

that the function $V(s)$ is given at all points of the boundary by

$$V(s) = (\tau''\lambda_{22})^{-1}\left[(\lambda_{21} + \tau'\lambda_{22})[T(s) - T(s_0)] + \int_{s_0}^{s} P(q)dq\right] \tag{80}$$

where $V(s_0)$ is taken to be zero. Then $\phi(z)$ on the boundary is given by

$$\phi(z) = \int_{z_0}^{z} \chi(t)\, dt \quad \text{for } z \in \partial\Omega \tag{81}$$

where the line integral is taken along boundary $\partial\Omega$ from z_0 to z. Also, for interior points Cauchy's integral formula provides

$$\chi(z) = \frac{1}{2\pi i}\int_{\partial\Omega} \frac{\chi(t)\, dt}{t - z} \quad \text{for } z \in \Omega$$

and integration gives $\phi(z)$ in the form

$$\phi(z) = \frac{-1}{2\pi i}\int_{\partial\Omega} \chi(t)\log(t - z)\, dt \quad \text{for } z \in \Omega \tag{82}$$

Substitution of the equations (81) and (82) into (49) provides a particular solution $u_k^{(1)}$ to the equilibrium (6) with the corresponding stresses $\sigma_{ij}^{(1)}$ given by (50) and (53). A solution $u_k^{(2)}$ to the associated homogeneous system (8) can be added to this particular solution to the equilibrium equations so that the total displacement and stress satisfies the boundary conditions on $\partial\Omega$. The standard boundary integral equation [8] which may be used to numerically calculate the desired solution to the associated homogeneous equation takes the form

$$\lambda u_j^{(2)}(\mathrm{x}_0) + \int_{\partial\Omega} \mathcal{P}_i(\mathrm{x})\Phi_{ij}(\mathrm{x},\mathrm{x}_0) - \Gamma_{ij}(\mathrm{x},\mathrm{x}_0)u_j^{(2)}(\mathrm{x})]\, ds(\mathrm{x}) = 0 \tag{83}$$

where $\lambda = 1$ if $\mathrm{x}_0 = (a, b) \in \Omega$ and $0 < \lambda < 1$ if $\mathrm{x}_0 \in \partial\Omega$,

$$\mathcal{P}_i = c_{ijkl}\frac{\partial u_k^{(2)}}{\partial x_l} n_j \tag{84}$$

$$\Phi_{km} = \frac{1}{2\pi}\Re\left[\sum_{\alpha} A_{k\alpha}N_{\alpha j}\log(z_\alpha - c_\alpha)\right] d_{jm} \tag{85}$$

$$\Gamma_{km} = c_{ijkl}\frac{\partial \Phi_{km}}{\partial x_l} n_j \tag{86}$$

where $N_{\alpha k}$ and c_α (for $\alpha = 1, 2, 3$) are defined by

$$\delta_{ik} = \sum_{\alpha=1}^{3} A_{i\alpha}N_{\alpha k} \quad \text{and} \quad c_\alpha = a + \tau_\alpha b \tag{87}$$

The procedure outlined in this section provides a boundary element method which may be used to numerically solve generalized plane thermoelastic contact problems for anisotropic materials. The method makes use of the standard boundary integral equations for anisotropic thermostatics (74) and anisotropic elastostatics (83) with the only additional calculation required being the simple boundary integrals in (80), (81), and (82).

References

1. Johnson K (1985) Contact mechanics. Cambridge University Press, Cambridge
2. Nowacki W (1962) Thermoelasticity. Addison-Wesley, Reading Mass
3. Sharma B (1958) Thermal stresses in transversely isotropic semi-infinite elastic solids. J Appl Mech, Trans ASME 80:86–88
4. Sneddon IN (1951) Fourier transforms. McGraw-Hill, New York
5. Tauchert TR (1975) A review: quasistatic thermal stresses in anisotropic elastic bodies, with applications to composite materials. Acta Mechanica 23:113–115
6. Grilitskii DV, Shelestovskii BG (1970) An axisymmetric contact problem of thermoelasticity for a transverse isotropic half-space. Prikladnaya Mekhanika 6:807–811
7. Clements DL (1973) Thermal stress in an anisotropic half-space. SIAM J APPL Math 24:332–337
8. Clements DL (1981) Boundary value problems governed by second order elliptic systems. Pitman, Boston
9. Ang WT, Clements DL, Cooke T (1999) A boundary element method for generalized plane thermoelastic deformations of anisotropic elastic media. Math Mech Solids 4:307–319

Anisotropy

▶ Thermal Stresses of Thin Films on Flexible Substrates
▶ Wave-Field in Anisotropic Thermoviscoelastic Media

Annular Problems with a Point Heat Source

Ching-Kong Chao
Department of Mechanical Engineering, National Taiwan University of Science and Technology, Taipei, Taiwan, Republic of China

Overview

One of the most difficult parts in solving the annular problem with doubly connected regions is that the single-valued condition of the displacements and the stresses must be satisfied. The problem will become more complicated if singularities or point heat sources reside in the annulus. In this work, we first determine the temperature distributions of the annular problem subject to a point heat source and then solve for the thermal stresses. In the derivation of the thermal field, the strength of a point heat source must be properly chosen. This is because that the condition of energy balance between a point heat source and the given prescribed temperature distributions along the inner and outer boundaries must be satisfied. Having the solution of the temperature field, the thermal stresses in the annular region is determined by the method based on analytic continuation theorem in conjunction with Laurent series expansions. The undetermined coefficients appearing in the series solution are solved using the Fourier series expansions. Both the stress-free and displacement-free conditions are considered either on the inner boundary or on the outer boundary. In the present analysis, we exclude the case of the displacement-free condition considered on the inner and outer boundaries of the annulus. However, the method is easily extended to solve the displacement-free boundary for which the resultant force over an annular region is not zero which must be determined after the solution is obtained. The solution derived in the present problem with a point heat source can be used as a Green's function which allows us to derive the solution for the problem with distributed sources that is frequently encountered in practical applications.

Formulation of the Annular Problem

For two-dimensional thermoelastic problems, the resultant force and displacements can be expressed in terms of two stress potentials $\phi(z)$, $\psi(z)$ and a single temperature potential $g'(z)$ as [1]

$$-Y + iX = \phi(z) + z\overline{\phi'(z)} + \overline{\psi(z)} \tag{1}$$

$$2\mu(u + iv) = \kappa\phi(z) - z\overline{\phi'(z)} + \overline{\psi(z)} + 2\mu\beta \int g'(z)dz \tag{2}$$

where $-Y + iX$ is the resultant force over an arc of the boundary measured from some fixed point; u and v are the displacements in the x-y plane; $\kappa = 3 - 4v$, $\beta = (1 + v)\alpha$ for plane strain and $\kappa = 3 - v/1 + v$, $\beta = \alpha$ for plane stress with α being thermal expansion coefficient and v the Poisson's ratio; μ is the shear modulus; and z is the complex coordinate: $z = x + iy$, and the bars denote complex conjugation. The components of stress in polar coordinate system are

$$\sigma_{rr} + \sigma_{\theta\theta} = 2\left[\phi'(z) + \overline{\phi'(z)}\right] \tag{3}$$

$$\sigma_{rr} + i\tau_{r\theta} = \phi'(z) + \overline{\phi'(z)} - \left[z\overline{\phi''(z)} + \frac{\overline{z}}{z}\overline{\psi'(z)}\right] \tag{4}$$

Consider a circular annulus with inner radius a and outer radius b which is subjected to a point heat source with the strength q_0 located at the

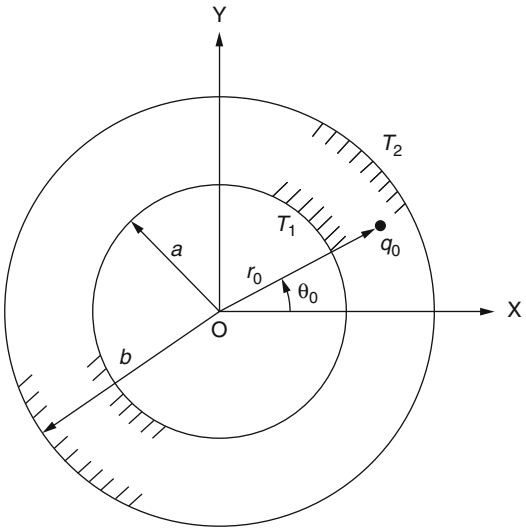

Annular Problems with a Point Heat Source, Fig. 1 Problem configuration for the annulus

point $z = z_0 = r_0 e^{i\theta}$ (see Fig. 1). For steady-state heat conduction problem, the temperature potential $g'(z)$ can be written as

$$g'(z) = Q_0 \ln(z - z_0) + \sum_{n=-\infty}^{\infty} \lambda_n z^n \qquad (5)$$

where $Q_0 = q_0/2\pi k$ with k being heat conductivity and λ_n are the unknown coefficients which will be determined as the thermal boundary condition is imposed. In the present analysis, the temperatures at the inner and outer boundaries of the annulus are denoted by $T_1(\theta)$ and $T_2(\theta)$, respectively, i.e.,

$$T = \frac{1}{2}\left[g'(t) + \overline{g'(t)}\right] = T_1(\theta) = \sum_{m=0}^{\infty} (A_m \cos m\theta + B_m \sin m\theta) \quad \text{on } t = ae^{i\theta} \qquad (6)$$

$$T = \frac{1}{2}\left[g'(t) + \overline{g'(t)}\right] = T_2(\theta) = \sum_{m=0}^{\infty} (A'_m \cos m\theta + B'_m \sin m\theta) \quad \text{on } t = be^{i\theta} \qquad (7)$$

On substituting (5) into (6) and (7) and applying the techniques of Fourier series, we find

$$\lambda_0 = A_0 - \frac{Q_0}{4\pi} \times \int_0^{2\pi} \ln\left[a^2 + r_0^2 - 2ar_0\cos(\theta - \theta_0)\right] d\theta \qquad (8)$$

$$\lambda_n = \frac{1}{2\pi\left(b^{2n} - a^{2n}\right)} \int_0^{2\pi} \left\{ 2\left(b^n T_2 - a^n T_1\right) - Q_0\left[b^n \ln\left(b^2 + r_0^2 - 2br_0\cos(\theta - \theta_0)\right)\right] - a^n \ln\left(a^2 + r_0^2 - 2ar_0\cos(\theta - \theta_0)\right) \right\} e^{-in\theta} d\theta \quad (n \neq 0) \qquad (9)$$

and for consistency, we require

$$A'_0 = A_0 - \frac{Q_0}{4\pi} \times \int_0^{2\pi} \ln\left(a^2 + r_0^2 - 2ar_0\cos(\theta - \theta_0)\right) - \ln\left(b^2 + r_0^2 - 2br_0\cos(\theta - \theta_0)\right) \qquad (10)$$

It should be emphasized that the strength of a point heat source must be chosen to satisfy (10) such that the condition of energy balance between a point source and the temperatures prescribed at the inner and outer boundaries of the annulus is ensured within the context of steady-state heat conduction theory [2]. Mathematically, the difference between A'_0 and A_0 in (10), which accounts for the net heat flow from outside to inside the annulus, must be equal to the integral term which accounts for the heat generation due to the presence of a point heat source. For the problem with the absence of a point heat source, the temperature potential in (5) is replaced by

$$g'(z) = \lambda^* \ln z + \sum_{n=-\infty}^{\infty} \lambda_n z^n \qquad (11)$$

where the unknown coefficients λ^* and $\lambda^*\lambda_n$ can be obtained from (8)–(10) by putting $Q_0 = \lambda^*$and $r_0 = 0$ as

$$\lambda^* = \frac{A'_0 - A_0}{\ln b - \ln a}, \lambda_0 = \frac{A_0 \ln b - A'_0 \ln a}{\ln b - \ln a} \quad (12)$$

and

$$\lambda_n = \frac{(b^n A'_n - a^n A_n) - i(b^n B'_n - a^n B_n)}{b^{2n} - a^{2n}} \quad (n \neq 0) \quad (13)$$

$$\lambda_{-n} = \frac{(b^{-n} A'_n - a^{-n} A_n) - i(b^{-n} B'_n - a^{-n} B_n)}{b^{-2n} - a^{-2n}} \quad (n \neq 0) \quad (14)$$

Upon integration of (5) and (11), the temperature functions become

$$g(z) = Q_0[(z - z_0)(\ln(z - z_0) - 1)] + \lambda_{-1} \ln z + g^*(z) \quad (15)$$

and

$$g(z) = \lambda^* z(\ln z - 1) + \lambda_{-1} \ln z + g^*(z) \quad (16)$$

respectively, where

$$g^*(z) = \sum_{\substack{n=-\infty \\ n \neq -1}}^{\infty} \frac{\lambda_n}{n+1} z^{n+1} \quad (17)$$

is analytic and single-valued everywhere in the annulus.

Thermal Stresses in the Annulus

For the annular problem with a point heat source, the stress functions can be written as [3]

$$\phi(z) = Az \ln z + B \ln z + \phi^*(z) \quad (18)$$

$$\psi(z) = C \ln z + \psi^*(z) \quad (19)$$

where A is real constant and B, C are complex constants which are related by the following equations [3]:

$$(\kappa + 1)Az + \kappa B + \overline{C} = \frac{-2\mu\beta}{2\pi i}[g(z)]_c \quad (20)$$

$$B - \overline{C} = \frac{[-Y + iX]_c}{2\pi i} \quad (21)$$

where $[f(z)]_c = f(r, \theta + 2\pi) - f(r, \theta)$ which denotes the jump of the function $f(z)$ when enclosing the contour c within the annulus.

Note that the singularity of the term z ln zappearing in (18) results from the logarithmic singularity of thetemperature function induced by a point heat source. The two holomorphic functions in (18) and (19), respectively, can be expressed in a series form as

$$\phi^*(z) = \sum_{n=-\infty}^{\infty} L_n z^n, \psi^*(z) = \sum_{n=-\infty}^{\infty} M_n z^n \quad (22)$$

where the constant coefficients L_n and M_n may be determined asthe stress or displacement boundary condition is imposed. The boundary condition on the innerand outer boundaries of the annulus can be expressed, respectively, as

$$\gamma_1 \phi(t) + t\overline{\phi'(t)} + \overline{\psi(t)} + \delta_1 g(t) = f_1(t) \quad \text{on } t = ae^{i\theta} \quad (23)$$

$$\gamma \phi(t) + t\overline{\phi'(t)} + \overline{\psi(t)} + \delta_2 g(t) = f_2(t) \quad \text{on } t = ae^{i} \quad (24)$$

where $\gamma_1 = \gamma_2 = 1$, $\delta_1 = \delta_2 = 0$, $f_1(t) = f_2(t) = R(t)$ for the stress boundary value problem with $R(t)$ being a known resultant force on the inner and outerboundaries of the annulus, while $\gamma_1 = \gamma_2 = -k$, $\delta_1 = \delta_2 = -2\mu\beta$, $f_1(t) = f_2(t) = -2\mu\beta D(t)$ for the displacementboundary value problem with $D(t)$ being a single-valued displacementfunction. Since the case of the displacement-free condition on both the inner and outerboundaries of the annulus is excluded from our analysis, the resultant force

over the entiresystem becomes zero, and the unknown coefficients A, B, and C appearing in (18) and (19) can beobtained by substituting (15) and (16) into (20) and (21) as

$$A = \frac{-2\mu\beta Q_0}{1+\kappa},\ B = \overline{C} = \frac{-2\mu\beta(\lambda_{-1} - Q_0 z_0)}{1+\kappa},$$
$$\text{for } |z_0| < z < b \tag{25}$$

$$A = \frac{-2\mu\beta Q_0}{1+\kappa}, B = \overline{C} = \frac{-2\mu\beta\lambda_{-1}}{1+\kappa},$$
$$\text{for } a < z < |z_0| \tag{26}$$

where $Q_0 = -q_0/2\pi k$, $R_0 = 0$ for the problem with a point heat source and $Q_0 = R_0 = \lambda^*$, $z_0 = 0$ for the problem with theabsence of a point heat source. Substitution of (15), (16), (18), and (19) into (23) and (24) results in

$$\gamma_1\phi^*(t) + t\overline{\phi^{*\prime}(t)} + \overline{\psi^*(t)} + \delta_1 g^*(t) = F_1(t)$$
$$\text{on } t = ae^{i\theta} \tag{27}$$

$$\gamma_2\phi^*(t) + t\overline{\phi^{*\prime}(t)} + \overline{\psi^*(t)} + \delta_2 g^*(t) = F_2(t)$$
$$\text{on } t = ae^{i\theta} \tag{28}$$

where

$$\begin{aligned} F_1(t) = {} & f_1(t) \\ & + \gamma_1\left(\frac{2\mu\beta R_0}{1+\kappa} t\ln t + \frac{2\mu\beta\lambda_{-1}}{1+\kappa}\ln t\right) \\ & + \frac{2\mu\beta R_0}{1+\kappa} t(1+\ln t) + \frac{2\mu\beta\overline{\lambda_{-1}}}{1+\kappa}\frac{t}{\overline{t}} \\ & + \frac{2\mu\beta\lambda_{-1}}{1+\kappa}\ln\overline{t} \\ & - \delta_1 Q_0[(t-z_0)\ln(t-z_0)] \\ & - \delta_1\lambda_{-1}\ln t + \delta_1 Q_0(t-z_0) \end{aligned} \tag{29}$$

and

$$\begin{aligned} F_2(t) = {} & f_2(t) \\ & + \gamma_2\left(\frac{2\mu\beta Q_0}{1+\kappa} t\ln t + \frac{2\mu\beta(\lambda_{-1} - Q_0 z_0)}{1+\kappa}\ln t\right) \\ & + t\frac{2\mu\beta Q_0}{1+\kappa}(1+\ln t) \\ & + \frac{2\mu\beta(\overline{\lambda_{-1}} - Q_0\overline{z_0})}{1+\kappa}\frac{t}{\overline{t}} \\ & + \frac{2\mu\beta(\lambda_{-1} - Q_0 z_0)}{1+\kappa}\ln\overline{t} \\ & - \delta_2 Q_0[(t-z_0)\ln(t-z_0)] \\ & - \delta_2\lambda_{-1}\ln t + \delta_2 Q(t-z_0) \end{aligned} \tag{30}$$

Compatibility Identity

Consider the annular region $a < |z| < b$ by S and the annuli, $a^2b^{-1}|z| < a$, $b < |z| < b^2a^{-1}$ by S^- and S^+, respectively (see Fig. 2). If we use the continuation across each boundary, $\phi*(z)$ can be extended from S into the annuli S^- and S^+ by the definitions [4]

$$\phi^* = -\frac{1}{\gamma_1} \times \left\{\overline{z\phi^{*\prime}\left(\frac{a^2}{\overline{z}}\right)} + \overline{\psi^*\left(\frac{a^2}{\overline{z}}\right)} + \delta_1 g^*(z)\right\}$$
$$\text{for } z \in S^- \tag{31}$$

$$\phi^*(z) = -\frac{1}{\gamma_2}\left\{\overline{z\phi^{*\prime}\left(\frac{b^2}{\overline{z}}\right)} + \overline{\psi^*\left(\frac{b^2}{\overline{z}}\right)} + \delta_2 g^*(z)\right\}$$
$$\text{for } z \in S^+ \tag{32}$$

$\phi^*(z)$ is thus holomorphic in the three regions S^-, S, and S^+. Notice that $g^*(z)$ is also holomorphic and single-valued in S^- and S^+ because there is no singularity or point heat source located in the region $S^-$and S^+. If we invert these continuations, we find

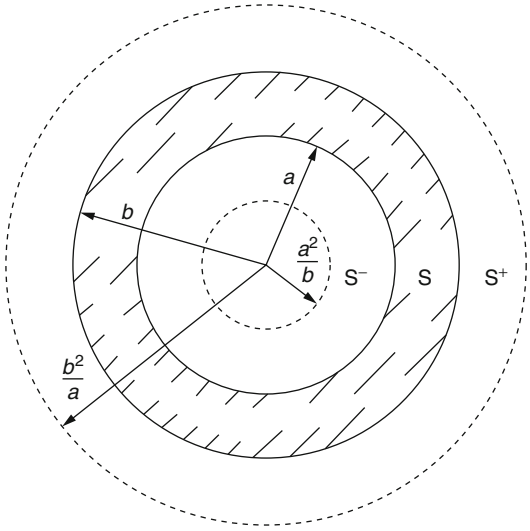

Annular Problems with a Point Heat Source, Fig. 2 Analytic regions of the annulus

$$\psi^*(z) = -\gamma_1\overline{\phi^*\left(\frac{a^2}{\overline{z}}\right)} - \frac{a^2}{z}\phi^{*\prime}(z) - \delta_1\overline{g^*\left(\frac{a^2}{\overline{z}}\right)} \quad \text{for } z \in S \tag{33}$$

$$\psi^*(z) = -\gamma_2\overline{\phi^*\left(\frac{b^2}{\overline{z}}\right)} - \frac{b^2}{z}\phi^{*\prime}(z) - \delta_2\overline{g^*\left(\frac{a^2}{\overline{z}}\right)} \quad \text{for } z \in S \tag{34}$$

and hence $\phi*(z)$ must satisfy the compatibility identity

$$\gamma_2\overline{\phi^*\left(\frac{b^2}{\overline{z}}\right)} - \gamma_1\overline{\phi^*\left(\frac{a^2}{\overline{z}}\right)} + \frac{b^2-a^2}{z}\phi^{*\prime}(z) + \delta_2\overline{g^*\left(\frac{b^2}{\overline{z}}\right)} - \delta_1\overline{g^*\left(\frac{a^2}{\overline{z}}\right)} = 0 \quad \text{for } z \in S \tag{35}$$

On substituting (31) and (32) into the boundary conditions (27) and (28), we obtain the following Hilbert problems:

$$\phi^*(t) - \phi^{*^-}(t) = \frac{1}{\gamma_1}[F_1(t) - \delta_1(g^*(t) - g^{*^-}(t))] \quad \text{on } t = ae^{i\theta} \tag{36}$$

$$\phi^*(t) - \phi^{*^+}(t) = \frac{1}{\gamma_2}[F_2(t) - \delta_2(g^*(t) - g^{*^+}(t))] \quad \text{on } t = e^{i\theta} \tag{37}$$

where $\phi^{*^+}(z)$ and $\phi^{*^-}(z)$ or ($g^{*^+}(z)$ and $g^{*^-}(z)$) denote the limits on $|z| = b$ and $|z| = a$ of $\phi^*(z)$ (or $g^*(z)$) in S^+ and S^- respectively. Since $\phi^*(z)$ and $g^*(z)$ are holomorphic and single-valued in S^-, S, and S^+, they may be represented by the Laurent series:

$$\phi^*(z) = \begin{cases} = \sum_{n=-\infty}^{\infty} L_n^- z^n & (z \in S^-) \\ = \sum_{n=-\infty}^{\infty} L_n z^n & (z \in S) \\ = \sum_{n=-\infty}^{\infty} L_n^+ z^n & (z \in S^+) \end{cases} \tag{38}$$

$$g^*(z) = \begin{cases} = \sum_{\substack{n=-\infty \\ n\neq -1}}^{\infty} \frac{\lambda_n^-}{n+1} z^{n+1} & (z \in S^-) \\ = \sum_{\substack{n=-\infty \\ n\neq -1}}^{\infty} \frac{\lambda_n}{n+1} z^{n+1} & (z \in S) \\ = \sum_{\substack{n=-\infty \\ n\neq -1}}^{\infty} \frac{\lambda_n^+}{n+1} z^{n+1} & (z \in S^+) \end{cases} \tag{39}$$

Hence the boundary conditions (36) and (37) take the form

$$a^n(L_n - L_n^-) = \frac{1}{2\pi\gamma_1}\int_0^{2\pi} F_1(ae^{i\theta})e^{-in\theta}d\theta - \frac{\delta_1}{\gamma_1}\frac{a^n(\lambda_{n-1} - \lambda_{n-1}^-)}{n} \quad (n \neq 0) \tag{40}$$

$$b^n(L_n - L_n^+) = \frac{1}{2\pi\gamma_2}\int_0^{2\pi} F_2(be^{i\theta})e^{-in\theta}d\theta - \frac{\delta_2}{\gamma_2}\frac{b^n(\lambda_{n-1} - \lambda_{n-1}^+)}{n}(n \neq 0) \tag{41}$$

and substituting in the compatibility identity (35), we obtain

$$\gamma_2 b^{2n}L_n^+ - \gamma_1 a^{2n}L_n^- + (b^2 - a^2)(2-n)\overline{L_{2-n}} + \delta_2 b^{2n}\frac{\lambda_{n-1}^+}{n} - \delta_1 a^{2n}\frac{\lambda_{n-1}^-}{n} = 0(n \neq 0) \tag{42}$$

On eliminating the coefficients $L_n{}^+$ and $L_n{}^-$ from (40)–(42), the constants L_n and λ_{n-1} satisfy the system of equations

$$(\gamma_2 b^{2n} - \gamma_1 a^{2n})L_n + (b^2 - a^2)(2-n)\overline{L_{2-n}} + (\delta_2 b^{2n} - \delta_1 a^{2n})\frac{\lambda_{n-1}}{n} = \frac{1}{2\pi}\int_0^{2\pi}(b^2 F_2(be^{i\theta}) - b^n F_1(ae^{i\theta}))e^{-in\theta}d\theta \ (n \neq 0) \tag{43}$$

Similar to the previous approach, the coefficient M_n associated with the stress function $\psi^*(z)$ can be found from (33) or (34) which satisfy the system of equations

$$(\gamma_2 b^{-(2n+1)} - \gamma_1 a^{-(2n+1)})\overline{L_{-n}} + (b^{-2} - a^{-2})M_n - (\delta_2 b^{-(2n+1)} - \delta_1 a^{-(2n+1)})\frac{\overline{\lambda_{-(n+1)}}}{n} = \frac{1}{2\pi}\int_0^{2\pi}[b^{-(n+2)}\overline{F_2(be^{i\theta})} - a^{-(n+2)}\overline{F_1(ae^{i\theta})}]e^{-in\theta}d\theta \quad (n \neq 0) \tag{44}$$

Once we obtain the coefficients L_n and M_n, the stress functions $\phi^*(z)$ and $\psi^*(z)$ are completely solved and the components of stress can be determined by substituting (18) and (19) into (3) and (4). Since no analytical solutions for annular problem with a point heat source are available in the literature, only special cases with the absence of a point heat source are considered here for demonstrating the use of the present approach. We consider the case that the inner and outer boundaries of the annulus are subjected to angled temperature distributions, i.e., $T_1 = A_1\cos\theta$ on $|z| = a$ and $T_2 = A_1{}'\cos\theta$ on $|z| = b$ and from (8)–(10) and (29)–(30) we have

$$\lambda^* = 0, \quad \lambda_0 = 0, \quad \lambda_1 = \frac{bA'_1 - aA_1}{b^2 - a^2},$$
$$\lambda_{-1} = \frac{a^2b^2}{a^2 - b^2}\left(\frac{A'_1}{b} - \frac{A_1}{a}\right)A = \frac{-2\mu\beta\lambda*}{1+\kappa} = 0$$
$$B = \overline{C} = \frac{-2\mu\beta\lambda_{-1}}{1+\kappa} = \frac{-2\mu\beta}{1+\kappa}\frac{a^2b^2}{a^2 - b^2}\left(\frac{A'_1}{b} - \frac{A_1}{a}\right)$$
$$F_1(t) = F_2(t) = \frac{2\mu\beta\lambda_{-1}}{1+\kappa}\left[\ln t + \frac{t}{t} + \ln\bar{t}\right] \tag{45}$$

$$L_2 = \frac{-\overline{B}}{(a^2 + b^2)}, \quad L_n = 0 \quad (n \neq 2)$$
$$M_{-2} = \frac{-a^2b^2B}{a^2 - b^2}, \quad M_n = 0 \quad (n \neq -2) \tag{46}$$

and the components of stress are

$$\sigma_{rr} = pr\left(1 - \frac{a^2}{r^2}\right)\left(\frac{b^2}{r^2} - 1\right)\cos\theta$$
$$\sigma_{\theta\theta} = pr\left(\frac{a^2b^2}{r^4} + \frac{a^2 + b^2}{r^2} - 3\right)\cos\theta \tag{47}$$
$$\tau_{r\theta} = pr\left(1 - \frac{a^2}{r^2}\right)\left(\frac{b^2}{r^2} - 1\right)\sin\theta$$

where

$$p = \frac{\alpha E}{2(1-\nu)}\frac{a^2b^2}{b^4 - a^4}\left(\frac{A_1}{a} - \frac{A_1{}'}{b}\right)$$

which are exactly the same as those given by [5] for a plane-strain condition.

Results and Discussion

For steady-state heat conduction problems, the strength q_0 cannot be arbitrarily chosen once

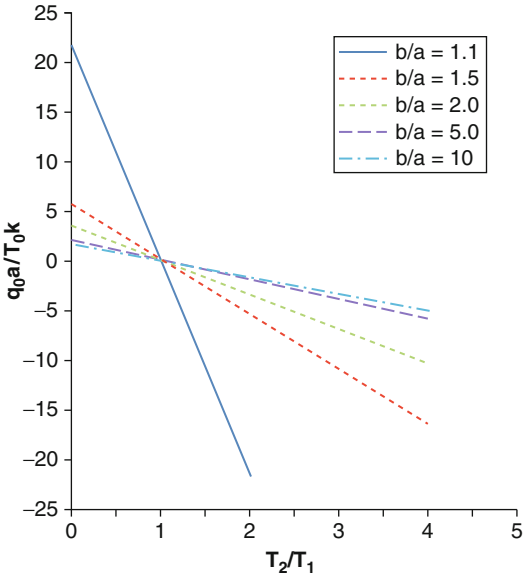

Annular Problems with a Point Heat Source, Fig. 3 Relationship between the strength of a point heat source and the temperatures at the boundaries of the annulus

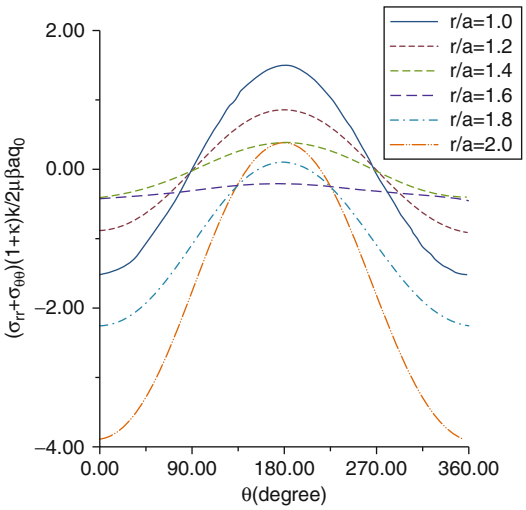

Annular Problems with a Point Heat Source, Fig. 4 Dilatation stress in the annulus for the stress-free boundary condition at the inner and outer boundaries

the temperature T_1 at the inner boundary and the temperature T_2 at the outer boundary are assumed as known values. The effect of changing the ratio T_2/T_1 and the wall thickness b/a on the dimensionless strength q_0a/T_0k (with the case

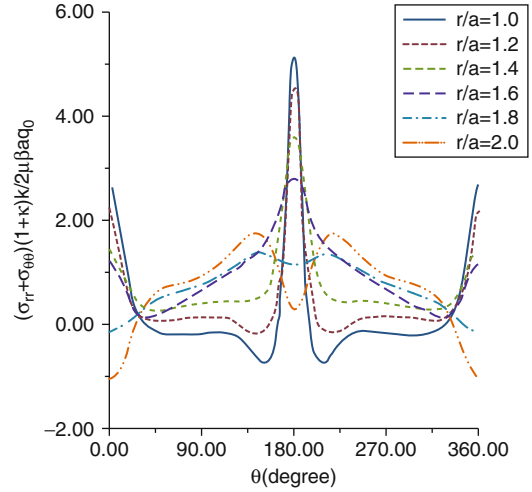

Annular Problems with a Point Heat Source, Fig. 5 Dilatation stress in the annulus for the displacement-free and stress-free boundary conditions at the inner and outer boundaries, respectively

$r_0 = (a+b)/2$, $\theta_0 = 0\ ^\circ\mathrm{C}$) can be evaluated from (10) and shown graphically in Fig. 3. For convenience of the calculation in (10), we assume the temperature T_1 and T_2 are kept at constant, i.e., $A_0 = T_1, A_0{}' = T_1$ from (6) and (7). Once A_0 and $\theta_0 = 0$ are given, the dimensionless strength q_0a/T_0k can be determined from (10) for different wall thickness b/a. The result indicates that the strength of a point heat source becomes a positive (or negative) value as the temperature at the outer boundary is lower or higher than that at the inner boundary. It is then understood that the condition $T_2 < T_1$ (or $T_1 < T_2$) will accompany with the presence of a heat source (or sink) such that the energy balance within the annular system is preserved. Furthermore, the strength q_0 changes dramatically with the ratio T_2/T_1 for the annulus with a relatively thin wall. The dilatation stress $\sigma_{rr} + \sigma_{\theta\theta}$, which is mainly responsible for the result of material failure by fracture, is found for three different cases of boundary value problems as displayed in Figs. 4–6. The conditions $T_2/T_1 = 3$, $b/a = 2$, $r_0/a = 1.5$, and $\theta_0 = 0^\circ\mathrm{C}$ are considered for all three cases, and the results shown in Figs. 4–6 are based on the series solutions up to the first 20 terms in (22) which are checked to preserve a good accuracy. It is shown that the maximum dilatation stress always occurs

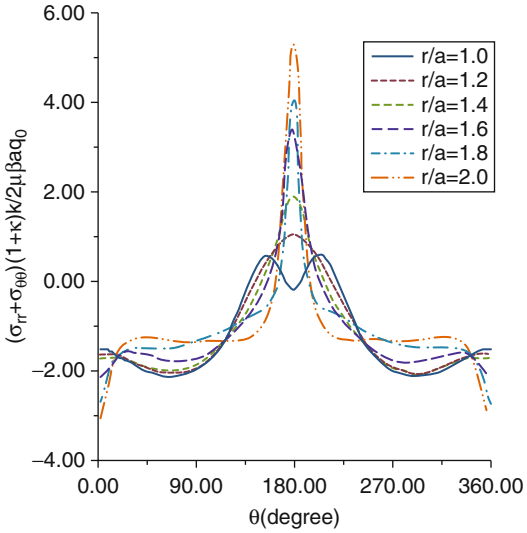

Annular Problems with a Point Heat Source, Fig. 6 Dilatation stress in the annulus for the stress-free and displacement-free boundary conditions at the inner and outer boundaries, respectively

at $\theta_0 = 180$ °C, which is farthest away from the position where a heat sink resides, for all three cases. For the traction-free boundary condition at both inner and outer boundaries of the annulus, the maximum dilatation stress occurs at the inner boundary with the lower temperature as shown in Fig. 4. For the displacement-free condition (or the traction-free condition) at the inner boundary and traction-free condition (or displacement-free condition) at the outer boundary, the maximum dilatation stress is found to take place at the inner boundary (or outer boundary) as displayed in Fig. 5 (or Fig. 6).

References

1. Bogdanoff JL (1954) Note on thermal stress. ASME J Appl Mech 21:88
2. Carslaw HS, Jaeger JC (1965) Conduction of heats in solids. Clarendon, Oxford
3. Chao CK, Shen MH (1997) On bonded circular inclusions in plane thermoelasticity. ASME J Appl Mech 64:1000–1004
4. Muskhelishvili NI (1954) Some basic problems of mathematical theory of elasticity. P. Noordhoff, Groningen
5. Timoshenko SP, Goodier JN (1970) Theory of elasticity, 3rd edn. McGraw-Hill, New York

Application of Boundary Integral Equation (BIE) Method in Thermoelastodynamic Problem

Seyed Mahmoud Hosseini[1], Jan Sladek[2] and Vladimir Sladek[2]
[1]Industrial Engineering Department, Ferdowsi University of Mashhad, Mashhad, Iran
[2]Department of Mechanics, Institute of Construction and Architecture, Slovak Academy of Sciences, Bratislava, Slovakia

Synonyms

Boundary integral equation method; Fundamental solution; Thermoelastodynamics; Uncoupled thermoelasticity

Definition

The boundary integral equation method (BIEM) is one of the most effective numerical methods in engineering analysis. The great advantage of the BIEM is the reduction of dimensions in the formulation for solution of boundary value problems since the unknowns are localized on the boundary instead of the whole analyzed domain. It should be stressed that the dimensional reduction is achieved only in problems when the fundamental solutions of the governing equations are available. Recall that the fundamental solutions are known only in linear theory of thermoelasticity. The temperature and displacement fields (the primary fields) are represented in terms of boundary integrals of relevant boundary densities (temperature, heat flux, displacements, and tractions) and domain integrals of known body sources. The integral representations of the derivatives of the primary fields are expressed in terms of the same boundary densities as in the case of the primary fields.

Overview

Since the fundamental solutions of the governing partial differential equations are the cornerstone

of pure boundary integral formulation for solution of any boundary value problem, we shall pay attention to the fundamental solutions for transient uncoupled thermoelastic problems. This class of thermoelastic 3-D problems has been selected because of their practical applicability (coupling can be often neglected in practical problems) and sufficient generality (it includes all special classes of uncoupled thermoelastic problems). In case of homogeneous media, the governing equations are given by partial differential equations (PDE) with constant coefficients, and the fundamental solutions are available in rather simple closed form for isotropic media in both the formulations for Laplace transform and the time-dependent fields. The boundary integral representation of field variables means that these fields are expressed in terms of complete set of relevant boundary quantities without having the need to know the solution at any interior point. In a well-posed boundary value problem, only half of the relevant boundary quantities are prescribed by the boundary conditions. The unknown boundary densities can be computed by solving the boundary integral equations (BIE). In case of uncoupled thermoelasticity, the thermal fields are independent of the elastic ones, though the elastic fields are influenced by the thermal fields. The integral representations for the primary thermal and elastic fields, as well as for their derivatives will be presented and supplemented with the BIE. Owing to the space limit, the details of the BIEM formulation as well as the numerical implementation by using the boundary elements cannot be discussed here, and we refer the reader to several works. The list of references is not complete and is restricted to works which are consistently written with the present text.

Fundamental Solutions in Uncoupled Thermoelastodynamics

In uncoupled thermoelasticity, the temperature field is independent of elastic fields, and the governing equation results from the energy balance assuming the heat transfer via heat conduction in continuous media. On the other hand, the elastic fields such as the displacements and stresses are influenced by the temperature distribution because of thermal expansion of elastic media. The governing equations for elastic fields result from the conservation of momentum. The time variable is very important dimension of transient problems as compared with the stationary ones. From the mathematical point of view, the stationary problems are described by the elliptic partial differential equations (PDE) while the transient problems by the parabolic and hyperbolic PDE. Applying the Laplace transformation with respect to the time variable, the latter are converted to the elliptic PDE which can be solved for discrete values of the transform parameter like the stationary problems. Finally, the inverse Laplace transformation is required in order to obtain time-dependent solutions. The BIEM formulations will be developed for both the time-dependent and the Laplace transforms of the field variables in uncoupled thermoelasticity [1].

Let us consider a homogenous, isotropic, perfectly elastic body. The governing equations for uncoupled thermoelasticity are given as [2]

$$\mu\, u_{i,kk} + (\lambda + \mu)\, u_{k,ki} - \gamma\, \theta_{,i} + F_i = \rho\, \ddot{u}_i \quad (1)$$

$$C\, \theta_{,kk} - \dot{\theta} = -Q \quad (2)$$

where "u_i" is the displacement vector; "θ" is the temperature change above the uniform reference temperature "T_0" or "$\theta = T - T_0$," "F_i" and "Q" are the volume densities of external forces and heat sources; "ρ" is the mass density; "C" is the thermal diffusivity; "λ" and "μ" are the Lame constants; and $\gamma = (2\mu + 3\lambda)\alpha$ with α being the coefficient of linear thermal expansion. The constitutive stress-strain equations and the linear expression for strains in terms of displacement gradients are given as

$$\sigma_{ij} = 2\,\mu\, e_{ij} + (\lambda\, e_{kk} - \gamma\, \theta)\, \delta_{ij}, e_{ij} = \frac{1}{2}\left(u_{i,j} + u_{j,i}\right) \quad (3)$$

Subscripts following a comma denote the partial derivative with respect to Cartesian

coordinates of the vector "**x**." Components of the traction vector on a surface with the normal "$n_i(\mathbf{x})$" take the form

$$s_i(\mathbf{x},t) = \sigma_{ji}(\mathbf{x},t)\, n_j(\mathbf{x}) = \hat{T}_{ij}(n_x,\partial_x)\, u_j(\mathbf{x},t) - \gamma\, n_i(\mathbf{x})\, \theta(\mathbf{x},t) \tag{4}$$

where

$$\hat{T}_{ij}(n_x,\partial_x) = \mu\,\delta_{ij}\, n_k(\mathbf{x})\,\partial_k + \mu\, n_j(\mathbf{x})\,\partial_i + \lambda\, n_i(\mathbf{x})\,\partial_j, \quad \partial_k \equiv \frac{\partial}{\partial x_k} \tag{5}$$

Excluding the time variable by using the Laplace transformation technique, we obtain

$$\mu\,\bar{u}_{i,kk} + (\lambda+\mu)\,\bar{u}_{k,ki} - \gamma\bar{\theta}_{,i} + \tilde{F}_i = \rho\, S^2\,\bar{u}_i \tag{6}$$

$$C\,\bar{\theta}_{,kk} - S\,\bar{\theta} = -\tilde{Q} \tag{7}$$

where

$$\bar{f}(\mathbf{x},S) = \int_0^\infty f(\mathbf{x},t)\, e^{-St}\, dt \tag{8}$$

S is the Laplace transform parameter, and the generalized body sources are given by

$$\tilde{F}_i(\mathbf{x},S) = \overline{F}_i(\mathbf{x},S) + \rho[Su_i(\mathbf{x}) + v_i(\mathbf{x})]$$
$$\tilde{Q}(\mathbf{x},S) = \tilde{\overline{Q}}(\mathbf{x},S) + \theta(\mathbf{x})$$

with $u_i(\mathbf{x})$, $v_i(\mathbf{x})$, and $\theta(\mathbf{x})$ being the initial values of displacements, displacement velocity, and temperature, respectively.

Let the body sources

$$\tilde{Q} = \delta(\mathbf{x}-\mathbf{y}), \quad \tilde{F}_i = 0 \tag{9}$$

determine the fundamental displacements $\bar{U}_i'$ and temperature $\bar{\theta}'$. The displacement vector can be decomposed into the potential and solenoid parts as

$$\bar{U}_i' = \bar{\phi}'_{,i} + \varepsilon_{ijk}\,\bar{\psi}'_{k,j} \tag{10}$$

Then, the governing (6) and (7) are converted into the system

$$\nabla^2\,\bar{\phi}' - \frac{\lambda+2\mu}{\rho}\,S^2\,\bar{\phi}' - \frac{\gamma}{\lambda+2\mu}\,\bar{\theta}' = 0$$
$$\nabla^2\,\bar{\theta}' - \frac{S}{C}\,\bar{\theta}' = -\frac{1}{C}\,\delta(\mathbf{x}-\mathbf{y}) \tag{11}$$

Having solved this system, one obtains the fundamental solutions generated by point heat source

$$\bar{U}_i'(\mathbf{r},S) = -\frac{r_{,i}}{C\,r}\,g_1, \quad g_1 = \frac{m}{4\,\pi\left({\lambda_1}^2 - {\lambda_2}^2\right)}\left[\left(\lambda_1 + \frac{1}{r}\right)e^{-\lambda_1 r} - \left(\lambda_2 + \frac{1}{r}\right)e^{-\lambda_2 r}\right] \tag{12}$$

and

$$\bar{\theta}'(r,S) = \frac{1}{C\,r}\,g_2, \quad g_2 = \frac{1}{4\,\pi\left({\lambda_1}^2 - {\lambda_2}^2\right)} \times \left[\left({\lambda_1}^2 - \frac{S^2}{c_1^2}\right)e^{-\lambda_1 r} - \left({\lambda_2}^2 - \frac{S^2}{c_1^2}\right)e^{-\lambda_2 r}\right] = \frac{1}{4\pi}\,e^{-r\sqrt{S/C}} \tag{13}$$

where

$$m = \frac{\gamma}{\rho\,{c_1}^2}, \quad {c_1}^2 = \frac{\lambda+2\mu}{\rho}, \quad {c_2}^2 = \frac{\mu}{\rho}$$
$$\mathbf{r} = \mathbf{x}-\mathbf{y}, \quad r = |\mathbf{r}|, \quad r_{,i} = (x_i - y_i)/r,$$
$${\lambda_1}^2 = S/C, \quad {\lambda_2}^2 = (S/c_1)^2 \tag{14}$$

The Laplace transform of the fundamental traction vector "$\bar{T}_i'(\mathbf{y}-\mathbf{x},S)$" is given as

$$\bar{T}_l'(\mathbf{y}-\mathbf{x},S) = \hat{T}_{lk}\left(n_y,\partial_y\right)\bar{U}_k'(\mathbf{y}-\mathbf{x},S) - \gamma\, n_l(\mathbf{y})\,\bar{\theta}'(r,S)$$
$$= \mu\, n_k(\mathbf{y})\left[\partial_k\,\bar{U}_l'(\mathbf{r},S) + \partial_l\,\bar{U}_k'(\mathbf{r},S)\right] + n_l(\mathbf{y})\left[\lambda\,\partial_k\,\bar{U}_k'(\mathbf{r},S) - \gamma\,\bar{\theta}'(r,S)\right] \tag{15}$$

with

$$\partial_j \bar{U}_i'(\mathbf{r},S) = \frac{1}{C}\left[\frac{r_{,i}\,r_{,j}}{r}\,g_3 - \frac{1}{r^2}\left(\delta_{ij} - 3\,r_{,i}\,r_{,j}\right)g_1\right]$$
$$g_3 = \frac{m}{4\,\pi\left(\lambda_1^2 - \lambda_2{}^2\right)}\left(\lambda_1^2\,e^{-\lambda_1 r} - \lambda_2{}^2\,e^{-\lambda_2 r}\right) \tag{16}$$

The Laplace transform of the fundamental flux is given by

$$\frac{\partial\,\bar{\theta}'(r,S)}{\partial\,n(y)} = \frac{r_{,i}\,n_i\,(y)}{C\,r}\,g_4,$$
$$g_4 = \frac{1}{4\,\pi}\left(\sqrt{\frac{S}{C}} + \frac{1}{r}\right)e^{-r\sqrt{\frac{S}{C}}} \tag{17}$$

As to the limit behavior when $r \to 0$, we have

$$\bar{\theta}'(r,S) \sim \frac{1}{4\,\pi\,C\,r} + 0(1),$$
$$\bar{U}_i'\,(\mathbf{r},S) = \frac{m r_{,i}}{4\pi C} + O(1) \tag{18}$$

$$\frac{\partial\,\bar{\theta}'(r,S)}{\partial\,n(y)} \sim \frac{\partial}{\partial\,n(y)}\,\frac{1}{4\,\pi\,C\,r} + 0\left(r^{-1}\right),$$
$$\bar{T}_l'(\mathbf{y}-\mathbf{x},S) = O(r^{-1}) \tag{19}$$

The fundamental displacements $\bar{u}_i^{(j)}(\mathbf{r},S) \equiv \bar{U}_{ij}(\mathbf{r},S)$ and tractions $\bar{T}_{ij}(\mathbf{y}-\mathbf{x},S)$ generated by point sources $\tilde{F}_i(\mathbf{x},S) = \delta_{ij}\delta(\mathbf{x}-\mathbf{y})$, $\tilde{Q}(\mathbf{x},S) = 0$ in the uncoupled theory of themoelastodynamics are given by

$$\bar{U}_{ij}\,(\mathbf{r},S) = \frac{U_1}{r}\,\delta_{ij} + \frac{U_2}{r}\,r_{,i}\,r_{,j} \tag{20}$$

and

$$\bar{T}_{ij}\,(\boldsymbol{\eta}-x,S) = -\,\mu\,n_k(\boldsymbol{\eta})\left[\partial_k\,\bar{U}_{ij}(\mathbf{r},S) + \partial_i\,\bar{U}_{kj}(\mathbf{r},S)\right]$$
$$-\,n_i(\boldsymbol{\eta})\,\lambda\,\partial_k\bar{U}_{kj}(\mathbf{r},S) \tag{21}$$

where

$$\partial_k\,\bar{U}_{ij}(\mathbf{r},S) = \frac{\delta_{ij}\,r_{,k}}{r^2}\,(U_2+U_3)$$
$$+\,\frac{\delta_{ik}\,r_{,j} + \delta_{jk}\,r_{,i}}{r^2}\,U_2$$
$$+\,\frac{r_{,i}\,r_{,j}}{r^2}\,U_4 \tag{22}$$

and

$$U_1 = \frac{1}{4\,\pi\,\rho}\left\{\frac{1}{c_2{}^2}\,e^{-\frac{Sr}{c_2}} + \frac{1}{S^2\,r^2}\left[\left(1+\frac{Sr}{c_2}\right)e^{-\frac{Sr}{c_2}}\right.\right.$$
$$\left.\left. -\left(1+\frac{Sr}{c_1}\right)e^{-\frac{Sr}{c_1}}\right]\right\} \tag{23}$$

$$U_2 = -\frac{1}{4\,\pi\,\rho}\left\{\left[\frac{1}{c_2{}^2} + \frac{3}{S^2\,r^2}\left(1+\frac{Sr}{c_2^2}\right)\right]e^{-\frac{Sr}{c_2}}\right.$$
$$\left. -\left[\frac{1}{c_1^2} + \frac{3}{S^2\,r^2}\left(1+\frac{Sr}{c_1^2}\right)\right]e^{-\frac{Sr}{c_1}}\right\} \tag{24}$$

$$U_3 = -\frac{1}{4\,\pi\,\rho\,c_2{}^2}\left(1+\frac{S\,r}{c_2}\right)e^{-\frac{Sr}{c_2}} \tag{25}$$

$$U_4 = \frac{1}{4\,\pi\,\rho}\left[\frac{1}{c_2{}^2}\left(6+\frac{Sr}{c_2}\right) + \frac{15}{S^2\,r^2}\left(1+\frac{Sr}{c_2}\right)e^{-\frac{Sr}{c_2}}\right]$$
$$-\,\frac{1}{4\,\pi\,\rho}\left[\frac{1}{c_1{}^2}\left(6+\frac{Sr}{c_1}\right) + \frac{15}{S^2\,r^2}\left(1+\frac{Sr}{c_1}\right)e^{-\frac{Sr}{c_1}}\right] \tag{26}$$

Boundary Integral Representations and Boundary Integral Equations

Assuming the governing equations in weak sense with taking adequate fundamental solutions for the weight functions and making use of the Gauss divergence theorem, one can derive the following integral representations [6]:

$$h(\mathbf{x})\,\theta(\mathbf{x},S) = \int_V \bar{Q}(\mathbf{y},S)\,\bar{\theta}'(|\mathbf{x}-\mathbf{y}|,S)\,dV_y$$
$$+\,C\int_{S_A}\left[\frac{\partial\bar{\theta}(\boldsymbol{\eta},S)}{\partial\mathbf{n}(\boldsymbol{\eta})}\,\bar{\theta}'\left(|\mathbf{x}-\boldsymbol{\eta}|,S\right)\right.$$
$$\left. -\,\bar{\theta}(\boldsymbol{\eta},\boldsymbol{S})\,\frac{\partial\bar{\theta}'\left(|\mathbf{x}-\boldsymbol{\eta}|,S\right)}{\partial\mathbf{n}(\boldsymbol{\eta})}\right]dS_\eta \tag{27}$$

$$h(\mathbf{x})\,\mathbf{u_j}(\mathbf{x},S)$$
$$= \int_V \left[\bar{F}_i(\mathbf{y},S) - \gamma\,\bar{\theta}_{,i}(\mathbf{y},S)\right]\bar{U}_{ij}(\mathbf{y}-\mathbf{x},S)\,dV_y$$
$$+\int_{S_A}\left\{\left[\bar{t}_i(\boldsymbol{\eta},\boldsymbol{S}) + \gamma\,n_i(\boldsymbol{\eta})\,\bar{\theta}(\boldsymbol{\eta},S)\right]\bar{U}_{ij}(\boldsymbol{\eta}-\mathbf{x},S)\right.$$
$$\left. -\,\bar{u}_i(\boldsymbol{\eta},S)\,\bar{T}_{ij}(\boldsymbol{\eta}-\mathbf{x},S)\right\}dS_\eta \tag{28}$$

Applying the inverse Laplace transformation to the previous two equations, one obtains

$$h(\mathbf{x})\,\theta(\mathbf{x},t) = \int_0^t \int_V Q(\mathbf{y},\tau)\,\theta'(|\mathbf{x}-\mathbf{y}|,t-\tau)\,dV_y\,d\tau + C\int_0^t \int_{S_A} \left[\frac{\partial\,\theta(\boldsymbol{\eta},\tau)}{\partial\,\mathbf{n}(\boldsymbol{\eta})}\,\theta'(|\mathbf{x}-\boldsymbol{\eta}|,t-\tau)\right.$$
$$\left. - \theta(\boldsymbol{\eta},\tau)\,\frac{\partial\,\theta'(|\mathbf{x}-\boldsymbol{\eta}|,t-\tau)}{\partial\,\mathbf{n}(\boldsymbol{\eta})}\right] dS_\eta \tag{29}$$

$$h(\mathbf{x})\,\mathbf{u_j}(\mathbf{x},t) = \int_0^t \int_V [F_i(\mathbf{y},\tau) - \gamma\,\theta_{,i}(\mathbf{y},\tau)]\,U_{ij}(\mathbf{y}-\mathbf{x},t-\tau)\,dV_y\,d\tau + \int_0^t \int_{S_A} \{[t_i(\boldsymbol{\eta},\tau) + \gamma\,n_i(\boldsymbol{\eta})\,\theta(\boldsymbol{\eta},\tau)]\,U_{ij}(\boldsymbol{\eta}-\mathbf{x},t-\tau)$$
$$- u_i(\boldsymbol{\eta},\tau)\,T_{ij}(\boldsymbol{\eta}-\mathbf{x},t-\tau)\}\,dS_\eta\,d\tau \tag{30}$$

where

$$h(\mathbf{x}) = \begin{cases} 1, & \mathbf{x} \in V \\ h(\zeta), & \mathbf{x} = \zeta \in S_A \\ 0, & \mathbf{x} \notin (V \cup S_A) \end{cases} \tag{31}$$

$$h(\zeta)\delta_{ij} = -\int_{S_A} T_{ij}(\boldsymbol{\eta}-\zeta)\,dS_\eta$$

$$\text{and/or} \quad h(\zeta) = -\int_{S_A} \frac{\partial}{\partial\mathbf{n}(\boldsymbol{\eta})}\,\theta'(|\boldsymbol{\eta}-\zeta|)\,dS_\eta$$

$$\text{with} \quad h(\zeta) = 0.5 \quad \text{on smooth boundary}$$

Note that the kernels $T_{ij}(\boldsymbol{\eta}-\zeta)$ and $\partial\theta'(|\boldsymbol{\eta}-\zeta|)/\partial\mathbf{n}(\boldsymbol{\eta})$ exhibit strong singularity $r^{-2} = |\boldsymbol{\eta}-\zeta|^{-2}$. Therefore, the strongly singular boundary integrals in (27)–(30) for $\mathbf{x} = \zeta \in S_A$ exist in the Cauchy principal value sense. Nevertheless, bearing in mind that the transient fundamental solutions exhibit the same singularity as the stationary ones, one can easily regularize [3–7] the integral equations by making use of the integral representations of the coefficient $h(\zeta)$ given in (31). According to the Gauss divergence theorem, the temperature terms in (28) can be rewritten into a volume integral as

$$-\gamma\int_V \bar{\theta}_{,i}(\mathbf{y},S)\,\bar{U}_{ij}(\mathbf{y}-\mathbf{x},S)\,dV_y + \gamma\int_{S_A} n_i(\boldsymbol{\eta})\bar{\theta}(\boldsymbol{\eta},S)\,\bar{U}_{ij}(\boldsymbol{\eta}-\mathbf{x},S)\,dS_\eta = \gamma\int_V \bar{\theta}(\mathbf{y},S)\,\bar{U}_{ij,i}(\mathbf{y}-\mathbf{x},S)\,dV_y \tag{32}$$

From (22), the term "$\bar{U}_{ij,i}(\mathbf{r},S)$" can be expressed as

$$\partial_i\,\bar{U}_{ij}(\mathbf{r},S) = \frac{C}{\gamma}\left(\nabla^2 - \frac{S}{C}\right)\bar{U}'_j(\mathbf{r},S) \tag{33}$$

with $\bar{U}'_j(\mathbf{r},S)$ being given in (12). Inserting (33) into the r.h.s. of (32) and utilizing the Gauss divergence theorem, one obtains finally in view of (7)

$$\gamma\int_V \bar{\theta}(\mathbf{y},S)\,\bar{U}_{ij,i}(\mathbf{y}-\mathbf{x},S)\,dV_y = -\int_V \bar{Q}(\mathbf{y},S)\,\bar{U}'_j(\mathbf{y}-\mathbf{x},S)\,dV_y + C\int_{S_A} [n_i(\boldsymbol{\eta})\bar{\theta}(\boldsymbol{\eta},S)\,\partial'_i\,\bar{U}'_j(\boldsymbol{\eta}-\mathbf{x},S)$$
$$- \bar{q}(\boldsymbol{\eta},S)\bar{U}'_j(\boldsymbol{\eta}-\mathbf{x},S)]\,dS_\eta, \quad \partial'_i = \partial/\partial\eta_i$$

and the integral representation of the displacement field given by (28) can be rewritten into an equivalent form as

$$h(\mathbf{x})\,\bar{u}_j(\mathbf{x},S) = \int_V [\bar{F}_i(\mathbf{y},S)\,\bar{U}_{ij}(\mathbf{y}-\mathbf{x},S) - \bar{Q}(\mathbf{y},S)\,\bar{U}'_j(\mathbf{y}-\mathbf{x},S)]\,dV_y + \int_{S_A} [\bar{t}_i(\boldsymbol{\eta},S)\,\bar{U}_{ij}(\boldsymbol{\eta}-\mathbf{x},S) - \bar{u}_i(\boldsymbol{\eta},S)\,\bar{T}_{ij}(\boldsymbol{\eta}-\mathbf{x},S)]\,dS_\eta$$
$$+ C\int_{S_A} [\bar{\theta}(\boldsymbol{\eta},S)\,n_i(\boldsymbol{\eta})\,\partial'_i\,\bar{U}'_j(\boldsymbol{\eta}-\mathbf{x},S) - \bar{q}(\boldsymbol{\eta},S)\bar{U}'_j(\boldsymbol{\eta}-\mathbf{x},S)]\,dS_\eta \tag{34}$$

where the domain integral involves only the prescribed densities of body sources.

Making use of the definition of the stress field by (3) as well as the governing (1), after certain lengthy derivation [6], one can obtain from (34) the integral representation of the stress field

$$\begin{aligned}
&\bar{\sigma}_{lp}(\mathbf{x},S)+\gamma\delta_{lp}\,\bar{\theta}(\mathbf{x},S)\\
&\quad= c_{lpjr}\left\{\int_V\left[\tilde{F}_i(\mathbf{y},S)\partial_r\,\bar{U}_{ij}(\mathbf{y}-\mathbf{x},S)\right.\right.\\
&\quad-\tilde{Q}(\mathbf{y},S)\partial_r\,\bar{U}'_j(\mathbf{y}-\mathbf{x},S)\big]dV_y\\
&\quad-\int_{S_A}\bar{t}_i(\boldsymbol{\eta},S)\partial'_r\,\bar{U}_{ij}(\boldsymbol{\eta}-\mathbf{x},S)\,dS_\eta\\
&\quad+c_{iskt}\int_{S_A}\bar{k}_{rst}\partial'_t\,\bar{U}_{kj}(\boldsymbol{\eta}-\mathbf{x},S)\,dS_\eta\\
&\quad+\rho S^2\int_{S_A}\bar{u}_i(\boldsymbol{\eta},S)\,n_r(\boldsymbol{\eta})\,\bar{U}_{ij}(\mathbf{y}-\mathbf{x},S)\,dS_\eta\\
&\quad-C\int_{S_A}\big[\bar{\theta}(\boldsymbol{\eta},S)\,n_i(\boldsymbol{\eta})\,\partial'_i\,\partial'_r\,\boldsymbol{U}'_j(\boldsymbol{\eta}-\mathbf{x},S)\\
&\quad\left.-\bar{q}(\boldsymbol{\eta},S)\partial'_r\,\bar{U}'_j(\boldsymbol{\eta}-\mathbf{x},S)\big]\,dS_\eta\right\}
\end{aligned}\tag{35}$$

where $\bar{k}_{rsi}=\hat{D}'_{rs}\,\bar{u}_i(\boldsymbol{\eta},S),\hat{D}'_{rs}=n_r(\boldsymbol{\eta})\,\partial'_s-n_s(\boldsymbol{\eta})\,\partial'_r$

$$\begin{aligned}
&\partial_i\partial_r\,\bar{U}'_j(\mathbf{r},S)\\
&\quad=\frac{1}{Cr^2}\left(r_{,k}\delta_{ij}+r_{,i}\delta_{kj}+r_{,j}\delta_{ik}-3r_{,i}r_{,j}r_{,k}\right)\left(g_3+3\frac{g_1}{r}\right)\\
&\qquad-r_{,i}r_{,j}r_{,k}\frac{1}{Cr}\left[g_7+\frac{3}{r}\left(g_3+2\frac{g_1}{r}\right)\right],\\
&g_7=\frac{m}{4\pi\left[\lambda_1^2-\lambda_2^2\right]}\left[\lambda_1^3e^{-r\lambda_1}-\lambda_2^3e^{-r\lambda_2}\right]
\end{aligned}\tag{36}$$

Approaching the field point $\mathbf{x}$ in (35) to the boundary point $\boldsymbol{\zeta}\in S_A$ and multiplying this equation by the normal vector $n_p(\boldsymbol{\zeta})$, one can derive the traction BIE with strongly singular integrals being taken in the Cauchy principal value sense. However, a more advanced regularized form of the traction BIE is available too (see, e.g., [6]).

Finally, performing the inverse Laplace transformation in (35) and (36), one obtains

$$\begin{aligned}
&h(\mathbf{x})\,\mathbf{u_j}(\mathbf{x},t)\\
&\quad=\int_0^t\{\int_V\left[F_i(\mathbf{y},\tau)\,U_{ij}(\mathbf{y}-\mathbf{x},t-\tau)\right.\\
&\quad-Q\,(\mathbf{y},\tau)U'_j(\mathbf{y}-\mathbf{x},t-\tau)\big]\,dV_y\\
&\quad+\int_{S_A}\left[t_i(\boldsymbol{\eta},\tau)\,U_{ij}(\boldsymbol{\eta}-\mathbf{x},t-\tau)\right.\\
&\quad-u_i(\boldsymbol{\eta},\tau)\,T_{ij}(\boldsymbol{\eta}-\mathbf{x},t-\tau)\big]\,dS_\eta\\
&\quad+C\int_{S_A}\left[\theta(\boldsymbol{\eta},\tau)\,n_i(\boldsymbol{\eta})\,\partial_i\,U'_j(\boldsymbol{\eta}-\mathbf{x},t-\tau)\right.\\
&\quad\left.-q(\boldsymbol{\eta},\tau)U'(\boldsymbol{\eta}-\mathbf{x},t-\tau)\big]\,dS_\eta\right\}d\tau\\
&\quad+\rho\int_V\left(u_i(\mathbf{x})\frac{\partial}{\partial t}+v_i(\mathbf{x})\right)U_{ij}(\mathbf{x}-\mathbf{y},t)dV_y\\
&\quad-\int_V\theta(\mathbf{x})U'_j(\mathbf{x}-\mathbf{y},t)dV_y
\end{aligned}\tag{37}$$

and

$$\begin{aligned}
&\sigma_{lp}(\mathbf{x},t)+\gamma\delta_{lp}\,\theta(\mathbf{x},t)\\
&\quad=c_{lpjr}\left\{\int_V\left[F_i(\mathbf{y},\tau)\partial_r\,U_{ij}(\mathbf{y}-\mathbf{x},t-\tau)\right.\right.\\
&\quad\left.-Q(\mathbf{y},\tau)\partial_r\,U'_j(\mathbf{y}-\mathbf{x},t-\tau)\right].dV_y\\
&\quad-\int_{S_A}t_i(\boldsymbol{\eta},\tau)\partial'_r\,U_{ij}(\boldsymbol{\eta}-\mathbf{x},t-\tau)\,dS_\eta\\
&\quad+c_{iskt}\int_{S_A}k_{rst}\partial'_t\,U_{kj}(\boldsymbol{\eta}-\mathbf{x},t-\tau)\,dS_\eta\\
&\quad+\rho\int_{S_A}\ddot{u}_i(\boldsymbol{\eta},\tau)\,n_r(\boldsymbol{\eta})\,\boldsymbol{U_{ij}}(\boldsymbol{\eta}-\mathbf{x},t-\tau)\,dS_\eta\\
&\quad-C\int_{S_A}\left[\theta(\boldsymbol{\eta},\tau)\,n_i(\boldsymbol{\eta})\,\partial'_i\,\partial'_r\,U'_j(\boldsymbol{\eta}-\mathbf{x},\mathbf{t}-\tau)\right.\\
&\quad\left.-\bar{q}(\boldsymbol{\eta},\tau)\partial'_r\,U'_j(\boldsymbol{\eta}-\mathbf{x},t-\tau)\right]\,dS_\eta\\
&\quad+\int_V\left[\rho\left(u_i(\mathbf{x})\frac{\partial}{\partial t}+v_i(\mathbf{x})\right)\partial_r\,U_{ij}(\mathbf{y}-\mathbf{x},t-\tau)\right.\\
&\quad\left.\left.-\theta(\mathbf{x})\partial_r\,U'_j(\mathbf{y}-\mathbf{x},t-\tau)\right]dV_y\right\}
\end{aligned}\tag{38}$$

Future Directions for Research

Although the fundamental solutions are available even for some special kinds of gradation of material coefficients, they are not available in general case of non-homogeneous media and/or for nonlinear problems. Nevertheless, having used the fundamental solutions for simplified operators, one can derive the boundary-domain integral formulations in such more complex problems. The domain integrals involving unknown fields occur also in time-stepping techniques for solution of transient problems. Such domain integrals, however, partially decrease the advantage of pure boundary integral formulations. Note that there are under development some approaches for treatment of such domain integrals. Instead of discretization of the analyzed domain with using domain cells only, some additional interior nodes are required [8–10]. Such sophisticated formulations utilize the advantages of the BIEM formulations without losing the universality of formulation. Another extension of universality and simplification of formulation consists in using the integral equation formulations with mesh-free approximations of field variables [11].

References

1. Sladek V, Sladek J (1983) Boundary integral equation method in thermoelasticity. Part I: general analysis. Appl Math Model 7:241–253
2. Sladek V, Sladek J (1984) Boundary integral equation method in thermoelasticity. Part III: uncoupled thermoelasticity. Appl Math Model 8:413–418
3. Sladek V, Sladek J (1990) Nonsingular BIE for transient heat conduction. Eng Anal Bound Elem 7:113–118
4. Sladek J, Sladek V (1991) Regularized integral representation of thermoelastic stresses. Eng Anal Bound Elem 8:224–230
5. Sladek V, Sladek J (1992) Non-singular boundary integral representation of potential field gradients. Int J Numer Method Eng 33:1181–1195
6. Balas J, Sladek J, Sladek V (1989) Stress analysis by boundary element methods. Elsevier, Amsterdam
7. Sladek V, Sladek J (1998) Singular integrals in boundary element methods. CMP, Southampton
8. Ochiai Y, Sladek V (2004) Numerical treatment of domain integrals without internal cells in three-dimensional BIEM formulations. CMES Comp Model Eng Sci 6:525–536
9. Ekhlakov AV, Khay OM, Zhang C, Sladek J, Sladek V (2010) Transient coupled thermoelastic crack analysis in functionally graded materials. SDHM Struct Durabil Health Monitor 6:329–350
10. Ekhlakov AV, Khay OM, Zhang C, Sladek J, Sladek V (2011) A meshless BEM for transient thermoelastic crack analysis in functionally graded materials. In: Albquerque EL, Aliabadi MH (eds) Advances in boundary element techniques XII. Ltd Publications, Eastleigh/Hampshire, pp 38–43
11. Sladek J, Sladek V, Solek P, Tan CL, Zhang CH (2009) Two- and three-dimensional transient thermoelastic analysis by the MLPG method. CMES Comp Model Eng Sci 47:61–95

Application of GS4-1 Time Integration Framework to Linear Heat Transfer: Transient Heat Conduction

Siti Ujila Masuri[1] and Kumar K. Tamma[2]
[1]Department of Mechanical and Manufacturing Engineering, Universiti Putra Malaysia, UPM Serdang, Selangor, Malaysia
[2]Department of Mechanical Engineering, University of Minnesota, Minneapolis, MN, USA

Overview

Many problems to be solved by engineers and researchers are dynamics or time-dependent systems. Dynamic systems mean that the solutions of the problem change with time. In the heat transfer, the heat conduction problems, which describe the transfer of thermal energy between regions of an object due to difference in temperature, could become time-dependent due to an imposed change in temperature at the object's boundary. This time-dependent heat conduction may also occur when a source (or sink) of heat is suddenly applied within the object and subsequently causes change in the nearby temperatures.

Solving time-dependent engineering problems is not always simple. In practice or even in the academic world, the engineers or researchers often have to deal with engineering problems whose equations involve multiple physics, and

geometries are large scale if not complex. For such problems, it is almost impossible to derive analytical solutions to problems. Therefore, it has become a common practice for engineers and scientists to rely on numerical methods or computational softwares to obtain the solutions.

Basic Concepts

Solving these problems numerically or computationally usually involves two major steps. Firstly, the whole spatial domain of the problem, as enclosed by the geometry, is broken into discrete elements. These discrete elements are interconnected between one another such that their assembly represents the problem's actual continuous spatial domain. By doing so, one is allowed to create elemental equations that approximate the actual equation of the problem, given enough discrete elements. This step, known as spatial discretization, transforms the problem's actual equation (that is complicated due to its nature of being partial differential) to a set of ordinary differential equations that is easier to be solved. A number of different spatial discretization methods are available including finite element method, finite difference method, finite volume method, and boundary element method, to name a few. When the problem is time dependent, the resulting set of ordinary differential equations will be time dependent. Some problems are dependent on time to a first order, such as parabolic heat conduction problems. Others are second order in time such as hyperbolic heat conduction problems.

Once the problem's equation is written as a set of ordinary differential equations after use of any spatial discretization method, the next step in the numerical method is to solve such set of equations using a solver or method that can give the solutions to the problem at each time level and throughout the whole simulation period. Such a method is called time integrator. To date, there exist in the literature a variety of different classes of time integrators for solving time-dependent engineering problems, such as the so-called linear multistep methods, sub-stepping methods, Runge–Kutta type methods, and higher-order time-accurate methods. Of particular interest is a class of time integrators characterized as a single-system and a single-solve method. A single step means that the time integrator requires solutions of only one previous time level, while a single solve implies that the method needs to solve only one system of equations. These characteristics of such class of time integrators make it probably the simplest of its kind, which subsequently require the least computational effort. Due to such a convenience of this class of time integrators, we have been focusing much of our previous effort on its development and improvement.

Looking at the big picture of time integrators, under the class of single step and single solve, a new design concept, namely, the notion of *Algorithms by Design*, was first introduced for applications in linear structural dynamics problems [1, 2]. This relatively new design concept describes how to design time integrators via a unified theory which encompasses existing and new time integrators under a generalized mathematical framework. In this design procedure, one can a priori tailor the design of a time integrator according to predetermined desirable attributes of the proposed time integrator. Extensions to nonlinear structural dynamic systems also appear in [3]. This is in contrast to classical design approach where one a posteriori studies the time integrator's properties resulting from an "idea" which could physically base interpretation or a mathematical representation of an assumed construct.

In these earlier studies, it was shown for linear structural dynamic problems (second-order time-dependent systems) that the *Algorithms by Design* procedure successfully leads to the design of a framework consisting of new and existing generalized single-step single-solve time integrators. This framework, formerly termed as GSSSS but herein referred to as GS4-2 (where "2" stands for second-order time-dependent system), uniquely enables most existing linear multistep (LMS) methods in the literature (for solving second-order time-dependent problems) to be cast into a single modular routine regardless of the original approach of how those time integrators were developed. These existing time integrators

include the midpoint rule, Newmark average acceleration [4], velocity-based scheme [5], HHT-α method [6, 7], and WBZ method [8]. This framework also provides new and optimal time integrators characterized by the underlying algorithmic overshoot behavior [1, 2]. As a result, the framework offers a wide variety of time integrator choices to the analyst.

For first-order time-dependent systems that frequently arise in engineering problems, there exist in the literature a number of time integrators that are single step and single solve. The popular and often used ones are those belonging to the so-called θ-family of time integrators including the Crank-Nicolson [9], Forward Euler, Backward Euler, and Galerkin methods. These time integrators are to be distinguished according to the order of accuracy in time discretization. An order of accuracy represents the order in which convergence to the exact solution of the ODE can be obtained. Some of these time integrators are only first-order accurate, such as the Forward Euler, Backward Euler, and Galerkin methods. The Crank-Nicolson method, although is second-order accurate, is also well known to cause instabilities or oscillations in the resulting solutions. Such unrealistic behavior is due to the fact that the Crank-Nicolson method is characterized by a zero numerical damping property.

Numerical damping is an interesting attribute of a time integrator that is artificially added in order to obtain more stable solutions. The need for numerical damping frequently arises in simulation of fluid dynamics and flow transport problems especially those of turbulent flows. These problems require robust and efficient computational methods that possess numerical damping attribute to meet the strict needs in running simulation of such problems for very long time periods. Especially for fluid dynamics problems where the equation is nonlinear, it has long been recognized that the numerical damping of the time integrator is of great interest to obtain physically meaningful numerical solutions. However, because this damping is artificially added into the system, it may drain the energy out of the system leading to physically incorrect dynamics of the systems for long-term simulations. Therefore, while numerical damping is needed to suppress the numerical oscillation, there is a crucial need to balance between this need and the resulting amount of artifact added into the system to ensure that the dynamics of the system is correctly represented. Because of this required balancing act, it is desirable that the time integrator can produce acceptable solutions with minimal amount of numerical damping. For this reason, it is desirable that the numerical damping attribute can be selectively controlled by the analyst.

Controllable numerical dissipative methods including optimal algorithm designs exist for integrating second-order dynamic systems such as elastodynamics problems and to a limited extent have also been applied to first-order systems for integrating the transient system of equations [1, 2, 10, 11]. Recently, a generalized single-system single-solve computational approach has been developed that permits order preservation with second-order time-accurate features and unconditionally stability with zero-order overshoot behavior for a family of time integrators in conjunction with possessing a new feature of selective control of high-frequency damping for the integration of transient first-order parabolic systems such as the heat-conduction type, termed as GS4-1 framework [10]. Such a family of methods were developed by utilizing in a consistent manner the *Algorithms by Design* procedure previously introduced for second-order systems via a generalized time-weighted residual approach [1, 2]. This approach is introduced to the discretized system of equations with free parameters, which are then adjusted to suit the desired algorithmic attributes, which are (1) second-order accurate, (2) unconditionally stable, (3) zero-order overshoot, and (4) selective and controllable numerical dissipation. Detailed derivation of this new framework can be found elsewhere [10].

The key feature in this framework is the incorporation of a spurious root (ρ_∞^s), in addition to the principal root (ρ_∞), to allow for selective and more flexible control of the high-frequency damping (for both the primary variable and its time derivative, respectively) for a successful simultaneous elimination of the numerical oscillation associated with these variables. Such a

design thereby yields a two-parameter (ρ_∞ and ρ_∞^s) family of methods with a more flexible user control of high-frequency damping for the two variables, respectively. By allowing the two parameters to be equal (i.e., $\rho_\infty = \rho_\infty^s$), the amount of the high-frequency damping for the two variables is hence equal. However, the same amount of damping may not be sufficient to suppress the numerical oscillation in the time-derivative variable. This nonphysical instability in the time-derivative variable can lead to physically incorrect dynamics of the system for long-term simulations. This places a limitation. To overcome this drawback, we allow a more flexible control of the high-frequency damping by introducing different amounts of numerical dissipation in the two variables which is inherent in the present developments. Such a selective control of the high-frequency damping would allow simultaneous elimination of the numerical oscillation associated with the two variables. The GS4-1 computational framework that is described here is designed for first-order systems and encompasses algorithm designs with zero-order overshoot with selective controllable numerical dissipation in both the primary variable and its time derivative and inherits features that enable a family of second-order time-accurate preserving algorithms and designs.

Governing Equation of Transient Parabolic Heat Conduction

Before presenting the recently developed GS4-1 time integration solver, it would be useful to first describe the specific physical systems to be solved by the new solver. For this purpose, we consider the transient heat conduction problem defined by the following governing equation (for materials with constant specific heat (c), density (ρ), and conductivity (k)):

$$\rho c\,\frac{\partial T(\mathbf{x},t)}{\partial t} = k\nabla^2 T(\mathbf{x},t) + \mathbf{Q}, \quad \forall \mathbf{x} \in \Omega \subset R^d, t > 0 \tag{1}$$

where $T(\mathbf{x},t)$ represents the temperature field at position $\mathbf{x}$ and time t, $\mathbf{Q}$ is the source or sink of heat introduced within the system, $\mathbf{x} = (x_1, x_2, ..., x_d)$ is the vector position, d is the dimension of the problem, and Ω is a bounded domain in R^d. This governing (1) is subject to the following conditions on the boundary Γ:

$$T(\mathbf{x},t) = T_\Gamma(\mathbf{x},t) \quad \forall \mathbf{x} \in \Gamma_1 \tag{2}$$

$$k\nabla T \cdot \vec{\mathbf{n}} = q(\mathbf{x}) \quad \forall \mathbf{x} \in \Gamma_2 \tag{3}$$

$$\Gamma = \Gamma_1 + \Gamma_2 \tag{4}$$

and initial conditions

$$T(\mathbf{x}, t=0) = T_0(\mathbf{x}) \quad \forall \mathbf{x} \in \Omega \tag{5}$$

where Γ is the boundary on Ω, while $T_\Gamma(\mathbf{x},t)$, $q(\mathbf{x})$, and T_0 are known vectors of boundary and initial conditions.

Spatial Discretization by Finite Element Method

As previously mentioned, the first step in solving the time-dependent problems numerically or computationally is to transform the problem continuous equation to a set of ordinary differential equations that is easier to be solved. Employing the finite element method, the spatial discretization can be done by applying the method of weighted residuals to (1) as

$$\int_{\Omega^{(e)}} W_i \left(\rho c\,\frac{\partial T(\mathbf{x},t)}{\partial t} - k\nabla^2 T(\mathbf{x},t) - \mathbf{Q} \right) \partial\Omega = 0 \tag{6}$$

where W_i is the weighting function and $\Omega^{(e)}$ is the domain for an element (e). We next apply Gauss's theorem to the diffusive term as follows:

$$\begin{aligned} &\int_{\Omega^{(e)}} W_i(\nabla \cdot k\nabla T(\mathbf{x},t))\partial\Omega \\ &\quad = \int_{\Gamma^{(e)}} W_i(k\nabla T(\mathbf{x},t)) \cdot \vec{\mathbf{n}}\ \ \partial\Gamma \\ &\quad\quad - \int_{\Omega^{(e)}} \nabla W_i \cdot (k\nabla T(\mathbf{x},t))\partial\Omega \end{aligned} \tag{7}$$

where $\vec{\mathbf{n}}$ is the normal direction at the boundary $\partial\Omega^{(e)}$ for this element. Substituting (7) into (6) yields

$$\int_{\Omega^{(e)}} W_i\left(\rho c\ \frac{\partial T(\mathbf{x},t)}{\partial t}\right)\partial\Omega + \int_{\Omega^{(e)}} \nabla W_i \cdot (k\nabla T(\mathbf{x},t))\partial\Omega = \int_{\Gamma^{(e)}} W_i(k\nabla T(\mathbf{x},t)) \cdot \vec{\mathbf{n}}\ \ \partial\Gamma \tag{8}$$

We next approximate the primary variable $T(\mathbf{x},t)$ as follows:

$$T(\mathbf{x},t) = N(\mathbf{x})_i T(t)_i \tag{9}$$

where $N(\mathbf{x})_i$ is the element shape function and $T(t)$ is the vector of nodal solutions of the element at time t. Substituting (9) into (8) and imposing the Neumann boundary condition yield the following first-order time-dependent ordinary differential equations:

$$\mathbf{M}\dot{\mathbf{T}} + \mathbf{K}\mathbf{T} = \mathbf{F} \tag{10}$$

where

$$\mathbf{M} = \sum_{e=1}^{n} \mathbf{M}^{(e)} = \sum_{e=1}^{n} \int_{\Omega^{(e)}} (W_i N_j)\ \ \partial\Omega$$
$$\mathbf{K} = \sum_{e=1}^{n} \mathbf{K}^{(e)} = \sum_{e=1}^{n} \int_{\Omega^{(e)}} (\nabla W_i \cdot k\nabla N_j)\ \ \partial\Omega$$
$$\mathbf{F} = \sum_{e=1}^{n} \mathbf{F}^{(e)} = \sum_{e=1}^{n} \int_{\Gamma^{(e)}} (W_i q(\mathbf{x}))\ \ \partial\Gamma \tag{11}$$

are the mass matrix, stiffness matrix due to diffusion, and force vector due to the Neumann boundary condition, respectively, while n is the total number of elements used in the spatial discretization. Equation (10) is a set of first-order time-dependent ordinary differential equations (after the summation over all elements). This completes the first step in the numerical or computational procedure to solve the problems.

As previously mentioned, the second step in the computation procedure is to solve the resulting set of first-order time-dependent ordinary differential equations using an appropriate time integrator to give the solutions of the primary variable (T) and its time derivative ($\dot{\mathbf{T}}$) at each time level and throughout the simulation period. In this work, we propose to perform this step using the GS4-1 framework, a new family of time integrators with optimal properties developed in this study. To show the improvement offered by this framework via its selective control features over the existing or current state of art, we will solve the problems using the GS4-1 framework, with and without the selective control features, in which case the former represents the new/present developments, whereas the latter is representative of past developments. Results are shown in section "Numerical Results". It is of great importance, however, to first present the development of this new time integration framework as described next.

Development of GS4-1 Time Integrator

We proceed in this section by introducing the GS4-1 time integration framework for solving the resulting set of first-order time-dependent ordinary differential equations (such as (10)) from one time level (t_n) to the next time level (t_{n+1}). The GS4-1 time integration framework can be derived by introducing a time-weighted residual approach with arbitrary-weighted time field $\mathcal{W}$ to the semi-discretized system of Equations (10) as follows:

$$\int_0^{\Delta t} \mathcal{W}[\mathbf{M}\dot{\mathbf{T}} + \mathbf{K}\mathbf{T} - \mathbf{F}]dt = 0 \tag{12}$$

The weighted time field, $\mathcal{W}$, in (12) is assumed to be a degenerated scalar polynomial function of the form

$$\mathcal{W} = 1 + w_1\Gamma + w_2\Gamma^2 \tag{13}$$

where $\Gamma = \frac{\tau}{\Delta t}$ and $\tau \in [0, \Delta t]$, while $\Delta t = t_{n+1} - t_n$.

The primary variable ($\mathbf{T}$) and its time derivative ($\dot{\mathbf{T}}$) in (12) are then approximated using an

asymptotic series type expansion, whereas the load term, **F**, is approximated using Taylor series expansion

$$\dot{\mathbf{T}} = \dot{\mathbf{T}}_n + \Lambda_6 \frac{\Delta\dot{\mathbf{T}}}{\Delta t}\tau \tag{14}$$

$$\mathbf{T} = \mathbf{T}_n + \Lambda_4 \dot{\mathbf{T}}_n \tau + \Lambda_5 \frac{\Delta\dot{\mathbf{T}}}{\Delta t}\tau^2 \tag{15}$$

$$\mathbf{F} = \mathbf{F}_n + \frac{\mathbf{F}_{n+1} - \mathbf{F}_n}{\Delta t}\tau \tag{16}$$

where

$$\Delta\dot{\mathbf{T}} = \dot{\mathbf{T}}_{n+1} - \dot{\mathbf{T}}_n \tag{17}$$

while Λ_6, Λ_5, and Λ_4 are at this point free parameters. Substituting the approximations, (14)–(16) into (12), dividing the resulting equation by $\int_0^{\Delta t} \mathcal{W}\, dt$, and defining for convenience

$$W_i = \frac{\int_0^{\Delta t} \mathcal{W} \left(\frac{\tau}{\Delta t}\right)^i dt}{\int_0^{\Delta t} \mathcal{W}\, dt} \tag{18}$$

yield the GS4-1 time integration framework in form of free parameters as follows:

$$\begin{aligned}\mathbf{M}[\dot{\mathbf{T}}_n + \Lambda_6 W_1 \Delta\dot{\mathbf{T}}] + \mathbf{K}[\mathbf{T}_n + \Lambda_4 W_1 \Delta t\, \dot{\mathbf{T}}_n \\ + \Lambda_5 W_2 \Delta t \Delta\dot{\mathbf{T}}] = (1 - W_1)\mathbf{F}_n + W_1 \mathbf{F}_{n+1}\end{aligned} \tag{19}$$

The above formulation can be represented as

$$\mathbf{M}\widetilde{\dot{\mathbf{T}}} + \mathbf{K}\widetilde{\mathbf{T}} = \widetilde{\mathbf{F}} \tag{20}$$

where

$$\widetilde{\dot{\mathbf{T}}} = \dot{\mathbf{T}}_n + \Lambda_6 W_1 \Delta\dot{\mathbf{T}} \tag{21}$$

$$\widetilde{\mathbf{T}} = \mathbf{T}_n + \Lambda_4 W_1 \Delta t\, \dot{\mathbf{T}}_n + \Lambda_5 W_2 \Delta t \Delta\dot{\mathbf{T}} \tag{22}$$

$$\widetilde{\mathbf{F}} = \mathbf{F}_n + W_1(\mathbf{F}_{n+1} - \mathbf{F}_n) \tag{23}$$

The associated expressions for the updates are chosen as

$$\mathbf{T}_{n+1} = \mathbf{T}_n + \lambda_4 \dot{\mathbf{T}}_n \Delta t + \lambda_5 \Delta\dot{\mathbf{T}} \Delta t \tag{24}$$

$$\dot{\mathbf{T}}_{n+1} = \dot{\mathbf{T}}_n + \Delta\dot{\mathbf{T}} \tag{25}$$

The above formulation is the GS4-1 time integration framework in generalized representation (in form of free parameters). These free parameters ($\Lambda_6 W_1$, $\Lambda_5 W_2$, $\Lambda_4 W_1$, W_1, λ_4, and λ_5) are related to W_i, Λ_i, and λ_i that are contained in the approximations for the primary variable, its time derivative, and the load term in the design of the integrator and updates. They uniquely define an algorithm and serves as the discrete numerically assigned (DNA) algorithmic markers which are an algorithm's signature. Utilizing the concept of *Algorithm by Design*, a priori decide (wish list) the desirable algorithmic properties and impose those wish list to the generalized framework to determine these free parameters. Such a procedure has been presented in detail in our previous exposition [10] and will not be repeated here.

The desirable algorithmic attributes considered are (1) second-order accurate, (2) unconditionally stable, (3) zero-order overshoot behavior, and (4) controllable numerical dissipation in both the primary variable and its time derivative with selective control feature (i.e., the numerical dissipation of these two variables can be controlled separately). These algorithmic properties are then imposed upon the generalized framework to determine the free parameters. These parameters are then expressed in terms of the spectral radius for an infinite time step to obtain a framework with strict control of high-frequency damping. Because our goal is to develop a method with a more flexible control of the high-frequency damping in contrast to limited control, we require that the high-frequency damping of both the primary variable and its time derivative to be expressed in terms of two parameters: (1) a principal root (ρ_∞) and (2) a spurious root (ρ_∞^s). These two parameters separately control the high-frequency damping of the primary variable (T) and its time

derivative ($\dot{T}$), respectively. Such an approach would allow for different amounts of numerical dissipation in T and $\dot{T}$ to obtain simultaneous elimination of the numerical oscillations associated with these two variables. This is in contrast to past developments which control the high-frequency damping on the primary variable and its time derivative indiscriminately, i.e., without the selective control features.

For a small amount of dissipation that is desirable, the case without the selective control features may result in a large error in $\dot{T}$, although it may yield an acceptable solution for T. This behavior can lead to physically incorrect dynamics of the systems for long-term simulations. Such a restriction hence places a limitation. On the other hand, the selective control of the high-frequency damping additionally featured within the GS4-1 framework offers solutions that are not only acceptable but also represent physically correct dynamics. Such a design thereby yields a two-parameter (ρ_∞ and ρ_∞^s) family of methods with a more flexible user control of high-frequency damping for the primary variable and its time derivative, respectively. Furthermore, by allowing the two parameters to be equal (i.e., $\rho_\infty = \rho_\infty^s$), the amount of the high-frequency damping for the two variables is hence equal. In this case, the framework replicates both practices without selective control and with limited control of high-frequency damping.

By imposing this new feature, we can express the algorithmic parameters ($\Lambda_6 W_1$, $\Lambda_5 W_2$, $\Lambda_4 W_1$, W_1, λ_4, and λ_5) in terms of ρ_∞ and ρ_∞^s as follows:

$$\begin{aligned}
\Lambda_6 W_1 &= \frac{3+\rho_\infty+\rho_\infty^s-\rho_\infty\rho_\infty^s}{2(1+\rho_\infty)(1+\rho_\infty^s)},\\
\Lambda_5 W_2 &= \frac{1}{(1+\rho_\infty)(1+\rho_\infty^s)},\\
\Lambda_4 W_1 &= \frac{1}{1+\rho_\infty}, W_1 = \frac{1}{(1+\rho_\infty)}, \quad \lambda_4 = 1,\\
\lambda_5 &= \frac{1}{1+\rho_\infty^s}
\end{aligned} \tag{26}$$

For convenience, we rearrange (20) and substitute (26) to represent the GS4-1 time integrator in terms of ρ_∞ and ρ_∞^s for integrating the resulting set of first-order time-dependent ordinary differential Equations (10) as follows (i.e., for linear case).

Algorithm 1. *GS4-1 Time Integrator for Solving Linear Ordinary Differential Equations Describing Linear First-Order Time-Dependent Engineering Problems*

Consider linear first-order time-dependent engineering problems of the following form (after space discretization): $\mathbf{M}\dot{\mathbf{T}} + \mathbf{K}\mathbf{T} = \mathbf{F}$. Given $\mathbf{T}_n$ and $\dot{\mathbf{T}}_n$, we can find $\mathbf{T}_{n+1}$ and $\dot{\mathbf{T}}_{n+1}$ by first solving for $\mathbf{T}_{n+1}$ from

$$\begin{aligned}
&\left\{\left(\frac{3+\rho_\infty+\rho_\infty^s-\rho_\infty\rho_\infty^s}{2(1+\rho_\infty)}\right)\frac{\mathbf{M}}{\Delta t}+\left(\frac{1}{1+\rho_\infty}\right)\mathbf{K}\right\}\mathbf{T}_{n+1}\\
&\quad=\left\{\left(\frac{3+\rho_\infty+\rho_\infty^s-\rho_\infty\rho_\infty^s}{2(1+\rho_\infty)}\right)\frac{\mathbf{M}}{\Delta t}+\left(\frac{1}{1+\rho_\infty}\right)\mathbf{K}\right\}\mathbf{T}_n\\
&\quad+\left\{\left(\frac{3+\rho_\infty+\rho_\infty^s-\rho_\infty\rho_\infty^s}{2(1+\rho_\infty)}\right)-1\right\}\mathbf{M}\dot{\mathbf{T}}_n-\mathbf{K}\mathbf{T}_n\\
&\quad+\mathbf{F}_n+\left(\frac{1}{1+\rho_\infty}\right)(\mathbf{F}_{n+1}-\mathbf{F}_n)
\end{aligned}$$

and followed by updating the time-derivative variable as follows:

$$\dot{\mathbf{T}}_{n+1} = (1+\rho_\infty^s)\left(\frac{\mathbf{T}_{n+1}-\mathbf{T}_n}{\Delta t}\right) - \rho_\infty^s\,\dot{\mathbf{T}}_n \tag{27}$$

Numerical Results

To illustrate the selective control feature of the GS4-1 framework, the following transient heat conduction problem is considered. The problem is a two-dimensional rectangular slab with initial temperature of unity which is uniform over the entire domain. On the left boundary ($x = 0$), the Dirichlet boundary condition for the temperature is set to zero (cooled side), while all other boundaries are insulated (zero heat flux). The physical properties of the material are $\rho = 1.0$ kg/m^3, $c = 1.0$ J/(kg°C), and $k = 1.0$ W/(m°C). The domain of the problem is discretized using 64 quadrilateral elements using the finite element method.

The problem was solved using the GS4-1 time integration framework, with and without the

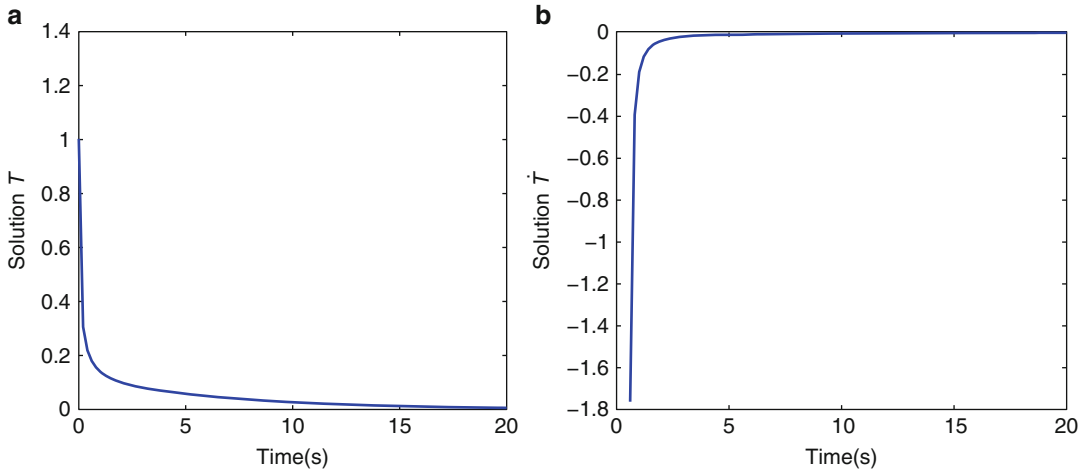

Application of GS4-1 Time Integration Framework to Linear Heat Transfer: Transient Heat Conduction, Fig. 1 Plot of analytical solutions T and $\dot{T}$ as a function of time for a specific node at ($x = 0.25$, $y = 0.5$)

selective control features, with a time step size (Δt) of 1 s and an end time of 20 s. While having two parameters (ρ_∞ and ρ_∞^s) in the GS4-1 framework has a certain appeal, we recall that our aim is to simultaneously suppress the nonphysical instabilities in both T and $\dot{T}$ to obtain solutions that are not only acceptable but also represent the correct dynamics of the problem. For this purpose, we let ρ_∞^s in the case with the selective control features to take a zero value regardless of the value of ρ_∞. Not only that this will ensure a successful elimination of the numerical oscillation associated with $\dot{T}$, such an approach would also allow for widest range of ρ_∞ to be tested (due to the restriction that $0 \leq \rho_{2\infty} \leq \rho_{1\infty} \leq 1$). Given this constraint on ρ_∞^s value, the GS4-1 framework with the selective control features turned on has only one parameter left to be specified (i.e., ρ_∞). We also recall that the case without the selective control features as in past developments can be recovered in the GS4-1 framework by defining $\rho_\infty = \rho_\infty^s$. For comparison purposes, we choose ρ_∞ for such case (i.e., the case without the selective control features) to take the same value as the ρ_∞ for the other case (i.e., the GS4-1 framework with the selective control features). For ρ_∞ we choose values ranging from 0 (i.e., maximal damping) to 1 (i.e., zero damping) in increments of 0.1. For each ρ_∞ value, we solve the problem using the two cases, i.e., the GS4-1 framework with and without the selective control features as defined above.

For analyses purposes, we compare the performance of the GS4-1 framework, with and without the selective control features, by first looking at the solutions of T and $\dot{T}$ as a function of time for a specific node. For this purpose, we chose ρ_∞ value of 0.4 and specific node at ($x = 0.25$, $y = 0.5$). The analytical solutions, as given in [12], are shown in Fig. 1. Meanwhile, the numerical solutions of T and $\dot{T}$ as a function of time for this node generated by the two representations, i.e., with and without selective control features, are illustrated in Fig. 2, which illustrates the improvement in the numerical solutions of T and $\dot{T}$ made by the GS4-1 framework with the selective control features turned on (i.e., the case with $\rho_\infty = 0.4, \rho_\infty^s = 0$), in contrast to the case without the selective control features (i.e., the case with $\rho_\infty = \rho_\infty^s = 0.4$) for the same value of $\rho_\infty = 0.4$. This difference in performance between these two cases highlights the role played by the selective control feature, which is the key desirable feature of the new GS4-1 framework not available in past developments.

For a complete investigation, we then compute and compare the errors in T and $\dot{T}$ generated by these two cases, respectively. An error is defined as

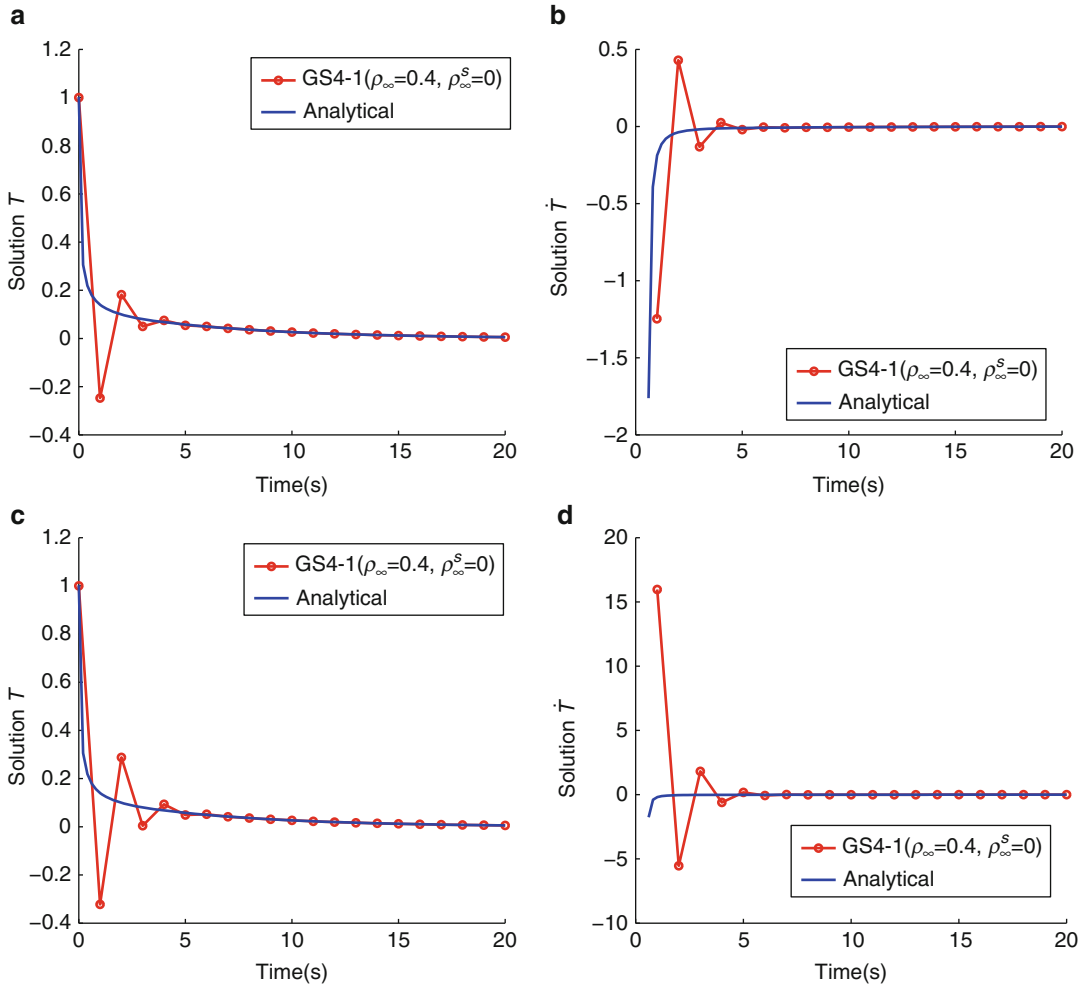

Application of GS4-1 Time Integration Framework to Linear Heat Transfer: Transient Heat Conduction, Fig. 2 Plot of T and $\dot{T}$ as a function of time for a specific node at ($x = 0.25$, $y = 0.5$) generated by (1) GS4-1 ($\rho_\infty = 0.4, \rho^s_\infty = 0$) and (2) GS4-1($\rho_\infty = 0.4$, $\rho^s_\infty = 0.4$), i.e., the case without selective control features

$$Error = |Numerical - Analytical| \tag{28}$$

Tables 1 and 2 compare the maximal and total errors in the solutions of primary variable (T) and its time derivative ($\dot{T}$), respectively, as generated by the two cases (i.e., the GS4-1 framework with and without the selective control features) for all ρ_∞ values considered. By looking at Table 1, it is obvious that the error in T generated by these two time integrators is very small. In other words, we can say that both cases perform well to obtain acceptable solutions of T. On the other hand, Table 2 shows that the errors in $\dot{T}$ (both maximal and total) generated by the case without the selective control features are large with exception for large amount of damping ($0 \leq \rho_{1\infty} \leq 0.6$) that is less desirable. Interestingly, these errors are significantly reduced by the GS4-1 time integration framework when the selective control feature is turned on. By looking at Table 2, therefore, we can say that the GS4-1 time integrator with the selective control feature provides improvement over the case without the selective control feature as in past development in generating solutions for $\dot{T}$.

Application of GS4-1 Time Integration Framework to Linear Heat Transfer: Transient Heat Conduction, Table 1 Comparison of error in T for the parabolic heat conduction problem between (1) the case without selective control features (i.e., GS4-1 framework with $\rho_\infty^s = \rho_\infty$) and (2) GS4-1 framework with selective control features with $\rho_\infty^s = 0$ for ρ_∞ values ranging from 1 (zero damping) to 0 (maximal damping) in decrements of 0.1

	Max error		Total error	
ρ_∞	Without selective control	Selective control	Without selective control	Selective control
1	0.0850	0.0850	0.3275	0.3275
0.9	0.0203	0.0101	0.1062	0.0479
0.8	0.0026	8.6609×10^{-4}	0.0217	0.0156
0.7	5.6841×10^{-4}	6.8083×10^{-4}	0.0117	0.0138
0.6	5.9327×10^{-4}	7.3724×10^{-4}	0.0121	0.0150
0.5	6.2957×10^{-4}	8.0159×10^{-4}	0.0128	0.0163
0.4	6.8459×10^{-4}	8.7569×10^{-4}	0.0139	0.0178
0.3	7.6622×10^{-4}	9.6192×10^{-4}	0.0156	0.0196
0.2	8.8666×10^{-4}	0.0011	0.0180	0.0216
0.1	0.0011	0.0012	0.0217	0.0241
0	0.0013	0.0013	0.0271	0.0271

Application of GS4-1 Time Integration Framework to Linear Heat Transfer: Transient Heat Conduction, Table 2 Comparison of error in $\dot{T}$ for the parabolic heat conduction problem between (1) the case without selective control features (i.e., GS4-1 framework with $\rho_\infty^s = \rho_\infty$) and (2) GS4-1 framework with selective control features with $\rho_\infty^s = 0$ for ρ_∞ values ranging from 1 (zero damping) to 0 (maximal damping) in decrements of 0.1

	Max error		Total error	
ρ_∞	Without selective control	Selective control	Without selective control	Selective control
1	70.2769	0.1757	226.9521	0.6587
0.9	8.5440	0.0222	24.6318	0.0843
0.8	0.8102	0.0022	48.7307	0.0091
0.7	0.0561	1.5954×10^{-4}	0.1437	0.0018
0.6	0.0026	6.7106×10^{-5}	0.0082	0.0014
0.5	8.2366×10^{-5}	7.1950×10^{-5}	0.0018	0.0015
0.4	8.5200×10^{-5}	7.7475×10^{-5}	0.0017	0.0016
0.3	8.8950×10^{-5}	8.3826×10^{-5}	0.0018	0.0017
0.2	9.4064×10^{-5}	9.1198×10^{-5}	0.0019	0.0019
0.1	1.0097×10^{-4}	9.9841×10^{-5}	0.0021	0.0020
0	1.1008×10^{-4}	1.1008×10^{-4}	0.0022	0.0022

Conclusions

A two-parameter GS4-1 time integration framework is presented for use in solving first-order time-dependent engineering problems. A key desirable feature of the new time integration framework is that it allows for a more flexible control of the numerical damping as compared to existing/past developments. In this time integration framework, the two parameters separately control the numerical damping of the primary variable and its time derivative, allowing for different amount of damping for these variables. This feature, termed as selective control feature, is not available in the existing time integrators for applications in first-order time-dependent engineering problems.

The application of GS4-1 time integration framework to a transient parabolic heat conduction problem was presented to illustrate the ability of the new solver to generate acceptable solutions of both the primary and time-derivative

variables using minimum numerical damping, which is a key desirable attribute of the newly developed GS4-1 time integration framework.

Acknowledgments The authors are very pleased to acknowledge support from Mighty River Power, New Zealand, under research contract number E5653. Thanks are also due to computer grants from the Minnesota Supercomputing Institute (MSI) at the University of Minnesota, Minneapolis, Minnesota.

References

1. Zhou X, Tamma KK (2004) Design, analysis, and synthesis of generalized single step single solve and optimal algorithms for structural dynamics. Int J Numer Methods Eng 59:597–668
2. Zhou X, Tamma KK (2006) Algorithms by design with illustrations to solid and structural mechanics/dynamics. Int J Numer Methods Eng 66:1738–1790
3. Masuri SU, Hoitink A, Zhou X, Tamma KK (2009) Algorithms by design: a new normalized time-weighted residual methodology and design of a family of energy-momentum conserving algorithms for non-linear structural dynamics. Int J Numer Methods Eng 79:1094–1146
4. Newmark NM (1959) A method of computation for structural dynamics. J Am Soc Civ Eng 1:67–94
5. Tamma KK, Namburu RR (1990) Applicability and evaluation of an implicit self-starting unconditionally stable methodology for the dynamics of structures. Comput Struct 34:835–842
6. Taylor RL, Hilber HM, Hughes TJR (1977) Improved numerical dissipation for time integration algorithms in structural dynamics. Earthq Eng Struct Dyn 5:283
7. Hilber HM (1977) Analysis and design of numerical integration methods in structural dynamics. PhD thesis, University of California
8. Zienkiewicz OC, Wood WL, Bossak M (1980) An alpha modification of Newmark's method. Int J Numer Methods Eng 15:1562
9. Crank J, Nicolson P (1947) Practical method for numerical evaluation of solutions of partial differential equations of the heat-conduction type. Math Proc Camb Philos Soc 43:50–67
10. Masuri S, Sellier M, Zhou X, Tamma KK (2011) Design of order-preserving algorithms for transient first-order systems with controllable numerical dissipation. Int J Numer Methods Eng. doi:10.1002/nme.3228
11. Jansen KE et al (2000) A generalized-α method for integrating the filtered Navier–Stokes equations with a stabilized finite element method. Comput Methods Appl Mech Eng 190:305–319
12. Loureiro FS, Mansur WJ (2009) A new family of time integration methods for heat conduction problems using numerical green's functions. Comput Mech 44(4):519–531

Application of GS4-1 Time Integration Framework to Nonlinear Heat Transfer: Heat Conduction in Medium with Temperature-Dependent Velocity

Siti Ujila Masuri[1] and Kumar K. Tamma[2]
[1]Department of Mechanical and Manufacturing Engineering, Universiti Putra Malaysia, UPM Serdang, Selangor, Malaysia
[2]Department of Mechanical Engineering, University of Minnesota, Minneapolis, MN, USA

Overview

Computational techniques, especially for proper time integration of transient nonlinear heat transfer and related applications, need to be not only robust but also should possess controllable numerical dissipative features to selectively control the high-frequency damping associated with all relevant variables describing the problem physics, should facilitate completion of the analysis, and should enable long simulation times. An overview of existing time discretized operators for transient first-order systems is described in Masuri et al. (ETS entry "► Application of GS4-1 Time Integration Framework to Linear Heat Transfer: Transient Heat Conduction" [1], wherein the new GS4-1 computational framework [2] is described. The new framework permits order preservation with computationally attractive numerical features and second-order time accuracy with and without controllable numerical dissipation. It additionally inherits a new feature of selective control of high-frequency damping for the relevant variables. Such a selective control of the high-frequency damping adequately permitted the simultaneous elimination of the numerical oscillations associated with the variables of physical interest. In this synopsis, we present the computational methodology with extensions to nonlinear first-order transient systems from the basic linear transient framework for application in a simple transient nonlinear heat transfer problem, with particular

illustration to nonlinear problem of heat conduction in a medium with temperature-dependent velocity, to highlight the essential aspects of the computational methodology that are needed to correctly capture the problem physics.

The Governing Equations

From the equation of continuity in hydrodynamics, one can derive for any time t and any point (x, y, z) of a solid, through which heat is flowing but within which no heat is supplied at the point, the temperature as a continuous function of x, y, z, and t satisfying [3]

$$\rho c \frac{\partial T}{\partial t} + \left(\frac{\partial f_x}{\partial x} + \frac{\partial f_y}{\partial y} + \frac{\partial f_z}{\partial z} \right) = 0 \tag{1}$$

where ρ is the density, c is the constant specific heat, while f_x, f_y, and f_z are the components of the heat flux vector at which heat crosses any plane of the isotropic surface per unit area per unit time at a point. We consider, for purpose of illustration of the proposed numerical methodology, the conduction of heat in an isotropic solid medium whose temperature field is governed by (1), while the medium is moving with a velocity whose components are (u_x, u_y, u_z). For such a case, the heat flux components (f_x, f_y, and f_z) can be expressed as

$$f_x = -k \frac{\partial T}{\partial x} + \rho c T u_x \tag{2}$$

$$f_y = -k \frac{\partial T}{\partial y} + \rho c T u_y \tag{3}$$

$$f_z = -k \frac{\partial T}{\partial z} + \rho c T u_z \tag{4}$$

where k is the temperature-independent thermal conductivity of the medium. The first term in the expressions of the heat flux components (2)–(4) represents the conduction part (i.e., the terms $-k\frac{\partial T}{\partial x}$, $-k\frac{\partial T}{\partial y}$, and $-k\frac{\partial T}{\partial z}$), while the latter term represents the convective part (i.e., the terms $\rho c T u_x$, $\rho c T u_y$, and $\rho c T u_z$) of the respective heat flux components. Substituting (2)–(4) into (1), the partial differential equation describing the conduction of heat in the moving medium can be expressed as

$$\rho c \frac{\partial T}{\partial t} + u_x \frac{\partial T}{\partial x} + u_y \frac{\partial T}{\partial y} + u_z \frac{\partial T}{\partial z} = k \left(\frac{\partial^2 T}{\partial x^2} + \frac{\partial^2 T}{\partial y^2} + \frac{\partial^2 T}{\partial z^2} \right) \tag{5}$$

If the velocity is dependent on the temperature, that is,

$$u_i = u_i(T), i = x, y, z \tag{6}$$

the partial differential (5) becomes nonlinear, that is,

$$\rho c \frac{\partial T}{\partial t} + u_x(T) \frac{\partial T}{\partial x} + u_y(T) \frac{\partial T}{\partial y} + u_z(T) \frac{\partial T}{\partial z} = k \left(\frac{\partial^2 T}{\partial x^2} + \frac{\partial^2 T}{\partial y^2} + \frac{\partial^2 T}{\partial z^2} \right) \tag{7}$$

To evaluate the relative performance of the present GS4-1 framework and the existing method and to demonstrate the ability of the proposed numerical methodology to solve such nonlinear heat conduction problems, we consider a one-dimensional heat conduction problem with temperature-dependent velocity, in which the partial differential (7) reduces to

$$\rho c \frac{\partial T}{\partial t} + u_x(T) \frac{\partial T}{\partial x} = k \frac{\partial^2 T}{\partial x^2} \tag{8}$$

Consider the case where the velocity is defined in terms of the temperature as

$$u_x = \alpha_0 + \alpha_1 T \tag{9}$$

where the coefficient $\alpha_0 + \alpha_1 T$ could be regarded as a temperature-dependent convection coefficient (where α_0 and α_1 are units of m/s and $m/s/K$, respectively). The physical heat transfer system that can be represented by such a coefficient is the cooling of a small metal casting or billet in a quenching bath after its removal

from a hot furnace [4]. Substituting (9) into (8) yields the governing equation of the illustrative problem as follows:

$$\rho c\left[\frac{\partial T}{\partial t}+(\alpha_0+\alpha_1 T)\frac{\partial T}{\partial x}\right]=k\frac{\partial^2 T}{\partial x^2}, \quad \forall x\in\Omega\subset R, t>0 \tag{10}$$

where Ω is a bounded domain in R defined by $0<x<L$ and where L is the length of the one-dimensional domain. The physical problem may be specified on the boundary, denoted Γ, by the Dirichlet and/or the Neumann boundary conditions

$$T=T_\Gamma \quad \forall x\in\Gamma_1 \tag{11}$$

$$k\frac{\partial T}{\partial n}=q \quad \forall x\in\Gamma_2 \tag{12}$$

$$\Gamma=\Gamma_1+\Gamma_2 \tag{13}$$

where $\partial/\partial n$ denotes differentiation along the outward-drawn normal to the surface Γ_2, while T_Γ and q are the known vectors of the prescribed temperature and flux. Furthermore, a known initial temperature must be specified to complete the problem description

$$T(t=0)=T_0 \quad \forall x\in\Omega \tag{14}$$

Spatial Discretization by Finite Element Method

We proceed in this section with the spatial discretization of nonlinear problems of the above type by employing the finite element method. To discretize the described problem in space using the standard Galerkin finite element method, we apply the method of weighted residuals to (10) (with the superscripts intentionally dropped for convenience and simplicity of notation). The temperature field of an element with N nodes is approximated by a linear combination of time-independent element shape functions $\psi_n(n=1,\ldots,N)$

$$T=\sum_{n=1}^{N}T_n\psi_n \tag{15}$$

The shape function ψ_n is used as the weighting function in the weighted residual equation. After use of (15), we obtain the following nonlinear ordinary differential equations

$$\mathbf{M}\dot{\mathbf{T}}+\mathbf{P}(\mathbf{T})+\mathbf{K}\mathbf{T}=\mathbf{F} \tag{16}$$

where $\mathbf{T}$ a vector of length N containing the nodal temperatures $T_n(n=1,....N)$, $\dot{\mathbf{T}}$ is the time derivative of $\mathbf{T}$, while $\mathbf{M}$ is the mass matrix of size $N\times N$ and is defined as ($p=1,\ldots,N$ and $q=1,\ldots,N$)

$$\mathbf{M}(p,q)=\int_\Omega \psi_p\psi_q d\,\Omega \tag{17}$$

Furthermore, $\mathbf{P}(\mathbf{T})$ is a vector of length N containing the nonlinear term and is defined as ($p=1,\ldots,N$)

$$\mathbf{P}(p)=\int_\Omega\left(\sum_{n=1}^{N}T_n\psi_n\sum_{l=1}^{N}T_l\frac{\partial\psi_l}{\partial x}\right)\psi_p d\Omega \tag{18}$$

In addition, $\mathbf{K}$ is the diffusion matrix of size $N\times N$ and is defined as ($p=1,\ldots,N$ and $q=1,\ldots,N$)

$$\mathbf{K}(p,q)=\int_\Omega\frac{\partial\psi_p}{\partial x}\frac{\partial\psi_q}{\partial x}d\Omega \tag{19}$$

and $\mathbf{F}$ is the force vector of length N resulting from integration by parts of the diffusive term in the governing equation. It is defined as ($p=1,\ldots,N$ and $i=1,2$)

$$\mathbf{F}(p)=\int_\Omega q^*\psi_p d\Omega \tag{20}$$

The ordinary differential equation (16) is consistently assembled for all elements in the domain to yield a system of nonlinear transient ordinary differential equations to be solved using specially tailored time discretization techniques to effectively capture the problem

physics (in contrast to following traditional practices which fail to capture the problem physics). This is described next.

Time Discretization by GS4-1 Framework via Normalized Time-Weighted Residual Approach

The system of ordinary differential equations given by (16) is nonlinear, which requires accurate treatment of the nonlinear terms in the time integration procedure to ensure satisfactory convergence of the nonlinear iterations during each time step. This can be achieved by employing the so-called and well-known normalized time-weighted residual approach which is new; it has been previously shown to provide significant improvement and also explain how to provide proper and accurate extensions to nonlinear structural dynamic type problems [5–7] in contrast to traditional practices. The idea behind the developed normalized time-weighted residual approach is to provide the necessary avenue to individually weigh and normalize each term in the nonlinear semi-discretized equation of motion. In contrast to the classical time-weighted residual approach and counterpart, this new approach is a general theoretical idea that inherently enables the nonlinear terms in the equation of motion to be treated specifically and consequently leads to a more appropriate treatment of the nonlinear terms. This approach can also explain and yields all possible treatments of the nonlinear term for implementation in a computational framework. For the nonlinear heat transfer problem considered here, the normalized time-weighted residual approach yields only one type of nonlinear treatment. Here, we illustrate the use of this treatment with the GS4-1 framework employed as the basic primitive time integrator to march the solutions in time. Employing such a method, the system of ordinary differential equations (16) becomes

$$\mathbf{M}\widetilde{\dot{\mathbf{T}}} + \mathbf{P}(\widetilde{\mathbf{T}}) + \mathbf{K}\widetilde{\mathbf{T}} = \widetilde{\mathbf{F}} \tag{21}$$

where

$$\widetilde{\dot{\mathbf{T}}} = \dot{\mathbf{T}}_n + \Lambda_6 W_1 \Delta\dot{\mathbf{T}} \tag{22}$$

$$\widetilde{\mathbf{T}} = \mathbf{T}_n + \Lambda_4 W_1 \Delta t\, \dot{\mathbf{T}}_n + \Lambda_5 W_2 \Delta t \Delta\dot{\mathbf{T}} \tag{23}$$

$$\widetilde{\mathbf{F}} = \mathbf{F}_n + W_1(\mathbf{F}_{n+1} - \mathbf{F}_n) \tag{24}$$

and

$$\Delta\dot{\mathbf{T}} = \dot{\mathbf{T}}_{n+1} - \dot{\mathbf{T}}_n \tag{25}$$

In (21)–(25), subscripts $()_n$ and $()_{n+1}$ denote the time levels t_n and t_{n+1} (where $t_{n+1} - t_n = \Delta t$), while the superposed $()$ denotes the algorithmic time level $\hat{t}$ between t_n and t_{n+1} (i.e., $t_n \le \hat{t} \le t_{n+1}$).

In this framework, the expressions for the update on the primary variable and its time derivative at the end of t_{n+1} time level are chosen as

$$\mathbf{T}_{n+1} = \mathbf{T}_n + \lambda_4\, \dot{\mathbf{T}}_n\, \Delta t + \lambda_5 \Delta\dot{\mathbf{T}} \Delta t \tag{26}$$

$$\dot{\mathbf{T}}_{n+1} = \dot{\mathbf{T}}_n + \Delta\dot{\mathbf{T}} \tag{27}$$

In (22)–(27), the algorithmic parameters $\Lambda_6 W_1$, $\Lambda_5 W_2$, $\Lambda_4 W_1$, W_1, λ_4, and λ_5 can be expressed in terms of the principal root (ρ_∞) and the spurious root (ρ_∞^s) as follows [2]:

$$\begin{aligned}
\Lambda_6 W_1 &= \frac{3 + \rho_\infty + \rho_\infty^s - \rho_\infty \rho_\infty^s}{2(1+\rho_\infty)(1+\rho_\infty^s)},\\
\Lambda_5 W_2 &= \frac{1}{(1+\rho_\infty)(1+\rho_\infty^s)},\\
\Lambda_4 W_1 &= \frac{1}{1+\rho_\infty}, W_1 = \frac{1}{(1+\rho_\infty)}, \lambda_4 = 1,\\
\lambda_5 &= \frac{1}{1+\rho_\infty^s}
\end{aligned} \tag{28}$$

where ρ_∞ and ρ_∞^s are the two, user-defined parameters satisfying the following conditions [2]

$$0 \le \rho_\infty^s \le \rho_\infty \le 1 \tag{29}$$

and defining the GS4-1 algorithm (i.e. the algorithms in GS4-1 framework are usually represented/defined as: GS4-1($\rho_\infty, \rho_\infty^s$)).

These two parameters, namely, ρ_∞ and ρ_∞^s, represent the selective, controllable numerical dissipative property of $\mathbf{T}$ and $\dot{\mathbf{T}}$, respectively, due to high-frequency damping. That is [2],

- ρ_∞ is associated with the numerical dissipative property of $\mathbf{T}$.
  $\rho_\infty = 1$ means that $\mathbf{T}$ is numerically nondissipative.
- ρ_∞^s is associated with the numerical dissipative property of $\dot{\mathbf{T}}$.
  $\rho_\infty^s = 1$ means that $\dot{\mathbf{T}}$ is numerically nondissipative.

By introducing ρ_∞^s in addition to ρ_∞, we are able to introduce selective control of the numerical dissipation at high frequency for the two variables ($\mathbf{T}$ and $\dot{\mathbf{T}}$) in the developed framework, allowing for different amount of numerical damping for these two variables. Such a feature is necessary for obtaining acceptable solutions of the two variables as often the time derivative variable ($\dot{\mathbf{T}}$) would require more numerical damping than that of the primary variable ($\mathbf{T}$). This selective control feature is a new desirable feature not available in any existing methods to date. More importantly is the fact that we are able to introduce an important feature while preserving second-order accuracy (i.e., order-preserving feature) resulting in a two-root system. This is in contrast to the classical Trapezoidal family of algorithms which is only a single root system.

Upon rearrangement, (22)–(27) can also be represented as follows:

$$\widetilde{\dot{\mathbf{T}}} = \left(1 - \frac{\lambda_4}{\lambda_5}\Lambda_6 W_1\right)\dot{\mathbf{T}}_n + \frac{\Lambda_6 W_1}{\lambda_5}\frac{\Delta\mathbf{T}}{\Delta t} \tag{30}$$

$$\widetilde{\mathbf{T}} = \mathbf{T}_n + \frac{\Lambda_5 W_2}{\lambda_5}\Delta\mathbf{T} \tag{31}$$

$$\widetilde{\mathbf{F}} = \mathbf{F}_n + W_1(\mathbf{F}_{n+1} - \mathbf{F}_n) \tag{32}$$

with the update equations

$$\mathbf{T}_{n+1} = \mathbf{T}_n + \Delta\mathbf{T} \tag{33}$$

$$\dot{\mathbf{T}}_{n+1} = \frac{1}{\lambda_5}\frac{\Delta\mathbf{T}}{\Delta t} + \left(1 - \frac{\lambda_4}{\lambda_5}\right)\dot{\mathbf{T}}_n \tag{34}$$

The two sets of equations, that is, (22)–(27) and (30)–(34), represent two different forms of the expressions for the algorithmic variables ($\dot{\mathbf{T}}$ and $\widetilde{\mathbf{T}}$) and the update expressions for the variable at end of time step ($\dot{\mathbf{T}}_{n+1}$ and $\mathbf{T}_{n+1}$). The equations in the former set (i.e., (22)–(27)) represent the algorithmic variables in terms of the increment of the time derivative variable ($\Delta\dot{\mathbf{T}}$), whereas in the latter set (i.e., equations (30) to (34) the equations represent the algorithmic variables in terms of the increment of the primary variable ($\Delta\mathbf{T}$). In the numerical methodology to be described next, we will make use of these two forms interchangeably as deemed necessary.

Numerical Methodology Via the GS4-1 Framework

In this section, we show how to use the GS4-1 computational framework with the midpoint rule representation for the nonlinear term, described in sect "Time Discretization by GS4-1 Framework via Normalized Time-Weighted Residual Approach," in a general mathematical setting, suitable for use in solving any nonlinear heat transfer problems. For this purpose, because the semi-discretized equation to be solved is nonlinear (21), we now employ the Newton–Raphson method to iteratively solve the equation at each time level. The computational details follow next.

Given/knowing the solutions at previous time level t_n (i.e., $\mathbf{T}_n$ and $\dot{\mathbf{T}}_n$), we seek the solutions of the nodal primary variable and its time derivative at the next time level t_{n+1} (i.e., $\mathbf{T}_{n+1}$ and $\dot{\mathbf{T}}_{n+1}$). At the beginning of t_{n+1} time level, we initially predict the solutions using known values at previous time level as follows:

$$\begin{aligned}\mathbf{T}_{n+1}^k &= \mathbf{T}_n \\ \dot{\mathbf{T}}_{n+1}^k &= \dot{\mathbf{T}}_n\left(1 - \frac{\lambda_4}{\lambda_5}\right)\end{aligned} \tag{35}$$

where k is the nonlinear iteration counter. We then calculate the algorithmic variables $\widetilde{\dot{\mathbf{T}}}^k$ and $\widetilde{\mathbf{T}}^k$ in terms of the predicted (i.e., $k = 1$) values $\mathbf{T}_{n+1}^k$ and $\dot{\mathbf{T}}_{n+1}^k$ using (31) and (22), respectively,

$$\widetilde{\mathbf{T}}^{k} = \mathbf{T}_n + \frac{\Lambda_5 W_2}{\lambda_5}(\mathbf{T}^{k}_{n+1} - \mathbf{T}_n) \tag{36}$$

$$\widetilde{\dot{\mathbf{T}}}^{k} = \dot{\mathbf{T}}_n + \Lambda_6 W_1(\dot{\mathbf{T}}^{k}_{n+1} - \dot{\mathbf{T}}_n) \tag{37}$$

We next enter the nonlinear iteration loop. This is done as follows:

1. In this nonlinear iteration loop, we first calculate the residual resulting from using the predicted algorithmic variables at the kth iteration. From use of (21), we have the residual at the kth iteration as

$$\widetilde{\mathbf{R}}^{k} = \mathbf{M}\,\widetilde{\dot{\mathbf{T}}}^{k} + \mathbf{P}(\widetilde{\mathbf{T}}^{k}) + \mathbf{K}\,\widetilde{\mathbf{T}}^{k} - \widetilde{\mathbf{F}}^{k} \tag{38}$$

2. We next linearize the residual using Taylor expansion, truncate after the linear term and set the residual to vanish. This step yields the following equation

$$\frac{\partial \widetilde{\mathbf{R}}^{k}}{\partial \widetilde{\mathbf{T}}^{k}}\Delta\widetilde{\mathbf{T}} = -\widetilde{\mathbf{R}}^{k} \tag{39}$$

where

$$\Delta\widetilde{\mathbf{T}} = \widetilde{\mathbf{T}}^{k+1} - \widetilde{\mathbf{T}}^{k} \tag{40}$$

and $\frac{\partial \widetilde{\mathbf{R}}^{k}}{\partial \widetilde{\mathbf{T}}^{k}}$ is the Jacobian given by

$$\begin{aligned}\frac{\partial \widetilde{\mathbf{R}}^{k}}{\partial \widetilde{\mathbf{T}}^{k}} &= \mathbf{M}\frac{\partial \widetilde{\dot{\mathbf{T}}}^{k}}{\partial \widetilde{\mathbf{T}}^{k}} + \frac{\partial \mathbf{P}(\widetilde{\mathbf{T}}^{k})}{\partial \widetilde{\mathbf{T}}^{k}} + K \\ &= \mathbf{M}\left(\frac{\Lambda_6 W_1}{\Lambda_5 W_2 \Delta t}\right) + \frac{\partial \mathbf{P}(\widetilde{\mathbf{T}}^{k})}{\partial \widetilde{\mathbf{T}}^{k}} + \mathbf{K}\end{aligned} \tag{41}$$

The term $\frac{\partial \mathbf{P}(\widetilde{\mathbf{T}}^{k})}{\partial \widetilde{\mathbf{T}}^{k}}$ in (41) is the derivative of the nonlinear vector $\mathbf{P}$ ((18) in terms of the algorithmic primary variable $\widetilde{\mathbf{T}}^{k}$) with respect to $\widetilde{\mathbf{T}}^{k}$. Because the evaluation of the $\mathbf{P}$ is dependent upon the choice of the element shape function (see (18)) and the type of element used in the finite element spatial discretization, a closed form equation for this term will also be dependent upon these factors and therefore will be given in section "Numerical Illustrations" where we discuss the benchmark numerical example of the considered transient nonlinear heat transfer problem.

Equation (39) can be rearranged to the following form

$$\widetilde{\mathbf{T}}^{k+1} = \left(\frac{\partial \widetilde{\mathbf{R}}^{k}}{\partial \widetilde{\mathbf{T}}^{k}}\right)^{-1} * \left(-\widetilde{\mathbf{R}}^{k} + \frac{\partial \widetilde{\mathbf{R}}^{k}}{\partial \widetilde{\mathbf{T}}^{k}}\,\widetilde{\mathbf{T}}^{k}\right) \tag{42}$$

3. We next impose the Dirichlet boundary condition (if any) to (42), and this can be done from the use of (36) by imposing that $\widetilde{\mathbf{T}}^{k}$ takes the following value

$$\widetilde{\mathbf{T}}^{k} = \mathbf{T}_n + \frac{\Lambda_5 W_2}{\lambda_5}(\mathbf{T}_\Gamma - \mathbf{T}_n) \tag{43}$$

where $\mathbf{T}_\Gamma$ is the known prescribed temperature at the boundary (see (11)).

4. We then solve for $\widetilde{\mathbf{T}}^{k+1}$ from (42) after imposing the boundary conditions appropriately.
5. Subsequently, we correct the time derivative variable using (30) as follows:

$$\widetilde{\dot{\mathbf{T}}}^{k+1} = \left(1 - \frac{\lambda_4}{\lambda_5}\Lambda_6 W_1\right)\dot{\mathbf{T}}_n + \frac{\Lambda_6 W_1}{\Lambda_5 W_2}\frac{(\widetilde{\mathbf{T}}^{k+1} - \mathbf{T}_n)}{\Delta t} \tag{44}$$

6. Upon obtaining the algorithmic variables at the $(k+1)$-th nonlinear iteration counter for the t_{n+1} time level, we have to check if convergence is met

$$|\,\widetilde{\mathbf{T}}^{k+1} - \widetilde{\mathbf{T}}^{k}\,| = tol \tag{45}$$

where tol is the user-specified tolerance value.

We repeat the nonlinear iteration (i.e., steps 1 to 6 described above) until the solution is converged (i.e., until (45) is satisfied). Upon convergence, we update the variables at the end of t_{n+1} time level as follows:

$$\begin{aligned}\mathbf{T}_{n+1} &= (\widetilde{\mathbf{T}}^{k+1} - \mathbf{T}_n)\frac{\lambda_5}{\Lambda_5 W_2} + \mathbf{T}_n \\ \dot{\mathbf{T}}_{n+1} &= \frac{(\mathbf{T}_{n+1} - \mathbf{T}_n)}{\lambda_5 \Delta t} + \dot{\mathbf{T}}_n\left(1 - \frac{\lambda_4}{\lambda_5}\right)\end{aligned} \tag{46}$$

Numerical Illustrations

In this section, we illustrate the advantage of the selective control features (i.e., by allowing $\rho_\infty \neq \rho_\infty^s$) inherent within the GS4-1 framework as compared to traditional practices without the selective control features (i.e., $\rho_\infty = \rho_\infty^s$) by solving a one-dimensional case of the transient nonlinear heat transfer problem governed by (10). In the spatial discretization by the finite element method, use 1D linear elements whose element shape functions are given by

$$\psi = \left[1 - \frac{x}{l}\ \frac{x}{l}\right] \tag{47}$$

where l is the length of each element. We discretize the spatial domain using 30 elements such that the Galerkin FEM can be appropriately used. These choices of the element type and the element shape functions (ψ) result in the following elemental nonlinear vector ($\mathbf{P}$, defined in (18)) for this particular problem

$$\mathbf{P} = \frac{1}{6}\begin{Bmatrix} -2T_1^2 + T_1T_2 + T_2^2 \\ -T_1^2 - T_1T_2 + 2T_2^2 \end{Bmatrix} \tag{48}$$

where T_1 and T_2 are the values of the nodal primary variable at node 1 and 2 of each element, respectively. Using (48), we can find the derivative of this vector with respect to the primary variable in a general form as follows:

$$\frac{\partial \mathbf{P}(\mathbf{T})}{\partial \mathbf{T}} = \frac{1}{6}\begin{bmatrix} -4T_1 + T_2 & T_1 + 2T_2 \\ -2T_1 - T_2 & -T_1 + 4T_2 \end{bmatrix} \tag{49}$$

Therefore, for the computation of the Jacobian in the Newton–Raphson iteration method (see (41)) we have

$$\frac{\partial \mathbf{P}(\widetilde{\mathbf{T}}^k)}{\partial \widetilde{\mathbf{T}}^k} = \frac{1}{6}\begin{bmatrix} -4\widetilde{T}_1^k + \widetilde{T}_2^k & \widetilde{T}_1^k + 2\widetilde{T}_2^k \\ -2\widetilde{T}_1^k - \widetilde{T}_2^k & -\widetilde{T}_1^k + 4\widetilde{T}_2^k \end{bmatrix} \tag{50}$$

where $\widetilde{T}_1^k$ and $\widetilde{T}_2^k$ are the values of the nodal algorithmic primary variable at node 1 and 2 of each element, respectively.

As mentioned earlier, we have previously seen in our earlier studies on transient linear first-order systems that the GS4-1 framework with the selective control features yields physically accurate and acceptable solutions for both the primary variable and its time derivative with only minimal numerical dissipation; this is sharp contrast to the case without employing the selective control features for which case numerical instabilities in the time derivative variable were observed for such transient linear situations. Our objective in this synopsis is to demonstrate that indeed, for extensions to transient nonlinear cases, the analogous algorithmic property of the recently developed GS4-1 framework with the selective control features holds for the transient nonlinear cases as well.

Results Illustrating the Method's Ability Via the Selective Control Feature

For this purpose, we solve the problem using the approach described and outlined above with a time step size $\Delta t = 5s$ and an end time of 50 s. We let the ρ_∞^s of the GS4-1 framework with the selective control features to take on a zero value, while the ρ_∞ values tested range from 1 (i.e., non-dissipative/zero damping) to 0 (i.e., maximal damping) in decrements of 0.1. The parameter defining the case without the selective control features (ρ_∞) will take the same value as the ρ_∞ for the present case (i.e., with the selective control features) to enable valid comparisons between the two cases, from which the ability and advantage of the selective control feature will be made transparent.

We first compare the performance of the GS4-1 framework (employing the numerical methodology described in section "Numerical Methodology Via the GS4-1 Framework") with and without the selective control features, by comparing the solutions of $\mathbf{T}$ and $\dot{\mathbf{T}}$ generated by these two cases as a function of time for a specific node number 2 ($x = 0.0333$) using ρ_∞ value of 1 for illustration. The numerical

solutions generated by the two algorithms (i.e., the case with and without selective control feature) are illustrated in Fig. 1. This figure shows that for the solutions of the primary variable ($\mathbf{T}$) both cases (i.e., with and without selective control feature) yield good results. However, for the solutions of the time derivative variable ($\dot{\mathbf{T}}$), it is clear from the figure that the case without the selective control features (i.e., $\rho_\infty = \rho_\infty^s$) results in large oscillations (it is to be noted that due to the automatic scale generated by the plotting routine employed, although not representative, this oscillation makes the analytical solution simply appear as a straight line due to the different ranges on the $\dot{\mathbf{T}}$ solution values; see Fig. 1d; alternately, the GS4-1 framework with the selective control features (i.e., $\rho_\infty \neq \rho_\infty^s$, with $\rho_\infty^s = 0$) indeed yields good agreement with the analytical solution with the same ρ_∞ value (hence is capable to capture the analytical solution curve; see Fig. 1b. This is because the GS4-1 framework with the selective control feature is able to successfully suppress the numerical oscillations associated with $\dot{\mathbf{T}}$ solution via such an important and practically useful feature. That is, by allowing the ρ_∞^s value to take on zero value, regardless of the choice of ρ_∞, the GS4-1 framework with the selective control features could guarantee that sufficient numerical damping is given to the time derivative variable ($\dot{\mathbf{T}}$) such that the large oscillations are successfully eliminated. Such a new feature is necessary as often the time derivative variable requires more numerical damping than the primary variable does. This requirement, however, cannot be achieved without the selective control feature as in the past practices since the numerical damping of both $\mathbf{T}$ and $\dot{\mathbf{T}}$ is of limited control, often indiscriminately; hence, a ρ_∞ value of 1 means a corresponding ρ_∞^s value of 1 as well. However, with the selective control features, the GS4-1 framework can enable algorithm designs defined by ρ_∞ value of 1 and ρ_∞^s value of 0 and subsequently could satisfy the need for larger numerical damping for the $\dot{\mathbf{T}}$ variable resulting in good agreement with the analytical solutions for both the $\mathbf{T}$ and $\dot{\mathbf{T}}$ variables. This clearly indicates the significance and advantage of the GS4-1 computational framework with the selective control features over the past practices wherein such a feature is not inherent.

In general, for problems involving thermal shock, the numerical solution of the primary variable ($\mathbf{T}$) will be oscillating, in which case numerical damping for this variable is needed to obtain physically representative solution. This type of problem is considered in [2] where the GS4-1 framework with the selective control feature is applied to solve linear transient parabolic heat conduction problem. It is however, beyond the discussion here since the problem considered in this synopsis does not involve any thermal shock. Our objective here is to demonstrate the ability of the present numerical methodology via the GS4-1 framework with selective control feature to give physically accurate and representative solutions of primary variable and its time derivative, even without having to impose numerical damping on the primary variable (i.e., $\rho_\infty = 1$). For illustration purpose only, we also show the solutions when numerical damping is imposed. Figure 2 shows the results when $\rho_\infty = 0.9$ with time step size of $\Delta t = 5s$. As suspected, the solutions of $\mathbf{T}$ generated by the two cases (with and without selective control feature) agree well with the analytical solution (see Fig. 2a, c). The numerical solution of $\dot{\mathbf{T}}$ is acceptable for the case with the selective control feature (see Fig. 2b) but is still oscillating for the case without the selective control feature (see Fig. 2d) although the amount of oscillation is reduced (as compared to Fig. 1d) due to the effect of numerical damping into the algorithm. When time step size is reduced to $\Delta t = 1s$, the oscillation in $\dot{\mathbf{T}}$ is still apparent as seen in Fig. 3d although is less than that for the case with $\Delta t = 5s$ (Fig. 2d).

Further attempt is made to investigate the performance of the algorithm without selective control feature (i.e., GS4-1 with $\rho_\infty = \rho_\infty^s$) when the numerical damping is further increased to approach the maximal value (i.e. $\rho_\infty \to 0$). For this purpose, we solve the problem using $\rho_\infty = 0.1$ with a time step size of $\Delta t = 1s$ and show results of $\mathbf{T}$ and $\dot{\mathbf{T}}$ generated by the two cases (i.e., with and without selective control

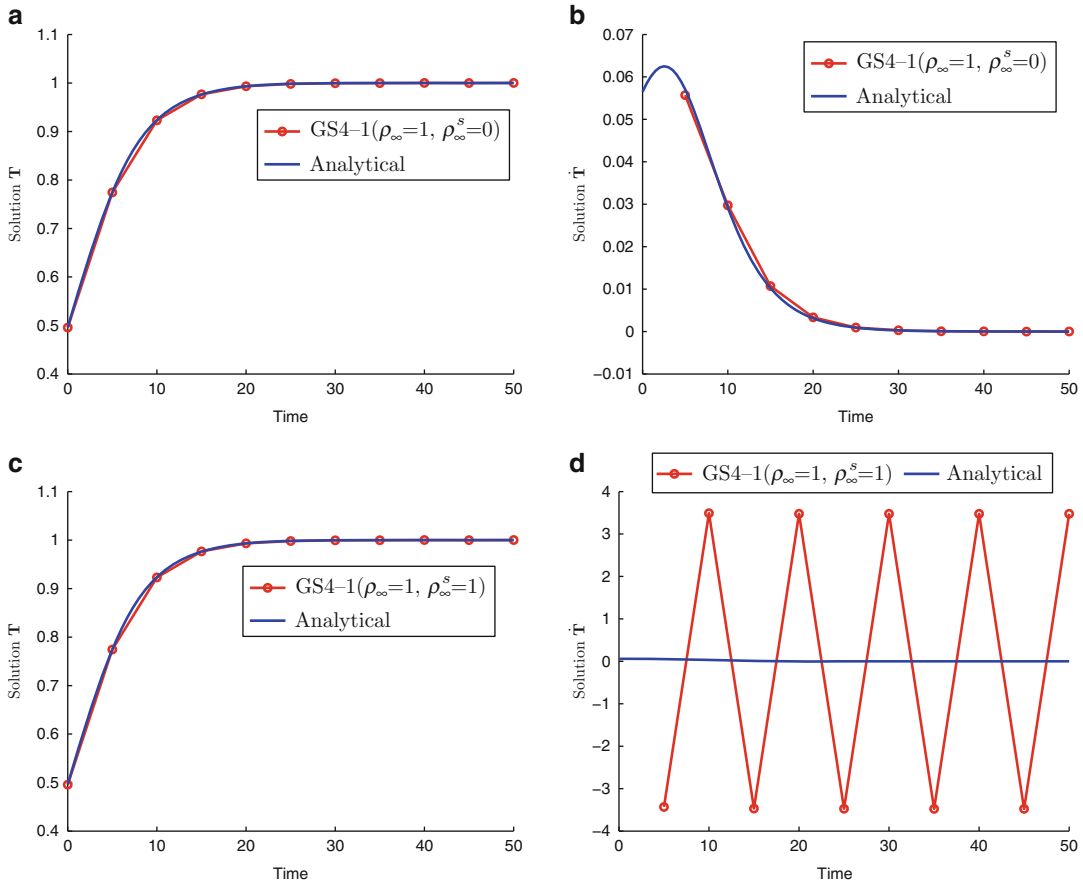

Application of GS4-1 Time Integration Framework to Nonlinear Heat Transfer: Heat Conduction in Medium with Temperature-Dependent Velocity, Fig. 1 Plot of $\mathbf{T}$ and $\dot{\mathbf{T}}$ as a function of time for node number 2 ($x = 0.0333$) and $\Delta t = 5s$ generated by (**a**, **b**) GS4-1($\rho_\infty = 1, \rho^s_\infty = 0$) and (**c**, **d**) GS4-1 ($\rho_\infty = 1, \rho^s_\infty = 1$), that is, the case without selective control features

feature) in Fig. 4. Consistently and as expected, the numerical solution of the primary variable generated by the two cases agrees well with the analytical solution as seen in Fig. 4a, c. Focusing on the numerical solution of the time derivative variable, Fig. 4d shows that the algorithm without the selective control feature (i.e. $\rho_\infty = \rho^s_\infty = 0.1$ in this case) still results in numerical oscillation in $\dot{\mathbf{T}}$. This numerical oscillation could only be eliminated in this method by strictly imposing maximal numerical damping to both $\mathbf{T}$ and $\dot{\mathbf{T}}$ (i.e., $\rho_\infty = \rho^s_\infty = 0$) as illustrated in Fig. 5. This shows that even for this simple, illustrative numerical example where thermal shock is not involved, it is only when maximal damping to both $\mathbf{T}$ and $\dot{\mathbf{T}}$ is imposed that the existing method without selective control feature could yield physically representative and accurate solutions. In this case, imposing maximal damping to $\mathbf{T}$ means over-dissipating, since the numerical solution of this variable can already/easily be obtained with good accuracy without having to impose any numerical dissipation even with relatively larger time step size (see Fig. 1c). While numerical damping is handy in one way if one could control it smartly, but in another way over-dissipation may also lead to physically incorrect dynamics of the system due to the fact that numerical damping is an artifact added into the system to yield acceptable solutions; hence,

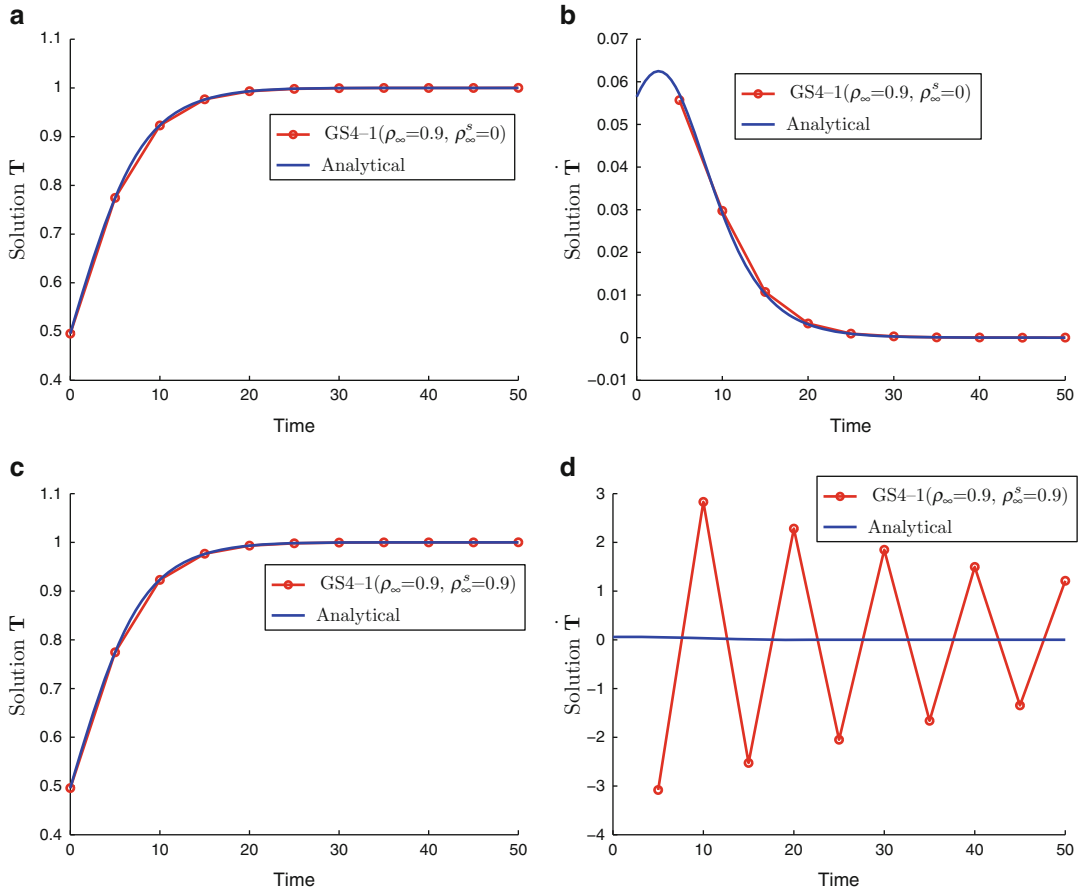

Application of GS4-1 Time Integration Framework to Nonlinear Heat Transfer: Heat Conduction in Medium with Temperature-Dependent Velocity, Fig. 2 Plot of $\mathbf{T}$ and $\dot{\mathbf{T}}$ as a function of time for node number 2 ($x = 0.0333$) and $\Delta t = 5s$ generated by (**a**, **b**) GS4-1($\rho_\infty = 0.9, \rho^s_\infty = 0$) and (**c**, **d**) GS4-1($\rho_\infty = 0.9, \rho^s_\infty = 0.9$), that is, the case without selective control features

caution has to be exercised. The GS4-1 framework with selective control feature, on the other hand, is capable of giving physically accurate and representative solutions of primary variable and its time derivative, even without having to impose numerical damping on the primary variable (i.e., $\rho_\infty = 1$) for this particular problem without thermal shock, hence the clear improvement and advantage of the present approach.

The next comparison between the two cases (i.e., GS4-1 framework with and without selective control features) is done by looking at the solutions of both $\mathbf{T}$ and $\dot{\mathbf{T}}$ for the whole spatial domain at a specific time of $t = 10s$ and using a time step size of $\Delta t = 1s$. For this purpose, we show the results using ρ_∞ value of 1 to consistently demonstrate the ability of the GS4-1 algorithm with $\rho_\infty = 1$ and $\rho^s_\infty = 0$. The numerical solutions of these variables as generated by the two cases (with and without selective control features) are illustrated in Fig. 6, from which a comparison of the performance between these two different algorithmic structures can be made. We can see from this figure that the same observations seen previously in Fig. 1 are repeated here. That is, (1) that both algorithms yield good agreement with the analytical solution for $\mathbf{T}$, (2) that the case without selective control features results in oscillations for $\dot{\mathbf{T}}$, and (3) that the GS4-1 framework with the selective control features could suppress such

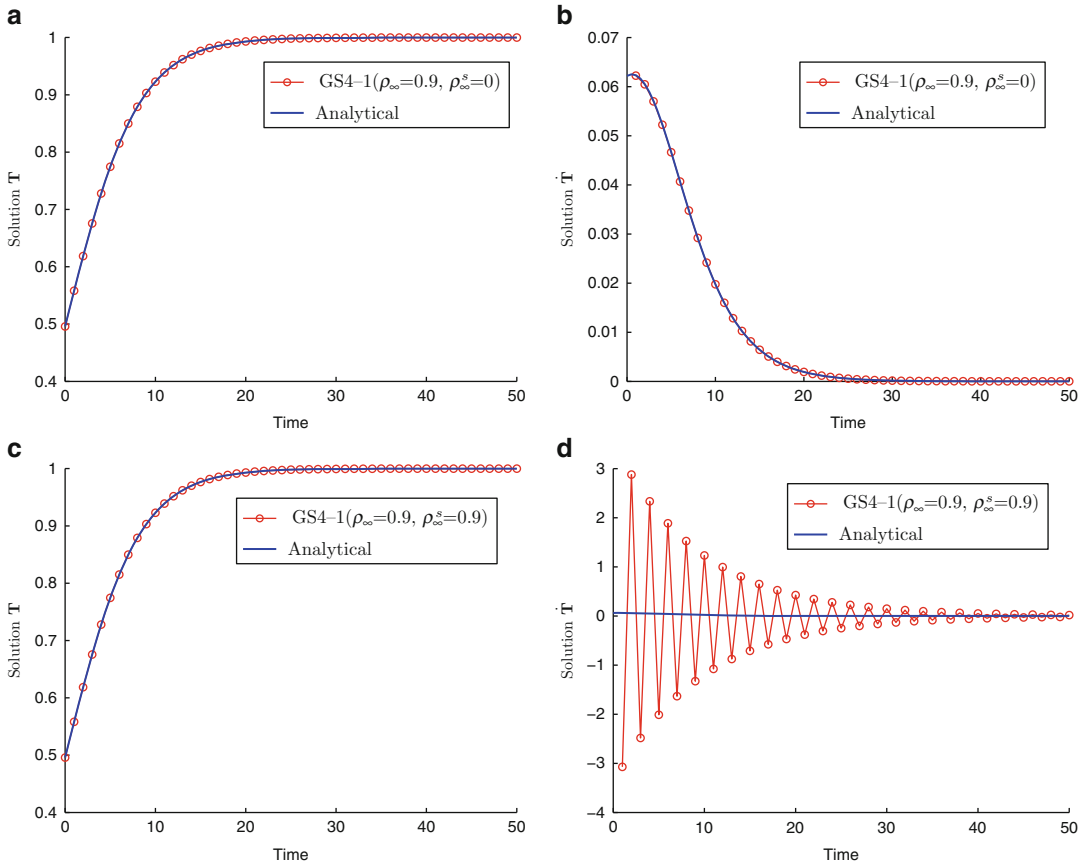

Application of GS4-1 Time Integration Framework to Nonlinear Heat Transfer: Heat Conduction in Medium with Temperature-Dependent Velocity, Fig. 3 Plot of $\mathbf{T}$ and $\dot{\mathbf{T}}$ as a function of time for node number 2 ($x = 0.0333$) and $\Delta T = 1s$ generated by (**a**, **b**) GS4-1 ($\rho_\infty = 0.9, \rho^s_\infty = 0$) and (**c**, **d**) GS4-1 ($\rho_\infty = 0.9, \rho^s_\infty = 0.9$), that is, the case without selective control features

oscillations and subsequently yields good agreement with the analytical solution even with the same ρ_∞ value that was employed for the case without selective control. For the $\dot{\mathbf{T}}$ solution, it is to be again noted that the oscillations generated by the case without the selective control feature, due to the scale of the plotting routine employed, make the analytical solution appear as a straight line due to the different ranges on the $\dot{\mathbf{T}}$ solution values (see Fig. 6d); alternately, the GS4-1 framework with the selective control features (i.e., $\rho_\infty \neq \rho^s_\infty$, with $\rho^s_\infty = 0$) readily captures the proper physics as seen in the analytical solution curve due to the excellent agreement between the numerical results and the analytical solutions (see Fig. 6b). These observations consistently illustrate the importance of and the significant role played by the new features introduced within the GS4-1 computational framework, which is its selective control of the high-frequency damping for both $\mathbf{T}$ and $\dot{\mathbf{T}}$ that is not available in the existing methods to date, for obtaining physically representative and accurate solutions of both the primary variable and its time derivative constituting the transient first-order system.

For completeness of the comparisons between the two cases (i.e., with and without the selective control feature), we next compute and compare the errors in $\mathbf{T}$ and $\dot{\mathbf{T}}$ generated by these two time integrators with time step size of $\Delta t = 1s$ and an end time of $t = 10s$, for a given set of ρ_∞ value ranging from 0 (maximal numerical damping)

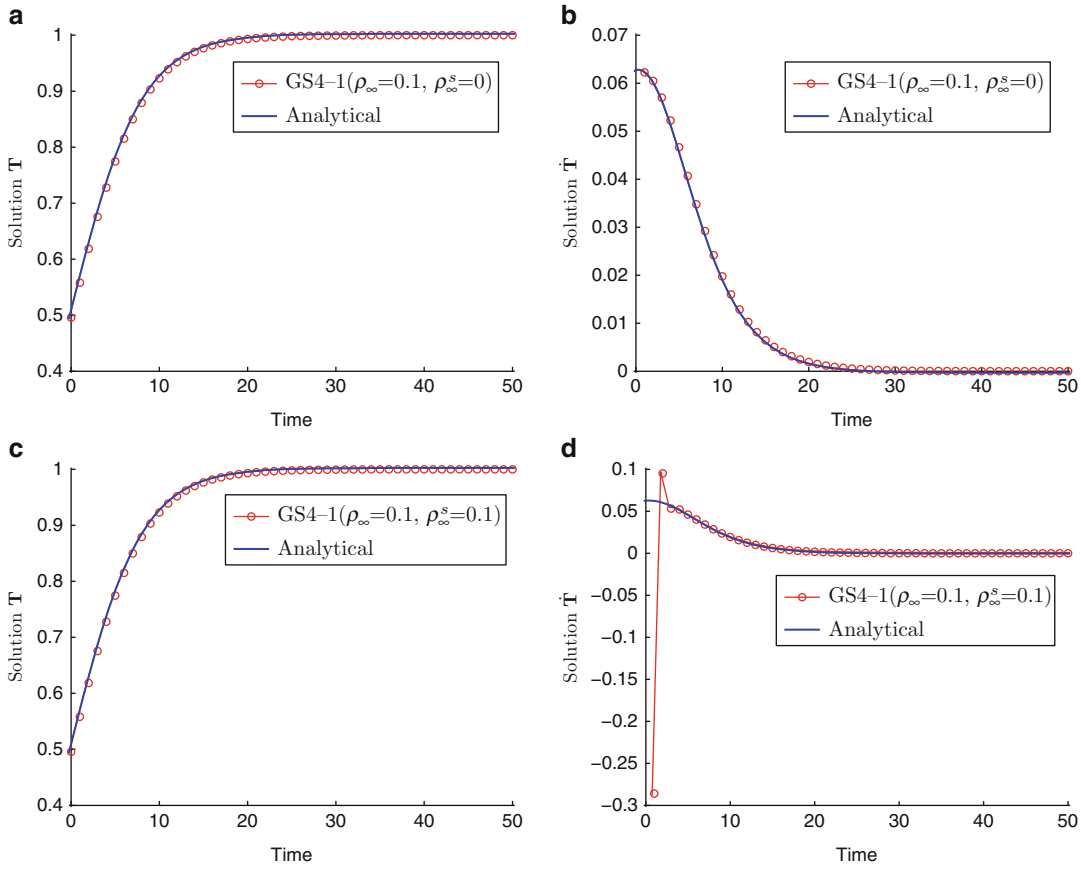

Application of GS4-1 Time Integration Framework to Nonlinear Heat Transfer: Heat Conduction in Medium with Temperature-Dependent Velocity, Fig. 4 Plot of $\mathbf{T}$ and $\dot{\mathbf{T}}$ as a function of time for node number 2 ($x = 0.0333$) and $\Delta t = 1s$ generated by (**a**, **b**) GS4-1 ($\rho_\infty = 0.1, \rho^s_\infty = 0$) and (**c**, **d**) GS4-1 ($\rho_\infty = 0.1, \rho^s_\infty = 0.1$), that is, the case without selective control features

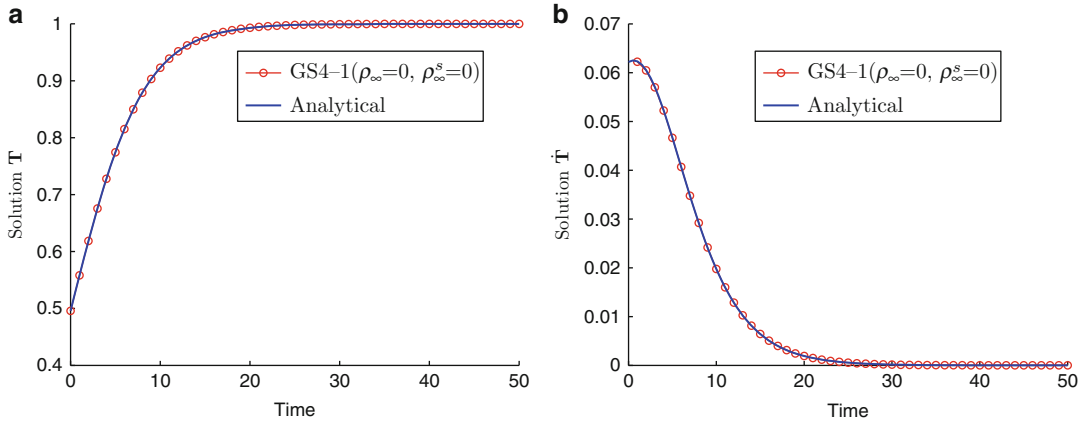

Application of GS4-1 Time Integration Framework to Nonlinear Heat Transfer: Heat Conduction in Medium with Temperature-Dependent Velocity, Fig. 5 Plot of $\mathbf{T}$ and $\dot{\mathbf{T}}$ as a function of time for node number 2 ($x = 0.0333$) and $\Delta t = 1s$ generated by GS4-1 ($\rho_\infty = 0, \rho^s_\infty = 0$), that is, the case without selective control features but with maximal numerical damping

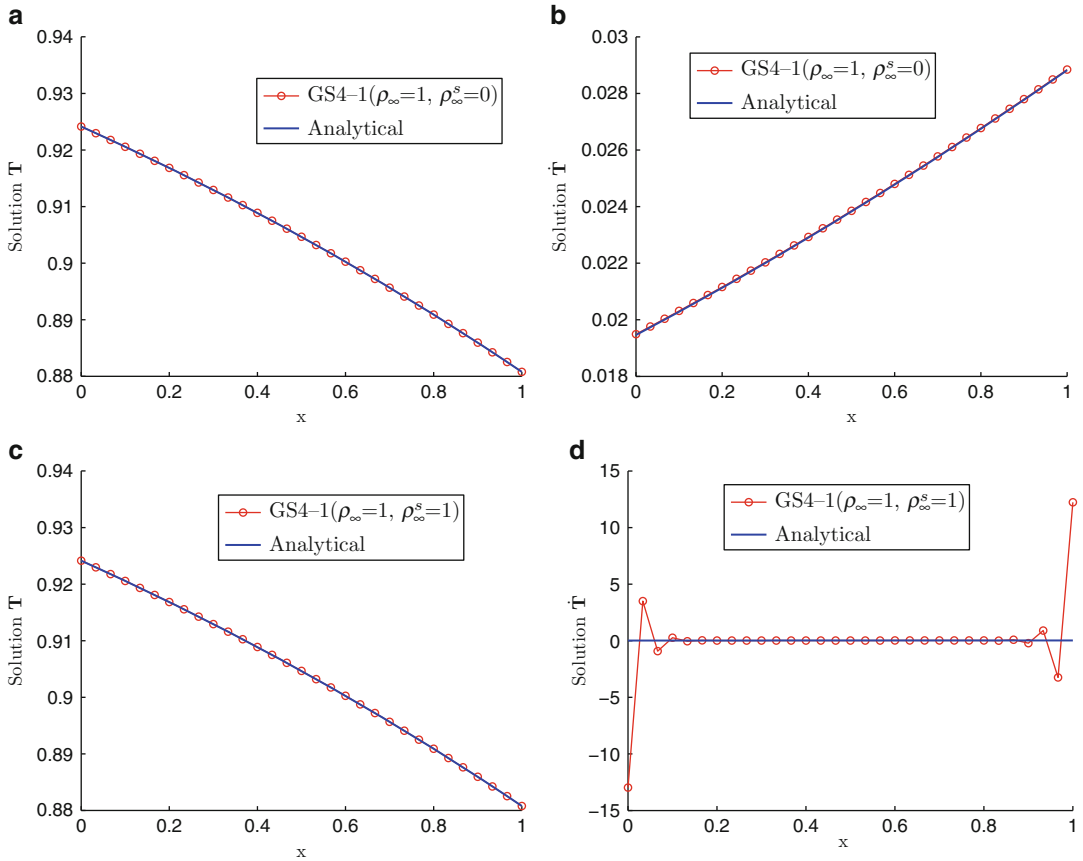

Application of GS4-1 Time Integration Framework to Nonlinear Heat Transfer: Heat Conduction in Medium with Temperature-Dependent Velocity, Fig. 6 Plot of **T** and $\dot{\mathbf{T}}$ as a function of x for a specific time of $t = 10s$ generated by (**a**, **b**) GS4-1 ($\rho_\infty = 1, \rho^s_\infty = 0$) and (**c**, **d**) GS4-1 ($\rho_\infty = 1, \rho^s_\infty = 1$), that is, the case without selective control features

to 1 (zero numerical damping) in a decrement of 0.1. The error is defined as

$$\text{Error} = \left| \frac{\text{numerical} - \text{exact}}{\text{exact}} \right| \tag{51}$$

Table 1 shows the comparison of maximal and total errors in the primary variable (**T**) within the GS4-1 framework, with and without the selective control features, for all ρ_∞ values considered. It is clear from this table that the two cases yield acceptable solutions of **T**. The focus is however on the performance of the different time integrators with and without selective control features in computing the solutions of the time derivative variables ($\dot{\mathbf{T}}$). The maximal and total errors in this quantity are shown in Table 2. From this table, we can easily see that the GS4-1 framework with the selective control features outperforms the case without such features. The former yields satisfactory results for all ρ_∞ values considered, whereas the latter results in large errors as the numerical damping is minimal (i.e., ρ_∞ approaches unity). Because our aim is to obtain physically representative and accurate solutions at minimal damping to preserve the system dynamics and the associated physics, the GS4-1 framework with the selective control features is clearly at an advantage, even without having to introduce numerical damping to the primary variable (i.e., GS4-1 with $\rho_\infty = 1$ and $\rho^s_\infty = 0$). Meanwhile, the large errors in $\dot{\mathbf{T}}$ generated by

Application of GS4-1 Time Integration Framework to Nonlinear Heat Transfer: Heat Conduction in Medium with Temperature-Dependent Velocity, Table 1 Comparison of error in $\mathbf{T}$ between (a) the case without selective control features with $\rho_\infty = \rho_\infty$ and (b) GS4-1 framework with selective control features with $\rho_\infty^s = 0$, for ρ_∞ values ranging from 1 (zero damping) to 0 (maximal damping) in decrements of 0.1

	Max error		Total error	
ρ_∞	Without selective control	Selective control	Without selective control	Selective control
1	1.4140×10^{-5}	1.4140×10^{-5}	2.9509×10^{-4}	2.9509×10^{-4}
0.9	1.3079×10^{-5}	1.5227×10^{-5}	2.6847×10^{-4}	3.0655×10^{-4}
0.8	1.3782×10^{-5}	1.6533×10^{-5}	2.7631×10^{-4}	3.2925×10^{-4}
0.7	1.4687×10^{-5}	1.7917×10^{-5}	2.9170×10^{-4}	3.5601×10^{-4}
0.6	1.5407×10^{-5}	1.9365×10^{-5}	3.0553×10^{-4}	3.8484×10^{-4}
0.5	1.6224×10^{-5}	2.0891×10^{-5}	3.2198×10^{-4}	4.1525×10^{-4}
0.4	1.7381×10^{-5}	2.2476×10^{-5}	3.4530×10^{-4}	4.4687×10^{-4}
0.3	1.9009×10^{-5}	2.4082×10^{-5}	3.7786×10^{-4}	4.7892×10^{-4}
0.2	2.1218×10^{-5}	2.5630×10^{-5}	4.2193×10^{-4}	5.0986×10^{-4}
0.1	2.4128×10^{-5}	2.6966×10^{-5}	4.8008×10^{-4}	5.3665×10^{-4}
0	2.7793×10^{-5}	2.7793×10^{-5}	5.5342×10^{-4}	5.5342×10^{-4}

Application of GS4-1 Time Integration Framework to Nonlinear Heat Transfer: Heat Conduction in Medium with Temperature-Dependent Velocity, Table 2 Comparison of error in $\dot{\mathbf{T}}$ between (a) the case without selective control features with $\rho_\infty = \rho_\infty$ and (b) GS4-1 framework with selective control features with $\rho_\infty^s = 0$, for ρ_∞ values ranging from 1 (zero damping) to 0 (maximal damping) in decrements of 0.1

	Max error		Total error	
ρ_∞	Without selective control	Selective control	Without selective control	Selective control
1	741.2217	0.0014	1.6459×10^3	0.0341
0.9	257.0124	0.0014	570.8179	0.0332
0.8	78.6596	0.0014	174.7673	0.0331
0.7	20.5530	0.0014	45.7032	0.0332
0.6	4.3676	0.0014	9.7434	0.0335
0.5	0.7013	0.0014	1.5961	0.0338
0.4	0.0764	0.0014	0.2068	0.0342
0.3	0.0058	0.0014	0.0460	0.0348
0.2	0.0010	0.0014	0.0231	0.0356
0.1	1.2102×10^{-4}	0.0014	0.0025	0.0367
0	0.0014	0.0014	0.0382	0.0382

the case without the selective control features indicate that such a method is not capable of eliminating the numerical oscillation associated with $\dot{\mathbf{T}}$ for the given minimal amount of damping. Although such error can be greatly reduced by the method as numerical damping is approaching its maximal value (i.e., ρ_∞ approaches zero), such over-dissipative algorithm is unnecessary when it can easily be achieved by using the GS4-1 framework with $\rho_\infty = 1$ (i.e., non-dissipative for $\mathbf{T}$) and $\rho_\infty^s = 0$ via the selective control feature inherent in the GS4-1 framework.

Convergence Rate in Time of the Method

The developed GS4-1 framework is second-order accurate in time. For completeness of the analyses, we explicitly demonstrate in this section the rate of convergence in time of the GS4-1 framework employing the numerical methodology described in section "Numerical Methodology Via the GS4-1 Framework Numerical Methodology Via the GS4-1 Framework" for the one-dimensional transient nonlinear heat transfer problem considered in this synopsis. For this purpose and for consistency, we show

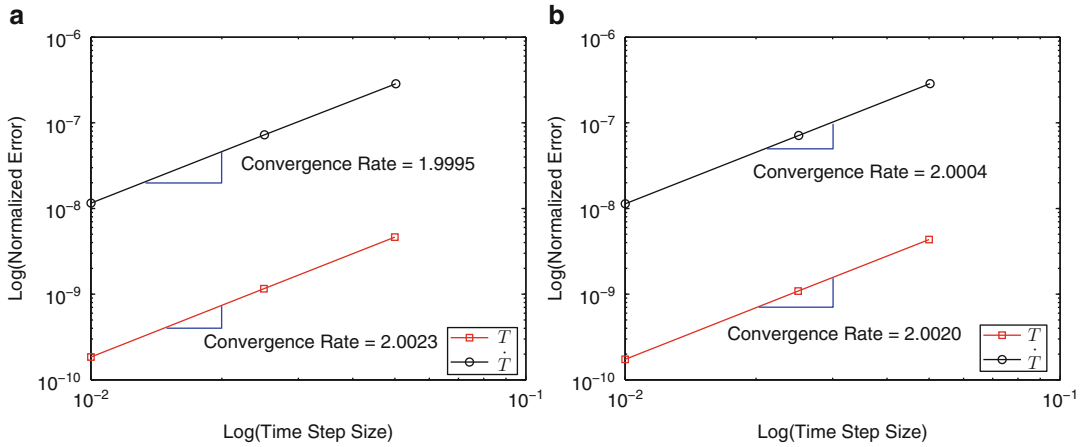

Application of GS4-1 Time Integration Framework to Nonlinear Heat Transfer: Heat Conduction in Medium with Temperature-Dependent Velocity, Fig. 7 Convergence plot of the GS4-1 algorithm with (**a**) $(\rho_\infty, \rho_\infty^s) = (1, 0)$ and (**b**) $(\rho_\infty, \rho_\infty^s) = (0.9, 0)$ utilizing the standard convergence plot for $\mathbf{T}$ and the time level aligned convergence plot for $\dot{\mathbf{T}}$

the convergence plots of the algorithms used in obtaining the numerical results shown in section Results Illustrating the Method's Ability Via the Selective Control Feature," namely, (1) GS4-1 with $(\rho_\infty, \rho_\infty^s) = (1,0)$ and (2) GS4-1 with $(\rho_\infty, \rho_\infty^s) = (0.9,0)$. The set for the number of time steps used to construct the plots is $N_i = [10000, 500, 200, 100]$, and the end time at which the solutions are evaluated is 5 s. In constructing the convergence plots, we use the standard convergence plot for $\mathbf{T}$ and the time level aligned convergence plot for $\dot{\mathbf{T}}$ (description and discussion of these different ways of constructing the convergence plot has been discussed in [2] and will not be repeated here). Figure 7 shows the convergence plots of $\mathbf{T}$ and $\dot{\mathbf{T}}$ generated by (a) the GS4-1 algorithm with $(\rho_\infty, \rho_\infty^s) = (1,0)$ and (b) the GS4-1 algorithm with $(\rho_\infty, \rho_\infty^s) = (0.9, 0)$, respectively.

Concluding Remarks

For transient nonlinear heat transfer type applications dealing with first-order systems, a novel computational methodology under the umbrella of the so-called GS4-1 framework was presented. The original transient linear algorithms and designs under the GS4-1 framework were properly extended to an illustrative transient nonlinear heat transfer application to satisfactorily capture the problem physics. The GS4-1 computational framework naturally inherits features with and without selective control of high-frequency damping for both the primary variable and its time derivative. This is extremely noteworthy and significant. The numerical features with selective control enable the optimal suppression of the numerical oscillations selectively for each of the variables and thereby enable not only the analysis of long-term system dynamics to be satisfactory but also readily enable the capture of the underlying physics. The current state of the art do not permit such features and consequently lead to physically incorrect dynamics of the system. The simple illustration to a one-dimensional transient nonlinear heat transfer application wherein an analytic solution is available was purposely chosen to highlight the essential aspects and to demonstrate the significance of the present developments in capturing the problem physics.

Acknowledgments The authors are very pleased to acknowledge support and funding from Mighty River Power, New Zealand, under research contract number E5653. Acknowledgment is also due the Minnesota Supercomputer Institute (MSI), Minneapolis, Minnesota, for computer grants.

References

1. Masuri S, Tamma KK (2012) Application of GS4-1 time integration framework to linear heat transfer: transient heat conduction. ETS entry 00759
2. Masuri S, Sellier M, Zhou X, Tamma KK (2011) Design of order-preserving algorithms for transient first-order systems with controllable numerical dissipation. Int J Numer Methods Eng. doi:10.1002/nme.3228
3. Carslaw HS, Jaeger JC (1959) Conduction of heat in solids. Oxford University Press, Oxford
4. Huebner KH, Thornton EA, Byrom TG (1995) The finite element method for engineers. Wiley, New York
5. Masuri SU, Hoitink A, Zhou X, Tamma KK (2009) Algorithms by design: a new normalized time-weighted residual methodology and design of a family of energy-momentum conserving algorithms for nonlinear structural dynamics. Int J Numer Methods Eng 79:1094–1146
6. Masuri S, Hoitink A, Zhou X, Tamma KK (2009) Algorithms by design: Part II – a novel normalized time-weighted residual methodology and design leading to a family of symplectic-momentum conserving algorithms for non-linear structural dynamics. Int J Comput Methods Eng Sci Mech 10:27–56
7. Masuri S, Hoitink A, Zhou X, Tamma KK (2009) - Algorithms by design: Part III – a novel normalized time weighted residual methodology and design of optimal symplectic-momentum based controllable numerical dissipative algorithms for nonlinear structural dynamics. Int J Comput Methods Eng Sci Mech 10:57–90

Application of Isochronous Integration Framework to Dynamic Thermoelasticity

Siti Ujila Masuri[1] and Kumar K. Tamma[2]
[1]Department of Mechanical and Manufacturing Engineering, Universiti Putra Malaysia, UPM Serdang, Selangor, Malaysia
[2]Department of Mechanical Engineering, University of Minnesota, Minneapolis, MN, USA

Overview

Dynamic thermoelasticity involves generalization of both the fields of heat conduction in solids and continuum elasticity. The thermoelastic behavior of solids and engineering structures has long been a subject of widespread research activity and interest, and numerous publications exist to date including a review article by Tamma and Namburu [1], as the problem has a significant number of general engineering applications in mechanical, aerospace, chemical, civil, electronic, and nuclear engineering disciplines. Therefore, an accurate understanding of the interdisciplinary thermal-structural interactions is of utmost importance and concern especially in the design and analysis stage. The complexity and interdisciplinary nature of these structures significantly influences the response characteristics and makes the combined modeling and analysis a formidable and challenging task.

In this regard, numerical computational methods play an important role for both the fields of heat transfer and the associated structural analysis especially due to the complex nature of the structural components and configurations encountered in engineering practice. Here, we consider the classical model with particular case of ramp-type surface heating known as the Sternberg-Chakravorty boundary condition [2] and describe how the problem can be solved by the isochronous integration (*i*Integration) framework. The framework is suitable for use in both first- and second-order systems, such as the classical model of dynamic thermoelasticity problem described in this synopsis, with optimal algorithms, numerical, and order-preserving attributes (in particular, second-order time accuracy) as well. The principal contribution emanating from such unified framework is the practicality and convenience of using the same computational framework and implementation when solving first- and/or second-order systems without having to resort to the individual framework especially when there is a need to switch from one system to another.

Governing Equations

For homogeneous and isotropic continuum, the governing equations for the temperature and displacement fields are the following coupled differential equations [3]:

$$\frac{E}{2(1+\nu)}\left(u_{i,\,kk}+\frac{1}{1-2\nu}u_{k,\,ki}\right)+\rho f_i - \rho\,\ddot{u}_i-\frac{E\alpha}{1-2\nu}T_{,i}=0 \tag{1}$$

$$\lambda T_{,kk}+\ r-\rho c_v\dot{T}-\frac{E\alpha T_0}{1-2\nu}\,\dot{u}_{k,\,k}=0 \tag{2}$$

where E is Young's modulus; ν is Poisson's ratio; u_i and f_i are the Cartesian components of displacement and body force vector, respectively; ρ is the mass density; α is the coefficient of linear thermal expansion; T is the absolute temperature; λ is the thermal conductivity; r is the heat source; c_v is the specific heat at constant strain; and T_0 is the reference temperature of the natural, stress-free state. Meanwhile, superposed dots $\dot{(\,)}$ and commas $(\,)_{,i}$ denote time differentiation and partial differential with respect to Cartesian coordinates $x_i (i = 1, 2, 3)$, respectively.

The equation of motion for the displacement field (1) is a hyperbolic, second-order (in time) system. Meanwhile, the governing equation for the temperature field (2) is parabolic, first-order (in time) system. Since the developed *i* Integration framework described in here is meant to be used to solve first- and second-order systems, such classical thermoelasticity problems governed by the above equations are well suited for consideration here to truly illustrate the method's ability to solve first- and second-order systems. Although nonclassical thermoelastic models also frequently appear in technical literature, the governing equations for the displacement and temperature fields in this nonclassical category are both second order in time, hence are not appropriate for consideration here. The discussion from here onward will therefore be focused on the classical thermoelasticity problems involving first- and second-order systems.

In the theoretical studies as well as engineering practice of thermoelasticity problems, simplifications to the above fully coupled equations are usually made, from which adequate results can be obtained relatively more easily. These simplifications involve neglecting the inertia term in the equation of motion (1) to arrive at a quasi-static model and/or eliminating the coupling term from the heat conduction (2) to arrive at an uncoupled model. Only the latter model is of interest here due to the reason cited above. Furthermore, analytical solutions to the uncoupled classical thermoelastic model are available in literature [4], enabling the validation of the developed numerical method. For the uncoupled classical thermoelastic model, the heat conduction (2) becomes

$$\lambda T_{,kk}+\ r-\rho c_v\dot{T}=0 \tag{3}$$

We shall now consider particular dynamic thermoelasticity problem described as follows: Take a Cartesian coordinate system (x, y, z) and consider a homogeneous, isotropic, thermoelastic solid occupying the half-space $x \geq 0$. Suppose that the solid is initially at rest, in stress-free state, at a uniform temperature of $T = T_0$. At time $t = 0^+$, however, the temperature at boundary of the solid ($x = 0$) is changed from $T = T_0$ with a ramp-type surface heating (i.e., Sternberg-Chakravorty Problem) to $T = T_1$ according to

$$f(t)=T_0+\frac{(T_1-T_0)t}{t_0}[H(t)-H(t-t_0) + (T_1-T_0)H(t-t_0) \tag{4}$$

where $H(t)$ is the Heaviside unit step-function and then is maintained steadily at $T = T_1$. The boundary is let to move without any restrictions (i.e., is maintained stress-free). The temperature, displacement, and stress fields after the sudden heating can be expressed as

$$u_x = u_x(x,t),\quad u_y = 0,\quad u_z = 0,\quad T = T(x,t) \tag{5}$$

$$\sigma_x=\frac{E(1-\nu)}{(1+\nu)(1-2\nu)}\frac{\partial u_x}{\partial x}-\frac{E\alpha}{1-2\nu}(T-T_0) \tag{6}$$

$$\sigma_y=\sigma_z=\frac{\nu}{1-\nu}\sigma_x-\frac{E\alpha}{1-\nu}(T-T_0) \tag{7}$$

An observation of (6)–(7) indicate that the determination of the temperature (T), x-direction displacement (u_x), and normal stress (σ_x) are of interest for a complete analysis. From the value of the temperature and normal stress, the stresses σ_y

and σ_z can be determined from (7). For this case, and in the absence of body forces (f_i) and heat source (r), (1) and (3) can be expressed as

$$\frac{\partial^2 u_x}{\partial x^2} - \frac{(1+\nu)(1-2\nu)\rho}{(1-\nu)E}\frac{\partial^2 u_x}{\partial t^2} - \frac{(1+\nu)\alpha}{1-\nu}\frac{\partial T}{\partial x} = 0 \tag{8}$$

$$\frac{\partial^2 T}{\partial x^2} - \frac{\rho c_v}{\lambda}\frac{\partial T}{\partial t} = 0 \tag{9}$$

To complete the description of the problem, the associated initial and boundary conditions can be expressed as follows:

$$u_x(x,0) = 0, \quad \frac{\partial}{\partial t}u_x(x,0) = 0, \quad T(x,0) = 0 \tag{10}$$

$$u_x(x \to \infty, t) \to 0, \quad \frac{\partial}{\partial x}u_x(x \to \infty, t) \to 0, \quad T(x \to \infty, t) \to T_0 \tag{11}$$

$$\sigma_x(0,t) = 0, \quad T(0,t) = f(t) \tag{12}$$

The governing equation can be represented in dimensionless form by assigning dimensionless temperature, displacement, and normal stress as follows:

$$\theta = \frac{T - T_0}{T_0}, \quad u = \frac{(1-\nu)c}{\kappa(1+\nu)\alpha T_0}u_x, \quad \sigma = \frac{(1-2\nu)}{E\alpha T_0}\sigma_x \tag{13}$$

where $\kappa = \dfrac{\lambda}{\rho c_v}$, $c = \left[\dfrac{(1-\nu)E}{(1+\nu)(1-2\nu)\rho}\right]^{1/2}$, $\xi = \dfrac{cx}{\kappa}$, $\tau = \dfrac{c^2 t}{\kappa}$ to yield (in concise form)

$$u'' - \ddot{u} - \theta' = 0 \tag{14}$$

$$\theta'' - \dot{\theta} = 0 \tag{15}$$

$$\sigma = u' - \theta \tag{16}$$

the primes $()'$ and superposed dots $\dot{()}$ denote partial differentiations with respect to the nondimensional variables ξ and τ, respectively. Likewise, the initial and boundary conditions can be expressed in dimensionless forms as follows:

$$u(\xi,0) = 0, \quad \dot{u}(\xi,0) = 0, \quad \theta(\xi,0) = 0 \tag{17}$$

$$u(\xi \to \infty, \tau) \to 0, \quad u'(\xi \to \infty, \tau) \to 0, \quad \theta(\xi \to \infty, \tau) \to 0 \tag{18}$$

$$\sigma(0,\tau) = 0, \quad \theta(0,\tau) = \varphi(\tau) \tag{19}$$

For simplification purpose, we suppose that $T_1 = 2T_0$, in which case $\varphi(\tau)$ can be expressed for the Sternberg-Chakravorty boundary condition as

$$\varphi(\tau) = \frac{\tau}{\tau_0}[H(\tau) - H(\tau - \tau_0)] + H(\tau - \tau_0) \tag{20}$$

Equations (14) and (15) indicate that the equation of motion describing the displacement field is a second-order transient system, while the heat conduction equation describing the temperature field is a first-order transient system. Solving such problem would require appropriate time integration solvers for both second- and first-order systems, respectively. Therefore, this illustrative example serves well to demonstrate the applicability of the present isochronous integration framework. The descriptions of how this example (or any problems involving first- and/or second-order systems) can be solved effectively and practically using the proposed *i*Integration framework will be presented in section Time Discretization by *i*Integration Framework where we discuss the time discretization of such problems. In the next section, we first present the spatial discretization procedures for the problem, employing the Finite Element Method.

Spatial Discretization by Finite Element Method

We now proceed in this section to describe how the governing equations of interest can be discretized in space using the Galerkin Finite Element Method. Observation of the governing equations,

namely, (14) and (15), indicates that the equation of motion describing the displacement field (14) is dependent on the temperature field that is to be solved from the heat conduction (15). Therefore, in the computational procedures to be described hereafter, we first discuss the heat conduction model, followed by the discussion on the equation of motion describing the displacement field.

Heat Conduction Equation for the Temperature Field

To discretize the heat conduction equation using the Galerkin Finite Element Method, we apply the method of weighted residuals to (15). The temperature field of an element with N nodes is approximated by a linear combination of time-dependent nodal temperatures $\theta_n(n = 1, \ldots, N)$ and time-independent element shape functions $\psi_n(n = 1, \ldots, N)$

$$\theta = \sum_{n=1}^{N} \theta_n \psi_n \tag{21}$$

The shape function ψ_n is used as the weighting function in the weighted residual equation. After use of (21), we obtain the following linear ordinary differential equation that is first order in time:

$$\mathbf{M}\dot{\theta} + \mathbf{K}\theta = \mathbf{F} \tag{22}$$

where θ is a vector of length N containing the nodal temperatures $\theta_n(n = 1, \ldots N)$, $\dot{\theta}$ is the time derivative of θ, while $\mathbf{M}$ is the mass matrix of size N x N and is defined as ($p = 1, \ldots, N$ and $q = 1, \ldots, N$)

$$\mathbf{M}(p, q) = \int_{\Omega} \psi_p \psi_q d\xi \tag{23}$$

Furthermore, $\mathbf{K}$ is the stiffness matrix of size N x N and is defined as ($p = 1, \ldots, N$ and $q = 1, \ldots, N$)

$$\mathbf{K}(p, q) = \int_{\Omega} \frac{d\psi_p}{d\xi} \frac{d\psi_q}{d\xi} d\xi \tag{24}$$

Meanwhile, $\mathbf{F}$ is zero vector of length N. The ordinary differential equation (22) is consistently assembled for all elements in the spatial domain to yield a system of linear ordinary differential equations that is first order in time, to be solved using the specially tailored *i*Integration framework to effectively capture the problem physics.

Equation of Motion for the Displacement Field

Employing the Finite Element Method to (14), following the same procedure as done for the heat conduction equation (section Heat Conduction Equation for the Temperature Field), we obtain for the displacement equation of motion the following linear ordinary differential equation that is second order in time:

$$\mathbf{M}\ddot{\mathbf{u}} + \mathbf{K}\mathbf{u} = \mathbf{F} \tag{25}$$

where $\mathbf{u}$ is a vector of length N containing the nodal displacements $u_n(n = 1, \ldots N)$, $\ddot{\mathbf{u}}$ is the time derivative of $\mathbf{u}$, while $\mathbf{M}$ and $\mathbf{K}$ are the mass and stiffness matrices of size N x N defined by (23) and (24), respectively.

Meanwhile, for this model, $\mathbf{F}$ is the force vector of length N defined as ($p = 1, \ldots, N$ and $q = 1, \ldots, N$)

$$\mathbf{F}(p) = \left(\int_{\Omega} \frac{d\psi_p}{d\xi} \psi_q d\xi \right) \theta_p \tag{26}$$

where θ_p is nodal temperature value at node p ($p = 1, \ldots, N$) to be obtained from solving (22) using the present *i*Integration framework as described in section Time Discretization by *i* Integration Framework. The ordinary differential equation (25) is consistently assembled for all elements in the spatial domain to yield a system of linear ordinary differential equations that is second order in time, to be solved using the specially tailored *i*Integration framework to effectively capture the problem physics. This is described next.

Time Discretization by *i*Integration Framework

The *i*Integration framework, in its natural form, is a time integration solver originally developed for

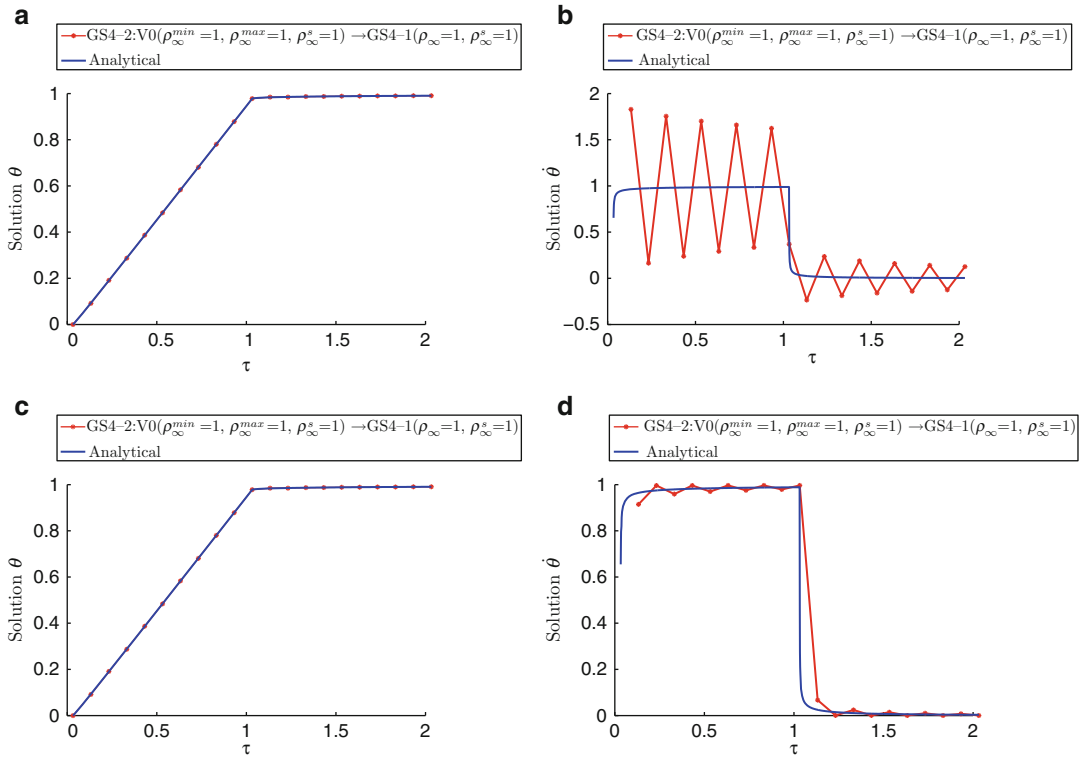

Application of Isochronous Integration Framework to Dynamic Thermoelasticity, Fig. 1 Plot of θ and $\dot{\theta}$ as a function of time for node 2 ($\xi = 0.02$) employing (**a**, **b**) GS4-1($\rho_\infty = \rho_\infty^s = 1$), that is, the case without selective control feature, and (**c**, **d**) GS4-1($\rho_\infty = 1, \rho_\infty^s = 0$), that is, the case with selective control feature

second-order transient system, identical to the V0-family of the GS4-2 framework previously presented in [5]. It is described as follows:

Given $\mathbf{u}_n$, $\dot{\mathbf{u}}_n$, and $\ddot{\mathbf{u}}_n$, one can find $\mathbf{u}_{n+1}$, $\dot{\mathbf{u}}_{n+1}$, and $\dot{\mathbf{u}}_{n+1}$ by first solving for $\Delta\ddot{\mathbf{u}}$ from

$$\begin{aligned}(\Lambda_6 W_1\mathbf{M} + \Lambda_5 W_2 \Delta t\mathbf{C} + \Lambda_3 W_3 \Delta t^2\mathbf{K})\Delta\ddot{\mathbf{u}}\\ = -\mathbf{M}\,\ddot{\mathbf{u}}_n - \mathbf{C}(\dot{\mathbf{u}}_n + \Lambda_4 W_1 \Delta t\,\ddot{\mathbf{u}}_n)\\ - \mathbf{K}(\mathbf{u}_n + \Lambda_1 W_1 \Delta t\,\dot{\mathbf{u}}_n + \Lambda_2 W_2 \Delta t^2\,\ddot{\mathbf{u}}_n)\\ + \mathbf{F}_n + W_1(\mathbf{F}_{n+1} - \mathbf{F}_n)\end{aligned}$$

followed by updating the variables as follows:

$$\mathbf{u}_{n+1} = \mathbf{u}_n + \lambda_1\,\dot{\mathbf{u}}_n\Delta t + \lambda_2\,\ddot{\mathbf{u}}_n\Delta t^2 + \lambda_3\Delta\ddot{\mathbf{u}}\Delta t^2 \quad (27)$$

$$\dot{\mathbf{u}}_{n+1} = \dot{\mathbf{u}}_n + \lambda_4\,\ddot{\mathbf{u}}_n\,\Delta t + \lambda_5\Delta\ddot{\mathbf{u}}\Delta t^2 \quad (28)$$

$$\ddot{\mathbf{u}}_{n+1} = \ddot{\mathbf{u}}_n + \Delta\ddot{\mathbf{u}} \quad (29)$$

where

$$\begin{aligned}\Lambda_1 W_1 &= \frac{3 + \rho_\infty^{\min} + \rho_\infty^{\max} - \rho_\infty^{\min}\rho_\infty^{\max}}{2(1+\rho_\infty^{\min})(1+\rho_\infty^{\max})}, \quad \lambda_1 = 1\\ \Lambda_2 W_2 &= \frac{1}{(1+\rho_\infty^{\min})(1+\rho_\infty^{\max})}, \quad \lambda_2 = 1/2\\ \Lambda_3 W_3 &= \frac{1}{(1+\rho_\infty^{\min})(1+\rho_\infty^{\max})(1+\rho_\infty^s)}\\ \lambda_3 &= \frac{1}{2(1+\rho_\infty^s)}\\ \Lambda_4 W_1 &= \frac{3 + \rho_\infty^{\min} + \rho_\infty^{\max} - \rho_\infty^{\min}\rho_\infty^{\max}}{2(1+\rho_\infty^{\min})(1+\rho_\infty^{\max})}, \quad \lambda_4 = 1\\ \Lambda_5 W_2 &= \frac{2}{(1+\rho_\infty^{\min})(1+\rho_\infty^{\max})(1+\rho_\infty^s)}\\ \lambda_5 &= \frac{1}{1+\rho_\infty^s}\\ \Lambda_6 W_1 &= \frac{2 + \rho_\infty^{\min} + \rho_\infty^{\max} + \rho_\infty^s - \rho_\infty^{\min}\rho_\infty^{\max}\rho_\infty^s}{(1+\rho_\infty^{\min})(1+\rho_\infty^{\max})(1+\rho_\infty^s)}\\ W_1 &= \frac{3 + \rho_\infty^{\min} + \rho_\infty^{\max} - \rho_\infty^{\min}\rho_\infty^{\max}}{2(1+\rho_\infty^{\min})(1+\rho_\infty^{\max})}\end{aligned} \quad (30)$$

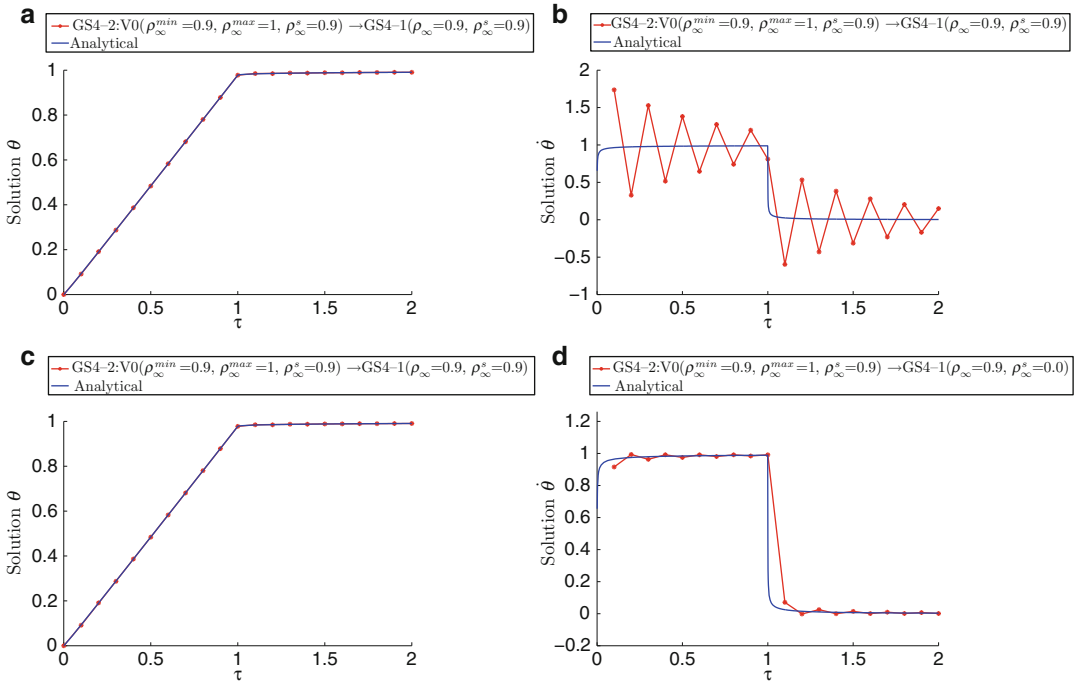

Application of Isochronous Integration Framework to Dynamic Thermoelasticity, Fig. 2 Plot of θ and $\dot{\theta}$ as a function of time for node 2 ($\xi = 0.02$) employing (**a**, **b**) GS4-1($\rho_\infty = \rho_\infty^s = 0.9$), that is, the case without selective control feature, and (**c**, **d**) GS4-1($\rho_\infty = 0.9, \rho_\infty^s = 0$), that is, the case with selective control feature

Meanwhile, **M**, **C**, **K**, and **F** are matrices of the second-order system: $\mathbf{M}\ddot{\mathbf{u}} + \mathbf{C}\dot{\mathbf{u}} + \mathbf{K}\mathbf{u} = \mathbf{F}$. The user-defined parameters, $\rho_{infty}^{\min}$, $\rho_\infty^{\max}$, and ρ_∞^s, are the two principal and spurious roots at the high-frequency limit satisfying the following relation:

$$0 \le \rho_\infty^s \le \rho_\infty^{\min} \le \rho_\infty^{\max} \le 1 \qquad (31)$$

The above framework can also be used to solve first-order transient system $\mathbf{M}\dot{\mathbf{u}} + \mathbf{K}\mathbf{u} = \mathbf{F}$ by carefully adapting it for such purpose as follows, hence the name isochronous integration (*i*Integration) framework.

For the matrices:

- Assign **M** in the *i*Integration as **M** in the first-order system.
- Assign **C** in the *i*Integration as **K** in the first-order system.
- Set **K** in the *i*Integration to equal 0.
- Assign **F** in the *i*Integration as **F** in the first-order system.

For the variables:

- Treat $\ddot{\mathbf{u}}$ in the *i*Integration as $\dot{\mathbf{u}}$ in the first-order system.
- Treat $\dot{\mathbf{u}}$ in the *i*Integration as **u** in the first-order system.
- Neglect **u** (i.e., dummy variable).

For the parameters:

- Set ρ_∞^s in the *i*Integration that controls $\dot{\mathbf{u}}$ in the first-order system.
- Set $\rho_\infty^{\max}$ in the *i*Integration to equal 1.
- Set $\rho_\infty^{\min}$ in the *i*Integration that controls **u** in the first-order system.

and the above *i*Integration framework results in the original GS4-1 framework [6] originally developed for first-order system, whose algorithms are defined by choice of the principal root (ρ_∞) and the spurious root (ρ_∞^s), with or without the selective control feature ($\rho_\infty \neq \rho_\infty^s$ or $\rho_\infty = \rho_\infty^s$, respectively) satisfying $0 \le \rho_\infty^s \le \rho_\infty \le 1$.

The heat conduction model results in a system of ordinary differential equations that is first order in time (see (22)). Therefore, we readily

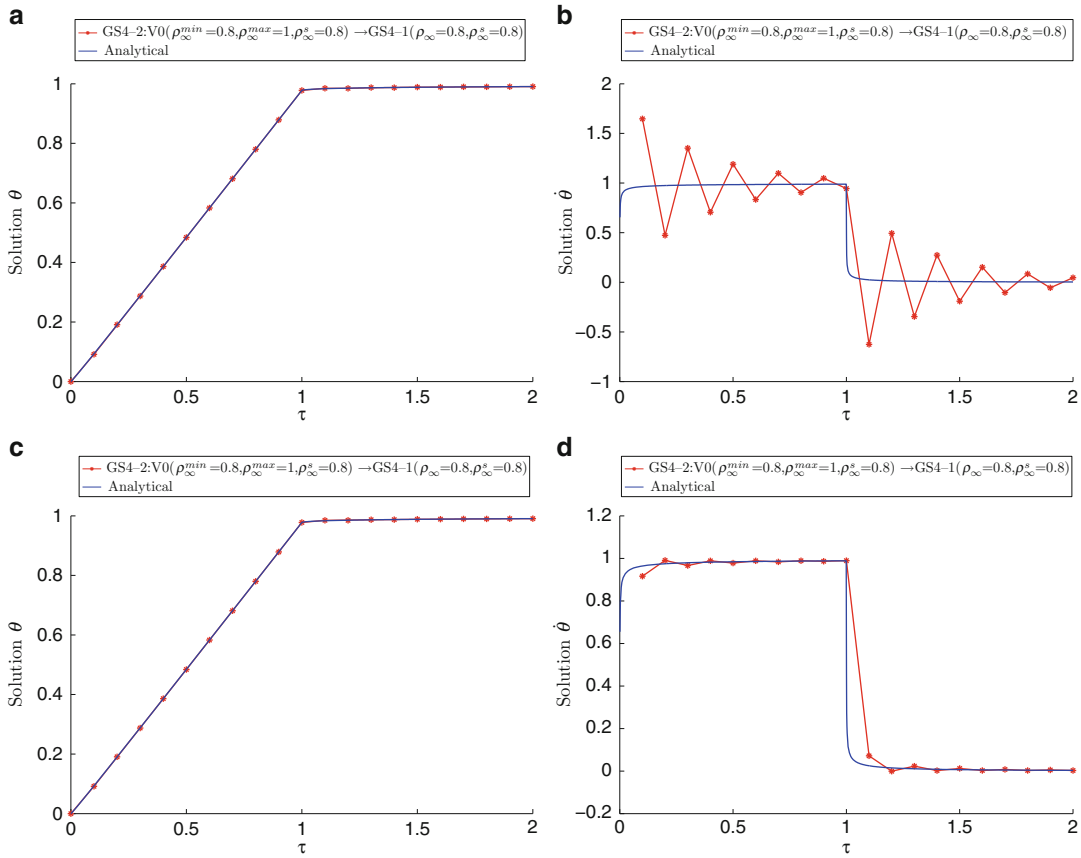

Application of Isochronous Integration Framework to Dynamic Thermoelasticity, Fig. 3 Plot of θ and $\dot{\theta}$ as a function of time for node 2 ($\xi = 0.02$) employing (**a**, **b**) GS4-1($\rho_\infty = \rho_\infty^s = 0.8$), that is, the case without selective control feature, and (**c**, **d**) GS4-1($\rho_\infty = 0.8, \rho_\infty^s = 0$), that is, the case with selective control feature

adapt the *i*Integration framework for solving such system as described above. This way, the original GS4-1 framework described in [6] need not be programmed directly, since the *i*Integration framework automatically adapts to first-/second-order systems. Performing the assignment operations as described above, this framework is recovered directly (from the *i*Integration framework). This demonstrates the practicality of the framework, that is, it readily enables the use of the same computational code to solve both first and second-order systems.

We employ the *i*Integration framework for solving the heat transfer model as described above using the nondimensional time step size ($\Delta\tau$) of 0.1 and nondimensional end time of $\tau = 2$. Additionally, we demonstrate the ability of the selective control feature inherent in the framework. Such a feature can be turned on by choosing $\rho_\infty^{\min} \neq \rho_\infty^s$, which is equivalent to the GS4-1 framework with $\rho_\infty \neq \rho_\infty^s$. On the other hand, when $ho_\infty^{\min} = \rho_\infty^s$, the framework recovers the GS4-1 framework without the selective control feature as in the existing/past methods. The advantage of this feature will be made apparent by comparing the numerical results generated by the two cases, that is, with and without the selective control feature. For this purpose, we let the ρ_∞^s of the GS4-1 framework with the selective control feature to take on zero value, while the $\rho_\infty^{\min}$ values tested may range from 1 (i.e., nondissipative/zero damping) to 0 (i.e., maximal

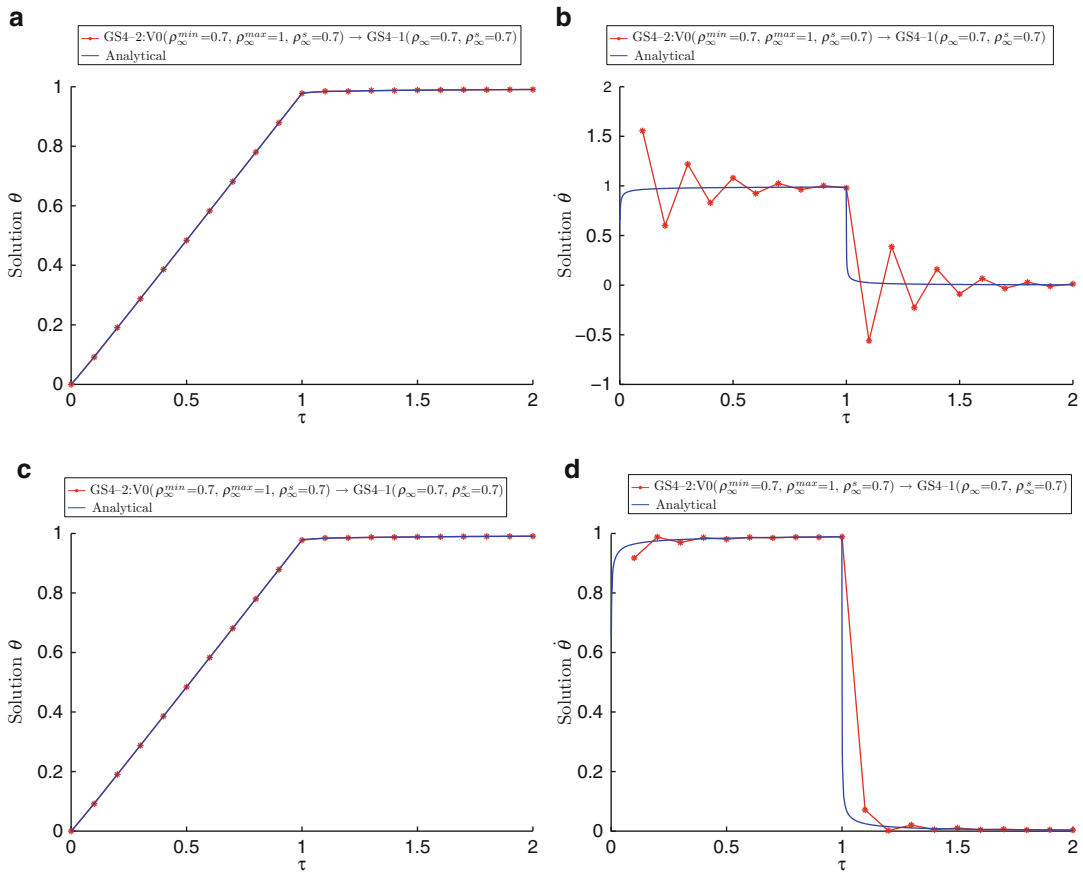

Application of Isochronous Integration Framework to Dynamic Thermoelasticity, Fig. 4 Plot of θ and $\dot{\theta}$ as a function of time for node 2 ($\xi = 0.02$) employing (**a**, **b**) GS4-1($\rho_\infty = \rho_\infty^s = 0.7$), that is, the case without selective control feature, and (**c**, **d**) GS4-1($\rho_\infty = 0.7, \rho_\infty^s = 0$), that is, the case with selective control feature

damping) in decrements of 0.1. The parameter defining the case without the selective control feature ($\rho_\infty^{\min} = \rho_\infty^s$) takes on the same value as the $\rho_\infty^{\min}$ for the other case with the selective control feature to enable valid comparisons between the cases.

Figures 1 to 4 show the plots of θ and $\dot{\theta}$ as a function of time for node 2 ($\xi = 0.02$) employing the two cases, that is, GS4-1 framework with and without selective control feature for ρ_∞ values of 1, 0.9, 0.8, and 0.7. It can be seen from these figures that the two cases yield good results of θ. However, for the solutions of $\dot{\theta}$, the case without the selective control feature results in large oscillations. These oscillations can be easily reduced when the selective control feature is turned on (i.e., by choosing $\rho_\infty^s = 0$). This shows the advantage of the GS4-1 framework with the selective control feature in contrast to past methods without such feature.

We next solve the system of ordinary differential equations describing the displacement field as given by (25) as follows:

$$\mathbf{M\ddot{u}} + \mathbf{Ku} = \mathbf{F} \tag{32}$$

In this case, the system is second order in time, and therefore, we employ the *i* Integration framework in its natural form, in which case the framework recovers the original V0-family of

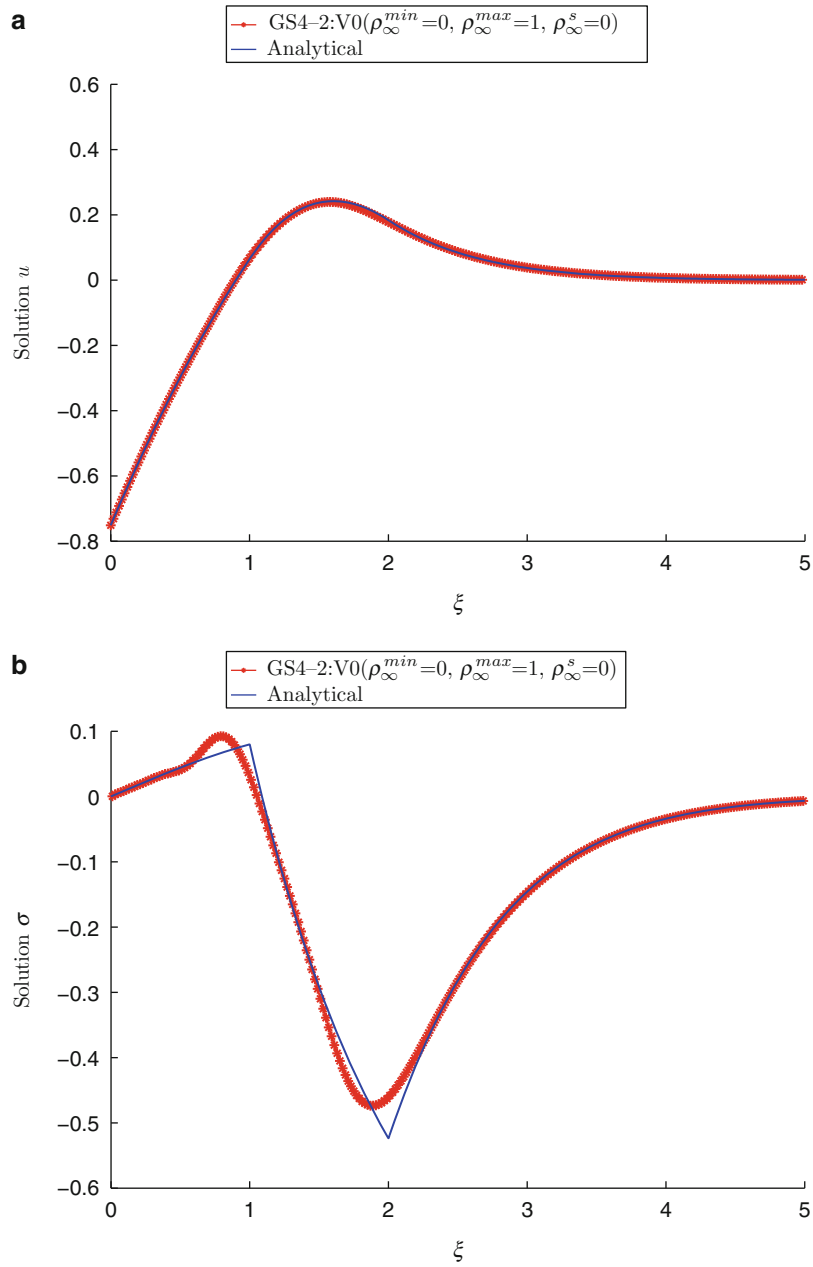

Application of Isochronous Integration Framework to Dynamic Thermoelasticity, Fig. 5 Plot of u and σ as a function of the spatial coordinate ξ at $\tau = 2$ employing GS4-2: V0 ($\rho_\infty^{min} = 0, \rho_\infty^{max} = 1$, $\rho_\infty^{s} = 0$), that is, the $\mathrm{U0} - \mathrm{V0}_{optimal}$ with $\Delta\tau = 0.1$

GS4-2 framework [5]. For this model, we employ the $\mathrm{U0} - \mathrm{V0}_{\mathrm{optimal}}$ defined by GS4-2: V0 ($\rho_\infty^{\min} = 0$, $\rho_\infty^{\max} = 1$, $\rho_\infty^{s} = 0$). Since the computational procedure to solve this system requires the solution of the heat conduction model (the first-order system), we use the solutions of θ generated by the GS4-1 framework with the selective control feature defined by $\rho_\infty = 0.7$ and $\rho_\infty^{s} = 0$. The numerical results on the nondimensional displacement (u) and stress (σ) as a function of the spatial coordinate ξ at $\tau = 2$ are shown in Figs. 5 and 6 for $\Delta\tau$ values of 0.1 and 0.01, respectively. From these figures, it can be seen that the numerical solutions of these variables employing the $\mathrm{U0} - \mathrm{V0}_{\mathrm{optimal}}$ is satisfactory.

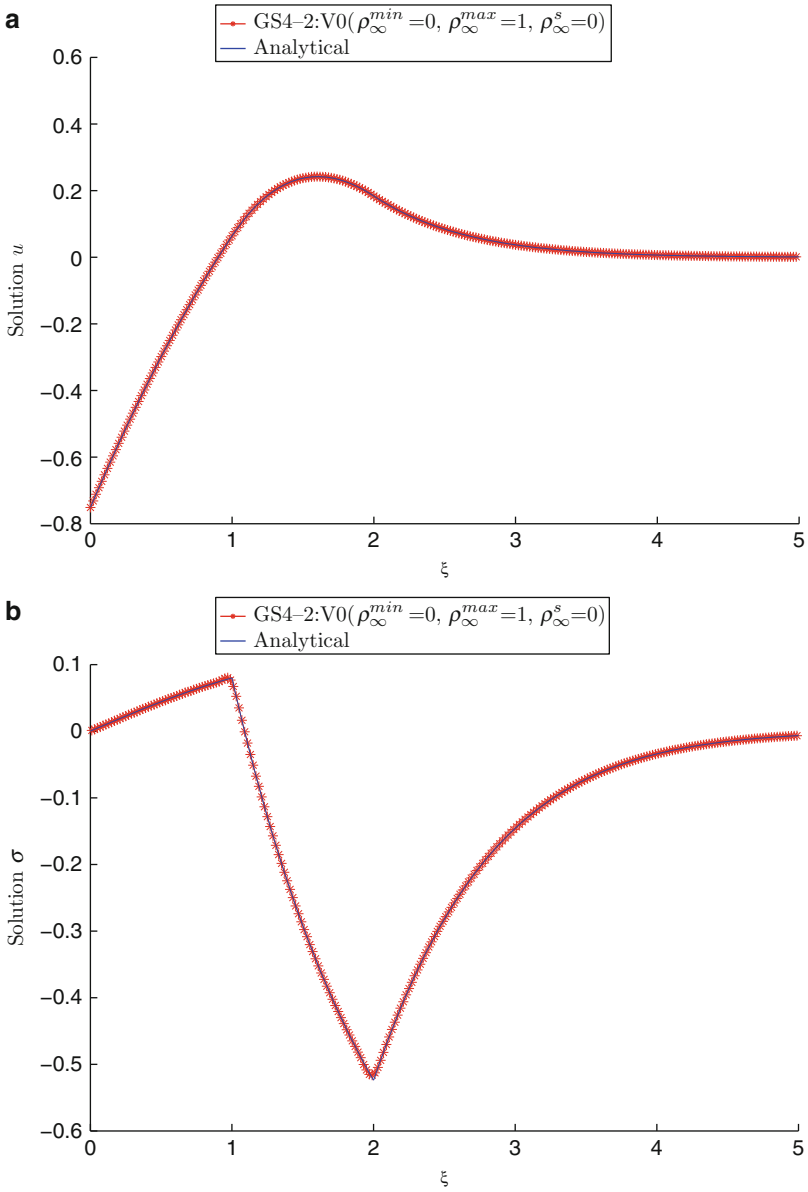

Application of Isochronous Integration Framework to Dynamic Thermoelasticity, Fig. 6 Plot of u and σ as a function of the spatial coordinate ξ at $\tau = 2$ employing GS4-2: V0($\rho_\infty^{min} = 0, \rho_\infty^{max} = 1, \rho_\infty^{s} = 0$), that is, the $\mathrm{U0} - \mathrm{V0}_{optimal}$ with $\Delta\tau = 0.01$

Conclusions

In this work, we describe the significance and also how the *i*Integration framework can be used to solve a dynamic thermoelasticity problem, in particular with ramp-type surface heating (Sternberg-Chakravorty Boundary Condition). The framework is suitable for use in both first- and second-order systems, such as the dynamic thermoelasticity problem described in this synopsis, with optimal algorithms, numerical, and order-preserving attributes (in particular, second-order time accuracy) as well. The principal contribution emanating from such unified framework is the practicality and convenience of using the same computational framework and implementation when solving first- and/or second-order systems without having to resort to the individual framework especially when there is a need to switch from one system to another.

References

1. Tamma KK, Namburu RR (1997) Computational approaches with applications to non-classical and classical thermomechanical problems. Appl Mech Rev 50(9):514–551
2. Sternberg E, Chakravorty JG (1959) On inertia effects in a transient thermoelastic problem. J Appl Mech 26:503–509
3. Nowinski JL (1978) Theory of thermoelasticity with applications. Sijthoff & Noordhoff International, The Netherlands
4. Balla M (1991) Analytical study of the thermal shock problem of a half-space with various thermoelastic models. Acta Mech 89:73–92
5. Zhou X, Tamma KK (2006) Algorithms by design with illustrations to solid and structural mechanics/dynamics. Int J Numer Methods Eng 66:1738–1790
6. Masuri S, Sellier M, Zhou X, Tamma KK (2011) Design of order-preserving algorithms for transient first-order systems with controllable numerical dissipation. Int J Numer Methods Eng. doi:10.1002/nme.3228

Application of Meshless Local Petrov-Galerkin (MLPG) and Generalized Finite Difference (GFD) Methods in Coupled Thermoelasticity Analysis of Thick Hollow Cylinder

Seyed Mahmoud Hosseini
Industrial Engineering Department, Ferdowsi University of Mashhad, Mashhad, Iran

Synonyms

Coupled thermoelasticity; Green-Naghdi theory; Meshless methods; Thick cylinder

Definition

The mesh-free or meshless methods are some of the most effective numerical methods in engineering analysis. In meshless methods, it is not required to generate any mesh on the whole analyzed domain which can be considered as the great advantage of meshless methods. The governing equations of coupled thermoelasticity based on Green-Naghdi theory without energy dissipation in thick hollow cylinder are solved using two meshless methods including meshless local Petrov-Galerkin (MLPG) and generalized finite difference (GFD). In both methods, the governing equations are discretized in matrix forms in the temperature and displacement fields. The boundary conditions are represented in MLPG and GFD discretized forms of relevant boundary densities (temperature, heat flux, displacements, and tractions).

Overview

In many problems of thermoelasticity, the temperature field is directly obtained from the first law of thermodynamics and the temperature is independent of displacements. Coupled problems of thermoelasticity take into account the time rate of the first invariant change of strain tensor in the first law of thermodynamics. This causes dependency between the temperature and displacement fields and, thus, coupling between elasticity and energy equations. This situation happens when the time rate of change of thermal boundary conditions is comparable with the time rate of structural disturbances. When characteristic times of structural and thermal disturbances are of comparable magnitudes, the equations of motion of an elastic body are coupled with the energy equation. Green and Naghdi presented a model in coupled thermoelasticity which is called the GN theory of thermoelasticity [1].

The meshless local Petrov-Galerkin (MLPG) method is based on local (symmetric or unsymmetric) weak forms over intersecting subdomains, which are distributed over an analyzed domain of problem in both temperature and displacement fields. Physically the considered problem is three dimensional though some components of the physical fields are vanishing and each physical field is dependent only on the radial coordinate due to the axial symmetry and independence on the axial coordinate.

In generalized finite difference (GFD) method, the partial derivatives are linearly approximated by Taylor series expansion on

some nodes (center nodes) in the analyzed domain such that each center node is surrounded by some other nodes in both temperature and displacement fields. Consequently, partial derivatives are obtained at the rest of each center nodes and the group of nodes with a center node and surrounding other nodes is called a star in this method.

Green-Naghdi Coupled Thermoelasticity in Thick Hollow Cylinder

Consider a thick hollow cylinder made of functionally graded materials (FGMs) with inner radius "r_{in}" and outer radius "r_{out}", which is subjected to thermal shock loading. To find the dynamic response of displacement field, the coupled thermoelasticity governing equations should be considered for the problem. In coupled thermoelasticity, the time rate of the first invariant change of strain tensor is employed in the first law of thermodynamics. Consequently, this causes dependency between the temperature and displacement fields and, thus, coupling between elasticity and energy equations. To find the dynamic behaviors of displacement field, the temperature field and elastic field should be solved together as a coupled system of partial differential equations. The governing coupled thermoelasticity equations based on GN theory without energy dissipation are given as:

$$\nabla\cdot\boldsymbol{\sigma} + \rho\mathbf{F} = \rho\ddot{\mathbf{u}} \tag{1}$$

$$c\,\ddot{T} + \gamma\, T_0\, \nabla\cdot\ddot{\mathbf{u}} = \rho\,\dot{g} + \nabla\cdot(k^*\nabla T) \tag{2}$$

where "$\mathbf{u}$" is the displacement vector, "T" is the temperature change above the uniform reference temperature "T_0", "$\mathbf{F}$" is the external force, and "$\dot{g}$" is the external rate of supply of heat. Both the "$\mathbf{F}$" and "$\dot{g}$" are assumed to be absent in this work. Furthermore, "ρ" is the mass density, "c" is the specific heat, "λ" and "μ" are the Lame constants and

$$\gamma = (3\lambda + 2\mu)\beta^* \tag{3}$$

where "β^*" is the coefficient of linear thermal expansion and "k^*" is a material parameter of the GN theory. The dot over the symbol denotes the time differentiation. The stress field can be reached using following equation:

$$\sigma_{ij} = \delta_{ij}\left(\lambda\, u_{k,k} - \gamma T\right) + \mu\,(u_{i,j} + u_{j,i}) \tag{4}$$

The axisymmetry and plane strain conditions are assumed for the problem to find natural frequencies of FG thick hollow cylinder from dynamic response of radial displacement. Consequently, the following relations are taken into account to calculate the parameters:

$$u_\theta = 0,\ \ u_z = 0,\ \ \sigma_{rr} = 2\,\mu\, u_{r,r} + (\lambda\, e - \gamma T),$$
$$\sigma_{\theta\theta} = 2\,\mu\, u_r/r + (\lambda\, e - \gamma T),\ \ \sigma_{zz} = \lambda\, e - \gamma T,$$
$$\sigma_{r\theta} = 0 = \sigma_{rz} = \sigma_{z\theta},\ \ e = u_{r,r} + u_r/r$$

The governing equations (1) and (2) are reduced to the equations:

$$\mu\nabla^2 u + (\lambda + \mu)\nabla div u - \gamma\nabla T + \rho F = \rho\ddot{u} \tag{5}$$

$$c\ddot{T} + \gamma\, T_0 div\ddot{u} = \rho\,\dot{g} + k^*\nabla^2 T \tag{6}$$

where "u" is the displacement vector, "T" is the temperature change above the uniform reference temperature "T_0", "F" is the external force, and "$\dot{g}$" is the external rate of supply of heat that both "F" and "$\dot{g}$" are not considered in this work. "ρ" is the mass density, "c" is the specific heat, "λ" and "μ" are the Lame constants, and

$$\gamma = (3\,\lambda + 2\,\mu)\,\beta^* \tag{7}$$

where "β^*" is the coefficient of volume expansion and "k^*" is a material constant characteristic of the theory.

To analyze the problem, we use the nondimensional parameters as follows:

$$\bar{r} = \frac{r}{l},\ \ \bar{t} = \frac{v}{l}t,\ \bar{u} = \frac{1}{l}\,\frac{(\lambda + 2\mu)}{\gamma\, T_0}\,u$$
$$\bar{T} = \frac{T}{T_0},\ \ \bar{\sigma}_r = \frac{\sigma_r}{\gamma\, T_0},\ \ \bar{\sigma}_\theta = \frac{\sigma_\theta}{\gamma\, T_0} \tag{8}$$

where "l" is a standard length and "v" is a standard speed. The governing equation and heat transfer can be rewritten by using nondimensional parameters:

$$C_s{}^2\nabla^2\bar{u} + \left(C_p^2 - C_s{}^2\right)\nabla div\bar{u} - C_p{}^2\nabla\bar{T} = \ddot{\bar{u}} \quad (9)$$

$$C_T{}^2\nabla^2\bar{T} = \dot{\bar{T}} + \varepsilon^* div\ddot{\bar{u}} \quad (10)$$

where

$$C_p{}^2 = \frac{\lambda + 2\mu}{\rho\, v^2},\quad C_T{}^2 = \frac{k^*}{c\, v^2},$$
$$C_s{}^2 = \frac{\mu}{\rho\, v^2},\quad \varepsilon^* = \frac{\gamma^2\, T_0}{c\,(\lambda + 2\mu)} \quad (11)$$

We consider the axisymmetry and plane strain conditions for problem. The governing equations for axisymmetry and plane strain conditions can be obtained as follows:

$$C_p{}^2\frac{\partial^2\bar{u}}{\partial\bar{r}^2} + C_p{}^2\frac{1}{\bar{r}}\frac{\partial\bar{u}}{\partial\bar{r}} - \left(C_p^2 - C_s{}^2\right)\frac{\bar{u}}{\bar{r}^2} - C_p{}^2\frac{\partial\bar{T}}{\partial\bar{r}} = \ddot{u} \quad (12)$$

$$C_T{}^2\left[\frac{\partial^2\bar{T}}{\partial\bar{r}^2} + \frac{1}{\bar{r}}\frac{\partial\bar{T}}{\partial\bar{r}}\right] = \dot{\bar{T}} + \varepsilon^*\left[\frac{\partial\ddot{u}}{\partial\bar{r}} + \frac{\ddot{u}}{\bar{r}}\right] \quad (13)$$

To solve the aforementioned governing coupled thermoelasticity equations (12) and (13), there are some numerical methods such as finite element and other similar methods that are needed to mesh generations and also numerical methods based on mesh reduction or meshless techniques. In this entry, we present two efficient mesh-free methods, which are called meshless local Petrov-Galerkin (MLPG) and generalized finite difference (GFD) methods.

Meshless Local Petrov-Galerkin Method

The MLPG method is based on local weak forms over some subdomains, which are distributed over an analyzed domain of problem. In this problem, the analyzed domain is an abscissa along the radial coordinate of the FG cylinder. The analyzed domain is assumed to be covered by small subdomains in finite size line segments forms. Nodal points are randomly distributed in the global domain and each interior node $\bar{r}_I$ is surrounded by a subdomain (line segment) $\Omega_I = [\bar{r}_{I0}, \bar{r}_{I1}]$ on which a local weak formulation for the set of Green-Naghdi coupled thermoelasticity governing equations (12) and (13) is considered. Using $h(\bar{r})$ and $g(\bar{r})$ as the test functions, the local weak form of the coupled thermoelasticity governing equations can be written over subdomain Ω_I as:

$$\int_{\Omega_I}\left\{C_p^2\frac{\partial^2\bar{u}(\bar{r},\bar{t})}{\partial\bar{r}^2} + C_p{}^2\frac{1}{\bar{r}}\frac{\partial\bar{u}(\bar{r},\bar{t})}{\partial\bar{r}} - \left(C_p^2 - C_s{}^2\right)\frac{\bar{u}(\bar{r},\bar{t})}{\bar{r}^2} - C_p{}^2\frac{\partial\bar{T}(\bar{r},\bar{t})}{\partial\bar{r}} - \ddot{\bar{u}}(\bar{r},\bar{t})\right\}h(\bar{r})\bar{r}d\bar{r} = 0 \quad (14)$$

$$\int_{\Omega_I}\left\{C_T^2\left[\frac{\partial^2\bar{T}(\bar{r},\bar{t})}{\partial\bar{r}^2} + \frac{1}{\bar{r}}\frac{\partial\bar{T}(\bar{r},\bar{t})}{\partial\bar{r}}\right] - \dot{\bar{T}}(\bar{r},\bar{t}) - \varepsilon^*\left[\frac{\partial\ddot{\bar{u}}(\bar{r},\bar{t})}{\partial\bar{r}} + \frac{\ddot{\bar{u}}(\bar{r},\bar{t})}{\bar{r}}\right]\right\}g(\bar{r})\bar{r}d\bar{r} = 0 \quad (15)$$

for all interior nodes $I = 1, 2, \ldots, n$. Applying the integration by parts to equations (14) and (15), we obtain:

$$C_p^2\left(\frac{\partial\bar{u}(\bar{r},\bar{t})}{\partial\bar{r}} + \frac{\bar{u}(\bar{r},\bar{t})}{\bar{r}} - \bar{T}(\bar{r},\bar{t})\right)\bar{r}h(\bar{r})\Big|_{\bar{r}_{I0}}^{\bar{r}_{I1}} + \int_{\bar{r}_{I0}}^{\bar{r}_{I1}}\left[C_s^2\frac{\bar{u}(\bar{r},\bar{t})}{\bar{r}^2} - \ddot{\bar{u}}(\bar{r},\bar{t})\right]h(\bar{r})\bar{r}d\bar{r} - \int_{\bar{r}_{I0}}^{\bar{r}_{I1}}\left[C_p^2\left(\frac{\partial\bar{u}(\bar{r},\bar{t})}{\partial\bar{r}} + \frac{\bar{u}(\bar{r},\bar{t})}{\bar{r}} - \bar{T}(\bar{r},\bar{t})\right)\frac{\partial\bar{r}h(\bar{r})}{\partial\bar{r}}\right]d\bar{r} = 0 \quad (16)$$

$$\left[C_T^2\left(\frac{\partial\bar{T}(\bar{r},\bar{t})}{\partial\bar{r}} + \frac{\bar{T}(\bar{r},\bar{t})}{\bar{r}}\right) - \varepsilon^*\ddot{\bar{u}}(\bar{r},\bar{t})\right]\bar{r}g(\bar{r})\Big|_{\bar{r}_{I0}}^{\bar{r}_{I1}} + \int_{\bar{r}_{I0}}^{\bar{r}_{I1}}\left[C_T^2\frac{\bar{T}(\bar{r},\bar{t})}{\bar{r}^2} - \dot{\bar{T}}(\bar{r},\bar{t}) - \varepsilon^*\frac{\ddot{\bar{u}}(\bar{r},\bar{t})}{\bar{r}}\right]g(\bar{r})\bar{r}d\bar{r} - \int_{\bar{r}_{I0}}^{\bar{r}_{I1}}\left[C_T^2\left(\frac{\partial\bar{T}(\bar{r},\bar{t})}{\partial\bar{r}} + \frac{\bar{T}(\bar{r},\bar{t})}{\bar{r}}\right) - \varepsilon^*\ddot{\bar{u}}(\bar{r},\bar{t})\right]\frac{\partial\bar{r}g(\bar{r})}{\partial\bar{r}}d\bar{r} = 0 \quad (17)$$

For the problem in this entry, we assumed the test functions to be equal to Heaviside step unit function:

$$h(\bar{r}) = g(\bar{r}) = \begin{cases} 1 & at \quad \bar{r} \in \Omega_I \\ 0 & at \quad \bar{r} \notin \Omega_I \end{cases} \tag{18}$$

The local integral equations (16) and (17) are simplified as:

$$\begin{aligned} & C_p^2 \left(\frac{\partial \bar{u}(\bar{r},\bar{t})}{\partial \bar{r}} + \frac{\bar{u}(\bar{r},\bar{t})}{\bar{r}} - \bar{T}(\bar{r},\bar{t}) \right) \bar{r} \Big|_{\bar{r}_{I0}}^{\bar{r}_{I1}} \\ & - \int_{\bar{r}_{I0}}^{\bar{r}_{I1}} \left[C_p^2 \left(\frac{\partial \bar{u}(\bar{r},\bar{t})}{\partial \bar{r}} - \bar{T}(\bar{r},\bar{t}) \right) \right. \\ & \left. + \left(C_p^2 - C_s^2 \right) \frac{\bar{u}(\bar{r},\bar{t})}{\bar{r}} + \bar{r}\, \ddot{\bar{u}}(\bar{r},\bar{t}) \right] d\bar{r} = 0 \end{aligned} \tag{19}$$

$$\begin{aligned} & \left[C_T^2 \left(\frac{\partial \bar{T}(\bar{r},\bar{t})}{\partial \bar{r}} + \frac{\bar{T}(\bar{r},\bar{t})}{\bar{r}} \right) - \varepsilon^* \ddot{\bar{u}}(\bar{r},\bar{t}) \right] \bar{r} \Big|_{\bar{r}_{I0}}^{\bar{r}_{I1}} \\ & - \int_{\bar{r}_{I0}}^{\bar{r}_{I1}} \left[C_T^2 \frac{\partial \bar{T}(\bar{r},\bar{t})}{\partial \bar{r}} + \bar{r} \ddot{\bar{T}}(\bar{r},\bar{t}) \right] d\bar{r} = 0 \end{aligned} \tag{20}$$

The radial basis functions are used to approximate for the spatial distributions of functions "$\bar{u}(\bar{r},\bar{t})$" and "$\bar{T}(\bar{r},\bar{t})$" over a number of randomly located nodes "$\bar{r}_I$", $I = 1, 2, \ldots, N$. Consequently, assuming the separation of the spatial and temporal variables, the considered approximations take the form:

$$\bar{u}(\bar{r},\bar{t}) = R^T(\bar{r})\, A(\bar{t}) \tag{21}$$

$$\bar{T}(\bar{r},\bar{t}) = R^T(\bar{r})\, B(\bar{t}) \tag{22}$$

where "$R^T(\bar{r}) = [R_1(\bar{r}), R_2(\bar{r}), \ldots, R_n(\bar{r})]$" is the value of radial basis functions around "$\bar{r}_I$", and "$A(\bar{t})$" and "$B(\bar{t})$" are vectors containing the coefficients of "A_I" and "B_I", $I = 1, 2, \ldots, N$.

The radial basis function studied in this entry is [2]:

$$R_I(\bar{r}) = \left(|\bar{r} - \bar{r}_I|^2 + c^2 \right)^{\frac{m}{2}} \tag{23}$$

Form the interpolation equations (21) and (22) for the radial basis functions, the following systems of linear equations for the coefficients "$A(\bar{t})$" and "$B(\bar{t})$" are obtained:

$$R_0 A(\bar{t}) = \hat{u}(\bar{t}) \tag{24}$$

$$R_0\, B(\bar{t}) = \hat{T}(\bar{t}) \tag{25}$$

where

$$\hat{u}^T(\bar{t}) = \left[\bar{u}^1(\bar{t}), \bar{u}^2(\bar{t}), \ldots, \bar{u}^n(\bar{t}) \right] \tag{26}$$

$$\hat{T}^T(\bar{t}) = \left[\bar{T}^1(\bar{t}), \bar{T}^2(\bar{t}), \ldots, \bar{T}^n(\bar{t}) \right] \tag{27}$$

are composed of the time variable nodal values of displacements "$\bar{u}^I(\bar{t})$" and temperature "$\bar{T}^I(\bar{t})$", while "R_0" is the matrix defined by nodal values of the RBFs as:

$$R_0 = \begin{bmatrix} R_1(\bar{r}_1) & R_2(\bar{r}_1) & \ldots & R_n(\bar{r}_1) \\ R_1(\bar{r}_1) & R_2(\bar{r}_2) & \ldots & R_n(\bar{r}_2) \\ \cdot & \cdot & \cdot & \cdot \\ \cdot & \cdot & \cdot & \cdot \\ R_1(\bar{r}_n) & R_2(\bar{r}_n) & \ldots & R_n(\bar{r}_n) \end{bmatrix} \tag{28}$$

To calculate the vectors "$A(\bar{t})$" and "$B(\bar{t})$", we can write from equations (24) and (25):

$$A(\bar{t}) = {R_0}^{-1}\, \hat{u}(\bar{t}) \tag{29}$$

$$B(\bar{t}) = {R_0}^{-1}\, \hat{T}(\bar{t}) \tag{30}$$

The approximated functions can be expressed in terms of the nodal values and the shape functions as:

$$\begin{aligned} \bar{u}(\bar{r},\bar{t}) &= R^T(\bar{r})\, {R_0}^{-1}\, \hat{u}(\bar{t}) = \Phi^T(\bar{r})\, \hat{u}(\bar{t}) \\ &= \sum_{a=1}^{n} \phi^a(\bar{r})\, \bar{u}^a(\bar{t}) \end{aligned} \tag{31}$$

$$\begin{aligned} \bar{T}(\bar{r},\bar{t}) &= R^T(\bar{r})\, {R_0}^{-1}\, \hat{T}(\bar{t}) = \Phi^T(\bar{r})\, \hat{T}(\bar{t}) \\ &= \sum_{a=1}^{n} \phi^a(\bar{r})\, \bar{T}^a(\bar{t}) \end{aligned} \tag{32}$$

where "$\phi^a(\bar{r})$" is the shape function associated with the node a. The nodal shape functions are given by:

$$\Phi^T(\bar{r}) = R^T(\bar{r})\, R_0{}^{-1} \tag{33}$$

The local boundary integral equations (19) and (20) for all subdomains yield the following set of coupled equations:

$$\begin{aligned}
&\sum_{a=1}^{n} \bar{u}^a(\bar{t}) \left\{ C_p^2 \left(\bar{r} \frac{\partial \phi^a(\bar{r})}{\partial \bar{r}} + \phi^a(\bar{r}) \right) \Big|_{\bar{r}_{I0}}^{\bar{r}_{I1}} \right. \\
&\left. - \int_{\bar{r}_{I0}}^{\bar{r}_{I1}} \left[C_p^2 \frac{\partial \phi^a(\bar{r})}{\partial \bar{r}} + \left(C_p^2 - C_s{}^2 \right) \frac{\phi^a(\bar{r})}{\bar{r}} \right] d\bar{r} \right\} \\
&- \sum_{a=1}^{n} \ddot{\bar{u}}^a(\bar{t}) \int_{\bar{r}_{I0}}^{\bar{r}_{I1}} \bar{r} \phi^a(\bar{r}) d\bar{r} - C_p{}^2 \sum_{a=1}^{n} \bar{T}^a(\bar{t}) \\
&\left[\bar{r} \phi^a(\bar{r}) |_{\bar{r}_{I0}}^{\bar{r}_{I1}} - \int_{\bar{r}_{I0}}^{\bar{r}_{I1}} \phi^a(\bar{r}) d\bar{r} \right] = 0
\end{aligned} \tag{34}$$

$$\begin{aligned}
&\sum_{a=1}^{n} \bar{T}^a(\bar{t}) \left\{ C_T^2 \left(\bar{r} \frac{\partial \phi^a(\bar{r})}{\partial \bar{r}} + \phi^a(\bar{r}) \right) \Big|_{\bar{r}_{I0}}^{\bar{r}_{I1}} \right. \\
&\left. - \int_{\bar{r}_{I0}}^{\bar{r}_{I1}} C_T^2 \frac{\partial \phi^a(\bar{r})}{\partial \bar{r}} d\bar{r} \right\} - \sum_{a=1}^{n} \ddot{\bar{T}}^a(\bar{t}) \int_{\bar{r}_{I0}}^{\bar{r}_{I1}} \bar{r} \phi^a(\bar{r}) d\bar{r} \\
&- \varepsilon^* \sum_{a=1}^{n} \ddot{\bar{u}}^a(\bar{t}) \bar{r} \phi^a(\bar{r}) |_{\bar{r}_{I0}}^{\bar{r}_{I1}} = 0
\end{aligned} \tag{35}$$

It should be noted that the essential boundary conditions on "$\partial \Omega_s$" can be imposed directly using the interpolation approximation (31) and (32). In view of the considered spatial interpolations, the discretized boundary conditions and the integral equations on local subdomains can be written in the matrix form as a system of ordinary differential equations (ODEs) for the time dependent nodal values of the displacement and temperature.

$$[M] \left\{ \ddot{\phi} \right\} + [K] \{\phi\} = [f] \tag{36}$$

where

$$\{\phi\} = \begin{Bmatrix} [\hat{u}(\bar{t})] \\ [\hat{T}(\bar{t})] \end{Bmatrix}$$

$$\hat{u}^T(\bar{t}) = \left[\bar{u}^1(\bar{t}), \quad \bar{u}^2(\bar{t}), \quad \ldots, \quad \bar{u}^n(\bar{t}) \right] \tag{37}$$

$$\hat{T}^T(\bar{t}) = \left[\bar{T}^1(\bar{t}), \quad \bar{T}^2(\bar{t}), \ldots, \bar{T}^n(\bar{t}) \right]$$

Once the coupled differential equations are established, different numerical methods can be employed to solve them in time domain such as Newmark finite difference method or Laplace transformation.

Generalized Finite Difference (GFD) Method

In numerical methods that are needed to generate mesh on the problem domain such as finite element methods, the mesh generation takes a long time during the solving process. In this section, we develop the application of GFD method in which there is no need for any mesh generation for coupled thermoelasticity problem based on Green-Naghdi theory for thick hollow cylinder. In this method, the partial derivatives are linearly approximated by Taylor series expansion on some nodes (center nodes) in the analyzed domain such that each center node is surrounded by some other nodes. Consequently, partial derivatives are obtained at the rest of each center nodes and the group of nodes with a center node and surrounding other nodes is called a star in this method.

Consider the nondimensional radial displacement at a center node to be "$\bar{u}_0$" and nondimensional temperature to be "$\bar{T}_0$" and the terms "$\bar{u}_i$" and "$\bar{T}_i$" are the values of nondimensional radial displacement and temperature at the rest of surrounding nodes. The function values "$\bar{u}_i$" and "$\bar{T}_i$" can be approximated using Taylor expansion as:

$$\bar{u}_i = \bar{u}_0 + h_i \frac{\partial \bar{u}_0}{\partial \bar{r}} + \frac{1}{2} \left(h_i^2 \frac{\partial^2 \bar{u}_0}{\partial \bar{r}^2} \right) + \ldots \tag{38}$$

and

$$\bar{T}_i = \bar{T}_0 + h_i \frac{\partial \bar{T}_0}{\partial \bar{r}} + \frac{1}{2}\left(h_i^2 \frac{\partial^2 \bar{T}_0}{\partial \bar{r}^2}\right) + \ldots \quad (39)$$

The term "i" denotes the number of surrounding nodes. The analyzed domain in the problem is linear through radial direction on thickness of cylinder. Consequently, the term "h_i" can be calculated as $h_i = \bar{r}_i - \bar{r}_o$. The terms over second order are ignored in equations (38) and (39) and the linear approximation of second order can be obtained for radial displacement and temperature. To minimize the error in this method, the function of norm should be minimized. The functions of norm for radial displacement and temperature are:

$$Norm(u) = \sum_{i=1}^{N}\left[\left(\bar{u}_0 - \bar{u}_i + h_i \frac{\partial \bar{u}_0}{\partial \bar{r}} + \frac{1}{2}\left(h_i^2 \frac{\partial^2 \bar{u}_0}{\partial \bar{r}^2}\right)\right) w(h_i)\right]^2 \quad (40)$$

and

$$Norm(\bar{T}) = \sum_{i=1}^{N}\left[\left(\bar{T}_0 - \bar{T}_i + h_i \frac{\partial \bar{T}_0}{\partial \bar{r}} + \frac{1}{2}\left(h_i^2 \frac{\partial^2 \bar{T}_0}{\partial \bar{r}^2}\right)\right) w(h_i)\right]^2 \quad (41)$$

where "$w(h_i)$" is the weight function. In this entry, we assume that the weight function is defined by:

$$w(h_i) = \frac{1}{(dist)^3} = \frac{1}{h_i^3} \quad (42)$$

If the norms (40) and (41) are minimized with respect to the partial derivatives, a set of linear equations system is obtained as follows:

$$\psi^u{}_2 \, \mathbb{Q}_{u2} = \xi^u{}_2 \quad (43)$$

$$\psi^T{}_2 \, \mathbb{Q}_{T2} = \xi^T{}_2 \quad (44)$$

where the terms "$\psi^u{}_2$" and "$\psi^T{}_2$" stand for 2×2 matrices in displacement and temperature fields, respectively. The components of matrices "$\psi^u{}_2$" and "$\psi^T{}_2$" and vectors "$\xi^u{}_2$" and "$\xi^T{}_2$" are obtained in the Appendix. The vectors "$\mathbb{Q}_{u2}$" and "$\mathbb{Q}_{T2}$" are given, respectively, by:

$$\mathbb{Q}_{u2} = \left\{\frac{\partial \bar{u}_0}{\partial \bar{r}}, \frac{\partial^2 \bar{u}_0}{\partial \bar{r}^2}\right\}^T \quad (45)$$

$$\mathbb{Q}_{T2} = \left\{\frac{\partial \bar{T}_0}{\partial \bar{r}}, \frac{\partial^2 \bar{T}_0}{\partial \bar{r}^2}\right\}^T \quad (46)$$

There are some methods to solve the system of differential equations; one of them is Cholesky method [3]. In Cholesky method, the symmetric matrices "$\psi^u{}_2$" and "$\psi^T{}_2$" are decomposed to upper and lower triangular matrices. The first and second derivatives are calculated as:

$$\frac{\partial \bar{u}_0}{\partial \bar{r}} = A_1{}^u\left\{\sum_{i=1}^{N}(-\bar{u}_0 + \bar{u}_i) h_i \, w^2(h_i)\right\} - A_2{}^u\left\{\sum_{i=1}^{N}(-\bar{u}_0 + \bar{u}_i)\frac{h_i{}^2}{2} w^2(h_i)\right\} \quad (47)$$

$$\frac{\partial^2 \bar{u}_0}{\partial \bar{r}^2} = B_1{}^u\left\{\sum_{i=1}^{N}(-\bar{u}_0 + \bar{u}_i) h_i \, w^2(h_i)\right\} - B_2{}^u\left\{\sum_{i=1}^{N}(-\bar{u}_0 + \bar{u}_i)\frac{h_i{}^2}{2} w^2(h_i)\right\} \quad (48)$$

and

$$\frac{\partial \bar{T}_0}{\partial \bar{r}} = A_1{}^T\left\{\sum_{i=1}^{N}(-\bar{T}_0 + \bar{T}_i) h_i \, w^2(h_i)\right\} - A_2{}^T\left\{\sum_{i=1}^{N}(-\bar{T}_0 + \bar{T}_i)\frac{h_i{}^2}{2} w^2(h_i)\right\} \quad (49)$$

$$\frac{\partial^2 \bar{T}_0}{\partial \bar{r}^2} = B_1{}^T\left\{\sum_{i=1}^{N}(-\bar{T}_0 + \bar{T}_i) h_i \, w^2(h_i)\right\} - B_2{}^T\left\{\sum_{i=1}^{N}(-\bar{T}_0 + \bar{T}_i)\frac{h_i{}^2}{2} w^2(h_i)\right\} \quad (50)$$

where the coefficients "$A_1{}^u$", "$A_2{}^u$", "$B_1{}^u$", "$B_2{}^u$", "$A_1{}^T$", "$A_2{}^T$", "$B_1{}^T$", and "$B_2{}^T$" are obtained in detail as follows:

$$A_1{}^u = A_1{}^T = \frac{\left(\sum_{i=1}^{N} \frac{h_i{}^4}{4} w^2(h_i)\right)}{\left(\sum_{i=1}^{N} h_i{}^2 w^2(h_i)\right)\left(\sum_{i=1}^{N} \frac{h_i{}^4}{4} w^2(h_i)\right) - \left(\sum_{i=1}^{N} \frac{h_i{}^3}{2} w^2(h_i)\right)^2} \tag{51}$$

$$A_2{}^u = A_2{}^T = \frac{\left(\sum_{i=1}^{N} \frac{h_i{}^3}{2} w^2(h_i)\right)}{\left(\sum_{i=1}^{N} h_i{}^2 w^2(h_i)\right)\left(\sum_{i=1}^{N} \frac{h_i{}^4}{4} w^2(h_i)\right) - \left(\sum_{i=1}^{N} \frac{h_i{}^3}{2} w^2(h_i)\right)^2} \tag{52}$$

$$B_1{}^u = B_1{}^T = \frac{-\left(\sum_{i=1}^{N} \frac{h_i{}^3}{2} w^2(h_i)\right)}{\left(\sum_{i=1}^{N} h_i^2 w^2(h_i)\right)\left(\sum_{i=1}^{N} \frac{h_i{}^4}{4} w^2(h_i)\right) - \left(\sum_{i=1}^{N} \frac{h_i{}^3}{2} w^2(h_i)\right)^2} \tag{53}$$

$$B_2{}^u = B_2{}^T = \frac{-\left(\sum_{i=1}^{N} h_i{}^2 w^2(h_i)\right)}{\left(\sum_{i=1}^{N} h_i{}^2 w^2(h_i)\right)\left(\sum_{i=1}^{N} \frac{h_i{}^4}{4} w^2(h_i)\right) - \left(\sum_{i=1}^{N} \frac{h_i{}^3}{2} w^2(h_i)\right)^2} \tag{54}$$

The derivatives of radial displacement and temperature can be also rewritten in star forms as follows:

$$\frac{\partial \bar{u}_0}{\partial \bar{r}} = -\alpha_0 \bar{u}_0 + \sum_{i=1}^{N} \alpha_i \bar{u}_i \tag{55}$$

where

$$\alpha_0 = A_1{}^u \sum_{i=1}^{N} h_i{}^2 w^2(h_i) - A_2{}^u \sum_{i=1}^{N} \frac{h_i{}^2}{2} w^2(h_i),$$
$$\alpha_i = A_1{}^u h_i{}^2 w^2(h_i) - A_2{}^u \frac{h_i{}^2}{2} w^2(h_i),\ \alpha_0 = \sum_{i=1}^{N} \alpha_i \tag{56}$$

For second derivative of radial displacement, we have:

$$\frac{\partial^2 \bar{u}_0}{\partial \bar{r}^2} = -\beta_0 \bar{u}_0 + \sum_{i=1}^{N} \beta_i \bar{u}_i \tag{57}$$

where

$$\beta_0 = B_1{}^u \sum_{i=1}^{N} h_i{}^2 w^2(h_i) - B_2{}^u \sum_{i=1}^{N} \frac{h_i{}^2}{2} w^2(h_i),$$
$$\beta_i = B_1{}^u h_i{}^2 w^2(h_i) - B_2{}^u \frac{h_i{}^2}{2} w^2(h_i),\ \beta_0 = \sum_{i=1}^{N} \beta_i \tag{58}$$

The temperature derivatives can be obtained using the similar method:

$$\frac{\partial \bar{T}_0}{\partial \bar{r}} = -\gamma_0 \bar{T}_0 + \sum_{i=1}^{N} \gamma_i \bar{T}_i \tag{59}$$

where

$$\gamma_0 = A_1{}^T \sum_{i=1}^{N} h_i{}^2 w^2(h_i) - A_2{}^T \sum_{i=1}^{N} \frac{h_i{}^2}{2} w^2(h_i),$$
$$\gamma_i = A_1{}^T h_i{}^2 w^2(h_i) - A_2{}^T \frac{h_i{}^2}{2} w^2(h_i),\ \gamma_0 = \sum_{i=1}^{N} \gamma_i \tag{60}$$

For second derivative of temperature, we have:

$$\frac{\partial^2 \bar{T}_0}{\partial \bar{r}^2} = -\psi_0 \bar{u}_0 + \sum_{i=1}^{N} \psi_i \bar{u}_i \tag{61}$$

where

$$\psi_0 = B_1{}^T \sum_{i=1}^{N} h_i{}^2 w^2(h_i) - B_2{}^T \sum_{i=1}^{N} \frac{h_i{}^2}{2} w^2(h_i),$$
$$\psi_i = B_1{}^T h_i{}^2 w^2(h_i) - B_2{}^T \frac{h_i{}^2}{2} w^2(h_i),\ \psi_0 = \sum_{i=1}^{N} \psi_i \tag{62}$$

Also, the second derivative of radial displacement with respect to time can be approximated for first derivative with respect to radius as follows:

$$\frac{\partial \ddot{\bar{u}}_0}{\partial \bar{r}} = -\alpha_0 \bar{u}_0 + \sum_{i=1}^{N} \alpha_i \bar{u}_i \tag{63}$$

where the terms "α_0" and "α_i" were introduced in equations (56). By substituting the obtained relations in star forms for first and second derivatives in governing equations (12) and (13) at a center node, the coupled thermoelasticity governing equations can be obtained in new form based on GFD method. In other words, the governing equations should be valid at every center node on analyzed domain.

$$C_p{}^2 \frac{\partial^2 \bar{u}_0}{\partial \bar{r}^2} + C_p{}^2 \frac{1}{\bar{r}_0} \frac{\partial \bar{u}_0}{\partial \bar{r}} - \left(C_p{}^2 - C_s{}^2\right) \frac{\bar{u}_0}{\bar{r}_0{}^2} - C_p{}^2 \frac{\partial \bar{T}_0}{\partial \bar{r}} = \ddot{\bar{u}}_0 \tag{64}$$

$$C_p{}^2 \left(-\beta_0 \bar{u}_0 + \sum_{i=1}^{N} \beta_i \bar{u}_i\right) + C_p{}^2 \frac{1}{\bar{r}_0} \left(-\alpha_0 \bar{u}_0 + \sum_{i=1}^{N} \alpha_i \bar{u}_i\right) - \left(C_p^2 - C_s{}^2\right) \frac{\bar{u}_0}{\bar{r}_0{}^2} - C_p{}^2 \left(-\gamma_0 \bar{u}_0 + \sum_{i=1}^{N} \gamma_i \bar{u}_i\right) = \ddot{\bar{u}}_0 \tag{65}$$

$$\left\{-\beta_0 C_p{}^2 - \alpha_0 C_p{}^2 \frac{1}{\bar{r}_0} - \left(C_p^2 - C_s{}^2\right) \frac{1}{\bar{r}_0{}^2}\right\} \bar{u}_0 + \sum_{i=1}^{N} \left\{C_p{}^2 \beta_i + C_p{}^2 \frac{1}{\bar{r}_0} \alpha_i\right\} \bar{u}_i + \left\{C_p^2 \gamma_0\right\} T_0 + \sum_{i=1}^{N} \left\{-C_p{}^2 \gamma_i\right\} \bar{T}_i = \ddot{\bar{u}}_0 \tag{66}$$

and also we have:

$$C_T{}^2 \left[\frac{\partial^2 \bar{T}_0}{\partial \bar{r}^2} + \frac{1}{\bar{r}_0} \frac{\partial \bar{T}_0}{\partial \bar{r}}\right] = \ddot{\bar{T}}_0 + \varepsilon^* \left[\frac{\partial \ddot{\bar{u}}_0}{\partial \bar{r}} + \frac{\ddot{\bar{u}}_0}{\bar{r}_0}\right] \tag{67}$$

$$C_T{}^2 \left(-\psi_0 \bar{u}_0 + \sum_{i=1}^{N} \psi_i \bar{u}_i\right) + C_T{}^2 \frac{1}{\bar{r}_0} \left(-\gamma_0 \bar{T}_0 + \sum_{i=1}^{N} \gamma_i \bar{T}_i\right) = \ddot{\bar{T}}_0 + \varepsilon^* \left\{-\alpha_0 \ddot{\bar{u}}_0 + \sum_{i=1}^{N} \alpha_i \ddot{\bar{u}}_i\right\} + \frac{\varepsilon^*}{r_0} \ddot{\bar{u}}_0 \tag{68}$$

$$\left\{-\psi_0 C_T{}^2 - \gamma_0 C_T{}^2 \frac{1}{\bar{r}_0}\right\} \bar{T}_0 + \sum_{i=1}^{N} \left\{C_p{}^2 \psi_i + C_T{}^2 \frac{1}{\bar{r}_0} \gamma_i\right\} \bar{T}_i = \ddot{\bar{T}}_0 + \left\{-\varepsilon^* \alpha_0 + \frac{\varepsilon^*}{r_0}\right\} \ddot{\bar{u}}_0 + \sum_{i=1}^{N} \{\varepsilon^* \alpha_i\} \ddot{\bar{u}}_i \tag{69}$$

The following system of linear equations is obtained for the distributed nodes on the analyzed domain.

$$[M]_{(N+1)^*(N+1)} \left\{\ddot{\phi}\right\}_{(N+1)^*1} + [K]_{(N+1)^*(N+1)} \{\phi\}_{(N+1)^*1} = [f]_{(N+1)^*1} \tag{70}$$

where

$$\{\phi\}^T = \left\{\bar{u}_0 \quad \bar{T}_0 \quad \bar{u}_1 \quad \bar{T}_1 \quad . \quad . \quad . \quad \bar{u}_N \quad \bar{T}_N\right\}^T \tag{71}$$

and

$$\left\{\ddot{\phi}\right\}^T = \left\{\ddot{\bar{u}}_0 \quad \ddot{\bar{T}}_0 \quad \ddot{\bar{u}}_1 \quad \ddot{\bar{T}}_1 . \quad . \quad . \quad \ddot{\bar{u}}_N \quad \ddot{\bar{T}}_N\right\}^T \tag{72}$$

Similar to the previous section, different numerical methods can be employed to solve the obtained differential equations in time domain such as Newmark finite difference (NFD) or Laplace transformation.

Future Directions for Research

Although the MLPG and GFD methods are available to solve the governing equations of coupled thermoelasticity even for some cylinder, shells, and plates, they are not available in the general case of nonhomogeneous media and/or for geometrically nonlinear problems. Also the presented methods can be developed for other coupled thermoelasticity theories such as Lord-Shulman and Green-Lindsay and for calculation of thermoelastic damping in microscales and nanoscales of media.

Appendix

The components of matrices ψ_2^u and ψ_2^T and vectors ξ_2^u and ξ_2^T are given as

$$\psi_2^u = \begin{bmatrix} \sum_{i=1}^{N} h_i^2 w^2(h_i) & \sum_{i=1}^{N} \frac{h_i^3}{2} w^2(h_i) \\ \sum_{i=1}^{N} \frac{h_i^3}{2} w^2(h_i) & \sum_{i=1}^{N} \frac{h_i^4}{4} w^2(h_i) \end{bmatrix} \tag{73}$$

$$\xi_2^u = \begin{bmatrix} \sum_{i=1}^{N} (-\bar{u}_0 + -\bar{u}_i) h_i w^2(h_i) \\ \sum_{i=1}^{N} (-\bar{u}_0 + -\bar{u}_i) \frac{h_i^2}{2} w^2(h_i) \end{bmatrix} \tag{74}$$

$$\psi_2^T = \begin{bmatrix} \sum_{i=1}^{N} h_i^2 w^2(h_i) & \sum_{i=1}^{N} \frac{h_i^3}{2} w^2(h_i) \\ \sum_{i=1}^{N} \frac{h_i^3}{2} w^2(h_i) & \sum_{i=1}^{N} \frac{h_i^4}{4} w^2(h_i) \end{bmatrix} \tag{75}$$

$$\xi_2^T = \begin{bmatrix} \sum_{i=1}^{N} (-\bar{T}_0 + -\bar{T}_i) h_i w^2(h_i) \\ \sum_{i=1}^{N} (-\bar{T}_0 + -\bar{T}_i) \frac{h_i^2}{2} w^2(h_i) \end{bmatrix} \tag{76}$$

References

1. Green AE, Naghdi PM (1993) Thermoelasticity without energy dissipation. J Elasticity 31:189–208
2. Sladek V, Sladek J, Tanaka M, Zhang C (2005) Transient heat conduction in anisotropic and functionally graded media by local integral equations. Eng Anal Bound Elem 29:1047–1065
3. Benito JJ, Ureña F, Gavete L (2007) Solving parabolic and hyperbolic equations by the generalized finite difference method. J Comput Appl Math 209:208–233

Application of the Generalized Functions Method for Analysis of Thermal Stresses in Piecewise-Homogeneous Solids

Roman Kushnir and Vasyl Popovych
Pidstryhach Institute for Applied Problems of Mechanics and Mathematics, National Academy of Sciences of Ukraine, Lviv, Ukraine

Synonyms

Coupled problem of thermoelasticity: Solution in a series of functions form

Overview

We consider the piecewise-homogeneous bodies consisting of the separate parts with dissimilar physico-mechanical properties, which are constant within each part. The accurate analysis of thermal stresses in such structures presents a very important problem for engineering and requires effective approaches for its implementation. One of such approaches (Kolyano and Popovych, 1975) is based on the use of the generalized functions theory (the distribution technique) for describing of such structures in a comprehensive whole and utilizing thermoelasticity equations for nonhomogeneous bodies under ideal thermomechanical contact of the interfaces.

A different method within the framework of such approach has been suggested by Yu. M. Kolyano, O. M. Kulyk, and R. M. Kushnir in 1980. Its implementation involves the mathematical formulation of the generalized coupling problems for differential equations of thermoelasticity for homogeneous bodies (similar formulation has been provided for the Cauchy problem). For this purpose, the given and unknown functions, and the coefficients of the differential equations are extended by means of the characteristic functions on the entire domain occupied by the piecewise-homogeneous structure. Then the contact conditions on the interfaces are satisfied (in the cases of both ideal and nonideal contact). The partly degenerated differential equations of heat conduction and thermoelasticity with discontinuous coefficients arising in such problems for massive bodies and thin-walled plates and shells of piecewise-homogeneous structures are obtained. A procedure for finding their solutions is proposed.

Modeling of the Piecewise-Homogeneous Structures by Means of the Generalized Functions

A characterization of a piecewise-homogeneous body as a comprehensive whole can be performed by making use of a characteristic domain function defined for the domain occupied by the body.

In the case of one-dimensional nonhomogeneity, this function can be given through the asymmetric Heaviside function:

$$H_-(x_3) = \{(1,\ x_3 \geq 0) \cup (0,\ x_3 < 0)\} \quad (1)$$

Then, for instance, the thermostressed state of the multilayer body (Fig. 1) can be described by characteristic domain function in the form

$$p(\mathrm{x}) = p_1(\mathrm{x}) + \sum_{i=1}^{n-1} \left[p_{i+1}(\mathrm{x}) - p_i(\mathrm{x})\right] H_-(x_3 - d_i) \quad (2)$$

Here $p(\mathrm{x})$ and $p_i(\mathrm{x})$ denote the unknown (temperature, displacement-vector, and stress-tensor components) and given (thermal and mechanical characteristics, density of internal heat sources, etc.) functions in the regions, which are occupied by the multilayer body or its ith layer, respectively; n is the number of the layers; d_i, $i = \overline{1,n}$ are coordinates of interfaces; $\mathrm{x} = (x_1, x_2, x_3)$.

By making use of the representation (2), the solution of the thermoelasticity problems for the piecewise-homogeneous bodies can be reduced to the solution of the corresponding partly degenerated differential equations of heat conduction and thermoelasticity theories with discontinuous coefficients.

A Technique for Deriving of Thermoelasticity Equations by Means of the Corresponding Equations for Nonhomogeneous Bodies

A technique for determination and investigation of thermal stresses in piecewise-homogeneous bodies by making use of the distribution technique has been proposed by Kolyano and Popovych [1, 2]. This technique is based on application of the representation (2) and thermoelasticity equations for nonhomogeneous bodies for derivation of the corresponding partly degenerated differential equations of the heat conduction and thermoelasticity theories with discontinuous coefficients.

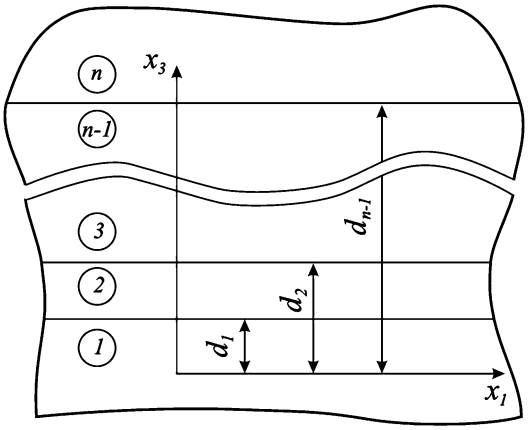

Application of the Generalized Functions Method for Analysis of Thermal Stresses in Piecewise-Homogeneous Solids, Fig. 1 Scheme of the multilayer body

Let us consider, for instance, how this technique can be applied for the above-considered multilayer body (Fig. 1). For determination of the nonstationary temperature field $T(\mathrm{x}, t)$ in this body, we employ the heat conduction equation

$$\Delta_2 T + k^{-1}(x_3)\partial_3[k(x_3)\partial_3 T] = \kappa^{-1}(x_3)\dot{T} - k^{-1}(x_3)w(\mathrm{x}, t) \quad (3)$$

for a body, which is nonhomogeneous with respect to the coordinate x_3. Here $k(x_3)$ and $\kappa(x_3)$ are the coefficients of thermal conductivity and thermal diffusivity, $w(\mathrm{x}, t)$ is the density of internal heat sources, $\Delta_2 = \partial_1^2 + \partial_2^2$ is the Laplacian with respect to x_1 and x_2, and $\partial_i = \frac{\partial}{\partial x_i}$.

For the case of the multilayer body, the functions $T(\mathrm{x}, t)$ and $w(\mathrm{x}, t)$, as well as the coefficients $k(x_3)$ and $\kappa(x_3)$, appear in the form (2). By putting them in an equation that is similar to (3) but with generalized derivatives, followed by differentiation with the following properties

$$\begin{aligned} &f(x_3)\delta_-(x_3 - d_i) = f(d_i - 0)\delta_-(x_3 - d_i) \\ &H_-(x_3 - d_i)\delta_-(x_3 - d_i) = 0 \\ &H_-(x_3 - d_i)\delta'_-(x_3 - d_i) = 0 \\ &H_-(x_3 - d_j)\delta_-(x_3 - d_i) \\ &= \{(0,\ d_i \leq d_j) \cup (\delta_-(x_3 - d_i),\ d_i > d_j)\} \end{aligned} \quad (4)$$

of the asymmetric Heaviside and impulse functions and their products [3] in view, we can obtain

the following partly degenerated differential equations of the heat conduction:

$$\Delta T = \kappa^{-1}(x_3)\dot{T} + \sum_{i=1}^{n-1}(1 - K_{i+1})\partial_3 T_{i+1}\Big|_{x_3=d_i}\delta_-(x_3 - d_i) - k^{-1}(x_3)w(\mathrm{x}, t) \tag{5}$$

Here $f(x_3)$ is an arbitrary piecewise-continuous function, $\Delta = \partial_1^2 + \partial_2^2 + \partial_3^2$ is the Laplacian, $K_{i+1} = k_{i+1}/k_i$, and $\delta_-(x_3)$ is the Dirac delta function, which can be determined, along with its derivative, as the generalized derivatives of the asymmetric Heaviside function:

$$\delta_-^l(x_3) = d_3^{l+1}H_-(x_3) \quad l = 0, 1$$

Due to the fact that the derivatives in the heat conduction equation (3) for a nonhomogeneous body are used in a classical meaning and meanwhile the ones in the equation (5) for the multilayer body are used in generalized meaning, the equivalence of the solutions of the mentioned equations can be achieved under matching condition for the classical and generalized derivatives. This requirement yields the equivalence conditions for the temperature and the interfacial heat fluxes in the multilayer body. Consequently, the partly degenerated differential equations of the heat conduction (5) must be equivalent to the system of equations

$$\Delta T_i = \kappa_i^{-1}T_i - k_i^{-1}w_i \quad i = \overline{1, n} \tag{6}$$

$$T_i = T_{i+1} \quad k_i\partial_3 T_i = k_{i+1}\partial_3 T_{i+1} \quad \text{at} \quad x_3 = d_i \tag{7}$$

which correspond to equation (3) for a homogeneous body within each of the parts of the multilayer body and to the conditions of the ideal thermal contact on the interfaces that has been shown in [3]. In accordance to the expression (2) and the first contact condition, the equality $\partial_3 T_{i+1}\big|_{x_3=d_i} = \partial_3 T\big|_{x_3=d_i}$ holds. This condition must be accounted in the right-hand part of equation (5).

For obtaining of the corresponding equations of the quasistatic thermoelasticity problem for the multilayer body, we depart from the thermoelastic equilibrium equations in terms of displacements for nonhomogeneous body. By putting the expressions for the Lamé coefficients, λ and μ, and the thermal expansion coefficient, α, written in the form (2), into the aforementioned equations and then providing the same mathematical treatment as in the case of derivation of the heat conduction equation, we arrive at the system of three partly degenerated differential equations of thermoelasticity:

$$\begin{aligned}
&\Delta u_1 + [1 + \omega_\lambda(x_3)]\partial_1 e = \omega_\beta(x_3)\partial_1 T \\
&- \sum_{i=1}^{n-1}\mu_i^{-1}(\mu_{i+1} - \mu_i)\left(\partial_1 u_3^{i+1} + \partial_3 u_1^{i+1}\right)\Big|_{x_3=d_i} \\
&\times \delta_-(x_3 - d_i) \\
&(u_1, x_1) \rightleftarrows (u_2, x_2) \\
&\Delta u_3 + [1 + \omega_\lambda(x_3)]\partial_3 e \\
&= \omega_\beta(x_3)\partial_3 T - \sum_{i=1}^{n-1}\mu_i^{-1}[(\lambda_{i+1} - \lambda_i)e \\
&+ 2(\mu_{i+1} - \mu_i)\partial_3 u_{3,i+1} - (\beta_{i+1} - \beta_i)T_{i+1}]_{x_3=d_i} \\
&\times \delta_-(x_3 - d_i)
\end{aligned} \tag{8}$$

with discontinuous coefficients for determination of the components of the displacement-vector components $\mathbf{u} = (u_1, u_2, u_3)$ for the considered multilayer body. Here

$$\omega_\gamma(x_3) = \gamma_1\mu_1^{-1} + \sum_{i=1}^{n-1}(\gamma_{i+1}\mu_{i+1}^{-1} - \gamma_i\mu_i^{-1})H_-(x_3 - d_i)$$
$$\gamma = \lambda, \beta \quad e = \partial_1 u_1 + \partial_2 u_2 + \partial_3 u_3$$
$$\beta = \alpha(3\lambda + 2\mu)$$

Note that for the case when the parts of the multilayer body are made of the metals or other materials with neighbor Poisson ratios ν, the coefficients of the differential operators in the above system are constant due to $\omega_\lambda(x_3) = \omega = (1 - 2\nu)^{-1}$.

Analogously to the case of the heat conduction equation, it is shown that the system of three equations (8) is equivalent to n systems of the Lamé equations consisting of the three equations for each part of the multilayer body

along with the conditions of ideal thermomechanical contact on the interfaces. In accordance to (2), the satisfaction of the later conditions yields the equalities $\partial_l u_{m,i+1}\big|_{x_3=d_i} = \partial_l u_m\big|_{x_3=d_i}$, $l,\ m = \overline{1,3},\ T_{i+1}\big|_{x_3=d_i} = T\big|_{x_3=d_i}$, which must be taken into consideration in the right-hand side parts of the equations (8).

The results of applications of this approach to study of thermal fields and stresses caused by them in massive and thin-walled bodies of piecewise-homogeneous structures are presented in [1–6].

Generalized Coupling Problems for Thermoelasticity Equations for Homogeneous Bodies

In the above-considered technique for derivation of the governing thermoelasticity equations for piecewise-homogeneous bodies, the equations for nonhomogeneous bodies were regarded as the input ones, and the ideal thermomechanical contact conditions were imposed on the interfaces. For simplification of the procedure for derivation of the partly degenerated differential equations of the heat conduction and thermoelasticity theories with discontinuous coefficients and application of the distribution technique for determination of the thermal and, consequently, the thermostressed states of the piecewise-homogeneous bodies under more general contact conditions, an alternative method has been proposed by Kolyano et al. [7]. The basic idea of this method is to obtain the governing equations using the procedure of mathematical statement of generalized coupling problem for the thermoelasticity equations of homogeneous bodies. The main stages of this method are the following:

- According to representation (2), extend the required and given functions to the entire region occupied by the piecewise-homogeneous structure.
- Take the connections between the generalized and classical derivates into account along with the conditions of nonideal contact at interfaces between its homogeneous components.

Let us consider an application of this method for derivation of the heat conduction equation for the above-mentioned multilayer body under nonideal thermal contact on the interfaces between the homogeneous layers.

As a result of implementation of this procedure for mathematical statement of generalized coupling problem, we can obtain the following partly degenerated heat conduction equation:

$$\Delta T = \kappa^{-1}(x_3)\dot{T} + \sum_{i=1}^{n-1}\left\{[\partial_3 T]_i\delta_-(x_3 - d_i) + [T]_i\delta'_-(x_3 - d_i)\right\} - k^{-1}(x_3)w(\mathrm{x}, t) \tag{9}$$

with discontinuous coefficients for the laminated body under consideration. Here $[p]_i = \left(p_{i+1} - p_i\right)\big|_{x_3=d_i}$.

If the nonideal contact with thermal resistance R_i (the simplest condition of the nonideal thermal contact) is assumed on the interfaces $x_3 = d_i$, then the jumps of the temperature function and its derivative, those occur in the right-hand side of heat conduction equation, can be determined as follows:

$$\begin{aligned}[T]_i &= R_i k_{i+1}\partial_3 T_{i+1}\big|_{x_3=d_i}\\ [\partial_3 T]_i &= (1 - K_{i+1})\partial_3 T_{i+1}\big|_{x_3=d_i}\end{aligned} \tag{10}$$

Note that $[T]_i = 0$ in the case of the ideal thermal contact. Then the heat conduction equation (9) coincides with equation (5).

In a similar manner, by means of the formulation of the generalized coupling problem for the system of thermoelasticity equations in terms of displacements for a homogeneous body, the corresponding partially degenerated thermoelasticity equations for piecewise-homogeneous bodies can be obtained. In [8–11], such equations are given for the quasistatic thermoelasticity problems in multilayer bodies under conditions of the nonideal thermal contact in more general in comparison to (10) form, for example, the conditions which account the heat generation due the friction between moving contacting layers or connection of the layers through the thin intermediate layer.

By means of this method, many quasistatic problems for piecewise-homogeneous massive bodies and thin-walled plates and shells and plates with coordinate-dependent heat exchange coefficients were solved and numerically verified [8–19].

To construct the solutions of partly degenerated thermoelasticity differential equations with discontinuous coefficients, a method-based construction of a fundamental system of solutions of the corresponding homogeneous ordinary differential equations of arbitrary order with discontinuous coefficients is developed [3, 20]. The need to solve these equations arises in the application of integral transforms to the key equations of thermoelasticity or for construction of the corresponding Green functions for quasistatic thermoelasticity problems in multilayer bodies [16, 19]. The procedure for reducing the above-mentioned partly degenerated differential equations for bodies with cracks and inhomogeneous inclusions to the boundary integral equations is proposed in [14, 17].

Thermostressed State of a Piecewise-Homogeneous Friction System

For example, we consider a friction system modeled by two different elastic half-spaces and sufficiently thick layer parallel to their boundary surfaces with physico-mechanical characteristics different from the characteristics of the half-spaces. This one-dimensional piecewise-homogeneous body is compressed at infinity from both directions parallel to the x_3-axis by forces P_0. From an initial moment of time, the intermediate layer begins to move with a low velocity v relative to the half-spaces. We determine the nonstationary temperature field that arises as a result of the contact interaction of the three-layer structure from the frictional forces. On the basis of the formulated one-dimensional generalized coupling problem, similarly to (9) with specified temperature jumps and derivative of the temperature, the following heat conduction equation [9] appears as

$$\begin{aligned}\partial_3^2 T = {} & k^{-1}(x_3)\dot{T} \\ & + \sum_{i=1}^{2}\Big\{(1-K_{i+1})\partial_3 T_{i+1}\big|_{x_3=d_i} \\ & - f_i P_0 \mathrm{v} k_i^{-1}\big]\delta_-(x_3-d_i) + \Big[2k_{i+1}h_i^{-1}\partial_3 T_{i+1}\big|_{x_3=d_i} \\ & + f_i P_0 \mathrm{v} h_i^{-1}\Big]\delta'_-(x_3-d_i)\Big\}\end{aligned} \tag{11}$$

and the initial and boundary conditions are

$$T(x_3,0)=0 \qquad \lim_{x_3\to\pm\infty} T(x_3,t)=0 \tag{12}$$

Here f_i and h_i are the coefficients of friction between $(i+1)$-th and ith components and the thermal conductivity of the contact surface $x_3 = d_i$, respectively. We construct a solution of the boundary-value problems (11) and (12) by applying the Laplace transform. To simplify the derivation of the governing equation, we set $\kappa(x_3) = \kappa$, that is, $\kappa_i = \kappa$, $i = \overline{1,3}$, and $d_1 = 0$. As a result, we obtain an expression for the transform of the temperature function:

$$\begin{aligned}\tilde{T}(x_3,s) = {} & C\exp(x_3\bar{s})[1-H_-(x_3)] \\ & + \big[C\Theta(x_3)+\Theta_1^0(x_3)\big]H_-(x_3) \\ & + \Big\{\big[Cd_3\Theta(x_3)+d_3\Theta_1^0(x_3)\big]_{x_3=d_2}\Theta_2^*(x_3) \\ & + \Theta_2^0(x_3)\Big\}H_-(x_3-d_2)\end{aligned} \tag{13}$$

Here

$$\tilde{T}(x_3,s)=\int_0^\infty T(x_3,t)\exp(-st)dt$$

$$\Theta(x_3)=\exp(x_3\bar{s})+\bar{s}\Theta_1^*(x_3)$$

$$\begin{aligned}\Theta_i^0(x_3) = {} & -F_i(s)\big[k_{i+1}^{-1}\sinh\bar{s}(x_3-d_i) \\ & + h_i^{-1}\bar{s}\cosh\bar{s}(x_3-d_i)\big]\end{aligned}$$

$$\begin{aligned}\Theta_i^*(x_3) = {} & \big[\big(K_{i+1}^{-1}-1\big)\bar{s}^{-1}\sinh\bar{s}(x_3-d_i) \\ & + 2k_{i+1}h_i^{-1}\cosh\bar{s}(x_3-d_i)\big]\end{aligned}$$

$$C = -\left[\overline{\Theta}_1^0 \exp(\bar{s}d_2) + \overline{\Theta}_2^* d_3 \Theta_1^0(x_3)\big|_{x_3=d_2} + \overline{\Theta}_2^0\right]$$

$$\times \left[\left(2 + \overline{\Theta}_1^* \bar{s}\right) \exp(\bar{s}d_2) + \overline{\Theta}_2^* d_3 \Theta(x_3)\big|_{x_3=d_2}\right]^{-1}$$

$$F_i(s) = f_i P_0 \mathrm{v}(s\bar{s})^{-1} \quad \overline{\Theta}_i^0 = -F_i(s)\left(k_{i+1}^{-1} + h_i^{-1}\bar{s}\right)$$

$$\overline{\Theta}_i^* = \bar{s}^{-1}\left(K_{i+1}^{-1} - 1\right) + 2k_i h_i^{-1} \quad \bar{s} = \sqrt{s/\kappa}$$

For determination of the thermoelastic state of the considered piecewise-homogeneous frictional structures on the basis of the one-dimensional quasistatic problem of thermoelasticity, the system of equations (8) can be simplified and takes the form

$$\partial_3^2 u_3 = \alpha(x_3)[1 + \nu(x_3)][1 - \nu(x_3)]^{-1}\partial_3 T + \sum_{i=1}^{n-1}\left\{[\partial_3 u_3]_i - \alpha_i(1+\nu_i)(1-\nu_i)^{-1}[T]_i\right\} \times \delta_-(x_3 - d_i) \tag{14}$$

Note that the conditions for equality of displacements $u_3(x_3, t)$ and normal stresses $\sigma_{33}(x_3, t)$ at the interfaces have been already taken into account in this equation.

By substituting the expression (13) into the Laplace transform of the equation (14) with $n = 3$ and integrating the result with the condition $\sigma_{33}|_{x_3 \to \pm\infty} = -P_0$ in view, the expression for the transform of the thermoelastic displacement $\tilde{u}_3(x_3, s)$ can be found in the form [10]

$$\tilde{u}_3(x_3, s) = C\beta_1 \bar{s}^{-1}\left\{\exp(x_3\bar{s})[1 - H_-(x_3)] + H_-(x_3)\right\} + \beta_2 H_-(x_3)\int_0^{x_3}[C\Theta(x_3) + \Theta_1^0(x_3)]dx_3 + (\beta_3 - \beta_2)H_-(x_3 - d_2)\int_{d_2}^{x_3}[C\Theta(x_3) + \Theta_1^0(x_3)]dx_3 + \beta_3 H_-(x_3 - d_2) \times \int_{d_2}^{x_3}\left\{\left[Cd_3\Theta(x_3) + d_3\Theta_1^0(x_3)\right]\big|_{x_3=d_2}\Theta_2^*(x_3) + \Theta_2^0(x_3)\right\}dx_3 + C_u x_3 \tag{15}$$

Here

$$C_u x_3 = C_u^{(1)} x_3 + \left[C_u^{(2)} - C_u^{(1)}\right]x_3 H_-(x_3) + \left[C_u^{(3)} - C_u^{(2)}\right](x_3 - d_2)H_-(x_3 - d_2)$$

$$C_u^{(i)} = -(\mu_i\eta_i s)^{-1}P_0 \quad \mu_i = E_i[2(1+\nu_i)]^{-1}$$

$$\eta_i = 2(1-\nu_i)(1-2\nu_i)^{-1}$$

$$\beta_i = \alpha_i(1+\nu_i)(1-\nu_i)^{-1}$$

E_i is Young's modulus of ith component.

Due to the cumbersomeness of the expressions (13) and (15), it makes sense to find the originals of the unknown functions by applying numerical inversion methods. In the considered case, for instance, the original functions $T(x_3, t)$ and $u_3(x_3, t)$ can be found by using the spectral method with Jacobi orthogonal polynomials [10].

To illustrate this method, we consider its numerical implementation for a three-layer (steel-aluminum-steel) frictional system with the following parameters: $f_1 = f_2 = 0.3$, $h_1 = h_2 = 0.5 \cdot 10^4$ W/(m$^2 \cdot$ °C), $P_0 = 0.5$ MPa, $d_1 = 0$, $d_2 = 0.2$ m.

In Fig. 2, the time dependences of the contact temperature T_{d_i} for various velocities of motion of interlayer with respect to the half-spaces are shown.

We can observe that the contact temperatures increase with the velocity of motion. It can be shown [10] that the contact displacements have a similar behavior. The temperature has jumps at the interfaces due to nonideal thermal contact, while the thermoelastic displacement is continuous. The comparison of the temperature distributions $T(x_3, t)$ versus coordinate x_3 in the considered structure to the temperature in a two-layer (steel-aluminum) space for the same values of t and v shows the redistribution and equalization of temperature across the structure due to the presence of the interlayer and the choice of the materials of both half-spaces to be identical. Since the contact temperature T_{d_1} significantly decreases, the temperature jump in the three-layer structure at the interfaces $x_3 = 0$ is smaller than in the case of the two-layer structure.

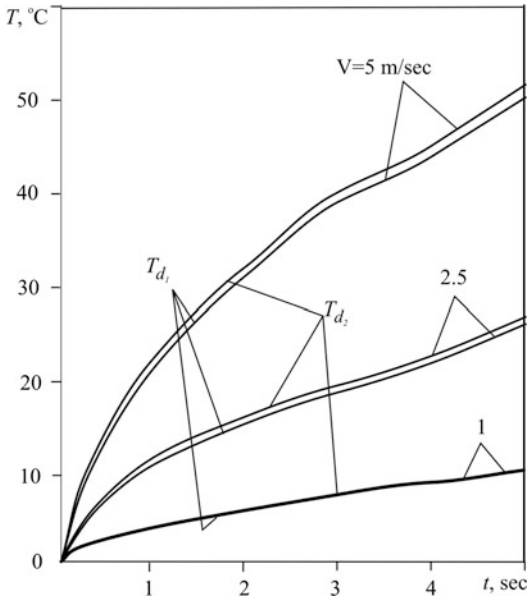

Application of the Generalized Functions Method for Analysis of Thermal Stresses in Piecewise-Homogeneous Solids, Fig. 2 The time dependences of the contact temperature

Cross-References

► Application of the Generalized Functions Method for Analysis of Thermal Stresses in Piecewise-Homogeneous Solids

References

1. Kolyano YM, Popovych VS (1975) Thermoelasticity of laminated solids. Dopov AN Ukr RSR Ser A 12:1112–1117 (in Ukrainian)
2. Kolyano YM, Popovych VS (1976) On an efficient method for solution of the thermoelasticity problems for piecewise-homogeneous bodies heated by a surrounding. Phizyko-khim mekhanika meterialov 2:108–112 (in Russian)
3. Podstrigach YS, Lomakin VA, Kolyano YM (1984) Thermoelasticity of solids of heterogeneous structure. Nauka, Moscow (in Russian)
4. Lavrenyuk VI (1979) On solving spatial quasi-static thermoelastic problem for piecewise-homogeneous solids. Izv AN SSSR Mechanics of Solids 3:63–69 (in Russian)
5. Kolyano YM (1992) Methods of heat conduction and thermoelasticity of heterogeneous solid. Naukova Dumka, Kyiv (in Russian)
6. Lavrenyuk VI, Tereshchenko VM (1998) The stressed state of piecewise-homogeneous bodies subject to nonsteady thermal fields. J Math Sci 88(3):368–373
7. Kolyano YM, Kulyk OM, Kushnir RM (1980) On formulation of a generalized coupling problem for thermoelasticity equations of piecewise-homogeneous solids. Dopov AN Ukr RSR Ser A 2:43–47 (in Ukrainian)
8. Kolyano YM, Kushnir RM, Muzychuk YA (1987) Thermal stresses in laminated solids with non-ideal thermomechanical contact at the interfaces. Sov Appl Mech 5:1036–1043
9. Kushnir RM (1999) Application of the method of generalized coupling problems in the thermoelasticity of piecewise-homogeneous bodies under non-ideal contact. J Math Sci 97(1):3854–3861
10. Kushnir RM, P'yanylo YD (2001) Study of the thermostressed state of a piecewise-homogeneous friction assembly. J Math Sci 104(5):1515–1520
11. Horechko NO, Kushnir RM (2005) Numerical analysis of the quasistatic thermal stresses state for semiinfinite contacting bodies. Matematychni Metody & Fizyko-Mekhanichni Polya 48(3):82–87 (in Ukrainian)
12. Kushnir RM (1996) Generalized conjugation problem in mechanics of piecewise-homogeneous elements of constructions. Z angew Math Mech (ZAMM) 76(5):283–284
13. Kushnir RM (1997) Thermoelasticity of piecewise-homogeneous structures: method of investigation utilizing the distribution technique. Proc Thermal Stresses 97:557–560
14. Vishnevskii KV, Kushnir RM (1997) Boundary integral equations for a body with inhomogeneous inclusions. J Math Sci 86(2):2552–2555
15. Kushnir RM, Popovych VS, Harmatii HY (2001) Analytic-numerical solution of contact problems of thermoelasticity for thermal sensitive bodies. Mater Sci 37(6):893–901
16. Kushnir RM, Protsyuk BV, Synyuta VM (2004) Quasistatic temperature stresses in a multiplayer thermally sensitive cylinder. Mater Sci 40(4):433–445
17. Kushnir RM, Osadchuk VA (2002) Temperature stresses in a piecewise-homogeneous cylindrical shell caused by the presence of a longitudinal crack. J Math Sci 109(1):1283–1289
18. Khapko BS, Chyzh AI (2011) Thermal bending of a strip and a rectangular plate with coordinate-dependent heat exchange coefficients. J Math Sci 174(3):375–386
19. Kushnir R, Protsiuk B (2009) A method of the Green's functions for quasistatic thermoelasticity problems in layered thermosensitive bodies under complex heat exchange. Operator theory: advances and applications 191:143–154
20. Kushnir RM (1980) On the construction of solutions of ordinary linear differential equations with piecewise-constant coefficients. Dopov AN Ukr RSR Ser A 9:54–57 (in Ukrainian)

Approximate Boundary Conditions

▶ Generalized Boundary Conditions to Solving Thermal Stress Problems for Bodies with Thin Coatings

Arbitrarily Shaped Hole

▶ Thermal Stress for Mixed Heat Conduction Boundary Around an Arbitrarily Shaped Hole Under Uniform Heat Flux

Area Array Package/Assembly Under Thermal Stress

Reza Ghaffarian
Jet Propulsion Laboratory, California Institute of Technology, Pasadena, CA, USA

Overview

Understanding reliability of microelectronics under thermal cycling stresses is an integral part of implementation of advanced area array packaging technologies, especially those considered for high reliability applications. In the past, there was always a ceramic version of a plastic package for high reliability use, including the plastic-ball-grid-array (PBGA) which has the analogous ceramic-ball-grid-array (and column-grid-array) (CBGA & CGA). Today, there are fewer ceramic versions with time-delay of the latest technologies. In fact, under thermal stresses, even though ceramic packages are individually more reliable compared to their plastic BGA versions, they may not always be the most reliable choice when assembled onto polymeric board due to generation of much larger coefficient of thermal mismatch.

This entry discusses important parameter affecting surface mount packaging and assembly solder joint degradation due to thermal cycling fatigue stresses. The key parameters include coefficient of thermal mismatches due to global, local, and solder alloy. Specifically literature data gathered for ceramic-ball-grid-array (CBGA) and ceramic-column-grid-array (CCGA or CGA) were classified into different sets to delineate packaging and assembly parameters influencing cycles to failure. It briefly discusses various modeling approaches for predicting solder joint reliability of microelectronics packaging and assemblies.

Package/Assembly Under Thermal Stresses

High Reliability Applications

Contrary to early development of microelectronic technologies that aimed mostly at meeting high reliability applications, however, in the past decades, consumer electronics is driving the trends for electronic packaging and assembly. With that being the primary driver, materials and processes are transitioned to Pb-free solder alloy due to restriction of hazardous substances (ROHS) implementation. While there is a drive to develop new low-k dielectrics and advanced organic substrate materials, the higher melting temperature of these solder alloys is pushing the limits of the reliability of these material sets. High reliability industry now uses both specialty electronics as well either adapted consumer electronics or their tailored versions for higher reliability applications.

In the past, for high reliability applications, there was always a ceramic version of a plastic package, including the plastic-ball-grid-array (PBGA) which has the analogous ceramic-ball-grid-array (and column-grid-array) (CBGA & CGA). Today, there are fewer ceramic versions with time-delay of the latest technologies for harsher environmental applications. In fact under thermal stresses, even though ceramic packages are individually more reliable compared to their plastic BGA versions, they may not always be the most reliable choice when assembled onto polymeric board due to generation of much larger coefficient of thermal

mismatch. Solder joint reliability under thermal stress, especially thermal cycling, has become an integral part of the microelectronic packaging equation for overall system reliability, especially those for high reliability applications discussed in this entry [1–10].

Reliability for Package/Assembly

Reliability under thermal stress for package and assembly depends on the reliability of constituent elements and global/local interfaces (attachments) [11]. Solders in surface mount are unique since they provide both electrical interconnection and mechanical load-bearing element for attachment of package on PCB and often also function as a critical heat conduit too. A solder joint in isolation is neither reliable nor unreliable; reliability has meaning only in the context of interconnections either within package or outside of package on PCB. Solder joints are a key interface element for BGA/CBGA/CGA package and assembly on PCB. As schematically shown in Fig. 1, three elements play key roles in defining reliability for CGA, global, local, and solder alloy. In CGA, solder columns also act as load carrying element between package and boards similar to metallic leads such as those for CQFP. The characteristics of these three elements – package (e.g., die, substrate, solder joint, underfill), PCB (e.g., polymer, Cu, plated through hole, microvia), solder joints (e.g., via balls, columns) – together with the use conditions, the design life, and acceptance failure probability for the electronic assembly determine the reliability of BGA/CBGA/CGA assemblies.

In other words, reliability is the ability of a system (here microelectronics) to function as expected under the expected operating conditions for an expected time period without exceeding the expected failure levels. However, reliability is threatened by infant mortality due to workmanship defect and lack of sound manufacturing, and reliability design. Designs for manufacturability, design for assembly, design for testability, and so on are prerequisite to assure the reliability of the product. Only design for reliability can assure that manufactured-to-quality product will be reliable. The elements of the system

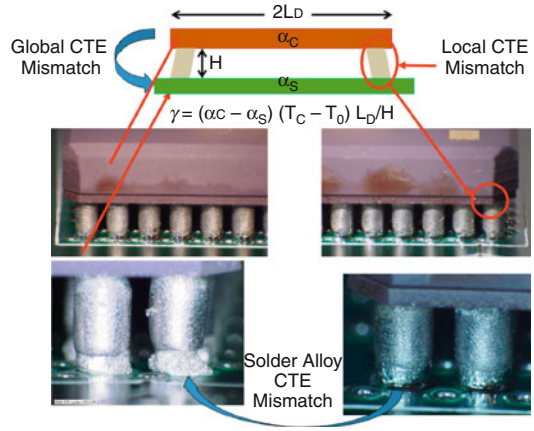

Area Array Package/Assembly Under Thermal Stress, Fig. 1 Reliability under thermal stresses are defined by: global, local, and solder alloy coefficient of thermal expansion (CTE) mismatches

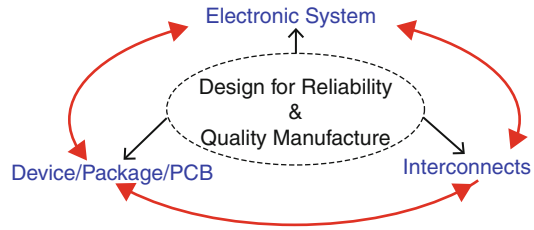

Area Array Package/Assembly Under Thermal Stress, Fig. 2 System reliability achieved through design for reliability (DfR), sound manufacturing, and quality to packaging/device/PCB and interconnections

reliability are schematically shown in Fig. 2 which are comprised of device/package/PCB and interconnections and also include consideration of design for reliability prior to assembly and subsequent manufacturing and quality assurance implementation.

Package Reliability

Typical packaging build steps are schematically shown in Fig. 3. After wafer processing and testing, the wafer is generally sawed into die, which are then packaged or used as chip-on-board flip chip direct attachment. In wafer level packaging (WLP), protection and testing are first performed on the wafer and then dicing in preparation for surface mount assembly (SMA). There is a great contrast between processing at the chip and

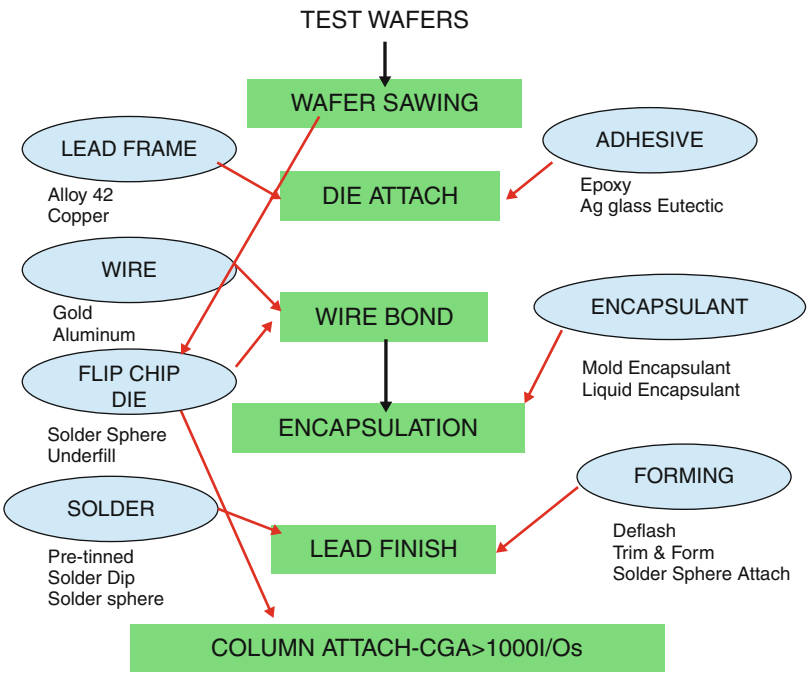

Area Array Package/Assembly Under Thermal Stress, Fig. 3 Microelectronic packaging steps

package levels, including the defects created and the reliability implications involved. Materials and process steps involved may need to be modified in order to achieve reliable package for application in a harsher environment including extremely cold or extremely hot environments.

Packaging materials and structures are chosen to meet the demands of device used in conventional environments. Thus, metals are selected according to how well they conduct current into and out of chips, and encapsulants on their ability to encase and protect the die over commercial temperature ranges. In addition to their electrical conduction function, metals are used in packaging as mechanical supports, to conduct heat away (heat sinks), and to seal the contents. Ceramics like alumina also serve as containers for chips and often the substrates for mounting semiconductor devices. Polymers are used to hermetically encase the chips and are employed in printed circuit boards for mounting the packages.

Silicon of chip in package degrades under thermal stresses. Most Si device degradation mechanisms are thermally activated and the device reliability is a strong function of temperature and operating voltage. The higher the temperature, the greater are degradation mechanisms such as inter-diffusion through interconnection, latch-up, noise, and heat. For thermally activated failure mechanisms, the relative improvement in mean-time-to-failure (MTTF) is proportional to a temperature-dependent term expressed by the Arrhenius relation:

$$\text{MTTF} \sim \exp(E_a/KT) \tag{1}$$

where E_a is the activation energy of a given thermal process, T is absolute temperature, and K is Boltzmann's constant. E_a will typically range between 0.3 and 1.2 eV. A lower value of E_a implies that the temperature effect is less significant for a failure mechanism than the one with higher E_a.

SMT Assembly Reliability

Majority of fatigue failures of solder joints in surface mount assemblies are due to global CTE mismatch induced damage while early premature failure may be due to workmanship anomalies and local interfacial integrity deficiencies [11]. The global expansion mismatches result from differential thermal expansions of a package and the PCB

assembly. These thermal expansion differences stem from differences in the coefficients of thermal expansion (CTEs) and thermal gradients as the result of heat dissipation from functional die within package. Global CTE mismatches typically range from $\Delta\alpha \sim 2$ ppm/°C (2×10^{-6}) for CTE-tailored high-reliability assemblies to $\Delta\alpha \sim 14$ ppm/°C for ceramic packages (e.g., CBGA/CGA) on FR-4 PCBs. The shear strain representative of the global CTE mismatch due to thermal excursion is given as follows:

$$\gamma = (\alpha_C - \alpha_S)(T_c - T_0)L/H = (\Delta\alpha)(\Delta T)L_D/H \quad (2)$$

Global CTE mismatches typically are the largest, since all three parameters determining the thermal expansion mismatch, i.e., the CTE mismatch ($\Delta\alpha$), the temperature swing (ΔT), and the largest acting package length (L_D), a.k.a., distance to neutral point (DNP), can be large. In thermal cycling, this global expansion thermal mismatch will induce cyclic stresses, and thus fatigue the solder joints. The cumulative fatigue damage will ultimately cause the failure of one of the solder joints, typically a corner joint in CBGA/CGA, causing permanent functional electrical failure that initially may be intermittent. The shear strain representing damage in each cycle is proportional to $\Delta\alpha$, ΔT, and L_D, and inversely proportional to the package /PCB separation height (H). For this reason, CGAs are selected for higher package sizes and I/Os since thermal strain is lower for higher column height (H) than their CBGA counterparts; therefore, it is expected to show better thermal cycling fatigue life.

The local expansion mismatch results from differential thermal expansions of the solder and the base material of the package or PCB assembly. These thermal expansion differences result from differences in the CTE of the solder and those of the base materials together with thermal excursions. Local CTE mismatches typically range from $\Delta\alpha \sim 7$ ppm/°C with copper to ~18 ppm/°C with ceramic. Local thermal expansion mismatches typically are smaller than the global expansion mismatches, since the acting distance, the maximum wetted area dimension, is much smaller in the order of tens of mils, e.g., 20 mils for a typical column diameter.

Solder alloy CTE mismatch covers microstructural changes as solder alloy is a mixture of two or more elements. The grain structure of tin-lead solder is inherently unstable. The grains will grow in size over time as the grain structure reduces the internal energy of a fine-grained structure. This grain growth process is increased by exposures at elevated temperatures as well as strain energy input during cyclic loading. The grain growth process is thus an indication of the accumulating fatigue damage. Figure 4 illustrated grain growth near cracks for a CGA assembly after 200 thermal cycles in the range of −55°C to 100°C. For tin-lead solder, an internal CTE mismatch of ~6 ppm/°C results from the different CTEs of the Sn-rich and Pb-rich phases of solder. Internal thermal expansion mismatches typically are the smallest, since the acting distance, the size of the grain structure, is much smaller than either the wetted length or the component dimension, in the order of mils.

Fatigue Models for SMT Reliability Prediction

Predicting solder joint fatigue failure under thermal cycling stress has been one of the challenging problems for microelectronic packaging and assembly [12]. Early solder joint fatigue models were developed based on experimental thermal cycling tests using strain gauge; therefore, most models are correlated to strains. As size of package decreased, finite element analyses (FEA) become a more popular approach for estimating strains in PBGA/CBGA/CGA assemblies. The Coffin-Manson relationship perhaps the best known and most widely used was developed for aerospace metals and was considered for tin-lead solder. The model relates the total number of cycles to failure (CTF) to the plastic strain amplitude and the fatigue ductility coefficient and exponential.

In a previous investigation, the modified Coffin-Manson relationship (a.k.a., Norris and Landzberg) was applied to correlate thermal cycle failure test data of CBGA assemblies from different thermal cycle regimes and ramp rates [5].

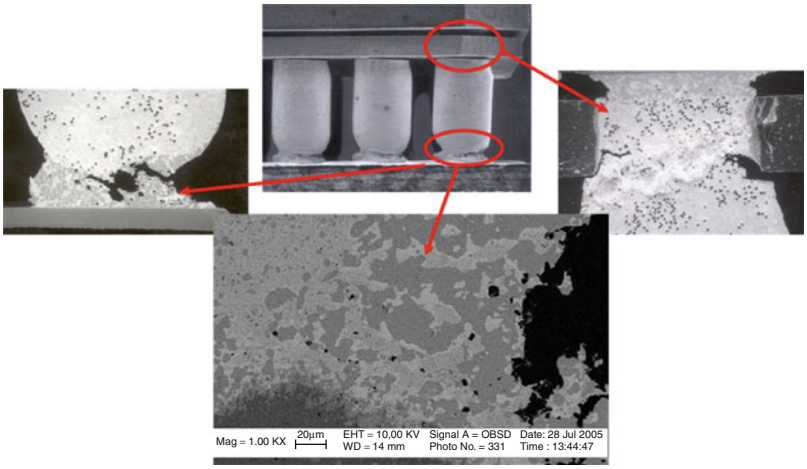

Area Array Package/Assembly Under Thermal Stress, Fig. 4 Tin-lead solder alloy phases and grain growth in CGA after thermal cycling

This relationship is one of many numerous parametric modeling analysis methods that have been proposed and used by industry for projection CTF from one thermal cycle condition to a field application. Table 1 lists a number of these models for reliability extrapolation of tin-lead solder joint attachments [10].

In the Coffin-Manson relationship, CTF is inversely proportional to the creep strain. Its modified version includes the effects of frequency as well as the maximum temperature and is given by:

$$(N_1/N_2) \propto (\Delta\gamma_2/\Delta\gamma_1)^{\beta}(f_1/f_2)^{\kappa} \exp\{(1414(1/T_1 - 1/T_2)\} \quad (3)$$

- N_1 and N_2 represent cycles to failure under two plastic strain conditions. β is the fatigue exponential and is generally assumed to be equal to 1.9 [13].
- $\Delta\gamma$ is proportional to (DNP/h) $\Delta\alpha$ ΔT, where DNP is the distance from the neutral point at the center of the package, h is equal to the solder joint height, $\Delta\alpha$ is the difference in the coefficient of thermal expansion of the package and PCB, and ΔT is the cycling temperature range.
- f_1 and f_2 are fatigue frequencies. κ is the frequency exponential varying from 0 to 1, with value 0 for no frequency effect and 1 for the maximum effect depending on the materials and testing conditions. A value equal to 1/3 is commonly used to extrapolate the laboratory accelerated thermal cycles-to-failure data with short duration (high frequency) to on/off field operating cycles with long duration (low frequency), i.e., a shorter field cycles-to-failure projection.
- T_1 and T_2 are maximum temperatures (in degrees Kelvin) under the two cycling conditions.

Key Parameters Affecting CBGA/CGA Assembly Under Thermal Cycles

Data on thermal cycles were gathered to illustrate the effects of package and assembly parameters (e.g., $\Delta\alpha$, ΔT, L_D, H) for CBGAs and CGAs. Table 2 lists cycles to failure for a number of CGA and CBGA package assembly having different configurations, selected from the limited data set reported in the literature [14–19]. Data were chosen to illustrate the effects of only a few key parameters on the reliability. The parameters listed in the following were considered for tabulating test data, even though in some cases specific information was not reported and missing.

- *Thermal cycle range, ramp rate, dwell times*
  - For example, the CT50%F (cycles-to-fifty percent-failure) for the CBGA 361 over the range of 0°/100°C was 4,535 cycles (Case #2); it diminished to 1,190 cycles when the temperature range was broadened to –55°/110 °C (Case #6)

Area Array Package/Assembly Under Thermal Stress, Table 1 Summary of various reliability models developed for plastic- and ceramic-grid-array packages

Model	Reliability/life-prediction representation	
Coffin-Manson	$N_f = 2.277 \times 10^{-3}(\text{Max}\varepsilon_{\text{eqv}})^{-2.61}$	J. H. Lau
	$N_f = 1.2938(\Delta\varepsilon_{\text{eqv}})^{-1.96}$	B. Z. Hong
	$N_f = 0.4405(\Delta\varepsilon_{\text{eqv}})^{-1.96}$	K. N. Chiang, et al.
	$N_f = K(\varepsilon_p{}^{-2})$	M. Farooq, et al.
	$N_f = 0.5(\Delta\gamma/2\varepsilon'_f)^{1/C}$	Howieson, M., et al
	$N_f = 82.4(De_{\text{in}})^{-0.863}$	Perkins, A., et al
Engelmaier	$N_f(x\%) = \frac{1}{2}\left[\frac{2\varepsilon'_f}{F}\frac{h}{L_D\Delta\alpha\Delta T_c}\right]^{-1/c}\cdot\left[\frac{\text{In}(1-0.01x)}{\text{In}(0.5)}\right]^{1/\beta}$	
Norris-Landzberg	$AF = \frac{N_p}{N_t} = \left(\frac{\Delta T_t}{\Delta T_p}\right)^{1.9}\left(\frac{f_p}{f_t}\right)^{1/3} e^{1414\left(\frac{1}{T_{\text{max},\,p}}-\frac{1}{T_{\text{max},\,t}}\right)}$	S. Y. Teng
	$N_{50\,\%} = \left(\frac{100}{\Delta T}\right)^{1.9}\left(\frac{f}{2}\right)e^{1414\left(\frac{1}{T_{\text{Max}}}-\frac{1}{373}\right)}(G)$ $G = (12439-70.1\text{A}-434\text{B}-1301\text{C}-930\text{D}-272\text{E}+302\text{CD})$; A : substrate size, B : board and substrate CTE mismatch C : substrate thickness, D : board thickness, E : ball pitch	A. Perkins, et al
Darveaux	$N_{\text{init}} = C_1(\Delta W_{\text{ave}})^{C_2}, da/dN = C_3(\Delta W_{\text{ave}})^{C_4}$ $C_1 = 13173$, $C_2 = -1.38$ to -1.45, $C_3 = 1.72$ to 3.92, $C_4 = 1.12$ to 1.15	
SRS	$N_{63.2\,\%}\ /\ A = C_1(\Delta W_{in})^{C_2}\ C_2 = -1$	J. Clech
	$N_f = (\Delta W)^{1.51}\left(\frac{A_L}{A_D}\right)A_D = 5.9 \times 10^{-3}\ \text{mm}^2$	Wong, T. E., et al

- *Package size, thickness, materials, configuration, and I/Os*
  - Comparing Case#2 to Case#3, a relatively large reduction in CT50%F is shown when the package thickness was increased from 0.8 to 1.2 mm (4,535 vs. 2,700 cycles). When the package thickness was further increased to 2.9 mm, the CT50%F was further reduced, a reduction by 3.2 times relative to the package with 0.8 mm thickness. A similar reduction was observed for the CGA 1657 I/Os when the package thickness was increased from 1.5 to 3.7 mm (Case #13). The reliability decreases by increasing the package I/O since the distance to the neutral point has increased. The CT50%F was reduced from 4,535 cycles to 2,462 cycles when the I/Os for the 0.8 mm thick package increased from 361 to 625 (Case #2 vs. Case #5). The use of higher CTE (HiCTE) ceramic materials – to better match the ceramic CTE to the PCB – also improved the reliability. For example, compare Case #6 to the Case #7 for the 361 I/O CBGA assemblies. The CT50%F increased from 1,190 to 2,160 cycles for the HiCTE package.
- *Die size and its relation to the package size and ball configuration*
  - The reliability effects of die size and package configuration (full vs. peripheral) arrays were more pronounced for plastic than for ceramic package assemblies.
- *PCB thickness, pad definition, surface finish*
  - The preferred thickness was defined as 2.3 mm in IPC-9701 [20] since plastic packages assembled on thinner PCBs generally show higher cycles to failure. The effect of board thickness for ceramic packages was not well established, but its effect may be less critical for column-grid-array assemblies than for plastic package assemblies, especially when the dominant failure is the columns rather than solder joints.

Area Array Package/Assembly Under Thermal Stress, Table 2 Cycles-to-failure data illustrating the effect of a number of key variables

#	Package I/O-pitch	Pkg size (die size, mm)	Thermal cycle condition (ramp, dwell, cycle/h)	First failure	Mean life (63.2 %)	Comments
1	CBGA-255-1.27	21 × 21 (1 mm substrate)	0–100 °C (10, 5, 2 cycles/h)	1,980 (1 % failure)	2,426 ($N_{50\ \%}$)	PCB, 0.55 mm thickness Ref. Burrnette [16]
2	CBGA-361-1.27	25 × 25 (substrate 0.8 mm thickness)	0–100 °C (3 cycles/h)	NA	4,535 ($N_{50\ \%}$)	Average solder paste vol 5,900 mil^3 PCB, 1.57 mm thickness Die 15 × 10 mm
3	CBGA-361-1.27	25 × 25 (substrate 1.2 mm thickness)	0–100 °C (3 cycles/h)	NA	2,700 ($N_{50\ \%}$)	Note: Increase from die thickness 0.8 to 1.2 and 2.9, reliability reduction by 1.8 and 3.2 times Ref [16]
4	CBGA-625-1.27	32.5 × 32.5 (substrate 0.8 mm thickness)	0–100 °C (3 cycles/h)	NA	2,462 ($N_{50\ \%}$)	PCB, 1.57 mm thickness Ref [17]
5	CBGA-361-1.27	25 × 25 (substrate 0.8 mm thickness)	–55 °C to 110 °C (2 cycles/h)	890 (100 ppm)	1,190 ($N_{50\ \%}$)	PCB, 1.57 mm thickness Ref [14]
6	CBGA-361-1.27-HiCTE Substrate	25 × 25 (substrate 0.8 mm thickness)	–55 °C to 110 °C (2 cycles/h)	1,310 (100 ppm)	2,160 ($N_{50\ \%}$)	Substrate CTE, 12.2 ppm Ref [14]
7	CGA-361-1.27-Interposer	25 × 25 (substrate 0.8 mm thickness)	–55 °C to 110 °C (2 cycles/h)	1,350 (100 ppm)	2,320 ($N_{50\ \%}$))	NTK interposer CGA PCB, 1.57 Ref [14]
8	CGA-361-1.27-IBM	25 × 25 (substrate 0.8 mm thickness)	–55 °C to 110 °C (2 cycles/h)	1,080 (100 ppm)	1,520 ($N_{50\ \%}$)	Ref [14]
9	CBGA-1681-1.27-HiTCE	42.5 × 42.5 × 1.85 (substrate)	–25 °C to 125 °C (1, 9 min, 3 cycles/h)	613 (1st failure)	1,142 ($N_{50\ \%}$)	PCB, 93 mm thickness Ref [18]
10	CBGA-625-1.0	32 × 32 × 2.4 mm (substrate)	0–100 °C (2 cycles/h)	NA	740 ($N_{50\ \%}$)	Ref [15] IBM-2003
11	CBGA937-1.0	32 × 32 × 1.5 (substrate) 32 × 32 × 2.4	0–100 °C (2 cycles/h)	NA	1,860 ($N_{50\ \%}$) 1,310 ($N_{50\ \%}$)	Reference M. Ref [15]
12	CGA1657-1.0	42 × 42 × 1.5 42 × 42 × 2.55 42 × 42 × 3.7	0–100 °C (2 cycles/h)	NA	1,530 ($N_{50\ \%}$) 990 620	Ref [15]
13	CGA 1657-1.0 Cu	42.5 × 42.5 × 2.55	0–100 °C (2 cycles/h)	1,660 (1st failure)	2,410 ($N_{50\ \%}$)	Cu Column, solder paste 96.5 Sn3.5Ag Ref [19]

- *Single side or double side, relative offset of package on top and bottom*
  - Double-sided, mirror-image PBGA assemblies have significantly lower CTF compared to their single-sided version. Ghaffarian in his 1999 article published in *Chip Scale Review Magazine* reported that the mean time to failure for mirror-imaged CSP assemblies in thermal cycling is 40–60 % less than that observed for single-sided CSP assemblies. The effect of mirror-image assemblies on reliability for CGAs is not presently known.

Effect of Solder Volume on CBGA/CGA Assembly Reliability

In contrast to PBGA assemblies, the reliability of CGAs/CBGAs assemblies is significantly affected by the amount of solder volume since contrary to PBGAs, solder columns/balls do not melt during reflow and remain intact. In fact, solder volume is the most important key process variable affecting the reliability of CGAs/CBGAs [13, 21]. As one might expect, higher solder volume for CBGAs increases the solder balls' standoff height, which affects reliability, but this is not the case for the CGA assemblies where the effect is more complex because column flexibility also plays a role in reliability.

For CGA, as the volume increases, so does the fillet height on the column. This increased fillet height reduces the effective length of the flexible column, thus making it stiffer. This effect – while true for both cast and wire – is more pronounced for the cast because it is stiffer in nature due to its larger diameter. In a comprehensive investigation performed for this category of packages, it has been shown [19] that assemblies with a minimum acceptable solder paste showed slightly higher reliability than those with nominal and much better than those with higher solder volume. To avoid inducing opens however, the use of nominal rather than minimum solder paste volume is recommended.

References

1. Ghaffarian R (2011) Thermal cycle and vibration/drop reliability of area array package assemblies. In: Suhir E, Connally E, Steinberg D (ed) Structural dynamics of electronics and photonic systems. John Wiley & Sons, Hoboken New Jersey
2. Ghaffarian R (2008) Thermal cycle reliability and failure mechanisms of CCGA and PBGA assemblies with and without corner staking. IEEE Trans Comp Packag Technol 31(2):285–296
3. Ghaffarian R (2006) Area array technology for high reliability applications. In: Suhir E (ed) Micro-and opto-electronic materials and structures: physics, mechanics, design, reliability, packaging. Springer, New York, Chapter 16
4. Ghaffarian R (2006) CCGA packages for space applications. Microelectron Reliab 46:2006–2024
5. Ghaffarian R (2004) BGA assembly reliability. In: Gilleo K (ed) Area array packaging handbook. McGraw-Hill, New York, Chapter 20
6. Fjelstad J, Ghaffarian R, Kim YG (2002) Chip scale packaging for modern electronics. Electrochemical Publications, Isle of Man
7. Ghaffarian R (2001) Chip scale package assembly reliability. In: Puttlitz K, Totta PA (eds) Area array interconnection handbook. Kluwer/Academic, Boston, Chapter 23
8. Tasooji A, Ghaffarian R, Rinaldi A (2006) Design parameters influencing reliability of CCGA assembly and sensitivity analysis. In: Proc Itherm, 30 May–2 June 2006, San Diego, CA
9. Ghaffarian R (2012) Assembly and reliability of 1704 I/O FCBGA and FPBGAs. In: Proceeding IPC APEX conference, San Diego, Feb–Mar 2012
10. Ghaffarian R (2005) Characterization and failure analyses of lead-free solder defects. In: Shangguan D (ed) Lead-free solder interconnect reliability book. ASM International Materials Park, OH, chapter 10
11. Engelmaier W (1990) Solder joint reliability, accelerated testing and result evaluation. In: Lau J (ed) Solder joint reliability: theory and applications. Van Nostrand Reinhold, New York
12. Lee W, Nguyen L, Selvaduray G (2000) Solder joints fatigue models: review and applicability to chip scale packages. Microelectron Reliab 40(2):231–244
13. Column Grid Array and Rework, IBM User's Guideline (July 22, 2002)
14. Master RN, Ong OT (2000) Ceramic grid array technologies for ACPI applications. In: The Proceedings of Surface Mount International, 25–28 Sept 2000, Chicago, IL
15. Farooq M, Goldmann L, Martin G, Goldsmith C, Bergeron C (2003) Thermo-mechanical fatigue reliability of Pb-free ceramic ball grid arrays: experimental data and lifetime prediction mounting. In: The Proceeding of IEEE Electronic Components and Technology, Orlando, pp 827–833
16. Burnette Z et al (2000) Underfilled BGAs for ceramic BGA packages and board-level reliability. In: The Proceeding of IEEE Electronic Components and Technology, Las Vegas, NV, pp 1221–1226
17. Master RN, Dobear TP, Cole Marie S, Martin GB (1998) Ceramic ball grid array for AMD K6 microprocessors applications. In: Proceedings of electronic components and technology conference, Seattle, WA
18. Teng SY, Brillhart M (2002) Reliability assessment of a high CTE CBGA for high availability systems. In: Proceedings of electronic components and technology conference, San Diego
19. Interrante M et al (2003) Lead-free package interconnection for ceramic grid arrays. IEEE/CPMT/SEMI international's electronics manufacturing technology symposium, San Jose
20. IPC-9701A (2006) Performance test methods and qualification requirements for surface mount solder attachments. IPC, Association Connecting Electronics Industries, Bannockburn
21. CBGA Assembly and Rework, IBM User's Guideline (May 23, 2002)

Artificial Muscle Materials

▶ Fracture of Electrostrictive Materials

Assumed Linear Temperature Profile

▶ Classical Governing Equations for the Thermomechanical Analysis of Shells
▶ Refined and Advanced Governing Equations for the Thermomechanical Analysis of Shells
▶ Thermal Stress Analysis of Functionally Graded Material Plates
▶ Thermomechanical Bending in Functionally Graded Material Shells

Assumed Temperature Profile

▶ Temperature Profiles in Composite and Sandwich Shells
▶ Temperature Profiles in One-Layered and Multilayered Isotropic Shells

Asymptotic Analysis of Heterogeneous Micromorphic Elastic Solids

Samuel Forest
Mines ParisTech/CNRS, Centre des Matériaux/ CNRS UMR 7633, Evry Cedex, France

Overview

Heterogeneous materials like metal polycrystals and metal matrix composites exhibit a size-dependent mechanical elastoplastic and fracture behavior. Generalized continuum theories can be used for the constitutive behavior of each constituent in order to predict such size effects. Extended homogenization methods are then needed to compute the effective properties of composite higher-order materials. Higher-order continua include the Cosserat medium for which the material point is endowed with independent translational and rotation degrees of freedom and the micromorphic continuum which accounts for the full microdeformation of a triad of directors attached to the material point. An asymptotic multiscale expansion method is used here to derive the effective properties of heterogeneous linear elastic micromorphic media. The type of continuum theory representing the effective medium is shown to be either a Cauchy, Cosserat, microstrain, or full micromorphic model, depending on the ratio between the characteristic lengths of the micromorphic constituents and the size of the heterogeneities. Applications deal with fiber size effects in metal matrix composites and with the grain-size effect in polycrystals.

Introduction

The mechanics of generalized continua represents extensions of the classical Cauchy continuum mechanics that incorporate some aspects of the microstructure underlying the material point. Directors can be attached to each material point that evolve in a different way than the material lines. They account for privileged physical directions existing in the microstructure like lattice or fiber directions. In addition to the usual motion of the material point, the associated directors can rotate or even deform with straining. The microrotation case corresponds to the Cosserat continuum, whereas microdeformation is possible in the micromorphic continuum [6]. The Cosserat and micromorphic media are examples of higher-order continuum theories that are characterized by additional degrees of freedom of the material points. In the micromorphic continuum designed by Eringen and Mindlin [7, 13], the directors can also be distorted, so that a second-order tensor is attributed to each material point. Such higher-order media are sometimes called continua with *microstructure*. This name has now become misleading in the sense that even Cauchy material models can integrate some

aspects of the underlying microstructure as illustrated by classical homogenization methods used to derive the effective properties of composites. However, generalized continua incorporate a feature of the microstructure which is not accounted for by standard homogenization methods, namely, their size-dependent material response. They involve intrinsic lengths directly stemming from the microstructure of the material.

The links between the micromorphic continuum and the behavior of crystalline solids have been recognized very early by Eringen himself [4]. Lattice directions in a single crystal can be regarded as directors that rotate and deform. The fact that lattice directions can be rotated and stretched in a different way than material lines connecting individual atoms, especially in the presence of static or moving dislocations, illustrates the independence between directors and material lines in a micromorphic continuum, even though their deformations can be related at the constitutive level.

The identification of a micromorphic continuum from the discrete atomic single-crystal model is possible based on suitable averaging relations proposed in [3]. These works contain virial formula for the higher-order stress tensors arising in the micromorphic theory. This atomistic-based approach can be used to predict phonon dispersion relations; see for instance [4] for the study of dispersion of waves in a dislocated crystal.

If single-crystalline materials can be regarded as micromorphic media, then polycrystalline materials must be seen as a mixture of micromorphic media. The effective behavior of such materials can therefore be obtained by means of homogenization methods well known in the mechanics of heterogeneous materials [16, 18]. Classical homogenization methods can be used to account for the influence of the volume fraction, distribution, and morphology of the different constituents of the heterogeneous material, but they are not able to predict size effects. The authors in [20] propose to incorporate intrinsic length scales in the constitutive behavior of the constituents by means of a strain-gradient theory of plasticity. Reasons for introducing generalized continuum models in the mechanics of heterogeneous materials are twofold. Firstly, it is a natural way to obtain an explicit dependence of the effective properties of composites or multiphase materials on the absolute size of the constituents within a continuum model and to account for size effects observed for instance in materials strengthened by inclusions, fibers, or precipitates [1]. On the other hand, generalized continua can be used to limit strain localization phenomena that may occur in one constituent when it exhibits a strain-softening behavior [14]. If the constituents of a heterogeneous material are described by a generalized continuum like second grade, Cosserat, or micromorphic media, specific homogenization methods must be designed to derive its effective behaviour. The questions are the following: Does a homogeneous substitute medium exist? Under which conditions does it still have a nonlocal character? What is the relation between the effective characteristic length and that of the constituents? Bounds and estimates of the overall properties of heterogeneous linear couple stress media have been proposed for instance in [17]. Although most physically relevant applications deal with plasticity or damage phenomena, a first step is to develop homogenization methods for generalized continua in the case of linear elasticity [9]. These methods can then be applied to nonlinear behavior by introducing some linear comparison solids.

In this entry, the attention is focused on the case of heterogeneous micromorphic media with periodic microstructure. For that purpose, asymptotic methods classically used for periodic heterogeneous materials [15] are applied to linear elastic micromorphic constituents. The main interest of asymptotic methods in homogenization theory lies in the fact that it can provide the form of the balance and constitutive equations of an effective medium without any assumption on their nature and form. In particular, the nature of the effective medium for a mixture of micromorphic media will not be assumed a priori but rather will be an essential outcome of the asymptotic analysis. Asymptotic methods have been used in [2] to get solutions of higher

orders to the problem of the effective properties of periodic heterogeneous classical media. In contrast, the present analysis is restricted to the first orders in the asymptotic developments, but the method is applied to the case of periodic heterogeneous micromorphic media.

Homogenization of Cosserat composites is considered in the reference [9, 12, 19]. It is a special case of the situation envisaged in this entry. Note that this situation is different from that of a classical heterogeneous Cauchy material that can be homogenized into a Cosserat continuum by suitable homogenization techniques [11].

Regarding notations, the tensor product of two vectors is $\otimes$, with $\overset{s}{\otimes}$ and $\overset{a}{\otimes}$ respectively delivering the symmetric and skew–symmetric parts of the tensor product of two vectors. A wide use of the nabla operator ∇ is made in the sequel. The notation used for the gradient and divergence operators are the following:

$$a\nabla = a_{,i}\underline{\boldsymbol{e}}_i,\ \underline{\boldsymbol{a}} \otimes \nabla = a_{i,j}\,\underline{\boldsymbol{e}}_i \otimes \underline{\boldsymbol{e}}_j,\ \underline{\underline{\boldsymbol{a}}}.\nabla = \underline{a}_{ij,j}\,\underline{\boldsymbol{e}}_i$$

where a, $\underline{\boldsymbol{a}}$ and $\underline{\underline{\boldsymbol{a}}}$ respectively denote scalar, first- and second-rank tensors. The $(\underline{\boldsymbol{e}}_i)_{i=1,2,3}$ are the vectors of an orthonormal basis of space, and the associated Cartesian coordinates have been used. Third-, fourth-, fifth-, and sixth-rank tensors are respectively denoted by $\underline{\underline{\underline{\boldsymbol{a}}}}$ (or $\underline{\underline{\underline{\boldsymbol{a}}}}$), $\underline{\underline{\underline{\underline{\boldsymbol{a}}}}}$, $\underline{\underline{\underline{\underline{\underline{\boldsymbol{a}}}}}}$, and $\underline{\underline{\underline{\underline{\underline{\underline{\boldsymbol{a}}}}}}}$. Indices can be contracted as follows: $\underline{\boldsymbol{a}} : \underline{\boldsymbol{b}} = a_{ij}b_{ij}$,

$$\underline{\underline{\underline{\boldsymbol{a}}}} : \underline{\boldsymbol{b}} = a_{ijk}b_{jk}\underline{\boldsymbol{e}}_i, \quad \underline{\underline{\underline{\underline{\boldsymbol{a}}}}} : \underline{\boldsymbol{b}} = a_{ijkl}b_{kl}\underline{\boldsymbol{e}}_i \otimes \underline{\boldsymbol{e}}_j,$$

$$\underline{\underline{\underline{\boldsymbol{a}}}} : \underline{\underline{\boldsymbol{A}}} : \underline{\boldsymbol{b}} = a_{ij}A_{ijkl}b_{kl}, \quad \underline{\underline{\underline{\boldsymbol{a}}}} \vdots \underline{\underline{\underline{\boldsymbol{b}}}} = a_{ijk}b_{ijk}$$

Linear Elastic Micromorphic Media

The balance and constitutive equations of the micromorphic continuum are recalled briefly in the linear elastic framework. The motion of a micromorphic body Ω is described by two independent sets of degrees of freedom: the displacement $\underline{\boldsymbol{u}}$ and the microdeformation $\underline{\underline{\boldsymbol{\chi}}}$ attributed to each material point. The microdeformation accounts for the rotation and distortion of a triad associated with the underlying microstructure [6]. The microdeformation field is generally not compatible. The microdeformation can be split into its symmetric and skew–symmetric parts:

$$\underline{\underline{\boldsymbol{\chi}}} = \underline{\underline{\boldsymbol{\chi}}}^s + \underline{\underline{\boldsymbol{\chi}}}^a \tag{1}$$

that are called respectively the microstrain and the Cosserat rotation. The associated deformation fields are the classical strain tensor $\underline{\underline{\boldsymbol{\varepsilon}}}$, the relative deformation $\underline{\underline{\boldsymbol{e}}}$, and the microdeformation gradient tensor $\underline{\underline{\underline{\boldsymbol{\kappa}}}}$ defined by:

$$\underline{\underline{\boldsymbol{\varepsilon}}} = \underline{\boldsymbol{u}} \overset{s}{\otimes} \nabla,\ \ \underline{\underline{\boldsymbol{e}}} = \underline{\boldsymbol{u}} \otimes \nabla - \underline{\underline{\boldsymbol{\chi}}},\ \ \underline{\underline{\underline{\boldsymbol{\kappa}}}} = \underline{\underline{\boldsymbol{\chi}}} \otimes \nabla \tag{2}$$

The symmetric part of $\underline{\underline{\boldsymbol{e}}}$ corresponds to the difference of material strain and microstrain, whereas its skew–symmetric part accounts for the relative rotation of the material with respect to microstructure. The analysis is restricted to small deformations, small micro-rotations, small microstrains, and small microdeformation gradients. The microdeformation gradient can be split into two contributions:

$$\underline{\underline{\underline{\boldsymbol{\kappa}}}} = \underline{\underline{\underline{\boldsymbol{\kappa}}}}^s + \underline{\underline{\underline{\boldsymbol{\kappa}}}}^a, \quad \text{with} \quad \underline{\underline{\underline{\boldsymbol{\kappa}}}}^s = \underline{\underline{\boldsymbol{\chi}}}^s \otimes \nabla, \underline{\underline{\underline{\boldsymbol{\kappa}}}}^a = \underline{\underline{\boldsymbol{\chi}}}^a \otimes \nabla \tag{3}$$

The statics of the micromorphic continuum is described by the symmetric simple stress tensor $\underline{\underline{\boldsymbol{\sigma}}}$, the generally non-symmetric relative force–stress tensor $\underline{\underline{\boldsymbol{s}}}$, and the third-rank double stress tensor $\underline{\underline{\underline{\boldsymbol{m}}}}$. These tensors must fulfill the local form of the balance equations in the static case, in the absence of body simple nor double forces for simplicity:

$$\left(\underline{\underline{\boldsymbol{\sigma}}} + \underline{\underline{\boldsymbol{s}}}\right) \cdot \nabla = 0, \quad \underline{\underline{\underline{\boldsymbol{m}}}} \cdot \nabla + \underline{\underline{\boldsymbol{s}}} = 0 \ \ \text{on}\ \Omega \tag{4}$$

The constitutive equations for linear elastic centrosymmetric micromorphic materials read

$$\underline{\underline{\boldsymbol{\sigma}}} = \underline{\underline{\underline{\underline{\boldsymbol{a}}}}} : \underline{\underline{\boldsymbol{\varepsilon}}}, \qquad \underline{\underline{\boldsymbol{s}}} = \underline{\underline{\underline{\boldsymbol{b}}}} : \underline{\underline{\boldsymbol{e}}}, \qquad \underline{\underline{\underline{\boldsymbol{m}}}} = \underline{\underline{\underline{\underline{\underline{\boldsymbol{c}}}}}} \vdots \underline{\underline{\underline{\boldsymbol{\kappa}}}} \tag{5}$$

The elasticity tensors display the major symmetries:

$$a_{ijkl} = a_{klij}, \qquad b_{ijkl} = b_{klij}, \quad c_{ijkpqr} = c_{pqrijk} \tag{6}$$

and $\underset{\approx}{\boldsymbol{a}}$ has also the usual minor symmetries. The last constitutive law can be written in the form

$$\underset{\sim}{\boldsymbol{m}} = \underset{\approx}{\boldsymbol{c}}^{s} : \underset{\sim}{\boldsymbol{\kappa}}^{s} + \underset{\approx}{\boldsymbol{c}}^{a} : \underset{\sim}{\boldsymbol{\kappa}}^{a} \tag{7}$$

For the sake of simplicity, the tensors $\underset{\approx}{\boldsymbol{c}}^{s}$ and $\underset{\approx}{\boldsymbol{c}}^{a}$ are supposed to fulfill the following conditions:

$$c^{s}_{ijkpqr} = c^{s}_{jikpqr}, c^{a}_{ijkpqr} = -c^{a}_{jikpqr} \tag{8}$$

thus assuming that there is no coupling between the contributions of the symmetric and skew–symmetric parts of $\underset{\sim}{\boldsymbol{\kappa}}$ to the third-rank stress tensor.

The setting of the boundary value problem on body Ω is then closed by the boundary conditions. In the following, Dirichlet boundary conditions are considered of the form

$$\underline{\boldsymbol{u}}(\underline{\boldsymbol{x}}) = 0, \quad \underset{\sim}{\boldsymbol{\chi}}(\underline{\boldsymbol{x}}) = 0, \quad \forall \underline{\boldsymbol{x}} \in \partial\Omega \tag{9}$$

where $\partial\Omega$ denotes the boundary of Ω. The equations (2), (4), (5), and (9) define the boundary value problem $\mathcal{P}$.

Multiscale Asymptotic Expansion Method

The multiscale asymptotic expansion method is exposed in details in the case of heterogeneous micromorphic media so that the reader will be in the position of applying it readily to other similar situations.

The heterogeneous material under study is a mixture of micromorphic constituents, i.e., a heterogeneous micromorphic medium. One investigates the nature of the resulting homogeneous equivalent medium by means of asymptotic methods. The multiscale asymptotic method from [15] is especially adequate for this purpose since the nature of the effective medium is not postulated a priori but rather is the result of the analysis. The microstructure of the material is assumed to be periodic. The heterogeneous material is then obtained by space tessellation with cells translated from a single cell Y^l. The period of the microstructure is described by three dimensionless independent vectors $(\underline{\boldsymbol{a}}_1, \underline{\boldsymbol{a}}_2, \underline{\boldsymbol{a}}_3)$ such that

$$Y^l = \left\{ \underline{\boldsymbol{x}} = x_i \underline{\boldsymbol{a}}_i, |x_i| < \frac{l}{2} \right\}$$

where l is the characteristic size of the cell. We call $\underset{\approx}{\boldsymbol{a}}^l$, $\underset{\sim}{\boldsymbol{b}}^l$ and $\underset{\approx}{\boldsymbol{c}}^l$ the elasticity tensor fields of the periodic micromorphic material. They are such that

$$\begin{aligned}
&\forall \underline{\boldsymbol{x}} \in \Omega, \forall (n_1, n_2, n_3) \in Z^3 / \underline{\boldsymbol{x}} \\
&\qquad + l(n_1 \underline{\boldsymbol{a}}_1 + n_2 \underline{\boldsymbol{a}}_2 + n_3 \underline{\boldsymbol{a}}_3) \in \Omega \\
&\underset{\approx}{\boldsymbol{a}}^l(\underline{x}) = \underset{\approx}{\boldsymbol{a}}^l(\underline{x} + l(n_1 \underline{\boldsymbol{a}}_1 + n_2 \underline{\boldsymbol{a}}_2 + n_3 \underline{\boldsymbol{a}}_3)) \\
&\underset{\sim}{\boldsymbol{b}}^l(\underline{x}) = \underset{\sim}{\boldsymbol{b}}^l(\underline{\boldsymbol{x}} + l(n_1 \underline{\boldsymbol{b}}_1 + n_2 \underline{\boldsymbol{b}}_2 + n_3 \underline{\boldsymbol{b}}_3)) \\
&\underset{\approx}{\boldsymbol{c}}^l(\underline{x}) = \underset{\approx}{\boldsymbol{c}}^l(\underline{\boldsymbol{x}} + l(n_1 \underline{\boldsymbol{a}}_1 + n_2 \underline{\boldsymbol{a}}_2 + n_3 \underline{\boldsymbol{a}}_3))
\end{aligned}$$

Dimensional Analysis

The first step of a multiscale expansion analysis is the dimensional analysis which is necessary to identify the small parameters of the problem. The size L of body Ω is defined for instance as the maximum distance between two points. Dimensionless coordinates and displacements are introduced:

$$\underline{\boldsymbol{x}}^* = \frac{\underline{\boldsymbol{x}}}{L}, \underline{\boldsymbol{u}}^*(\underline{\boldsymbol{x}}^*) = \frac{\underline{\boldsymbol{u}}(\underline{\boldsymbol{x}})}{L}, \underset{\sim}{\boldsymbol{\chi}}^*(\underline{\boldsymbol{x}}^*) = \underset{\sim}{\boldsymbol{\chi}}(\underline{\boldsymbol{x}}) \tag{10}$$

The corresponding strain measures are

$$\begin{aligned}
\underset{\sim}{\boldsymbol{\varepsilon}}^*(\underline{\boldsymbol{x}}^*) &= \underline{\boldsymbol{u}}^* \overset{s}{\otimes} \nabla^* = \underset{\sim}{\boldsymbol{\varepsilon}}(\underline{\boldsymbol{x}}), \\
\underset{\sim}{\boldsymbol{e}}^*(\underline{\boldsymbol{x}}^*) &= \underline{\boldsymbol{u}}^* \otimes \nabla^* - \underset{\sim}{\boldsymbol{\chi}}^* = \underset{\sim}{\boldsymbol{e}}(\underline{\boldsymbol{x}})
\end{aligned} \tag{11}$$

$$\underset{\sim}{\boldsymbol{\kappa}}^*(\underline{\boldsymbol{x}}^*) = \underset{\sim}{\boldsymbol{\chi}}^* \otimes \nabla^* = L \underset{\sim}{\boldsymbol{\kappa}}(\underline{\boldsymbol{x}}) \tag{12}$$

with $\nabla^* = \left(\frac{\partial \cdot}{\partial x_i^*}\right) \underline{\boldsymbol{e}}_i = L\nabla$. Similarly,

$$\begin{aligned}\underset{\sim}{\boldsymbol{\kappa}}^{s*}(\underline{x}^*) &= \underset{\sim}{\boldsymbol{\chi}}^{s*} \otimes \nabla^* = L\,\underset{\sim}{\boldsymbol{\kappa}}^{s}(\underline{x}) \\ \underset{\sim}{\boldsymbol{\kappa}}^{a*}(\underline{x}^*) &= \underset{\sim}{\boldsymbol{\chi}}^{a*} \otimes \nabla^* = L\,\underset{\sim}{\boldsymbol{\kappa}}^{a}(\underline{x})\end{aligned} \tag{13}$$

It is necessary to introduce next a norm of the elasticity tensors:

$$\begin{aligned}A &= \underset{\underline{x}\in Y^l}{\mathrm{Max}} \left(\left| a^l_{ijkl}(\underline{x}) \right|, \left| b^l_{ijkl}(\underline{x}) \right| \right) \\ C^s &= \underset{\underline{x}\in Y^l}{\mathrm{Max}} \left| c^{sl}_{ijkpqr}(\underline{x}) \right| \\ C^a &= \underset{\underline{x}\in Y^l}{\mathrm{Max}} \left| c^{al}_{ijkpqr}(\underline{x}) \right|\end{aligned}$$

whereby characteristic lengths l_s and l_a can be defined as $C^s = Al_s^2, C^a = Al_a^2$.

The definition of dimensionless stress and elasticity tensors is as follows:

$$\begin{aligned}&\underset{\sim}{\boldsymbol{\sigma}}^*(\underline{x}^*) = A^{-1}\underset{\sim}{\boldsymbol{\sigma}}(\underline{x}), \quad \underline{s}^*(\underline{x}^*) = A^{-1}\underline{s}(\underline{x}), \\ &\underset{\sim}{\boldsymbol{m}}^*(\underline{x}^*) = (AL)^{-1}\underset{\sim}{\boldsymbol{m}}(\underline{x}) \\ &\underset{\approx}{\boldsymbol{a}}^*(\underline{x}^*) = A^{-1}\underset{\approx}{\boldsymbol{a}}^l(\underline{x}), \ \underset{\approx}{\boldsymbol{b}}^*(\underline{x}^*) = A^{-1}\underset{\approx}{\boldsymbol{b}}^l(\underline{x}), \\ &\underset{\approx\approx}{\boldsymbol{c}}^{s*}(\underline{x}^*) = (Al_s^2)^{-1}\underset{\approx\approx}{\boldsymbol{c}}^{sl}(\underline{x}), \ \underset{\approx\approx}{\boldsymbol{c}}^{a*}(\underline{x}^*) = (Al_a^2)^{-1}\underset{\approx\approx}{\boldsymbol{c}}^{al}(\underline{x})\end{aligned}$$

Since the initial tensors $\underset{\approx}{\boldsymbol{a}}^l, \underset{\approx}{\boldsymbol{b}}^l$ and $\underset{\approx\approx}{\boldsymbol{c}}^l$ are Y^l-periodic, the dimensionless counterparts are Y^*-periodic:

$$Y^* = \frac{1}{l}Y, Y = \left\{ \underline{y} = y_i \underline{a}_i, \ |y_i| < \frac{1}{2} \right\} \tag{14}$$

Y is the (dimensionless) unit cell used in the following asymptotic analyses. As a result, the dimensionless stress and strain tensors are related by the following constitutive equations:

$$\begin{aligned}&\underset{\sim}{\boldsymbol{\sigma}}^* = \underset{\approx}{\boldsymbol{a}}^* : \underset{\sim}{\boldsymbol{\varepsilon}}^*, \quad \underline{s}^* = \underset{\approx}{\boldsymbol{b}}^* : \underset{\sim}{\boldsymbol{e}}^*, \\ &\underset{\sim}{\boldsymbol{m}}^* = \left(\frac{l_s}{L}\right)^2 \underset{\approx\approx}{\boldsymbol{c}}^{s*} \vdots \underset{\sim}{\boldsymbol{\kappa}}^{s*} + \left(\frac{l_a}{L}\right)^2 \underset{\approx\approx}{\boldsymbol{c}}^{a*} \vdots \underset{\sim}{\boldsymbol{\kappa}}^{a*}\end{aligned} \tag{15}$$

The dimensionless balance equations read

$$\forall \underline{x}^* \in \Omega^*, (\underset{\sim}{\boldsymbol{\sigma}}^* + \underline{s}^*) \cdot \nabla^* = 0, \underset{\sim}{\boldsymbol{m}}^* \cdot \nabla^* + \underline{s}^* = 0 \tag{16}$$

A boundary value problem $\mathcal{P}^*$ can be defined using equations (12), (15), and (16), complemented by the boundary conditions:

$$\forall \underline{x}^* \in \partial\Omega^*, \underline{u}^*(\underline{x}^*) = 0, \underset{\sim}{\boldsymbol{\chi}}^*(\underline{x}^*) = 0 \tag{17}$$

The Homogenization Problem

The boundary value problem $\mathcal{P}^*$ is treated here as an element of a series of problems $(\mathcal{P}_{\boldsymbol{\varepsilon}})_{\boldsymbol{\varepsilon}>0}$ on Ω^*. The homogenization problem consists in the determination of the limit of this series when the dimensionless parameter $\boldsymbol{\epsilon}$, regarded as small, tends towards 0. The series is chosen such that

$$\mathcal{P}_{\boldsymbol{\epsilon}=\frac{l}{L}} = \mathcal{P}^*$$

The unknowns of boundary value problem $\mathcal{P}_{\boldsymbol{\varepsilon}}$ are the displacement and microdeformation fields $\underline{\boldsymbol{u}}^{\boldsymbol{\epsilon}}$ and $\underset{\sim}{\boldsymbol{\chi}}^{\boldsymbol{\epsilon}}$ satisfying the following field equations on Ω^*:

$$\begin{aligned}&\underset{\sim}{\boldsymbol{\sigma}}^{\boldsymbol{\epsilon}} = \underset{\approx}{\boldsymbol{a}}^{\boldsymbol{\epsilon}} : (\underline{\boldsymbol{u}}^{\boldsymbol{\varepsilon}} \overset{s}{\otimes} \nabla^*), \quad \underline{s}^{\boldsymbol{\epsilon}} = \underset{\approx}{\boldsymbol{b}}^{\boldsymbol{\epsilon}} : (\underline{\boldsymbol{u}}^{\boldsymbol{\epsilon}} \otimes \nabla^* - \underset{\sim}{\boldsymbol{\chi}}^{\boldsymbol{\epsilon}}), \\ &\underset{\sim}{\boldsymbol{m}}^{\boldsymbol{\epsilon}} = \underset{\approx\approx}{\boldsymbol{c}}^{\boldsymbol{\epsilon}} \vdots (\underset{\sim}{\boldsymbol{\chi}}^{\boldsymbol{\epsilon}} \otimes \nabla^*)\end{aligned} \tag{18}$$

$$(\underset{\sim}{\boldsymbol{\sigma}}^{\boldsymbol{\epsilon}} + \underline{s}^{\boldsymbol{\epsilon}}) \cdot \nabla^* = 0, \quad \underset{\sim}{\boldsymbol{m}}^{\boldsymbol{\epsilon}} \cdot \nabla^* + \underline{s}^{\boldsymbol{\epsilon}} = 0 \tag{19}$$

Different cases must now be distinguished depending on the relative position of the constitutive lengths l_s and l_a with respect to the characteristic lengths l and L of the problem. Four special cases can be distinguished for the present asymptotic analysis. The first case corresponds to a limiting process for which l_s/l and l_a/l remain constant when l/L goes to zero. The second case corresponds to the situation for which l_s/L and l_a/L remain constant when l/L goes to zero. The third (resp. fourth) situation assumes that l_s/l and l_a/L (resp. l_s/L and l_a/l) remain constant when l/L goes to zero. These assumptions lead to four different homogenization schemes labeled *HS*1 to *HS*4 in the sequel. The homogenization scheme 1 (resp. 2) will be

relevant when the ratio l/L is small enough and when l_s, l_a and l (resp. L) have the same order of magnitude.

Accordingly, the following tensors of elastic moduli are defined:

$$\underset{\approx}{\boldsymbol{a}}^{(0)}\left(\underline{\boldsymbol{y}}\right)=\underset{\approx}{\boldsymbol{a}}^{*}\left(\tfrac{l}{L}\underline{\boldsymbol{y}}\right),\quad \underset{\approx}{\boldsymbol{b}}^{(0)}\left(\underline{\boldsymbol{y}}\right)=\underset{\approx}{\boldsymbol{b}}^{*}\left(\tfrac{l}{L}\underline{\boldsymbol{y}}\right) \tag{20}$$

$$\underset{\approx}{\boldsymbol{c}}^{(1)}\left(\underline{\boldsymbol{y}}\right)=\left(\tfrac{l_s}{l}\right)^2\underset{\approx}{\boldsymbol{c}}^{*}\left(\tfrac{l}{L}\underline{\boldsymbol{y}}\right),\quad \underset{\approx}{\boldsymbol{c}}^{(2)}\left(\underline{\boldsymbol{y}}\right)=\left(\tfrac{l_s}{L}\right)^2\underset{\approx}{\boldsymbol{c}}^{*}\left(\tfrac{l}{L}\underline{\boldsymbol{y}}\right) \tag{21}$$

$$\underset{\approx}{\boldsymbol{c}}^{s(1)}\left(\underline{y}\right)=\left(\tfrac{l_s}{l}\right)^2\underset{\approx}{\boldsymbol{c}}^{s*}\left(\tfrac{l}{L}\underline{\boldsymbol{y}}\right),\quad \underset{\approx}{\boldsymbol{c}}^{a(1)}\left(\underline{\boldsymbol{y}}\right)=\left(\tfrac{l_a}{l}\right)^2\underset{\approx}{\boldsymbol{c}}^{a*}\left(\tfrac{l}{L}\underline{\boldsymbol{y}}\right) \tag{22}$$

$$\underset{\approx}{\boldsymbol{c}}^{s(2)}\left(\underline{\boldsymbol{y}}\right)=\left(\tfrac{l_s}{L}\right)^2\underset{\approx}{\boldsymbol{c}}^{s*}\left(\tfrac{l}{L}\underline{\boldsymbol{y}}\right),\quad \underset{\approx}{\boldsymbol{c}}^{a(2)}\left(\underline{\boldsymbol{y}}\right)=\left(\tfrac{l_a}{L}\right)^2\underset{\approx}{\boldsymbol{c}}^{a*}\left(\tfrac{l}{L}\underline{\boldsymbol{y}}\right) \tag{23}$$

They are Y-periodic since $\underset{\approx}{\boldsymbol{a}}^{*}, \underset{\approx}{\boldsymbol{b}}^{*}$ and $\underset{\approx}{\boldsymbol{c}}^{*}$ are Y^{*}-periodic. Four different hypotheses will be made concerning the constitutive tensors of problem $\mathcal{P}_{\boldsymbol{\varepsilon}}$:

$$\begin{aligned}
\textit{Assumption } 1: &\ \underset{\approx}{\boldsymbol{a}}^{\boldsymbol{\epsilon}}\left(\underline{\boldsymbol{x}}^{*}\right)=\underset{\approx}{\boldsymbol{a}}^{(0)}\left(\boldsymbol{\epsilon}^{-1}\underline{\boldsymbol{x}}^{*}\right)\\
&\ \underset{\approx}{\boldsymbol{b}}^{\boldsymbol{\epsilon}}\left(\underline{\boldsymbol{x}}^{*}\right)=\underset{\approx}{\boldsymbol{b}}^{(0)}\left(\boldsymbol{\epsilon}^{-1}\underline{\boldsymbol{x}}^{*}\right)\ \text{and}\\
&\ \underset{\approx}{\boldsymbol{c}}^{\boldsymbol{\epsilon}}\left(\underline{\boldsymbol{x}}^{*}\right)=\boldsymbol{\epsilon}^{2}\underset{\approx}{\boldsymbol{c}}^{(1)}\left(\boldsymbol{\epsilon}^{-1}\underline{\boldsymbol{x}}^{*}\right)\\
\textit{Assumption } 2: &\ \underset{\approx}{\boldsymbol{a}}^{\boldsymbol{\epsilon}}\left(\underline{\boldsymbol{x}}^{*}\right)=\underset{\approx}{\boldsymbol{a}}^{(0)}\left(\boldsymbol{\epsilon}^{-1}\underline{\boldsymbol{x}}^{*}\right)\\
&\ \underset{\approx}{\boldsymbol{b}}^{\boldsymbol{\epsilon}}\left(\underline{\boldsymbol{x}}^{*}\right)=\underset{\approx}{\boldsymbol{b}}^{(0)}\left(\boldsymbol{\epsilon}^{-1}\underline{\boldsymbol{x}}^{*}\right)\ \text{and}\\
&\ \underset{\approx}{\boldsymbol{c}}^{\boldsymbol{\epsilon}}\left(\underline{\boldsymbol{x}}^{*}\right)=\underset{\approx}{\boldsymbol{c}}^{(2)}\left(\boldsymbol{\epsilon}^{-1}\underline{\boldsymbol{x}}^{*}\right)\\
\textit{Assumption } 3: &\ \underset{\approx}{\boldsymbol{a}}^{\boldsymbol{\epsilon}}\left(\underline{\boldsymbol{x}}^{*}\right)=\underset{\approx}{\boldsymbol{a}}^{(0)}\left(\boldsymbol{\epsilon}^{-1}\underline{\boldsymbol{x}}^{*}\right)\\
&\ \underset{\approx}{\boldsymbol{b}}^{\boldsymbol{\epsilon}}\left(\underline{\boldsymbol{x}}^{*}\right)=\underset{\approx}{\boldsymbol{b}}^{(0)}\left(\boldsymbol{\epsilon}^{-1}\underline{\boldsymbol{x}}^{*}\right)\ \text{and}\\
&\ \underset{\approx}{\boldsymbol{c}}^{s\boldsymbol{\epsilon}}\left(\underline{\boldsymbol{x}}^{*}\right)=\boldsymbol{\epsilon}^{2}\underset{\approx}{\boldsymbol{c}}^{s(1)}\left(\boldsymbol{\epsilon}^{-1}\underline{\boldsymbol{x}}^{*}\right)\\
&\ \underset{\approx}{\boldsymbol{c}}^{a\boldsymbol{\epsilon}}\left(\underline{\boldsymbol{x}}^{*}\right)=\underset{\approx}{\boldsymbol{c}}^{a(2)}\left(\boldsymbol{\epsilon}^{-1}\underline{\boldsymbol{x}}^{*}\right)\\
\textit{Assumption } 4: &\ \underset{\approx}{\boldsymbol{a}}^{\boldsymbol{\epsilon}}\left(\underline{\boldsymbol{x}}^{*}\right)=\underset{\approx}{\boldsymbol{a}}^{(0)}\left(\boldsymbol{\epsilon}^{-1}\underline{\boldsymbol{x}}^{*}\right)\\
&\ \boldsymbol{b}^{\boldsymbol{\epsilon}}\left(\underline{\boldsymbol{x}}^{*}\right)=\underset{\approx}{\boldsymbol{b}}^{(0)}\left(\boldsymbol{\epsilon}^{-1}\underline{\boldsymbol{x}}^{*}\right)\ \text{and}\\
&\ \underset{\approx}{\boldsymbol{c}}^{s\boldsymbol{\epsilon}}\left(\underline{\boldsymbol{x}}^{*}\right)=\underset{\approx}{\boldsymbol{c}}^{s(2)}\left(\boldsymbol{\epsilon}^{-1}\underline{\boldsymbol{x}}^{*}\right)\\
&\ \underset{\approx}{\boldsymbol{c}}^{a\boldsymbol{\epsilon}}\left(\underline{\boldsymbol{x}}^{*}\right)=\boldsymbol{\epsilon}^{2}\underset{\approx}{\boldsymbol{c}}^{a(1)}\left(\boldsymbol{\epsilon}^{-1}\underline{\boldsymbol{x}}^{*}\right)
\end{aligned}$$

Assumptions 1 and 2 respectively correspond to the homogenization schemes HS1 and HS2. Both choices meet the requirement that

$$\left(\boldsymbol{\epsilon}=\frac{l}{L}\right)\Rightarrow\left(\underset{\approx}{\boldsymbol{a}}^{\boldsymbol{\epsilon}}=\underset{\approx}{\boldsymbol{a}}^{*}\quad\text{and}\quad\underset{\approx}{\boldsymbol{c}}^{\boldsymbol{\epsilon}}=\left(\frac{l}{L}\right)^2\underset{\approx}{\boldsymbol{c}}^{*}\right)$$

Assumptions 3 and 4 respectively correspond to the homogenization schemes HS3 and HS4. Both choices meet the requirement that

$$\left(\boldsymbol{\epsilon}=\frac{l}{L}\right)\Rightarrow\left(\underset{\approx}{\boldsymbol{a}}^{\boldsymbol{\epsilon}}=\underset{\approx}{\boldsymbol{a}}^{*},\quad\underset{\approx}{\boldsymbol{c}}^{s\boldsymbol{\epsilon}}=\left(\frac{l_s}{L}\right)^2\underset{\approx}{\boldsymbol{c}}^{s*}\quad\text{and}\quad\underset{\approx}{\boldsymbol{c}}^{a\boldsymbol{\epsilon}}=\left(\frac{l_a}{L}\right)^2\underset{\approx}{\boldsymbol{c}}^{a*}\right)$$

It must be noted that, in our presentation of the asymptotic analysis, the lengths l, l_s, l_a and L are given and fixed, whereas parameter $\boldsymbol{\varepsilon}$ is allowed to tend to zero in the limiting process. In the sequel, the stars $*$ are dropped for conciseness.

Multiscale Asymptotic Expansion of the Fields

In the setting of the homogenization problems, two space variables have been distinguished: $\underline{\boldsymbol{x}}$ describes the macroscopic scale and $\underline{\boldsymbol{y}}$ is the local variable in the unit Y. According to the method of multiscale asymptotic developments, all fields are regarded as functions of both variables $\underline{\boldsymbol{x}}$ and $\underline{\boldsymbol{y}}$. It is assumed that they can be expanded in a series of powers of small parameter $\boldsymbol{\varepsilon}$. In particular, the displacement, microdeformation, and simple and double stress fields are supposed to take the form

$$\begin{aligned}
\underline{\boldsymbol{u}}^{\boldsymbol{\epsilon}}(\underline{\boldsymbol{x}})&=\underline{\boldsymbol{u}}_0(\underline{\boldsymbol{x}},\underline{\boldsymbol{y}})+\boldsymbol{\epsilon}\underline{\boldsymbol{u}}_1(\underline{\boldsymbol{x}},\underline{\boldsymbol{y}})+\boldsymbol{\epsilon}^2\underline{\boldsymbol{u}}_2(\underline{\boldsymbol{x}},\underline{\boldsymbol{y}})+\ldots\\
\underset{\sim}{\boldsymbol{\chi}}^{\boldsymbol{\epsilon}}(\underline{\boldsymbol{x}})&=\underset{\sim}{\boldsymbol{\chi}}_1(\underline{\boldsymbol{x}},\underline{\boldsymbol{y}})+\boldsymbol{\epsilon}\underset{\sim}{\boldsymbol{\chi}}_2(\underline{\boldsymbol{x}},\underline{\boldsymbol{y}})+\boldsymbol{\epsilon}\underset{\sim}{\boldsymbol{\chi}}_3(\underline{\boldsymbol{x}},\underline{\boldsymbol{y}})+\ldots\\
\underset{\sim}{\boldsymbol{\sigma}}^{\boldsymbol{\epsilon}}(\underline{\boldsymbol{x}})&=\underset{\sim}{\boldsymbol{\sigma}}_0(\underline{\boldsymbol{x}},\underline{\boldsymbol{y}})+\boldsymbol{\epsilon}\underset{\sim}{\boldsymbol{\sigma}}_1(\underline{\boldsymbol{x}},\underline{\boldsymbol{y}})+\boldsymbol{\epsilon}\underset{\sim}{\boldsymbol{\sigma}}_2(\underline{\boldsymbol{x}},\underline{\boldsymbol{y}})+\ldots\\
\underline{\boldsymbol{s}}^{\boldsymbol{\epsilon}}(\underline{\boldsymbol{x}})&=\underline{\boldsymbol{s}}_0(\underline{\boldsymbol{x}},\underline{\boldsymbol{y}})+\boldsymbol{\epsilon}\underline{\boldsymbol{s}}_1(\underline{\boldsymbol{x}},\underline{\boldsymbol{y}})+\boldsymbol{\epsilon}^2\underline{\boldsymbol{s}}_2(\underline{\boldsymbol{x}},\underline{\boldsymbol{y}})+\ldots\\
\underset{\sim}{\boldsymbol{m}}^{\boldsymbol{\epsilon}}(\underline{\boldsymbol{x}})&=\underset{\sim}{\boldsymbol{m}}_0(\underline{\boldsymbol{x}},\underline{\boldsymbol{y}})+\boldsymbol{\epsilon}\underset{\sim}{\boldsymbol{m}}_1(\underline{\boldsymbol{x}},\underline{\boldsymbol{y}})+\boldsymbol{\epsilon}^2\underset{\sim}{\boldsymbol{m}}_2(\underline{\boldsymbol{x}},\underline{\boldsymbol{y}})+\ldots
\end{aligned}$$

where the coefficients $\underline{\boldsymbol{u}}_i(\underline{\boldsymbol{x}},\underline{\boldsymbol{y}}), \underset{\sim}{\boldsymbol{\chi}}_i(\underline{\boldsymbol{x}},\underline{\boldsymbol{y}}), \underset{\sim}{\boldsymbol{\sigma}}_i(\underline{\boldsymbol{x}},\underline{\boldsymbol{y}}), \underline{\boldsymbol{s}}_i(\underline{\boldsymbol{x}},\underline{\boldsymbol{y}})$ and $\underset{\sim}{\boldsymbol{m}}_i(\underline{\boldsymbol{x}},\underline{\boldsymbol{y}})$ are assumed to have the same order of magnitude and to be Y-periodic with respect to variable $\underline{\boldsymbol{y}}\left(\underline{\boldsymbol{y}}=\underline{\boldsymbol{x}}/\boldsymbol{\epsilon}\right)$. The average operator over the unit cell Y is denoted by

$$\langle\cdot\rangle = \frac{1}{|Y|}\int_Y \cdot dV$$

As a result,

$$<\underline{\boldsymbol{u}}^{\boldsymbol{\epsilon}}> = \underline{\boldsymbol{U}}_0 + \boldsymbol{\epsilon}\underline{\boldsymbol{U}}_1 + \ldots \quad \text{and} \quad <\underset{\sim}{\boldsymbol{\chi}}^{\boldsymbol{\epsilon}}> = \underset{\sim}{\boldsymbol{\varepsilon}}\underset{\sim}{\boldsymbol{\Xi}}_2 + \ldots \tag{24}$$

where $\underline{\boldsymbol{U}}_i = <\underline{\boldsymbol{u}}_i>$ and $\underset{\sim}{\boldsymbol{\Xi}}_i = <\underset{\sim}{\boldsymbol{\chi}}_i>$. The gradient operator can be split into partial derivatives with respect to $\underline{\boldsymbol{x}}$ and $\underline{\boldsymbol{y}}$:

$$\nabla = \nabla_x + \frac{1}{\boldsymbol{\epsilon}}\nabla_y \tag{25}$$

This operator is used to compute the strain measures and balance equations:

$$\begin{aligned}
\underset{\sim}{\boldsymbol{\varepsilon}}^{\boldsymbol{\epsilon}} &= \underset{\sim}{\boldsymbol{\varepsilon}}^{-1}\underset{\sim}{\boldsymbol{\varepsilon}}_{-1} + \underset{\sim}{\boldsymbol{\varepsilon}}_0 + \boldsymbol{\epsilon}^1\underset{\sim}{\boldsymbol{\varepsilon}}_1 + \ldots \\
&= \boldsymbol{\epsilon}^{-1}\underline{\boldsymbol{u}}_0 \overset{s}{\otimes} \nabla_y + (\underline{\boldsymbol{u}}_0 \overset{s}{\otimes} \nabla_x + \underline{\boldsymbol{u}}_1 \overset{s}{\otimes} \nabla_y) \\
&\quad + \boldsymbol{\epsilon}(\underline{\boldsymbol{u}}_1 \overset{s}{\otimes} \nabla_x + \underline{\boldsymbol{u}}_2 \overset{s}{\otimes} \nabla_y) + \ldots \\
\underset{\sim}{\boldsymbol{e}}^{\boldsymbol{\epsilon}} &= \boldsymbol{\epsilon}^{-1}\underset{\sim}{\boldsymbol{e}}_{-1} + \underset{\sim}{\boldsymbol{e}}_0 + \boldsymbol{\epsilon}^1\underset{\sim}{\boldsymbol{e}}_{-1} + \ldots \\
&= \boldsymbol{\epsilon}^{-1}\underline{\boldsymbol{u}}_0 \otimes \nabla_y + (\underline{\boldsymbol{u}}_0 \otimes \nabla_x + \underline{\boldsymbol{u}}_1 \otimes \nabla_y - \underset{\sim}{\boldsymbol{\chi}}_1) \\
&\quad + \boldsymbol{\epsilon}(\underline{\boldsymbol{u}}_1 \otimes \nabla_x + \underline{\boldsymbol{u}}_2 \otimes \nabla_y - \underset{\sim}{\boldsymbol{\chi}}_2) + \ldots \\
\underset{\sim}{\boldsymbol{\kappa}}^{\boldsymbol{\epsilon}} &= \boldsymbol{\epsilon}^{-1}\underset{\sim}{\boldsymbol{\kappa}}_{-1} + \underset{\sim}{\boldsymbol{\kappa}}_0 + \boldsymbol{\epsilon}^1\underset{\sim}{\boldsymbol{\kappa}} + \ldots \\
&= \boldsymbol{\epsilon}^{-1}\underset{\sim}{\boldsymbol{\chi}}_1 \otimes \nabla_y + (\underset{\sim}{\boldsymbol{\chi}}_1 \otimes \nabla_x + \underset{\sim}{\boldsymbol{\chi}}_2 \otimes \nabla_y) \\
&\quad + \boldsymbol{\epsilon}(\underset{\sim}{\boldsymbol{\chi}}_2 \otimes \nabla_x\underset{\sim}{\boldsymbol{\chi}}_3 \otimes \nabla_y) + \ldots \\
&(\underset{\sim}{\boldsymbol{\sigma}}^{\boldsymbol{\epsilon}} + \underline{\boldsymbol{s}}^{\boldsymbol{\epsilon}}) \cdot \nabla_x + \boldsymbol{\epsilon}^{-1}(\underset{\sim}{\boldsymbol{\sigma}}^{\boldsymbol{\epsilon}} + \underline{\boldsymbol{s}}^{\boldsymbol{\epsilon}}) \cdot \nabla_y = 0, \\
&\underset{\sim}{\boldsymbol{m}}^{\boldsymbol{\epsilon}} \cdot \nabla_x + \boldsymbol{\epsilon}^{-1}\underset{\sim}{\boldsymbol{m}}^{\boldsymbol{\epsilon}} \cdot \nabla_y + \underline{\boldsymbol{s}}^{\boldsymbol{\epsilon}} = 0
\end{aligned} \tag{26}$$

Similar expansions are valid for the tensors $\underset{\sim}{\boldsymbol{\kappa}}^s, \underset{\sim}{\boldsymbol{\kappa}}^a$. The expansions of the stress tensors are then introduced in the balance equations (26), and the terms can be ordered with respect to the powers of $\boldsymbol{\epsilon}$. Identifying the terms of same order, we are lead to the following set of equations:

- *order* $\boldsymbol{\epsilon}^{-1}$, $(\underset{\sim}{\boldsymbol{\sigma}}_0 + \underline{\boldsymbol{s}}_0) \cdot \nabla_y = 0$ and $\underset{\sim}{\boldsymbol{m}}_0 \cdot \nabla_y = 0$
- *order* $\boldsymbol{\epsilon}^0$, $(\underset{\sim}{\boldsymbol{\sigma}}_0 + \underline{\boldsymbol{s}}_0) \cdot \nabla_x + (\underset{\sim}{\boldsymbol{\sigma}}_1 + \underline{\boldsymbol{s}}_1) \cdot \nabla_y = 0$ and $\underline{\boldsymbol{S}}_0 \cdot \nabla_x + \underline{\boldsymbol{S}}_1 \cdot \nabla_y + \underline{\boldsymbol{s}}_1 = 0$

The effective balance equations follow from the first above equation by averaging over the unit cell Y and, at the order $\boldsymbol{\epsilon}^0$, one gets

$$(\underset{\sim}{\boldsymbol{\Sigma}}_0 + \underline{\boldsymbol{S}}_0) \cdot \nabla = 0 \qquad \text{and} \qquad \underset{\sim}{\boldsymbol{M}}_0 \cdot \nabla + \underline{\boldsymbol{S}}_0 = 0 \tag{27}$$

where effective stress tensors are defined as the following averages $\underset{\sim}{\boldsymbol{\Sigma}}_0 = <\underset{\sim}{\boldsymbol{\sigma}}_0>, \underline{\boldsymbol{S}}_0 = <\underline{\boldsymbol{s}}_0>$ and $\underset{\sim}{\boldsymbol{M}}_0 = <\underset{\sim}{\boldsymbol{m}}_0>$.

Homogenization Scheme HS1

For the first homogenization scheme HS1 previously defined, the equations describing the local behavior are

$$\underset{\sim}{\boldsymbol{\sigma}}^{\boldsymbol{\epsilon}} = \underset{\sim}{\boldsymbol{a}}^{(0)}(\underline{\boldsymbol{y}}) : \underset{\sim}{\boldsymbol{\varepsilon}}^{\boldsymbol{\epsilon}}, \quad \underline{\boldsymbol{s}}^{\boldsymbol{\epsilon}} = \underset{\sim}{\boldsymbol{b}}^{(0)}(\underline{\boldsymbol{y}}) : \underset{\sim}{\boldsymbol{e}}^{\boldsymbol{\epsilon}} \quad \text{and} \quad \underset{\sim}{\boldsymbol{m}}^{\boldsymbol{\epsilon}} = \boldsymbol{\epsilon}^2\underset{\sim}{\boldsymbol{c}}^{(1)}(\underline{\boldsymbol{y}}) \vdots \underset{\sim}{\boldsymbol{\kappa}}^{\boldsymbol{\epsilon}} \tag{28}$$

At this stage, the expansion (26) can be substituted into the constitutive equations (28). Identifying the terms of same order, one gets

- *order* $\boldsymbol{\epsilon}^{-1}$,

$$\begin{aligned}
\underset{\sim}{\boldsymbol{a}}^{(0)} : \underset{\sim}{\boldsymbol{\varepsilon}}_{-1} &= \underset{\sim}{\boldsymbol{a}}^{(0)} : \left(\underline{\boldsymbol{u}}_0 \overset{s}{\otimes} \nabla_y\right) = 0 \\
\underset{\sim}{\boldsymbol{b}}^{(0)} : \underset{\sim}{\boldsymbol{e}}_0 &= \underset{\sim}{\boldsymbol{b}}^{(0)} : (\underline{\boldsymbol{u}}_0 \otimes \nabla_y) = 0
\end{aligned} \tag{29}$$

- *order* $\boldsymbol{\epsilon}^0$,

$$\underset{\sim}{\boldsymbol{\sigma}}_0 = \underset{\sim}{\boldsymbol{a}}^{(0)} : \underset{\sim}{\boldsymbol{\varepsilon}}_0, \quad \underline{\boldsymbol{s}}_0 = \underset{\sim}{\boldsymbol{b}}^{(0)} : \underset{\sim}{\boldsymbol{e}}_0, \quad \underset{\sim}{\boldsymbol{m}}_0 = 0 \tag{30}$$

- *order* $\boldsymbol{\epsilon}^1$,

$$\underset{\sim}{\boldsymbol{\sigma}}_1 = \underset{\sim}{\boldsymbol{a}}^{(0)} : \underset{\sim}{\boldsymbol{\varepsilon}}_1, \quad \underline{\boldsymbol{s}}_1 = \underset{\sim}{\boldsymbol{b}}^{(0)} : \underset{\sim}{\boldsymbol{e}}_1, \quad \underset{\sim}{\boldsymbol{m}}_1 = \underset{\sim}{\boldsymbol{c}}^{(1)} \vdots \underset{\sim}{\boldsymbol{\kappa}}_{-1} \tag{31}$$

The equation (21) implies that $\underline{\boldsymbol{u}}_0$ does not depend on the local variable $\underline{\boldsymbol{y}}$:

$$\underline{\boldsymbol{u}}_0(\underline{\boldsymbol{x}}, \underline{\boldsymbol{y}}) = \underline{\boldsymbol{U}}_0(\underline{\boldsymbol{x}})$$

At the order $\boldsymbol{\epsilon}^0$, the higher-order stress tensor vanishes, $\underset{\approx}{\boldsymbol{M}}_0 = <\underset{\approx}{\boldsymbol{m}}_0> = 0$.

Finally, the fields $(\underline{\boldsymbol{u}}_1, \underset{\sim}{\boldsymbol{\chi}}_1, \underset{\approx}{\boldsymbol{\sigma}}_0, \underset{\approx}{\boldsymbol{s}}_0, \underset{\approx}{\boldsymbol{m}}_1)$ are solutions of the following auxiliary boundary value problem defined on the unit cell:

$$\begin{cases} \underset{\approx}{\boldsymbol{\varepsilon}}_0 = \underline{\boldsymbol{U}}_0 \overset{s}{\otimes} \nabla_x + \underline{\boldsymbol{u}}_1 \overset{s}{\otimes} \nabla_y, \underset{\sim}{\boldsymbol{e}}_0 = \underline{\boldsymbol{U}}_0 \otimes \nabla_x \\ \qquad + \underline{\boldsymbol{u}}_1 \otimes \nabla_y - \underset{\sim}{\boldsymbol{\chi}}_1 \\ \underset{\approx}{\boldsymbol{\kappa}}_{-1} = \underset{\sim}{\boldsymbol{\chi}}_1 \otimes \nabla_y \\ \underset{\approx}{\boldsymbol{\sigma}}_0 = \underset{\approx\approx}{\boldsymbol{a}}^{(0)} : \underset{\approx}{\boldsymbol{\varepsilon}}_0, \quad \underset{\approx}{\boldsymbol{s}}_0 = \underset{\approx}{\boldsymbol{b}}^{(0)} : \underset{\sim}{\boldsymbol{e}}_0, \quad \boldsymbol{m}_1 = \underset{\approx\approx}{\boldsymbol{c}}^{(1)} : \underset{\approx}{\boldsymbol{\kappa}}_{-1} \\ (\underset{\approx}{\boldsymbol{\sigma}}_0 + \underset{\approx}{\boldsymbol{s}}_0) \cdot \nabla_y = 0, \quad \underset{\approx}{\boldsymbol{m}}_1 \cdot \nabla_y + \underset{\approx}{\boldsymbol{s}}_0 = 0 \end{cases} \tag{32}$$

The boundary conditions of this problem are given by the periodicity requirements for the unknown fields. A series of auxiliary problems similar to (32) can be defined to obtain the solutions at higher orders. It must be noted that these problems must be solved in cascade since, for instance, the solution of (32) requires the knowledge of $\underline{\boldsymbol{U}}_0$. A particular solution $\underset{\sim}{\boldsymbol{\chi}}$ for a vanishing prescribed $\underline{\boldsymbol{U}}_0 \overset{s}{\otimes} \nabla_x$ is $\underset{\sim}{\boldsymbol{\chi}} = \underline{\boldsymbol{U}}_0 \overset{a}{\otimes} \nabla_x$. It follows that the solution $(\underline{\boldsymbol{u}}_1, \underline{\boldsymbol{U}}_0 \overset{a}{\otimes} \nabla_x - \underset{\sim}{\boldsymbol{\chi}}_1)$ to problem (32) depends linearly on $\underline{\boldsymbol{U}}_0 \overset{s}{\otimes} \nabla_x$, up to a translation term, so that

$$\underline{\boldsymbol{u}}^{\boldsymbol{\epsilon}} = \underline{\boldsymbol{U}}_0(\underline{\boldsymbol{x}}) + \boldsymbol{\epsilon}(\underline{\boldsymbol{U}}_1(\underline{\boldsymbol{x}}) + \underset{\approx u}{\boldsymbol{\chi}}^{(1)}(\underline{\boldsymbol{y}}) : (\underline{\boldsymbol{U}}_0 \overset{s}{\otimes} \nabla)) + \ldots \tag{33}$$

$$\underset{\sim}{\boldsymbol{\chi}}^{\boldsymbol{\epsilon}} = \underline{\boldsymbol{U}}_0 \overset{a}{\otimes} \nabla_x + \underset{\approx\boldsymbol{\chi}}{\boldsymbol{\chi}}^{(1)}(\underline{y}) : \underline{\boldsymbol{U}}_0 \overset{s}{\otimes} \nabla + \ldots \tag{34}$$

where concentration tensors $\underset{\approx u}{\boldsymbol{X}}^{(1)}$ and $\underset{\approx\boldsymbol{\chi}}{\boldsymbol{X}}^{(1)}$ have been introduced, the components of which are determined by the successive solutions of the auxiliary problem for unit values of the components of $\underline{\boldsymbol{U}}_0 \overset{s}{\otimes} \nabla$. Concentration tensor $\underset{\approx u}{\boldsymbol{X}}^{(1)}$ is such that its mean value over the unit cell vanishes.

The macroscopic stress tensor is given by

$$\underset{\approx}{\boldsymbol{\Sigma}}_0 = <\underset{\approx}{\boldsymbol{\sigma}}_0> = <\underset{\approx\approx}{\boldsymbol{a}}^{(0)} : (\underset{\approx}{\boldsymbol{1}} + \nabla_x \overset{s}{\otimes} \underset{\approx u}{\boldsymbol{X}}^{(1)})> : (\underline{\boldsymbol{U}}_0 \overset{s}{\otimes} \nabla) = \underset{\approx\approx}{\boldsymbol{A}}^{(1)}_0 : (\underline{\boldsymbol{U}}_0 \overset{s}{\otimes} \nabla) \tag{35}$$

Accordingly, the tensor of effective moduli possesses all symmetries of classical elastic moduli for a Cauchy medium: $A^{(1)}_{0ijkl} = A^{(1)}_{0klij} = A^{(1)}_{0jikl} = A^{(1)}_{0ijlk}$.

The additional second-rank stress tensor can be shown to vanish:

$$\underset{\approx}{\boldsymbol{S}}_0 = <\underset{\approx}{\boldsymbol{s}}_0> = < -\underset{\approx}{\boldsymbol{m}}_1 \cdot \nabla_y> = 0 \tag{36}$$

The effective medium is therefore governed by the single equation:

$$\underset{\approx}{\boldsymbol{\Sigma}}_0 \cdot \nabla = 0 \tag{37}$$

The effective medium turns out to be a Cauchy continuum with symmetric stress tensor.

Homogenization Scheme HS2

For the second homogenization scheme HS2, the equations describing the local behavior are

$$\underset{\approx}{\boldsymbol{\sigma}}^{\boldsymbol{\epsilon}} = \underset{\approx\approx}{\boldsymbol{a}}^{(0)}(\underline{\boldsymbol{y}}) : \underset{\approx}{\boldsymbol{\varepsilon}}^{\boldsymbol{\epsilon}}, \ \underset{\approx}{\boldsymbol{s}}^{\boldsymbol{\epsilon}} = \underset{\approx}{\boldsymbol{b}}^{(0)}(\underline{\boldsymbol{y}}) : \underset{\sim}{\boldsymbol{e}}^{\boldsymbol{\epsilon}}, \quad \text{and} \quad \underset{\approx}{\boldsymbol{m}} = \underset{\approx\approx}{\boldsymbol{c}}^{(2)}(\underline{\boldsymbol{y}}) \vdots \underset{\approx}{\boldsymbol{\kappa}}^{\boldsymbol{\epsilon}} \tag{38}$$

The different steps of the asymptotic analysis are the same as in the previous section for HS1. We will only focus here on the main results. At the order $\boldsymbol{\epsilon}^{-1}$, one gets

$$\underset{\approx\approx}{\boldsymbol{a}}^{(0)} : \underset{\approx}{\boldsymbol{\varepsilon}}_{-1} = 0, \quad \underset{\approx}{\boldsymbol{b}}^{(0)} : \underset{\sim}{\boldsymbol{e}}_{-1} = 0, \quad \underset{\approx\approx}{\boldsymbol{c}}^{(2)} \vdots \underset{\approx}{\boldsymbol{\kappa}}_{-1} = 0 \tag{39}$$

This implies that the gradients of $\underline{\boldsymbol{u}}_0$ and $\underset{\sim}{\boldsymbol{\chi}}_1$ with respect to $\underline{\boldsymbol{y}}$ vanish, so that

$$\underline{\boldsymbol{u}}_0(\underline{x}, \underline{y}) = \underline{\boldsymbol{U}}_0(\underline{x}), \qquad \underset{\sim}{\boldsymbol{\chi}}_1(\underline{x}, \underline{y}) = \underset{\sim}{\boldsymbol{\Xi}}_1(\underline{x}) \tag{40}$$

The fields $(\underline{\boldsymbol{u}}_1, \underset{\sim}{\boldsymbol{\chi}}_1, \underset{\approx}{\boldsymbol{\sigma}}_0, \underset{\approx}{\boldsymbol{m}}_0)$ are solutions of the two following auxiliary boundary

value problems defined on the unit cell:

$$\begin{cases} \underset{\sim}{\boldsymbol{\varepsilon}}_0 = \underline{\boldsymbol{U}}_0 \overset{s}{\otimes} \nabla_x + \underline{\boldsymbol{u}}_1 \overset{s}{\otimes} \nabla_y \\ \underset{\sim}{\boldsymbol{e}}_0 = \underline{\boldsymbol{U}}_0 \otimes \nabla_x + \underline{\boldsymbol{u}}_1 \otimes \nabla_y - \underset{\sim}{\Xi}_1 \\ \underset{\sim}{\boldsymbol{\sigma}}_0 = \underset{\approx}{\boldsymbol{a}}^{(0)} : \underset{\sim}{\boldsymbol{\varepsilon}}_0, \quad \underline{\boldsymbol{s}}_0 = \underset{\approx}{\boldsymbol{b}}^{(0)} : \underset{\sim}{\boldsymbol{e}}_0 \\ (\underset{\sim}{\boldsymbol{\sigma}}_0 + \underline{\boldsymbol{s}}_0) \cdot \nabla_y = 0 \end{cases}$$

$$\begin{cases} \underset{\sim}{\boldsymbol{\kappa}}_0 = \underset{\sim}{\Xi}_1 \otimes \nabla_x + \underset{\sim}{\boldsymbol{\chi}}_2 \nabla_y \\ \underset{\sim}{\boldsymbol{m}}_0 = \underset{\approx}{\boldsymbol{c}}^{(2)} \vdots \underset{\sim}{\boldsymbol{\kappa}}_0, \quad \underset{\sim}{\boldsymbol{m}}_0 \cdot \nabla_y = 0 \end{cases}$$

We are therefore left with two decoupled boundary value problems: the first one with main unknown $\underline{\boldsymbol{u}}_1$ depends linearly on $\underline{\boldsymbol{U}}_0 \overset{s}{\otimes} \nabla_x$ and $\underline{\boldsymbol{U}}_0 \otimes \nabla_x - \underset{\sim}{\Xi}_1$, whereas the second one with unknown $\underset{\sim}{\boldsymbol{\chi}}_2$ is linear in $\underset{\sim}{\Xi}_1 \otimes \nabla_x$. The solutions take the form

$$\begin{aligned} \underline{\boldsymbol{u}}^{\boldsymbol{\epsilon}} &= \underline{\boldsymbol{U}}_0(\underline{x}) + \boldsymbol{\epsilon}(\underline{\boldsymbol{U}}_1(\underline{\boldsymbol{x}}) + \underset{\approx}{\boldsymbol{X}}_u^{(2)}(\underline{\boldsymbol{y}}) : (\underline{\boldsymbol{U}}_0 \overset{s}{\otimes} \nabla) \\ &\quad + \underset{\approx}{\boldsymbol{X}}_{\boldsymbol{\epsilon}}^{(2)}(\underline{\boldsymbol{y}}) : (\underline{\boldsymbol{U}}_0 \otimes \nabla - \underset{\sim}{\Xi}_1)) + \ldots, \\ \underset{\sim}{\boldsymbol{\chi}}^{\boldsymbol{\epsilon}} &= \underset{\sim}{\Xi}_1(\underline{\boldsymbol{x}}) + \boldsymbol{\epsilon}(\underset{\sim}{\Xi}_2(\underline{\boldsymbol{x}}) + \underset{\approx}{\boldsymbol{X}}_{\kappa}^{(2)}(\underline{\boldsymbol{y}}) \vdots (\underset{\sim}{\Xi}_1 \otimes \nabla)) + \ldots \end{aligned} \tag{41}$$

where concentration tensors $\underset{\approx}{\boldsymbol{X}}_u^{(2)}, \underset{\approx}{\boldsymbol{X}}_e^{(2)}$ and $\underset{\approx}{\boldsymbol{X}}_{\kappa}^{(2)}$ have been introduced. Their components are determined by the successive solutions of the auxiliary problem for unit values of the components of $\underline{\boldsymbol{U}}_0 \overset{s}{\otimes} \nabla, \underline{\boldsymbol{U}}_0 \otimes \nabla - \underset{\sim}{\Xi}_1$ and $\underset{\sim}{\Xi}_1 \otimes \nabla_y$. They are such that their mean value over the unit cell vanishes.

The macroscopic stress tensors and effective elastic properties are given by

$$\begin{aligned} \underset{\sim}{\boldsymbol{\Sigma}}_0 &= \langle \underset{\approx}{\boldsymbol{a}}^{(0)} : (\underset{\approx}{1} + \nabla_y \overset{s}{\otimes} \underset{\approx}{\boldsymbol{X}}_u^{(2)}) \rangle : (\underline{\boldsymbol{U}}_0 \overset{s}{\otimes} \nabla) \\ &\quad + \langle \underset{\approx}{\boldsymbol{a}}^{(0)} : (\nabla_y \overset{s}{\otimes} \underset{\approx}{\boldsymbol{X}}_e^{(2)}) \rangle : (\underline{\boldsymbol{U}}_0 \otimes \nabla - \underset{\sim}{\Xi}_1) \\ \underline{\boldsymbol{S}}_0 &= \langle \underline{\boldsymbol{s}}_0 \rangle = \langle \underset{\approx}{\boldsymbol{b}}^{(0)} : (\nabla_y \otimes \underset{\approx}{\boldsymbol{X}}_u^{(2)}) \rangle : (\underline{\boldsymbol{U}}_0 \overset{s}{\otimes} \nabla) \\ &\quad + \langle \underset{\approx}{\boldsymbol{b}}^{(0)} : (\nabla_y \otimes \underset{\approx}{\boldsymbol{X}}_u^{(2)}) \rangle : (\underline{\boldsymbol{U}}_0 \otimes \nabla - \underset{\sim}{\Xi}_1) \\ \underset{\sim}{\boldsymbol{M}}_0 &= \langle \underset{\sim}{\boldsymbol{m}}_0 \rangle = \langle \underset{\approx}{\boldsymbol{c}}^{(2)} \vdots \left(\underset{\approx}{1} + \nabla_y \otimes \underset{\approx}{\boldsymbol{X}}_{\kappa}^{(2)} \right) \rangle \vdots \underset{\sim}{\Xi}_1 \otimes \nabla \end{aligned}$$

None of these tensors vanishes in general, which means that the effective medium is a full micromorphic continuum governed by the balance equations (27).

Homogenization Scheme HS3

In the case HS3, the equations describing the local behavior are

$$\begin{aligned} \underset{\sim}{\boldsymbol{\sigma}}^{\boldsymbol{\epsilon}} &= \underset{\approx}{\boldsymbol{a}}^{(0)}(\underline{\boldsymbol{y}}) : \underset{\sim}{\boldsymbol{\varepsilon}}^{\boldsymbol{\epsilon}}, \underline{\boldsymbol{s}}^{\boldsymbol{\epsilon}} = \underset{\approx}{\boldsymbol{b}}^{(0)}(\underline{\boldsymbol{y}}) : \underset{\sim}{\boldsymbol{e}}^{\boldsymbol{\epsilon}} \\ \underset{\sim}{\boldsymbol{m}}^{\boldsymbol{\epsilon}} &= \boldsymbol{\epsilon}^2 \underset{\approx}{\boldsymbol{c}}^{s(1)}(\underline{\boldsymbol{y}}) \vdots \underset{\sim}{\boldsymbol{\kappa}}^{s\boldsymbol{\epsilon}} + \underset{\approx}{\boldsymbol{c}}^{s(2)}(\underline{\boldsymbol{y}}) \underset{\sim}{\boldsymbol{\kappa}}^{a\boldsymbol{\epsilon}} \end{aligned} \tag{42}$$

At the order $\boldsymbol{\epsilon}^{-1}$, one gets $\underset{\approx}{\boldsymbol{a}}^{(0)} : \underset{\sim}{\boldsymbol{\varepsilon}}_{-1} = 0, \quad \underset{\approx}{\boldsymbol{b}}^{(0)} : \underset{\sim}{\boldsymbol{e}}_{-1} = 0, \quad \underset{\approx}{\boldsymbol{c}}^{a(2)} \vdots \underset{\sim}{\boldsymbol{\kappa}}_{-1}^{a} = 0.$

This implies that the gradients of $\underline{\boldsymbol{u}}_0$ and $\underset{\sim}{\boldsymbol{\chi}}_1^0$ with respect to $\underline{\boldsymbol{y}}$ vanish, so that

$$\underline{\boldsymbol{u}}_0(\underline{\boldsymbol{x}}, \underline{\boldsymbol{y}}) = \underline{\boldsymbol{U}}_0(\underline{\boldsymbol{x}}), \quad \underset{\sim}{\boldsymbol{\chi}}_1^a(\underline{\boldsymbol{x}}, \underline{\boldsymbol{y}}) = \underset{\sim}{\Xi}_1^a(\underline{\boldsymbol{x}}) \tag{43}$$

The fields $(\underline{\boldsymbol{u}}_1, \underline{\boldsymbol{\chi}}_1^s, \underline{\boldsymbol{\chi}}_2^a, \underline{\boldsymbol{\chi}}_3^a, \underset{\sim}{\boldsymbol{\sigma}}_0, \underline{\boldsymbol{s}}_0, \underset{\sim}{\boldsymbol{m}}_0, \underset{\sim}{\boldsymbol{m}}_1)$ are solutions of the following auxiliary boundary value problem defined on the unit cell:

$$\begin{cases} \underset{\sim}{\boldsymbol{\varepsilon}}_0 = \underline{\boldsymbol{U}}_0 \overset{s}{\otimes} \nabla_x + \underline{\boldsymbol{u}}_1 \overset{s}{\otimes} \nabla_y, \underset{\sim}{\boldsymbol{e}}_0 \underline{\boldsymbol{U}}_0 \otimes \nabla_x \\ \qquad + \underline{\boldsymbol{u}}_1 \otimes \nabla_y - \underset{\sim}{\Xi}_1^a - \underset{\sim}{\boldsymbol{\chi}}_1^s \\ \underset{\sim}{\boldsymbol{\kappa}}_{-1}^s = \underset{\sim}{\boldsymbol{\chi}}_1^s \otimes \nabla_y, \underset{\sim}{\boldsymbol{\kappa}}_{-1}^s = \underset{\sim}{\Xi}_1^a \otimes \nabla_x \underset{\sim}{\boldsymbol{\chi}}_2^a \otimes \nabla_y \\ \underset{\sim}{\boldsymbol{\kappa}}_1^a = \underset{\sim}{\boldsymbol{\chi}}_3^a \otimes \nabla_y \\ \underset{\sim}{\boldsymbol{\sigma}}_0 = \underset{\approx}{\boldsymbol{a}}^{(0)} : \underset{\sim}{\boldsymbol{\varepsilon}}_0, \quad \underline{\boldsymbol{s}}_0 = \underset{\approx}{\boldsymbol{b}}^{(0)} : \underset{\sim}{\boldsymbol{e}}_0 \\ \underset{\sim}{\boldsymbol{m}}_0 = \underset{\approx}{\boldsymbol{c}}^{a(2)} \vdots \underset{\sim}{\boldsymbol{\kappa}}_0^a, \quad \underset{\sim}{\boldsymbol{m}}_1 = \underset{\approx}{\boldsymbol{c}}^{s(1)} \vdots \underset{\sim}{\boldsymbol{\kappa}}_{-1}^s + \underset{\approx}{\boldsymbol{c}}^{s(2)} \vdots \underset{\sim}{\boldsymbol{\kappa}}_1^a \\ (\underset{\sim}{\boldsymbol{\sigma}}_0 + \underline{\boldsymbol{s}}_0) \cdot \nabla_y = 0, \quad \underset{\sim}{\boldsymbol{m}}_0 \cdot \nabla_y = 0, \\ \underset{\sim}{\boldsymbol{m}}_0 \cdot \nabla_x + \underset{\sim}{\boldsymbol{m}}_1 \cdot \nabla_y + \underline{\boldsymbol{s}}_0 = 0 \end{cases}$$

This complex problem can be seen to depend linearly on $\underline{\boldsymbol{U}}_0 \overset{s}{\otimes} \nabla, \underline{\boldsymbol{U}}_0 \overset{a}{\otimes} -\underset{\sim}{\Xi}_1^a$ and $\underset{\sim}{\Xi}_1^a \otimes \nabla$. The solutions take the form

$$\begin{aligned} \underline{\boldsymbol{u}}^{\boldsymbol{\epsilon}} &= \underline{\boldsymbol{U}}_0(\underline{\boldsymbol{x}}) + \boldsymbol{\epsilon}(\underline{\boldsymbol{U}}_1(\underline{\boldsymbol{x}}) + \underset{\approx}{\boldsymbol{X}}_u^{(3)}(\underline{\boldsymbol{y}}) : \\ &\quad (\underline{\boldsymbol{U}}_0 \overset{s}{\otimes} \nabla + \underset{\approx}{\boldsymbol{X}}_e^{(3)}(\underline{\boldsymbol{y}}) : \underline{\boldsymbol{U}}_0 \overset{a}{\otimes} \nabla - \underset{\sim}{\Xi}_1^a)) + \ldots \end{aligned} \tag{44}$$

$$\underset{\approx}{\boldsymbol{\chi}}^{\boldsymbol{\epsilon}} = \underset{\approx}{\Xi}_1(\underline{x}) + \boldsymbol{\epsilon}(\underset{\approx}{\Xi}_2(\underline{x}) + \underset{\approx}{\boldsymbol{X}}^{(3)}_{\kappa}(\underline{y}) \vdots \underset{\approx}{\Xi}^a_1 \otimes \nabla)) + \ldots \tag{45}$$

where concentration tensors $\underset{\approx}{\boldsymbol{X}}^{(3)}_{u}, \underset{\approx}{\boldsymbol{X}}^{(3)}_{e}$ and $\underset{\approx}{\boldsymbol{X}}^{(3)}_{\kappa}$ have been introduced. Their components are determined by the successive solutions of the auxiliary problem for unit values of the components of $\underline{\boldsymbol{U}}_0 \overset{s}{\otimes} \nabla, \underline{\boldsymbol{U}}_0 \overset{a}{\otimes} \nabla - \underset{\approx}{\Xi}^a_1$ and $\underset{\approx}{\Xi}^a_1 \otimes \nabla_y$. They are such that their mean value over the unit cell vanishes.

The macroscopic stress tensors and effective elastic properties are given by

$$\begin{aligned}
\underset{\approx}{\boldsymbol{\Sigma}}_0 &= <\underset{\approx}{\boldsymbol{a}}^{(0)} : (\underset{\approx}{1}\nabla_x \overset{s}{\otimes} \underset{\approx}{\boldsymbol{X}}^{(3)}_{u})> : (\underline{\boldsymbol{U}}_0 \overset{s}{\otimes} \nabla) + <\underset{\approx}{\boldsymbol{a}}^{(0)} : \\
&\quad (\nabla_x \overset{s}{\otimes} \underset{\approx}{\boldsymbol{X}}^{(3)}_{u})> : (\underline{\boldsymbol{U}}_0 \overset{a}{\otimes} \nabla - \underset{\approx}{\Xi}^a_1) \\
\underset{\approx}{\boldsymbol{S}}_0 &= <\underset{\approx}{\boldsymbol{s}}_0> = <\underline{\boldsymbol{b}}^{(0)} : (\nabla_x \otimes \underset{\approx}{\boldsymbol{X}}^{(3)}_{u})> : (\underline{\boldsymbol{U}}_0 \overset{s}{\otimes} \nabla) \\
&\quad + <\underline{\boldsymbol{b}}^{(0)} : (\nabla_x \otimes \underset{\approx}{\boldsymbol{X}}^{(3)}_{e})> : (\underline{\boldsymbol{U}}_0 \overset{a}{\otimes} \nabla - \underset{\approx}{\Xi}^a_1) \\
\underset{\approx}{\boldsymbol{M}}_0 &= <\underset{\approx}{\boldsymbol{m}}_0> = <\underset{\approx}{\boldsymbol{c}}^{a(2)} \vdots (\underset{\approx}{1}\nabla_y \overset{s}{\otimes} \underset{\approx}{\boldsymbol{X}}^{(3)}_{\kappa})> \vdots \underset{\approx}{\Xi}^a_1 \otimes \nabla
\end{aligned}$$

They must fulfill the balance equations (27). Note that $\underset{\approx}{\boldsymbol{m}}_0$ and therefore $\underset{\approx}{\boldsymbol{M}}_0$ are skew symmetric with respect to their first two indices. The averaged equation of balance of moment of momentum implies that $\underset{\approx}{\boldsymbol{S}}_0$ is symmetric. The macroscopic degrees of freedom are the displacement field $\underline{\boldsymbol{U}}_0$ and the symmetric strain tensor $\underset{\approx}{\Xi}^a_1$. The found balance and constitutive equations are therefore that of a Cosserat effective medium. The more classical form of the Cosserat theory is retrieved once one rewrites the previous equations using the axial vector associated to the skew–symmetric tensor $\underset{\approx}{\Xi}^a$ [6].

Homogenization Scheme HS4

In the last considered case, the equations describing the local behavior are

$$\underset{\approx}{\boldsymbol{\sigma}}^{\boldsymbol{\epsilon}} = \underset{\approx}{\boldsymbol{a}}^{(0)}(\underline{\boldsymbol{y}}) : \underset{\approx}{\boldsymbol{\epsilon}}^{\boldsymbol{\epsilon}}, \qquad \underline{\boldsymbol{s}}^{\boldsymbol{\epsilon}} = \underline{\boldsymbol{b}}^{(0)}(\underline{\boldsymbol{y}}) : \underline{\boldsymbol{e}}^{\boldsymbol{\epsilon}}, \qquad \underset{\approx}{\boldsymbol{m}}^{\boldsymbol{\epsilon}} = \underset{\approx}{\boldsymbol{c}}^{s(2)}(\underline{\boldsymbol{y}}) \vdots \underset{\approx}{\boldsymbol{\kappa}}^{a\boldsymbol{\epsilon}} \tag{46}$$

At the order $\boldsymbol{\epsilon}^{-1}$, one gets $\underset{\approx}{\boldsymbol{a}}^{(0)} : \underset{\approx}{\boldsymbol{\epsilon}}_{-1} = 0$, $\underline{\boldsymbol{b}}^{(0)} : \underline{\boldsymbol{e}}_{-1} = 0$, $\underset{\approx}{\boldsymbol{c}}^{s(2)} \vdots \underset{\approx}{\boldsymbol{\kappa}}^s_{-1} = 0$

This implies that the gradients of $\underline{\boldsymbol{u}}_0$ and $\underset{\approx}{\boldsymbol{\chi}}^s_1$ with respect to $\underline{\boldsymbol{y}}$ vanish, so that

$$\underline{\boldsymbol{u}}_0(\underline{\boldsymbol{x}}, \underline{\boldsymbol{y}}) = \underline{\boldsymbol{U}}_0(\underline{\boldsymbol{x}}), \qquad \underset{\approx}{\boldsymbol{\chi}}^s_1(\underline{\boldsymbol{x}}, \underline{\boldsymbol{y}}) = \underset{\approx}{\Xi}^s_1(\underline{\boldsymbol{x}}) \tag{47}$$

The fields $(\underline{\boldsymbol{u}}_1, \underset{\approx}{\boldsymbol{\chi}}^a_1, \underset{\approx}{\boldsymbol{\chi}}^s_2, \underset{\approx}{\boldsymbol{\chi}}^s_3, \underset{\approx}{\boldsymbol{\sigma}}_0, \underline{\boldsymbol{s}}_0, \underset{\approx}{\boldsymbol{m}}_0, \underset{\approx}{\boldsymbol{m}}_1)$ are solutions of the following auxiliary boundary value problem defined on the unit cell:

$$\left\{\begin{array}{l}
\underset{\approx}{\boldsymbol{\epsilon}}_0 = \underline{\boldsymbol{U}}_0 \overset{s}{\otimes} \nabla_x + \underline{\boldsymbol{u}}_1 \overset{s}{\otimes} \nabla_y, \underline{\boldsymbol{e}}_0 = \underline{\boldsymbol{U}}_0 \otimes \nabla_x \\
\qquad + \underline{\boldsymbol{u}}_1 \otimes \nabla_y - \underset{\approx}{\Xi}^s_1 - \underset{\approx}{\boldsymbol{\chi}}^a_1 \\
\underset{\approx}{\boldsymbol{\kappa}}^a_{-1} = \underset{\approx}{\boldsymbol{\chi}}^a_1 \otimes \nabla_y, \underset{\approx}{\boldsymbol{\kappa}}^s_0 = \underset{\approx}{\Xi}^s_1 \otimes \nabla_x + \underset{\approx}{\boldsymbol{\chi}}^s_2 \otimes \nabla_y, \underset{\approx}{\boldsymbol{\kappa}}^a_{-1} \\
\qquad = \underset{\approx}{\boldsymbol{\chi}}^s_2 \otimes \nabla_x + \underset{\approx}{\boldsymbol{\chi}}^s_3 \otimes \nabla_y \\
\underset{\approx}{\boldsymbol{\sigma}}_0 = \underset{\approx}{\boldsymbol{a}}^{(0)} : \underset{\approx}{\boldsymbol{\epsilon}}_0, \quad \underline{\boldsymbol{s}}_0 = \underline{\boldsymbol{b}}^{(0)} : \underline{\boldsymbol{e}}_0 \\
\underset{\approx}{\boldsymbol{m}}_0 = \underset{\approx}{\boldsymbol{c}}^{s(2)} \vdots \underset{\approx}{\boldsymbol{\kappa}}^s_0, \quad \underset{\approx}{\boldsymbol{m}}_1 = \underset{\approx}{\boldsymbol{c}}^{a(1)} \vdots \underset{\approx}{\boldsymbol{\kappa}}^a_{-1} + \underset{\approx}{\boldsymbol{c}}^{s(2)} \underset{\approx}{\boldsymbol{\kappa}}^s_1 \\
(\underset{\approx}{\boldsymbol{\sigma}}_0 + \underline{\boldsymbol{s}}_0) \cdot \nabla_y = 0, \underset{\approx}{\boldsymbol{m}}_0 \cdot \nabla_y = 0, \underset{\approx}{\boldsymbol{m}}_0 \cdot \nabla_x \\
\qquad + \underset{\approx}{\boldsymbol{m}}_1 \cdot \nabla_y + \underline{\boldsymbol{s}}_0 = 0
\end{array}\right.$$

This complex problem can be seen to depend linearly on $\underline{\boldsymbol{U}}_0 \overset{s}{\otimes} \nabla, \underline{\boldsymbol{U}}_0 \overset{s}{\otimes} \nabla - \underset{\approx}{\Xi}^s_1$ and $\underset{\approx}{\Xi}^s_1 \otimes \nabla$. The solutions take the form

$$\begin{aligned}
\underline{u}^{\boldsymbol{\epsilon}} \underline{\boldsymbol{U}}_0(\underline{\boldsymbol{x}}) &+ \boldsymbol{\epsilon}(\underline{\boldsymbol{U}}_1(\underline{\boldsymbol{x}}) \underset{\approx}{\boldsymbol{X}}^{(4)}_{u}(\underline{\boldsymbol{y}}) : (\underline{\boldsymbol{U}}_1 \overset{s}{\otimes} \nabla) \\
&+ \underset{\approx}{\boldsymbol{X}}^{(4)}_{e} : (\underline{\boldsymbol{U}}_1 \overset{s}{\otimes} \nabla - \underset{\approx}{\Xi}^s_1)) + \ldots \\
\underset{\approx}{\boldsymbol{\chi}}^{\boldsymbol{\epsilon}} &= \underset{\approx}{\Xi}_1(\underline{\boldsymbol{x}}) + \boldsymbol{\epsilon}(\underset{\approx}{\Xi}_2(\underline{\boldsymbol{x}}) + \underset{\approx}{\boldsymbol{X}}^{(4)}_{\kappa}(\underline{\boldsymbol{y}}) \vdots (\underset{\approx}{\Xi}^s_1 \otimes \nabla)) + \ldots
\end{aligned}$$

where concentration tensors $\underset{\approx}{\boldsymbol{X}}^{(4)}_{u}, \underset{\approx}{\boldsymbol{X}}^{(4)}_{e}$ and $\underset{\approx}{\boldsymbol{X}}^{(4)}_{\kappa}$ have been introduced. Their components are determined by the successive solutions of the auxiliary problem for unit values of the components of $\underline{\boldsymbol{U}}_0 \overset{s}{\otimes} \nabla, \underline{\boldsymbol{U}}_0 \overset{s}{\otimes} \nabla - \underset{\approx}{\Xi}^s_1$ and $\underset{\approx}{\Xi}^s_1 \otimes \nabla_y$. They are such that their mean value over the unit cell vanishes.

The macroscopic stress tensors and effective elastic properties are given by

$$\underset{\approx}{\boldsymbol{\Sigma}}_0 = <\underset{\approx}{\boldsymbol{a}}^{(0)} : (\underset{\approx}{1} + \nabla_x \overset{s}{\otimes} \underset{\approx}{\boldsymbol{X}}_u^{(4)})> : (\underline{\boldsymbol{U}}_0 \overset{s}{\otimes} \nabla)$$
$$+ <\underset{\approx}{\boldsymbol{a}}^{(0)} : (\nabla_y \overset{s}{\otimes} \underset{\approx}{\boldsymbol{X}}_e^{(4)})> : (\underline{\boldsymbol{U}}_0 \overset{s}{\otimes} \nabla - \underset{\approx}{\Xi}_1^s)$$
$$\underset{\approx}{\boldsymbol{S}}_0 = <\underline{\boldsymbol{s}}_0> = <\underset{\approx}{\boldsymbol{b}}^{(0)} : (\nabla_y \overset{s}{\otimes} \underset{\approx}{\boldsymbol{X}}_u^{(4)})> : (\underline{\boldsymbol{U}}_0 \overset{s}{\otimes} \nabla)$$
$$+ <\underset{\approx}{\boldsymbol{b}}^{(0)}> : (\underline{\boldsymbol{U}}_0 \overset{s}{\otimes} \nabla - \underset{\approx}{\Xi}_1^s)$$
$$\underset{\approx}{\boldsymbol{M}}_0 = <\underset{\approx}{\boldsymbol{m}}_0> = <\underset{\approx\approx}{\boldsymbol{c}}^{s(2)} \vdots (\underset{\approx}{1} + \nabla_y \otimes \underset{\kappa}{\boldsymbol{X}}^{(4)})> \vdots (\underset{\approx}{\Xi}_1^s \otimes \nabla)$$

They must fulfill the balance equations (27). Note that $\underset{\approx}{\boldsymbol{m}}_0$ and therefore $\underset{\approx}{\boldsymbol{M}}_0$ are

symmetric with respect to their first two indices. The averaged equation of balance of moment of momentum implies that $\underset{\approx}{\boldsymbol{S}}_0 = -<\underset{\approx}{\boldsymbol{m}}_0> \cdot \nabla$ is symmetric. The macroscopic degrees of freedom are the displacement field $\underline{\boldsymbol{U}}_0$ and the symmetric strain tensor $\underset{\approx}{\Xi}_1^s$.

Such a continuum is called a microstrain medium [8].

As a conclusion, depending on the relative contributions of the various intrinsic length scales of the micromorphic continuum, different effective media are obtained, as summarized in Table 1. The effective medium can be of micromorphic, microstrain, Cosserat, or Cauchy type. A similar situation is found in the case of the homogenization of heterogeneous Cosserat media. Depending on the ratio between the Cosserat characteristic length l_a and the sizes l, L, the effective medium will be a Cauchy continuum with body couples or a full Cosserat continuum [9].

Asymptotic Analysis of Heterogeneous Micromorphic Elastic Solids, Table 1 Homogenization of heterogeneous micromorphic media: nature of the homogeneous equivalent medium depending on the values of the intrinsic lengths of the constituents

Homogenization scheme	Characteristic lengths	Effective medium
HS1	$l_s \sim l, l_a \sim l$	Cauchy
HS2	$l_s \sim L, l_a \sim L$	Micromorphic
HS3	$l_s \sim l, l_a \sim L$	Cosserat
HS4	$l_s \sim L, l_a \sim l$	Microstrain

Applications

The approach is applied to two important classes of materials, namely, composite and polycrystalline materials. The auxiliary problems evidenced in the previous homogenization method are solved by means of the finite element method with well-suited boundary conditions.

Fiber or Particle Composites

The reinforcement induced by fibers and particles embedded in a matrix material depends on their volume fraction and arrangement but also on their size compared to the characteristic size of the microstructure elements of the matrix. The former effect is satisfactorily accounted for by standard homogenization methods. The latter can be described by considering that both the matrix and inclusions are Cosserat materials having different intrinsic length l_a. The effective properties of such a composite are found by solving auxiliary problems of the unit cell. The unit cell corresponding to a square arrangement of fibers with a volume fraction of 0.4 is shown in Fig. 1. According to scheme HS3, the displacement microrotation fields are searched for in the following form in the unit cell:

$$\underline{\boldsymbol{u}}(\underline{\boldsymbol{y}}) = \underset{\approx}{\boldsymbol{E}} \cdot \underline{\boldsymbol{y}} + \underline{\boldsymbol{v}}(\underline{\boldsymbol{y}})$$
$$\underset{\approx}{\boldsymbol{\chi}}^a(\underline{\boldsymbol{y}}) = \underset{\approx}{\boldsymbol{K}} \cdot \underline{\boldsymbol{y}} + \underline{\boldsymbol{\xi}}^a(\underline{\boldsymbol{y}})$$

The fluctuation displacement $\underline{\boldsymbol{v}}$ and the skew–symmetric microrotation fluctuation $\underline{\boldsymbol{\xi}}^a$ are periodic. The macroscopic deformation $\underset{\approx}{\boldsymbol{E}}$ and curvature $\underset{\approx}{\boldsymbol{K}}$ are prescribed to the unit cell. The computation of the mean elastic energy contained in the deformed unit cell is used to identify the microscopic elastic moduli. According to Hill–Mandel's lemma that can be derived from the previous homogenization procedure, the macroscopic strain energy is the mean value of the local one over the volume element:

$$\underset{\approx}{\boldsymbol{\Sigma}} : \underset{\approx}{\boldsymbol{E}} + \underset{\approx}{\boldsymbol{M}} \vdots \underset{\approx}{\boldsymbol{M}} = <\underset{\approx}{\boldsymbol{\sigma}} : \underset{\approx}{\boldsymbol{e}} + \underset{\approx}{\boldsymbol{m}} \vdots \underset{\approx}{\boldsymbol{\kappa}}> \qquad (48)$$

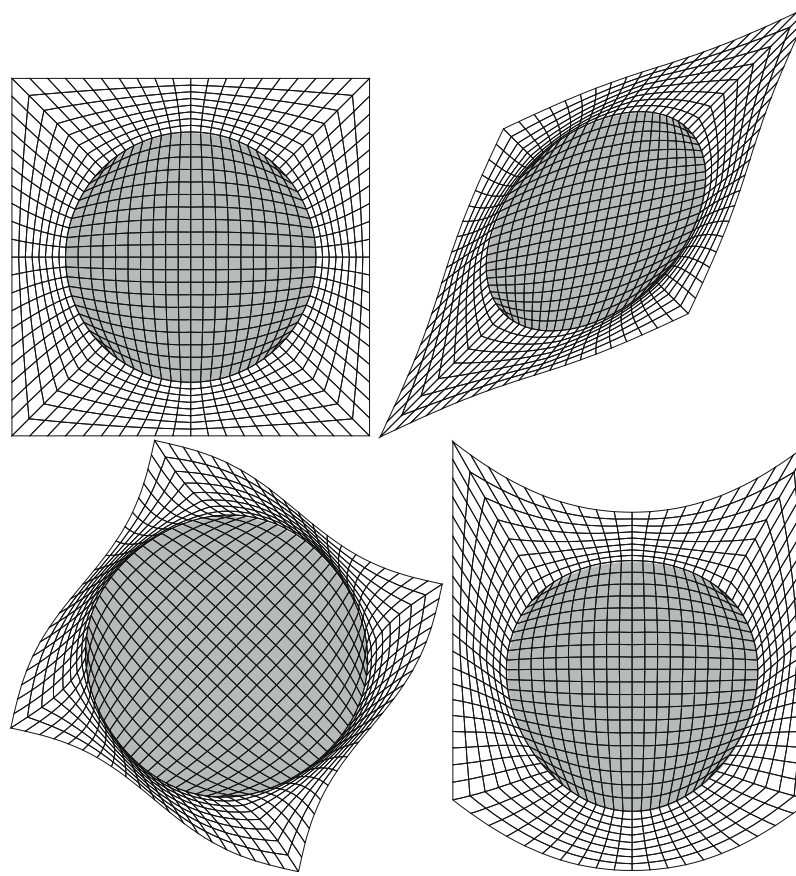

Asymptotic Analysis of Heterogeneous Micromorphic Elastic Solids, Fig. 1 Solution of the auxiliary problem in the homogenization of Cosserat fiber composites: unit cell of the composite material (*top right*), simple shear (*top right*), mean relative rotation (*bottom left*), and mean curvature (*bottom right*), under plane strain conditions

Figure 1 shows how mean shear, relative rotation, and curvature can be applied successively to a unit cell.

Polycrystalline Materials

The previous homogenization method can be extended, at least in a heuristic way, to nonlinear micromorphic constitutive equations in order to predict size effects in the plasticity of polycrystals. The reader is referred to [5] for a detailed presentation of such models and a more complete description of polycrystal homogenization. The computation of polycrystalline aggregates based on standard crystal plasticity models follows the rule of classical homogenization theory in the sense that a mean strain is prescribed to a volume element of polycrystalline materials using suitable boundary conditions like strain-based, stress-based, or periodic ones. The structure of the boundary value problem is modified if a generalized continuum approach is used inside the considered volume element. The grain boundary conditions represent an important new feature of the theory. At any interface of a micromorphic continuum, there may exist some jump conditions for the degrees of freedom of the theory and the associated reactions, namely, the simple and double tractions. As a first approximation, however, the displacement vector and the microdeformation tensor can be assumed to be continuous at grain boundaries. As a result, the simple and double tractions also are continuous. The continuity of microdeformation is a new grain boundary condition that does not exist in classical crystal plasticity. It will generate boundary layers at grain boundaries which are essential

for the observed size effects [5, 10]. In that way, material parameters of the micromorphic model can be identified in order to quantitatively describe the well-known Hall–Petch relationship which is a direct correspondence between the overall stress and the grain size at a given plastic strain.

References

1. Ashby M (1970) The deformation of plastically non–homogeneous materials. Philos Mag 21:399–424
2. Boutin C (1996) Microstructural effects in elastic composites. Int J Solids Struct 33:1023–1051
3. Chen Y, Lee J (2003) Connecting molecular dynamics to micromorphic theory. (I) instantaneous and averaged mechanical variables. Physica A 322:359–376
4. Claus W, Eringen A (1971) Dislocation dispersion of elastic waves. Int J Engin Sci 9:605–610
5. Cordero NM, Forest S, Busso EP, Berbenni S, Cherkaoui M (2012) Grain size effects on plastic strain and dislocation density tensor fields in metal polycrystals. Comput Mater Sci 52:7–13
6. Eringen A (1999) Microcontinuum field theories. Springer, New York
7. Eringen A, Suhubi E (1964) Nonlinear theory of simple microelastic solids. Int J Engng Sci 2(189–203):389–404
8. Forest S, Sievert R (2006) Nonlinear microstrain theories. Int J Solids Struct 43:7224–7245
9. Forest S, Pradel F, Sab K (2001) Asymptotic analysis of heterogeneous Cosserat media. Int J Solids Struct 38:4585–4608
10. Gurtin M (2002) A gradient theory of single–crystal viscoplasticity that accounts for geometrically necessary dislocations. J Mech Physics Solids 50:5–32
11. Lebée A, Sab K (2010) A cosserat multiparticle model for periodically layered materials. I J Solids Struct 37:293–297
12. Liu X, Hu G (2003) Inclusion problem of microstretch continuum. Int J Engin Sci 42:849–860
13. Mindlin R (1964) Micro–structure in linear elasticity. Arch Rat Mech Anal 16:51–78
14. Mühlhaus H (1995) Continuum models for materials with microstructure. Wiley, Chichester
15. Sanchez-Palencia E (1974) Comportement local et macroscopique d'un type de milieux physiques hétérogènes. Int J Engin Sci 12:331–351
16. Sanchez-Palencia E, Zaoui A (1987) Homogenization techniques for composite media, vol 272, Lecture Notes in Physics. Springer, Berlin
17. Smyshlyaev V, Fleck N (1994) Bounds and estimates for linear composites with strain gradient effects. J Mech Physics Solids 42:1851–1882
18. Suquet P (1997) Continuum micromechanics, vol 377, CISM courses and lectures. Springer, Udine \Berlin
19. Xun F, Hu G, Huang Z (2004) Size–dependence of overall in–plane plasticity for fiber composites. Int J Solids Struct 41:4713–4730
20. Zhu H, Zbib H, Aifantis E (1997) Strain gradients and continuum modeling of size effect in metal matrix composites. Acta Mechanica 121:165–176

Asymptotic Behavior in Time

Maria Grazia Naso
Università degli Studi di Brescia, Brescia, Italy

Synonyms

Decay rate; Longtime behavior in thermoelasticity

Overview

We are interested to study the longtime behavior for a linear one-dimensional thermoelastic system where the hyperbolic elastic system is joined with the parabolic heat equation. By some results in semigroup theory, we prove the exponential decay of the solutions related to the associated initial boundary value problem. For a detailed study in more general cases, some references are given at the end of this section.

A Simple Model in Thermoelasticity

The One-Dimensional Linear Thermoelastic System

For $T > 0$, we consider the following one-dimensional linear thermoelastic system:

$$u_{tt} - \alpha\, u_{xx} + \gamma\, \theta_x = 0 \qquad \text{in } (0,\ell) \times (0,T) \quad (1)$$

$$\theta_t - k\, \theta_{xx} + \gamma\, u_{xt} = 0 \qquad \text{in } (0,\ell) \times (0,T) \quad (2)$$

supplemented with initial conditions

$$u(x,0) = u_0(x), \quad u_t(x,0) = u_1(x) \qquad \text{in } (0,\ell) \tag{3}$$

$$\theta(x,0) = \theta_0(x) \qquad \text{in } (0,\ell) \tag{4}$$

and Dirichlet boundary conditions at both ends

$$u(0,t) = 0, \quad u(\ell,t) = 0 \qquad \text{in } (0,T) \tag{5}$$

$$\theta(0,t) = 0, \quad \theta(\ell,t) = 0 \qquad \text{in } (0,T) \tag{6}$$

in the unknown variables $u = u(x,t) : (0,\ell) \times (0,T) \to \mathbb{R}$ and $\theta = \theta(x,t) : (0,\ell) \times (0,T) \to \mathbb{R}$. With regard to the physical meaning of the variables in play, u represents the longitudinal deflection of a bar of length ℓ with unit reference density, while θ actually arises from the temperature variation with respect to a reference value. Constants α, $k \in \mathbb{R}^+$ and $\gamma \in \mathbb{R}\backslash\{0\}$ depend on the material properties. Here and in what follows, the subscripts x and t indicate partial derivatives.

For a detailed derivation of the modeling under consideration, we refer, e.g., to [2, 4].

Solutions in appropriate Hilbert spaces will be found by means of semigroup theory (see entry "▶ Existence and Uniqueness: Solutions of Thermoelastodynamics"). Without loss of generality, throughout this section, we choose $\alpha = 1$.

Notation

Putting $\Omega = (0,\ell)$, let us introduce the space

$$\mathcal{H} = H_0^1(\Omega) \times L^2(\Omega) \times L^2(\Omega)$$

with norm

$$\|(u,u_t,\theta)\|_{\mathcal{H}} = \left(\|u_x\|^2 + \|u_t\|^2 + \|\theta\|^2\right)^{1/2},$$

where

$$\|\varphi\| = \left[\int_0^\ell |\varphi(x)|^2\,dx\right]^{1/2}$$

is the L^2 norm in Ω. Furthermore, we denote by $\langle\cdot,\cdot\rangle_{\mathcal{H}}$ and $\langle\cdot,\cdot\rangle$ the inner products in $\mathcal{H}$ and L^2, respectively.

Formulation of the Problem

Setting $v = u_t$, $z = (u,v,\theta)^{\mathrm{T}}$, and $z_0 = (u_0,u_1,\theta_0)^{\mathrm{T}} \in \mathcal{H}$, system (1)–(2) can be rewritten as an evolution system in $\mathcal{H}$ of the form

$$z_t(t) = Az(t), \qquad t > 0 \tag{7}$$

$$z(0) = z_0 \tag{8}$$

The operator $A : \mathcal{D}(A) \subseteq \mathcal{H} \to \mathcal{H}$ is defined as

$$A = \begin{bmatrix} 0 & I & 0 \\ (.)_{xx} & 0 & -\gamma(.)_x \\ 0 & -\gamma(.)_x & k(.)_{xx} \end{bmatrix} \tag{9}$$

with domain

$$\mathcal{D}(A) = \left[H^2(\Omega) \cap H_0^1(\Omega)\right] \times H_0^1(\Omega) \times \left[H^2(\Omega) \cap H_0^1(\Omega)\right]$$

We can observe that A is a densely defined operator from $\mathcal{D}(A)$ to $\mathcal{H}$.

Useful Results in the Theory of Semigroups

We conclude this introductory part with a necessary and sufficient condition for a C_0-semigroup being exponentially stable. For a detailed exposition of the subject, the reader is referred to, e.g., [9, 25, 30].

Theorem 1. *Let $S(t) = e^{At}$ be a C_0 -semigroup of contractions (i.e., a C_0-semigroup $S(t) = e^{tA}$ such that $\|S(t)\|_{\mathcal{L}(\mathcal{H})} \le 1$ for every $t \ge 0$) on a Hilbert space $\mathcal{H}$. Then, $S(t)$ is exponentially stable if and only if*

$$\rho(A) \supseteq \{i\beta, \quad \beta \in \mathbb{R}\} =: i\mathbb{R} \tag{10}$$

and

$$\overline{\lim_{|\beta|\to\infty}} \left\|(i\beta I - A)^{-1}\right\|_{\mathcal{L}(\mathcal{H})} < +\infty \tag{11}$$

hold.

Here $\rho(A)$ denotes the resolvent set of A.

Exponential Decay

The presentation of this section is essentially based on [18, 19]. To study the exponential decay of the energy associated to system (1)–(6), we now analyze if the assumptions of Theorem 1 are satisfied.

- $$\rho(A) \supseteq \{i\beta, \quad \beta \in \mathbb{R}\} =: i\mathbb{R}$$

(i) Recalling that $0 \in \rho(A)$ (see entry "▶ Existence and Uniqueness: Solutions of Thermoelastodynamics") and by the contraction mapping theorem, it follows that for any $\beta \in \mathbb{R}$ with $|\beta| < \left\|A^{-1}\right\|^{-1}$, the operator

$$i\beta I - A = A(i\beta I A^{-1} - I)$$

is invertible. Moreover, $\left\|(i\beta I - A)^{-1}\right\|_{\mathcal{L}(\mathcal{H})}$ is a continuous function of β in the interval $\left(-\left\|A^{-1}\right\|^{-1}_{\mathcal{L}(\mathcal{H})}, \left\|A^{-1}\right\|^{-1}_{\mathcal{L}(\mathcal{H})}\right)$.

(ii) If $\sup_{|\beta|<\|A^{-1}\|^{-1}_{\mathcal{L}(\mathcal{H})}} \left\|(i\beta I - A)^{-1}\right\|_{\mathcal{L}(\mathcal{H})} = M < +\infty$, then, by the contraction mapping theorem, the operator

$$i\beta I - A = (i\beta_0 I - A) \times \left[I + i(\beta - \beta_0)(i\beta_0 I - A)^{-1}\right]$$

with $|\beta_0| < \left\|A^{-1}\right\|^{-1}$ is invertible for $|\beta - \beta_0| < \frac{1}{M}$. It turns out that by choosing $|\beta_0|$ as close to $\left\|A^{-1}\right\|^{-1}_{\mathcal{L}(\mathcal{H})}$ as we can, we find that

$$\left\{\beta : \quad |\beta| < \left\|A^{-1}\right\|^{-1}_{\mathcal{L}(\mathcal{H})} + \frac{1}{M}\right\} \subset \rho(A),$$

and $\left\|(i\beta I - A)^{-1}\right\|_{\mathcal{L}(\mathcal{H})}$ is a continuous function of β in the interval

$$\left(-\left\|A^{-1}\right\|^{-1}_{\mathcal{L}(\mathcal{H})} - \frac{1}{M}, \left\|A^{-1}\right\|^{-1}_{\mathcal{L}(\mathcal{H})} + \frac{1}{M}\right)$$

(iii) By argument in (ii), it follows that if (10) is not true, then there exists $\omega \in \mathbb{R}$ with $\left\|A^{-1}\right\|^{-1}_{\mathcal{L}(\mathcal{H})} \leq |\omega| < +\infty$ such that

$$\{i\beta : \quad |\beta| < |\omega|\} \subset \rho(A)$$

and

$$\sup_{|\beta|<|\omega|} \left\|(i\beta I - A)^{-1}\right\|_{\mathcal{L}(\mathcal{H})} = +\infty$$

It turns out that there exist a sequence $\beta_n \in \mathbb{R}$ with $\beta_n \to \omega$, $|\beta_n| < |\omega|$ and a sequence of complex vector functions $y_n = (u_n, v_n, \theta_n) \in \mathcal{D}(A)$ with $\|y_n\|^2_{\mathcal{H}} = \|u_{nx}\|^2 + \|v_n\|^2 + \|\theta_n\|^2 = 1$ such that

$$\|(i\beta_n I - A)y_n\|_{\mathcal{H}} \to 0, \qquad \text{as } n \to +\infty \quad (12)$$

namely,

$$i\beta_n u_n - v_n \to 0 \qquad \text{in } H^1_0(\Omega) \quad (13)$$

$$i\beta_n v_n - u_{nxx} + \gamma\theta_{nx} \to 0 \qquad \text{in } L^2(\Omega) \quad (14)$$

$$i\beta_n \theta_n - k\theta_{nxx} + \gamma v_{nx} \to 0 \qquad \text{in } L^2(\Omega) \quad (15)$$

Taking the real part of the inner product $\langle (i\beta_n I - A)y_n, y_n\rangle_{\mathcal{H}}$, we obtain

$$\text{Re}\,\langle (i\beta_n I - A)y_n, y_n\rangle_{\mathcal{H}} = k\|\theta_{nx}\|^2 \to 0 \quad (16)$$

By (15)–(16) and the Poincaré inequality, it follows that

$$k\theta_{nxx} - \gamma v_{nx} \to 0 \qquad \text{in } L^2(\Omega) \quad (17)$$

Integrating (17) from 0 to x, we find

$$k\theta_{nx}(x) - k\theta_{nx}(0) - \gamma v_n(x) \to 0 \qquad \text{in } L^2(\Omega) \quad (18)$$

The dependence on t is omitted. Combining (18) with (16), we have

$$k\theta_{nx}(0) + \gamma v_n(x) \to 0 \qquad \text{in } L^2(\Omega) \quad (19)$$

From $\|y_n\|_{\mathcal{H}} = 1$ and (13), we obtain that $\|v_{nx}\|$ is uniformly bounded with respect to n. Then, from (17), we find that $\|\theta_{nxx}\|$ is uniformly bounded with respect to n. By the Gagliardo-Nirenberg inequality (see, e.g., [6, 24]), we have

$$|\theta_{nx}(0)| \le \|\theta_{nx}\|_{L^\infty(\Omega)} \le C_1\|\theta_{nxx}\|^{1/2}\|\theta_{nx}\|^{1/2} + C_2\|\theta_{nx}\| \to 0 \tag{20}$$

From (19) and (20), we find

$$v_n(x) \to 0 \qquad \text{in } L^2(\Omega) \tag{21}$$

Taking the inner product of (14) with u_n in $L^2(\Omega)$ and integrating by parts also yield

$$u_n(x) \to 0 \qquad \text{in } L^2(\Omega) \tag{22}$$

Then (16), (21), and (22) contradict $\|y_n\|_{\mathcal{H}} = 1$, and the proof is complete.

- $\overline{\lim_{|\beta|\to\infty}} \left\|(i\beta I - A)^{-1}\right\|_{\mathcal{L}(\mathcal{H})} < +\infty$

We prove the second step by contradiction argument again. Suppose that (11) is not true. Then, there exist a sequence β_n with $|\beta_n| \to +\infty$ and a sequence of complex vector functions $y_n \in \mathcal{D}(A)$ with $\|y_n\|_{\mathcal{H}} = 1$ such that (12) holds. Again, we have (16). Dividing (15) by β_n and using the Poincaré inequality, we get

$$\frac{k\theta_{nxx} - \gamma v_{nx}}{\beta_n} \to 0 \qquad \text{in } L^2(\Omega) \tag{23}$$

Dividing (13) by β_n and using (23), we find

$$\frac{k\theta_{nxx}}{\beta_n} - i\gamma u_{nx} \to 0 \qquad \text{in } L^2(\Omega) \tag{24}$$

Since $\|u_{nx}\| \le 1$, (24) implies that $\left\|\frac{k\theta_{nxx}}{\beta_n}\right\|$ is bounded. Multiplying (24) by u_{nx} in $L^2(\Omega)$, it follows that

$$\left\langle \frac{k\theta_{nxx}}{\beta_n}, u_{nx} \right\rangle - i\gamma\|u_{nx}\|^2 \to 0 \tag{25}$$

An integration by parts gives

$$\left\langle \frac{k\theta_{nxx}}{\beta_n}, u_{nx} \right\rangle = \frac{k\theta_{nx}}{\beta_n}u_{nx}\Big|_{x=\ell} - \frac{k\theta_{nx}}{\beta_n}u_{nx}\Big|_{x=0} - \left\langle \frac{k\theta_{nx}}{\beta_n}, u_{nxx} \right\rangle \tag{26}$$

Dividing (14) by β_n and using (16) and the choice that $\|v_n\| \le 1$, we obtain that $\left\|\frac{u_{nxx}}{\beta_n}\right\|$ is bounded. Then, from (16) and the Cauchy-Schwarz inequality, it follows that

$$\left\langle \frac{k\theta_{nx}}{\beta_n}, u_{nxx} \right\rangle \to 0 \tag{27}$$

By the Gagliardo-Nirenberg inequality (see, e.g., [6, 24]), we have

$$\left\|\frac{\theta_{nx}}{\sqrt{|\beta_n|}}\right\|_{L^\infty(\Omega)} \le C_1\|\theta_{nx}\|^{1/2}\frac{\|\theta_{nxx}\|^{1/2}}{\sqrt{|\beta_n|}} + C_2\frac{\|\theta_{nx}\|}{\sqrt{|\beta_n|}} \to 0 \tag{28}$$

and

$$\left\|\frac{u_{nx}}{\sqrt{|\beta_n|}}\right\|_{L^\infty(\Omega)} \le C_1\|u_{nx}\|^{1/2}\frac{\|u_{nxx}\|^{1/2}}{\sqrt{|\beta_n|}} + C_2\frac{\|u_{nx}\|}{\sqrt{|\beta_n|}} \le C \tag{29}$$

with C being a positive constant independent of n. Thus, from (28)–(29), we have

$$\left\|\frac{\theta_{nx}u_{nx}}{\beta_n}\right\|_{L^\infty(\Omega)} \le \frac{\|\theta_{nx}\|_{L^\infty(\Omega)}}{\sqrt{|\beta_n|}}\frac{\|u_{nx}\|_{L^\infty(\Omega)}}{\sqrt{|\beta_n|}} \to 0 \tag{30}$$

Combining (30) with (25)–(27), we find

$$\|u_{nx}\| \to 0 \tag{31}$$

Then, by (27), we get

$$\frac{v_{nx}}{\beta_n} \to 0 \qquad \text{in } L^2(\Omega) \tag{32}$$

Multiplying (12) by $\frac{v_n}{\beta_n}$ in $L^2(\Omega)$, we find

$$i\|v_n\|^2 + \left\langle u_{nx}, \frac{u_{nx}}{\beta_n} \right\rangle \to 0 \tag{33}$$

Therefore, by (31)–(33), we find

$$v_n \to 0 \qquad \text{in } L^2(\Omega) \tag{34}$$

Thus, (34), (31), and (16) contradict $\|y_n\|_{\mathcal{H}} = 1$, and the proof is complete.

We can resume the analysis above on the asymptotic behavior of the solutions of problem (1)–(6) into the following theorem.

Theorem 2 (Exponential Decay). *The semigroup $S(t)$ generated by the operator A defined in (9) is exponentially stable, namely, there exist two positive constants M and α such that*

$$\|S(t)\| \leq Me^{-\alpha t} \qquad \forall t > 0$$

Remark 1. In [1], by using the same above approach, the exponential decay of the related energy has been shown for the following different boundary conditions:

$$u(0,t) = 0, \quad u(\ell,t) = 0 \qquad \text{in } (0,T)$$

$$\theta_x(0,t) = 0, \quad \theta_x(\ell,t) = 0 \qquad \text{in } (0,T)$$

or

$$u_x(0,t) - \gamma\theta(0,t) = 0 \qquad \text{in } (0,T)$$

$$u_x(\ell,t) - \gamma\theta(\ell,t) = 0 \qquad \text{in } (0,T)$$

$$\theta(0,t) = 0, \quad \theta(\ell,t) = 0 \qquad \text{in } (0,T)$$

or

$$u_x(0,t) - \gamma\theta(0,t) = 0 \qquad \text{in } (0,T)$$

$$u_x(\ell,t) - \gamma\theta(\ell,t) = 0 \qquad \text{in } (0,T)$$

$$\theta_x(0,t) = 0, \quad \theta_x(\ell,t) = 0 \qquad \text{in } (0,T)$$

Remark 2. In one space dimension, the longtime behavior of the solutions is dominated by the dissipation related to the variation of the temperature, and the associated energy decays exponentially as time goes to infinity (see, e.g., [7, 8, 10, 14, 15, 21, 26–29]). In general, for the linear higher-dimensional thermoelastic systems, we cannot expect to prove the exponential stability of the associated energy, unless some assumptions are made on the domain and initial data (cf., e.g., [16, 17]). For example, for materials that occupy the whole $\mathbb{R}^3$, Dassios and Grillakis [5] showed that the heat difference and the curl free part of the displacement vector field decay uniformly in time like $t^{3/2}$, while the divergence-free part conserves its energy. In the special case of symmetrical solutions, when the material has a spherical shape, it was shown in [11, 13, 20, 23] that the total energy decays exponentially. For bounded domain, Chiriţă [3] proved the asymptotic equipartition of the mean kinetic and strain energy and that the thermal difference decays to zero, but no rate of decay was obtained. In [22], Muñoz Rivera showed that the curl-free part of the displacement vector field, as well as the thermal difference, decays exponentially to zero as time goes to infinity, while the divergence free part conserves its energy. In fact, there exist oscillations that are not damped to zero.

The list of references is quite long but does not claim to be exhaustive, cf. [12] for further references on different topics.

In particular, the references under further reading section may be useful for those interested in learning more about the asymptotic behavior in time for the thermoelastic systems.

References

1. Burns JA, Liu Z, Zheng S (1993) On the energy decay of a linear thermoelastic bar. J Math Anal Appl 179(2):574–591
2. Carlson DE (1972) Linear thermoelasticity. In: Truesdell C (ed) Handbuch der Physik, vol VIA/2. Springer, Berlin, pp 297–345
3. Chiriţă S (1987) On the asymptotic partition of energy in linear thermoelasticity. Quart Appl Math 45(2):327–340
4. Dafermos CM (1968) On the existence and the asymptotic stability of solutions to the equations of linear thermoelasticity. Arch Ration Mech Anal 29:241–271
5. Dassios G, Grillakis M (1984) Dissipation rates and partition of energy in thermoelasticity. Arch Ration Mech Anal 87(1):49–91
6. Friedman A (1969) Partial differential equations. Holt Rinehart and Winston, New York
7. Hansen SW (1992) Exponential energy decay in a linear thermoelastic rod. J Math Anal Appl 167(2):429–442

8. Henry DB, Perissinitto A Jr, Lopes O (1993) On the essential spectrum of a semigroup of thermoelasticity. Nonlinear Anal 21(1):65–75
9. Huang FL (1985) Characteristic conditions for exponential stability of linear dynamical systems in Hilbert spaces. Annu Differ Equ 1(1):43–56
10. Jiang S (1992) Global solutions of the Neumann problem in one-dimensional nonlinear thermoelasticity. Nonlinear Anal 19(2):107–121
11. Jiang S (1998) Global existence and exponential decay of spherically symmetric solutions to thermoelasticity equations. Chinese Ann Math Ser A 19(5):629–640
12. Jiang S, Racke R (2000) Evolution equations in thermoelasticity, vol 112, Chapman & Hall/CRC monographs and surveys in pure and applied mathematics. Chapman & Hall/CRC, Boca Raton
13. Jiang S, Muñoz Rivera JE, Racke R (1998) Asymptotic stability and global existence in thermoelasticity with symmetry. Quart Appl Math 56(2):259–275
14. Kawashima S, Shibata Y (1995) On the Neumann problem of one-dimensional nonlinear thermoelasticity with time-independent external forces. Czechoslovak Math J 45(1):39–67
15. Kim JU (1992) On the energy decay of a linear thermoelastic bar and plate. SIAM J Math Anal 23(4):889–899
16. Lebeau G, Zuazua E (1997) Sur la décroissance non uniforme de l'énergie dans le système de la thermoélasticité linéaire. C R Acad Sci Paris Sér I Math 324(4):409–415
17. Lebeau G, Zuazua E (1999) Decay rates for the three-dimensional linear system of thermoelasticity. Arch Ration Mech Anal 148(3):179–231
18. Liu Z, Zheng S (1993) Exponential stability of the semigroup associated with a thermoelastic system. Quart Appl Math 51(3):535–545
19. Liu Z, Zheng S (1999) Semigroups associated with dissipative systems, vol 398, Chapman & Hall/CRC research notes in mathematics. Chapman & Hall/CRC, Boca Raton
20. Marzocchi A, Muñoz Rivera JE, Naso MG (2003) Transmission problem in thermoelasticity with symmetry. IMA J Appl Math 68(1):23–46
21. Muñoz Rivera JE (1992) Energy decay rates in linear thermoelasticity. Funkcial Ekvac 35(1):19–30
22. Muñoz Rivera JE (1997) Asymptotic behaviour in n-dimensional thermoelasticity. Appl Math Lett 10(5):47–53
23. Muñoz Rivera JE, Naso MG (2007) About asymptotic behavior for a transmission problem in hyperbolic thermoelasticity. Acta Appl Math 99(1):1–27
24. Nirenberg L (1959) On elliptic partial differential equations. Ann Scuola Norm Sup Pisa 13(3):115–162
25. Prüss J (1984) On the spectrum of C_0-semigroups. Trans Amer Math Soc 284(2):847–857
26. Racke R (1988) Initial boundary value problems in one-dimensional nonlinear thermoelasticity. Math Methods Appl Sci 10(5):517–529
27. Racke R, Shibata Y (1991) Global smooth solutions and asymptotic stability in one-dimensional nonlinear thermoelasticity. Arch Ration Mech Anal 116(1):1–34
28. Racke R, Shibata Y, Zheng S (1993) Global solvability and exponential stability in one-dimensional nonlinear thermoelasticity. Quart Appl Math 51(4):751–763
29. Slemrod M (1981) Global existence, uniqueness, and asymptotic stability of classical smooth solutions in one-dimensional nonlinear thermoelasticity. Arch Ration Mech Anal 76(2):97–133
30. Wyler A (1994) Stability of wave equations with dissipative boundary conditions in a bounded domain. Differ Integral Equ 7(2):345–366

Further Reading

Avalos G, Lasiecka I (1996) Exponential stability of a thermoelastic system without mechanical dissipation. Rend Istit Mat Univ Trieste 28(Suppl):1–28 (1997), dedicated to the memory of Pierre Grisvard

Avalos G, Lasiecka I (1998) Exponential stability of a thermoelastic system with free boundary conditions without mechanical dissipation. SIAM J Math Anal 29(1):155–182 (electronic)

Avalos G, Lasiecka I (1998) Exponential stability of an uncontrolled thermoelastic system with varying boundary conditions. Appl Anal 68(1–2):31–49

Avalos G, Lasiecka I (1998) Uniform decays in nonlinear thermoelastic systems. In: Optimal control (Gainesville, FL, 1997), vol 15, Applied optimization. Kluwer, Dordrecht, pp 1–23

Bonfanti G, Muñoz Rivera JE, Naso MG (2008) Global existence and exponential stability for a contact problem between two thermoelastic beams. J Math Anal Appl 345(1):186–202

Bonfanti G, Fabrizio M, Muñoz Rivera JE, Naso MG (2010) On the energy decay for a thermoelastic contact problem involving heat transfer. J Therm Stress 33(11):1049–1065

Chiriţă S, Ciarletta M (2008) On the structural stability of thermoelastic model of porous media. Math Methods Appl Sci 31(1):19–34

Ciarletta M, Chiriţă S (2002) Asymptotic partition in the linear thermoelasticity backward in time. In: Mathematical models and methods for smart materials: Cortona, 2001, vol 62, Series on advances in mathematics for applied sciences. World Scientific, River Edge, pp 31–41

D'Apice C, Ciarletta M, Chiriţă S (2011) Saint-Venant decay rates for an inhomogeneous isotropic linear thermoelastic strip. J Math Anal Appl 381(1):121–133

Fabrizio M, Lazzari B, Muñoz Rivera JE (1999) Asymptotic behavior in linear thermoelasticity. J Math Anal Appl 232(1):138–165

Fabrizio M, Lazzari B, Muñoz Rivera JE (2000) Asymptotic behaviour of a thermoelastic plate of weakly hyperbolic type. Differ Integral Equ 13(10–12): 1347–1370

Fabrizio M, Lazzari B, Muñoz Rivera JE (2007) Asymptotic behaviour for a twodimensional thermoelastic model. Math Methods Appl Sci 30(5):549–566
Fatori LH, Muñoz Rivera JE (2001) Energy decay for hyperbolic thermoelastic systems of memory type. Quart Appl Math 59(3):441–458
Giorgi C, Pata V (2001) Stability of abstract linear thermoelastic systems with memory. Math Models Methods Appl Sci 11(4):627–644
Giorgi C, Naso MG, Pata V, Potomkin M (2009) Global attractors for the extensible thermoelastic beam system. J Differ Equ 246(9):3496–3517
Grasselli M, Muñoz Rivera JE, Pata V (2005) On the energy decay of the linear thermoelastic plate with memory. J Math Anal Appl 309(1):1–14
Lasiecka I (1999) Uniform decay rates for full von Karman system of dynamic thermoelasticity with free boundary conditions and partial boundary dissipation. Commun Partial Differ Equ 24(9–10):1801–1847
Liu WJ, Zuazua E (2001) Uniform stabilization of the higher-dimensional system of thermoelasticity with a nonlinear boundary feedback. Q Appl Math 59(2):269–314
Muñoz Rivera JE, Qin Y (2002) Global existence and exponential stability in one-dimensional nonlinear thermoelasticity with thermal memory. Nonlinear Anal Ser A Theory Methods 51(1):11–32
Qin Y, Ma Z, Yang X (2010) Exponential stability for nonlinear thermoelastic equations with second sound. Nonlinear Anal Real World Appl 11(4):2502–2513
Zhang X, Zuazua E (2003) Decay of solutions of the system of thermoelasticity of type III. Commun Contemp Math 5(1):25–83

Asymptotic Expansions in Coupled and Generalized Thermoelasticity

Mohammed A. Elhagary
Department of Mathematics, Faculty of Science, Damietta University, New Damietta, Egypt

Synonyms

Coupled thermoelasticity

Overview

Asymptotic expansions technique is a method used to obtain approximately analytical solution for the inversion of Laplace transforms valid for short values of time. This method is based on expanding the solution of the problem in Laplace transform domain in the Maclaurin series of which the first selected terms then using the convolution theorem of the Laplace transform to obtain the inversion transforms for the solution.

The inversion technique used is an analytical one utilizing asymptotic expansions valid for short values of time. It was found that [1] generalized theories of thermoelasticity predict values quite different from those predicted by the coupled theories only when the time is small. For large values of time, both the coupled and the generalized theories differ numerically by very small amounts. It was used successfully by Hetnarski [2, 3] to solve problems in coupled thermoelasticity.

The advantages of using an analytical method over a numerical one are evident. The numerical program to find values of the functions is very simple, easy to implement, and very fast in execution.

The main advantage is that this method enables us to find exact values for the locations of the wave fronts and wave speeds associated with the problem. These values are exact, though the solution itself is approximate [4].

Sherief [5] and Sherief and Anwar [6] used this method to obtain the fundamental solutions for generalized thermoelasticity with one relaxation time for the point and line sources of heat, respectively. Sherief [7] used this method to obtain the fundamental solution for thermoelasticity with two relaxation times. The same method used by Sherief et al. to solve some problems in theory of generalized thermoelasticity in Cartesian, spherical, and cylindrical [8, 9] coordinate systems. The following section is an application of using this method to obtain the solution of a one-dimensional problem in Cartesian coordinate.

Fundamental Equations

We shall consider a homogeneous, isotropic, thermoelastic solid occupying the region $x > 0$. We shall also assume that the initial state of the medium is quiescent. The outer surface of this the half space is assumed traction-free and subject to a constant thermal shock. The equation of motion in the absence of body forces is given by

$$\rho\ddot{u}_i = (\lambda + \mu)u_{j,ij} + \mu u_{i,jj} - \gamma T_{,i} \quad (1)$$

where λ and μ are Lamé's constants, ρ is the density, and T is the absolute temperature.

The constitutive equation is given by

$$\sigma_{ij} = \lambda e_{kk}\delta_{ij} + 2\mu e_{ij} - \gamma(T - T_0)\delta_{ij} \quad (2)$$

where γ is a material constant given by $\gamma = (3\lambda + 2\mu)\alpha_t$. α_t is the coefficient of linear thermal expansion.

The energy equation has the form

$$kT_{,ii} = \rho c_E\left(\dot{T} + \tau_0\ddot{T}\right) + \gamma T_0(\dot{e}_{kk} + \tau_0\ddot{e}_{kk}) \quad (3)$$

where k is the thermal conductivity, τ_0 is a constant with the dimensions of time that act as a relaxation time, c_E is the specific heat at constant strain, and T_0 is the temperature of the medium in its natural state, assumed to be such that $|(T - T_0)/T_0| << 1$. τ_0 is the relaxation time, and e_{ii} is given *by*

$$e_{ij} = \frac{1}{2}\left(u_{i,j} + u_{j,i}\right) \quad (4)$$

The dot denotes differentiation with respect to time, while a comma denotes material. Derivatives and the summation notation are used throughout.

One-Dimensional Problem

For the one-dimensional problem, we assume displacement components of the form

$$u_x = u(x, t) \qquad u_y = u_z = 0 \quad (5)$$

The cubical dilatation e is given by

$$e = \frac{\partial u}{\partial x}.$$

Equations (1), (2), and (3), then, reduce to

$$\rho\frac{\partial^2 u}{\partial t^2} = (\lambda + 2\mu)\frac{\partial^2 u}{\partial x^2} - \gamma\frac{\partial T}{\partial x} \quad (6)$$

$$\sigma = (\lambda + 2\mu)\frac{\partial u}{\partial x} - \gamma(T - T_0) \quad (7)$$

$$k\frac{\partial^2 T}{\partial x^2} = \rho c_E\left(\frac{\partial T}{\partial t} + \tau_0\frac{\partial^2 T}{\partial t^2}\right) + \gamma T_0\left(\frac{\partial e}{\partial t} + \tau_0\frac{\partial^2 e}{\partial t^2}\right) \quad (8)$$

The governing equations can be put into a more convenient form by using the nondimensional variables

$$\begin{aligned} &x' = c_1\xi x,\ u' = c_1\xi u,\ t' = c_1^2\xi t,\\ &\tau_0' = c_1^2\xi\tau_0,\ \theta = \frac{\gamma(T - T_0)}{(\lambda + 2\mu)}\\ &\sigma' = \frac{\sigma_{ij}}{(\lambda + 2\mu)} \end{aligned} \quad (9)$$

where

$$c_1 = \sqrt{(\lambda + 2\mu)/\rho}, \xi = \rho c_E/k.$$

Substituting from (9) in (6), (7), and (8) and dropping the primes for convenience, we obtain the following set of nondimensional equations:

$$\frac{\partial^2 u}{\partial t^2} = \frac{\partial e}{\partial x} - \frac{\partial\theta}{\partial x} \quad (10)$$

$$\sigma = e - \theta \quad (11)$$

$$\frac{\partial^2\theta}{\partial x^2} = \left(\frac{\partial}{\partial t} + \tau_0\frac{\partial^2}{\partial t^2}\right)(\theta + \varepsilon e) \quad (12)$$

where

$$\varepsilon = \gamma^2 T_0/[\rho c_E(\lambda + 2\mu)]$$

Applying the operator $D = \left(\frac{\partial}{\partial x}\right)$ on both sides of (10), we obtain

$$\frac{\partial^2 e}{\partial t^2} = \frac{\partial^2 e}{\partial x^2} - \frac{\partial^2\theta}{\partial x^2} \quad (13)$$

The boundary conditions are assumed to be

$$\sigma(x,\,t)|_{x=0} = 0,\ \sigma(x,\,t)|_{x=\infty} = 0, \text{for} \quad t > 0 \tag{14}$$

$$\theta(x,\,t)|_{x=0} = \theta_0,\ \theta(x,\,t)|_{x=\infty} = 0, \text{for} \quad t > 0 \tag{15}$$

Solution in the Laplace Transform Domain

Introducing the Laplace transform defined by the formula

$$\bar{f}(p) = \int_0^\infty e^{-pt} f(t)\, dt$$

to both sides of (11)–(13), we obtain

$$\bar{\sigma} = \bar{e} - \bar{\theta} \tag{16}$$

$$D^2\bar{\theta} = \left(p + \tau_0\, p^2\right)\left(\,\bar{\theta} + \varepsilon\,\bar{e}\,\right) \tag{17}$$

$$D^2\bar{\theta} = \left(D^2 - p^2\right)\bar{e} \tag{18}$$

The transformed boundary conditions (14) and (15) become

$$\bar{\sigma}(x,\,p)|_{x=0} = 0,\ \bar{\sigma}(x,\,p)|_{x=\infty} = 0 \tag{19}$$

$$\bar{\theta}(x,\,p)\big|_{x=0} = \frac{\theta_0}{p},\ \bar{\theta}(x,\,p)\big|_{x=\infty} = 0 \tag{20}$$

Eliminating $\bar{e}$ between (17) and (18), we get

$$\left\{D^4 - \left[p^2 + (1+\varepsilon)\left(p + \tau_0\, p^2\right)\right]\nabla^2 + p^3(1 + \tau_0 p)\bar{\theta} = 0 \right. \tag{21}$$

The above equation can be factorized as

$$(\nabla^2 - k_1^2)(\nabla^2 - k_2^2)\bar{\theta} = 0 \tag{22}$$

where k_1 and k_2 are the roots with positive real parts of the characteristic equation

$$k^4 - \left[p^2 + (1+\varepsilon)\left(p + \tau_0 p^2\right)\right]k^2 + p^3(1 + \tau_0 p) = 0 \tag{23}$$

Since $\bar{\theta}$ must remain bounded as $x \to \infty$, the solution of (22) is given by

$$\bar{\theta} = \sum_{i=1}^{2} A_i\left(k_i^2 - p^2\right)e^{-k_i x} \tag{24}$$

where A_1 and A_2 are parameters depending on p.

Similarly, eliminating $\bar{\theta}$ between (17) and (18), we find that $\bar{e}$ satisfies an equation identical to (21). Thus, we obtain the solution compatible with (18) as

$$\bar{e} = \sum_{i=1}^{2} A_i k_i^2 e^{-k_i x} \tag{25}$$

Integrating both sides of (25) with respect to x, we obtain

$$\bar{u} = -\sum_{i=1}^{2} A_i k_i e^{-k_i x} \tag{26}$$

Substituting from (24) and (25) into (16), we get

$$\bar{\sigma} = \sum_{i=1}^{2} A_i p^2 e^{-k_i x} \tag{27}$$

From the boundary conditions (19) and (20), it follows that

$$A_1 = -A_2 = \frac{\theta_0}{p\left(k_1^2 - k_2^2\right)} \tag{28}$$

This completes the solution of the problem in the Laplace transform domain.

Inversion of the Laplace Transforms

Let us now determine inverse transforms for the case of small values of time (large values of p). We note first that the roots k_1 and k_2 of the characteristic equation (23) have the form

$$k_1 = \left\{\frac{p}{2}\left[p + (1+\varepsilon)(1+\tau_0 p) + \left(p^2 + 2p(\varepsilon-1)(1+\tau_0 p) + (1+\varepsilon)^2(1+\tau_0 p)^2\right)^{1/2}\right]\right\}^{1/2} \quad (29)$$

$$k_2 = \left\{\frac{p}{2}\left[p + (1+\varepsilon)(1+\tau_0 p) - \left(p^2 + 2p(\varepsilon-1)(1+\tau_0 p) + (1+\varepsilon)^2(1+\tau_0 p)^2\right)^{1/2}\right]\right\}^{1/2} \quad (30)$$

Denoting $q = p^{-1}$, we have

$$k_i = q^{-1}[f_i(q)]^{1/2} \quad (31)$$

where

$$f_1(q) = \left\{\frac{1}{2}\left[1 + (1+\varepsilon)(q+\tau_0) + \left(1 + 2(\varepsilon-1)(q+\tau_0) + (1+\varepsilon)^2(q+\tau_0)^2\right)^{1/2}\right]\right\}$$

$$f_2(q) = \left\{\frac{1}{2}\left[1 + (1+\varepsilon)(q+\tau_0) - \left(1 + 2(\varepsilon-1)(q+\tau_0) + (1+\varepsilon)^2(q+\tau_0)^2\right)^{1/2}\right]\right\}$$

Expanding $f_1(q)$ and $f_2(q)$ in the Maclaurin series of which the first four terms are retained, we have

$$f_i(q) = f_i(0) + f'_i(0)q + \frac{f''_i(0)q^2}{2} + \frac{f'''_{ii}(0)q^3}{6}, \quad i = 1,\ 2$$

and we have

$$f_i(q) = a_{i0} + a_{i1}q + a_{i2}q^2 + a_{i3}q^3 \quad (32)$$

where

$$a_{10} = \frac{1}{2}[1 + (\varepsilon+1)\tau_0 + A]$$

$$a_{11} = \frac{1}{2}\left[\varepsilon + 1 + \frac{(\varepsilon-1) + (\varepsilon+1)^2\tau_0}{A}\right]$$

$$a_{12} = -a_{22} = \frac{\varepsilon}{A_3}a_{20} = \frac{1}{2}[1 + (\varepsilon+1)\tau_0 - A]a_{21} = \frac{1}{2}\left[\varepsilon + 1 - \frac{(\varepsilon-1) + (\varepsilon+1)^2\tau_0}{A}\right] \quad (33)$$

and $A = \left[1 + 2(\varepsilon-1)\tau_0 + (\varepsilon+1)^2\tau_0^2\right]^{1/2}$

Next, we expand the expressions $[f_1(q)]^{1/2}$ and $[f_2(q)]^{1/2}$ in the Maclaurin series, and retaining the first three terms, we obtain finally the expressions for k_1 and k_2 in the form

$$k_i = q^{-1}\left\{b_{i0} + b_{i1}q + b_{i2}q^2\right\}, i = 1, 2 \quad (34)$$

where

$$b_{i0} = \sqrt{a_{i0}}$$
$$b_{11} = \frac{a_{i1}}{2b_{i0}}$$
$$b_{i2} = \frac{4a_{i0}a_{i2} - a_{i1}^2}{8b_{i0}^3} \quad (35)$$

Using similar expansion methods, we get

$$\frac{1}{k_1^2 - k_2^2} = q^2\left\{b_0 + b_1 q + b_2 q^2 + b_3 q^3\right\} \quad (36)$$

where

$$b_0 = \frac{1}{A}$$

$$b_1 = -\frac{\left[(\varepsilon-1) + (\varepsilon+1)^2\tau_0\right]}{A^3}$$

$$b_2 = \left[\frac{\left(\varepsilon^2 - 4\varepsilon + 1\right) + 2(\varepsilon-1)(\varepsilon+1)^2\tau_0 + (\varepsilon+1)^4\tau_0}{A^5}\right]$$

$$b_3 = \left[\frac{(\varepsilon-1)\left(\varepsilon^2 - 8\varepsilon + 1\right) + 3(\varepsilon+1)^2\left(\varepsilon^2 - 4\varepsilon + 1\right)\tau_0 + 3(\varepsilon-1)(\varepsilon+1)^4\tau_0^2 + (\varepsilon+1)^6\tau_0^3}{A^7}\right] \quad (37)$$

Stress Distribution

Let us substitute the expressions (28), (34), and (36) in (27) to obtain

$$\bar{\sigma} = \theta_0 \left[\frac{b_0}{p} + \frac{b_1}{p^2} + \frac{b_2}{p^3} + \frac{b_3}{p^4}\right] \cdot \left\{\exp(-b_{11}x)\exp(-b_{10}x)\exp\left(\frac{-b_{12}x}{p}\right) - \exp(-b_{21}x)\exp(-b_{20}x)\exp\left(\frac{-b_{22}x}{p}\right)\right\} \tag{38}$$

which can be written more concisely as

$$\bar{\sigma} = \theta_0 e^{-b_{11}x}\sum_{j=0}^{3}\frac{b_j}{p^{j+1}}e^{-b_{10}x}\exp\left(\frac{-b_{12}x}{p}\right) - \theta_0 b e^{-b_{21}x}\sum_{j=0}^{3}\frac{b_j}{p^{j+1}}e^{-b_{20}x}\exp\left(\frac{-b_{22}x}{p}\right) \tag{39}$$

In order to invert the Laplace transform, we shall use the convolution theorem for the Laplace transforms, namely,

$$L^{-1}[\bar{f}(p)\,.\,\bar{g}(p)] = \int_0^t L^{-1}[\bar{f}(p)]_{t=t-z}L^{-1}[\bar{g}(p)]_{t=z}dz$$

and the following three formulas from the table of Laplace transforms [10]:

$$L^{-1}[p^n e^{-ap}] = \delta^{(n)}(t-a)$$

$$L^{-1}\left[\frac{e^{-a/p}}{p^{j+1}}\right] = \left(\frac{t}{a}\right)^{\frac{j}{2}}J_j\left(2\sqrt{at}\right),\ \mathrm{Re}(j) > -1,\ a > 0$$

$$L^{-1}\left[\frac{e^{a/p}}{p^{j+1}}\right] = \left(\frac{t}{a}\right)^{\frac{j}{2}}I_j\left(2\sqrt{at}\right),\ \ \mathrm{Re}(j) > -1,\ a > 0$$

Using these formulas, (39) transforms to

$$\bar{\sigma} = \theta_0 e^{-b_{11}x}\sum_{j=0}^{3}b_j\int_0^{\infty}\delta[t-b_{10}x-u]\left(\frac{u}{b_{10}x}\right)^{j/2}J_j\left(2\sqrt{b_{12}x\,u}\right)du - \theta_0 b e^{-b_{21}x}\sum_{j=0}^{3}b_j\int_0^{\infty}\delta[t-b_{20}x-u]\left(\frac{u}{-b_{20}x}\right)^{j/2}I_j\left(2\sqrt{-b_{22}x\,u}\right)du$$

or

$$\sigma = \theta_0\eta(t-b_{10}x)e^{-b_{11}x}\sum_{j=0}^{3}b_j\left(\frac{t-b_{10}x}{b_{10}x}\right)^{j/2}J_j\left(2\sqrt{b_{12}x\,(t-b_{10}x)}\right) - \theta_0\eta(t-b_{20}x)be^{-b_{21}x}\sum_{j=0}^{3}b_j\left(\frac{t-b_{20}x}{-b_{20}x}\right)^{j/2}I_j\left(2\sqrt{-b_{22}x\,(t-b_{20}x)}\right)$$

or, written in full, we have

$$\sigma = \theta_0\left\{\eta(t-b_{10}x)e^{-b_{11}x}\left[b_0J_0(z_1) + b_1\left(\frac{t-b_{10}x}{b_{10}x}\right)^{1/2}J_1(z_1) + b_2\left(\frac{t-b_{10}x}{b_{10}x}\right)J_2(z_1) + b_3\left(\frac{t-b_{10}x}{b_{10}x}\right)^{3/2}J_3(z_1)\right] - \eta(t-b_{20}x)e^{-b_{21}x}\left[b_0I_0(z_2) + b_1\left(\frac{t-b_{20}x}{-b_{20}x}\right)^{1/2}I_1(z_2) + b_2\left(\frac{t-b_{20}x}{-b_{20}x}\right)I_2(z_2) + b_3\left(\frac{t-b_{20}x}{-b_{20}x}\right)^{3/2}I_3(z_2)\right]\right\} \tag{40}$$

where

$$z_1 = 2\sqrt{b_{12}x\,(t-b_{10}x)}$$
$$z_2 = 2\sqrt{-b_{22}x\,(t-b_{20}x)} \tag{41}$$

In (40), $\eta(x)$ denotes the Heaviside step function, and J_n and I_n are Bessel functions of the first and second kind of order n, respectively.

Temperature Distribution

Substituting from (28), (34), and (36) in (24), we get

$$\bar{\theta} = \theta_0 \left\{ \left[\frac{c_{10}}{p} + \frac{c_{11}}{p^2} + \frac{c_{12}}{p^3} + \frac{c_{13}}{p^4} \right] e^{-k_1 x} - \left[\frac{c_{10}}{p} + \frac{c_{11}}{p^2} + \frac{c_{12}}{p^3} + \frac{c_{13}}{p^4} \right] e^{-k_2 x} \right\} \tag{42}$$

where

$$\begin{aligned}
c_{10} &= \frac{1}{2}\left[1 + \frac{(\varepsilon+1)\tau_0 - 1}{A}\right] \\
c_{20} &= \frac{1}{2}\left[-1 + \frac{(\varepsilon+1)\tau_0 - 1}{A}\right] \\
c_{11} = c_{21} &= \left[\frac{\varepsilon((\varepsilon+1)\tau_0 + 1)}{A^3}\right] \\
c_{12} = c_{22} &= \left[\frac{-\varepsilon[(\varepsilon-2)] + (\varepsilon+1)(2\varepsilon+1)\tau_0 + (\varepsilon+1)^3\tau_0^3}{A^5}\right] \\
c_{13} = c_{23} &= \left[\frac{\varepsilon[(\varepsilon^2 - 6\varepsilon + 3) + (\varepsilon+1)(3\varepsilon^2 - 4\varepsilon - 5)\tau_0 + (\varepsilon+1)^3(3\varepsilon+1)\tau_0^2 + (\varepsilon+1)^5\tau_0^3}{A^7}\right]
\end{aligned} \tag{43}$$

Now, substituting from (34) and (42), we get

$$\begin{aligned}
\bar{\theta} = \theta_0 \Bigg\{ & \left[\frac{c_{10}}{p} + \frac{c_{11}}{p^2} + \frac{c_{12}}{p^3} + \frac{c_{13}}{p^4} \right] \exp(-b_{11}x) \\
& \exp(-b_{10}x) \exp\left(\frac{-b_{12}x}{p}\right) \\
& - \left[\frac{c_{20}}{p} + \frac{c_{21}}{p^2} + \frac{c_{22}}{p^3} + \frac{c_{23}}{p^4} \right] \\
& \exp(-b_{21}x) \exp(-b_{20}x) \exp\left(\frac{-b_{22}x}{p}\right) \Bigg\}
\end{aligned}$$

Performing the inverse Laplace transform, using the general inversion formulas used before, we obtain

$$\begin{aligned}
\theta = {} & \theta_0 \eta(t - b_{10}x) e^{-b_{11}x} \sum_{j=0}^{3} c_{1j} \left(\frac{t - b_{10}x}{b_{10}x}\right)^{j/2} J_j(z_1) \\
& - \theta_0 \eta(t - b_{20}x) e^{-b_{21}x} \sum_{j=0}^{3} c_{2j} \left(\frac{t - b_{20}x}{-b_{20}x}\right)^{j/2} I_j(z_2)
\end{aligned}$$

where z_1 and z_2 are given in (41).

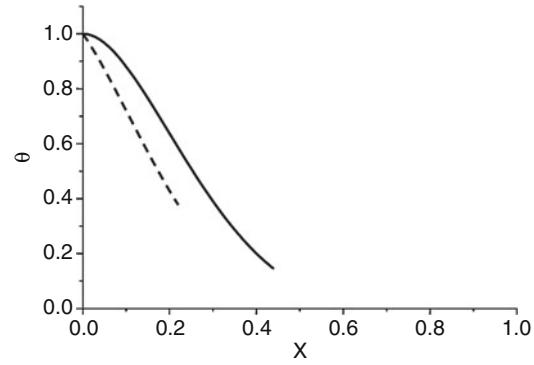

Asymptotic Expansions in Coupled and Generalized Thermoelasticity, Fig. 1 Temperature distribution

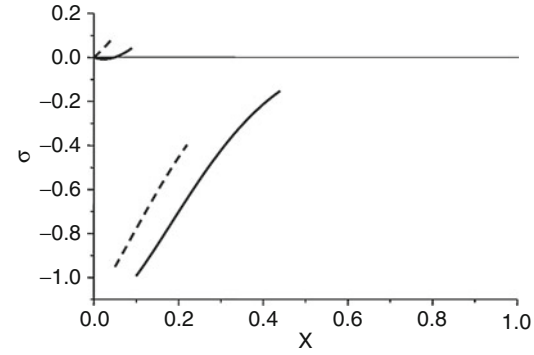

Asymptotic Expansions in Coupled and Generalized Thermoelasticity, Fig. 2 Stress distribution

Numerical Results

The copper material was chosen for purposes of numerical evaluations. The constants of the problem were taken as $\varepsilon = 0.0168$ and $\tau_0 = 0.05$.

The computations were carried out for two values of time, namely, for $t = 0.05$ and 0.1. The results are illustrated graphically in Figs. 1 and 2 for the temperature increment θ and stress component σ distributions, respectively. The dashed lines represent the case when $t = 0.05$, while the solid lines represent the case when $t = 0.1$.

All the functions considered here have two singularities at the points $x = t/b_{10}$ and $x = t/b_{20}$. The locations of these singularities are shown in Table 1. At these singularities, the

Asymptotic Expansions in Coupled and Generalized Thermoelasticity, Table 1 Location of singularities

t	Singularity 1	Singularity 2
0.05	0.043459	0.222650
0.10	0.092914	0.440376

temperature and stress distributions are discontinuous. The first singularity in the temperature is very small in magnitude and does not show in the figures.

All the figures show that, as expected, the heat and elastic effects propagate with finite speeds. It was found that dimensionless speeds for the two waves are $v_1 = 0.999556$ and $v_2 = 4.474124$. As seen in the figures, the effect of the thermal shock propagates into the medium with a finite speed. For $t = 0.05$, for example, the wave front has reached the location $x = 0.22265$. For $t = 0.1$, the temperature has nonzero value only in the region $x < 0.440376$ and is identically zero everywhere else. This region expands with the passage of time.

This is different from the cases in both the uncoupled and the coupled theories of thermoelasticity [2]. There, the effect of the thermal shock fills the whole space immediately, signifying an infinite speed of propagation for thermal waves.

References

1. Sherief H, Dhaliwal R (1981) A generalized one-dimensional thermal shock problem for small times. J Therm Stress 4:407–420
2. Hetnarski R (1961) Coupled one-dimensional thermal shock problem for small times. Arch Mech 13:295–306
3. Hetnarski R (1964) The fundamental solution of the coupled thermoelastic problem for small times. Arch Mech 16:23–32
4. Boley B (1962) Discontinuities in integral-transform solutions. Quart Appl Math 19:273–284
5. Sherief H (1986) Fundamental solution of the generalized thermoelastic problem for short times. J Therm Stress 9:151–164
6. Sherief H, Anwar M (1986) Problem in generalized thermoelasticity. J Therm Stress 9:165–181
7. Sherief H (1992) Fundamental solution for thermoelasticity with two relaxation times. Int J Eng Sci 30:313–325
8. Sherief H, Darwish A (1998) A short time solution for a problem in thermoelasticity of an infinite medium with a spherical cavity. J Therm Stress 21:811–828
9. Sherief H, Elmisiery A, Elhagary M (2004) Generalized thermoelastic problem for an infinitely long hollow cylinder for short times. J Therm Stress 27:885–902
10. Oberhettinger F, Badii L (1973) Tables of laplace transforms. Springer, New York

Asymptotic Partition Backward in Time

Vittorio Zampoli
Department of Electronic and Computer Science Engineering, University of Salerno, Fisciano, Italy

Overview

The problem concerning the ▶ partition of energy in asymptotic form was first approached in the 1960s (Lax and Phillips [1] and Brodsky [2]). Afterwards, Goldstein [3, 4], applying the semigroup theory, proved an equipartition theorem asserting that the difference between kinetic and potential energies vanishes as the time tends to infinity. Later, using the Lagrange identity method, Levine [5] proved in a simplified way with respect to Goldstein [4] that asymptotic equipartition occurs between the Cesàro means of kinetic and potential energies. In the context of linear elastodynamics, Day [6] established the asymptotic equipartition between the mean kinetic and strain energies. Such result has been extended by Chiriţă [7] to the theory of linear thermoelasticity.

On the other side, ▶ backward-in-time problems were initially considered by Serrin [8], who established uniqueness results for the Navier–Stokes equations. In such a context, interesting results have been obtained by Knops and Payne [9], Galdi and Straughan [10], and Payne and Straughan [11]. Subsequently, Ames and Payne [12] introduced the study of the dynamical linear theory for thermoelasticity backward in time, and

in this regard, other important results have been recently achieved by Ciarletta [13], Ciarletta and Chiriţă [14, 15], Iovane and Passarella [16], Passarella and Tibullo [17], and Passarella, Tibullo and Zampoli [18]. In particular, the asymptotic partition backward-in-time shown in [15] is here reported, likewise with regard to the contents but with an additional level of detail in terms of mathematical description.

In the context of the linear theory of thermoelasticity backward in time, a final-boundary value problem is considered such that the *final data* are assigned at time $t = 0$ and the extrapolation of the solution to the time interval $(-\infty, 0)$ is performed. To this end and through some auxiliary Lagrange-Brun identities (see [19, 20]), the Cesàro means of various parts of the total energy are introduced, and the relations describing the ▶ asymptotic behavior in time of mean energies are established, provided that some mild restrictions are imposed on the considered process.

Formulation of the Backward-in-Time Problem

A bounded regular region of the physical space E^3 will be denoted by B, and ∂B will be its piecewise smooth boundary surface; B is supposed filled by an anisotropic and inhomogeneous thermoelastic medium. An orthonormal system of reference is introduced such that all vectors and tensors have components denoted by Latin subscripts (ranging over 1,2,3). Summation over repeated subscripts and other typical conventions for differential operations are implied: a superposed dot or a comma followed by a subscript will denote partial derivative with respect to time or to the corresponding Cartesian coordinate, respectively. Moreover, regularity questions will be disregarded for all involved functions, simply understanding a degree of smoothness sufficient to ensure analysis to be valid. In the context of the linear theory of thermoelasticity, a final-boundary value problem will be considered in the time interval $(-\infty, 0]$.

Following [21] and neglecting supply terms, the fundamental system of field equations can be summarized as follows:

Equation of motion

$$S_{ji,j} = \rho \ddot{u}_i \qquad \text{in } B \times (-\infty, 0] \tag{1}$$

Energy equation

$$T_0 M_{ij} \dot{e}_{ij} - q_{i,i} = c\dot{\theta} \qquad \text{in } B \times (-\infty, 0] \tag{2}$$

Stress–strain-temperature relation

$$S_{ij} = C_{ijkl} e_{kl} + M_{ij}\theta \qquad \text{in } \bar{B} \times (-\infty, 0] \tag{3}$$

Heat conduction equation

$$q_i = -K_{ij} g_j \qquad \text{in } \bar{B} \times (-\infty, 0] \tag{4}$$

Strain–displacement relation

$$e_{ij} = \frac{1}{2}\left(u_{i,j} + u_{j,i}\right) \qquad \text{in } \bar{B} \times (-\infty, 0] \tag{5}$$

Thermal gradient-temperature relation

$$g_i = \theta_{,i} \qquad \text{in } \bar{B} \times (-\infty, 0] \tag{6}$$

In the above system of equations, the following notations have been used: S_{ij} are the components of the stress tensor, u_i are the components of the displacement vector, and θ is the temperature variation from the uniform strictly positive reference temperature T_0. Moreover, M_{ij} are the components of the stress-temperature tensor, e_{ij} are the components of the strain tensor, q_i are the components of the heat flux vector, C_{ijkl} are the components of the elasticity tensor, K_{ij} are the components of the conductivity tensor, and g_i are the components of the thermal gradient vector. Furthermore, ρ (mass density) and c (specific heat) are assumed to be strictly positive continuous functions of the position $\mathbf{x}$ on $\bar{B}$, and tensors C_{ijkl}, M_{ij}, and K_{ij} are continuous differentiable functions of the position $\mathbf{x}$ on $\bar{B}$ and satisfy the following symmetry relations:

$$C_{ijkl} = C_{klij} = C_{jikl} \tag{7}$$

$$M_{ij} = M_{ji} \tag{8}$$

$$K_{ij} = K_{ji} \tag{9}$$

The considered final-boundary value problem $\mathcal{P}$ is thus defined by the relations (1)–(6), by the final conditions

$$\begin{aligned} u_i(\mathbf{x},\ 0) &= u_i^0(\mathbf{x}) \qquad \dot{u}_i(\mathbf{x},\ 0) = \dot{u}_i^0(\mathbf{x}) \\ \theta(\mathbf{x},0) &= \theta^0(\mathbf{x}) \qquad \text{with } \mathbf{x} \in \bar{B} \end{aligned} \tag{10}$$

and by the homogeneous boundary conditions

$$\begin{aligned} u_i(\mathbf{x},t) &= 0 \quad \text{on} \quad \Sigma_1 \times (-\infty, 0] \\ s_i(\mathbf{x},t) &= 0 \quad \text{on} \quad \Sigma_2 \times (-\infty, 0] \\ \theta(\mathbf{x},t) &= 0 \quad \text{on} \quad \Sigma_3 \times (-\infty, 0] \\ q(\mathbf{x},t) &= 0 \quad \text{on} \quad \Sigma_4 \times (-\infty, 0] \end{aligned} \tag{11}$$

where u_i^0, $\dot{u}_i^0$, and θ^0 are assigned functions and

$$\begin{aligned} s_i(\mathbf{x},t) &= S_{ji}(\mathbf{x},t)\ \ n_j(\mathbf{x}) \\ q\ (\mathbf{x},t) &= q_i(\mathbf{x},t)\ n_i(\mathbf{x}) \end{aligned} \tag{12}$$

Moreover, n_i are the components of the outward unit normal vector to the boundary surface and $\Sigma_1, \Sigma_2, \Sigma_3, \Sigma_4$ are subsurfaces of ∂B such that $\Sigma_1 \cup \bar{\Sigma}_2 = \Sigma_3 \cup \bar{\Sigma}_4 = \partial B$ and $\Sigma_1 \cap \Sigma_2 = \Sigma_3 \cap \Sigma_4 = \emptyset$, where the closure is relative to ∂B.

Through an appropriate change of variables and referring to suitable notations, it is possible to transform the considered final-boundary value problem $\mathcal{P}$ into an initial-boundary value problem $\mathcal{P}^*$. For each function depending on time $f(t)$, it is considered that $f^*(t^*) = f(t)$, with $t^* = -t$. Removing the star signs for the sake of simplicity, the following set of equations can be defined:

$$S_{ji,j} = \rho \ddot{u}_i \qquad \text{in } B \times [0, \infty) \tag{13}$$

$$T_0 M_{ij} \dot{e}_{ij} + q_{i,i} = c\dot{\theta} \qquad \text{in } B \times [0, \infty) \tag{14}$$

$$S_{ij} = C_{ijkl} e_{kl} + M_{ij}\theta \qquad \text{in } \bar{B} \times [0, \infty) \tag{15}$$

$$q_i = -K_{ij} g_j \qquad \text{in } \bar{B} \times [0, \infty) \tag{16}$$

$$e_{ij} = \frac{1}{2}\left(u_{i,j} + u_{j,i}\right) \qquad \text{in } \bar{B} \times [0, \infty) \tag{17}$$

$$g_i = \theta_{,i} \qquad \text{in } \bar{B} \times [0, \infty) \tag{18}$$

To the previous equations, the following initial conditions have to be added:

$$\begin{aligned} u_i(\mathbf{x},\ 0) &= u_i^0(\mathbf{x}) \qquad \dot{u}_i(\mathbf{x}, 0) = \dot{u}_i^0(\mathbf{x}) \\ \theta(\mathbf{x},0) &= \theta^0(\mathbf{x}) \qquad \text{with } \mathbf{x} \in \bar{B} \end{aligned} \tag{19}$$

together with the boundary conditions

$$\begin{aligned} u_i(\mathbf{x},t) &= 0 \quad \text{on} \quad \Sigma_1 \times [0, \infty) \\ s_i(\mathbf{x},t) &= 0 \quad \text{on} \quad \Sigma_2 \times [0, \infty) \\ \theta(\mathbf{x},t) &= 0 \quad \text{on} \quad \Sigma_3 \times [0, \infty) \\ q(\mathbf{x},t) &= 0 \quad \text{on} \quad \Sigma_4 \times [0, \infty) \end{aligned} \tag{20}$$

A solution of the considered initial-boundary value problem $\mathcal{P}^*$ will be identified with an ordered array $\pi = \left[u_i, e_{ij}, S_{ij}, \theta, g_i, q_i\right]$ satisfying (13)–(20) and with the following properties:

a. $u_i, \dot{u}_i, \ddot{u}_i, \left(u_{i,j} + u_{j,i}\right), \left(\dot{u}_{i,j} + \dot{u}_{j,i}\right)$ continuous on $\bar{B} \times [0, \infty)$

b. e_{ij} continuous symmetric tensor field on $\bar{B} \times [0, \infty)$

c. $S_{ij}, S_{ji,j}$ continuous on $\bar{B} \times [0, \infty)$

d. $\theta, \theta_{,i}, \dot{\theta}$ continuous on $\bar{B} \times [0, \infty)$

e. g_i continuous on $\bar{B} \times [0, \infty)$

f. $q_i, q_{i,i}$ continuous on $\bar{B} \times [0, \infty)$

Some Auxiliary Integral Identities

It is now necessary to preliminarily establish some auxiliary identities useful in order to investigate the temporal behavior of the solutions of the considered initial-boundary value problem $\mathcal{P}^*$.

Lemma 1. Assuming that $\pi = \left[u_i, e_{ij}, S_{ij}, \theta, g_i, q_i\right]$ represents a solution of $\mathcal{P}^*$, then it results

$$\frac{1}{2}\int_B\left[\rho\dot{u}_i(t)\dot{u}_i(t)+C_{ijkl}e_{ij}(t)e_{kl}(t)+\frac{c}{T_0}\theta(t)^2\right]dv$$
$$=\frac{1}{2}\int_B\left[\rho\dot{u}_i(0)\dot{u}_i(0)+C_{ijkl}e_{ij}(0)e_{kl}(0)+\frac{c}{T_0}\theta(0)^2\right]dv$$
$$+\int_0^t\int_B\frac{1}{T_0}K_{ij}g_i(s)g_j(s)dvds \qquad \text{for all } t\in[0,\infty) \tag{21}$$

Proof. Equations (7), (8), (13), and (17) imply that

$$\rho\dot{u}_i(s)\ddot{u}_i(s)=\left[S_{ji}(s)\dot{u}_i(s)\right]_{,j}-S_{ij}(s)\dot{e}_{ij}(s) \tag{22}$$

and then, taking into account (14), (15), and (18), it can be easily deduced that

$$\frac{\partial}{\partial s}\left\{\frac{1}{2}\left[\rho\dot{u}_i(s)\dot{u}_i(s)+C_{ijkl}e_{ij}(s)e_{kl}(s)+\frac{c}{T_0}\theta(s)^2\right]\right\}$$
$$=\left[S_{ji}(s)\dot{u}_i(s)+\frac{1}{T_0}q_j(s)\theta(s)\right]_{,j}-\frac{1}{T_0}q_j(s)g_j(s) \tag{23}$$

Substituting (16) into (23) and integrating the result over $B\times[0,t]$, with the aid of divergence theorem and in view of boundary conditions (20), identity (21) is obtained and the proof is complete.

Lemma 2. Assuming that $\pi=\left[u_i,e_{ij},S_{ij},\theta,g_i,q_i\right]$ represents a solution of $\mathcal{P}^*$, then it results

$$2\int_B\rho u_i(t)\dot{u}_i(t)dv$$
$$-\frac{1}{T_0}\int_B K_{ij}\int_0^t g_i(z)dz\int_0^t g_j(z)dzdv$$
$$=2\int_0^t\int_B\left\{\rho\dot{u}_i(s)\dot{u}_i(s)\right.$$
$$\left.-\left[C_{ijkl}e_{ij}(s)e_{kl}(s)+\frac{c}{T_0}\theta(s)^2\right]\right\}dvds \tag{24}$$
$$+2\int_B\rho u_i(0)\dot{u}_i(0)dv$$
$$-2\int_0^t\int_B\theta(s)\left[M_{ij}e_{ij}(0)-\frac{c}{T_0}\theta(0)\right]dvds$$
for all $t\in[0,\infty)$

Proof. Integrating over the interval $[0,t]$ the following identity

$$\frac{\partial}{\partial s}[\rho u_i(s)\dot{u}_i(s)]=\rho\dot{u}_i(s)\dot{u}_i(s)+\rho u_i(s)\ddot{u}_i(s) \tag{25}$$

it results

$$\rho u_i(t)\dot{u}_i(t)=\rho u_i(0)\dot{u}_i(0)$$
$$+\int_0^t[\rho\dot{u}_i(s)\dot{u}_i(s)+\rho u_i(s)\ddot{u}_i(s)]ds \tag{26}$$

Now, considering (7), (8), (13), and (17), it is possible to write

$$\rho u_i(s)\ddot{u}_i(s)=\left[S_{ji}(s)u_i(s)\right]_{,j}-S_{ij}(s)e_{ij}(s) \tag{27}$$

and then, using (15), it can be seen that

$$\rho u_i(s)\ddot{u}_i(s)=\left[S_{ji}(s)u_i(s)\right]_{,j}-C_{ijkl}e_{ij}(s)e_{kl}(s)$$
$$-M_{ij}e_{ij}(s)\theta(s) \tag{28}$$

On the other side, (14) can be integrated over $[0,t]$ in order to obtain

$$M_{ij}e_{ij}(t)=-\frac{1}{T_0}\int_0^t q_{i,i}(s)ds+\frac{c}{T_0}\theta(t)+\eta_0 \tag{29}$$

where η_0 is defined as follows:

$$\eta_0=M_{ij}e_{ij}(0)-\frac{c}{T_0}\theta(0) \tag{30}$$

So, taking into account (9), (16), (18), (28), and (29), one can write

$$\rho\, u_i(s)\ddot{u}_i(s)=\left[S_{ji}(s)u_i(s)+\frac{1}{T_0}\theta(s)\int_0^s q_j(z)dz\right]_{,j}$$
$$-\left[C_{ijkl}e_{ij}(s)e_{kl}(s)+\frac{c}{T_0}\theta(s)^2\right]$$
$$-\eta_0\theta(s)+\frac{1}{T_0}K_{ij}g_i(s)\int_0^s g_j(z)dz \tag{31}$$

Substituting (31) into (26) and integrating the result over B, identity (24) is achieved with the

help of divergence theorem and boundary conditions (20). The proof can be completed underlining that, through an integration by parts, it results

$$\begin{aligned}&\frac{1}{T_0}\int_B\int_0^t\left[K_{ij}g_i(s)\int_0^s g_j(z)dz\right]dsdv\\&=\frac{1}{T_0}\int_B\left[K_{ij}\int_0^t g_i(z)dz\int_0^t g_j(z)dz\right]dv\\&\quad-\frac{1}{T_0}\int_B\int_0^t\left[K_{ij}g_j(s)\int_0^s g_i(z)dz\right]dsdv\end{aligned}\tag{32}$$

where symmetry relation (9) has been used.

Lemma 3. Assuming that $\pi=[u_i,e_{ij},S_{ij},\theta,g_i,q_i]$ represents a solution of $\mathcal{P}^*$, then it results

$$\begin{aligned}&2\int_B\rho u_i(t)\dot{u}_i(t)dv\\&-\frac{1}{T_0}\int_B K_{ij}\int_0^t g_i(z)dz\int_0^t g_j(z)dzdv\\&=\int_B\rho[u_i(2t)\dot{u}_i(0)+\dot{u}_i(2t)u_i(0)]dv\\&+\int_0^t\int_B\eta_0[\theta(t+s)-\theta(t-s)]dvds\\&\text{for all } t\in[0,\infty)\end{aligned}\tag{33}$$

Proof. Integrating with respect to the variable s and over the interval $[0,t]$ the following identity

$$\begin{aligned}&\frac{\partial}{\partial s}\{\rho[u_i(t+s)\dot{u}_i(t-s)+\dot{u}_i(t+s)u_i(t-s)]\}\\&=\rho[u_i(t-s)\ddot{u}_i(t+s)-u_i(t+s)\ddot{u}_i(t-s)]\end{aligned}\tag{34}$$

one can obtain

$$\begin{aligned}2\rho u_i(t)\dot{u}_i(t)=&\rho[u_i(2t)\dot{u}_i(0)+\dot{u}_i(2t)u_i(0)]\\&+\int_0^t\rho[u_i(t+s)\ddot{u}_i(t-s)\\&-u_i(t-s)\ddot{u}_i(t+s)]ds\end{aligned}\tag{35}$$

Furthermore, in view of (7), (8), (13), (15), and (17), it can be deduced that

$$\begin{aligned}&\rho[u_i(t+s)\ddot{u}_i(t-s)-u_i(t-s)\ddot{u}_i(t+s)]\\&=[S_{ji}(t-s)u_i(t+s)-S_{ji}(t+s)u_i(t-s)]_{,j}\\&\quad+[S_{ij}(t+s)e_{ij}(t-s)-S_{ij}(t-s)e_{ij}(t+s)]\end{aligned}\tag{36}$$

and then

$$\begin{aligned}&S_{ij}(t+s)e_{ij}(t-s)-S_{ij}(t-s)e_{ij}(t+s)\\&=\theta(t+s)M_{ij}e_{ij}(t-s)-\theta(t-s)M_{ij}e_{ij}(t+s)\end{aligned}\tag{37}$$

By means of (16), (18), and (29), the following relation can be derived

$$\begin{aligned}&S_{ij}(t+s)e_{ij}(t-s)-S_{ij}(t-s)e_{ij}(t+s)\\&=\eta_0[\theta(t+s)-\theta(t-s)]\\&+\left\{\frac{1}{T_0}\left[\theta(t-s)\int_0^{t+s}q_i(z)dz-\theta(t+s)\int_0^{t-s}q_i(z)dz\right]\right\}_{,i}\\&+\frac{1}{T_0}\left[g_i(t-s)K_{ij}\int_0^{t+s}g_j(z)dz-g_i(t+s)K_{ij}\int_0^{t-s}g_j(z)dz\right]\end{aligned}\tag{38}$$

and substituted into (36); the result has to be placed into (35).

Integrating the obtained relation over B, identity (33) is proved with the help of divergence theorem and boundary conditions (20). The proof is then complete.

Corollary 1. Assuming that $\pi=[u_i,e_{ij},S_{ij},\theta,g_i,q_i]$ represents a solution of $\mathcal{P}^*$, then it results

$$\begin{aligned}&2\int_0^t\int_B\left\{\rho\dot{u}_i(s)\dot{u}_i(s)-\left[C_{ijkl}e_{ij}(s)e_{kl}(s)\right.\right.\\&\left.\left.+\frac{c}{T_0}\theta(s)^2\right]\right\}dvds=-2\int_B\rho u_i(0)\dot{u}_i(0)dv\\&+\int_B\rho[u_i(2t)\dot{u}_i(0)+\dot{u}_i(2t)u_i(0)]\,dv\\&+\int_0^t\int_B\eta_0[2\theta(s)+\theta(t+s)\\&-\theta(t-s)]dvds\qquad\text{for all } t\in[0,\infty)\end{aligned}$$

Proof. Remembering (30), it is sufficient to note that a combination of (24) and (33) implies identity (39). The proof is then complete.

Asymptotic Partition of Energy

In order to derive the relations that exhibit the asymptotic partition of energy, $\mathcal{M}$ has to be identified as the set of all thermoelastic processes $\pi = \left[u_i, e_{ij}, S_{ij}, \theta, g_i, q_i\right]$ defined on $B \times [0, \infty)$ such that

$$\int_0^t \int_B \frac{1}{T_0} K_{ij} g_i(s) g_j(s) dv ds \leq M \qquad \text{for all } t \in [0, \infty) \tag{40}$$

and where M is a positive constant. The asymptotic partition in concern can be shown provided that the considered thermoelastic process π is constrained to lie into the set $\mathcal{M}$.

Let $\pi = \left[u_i, e_{ij}, S_{ij}, \theta, g_i, q_i\right]$ be a solution of the initial-boundary value problem $\mathcal{P}^*$, and let the following Cesàro means be associated with it:

$$\mathcal{K}_C(t) = \frac{1}{2t} \int_0^t \int_B \rho \dot{u}_i(s) \dot{u}_i(s) dv ds \tag{41}$$

$$\mathcal{S}_C(t) = \frac{1}{2t} \int_0^t \int_B C_{ijkl} e_{ij}(s) e_{kl}(s) dv ds \tag{42}$$

$$\mathcal{T}_C(t) = \frac{1}{2t} \int_0^t \int_B \frac{c}{T_0} \theta(s)^2 dv ds \tag{43}$$

$$\mathcal{D}_C(t) = \frac{1}{t} \int_0^t \int_0^s \int_B \frac{1}{T_0} K_{ij} g_i(z) g_j(z) dv dz ds \tag{44}$$

It will be convenient, in order to perform the incoming analysis, to assume that *meas* $\Sigma_3 \neq 0$, also if the procedure that is going to be shown could also be extended in theory to the case when *meas* $\Sigma_3 = 0$. It is noticeable that if *meas* $\Sigma_1 = 0$, then there exists a set of rigid motions and null temperatures satisfying (13)–(18) and boundary conditions (20). It is thus possible to decompose the initial data u_i^0 and $\dot{u}_i^0$ as follows:

$$u_i^0 = u_i^* + U_i^0 \qquad \dot{u}_i^0 = \dot{u}_i^* + \dot{U}_i^0 \tag{45}$$

where u_i^* and $\dot{u}_i^*$ are determined in such a way that

$$\begin{aligned} &\int_B \rho U_i^0 dv = 0 \qquad \int_B \rho \varepsilon_{ijk} x_j U_k^0 dv = 0 \\ &\int_B \rho \dot{U}_i^0 dv = 0 \qquad \int_B \rho \varepsilon_{ijk} x_j \dot{U}_k^0 dv = 0 \end{aligned} \tag{46}$$

where ε_{ijk} is the alternating symbol.

The following notations are now introduced:

$$\hat{\mathbf{C}}^1(B) = \Big\{ \mathbf{v} = (v_1, v_2, v_3), \quad v_i \in C^1(\bar{B}) : v_i = 0 \quad \text{on} \quad \Sigma_1$$
$$\text{and if } meas\ \Sigma_1 = 0, \text{then} \int_B \rho v_i dv = \int_B \rho \varepsilon_{ijk} x_j v_k dv = 0 \Big\}$$
$$\hat{C}^1(B) = \left\{ \gamma \in C^1(B) : \gamma = 0 \quad \text{on } \Sigma_3 \right\}$$
$$\hat{\mathbf{W}}_1(B) \text{ is the completion of } \hat{\mathbf{C}}^1(B) \text{ by means of } \|\cdot\|_{\mathbf{W}_1(B)}$$
$$\hat{W}_1(B) \text{ is the completion of } \hat{C}^1(B) \text{ by means of } \|\cdot\|_{W_1(B)}$$

where

$C^1(\bar{B})$ is the set of scalar functions continuous and continuously differentiable on $\bar{B}$

$W_m(B)$ represents the familiar Sobolev space

$\mathbf{W}_m(B) = [W_m(B)]^3$

It has to be underlined that the following inequality

$$\frac{1}{4}\int_B C_{ijkl}\left(v_{i,j}+v_{j,i}\right)\left(v_{k,l}+v_{l,k}\right)dv \geq m_1\int_B v_i v_i dv \tag{47}$$

with m_1 suitable strictly positive constant and for all $\mathbf{v} \in \hat{\mathbf{W}}_1(B)$, holds in view of the fact that C_{ijkl} is a positive definite tensor (see [22]).

Moreover, taking into account that *meas* $\Sigma_3 \neq 0$ and that the conductivity tensor is positive definite, the following Poincaré inequality holds in view of boundary conditions (20):

$$\int_B K_{ij}\gamma_{,i}\gamma_{,j}dv \geq m_2\int_B \gamma^2 dv \tag{48}$$

with m_2 suitable strictly positive constant and for all $\gamma \in \hat{W}_1(B)$.

If *meas* $\Sigma_1 = 0$, then it will be convenient to decompose $\{u_i, \theta\}$ as follows:

$$\begin{aligned} u_i(\mathbf{x},t) &= u_i^*(\mathbf{x}) + t\dot{u}_i^*(\mathbf{x}) + v_i(\mathbf{x},t) \\ \theta(\mathbf{x},t) &= \gamma(\mathbf{x},t) \end{aligned} \tag{49}$$

where $\{\mathbf{v}, \gamma\} \in \hat{\mathbf{W}}_1(B) \times \hat{W}_1(B)$ represents the solution of the initial-boundary value problem $\mathcal{P}^*$ in which initial conditions (19) are substituted by

$$\begin{aligned} v_i(\mathbf{x},0) &= U_i^0(\mathbf{x}) \qquad \dot{v}_i(\mathbf{x},0) = \dot{U}_i^0(\mathbf{x}) \\ \gamma(\mathbf{x},0) &= \theta^0(\mathbf{x}) \qquad \text{with } \mathbf{x} \in \bar{B} \end{aligned} \tag{50}$$

Introducing the total energy associated with the solution $\pi = \left[u_i, e_{ij}, S_{ij}, \theta, g_i, q_i\right]$ as

$$U(t) = \frac{1}{2}\int_B \left[\rho\dot{u}_i(t)\dot{u}_i(t) + C_{ijkl}e_{ij}(t)e_{kl}(t) + \frac{c}{T_0}\theta(t)^2\right]dv \tag{51}$$

then it is possible to derive the asymptotic partition in terms of the Cesàro means (41)–(44).

Theorem 1. Let $\pi = \left[u_i, e_{ij}, S_{ij}, \theta, g_i, q_i\right]$ be a solution of the initial-boundary value problem $\mathcal{P}^*$ lying in the set $\mathcal{M}$ defined by (40). Then, for all choices of the initial data $\mathbf{u}^0 \in \mathbf{W}_1(B)$, $\dot{\mathbf{u}}^0 \in \mathbf{W}_0(B)$, and $\theta^0 \in W_0(B)$, it results

$$\lim_{t\to\infty} \mathcal{T}_C(t) = 0 \tag{52}$$

Furthermore, it is possible to distinguish two cases:

a. If *meas* $\Sigma_1 \neq 0$, then

$$\lim_{t\to\infty} \mathcal{K}_C(t) = \lim_{t\to\infty} \mathcal{S}_C(t) \tag{53}$$

$$\begin{aligned} \lim_{t\to\infty} \mathcal{D}_C(t) &= 2\lim_{t\to\infty} \mathcal{K}_C(t) - \mathcal{U}(0) \\ &= 2\lim_{t\to\infty} \mathcal{S}_C(t) - \mathcal{U}(0) \end{aligned} \tag{54}$$

b. If *meas* $\Sigma_1 = 0$, then

$$\lim_{t\to\infty} \mathcal{K}_C(t) = \lim_{t\to\infty} \mathcal{S}_C(t) + \frac{1}{2}\int_B \rho\dot{u}_i^*\dot{u}_i^* dv \tag{55}$$

$$\begin{aligned} \lim_{t\to\infty} \mathcal{D}_C(t) &= 2\lim_{t\to\infty} \mathcal{K}_C(t) - \mathcal{U}(0) \\ &\quad - \frac{1}{2}\int_B \rho\dot{u}_i^*\dot{u}_i^* dv = 2\lim_{t\to\infty} \mathcal{S}_C(t) \\ &\quad - \mathcal{U}(0) + \frac{1}{2}\int_B \rho\dot{u}_i^*\dot{u}_i^* dv \end{aligned} \tag{56}$$

Proof. From Lemma 1 and (51), it follows that

$$\mathcal{U}(t) = \mathcal{U}(0) + \int_0^t \int_B \frac{1}{T_0} K_{ij} g_i(s) g_j(s) dv ds \tag{57}$$

for $t \in [0, \infty)$

Taking into account (41)–(44) and (57), it is possible to deduce that

$$\begin{aligned}
&\mathcal{K}_C(t)+\mathcal{S}_C(t)+\mathcal{T}_C(t)\\
&=\frac{1}{2t}\int_0^t\int_B[\rho\dot{u}_i(s)\dot{u}_i(s)\\
&+C_{ijkl}e_{ij}(s)e_{kl}(s)+\frac{c}{T_0}\theta(s)^2\Big]dvds\\
&=\frac{1}{t}\int_0^t\mathcal{U}(s)ds\\
&=\frac{1}{t}\int_0^t\left[\mathcal{U}(0)+\int_0^s\int_B\frac{1}{T_0}K_{ij}g_i(z)g_j(z)dvdz\right]ds\\
&=\mathcal{U}(0)+\frac{1}{t}\int_0^t\int_0^s\int_B\frac{1}{T_0}K_{ij}g_i(z)g_j(z)dvdzds\\
&=\mathcal{U}(0)+\mathcal{D}_C(t)\\
&\text{for all } t\in(0,\infty)
\end{aligned}\tag{58}$$

From (40), (43), and (48), it can also be shown that

$$\begin{aligned}
&\mathcal{T}_C(t)\le\frac{1}{2t}\left[\frac{1}{T_0}\max_{\bar{B}}c(x)\right]\int_0^t\int_B\theta(s)^2dvds\\
&\le\frac{1}{2m_2t}[\max_{\bar{B}}c(\mathbf{x})]\int_0^t\int_B\frac{1}{T_0}K_{ij}g_i(s)g_j(s)dvds\\
&\le\frac{M}{2m_2t}[\max_{\bar{B}}c(\mathbf{x})]\quad\text{for } t\in(0,\infty)
\end{aligned}\tag{59}$$

So if t tends to infinity, the condition (52) is proved, and (58) trivially implies that

$$\lim_{t\to\infty}\mathcal{K}_C(t)+\lim_{t\to\infty}\mathcal{S}_C(t)=\mathcal{U}(0)+\lim_{t\to\infty}\mathcal{D}_C(t)\tag{60}$$

On the other side, taking into account (39) and (41)–(43), it is possible to write

$$\begin{aligned}
&\mathcal{K}_C(t)-\mathcal{S}_C(t)-\mathcal{T}_C(t)=-\frac{1}{2t}\int_B\rho u_i(0)\dot{u}_i(0)dv\\
&+\frac{1}{4t}\int_0^t\int_B\eta_0[2\theta(s)+\theta(t+s)-\theta(t-s)]dvds\\
&+\frac{1}{4t}\int_B\rho[u_i(2t)\dot{u}_i(0)+\dot{u}_i(2t)u_i(0)]dv\quad\text{for } t\in(0,\infty)
\end{aligned}\tag{61}$$

From (40), (51), and (57), it can also be considered that

$$\int_B\rho\dot{u}_i(s)\dot{u}_i(s)dv\le 2\mathcal{U}(s)\le 2[\mathcal{U}(0)+M]\tag{62}$$

and

$$\begin{aligned}
\int_B\theta(s)^2dv&\le\frac{T_0}{\min_{\bar{B}}c(\mathbf{x})}\int_B\frac{c}{T_0}\theta(s)^2dv\\
&\le\frac{2T_0}{\min_{\bar{B}}c(\mathbf{x})}\mathcal{U}(s)\\
&\le\frac{2T_0}{\min_{\bar{B}}c(\mathbf{x})}[\mathcal{U}(0)+M]
\end{aligned}\tag{63}$$

Furthermore, using into (61) the Schwarz's inequality and (52), (62), and (63), it is easy to prove that

$$\begin{aligned}
&\lim_{t\to\infty}\mathcal{K}_C(t)-\lim_{t\to\infty}\mathcal{S}_C(t)\\
&=\lim_{t\to\infty}\frac{1}{4t}\int_B\rho\dot{u}_i(0)u_i(2t)dv
\end{aligned}\tag{64}$$

Case A. $(meas\ \Sigma_1\neq 0)$

Since $\mathbf{u}\in\hat{\mathbf{W}}_1(B)$, from (40), (47), (51), and (57), it can be deduced that

$$\int_B u_i(s)u_i(s)dv\le\frac{2}{m_1}\mathcal{U}(s)\le\frac{2}{m_1}[\mathcal{U}(0)+M]\tag{65}$$

and using again Schwarz's inequality, it results

$$\lim_{t\to\infty}\frac{1}{4t}\int_B\rho\dot{u}_i(0)u_i(2t)dv=0\tag{66}$$

So (64) and (66) lead to (53), while (54) follows from (53) and (60).

Case B. $(meas\ \Sigma_1=0)$

From (46), (49), and (50), it is possible to deduce that

$$\frac{1}{4t}\int_B \rho\dot{u}_i(0)u_i(2t)dv = \frac{1}{4t}\int_B \rho\dot{u}_i^* u_i^* dv + \frac{1}{4t}\int_B \rho\left(\dot{u}_i^* + \dot{U}_i^0\right)v_i(2t)dv + \frac{1}{2}\int_B \rho\dot{u}_i^*\dot{u}_i^* dv \tag{67}$$

On the other hand, from (40), (47), (51), and (57), it is noticeable that

$$\int_B v_i(s)v_i(s)dv \le \frac{2}{m_1}\mathcal{U}(s) \le \frac{2}{m_1}[\mathcal{U}(0) + M] \tag{68}$$

and so (67) leads to

$$\lim_{t\to\infty}\frac{1}{4t}\int_B \rho\dot{u}_i(0)u_i(2t)dv = \frac{1}{2}\int_B \rho\dot{u}_i^*\dot{u}_i^* dv \tag{69}$$

Then, substituting (69) into (64), (55) is obtained, while (56) follows from coupling (55) and (60). The proof is then complete.

The performed analysis has to be concluded underlining that the restriction (40), used in order to establish *Theorem 1*, exists in connection with uniqueness and ▶ continuous dependence results obtained by Ames and Payne [12] and Ciarletta [13].

Cross-References

▶ Backward in Time Problems

References

1. Lax PD, Phillips RS (1967) Scattering theory. Academic, New York
2. Brodsky AR (1967) On the asymptotic behavior of solutions of the wave equation. Proc Amer Math Soc 18:207–208
3. Goldstein JA (1969) An asymptotic property of solutions of wave equations. Proc Amer Math Soc 23:359–363
4. Goldstein JA (1970) An asymptotic property of solutions of wave equations II. J Math Anal Appl 32:392–399
5. Levine HA (1977) An equipartition of energy theorem for weak solutions of evolutionary equations in Hilbert space: the Lagrange identity method. J Differ Equ 24:197–210
6. Day WA (1980) Means and autocorrelations in elastodynamics. Arch Ration Mech Anal 73:243–256
7. Chiriţă S (1987) On the asymptotic partition of energy in linear thermoelasticity. Quart Appl Math 45:327–340
8. Serrin J (1963) The initial value problem for the Navier–Stokes equations. In: Proceeding of a Symposium Non-Linear Problems, Madison, University Wisconsin Press, pp 69–98
9. Knops RJ, Payne LE (1968) On the stability of solutions of the Navier–Stokes equations backward in time. Arch Ration Mech Anal 29:331–335
10. Galdi GP, Straughan B (1988) Stability of solutions of the Navier–Stokes equations backward in time. Arch Ration Mech Anal 101:107–114
11. Payne LE, Straughan B (1990) Improperly posed and non-standard problems for parabolic partial differential equations. In: Eason G, Ogden RW (eds) Elasticity: mathematical methods and applications, the Ian N. Sneddon 70th birthday volume. Ellis Horwood, Chichester, pp 273–299
12. Ames KA, Payne LE (1991) Stabilizing solutions of the equations of dynamical linear thermoelasticity backward in time. Stab Appl Anal Contin Media 1:243–260
13. Ciarletta M (2002) On the uniqueness and continuous dependence of solutions in dynamical thermoelasticity backward in time. J Therm Stress 25:969–984
14. Ciarletta M, Chiriţă S (2001) Spatial behavior in dynamical thermoelasticity backward in time. Fourth International Congress on Thermal Stresses, Osaka, Japan, pp 485–488
15. Ciarletta M, Chiriţă S (2001) Asymptotic partition in the linear thermoelasticity backward in time. Mathematical models and methods for smart materials. World Sci 62:31–41
16. Iovane G, Passarella F (2004) Spatial behavior in dynamical thermoelasticity backward in time for porous media. J Therm Stress 27:97–109
17. Passarella F, Tibullo V (2010) Some results in linear theory of thermoelasticity backward in time for microstretch materials. J Therm Stress 33:559–576
18. Passarella F, Tibullo V, Zampoli V (in press) On the uniqueness in dynamical thermoelasticity backward in time for porous media. Int. Journal of Thermal Stresses
19. Brun L (1965) Sur l'unicité en thermoelasticité dynamique et diverses éxpressions analogues à la formule de Clapeyron. CR Acad Sci Paris 261:2584–2587
20. Brun L (1969) Méthodes énergétiques dans les systèmes évolutifs linéaires. J Méc 8:125–192
21. Carlson DE (1972) Linear thermoelasticity. In: Truesdell C (ed) Handbuch der physik VIa/2. Springer, Berlin
22. Hlaváček I, Nečas J (1970) On inequalities of Korn's type. Arch Rational Mech Anal 36:305–334

Atomic-Level Hybrid Modeling of Thermomechanical Stress Wave in Metal Thin Films Induced by Ultrashort Laser Pulses

Yong Gan[1] and Jinn-Kuen Chen[2]
[1]School of Aeronautics and Astronautics, Zhejiang University, Hangzhou, Zhejiang, People's Republic of China
[2]Department of Mechanical and Aerospace Engineering, University of Missouri, Columbia, MO, USA

Overview

Ultrashort laser pulses are cataloged for those whose durations are in the range of femtoseconds ($1\ \text{fs} = 10^{-15}$ s) to a few picoseconds ($1\ \text{ps} = 10^{-12}$ s), depending on the interacted materials. Comparing with conventional laser pulses that have a duration of nanoseconds ($1\ \text{ns} = 10^{-9}$ s) or longer, these laser pulses have two exceptional features: (1) ultrashort pulse duration and (2) extremely high laser power, leading to a wide spectrum of application in the fields of chemistry, physics, biology, medicine, and engineering. For example, ultrashort-pulsed lasers have been used to observe chemical bond formation and breaking [1, 2], generate high-density plasma [3], image and manipulate biological systems [4], deliver foreign gene into cells in vitro [5], synthesize metal and semiconductor nanoparticles [6], etc.

Over the past two decades, many efforts have been stimulated to explore micro-/nanoprocessing of solid thin films by ultrashort-pulsed lasers. The ultrafast laser processing of metal films can generally be categorized into two main regimes: nanostructure fabrication and ultrahigh-precision machining. The former is to change film surface topography and controllably generate nanostructures, such as nanojets and nanobumps [7, 8], on a film surface; the latter is to machine metal films through material removal with minimal burr formation and collateral damage [9, 10].

Under the ultrafast laser irradiation, temperature in a metal target can easily shoot up to several thousand degrees and the strain rate up to $10^{10}\ \text{s}^{-1}$. In addition, the interacted material could exhibit a very different thermomechanical behavior from those caused by conventional pulse lasers. The behaviors of metal thin films induced by ultrafast laser heating can be simulated using an integrated numerical method coupling the molecular dynamics (MD) for lattice and the energy transport model for electron gas (continuum). This atomic-level hybrid approach vitally does not require *a priori* knowledge of lattice thermomechanical properties at extremely high temperature and strain-rate conditions, which, however, are barely available thus far.

Theory

When a metal target is irradiated by an ultrashort laser pulse, the incident laser energy is first absorbed by those electrons located within the skin (optical penetration) depth. During this short period of time, temperature (T_e) of the excited electrons can be very high due to the extremely high laser energy density and the small electron heat capacity, while the lattice temperature (T_l) basically remains unchanged. Then, a portion of the electron thermal energy diffuses, through electrons, into the deeper region, while the other part of the electron thermal energy transfers to the neighboring lattice via collision between electrons and phonons. Eventually, a thermal equilibrium state (i.e., $T_e = T_l$) will be established, and the subsequent thermal transport process can then be characterized by the classical heat conduction theory. The above two-step thermal process of ultrafast laser heating can be described by a two-temperature model (TTM) (e.g., [11])

$$C_e \frac{\partial T_e}{\partial t} = \nabla(K_e \nabla T_e) - G\,(T_e - T_l) + S \qquad (1)$$

$$C_l \frac{\partial T_l}{\partial t} = \nabla(K_l \nabla T_l) + G\,(T_e - T_l) \qquad (2)$$

where C is the heat capacity, K is the thermal conductivity, G is the electron-phonon coupling factor, S is the volumetric laser heat source, t represents time, and the subscripts e and l denote the quantities associated with the electron and lattice, respectively. The term $G(T_e - T_l)$ in the two equations is the thermal energy exchanged between the electrons and lattice. For a slow laser heating, the thermalization time for electrons and lattice to reach equilibrium is much shorter than the lasing time, and thus, the equilibrium temperature ($T_e = T_l$) is assumed for the entire heating process. In that case, the above two-temperature model can be reduced, by combining (1) and (2) with $T_e = T_l$, to the classical Fourier heat conduction equation.

Since thermal expansion in lattice occurs in such extremely short time ($\sim$ ps) when the lattice is heated up, the rate of change of the lattice dilation could be on the order of magnitude same as that of the lattice temperature. For that reason, the exchange of the thermal and mechanical energy in the lattice should be accommodated so that the temperature response can be better described. Thus, (2) is modified to

$$C_l \frac{\partial T_l}{\partial t} = \nabla(K_l \nabla T_l) + G\,(T_e - T_l) - (3\lambda + 2\mu)\alpha T_l \dot{\varepsilon}_{kk} \tag{3}$$

where λ is the Lamb constant, μ is the shear modulus, α is the thermal expansion coefficient, and $\dot{\varepsilon}_{kk}$ is the time rate of change of the lattice dilation with ε_{kk} denoting the sum of the three normal strains ε_{xx}, ε_{yy}, and ε_{zz}.

Because the dilation ($\dot{\varepsilon}_{kk}$) of lattice is involved in (3), the momentum equation of lattice should also be considered for solving the displacement field for the strains. For a metal material subjected to ultrashort-pulsed laser heating, the momentum equation of lattice is written in the following form [12]:

$$\rho \ddot{u}_\zeta = \sigma_{\eta\zeta,\eta} + \frac{2}{3}(C_e T_e)_{,\zeta} \tag{4}$$

where ρ is mass density of lattice, $\ddot{u}_\zeta$ are acceleration components ($\zeta = x, y, z$), $\sigma_{\eta\zeta}$ are stress components ($\eta = x, y, z$), and the subindices after "," denote the first spatial derivative with respect to the corresponding coordinate, respectively. Deviating from the classical momentum equation, the second term on the right-hand side of (4) is the so-called hot-electron blast force [13] that results from the electric kinetic pressure [12]. This hot-electron blast force could be quite significant during the early nonequilibrium stage, when both the electron temperature and its spatial gradient are very high. The stresses in (4) can be expressed in terms of strains and then displacements. Hence, the above ultrafast thermomechanical model, including five equations in (1), (3), and (4), can be solved for the five unknowns T_e, T_l, u_x, u_y, and u_z and subsequently the strains and stresses.

The main challenges in solving the continuum-based ultrafast thermomechanical model include the following: (1) the temperature-dependent thermal and mechanical properties of lattice, such as thermal conductivity, heat capacity, thermal expansion coefficients, and moduli, under the extremely high temperature and strain-rate conditions are barely available, and (2) the progressive lattice deformation, e.g., crack formation and propagation, is difficult to be accurately described. The latter usually is compounded by the former. To overcome these predicaments, an MD model for the lattice can be introduced to replace (3) and (4) since it has been shown that MD is an efficient tool for modeling ultrafast thermomechanical behavior of metal materials [14–16]. In the MD simulation, the lattice properties are characterized implicitly through the interatomic potential. The lattice temperature can be evaluated with the simulated velocities of atoms, and the deformation can be tracked and examined by the atom's trajectory.

The classical MD equations of motion for the lattice are given as follows [17]:

$$m_i \frac{d^2 \mathbf{r}_i}{dt^2} = -\sum_{j=1, j\neq i}^{N} \frac{\partial U(\mathbf{r}_{ij})}{\partial \mathbf{r}_{ij}} \tag{5}$$

in which m_i and $\mathbf{r}_i$ are the mass and position vector of atom i, respectively; $U(\mathbf{r}_{ij})$ is the interatomic potential between atoms i and j

separated by a distance $\mathbf{r}_{ij}$; N is the total number of atoms in the MD system; and the subscripts i and j run over all the atoms in the system. To take account of the thermal energy exchange between the electron gas and atoms in the MD model, an alternative form of the term $G(T_l - T_e)$ in (2) is inserted into the MD equations [18],

$$m_i \frac{d^2\mathbf{r}_i}{dt^2} = -\sum_{j=1, j\neq i}^{N} \frac{\partial U(\mathbf{r}_{ij})}{\partial \mathbf{r}_{ij}} - \xi m_i \mathbf{v}_i^T \tag{6}$$

$$\xi = \frac{\frac{1}{n} V_c \sum_{m=1}^{n} G\left(T_l - T_e^m\right)}{\sum_{k=1}^{N_V} m_k \left(v_k^T\right)^2} \tag{7}$$

The new symbols in (6) and (7) are explained below. Equation 1 governs the electron temperature and can be solved numerically using an explicit finite difference (FD) method. To couple with the FD method, the entire MD model is discretized into a collection of volumes corresponding to the FD cells. The maximum time step allowed for integrating the finite difference equations is determined by the von Neumann stability criterion and typically is much smaller than the time step employed in the integration of the MD equations of motion. Therefore, the time step for the MD simulation should be chosen to be multiple times that for the FD simulation. The symbols in (6) and (7) thus are defined as follows: V_c is the volume of the FD cell in which atom i exists, $\mathbf{v}_k^T$ is the velocity of an atom k after subtracting out the center-of-mass velocity of the atom group in V_c, n is the number of the total FD time steps in a single MD time step, T_e^m is the electron temperature obtained at the m-th FD time step, and N_V is the number of atoms in the volume of V_c. Under this manner, the lattice temperature of a FD cell is computed by

$$T_l = \frac{\sum_{k=1}^{N_V} m_k \left(v_k^T\right)^2}{3 N_V k_B} \tag{8}$$

with k_B being the Boltzmann constant.

Similar to the damping force converted for the thermal energy exchange between electrons and lattice, the hot-electron blast force, i.e., the last term in (4), needs to be modified so that it can be applied to the MD equations. By recalling the discretion of the FD cells, the hot-electron blast force $\mathbf{B}_i$ exerting on an atom i in the volume V_c can be computed by [14]

$$\mathbf{B}_i = \frac{2\nabla (C_e T_e)_i}{3} \frac{V_c}{N_V} \tag{9}$$

leading the MD equation of motion (6) to

$$m_i \frac{d^2\mathbf{r}_i}{dt^2} = -\sum_{j=1, j\neq i}^{N} \frac{\partial U(\mathbf{r}_{ij})}{\partial \mathbf{r}_{ij}} - \xi m_i \mathbf{v}_i^T + \mathbf{B}_i \tag{10}$$

The embedded atom method (EAM) potential proposed by Daw and Baskes [19] can be employed for the interatomic interaction between atoms. For atom i, the EAM potential U_i is expressed as

$$U_i = F_i(\theta_i) + \frac{1}{2} \sum_{j=1, j\neq i}^{N} \phi_{ij}\left(r_{ij}\right) \tag{11}$$

$$\theta_i = \sum_{j=1, j\neq i}^{N} g_j(r_{ij}) \tag{12}$$

in which g_j is the electron density at embedded atom i contributed from atom j with a distance r_{ij} between the two centers, θ_i is the electron density at the atom i contributed from all other atoms, F_i is the energy function of atom i in an electron density θ_i, and ϕ_{ij} is a short-range pair potential function. The embedded function F_i is universal and does not depend on the source of the background electron density, the pair interaction term ϕ_{ij} is purely repulsive, and the electron density g_j can be computed from the Hartree-Fock wave functions [19].

The continuum-based energy and momentum equations for lattice, (3) and (4), have been replaced by the MD equations of motion (10) with the additions of thermal energy exchange between electrons and lattice and the hot-electron

blast force. The temperature field, locations, and stresses of lattice can be computed from the MD results. On the other hand, the following temperature-dependent material parameters C_e, K_e, and G are employed to solve the electron temperature from the energy balance equation (1) [12, 20, 21]:

$$K_e = \chi \vartheta_e \frac{\left(\vartheta_e^2 + 0.16\right)^{5/4}\left(\vartheta_e^2 + 0.44\right)}{\left(\vartheta_e^2 + 0.092\right)^{1/2}\left(\vartheta_e^2 + \kappa\vartheta_l\right)} \tag{13}$$

$$G = G_{RT}\left[\frac{A_e}{B_l}\left(T_e + T_l\right) + 1\right] \tag{14}$$

$$C_e = \begin{cases} C_{e0}T_e, & T_e < \frac{T_F}{\pi^2} \\ \frac{2C_{e0}T_e}{3} + \frac{C'_e}{3}, & \frac{T_F}{\pi^2} \le T_e < \frac{3T_F}{\pi^2} \\ N_d k_B + \frac{C'_e}{3}, & \frac{3T_F}{\pi^2} \le T_e < T_F \\ \frac{3N_d k_B}{2}, & T_e \ge T_F \end{cases} \tag{15}$$

with

$$C'_e = \frac{\frac{3N_d k_B}{2} - \frac{C_{e0}T_F}{\pi^2}}{T_F - \frac{T_F}{\pi^2}}\left(T_e - \frac{T_F}{\pi^2}\right) + \frac{C_{e0}T_F}{\pi^2} \tag{16}$$

In the above (13)–(16), χ and κ are material parameters, $\vartheta_e = T_e/T_F$ and $\vartheta_l = T_l/T_F$ with T_F denoting the Fermi temperature, G_{RT} is the electron-phonon coupling factor at room temperature, A_e and B_l are material constants in the characterization of electron relaxation time, C_{eo} is the slope of C_e in the first range of $T_e < T_F/\pi^2$, and N_d is the number density of atoms.

Numerical Analysis

Consider that a gold film is irradiated by a flat-top, ultrashort laser pulse whose spot size is much larger than the film thickness. The time period of interest for the numerical simulation here is significantly shorter than that for the outgoing lateral stress wave to reflect back to the heated spot, due to the assumption that the in-plane dimensions are much larger than the thickness. Under these conditions, the thermomechanical problem can be treated as a case of one-dimensional (1-D) thermal transport and uniaxial strain in the film thickness direction. Let the z axis be along the film thickness direction. The 1-D form of (1) becomes

$$C_e(T_e)\frac{\partial T_e}{\partial t} = \frac{\partial}{\partial z} \times \left(K_e \frac{\partial T_e}{\partial z}\right) - G\left(T_e - T_l\right) + S \tag{17}$$

For a Gaussian beam with a FWHM (full width at half maximum) duration t_p, the 1-D form of the laser heat source S in (17) is described as

$$S(z,t) = 0.94\frac{J_{abs}}{t_p d_s} \times \exp\left[-\frac{z}{d_s} - 2.77\left(\frac{t - 2t_p}{t_p}\right)^2\right] \tag{18}$$

where J_{abs} is the absorbed laser fluence and d_s is the optical penetration depth. Equation 18 indicates that the laser pulse is impinged on the front film surface ($z = 0$). The lasing starts at $t = 0$ with the peak power occurring at $t = 2t_p$. The laser is assumed to be off at $t = 4t_p$ since the laser power after then is very small and can be neglected.

The MD equations of motion are solved using the Velocity Verlet algorithm. At time $t + \Delta t$, the acceleration $\mathbf{a}_i$, velocity $\mathbf{v}_i$, and position vector $\mathbf{r}_i$ of each atom i are updated by [15],

$$\mathbf{r}_i(t + \Delta t) = \mathbf{r}_i(t) + \mathbf{v}_i(t)\Delta t + \frac{1}{2}(\Delta t)^2\mathbf{a}_i(t) \tag{19}$$

$$\mathbf{v}_i\left(t + \frac{1}{2}\Delta t\right) = \mathbf{v}_i(t) + \frac{1}{2}\mathbf{a}_i(t)\Delta t \tag{20}$$

$$\mathbf{a}_i(t + \Delta t) = \frac{-\sum_{j=1, j\neq i}^{N} \frac{\partial U(\mathbf{r}_{ij})}{\partial \mathbf{r}_{ij}}\Big|_{t+t} - \xi m_i \mathbf{v}_i^T + \mathbf{B}_i}{m_i} \tag{21}$$

$$\mathbf{v}_i(t + \Delta t) = \mathbf{v}_i\left(t + \frac{1}{2}\Delta t\right) + \frac{1}{2}\mathbf{a}_i(t + \Delta t)\Delta t \tag{22}$$

Atomic-Level Hybrid Modeling of Thermomechanical Stress Wave in Metal Thin Films Induced by Ultrashort Laser Pulses, Table 1 Thermophysical parameters of gold

Parameter	Value
T_F (K)	64,000 [12]
C_{e0} (Jm^{-3} K^{-2})	71 [12]
N_d (m^{-3})	5.9×10^{28} [14]
G_{RT} (Wm^{-3} K^{-1})	2.1×10^{16} [12]
A_e (K^{-2} s^{-1})	1.2×10^{7} [20]
B_l (K^{-1} s^{-1})	1.23×10^{11} [20]
d_s (nm)	15.3 [12]
χ (Wm^{-1} K^{-1})	353 [12]
κ	0.16 [12]

The virial stress in atomistic simulations and its potential part have been demonstrated equivalent to the continuum stresses in either the Eulerian or Lagrangian configuration [22]. The thermomechanical stresses in the films can be computed by the following equation [23]:

$$\sigma_{\eta\zeta} = -\frac{1}{V}\sum_{i=1}^{N_c}\left(\frac{v_{i\eta}v_{i\zeta}}{m_i} + \frac{1}{2}\sum_{j=1}^{N_i} r_{ij\eta} f_{ij\zeta}\right) \quad (23)$$

where $v_{i\eta}$ and $v_{i\zeta}$ are the momentums of atom i in the η and ζ directions, respectively; $r_{ij\eta}$ is the component of the position vector $\mathbf{r}_{ij}$ between atoms i and j in the η direction; $f_{ij\zeta}$ is the component of the force vector on atom i due to atom j in the ζ direction; V is the current volume corresponding to the FD cell; N_c is the total number of atoms in the volume V; and N_i is the number of neighbor atoms to the atom i.

The MD system for the thin films are created out of a bulk fcc gold crystal with the [1 0 0], [0 1 0], and [0 0 1] crystallographic directions along the x, y, and z axes, respectively. The film surfaces normal to the z axis are free, and periodic boundaries are applied in the x and y direction. The two initial MD models have the same length of 4.08 nm in each of the x and y directions and different lengths of 99.96 nm and 499.8 nm in the z direction.

In the following numerical demonstration, two thin gold films of thickness 100 nm and 500 nm irradiated by a laser pulse of $t_p = 150$ fs are considered. The electron temperature is

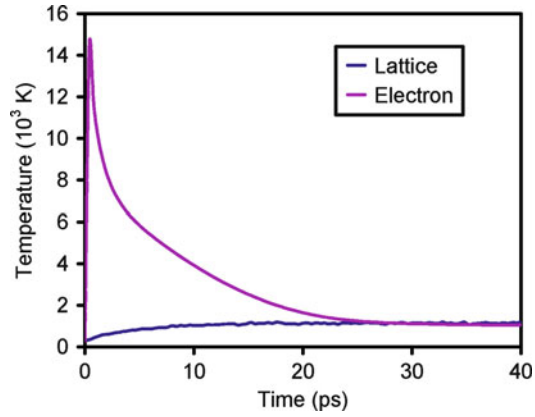

Atomic-Level Hybrid Modeling of Thermomechanical Stress Wave in Metal Thin Films Induced by Ultrashort Laser Pulses, Fig. 1 Time histories of lattice and electron temperatures at the irradiated surface of the 100-nm film heated by the 150-fs laser pulse of $J_{abs} = 175$ J/m^2

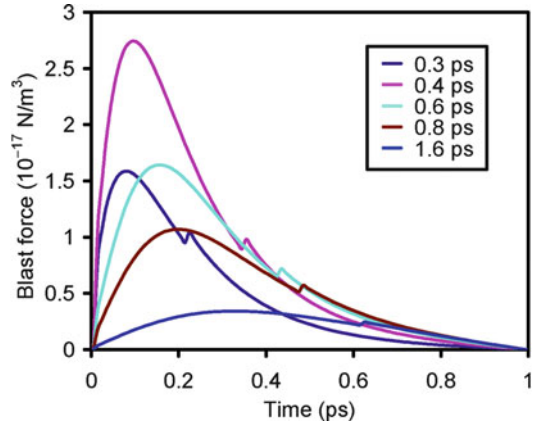

Atomic-Level Hybrid Modeling of Thermomechanical Stress Wave in Metal Thin Films Induced by Ultrashort Laser Pulses, Fig. 2 Hot-electron blast force profiles along the thickness of the 100-nm film

calculated from (1) with the adiabatic boundary conditions using the explicit FD method. The total numbers of cells in the FD model are 100 for the 100-nm film and 500 for the 500-nm film. The time step is 2.0 fs for the MD simulations and 0.005 fs for the FD calculations, giving $n = 400$ in (7). Before the laser beam is applied, the MD systems are equilibrated at 298 K and zero stress in both the x and y directions. The thermophysical parameters of gold is listed in Table 1.

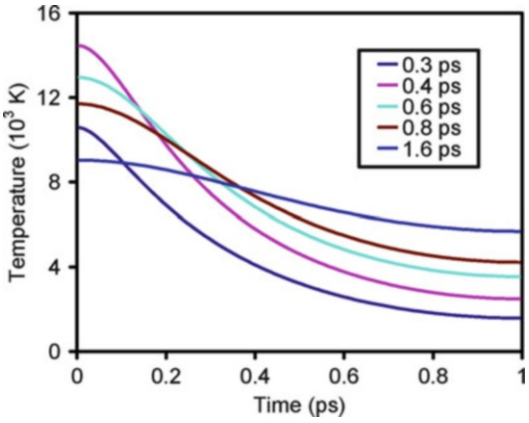

Atomic-Level Hybrid Modeling of Thermomechanical Stress Wave in Metal Thin Films Induced by Ultrashort Laser Pulses, Fig. 3 Distributions of the electron temperature along the thickness of the 100-nm film

Results

The simulated thermomechanical responses shown in Figs. 1–4 are for the 100-nm gold film heated by the laser pulse of $J_{abs} = 175$ J/m^2. Figure 1 shows the time histories of electron and lattice temperatures at the irradiated surface. It is obvious that the highly nonequilibrium thermal state exists in the early stage of the heating process as the significant difference between electron and lattice temperatures illustrated in Fig. 1. The maximum electron temperature is 14,494 K at $t = 0.41$ ps, while the lattice temperature only raises 49 K to 347 K at that time instant. The thermal equilibrium is established at about $t = 28$ ps when the lattice and electron temperatures becomes identical, about 1,150 K. Figure 2 plots the hot-electron blast force profiles

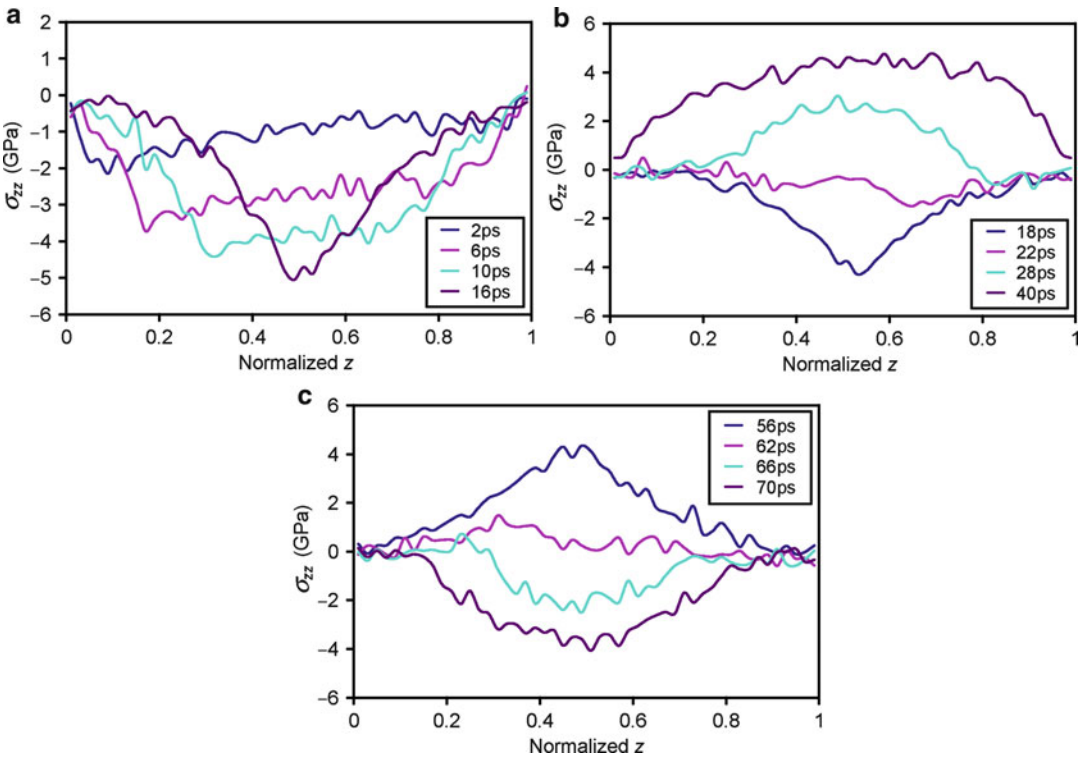

Atomic-Level Hybrid Modeling of Thermomechanical Stress Wave in Metal Thin Films Induced by Ultrashort Laser Pulses, Fig. 4 Distributions of normal stress σ_{zz} along the thickness of the 100-nm film: (**a**) $t = 2$, 6, 10, and 16 ps, (**b**) $t = 18$, 22, 28, and 40 ps, (**c**) $t = 56$, 62, 66, and 70 ps

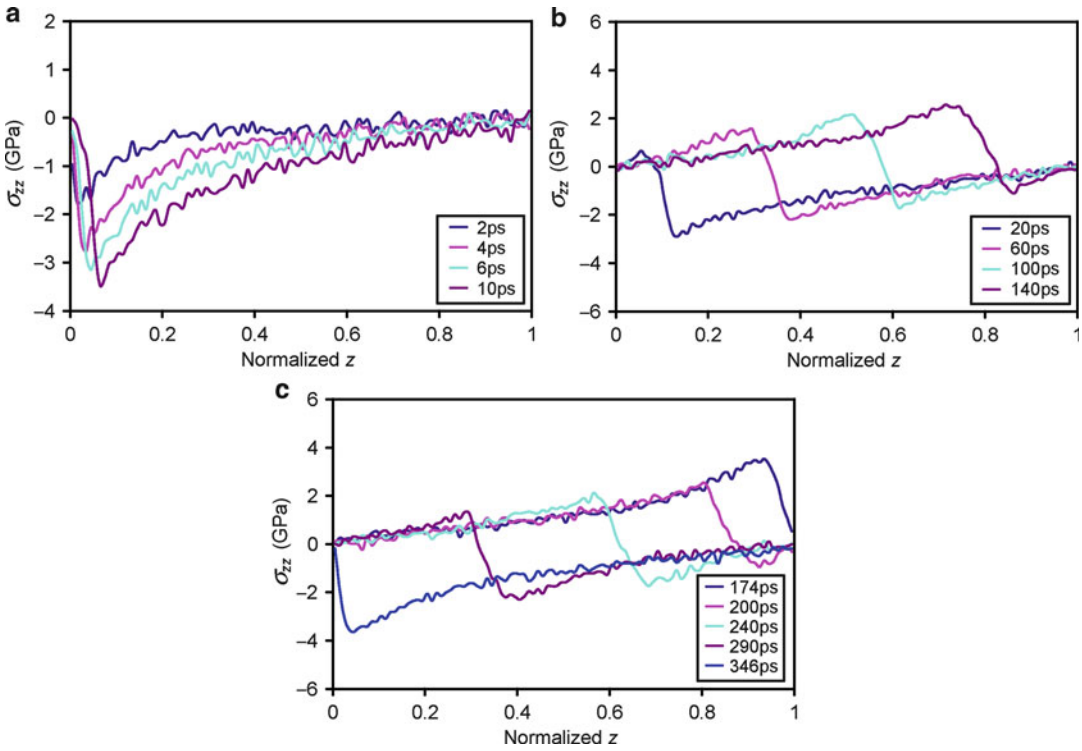

Atomic-Level Hybrid Modeling of Thermomechanical Stress Wave in Metal Thin Films Induced by Ultrashort Laser Pulses, Fig. 5 Distributions of normal stress σ_{zz} along the thickness of the 500-nm film heated by the laser pulse of $J_{abs} = 175$ J/m^2: (**a**) $t = 2, 4, 6,$ and 10 ps, (**b**) $t = 20, 60, 100,$ and 140 ps, (**c**) $t = 174, 200, 240, 290,$ and 346 ps

along the thickness direction (z axis) at different time instants, where the normalized values of $z = 0$ and 1 denote the irradiated and rear film surface, respectively. The hot-electron blast force reaches its maximum value of 2.74×10^{17} Nm^{-3} at about $t = 0.4$ ps and the normalized location $z = 0.095$ and then quickly drops down due to the fast decrease in the electron temperature and its gradient, as shown in Fig. 3. Those kicks in Fig. 2 are because the electron capacity is assumed to be a piecewise linear function of electron temperature (15).

Figure 4 presents the distributions of normal stress σ_{zz} along the z axis at various times. Initially, a compressive stress is generated in the front film side. While the peak of the compressive stress continues increasing, it also moves toward to the deeper part of the film. The maximum compressive stress is about 5 GPa occurring at $t = 16$ ps and the normalized location $z = 0.49$. Then, the stress wave becomes weaker and weaker and, further, converts into tension. At $t = 40$ ps, the peak of the tensile stress is 4.75 GPa, which is much larger than the ultimate strength of gold at room temperature (1.24 GPa). Afterward the stress oscillates like a standing wave as the film vibrates like a free-free spring.

The distributions of σ_{zz} in the thicker film of 500 nm induced by the same laser pulse of 150 fs and $J_{abs} = 175$ J/m^2 are shown in Fig. 5. Likewise, a compressive stress wave is first generated in the region near the irradiated surface. However, it can be seen in the figure that a tensile stress starts to emerge near the front film surface, instead of the middle film depth in the 100-nm film case. A twofold stress wave, comprising compression and tension, is consequently formed and propagates to the rear surface. As the twofold

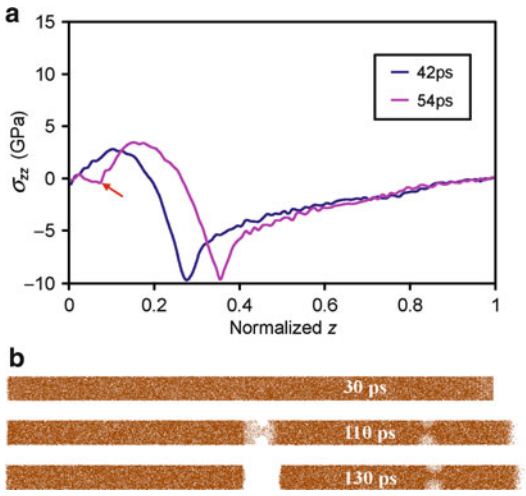

Atomic-Level Hybrid Modeling of Thermomechanical Stress Wave in Metal Thin Films Induced by Ultrashort Laser Pulses, Fig. 6 Results of the laser heating for the 500-nm thick film with $J_{abs} = 520$ J/m^2: (**a**) distributions of σ_{zz} along the film thickness (the stress drop is marked by *red arrow*), (**b**) snapshots for atoms in the region of normalized $z = 0.0$–0.16 at $t = 30$ ps

wave approaches the back surface, the leading compressive stress wave reverses to tension by the free surface reflection, and thereby transforming the twofold wave into a tensile stress wave. The superposition of the reflected and incoming tensile stress waves eventually results in the maximum tensile stress in the rear side, with the magnitude close to that of the maximum compressive stress initially generated in the front film side. Subsequently, the twofold wave appears again and travels back to the front film surface with a leading tensile wave instead. In this thicker film, the generation and propagation of the stress wave seems to be more conceivable though the wave is in a twofold form.

Figures 6 and 7 illustrate the results for the 500-nm film heated by the two laser pulses at higher absorbed fluences $J_{abs} = 520$ and 900 J/m^2, respectively. It is observed in Fig. 6a that a drop of the tensile stress σ_{zz} suddenly takes place at about $t = 54$ ps in the region of normalized $z = 0.1$. According to the snapshots shown in

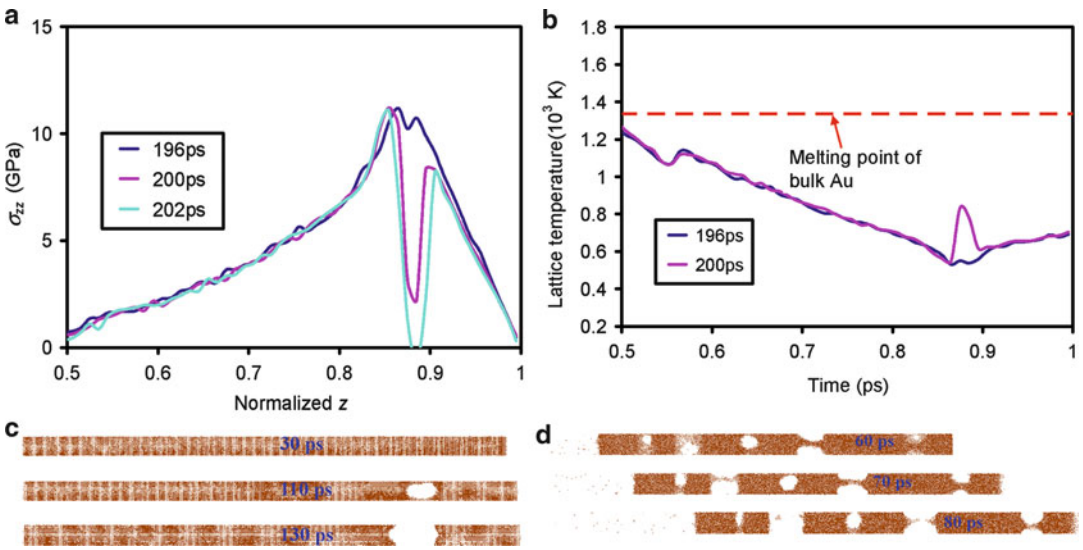

Atomic-Level Hybrid Modeling of Thermomechanical Stress Wave in Metal Thin Films Induced by Ultrashort Laser Pulses, Fig. 7 Results of the laser heating for the 500-nm thick film with $J_{abs} = 900$ J/m^2: (**a**) distributions of σ_{zz} along the film thickness, (**b**) lattice temperature distributions along the film thickness, (**c**) snapshots for atoms in the region of normalized $z = 0.824$–0.944 at $t = 180$ ps, and (**d**) snapshots for atoms in the region of normalized $z = 0.078$–0.22 at $t = 60$ ps

Fig. 6b, the stress drop can be attributed to the crack formation there. For the case of even higher absorbed fluence 900 J/m^2, as shown in Fig. 7a, the tensile stress abruptly drops also at about $t = 200$ ps in the region of normalized $z = 0.88$ and is accompanied by a sharp spike temperature. Those rapid changes are attributed to the spallation in the rear side of the film as found in Fig. 7c. By comparing with the case of $J_{abs} = 520$ J/m^2, this higher-fluence laser pulse removes much more material in the form of solid and nonsolid phases, as shown in Fig. 7d.

Future Research Direction

Ultrafast lasers have been demonstrated to be a promising and powerful tool for micro-/nanoprocessing of metal thin films. This work shows the simulated ultrafast thermomechanical response for gold films induced by ultrashort-pulsed lasers using an integrated atomic-level model. Future research should focus on multiscale modeling for the interactions with matter in three-dimensional space with affordable computational cost so that laser parameters could be optimized for enhancing the micro-/nanomaterial processing.

References

1. Zewail AH (2000) Femtochemistry: atomic-scale dynamics of the chemical bond using ultrafast lasers. Angew Chem Int Ed 39:2586–2631
2. Frischkorn C, Wolf M (2006) Femtochemistry at metal surfaces: nonadiabatic reaction dynamics. Chem Rev 106:4207–4233
3. Murnane MM, Kapteyn HC, Falcone RW (1989) High-density plasmas produced by ultrafast laser pulses. Phys Rev Lett 62:155–158
4. Sheetz KE, Squier J (2009) Ultrafast optics: imaging and manipulating biological systems. J Appl Phys 105:051101
5. Tirlapur UK, König K (2002) Targeted transfection by femtosecond laser. Nature 418:290–291
6. Besner S, Kabashin AV, Winnik FM, Meunier M (2008) Ultrafast laser based "green" synthesis of non-toxic nanoparticles in aqueous solutions. Appl Phys A 93:955–959
7. Nakata Y, Okada T, Maeda M (2003) Nano-sized hollow bump array generated by single femtosecond laser pulse. Jpn J Appl Phys 42:L1452–L1454
8. Korte F, Koch J, Chichkov BN (2004) Formation of microbumps and nanojets on gold targets by femtosecond laser pulses. Appl Phys A 79:879–881
9. Momma C, Chichkov BN, Nolte S, von Alvensleben F, Tunnermann A, Welling H, Wellegehausen B (1996) Short-pulse laser ablation of solid targets. Opt Commun 129:134–142
10. Perry MD, Staurt BC, Banks PS, Feit MD, Yanovsky V, Rubenchik AM (1999) Ultrashort-pulse laser machining of dielectric materials. J Appl Phys 85:6803–6810
11. Chen JK, Beraun JE (2001) Numerical study of ultrashort laser pulse interactions with metal films. Num Heat Transf A 40:1–20
12. Chen JK, Tzou DY, Beraun JE (2006) A semiclassical two-temperature model for ultrafast laser heating. Int J Heat Mass Trans 49:307–316
13. Falkovsky LA, Mishchenko EG (1999) Electron-lattice kinetics of metals heated by ultrashort laser pulses. J Exp Theor Phys 88:84–88
14. Gan Y, Chen JK (2009) Integrated continuum-atomistic modeling of nonthermal ablation of gold nanofilms by femtosecond lasers. Appl Phys Lett 94:201116
15. Gan Y, Chen JK (2010) Thermomechanical wave propagation in gold thin films induced by ultrashort laser pulses. Mech Mater 42:491–501
16. Gan Y, Chen JK (2010) An atomic-level study of material ablation and spallation in ultrafast laser processing of gold films. J Appl Phys 108:103102
17. Allen M, Tildesley D (1987) Computer simulation of liquids. Oxford University Press, New York
18. Ivanov DS, Zhigilei LV (2003) Combined atomistic-continuum modeling of short-pulse laser melting and disintegration of metal films. Phys Rev B 68:064114
19. Daw MS, Baskes MI (1984) Embedded-atom method: derivation and application to impurities, surfaces, and other defects in metals. Phys Rev B 29:6443–6453
20. Anismov SI, Rethfeld B (1997) On the theory of ultrashort laser pulse interaction with metal. SPIE 3093:192–203
21. Chen JK, Latham WP, Beraun JE (2005) The role of electron-phonon coupling in ultrafast laser heating. J Laser Appl 17:63–68
22. Subramaniyan AK, Sun CT (2008) Continuum interpretation of virial stress in molecular simulations. Int J Solids Struct 45:4340–4346
23. Tsai DH (1979) The virial theorem and stress calculation in molecular dynamics. J Chem Phys 70:1375–1382

Attenuation

▶ Wave-Field in Anisotropic Thermoviscoelastic Media

Axisymmetric Generalized Thermoelasticity Problems in Spherical Regions

Hany H. Sherief and Farid A. Hamza
Department of Mathematics, Faculty of Science, University of Alexandria, Alexandria, Egypt

Overview

In 1967, the theory of generalized thermoelasticity with one relaxation time was introduced by Lord and Shulman [1]. The motivation behind the introduction of this theory was to deal with the apparent paradox of infinite speeds of propagation predicted by the coupled theory of thermoelasticity introduced by Biot [2] in 1956. The generalized equation of heat conduction is hyperbolic and hence automatically ensures finite speeds of wave propagation. This theory was extended [3] by Dhaliwal and Sherief to anisotropic media. Among the contributions to this theory are the proofs of uniqueness theorems by Ignaczak [4] and by Sherief [5]. The state space formulation for one-dimensional problems was completed by Anwar and Sherief in [6] and by Sherief in [7]. The state space formulation for two-dimensional problems was done by Sherief and Anwar in [8]. The boundary element formulation was conducted by Anwar and Sherief in [9]. Sherief and Anwar also solved a two-dimensional problem of a thick plate with a moving heat source on its boundary and a two-dimensional problem for an infinite cylinder in [10] and [11], respectively. Sherief and Hamza solved a two-dimensional problem of a thick plate under axisymmetric temperature distribution and discussed wave propagation for this theory in [12].

The solutions of thermoelastic problems for spherical regions are not as numerous as those for Cartesian and cylindrical ones. Most of the treated problems are either one-dimensional spherically symmetric ones or axisymmetric two-dimensional problems under simplifying assumptions. Sternberg and Chakravorty [13] solved a thermal shock uncoupled one-dimensional problem. Hata solved a coupled one-dimensional thermal shock problem for a hollow sphere caused by rapid uniform heating in [14]. The general solution for spherically symmetric problems with a heat source in generalized thermoelasticity valid for short times was obtained by Sherief in [15]. Axially symmetric steady-state two-dimensional problems in spherical regions were solved by McDowell and Sternberg in [16] and by Ignaczak in [17]. Ignaaak [18] and Piechocki [19] solved dynamic problems in thermoelasticity by assuming that the time variable is harmonic, which tends to obscure the transient nature of the problems considered. Tanigawa and Kosako [20] solved a transient coupled axially symmetric thermal stress problem for an infinite medium with a spherical cavity by neglecting inertia terms in their solution. Tanigawa and Takeuti [21] obtained the three-dimensional solution to coupled thermoelastic problems in spherical regions again by neglecting inertia terms. Sherief and Hamza [22] obtained the solution in spherical regions for two-dimensional thermoelastic problems under axisymmetric temperature distributions within the context of the theory of generalized thermoelasticity with one relaxation time. Sherief and Megahed [23] did the same for thermoelasticity with two relaxation times. Sherief and Saleh [24] obtained the exact solution for a one-dimensional problem for a spherical cavity.

Formulation of the Problem

We consider a homogeneous isotropic thermoelastic solid under axisymmetric conditions. We shall take the axis of symmetry to be the z-axis and the origin of the system of coordinates at the center of the sphere. By denoting the spherical polar coordinates as (r, ϑ, φ) and the time variable by t, we can take the axisymmetric temperature distribution throughout the solid to be $T(r, \vartheta, \varphi)$. The solution of the problem requires the determination of the displacement components u and v in the r – and ϑ – directions, respectively, together with the nonvanishing

stress components σ_{ij} in the region under consideration.

We shall use the following nondimensional variables:

$$r' = c_1 \eta\, r,\ a' = c_1 \eta\, a,\ u' = c_1 \eta\, u,\ v' = c_1 \eta\, v,$$
$$t' = c_1^2 \eta\, t, \tau_0' = c_1^2 \eta\, \tau_0, \sigma_{ij}' = \frac{\sigma_{ij}}{\mu}, \theta = \frac{\gamma (T - T_0)}{\lambda + 2\mu}$$

where τ_0 is the relaxation time, a is a typical length, and T_o is a reference temperature chosen such that $\left|\frac{(T-T_0)}{T_0}\right| << 1$, c_1 is the velocity of propagation of longitudinal isothermal waves given by $c_1 = \sqrt{\frac{\lambda+2\mu}{\rho}}$, where λ and μ are Lame's constants and ρ is the density η is a constant given by $\eta = \rho\, C_E/k$, k being the thermal conductivity and C_E is the specific heat at constant strain. γ is a material constant given by $\gamma = (3\lambda + 2\mu)\, \alpha_t$ where α_t is the coefficient of linear thermal expansion.

The strain tensor components are given by [25]

$$e_{rr} = \frac{\partial u}{\partial r},\ e_{\vartheta\vartheta} = \frac{1}{r}\frac{\partial v}{\partial \vartheta} + \frac{u}{r},\ e_{\varphi\varphi} = \frac{v}{r}\cot\vartheta + \frac{u}{r}$$
$$e_{r\vartheta} = \frac{1}{2}\left[\frac{\partial v}{\partial \vartheta} + \frac{1}{r}\left\{\frac{\partial u}{\partial \vartheta} - v\right\}\right],\ e_{r\varphi} = e_{\vartheta\varphi} = 0$$

The cubical dilatation thus has the form

$$e = \frac{\partial u}{\partial r} + \frac{2u}{r} + \frac{1}{r\sin\vartheta}\frac{\partial (v\sin\vartheta)}{\partial \vartheta} \tag{1}$$

The constitutive equations have the form

$$\sigma_{rr} = 2\frac{\partial u}{\partial r} + \left(\beta^2 - 2\right)e - \beta^2\theta \tag{2a}$$

$$\sigma_{\vartheta\vartheta} = \frac{2}{r}\frac{\partial v}{\partial \vartheta} + \frac{2u}{r} + \left(\beta^2 - 2\right)e - \beta^2\theta \tag{2b}$$

$$\sigma_{\varphi\varphi} = \frac{2\cot\vartheta}{r}v + \frac{2u}{r} + \left(\beta^2 - 2\right)e - \beta^2\theta \tag{2c}$$

$$\sigma_{r\vartheta} = \frac{\partial v}{\partial \vartheta} + \frac{1}{r}\frac{\partial u}{\partial \vartheta} - \frac{v}{r} \tag{2d}$$

$$\sigma_{r\varphi} = \sigma_{\vartheta\varphi} = 0 \tag{2e}$$

where $\beta^2 = (\lambda + 2\mu)/\mu$.

The equations of motion, after applying the Laplace transform and using the homogeneous initial conditions, can be written as [22]

$$\beta^2\frac{\partial}{\partial r}\left[\overline{e} - \overline{\theta}\right] + \nabla^2\overline{u} - \frac{1}{r^2}\frac{\partial}{\partial r}\left[r^2\frac{\partial \overline{u}}{\partial r}\right] - \frac{1}{r^2\sin\vartheta}\frac{\partial^2}{\partial r\partial\vartheta}\left[r\overline{v}\sin\vartheta\right] = \beta^2 s^2\overline{u} \tag{3a}$$

$$\frac{1}{r}\frac{\partial}{\partial\vartheta}\left[\beta^2(\overline{e} - \overline{\theta}) - \frac{\partial \overline{u}}{\partial r}\right] + \frac{1}{r^2}\frac{\partial}{\partial r}\left[r^2\frac{\partial \overline{v}}{\partial r}\right] = \beta^2 s^2\overline{v} \tag{3b}$$

The heat equation in Laplace transform domain has the form

$$\nabla^2\overline{\theta} = s\left(1 + \tau_0 s\right)\left(\overline{\theta} + \varepsilon\,\overline{e}\right) \tag{4a}$$

where $\varepsilon = \gamma^2 T_0/[\rho C_E(\lambda + 2\mu)]$ and ∇^2 is Laplace's operator given by

$$\nabla^2 \equiv \frac{1}{r^2}\frac{\partial}{\partial r}\left[r^2\frac{\partial}{\partial r}\right] + \frac{1}{r^2\sin\vartheta}\frac{\partial}{\partial\vartheta}\left[\sin\vartheta\frac{\partial}{\partial\vartheta}\right]$$

Equations (3a) and (3b) can be combined to give

$$\left(\nabla^2 - s^2\right)\bar{e} = \nabla^2\bar{\theta} \tag{4b}$$

Eliminating $\bar{e}$ between (4a) and (4b), we get

$$\left[\nabla^4 - \left[s^2 + (1+\varepsilon)\left(s + \tau_0 s^2\right)\right]\nabla^2 + s^3\left(1 + \tau_0 s\right)\right]\bar{\theta} = 0$$

This can be factorized as

$$\left(\nabla^2 - k_1^2\right)\left(\nabla^2 - k_2^2\right)\bar{\theta} = 0 \tag{5}$$

where $k_i^2, i = 1, 2$ are the roots with positive real parts of the characteristic equation

$$k^4 - \left[s^2 + (1+\varepsilon)\left(s + \tau_0 s^2\right)\right]k^2 + s^3\left(1 + \tau_0 s\right) = 0$$

The solution of (5) can be written in the form

$$\bar{\theta} = \bar{\theta}_1 + \bar{\theta}_2$$

where $\bar{\theta}_i, i = 1, 2$ is the solution of the equation

$$\left(\nabla^2 - k_i^2\right)\ \bar{\theta}_i = 0, \mathrm{i} = 1, 2$$

Solving the above equation [22], we obtain

$$\bar{\theta} = \frac{1}{\sqrt{r}} \sum_{n=0}^{\infty} P_n(\mu) \sum_{i=1}^{2} \left(k_i^2 - s^2\right) \left[A_{ni}\, I_{n+1/2}(k_i r) + B_{ni}\, K_{n+1/2}(k_i r)\right] \tag{6a}$$

Similarly, eliminating $\bar{\theta}$ between (4a) and (4b), we get

$$\left(\nabla^2 - k_1^2\right)\ \left(\nabla^2 - k_2^2\right)\ \bar{e} = 0$$

The solution of this equation compatible with (4b) and (6a) is given by

$$\bar{e} = \frac{1}{\sqrt{r}} \sum_{n=0}^{\infty} P_n(\mu) \sum_{i=1}^{2} k_i^2 \left[A_{ni}\, I_{n+1/2}(k_i r) + B_{ni}\, K_{n+1/2}(k_i r)\right] \tag{6b}$$

In the above equations, I_n and K_n denote the modified Bessel functions of the first and second kinds of order n, respectively. P_n is the Legendre polynomial of degree n of argument $\mu = \cos\vartheta$, and A_{ni},B_{ni} are parameters depending on s only to be determined from the boundary conditions.

Using (1) to eliminate the last term in the left-hand side of (3a),we obtain the following equation satisfied by the displacement component u:

$$\nabla^2 \overline{u} + \frac{2}{r}\frac{\partial \bar{u}}{\partial r} + \frac{2\,\bar{u}}{r^2} - \beta^2 s^2 \overline{u} = (1 - \beta^2)\frac{\partial \bar{e}}{\partial r} + \frac{2\,\bar{e}}{r} + \beta^2 \frac{\partial \overline{\theta}}{\partial r} \tag{7a}$$

Substituting for $\bar{e}$ and $\bar{\theta}$ from (6a, b) into (7a), we get

$$\nabla^2 \overline{u} + \frac{2}{r}\frac{\partial \overline{u}}{\partial r} + \frac{2\,\overline{u}}{r^2} - \beta^2 s^2 \overline{u} = \frac{c}{r^{3/2}} \sum_{n=0}^{\infty} P_n(\mu)\ \left[\bar{f}_{n1}(r) + \bar{f}_{n2}(r)\right] \tag{7b}$$

where

$$\bar{f}_{n1}(r) = \sum_{i=1}^{2} A_{ni} \left\{ \left(k_i^2 - \beta^2 s^2\right) k_i\, r\, I_{n+3/2}(k_i r) + \left[(n+2)k_i^2 - n\,\beta^2 s^2\right] I_{n+1/2}(k_i r) \right\}$$

$$\bar{f}_{n2}(r) = \sum_{i=1}^{2} B_{ni} \left\{ -\left(k_i^2 - \beta^2 s^2\right) k_i\, r\, K_{n+3/2}(k_i r) + \left[(n+2)k_i^2 - n\,\beta^2 s^2\right] K_{n+1/2}(k_i r) \right\}$$

In obtaining (7b), we have used the following well-known formulas of the Legendre functions [26]

$$\frac{dI_{n+1/2}(kr)}{dr} = k\, I_{n+3/2}(kr) + \frac{n+1/2}{r} I_{n+1/2}(kr)$$

$$\frac{dK_{n+1/2}(kr)}{dr} = -k\, K_{n+3/2}(kr) + \frac{n+1/2}{r} K_{n+1/2}(kr)$$

Solving (7b), we obtain the solution in the form

$$\overline{u} = \overline{u_1} + \overline{u_1} \tag{7c}$$

where

$$\bar{u}_1 = \frac{1}{r^{3/2}} \sum_{n=1}^{\infty} P_n(\mu) \left\{ \sum_{i=1}^{2} A_{ni} \left[k_i\, r\, I_{n+3/2}(k_i r) + n\, I_{n+1/2}(k_i r)\right] + C_n\, I_{n+1/2}(\beta\, s\, r) \right\}$$

$$\bar{u}_2 = \frac{1}{r^{3/2}} \sum_{n=1}^{\infty} P_n(\mu) \left\{ \sum_{i=1}^{2} B_{ni} \left[-k_i\, r\, K_{n+3/2}(k_i r) + n\, K_{n+1/2}(k_i r)\right] + D_n\, K_{n+1/2}(\beta\, s\, r) \right\}$$

where C_n and D_n are parameters depending on s only. In obtaining (7b), we have used the

following well-known formulas of the Legendre functions [26]

$$\frac{dI_{n+3/2}(kr)}{dr} = k\,I_{n+1/2}(kr) - \frac{n+3/2}{r} I_{n+3/2}(kr)$$

$$\frac{dK_{n+3/2}(kr)}{dr} = -k\,K_{n+1/2}(kr) - \frac{n+1/2}{r} K_{n+3/2}(kr)$$

Substituting from (6b) and (7b) into (1), we obtain

$$\frac{\partial(\bar{v}\,\sin\vartheta)}{\partial\mu} = \frac{1}{r^{3/2}} \sum_{n=1}^{\infty} P_n(\mu)\,\left[\bar{g}_{n1}(r) + \bar{g}_{n2}(r)\right] \tag{8}$$

where

$$\bar{g}_{n1}(r) = n(n+1)\sum_{i=1}^{2} A_{ni}\,I_{n+1/2}(k_i r) + C_n\left[(n+1)I_{n+1/2}(\beta s r) + \beta s r I_{n+3/2}(\beta s r)\right]$$

$$\bar{g}_{n2}(r) = n(n+1)\sum_{i=1}^{2} B_{ni}\,K_{n+1/2}(k_i r) + D_n\left[(n+1)K_{n+1/2}(\beta s r) - \beta s r K_{n+3/2}(\beta s r)\right]$$

For convenience, from now on, we shall write simply P_n instead of $P_n(\mu)$.

Integrating both sides of (8) with respect to μ, we obtain

$$\bar{v} = \overline{v_1} + \overline{v_1} \tag{9}$$

where

$$\bar{v}_1 = \frac{1}{r^{3/2}} \sum_{n=1}^{\infty} \left[\frac{\mu P_n - P_{n-1}}{\sin\vartheta}\right] \left\{ \sum_{i=1}^{2} n A_{ni} I_{n+1/2}(k_i r) + C_n \left[I_{n+1/2}(\beta s r) + \frac{\beta s r}{n+1} I_{n+3/2}(\beta s r) \right] \right\}$$

$$\bar{v}_2 = \frac{1}{r^{3/2}} \sum_{n=1}^{\infty} \left[\frac{\mu P_n - P_{n-1}}{\sin\vartheta}\right] \left\{ \sum_{i=1}^{2} n B_{ni} K_{n+1/2}(k_i r) + D_n \left[K_{n+1/2}(\beta s r) - \frac{\beta s r}{n+1} K_{n+3/2}(\beta s r) \right] \right\}$$

In obtaining (9), we have used the following integral relation of the Legendre polynomials [26]:

$$\int P_n(\mu)\,d\mu = \frac{\mu P_n(\mu) - P_{n-1}(\mu)}{n+1}$$

Although $\bar{v}$ contains $\sin\vartheta$ in the denominator, it can be shown that it is bounded as $\vartheta \to 0$. In fact $\lim_{\vartheta\to 0} \bar{v} = 0$.

Substituting from (6a, b) and (7c) into (2a), we obtain

$$\bar{\sigma}_{rr} = \bar{\sigma}_{rr1} + \bar{\sigma}_{rr2} \tag{10}$$

where

$$\bar{\sigma}_{rr1} = \frac{1}{r^{5/2}} \sum_{n=0}^{\infty} P_n \sum_{i=1}^{2} A_{ni} \left\{ \left[\beta^2 s^2 r^2 + 2n(n-1)\right] I_{n+1/2}(k_i r) - 4 k_i r I_{n+3/2}(k_i r) \right\} + \frac{2}{r^{5/2}} \sum_{n=1}^{\infty} P_n C_n \left[(n-1) I_{n+1/2}(\beta s r) + \beta s r I_{n+3/2}(\beta s r)\right]$$

$$\bar{\sigma}_{rr2} = \frac{1}{r^{5/2}} \sum_{n=0}^{\infty} P_n \sum_{i=1}^{2} B_{ni} \left\{ \left[\beta^2 s^2 r^2 + 2n(n-1)\right] K_{n+1/2}(k_i r) + 4 k_i r K_{n+3/2}(k_i r) \right\} + \frac{2}{r^{5/2}} \sum_{n=1}^{\infty} P_n D_n \left[(n-1) K_{n+1/2}(\beta s r) - \beta s r K_{n+3/2}(\beta s r)\right]$$

Substituting from (6a, b) and (7c) into (2d), we obtain

$$\bar{\sigma}_{r\vartheta} = \bar{\sigma}_{r\vartheta 1} + \bar{\sigma}_{r\vartheta 2} \tag{11}$$

where

$$\bar{\sigma}_{r\vartheta 1} = \frac{2}{r^{5/2}\sin\vartheta} \sum_{n=0}^{\infty} n(\mu P_n - P_{n-1}) \sum_{i=1}^{2} A_{ni} \left[(n-1) I_{n+1/2}(k_i r) + k_i r I_{n+3/2}(k_i r)\right] + \frac{1}{r^{5/2}\sin\vartheta} \sum_{n=1}^{\infty} C_n \frac{(\mu P_n - P_{n-1})}{n+1} \left[(\beta^2 s^2 r^2 + 2n^2 - 2) I_{n+1/2}(\beta s r) - 2\beta s r I_{n+3/2}(\beta s r)\right]$$

$$\bar{\sigma}_{r\vartheta 2} = \frac{2}{r^{5/2}\sin\vartheta}\sum_{n=0}^{\infty} n\,(\mu P_n - P_{n-1})$$
$$\sum_{i=1}^{2} B_{ni}\left[(n-1)K_{n+1/2}(k_i r) - k_i r\,K_{n+3/2}(k_i r)\right]$$
$$+\frac{1}{r^{5/2}\sin\vartheta}\sum_{n=1}^{\infty} D_n \frac{(\mu P_n - P_{n-1})}{n+1}$$
$$\left[\left(\beta^2 s^2 r^2 + 2n^2 - 2\right)K_{n+1/2}(\beta s r) + 2\beta s r\,K_{n+3/2}(\beta s r)\right]$$

The remaining stress components can be obtained in a similar manner.

Equations (6a, b), (7c), (9), (10), and (11) give the general solution of the problem in the Laplace transform domain in terms of the parameters A_{ni}, B_{ni}, C_n, and D_n. These parameters can be obtained from the boundary conditions of the problem under consideration.

Application and Numerical Results

We consider a solid sphere of radius "a" with center at the origin. For the present problem, we keep in the solution only the terms with a suffix of 1 and discard those with a suffix of 2 that are not bounded at the origin (i.e., we take $\theta = \theta_1$, $u = u_1, .., ..$). The surface of the sphere is assumed to be traction free and is immersed in a medium with Biot's number L whose temperature F on the surface of the sphere is a function of ϑ and t. The boundary conditions thus have the form

$$\sigma_{rr} = 0 \text{ at } r = a \tag{12}$$

$$\sigma_{r\vartheta} = 0 \text{ at } r = a \tag{13}$$

$$q_r = L(\theta - F) \text{ at } r = a \tag{14}$$

where q_r is the component of the heat flux vector in the radial direction. The generalized Fourier's law of heat conduction in nondimensional form can be written as

$$q_r + \tau_0 \frac{\partial q_r}{\partial t} = -\frac{\partial \theta}{\partial r}$$

Taking Laplace transforms of both sides, we obtain

$$\bar{q}_r = -\frac{1}{1+\tau_0 s}\frac{\partial \overline{\theta}}{\partial r}$$

Using the above relation, the boundary condition (14) takes the form

$$\frac{\partial \overline{\theta}}{\partial r} + (1+\tau_0 s)\,L\left(\overline{\theta} - \overline{F}\right) = 0 \text{ at } r = a \tag{15}$$

Expanding the function $\overline{F}(\mu, s)$ in a series of Legendre polynomials, we obtain

$$\overline{F}(\mu, s) = \sum_{n=0}^{\infty} f_n(s)\,P_n(\mu) \tag{16a}$$

where

$$f_n(s) = \frac{2n+1}{2}\int_{-1}^{1} \overline{F}(\mu, s)\,P_n(\mu)\,d\mu \tag{16b}$$

Using (6a), (10), (12), (15), and (16a), we obtain upon equating the coefficients of $P_0(\mu)$ on both sides the following two linear equations in A_{01} and A_{02}

$$\sum_{i=1}^{2} A_{0i}\left[\beta^2 s^2 a\,I_{1/2}(k_i a) - 4\,k_i\,I_{3/2}(k_i a)\right] = 0$$

$$\sum_{i=1}^{2} A_{0i}(k_i^2 - s^2)\left[k_i I_{3/2}(k_i a) + L(1+\tau_0 s)\,I_{1/2}(k_i a)\right]$$
$$= L(1+\tau_0 s)\sqrt{a} f_0(s)$$

Solving the above two equations, we obtain

$$A_{01} = \frac{-L(1+\tau_0 s)\sqrt{a} f_0(s)}{\psi}\left[\beta^2 s^2 a\,I_{1/2}(k_2 a) - 4\,k_2\,I_{3/2}(k_2 a)\right]$$

$$A_{02} = \frac{L(1+\tau_0 s)\sqrt{a} f_0(s}{\psi}\left[\beta^2 s^2 a\,I_{1/2}(k_1 a) - 4\,k_1\,I_{3/2}(k_1 a)\right]$$

where

$$\psi = (k_2^2 - s^2)\left[k_2 I_{3/2}(k_2 a) + L(1+\tau_0 s) I_{1/2}(k_2 a)\right] \left[\beta^2 s^2 a I_{1/2}(k_1 a) - 4 k_1 I_{3/2}(k_1 a)\right] - (k_1^2 - s^2)\left[k_1 I_{3/2}(k_1 a) + L(1+\tau_0 s) I_{1/2}(k_1 a)\right] \left[\beta^2 s^2 a I_{1/2}(k_2 a) - 4 k_2 I_{3/2}(k_2 a)\right]$$

For n > 0, using (6a), (10), (11), (12), (13), (15), and (16a), we obtain upon equating the coefficients of $P_n(\mu)$ on both sides a system of three linear equations in the unknowns A_{n1}, A_{n2}, and C_n whose solution gives

$$A_{n1} = \frac{L(1+\tau_0 s) a^{3/2} f_n(s)}{\Omega} \left[\frac{m_{22}}{m_{23}} - \frac{m_{12}}{m_{13}}\right]$$

$$A_{n2} = \frac{L(1+\tau_0 s) a^{3/2} f_n(s)}{\Omega} \left[\frac{m_{11}}{m_{13}} - \frac{m_{21}}{m_{23}}\right]$$

$$C_n = \frac{-L(1+\tau_0 s) a^{3/2} f_n(s)}{\Omega m_{13}} \left\{ m_{11}\left[\frac{m_{22}}{m_{23}} - \frac{m_{12}}{m_{13}}\right] + m_{12}\left[\frac{m_{11}}{m_{13}} - \frac{m_{21}}{m_{23}}\right]\right\}$$

where

$$\Omega = m_{31}\left[\frac{m_{22}}{m_{23}} - \frac{m_{12}}{m_{13}}\right] + m_{32}\left[\frac{m_{11}}{m_{13}} - \frac{m_{21}}{m_{23}}\right]$$

$$m_{1i} = \left[(\beta^2 s^2 a^2 + 2n^2 - 2n) I_{n+1/2}(k_i a) - 4 k_i a\, I_{n+3/2}(k_i a)\right],\ \mathrm{i} = 1,\ 2$$

$$m_{13} = 2\left[(n-1) I_{n+1/2}(\beta s a) + \beta s a\, I_{n+3/2}(\beta s a)\right]$$

$$m_{2i} = 2n(n+1)\left[(n-1) I_{n+1/2}(k_i a) + k_i a\, I_{n+3/2}(k_i a)\right],\ \mathrm{i} = 1,\ 2$$

$$m_{23} = \left[(\beta^2 s^2 a^2 + 2n^2 - 2) I_{n+1/2}(\beta s a) - 2\beta s a\, I_{n+3/2}(\beta s a)\right]$$

$$m_{3i} = (k_i^2 - s^2)\left[k_i a I_{n+3/2}(k_i a) + \{n + aL(1+\tau_0 s)\} I_{n+1/2}(k_i a)\right],\ \mathrm{i} = 1,\ 2$$

During subsequent calculations, the functions $F(\vartheta, t)$ will be taken in the form $F(\vartheta, t) = \sin^2\vartheta$

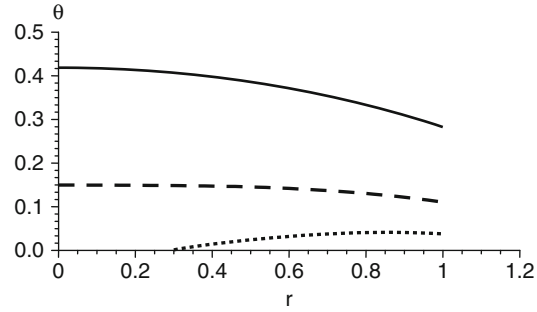

Axisymmetric Generalized Thermoelasticity Problems in Spherical Regions, Fig. 1 Temperature distribution against r

This gives $\overline{F}(\vartheta, s) = \sin^2\vartheta / s$. It follows from (16b) that

$$f_0(s) = \frac{2}{s},\ f_2(s) = \frac{-2}{3s} \text{ and } f_i(s) = 0,\ i \neq 0 \text{ or } 2$$

The copper material was chosen for purposes of numerical evaluations. The constants for the problem were taken as $\varepsilon = 0.0168$, $\beta^2 = 3.5$, $L = 1$, $a = 1$, and $\tau_0 = 0.02$. The numerical computations were carried out for three values of time, namely, for $t = 0.1$ (dotted lines), $t = 0.2$ (dashed lines), and $t = 0.5$ (solid lines). A numerical method [27] was used to invert the Laplace transform to obtain the temperature, displacement, and radial stress distributions in the physical domain.

The radial variation of the temperature θ, the radial displacement component u, and the radial stress σ_{rr} on the plane $\vartheta = \pi/2$, $0 \le r \le 1$ are shown in Figs. 1, 2, and 3, respectively. The displacement component v is identically zero on this plane due to symmetry. Variation of θ, u, and v on the surface of the sphere ($r = 1$, $0 \le \vartheta \le \pi/2$) is shown in Figs. 4, 5, and 6, respectively. Of course, on the surface $\sigma_{rr} = 0$ from the boundary conditions.

The computations were carried out also for the coupled theory of thermoelasticity ($\tau_0 = 0$). It was found that for large values of time, the coupled and the generalized theories give close results. The case is quite different when we consider small values of time. The coupled theory

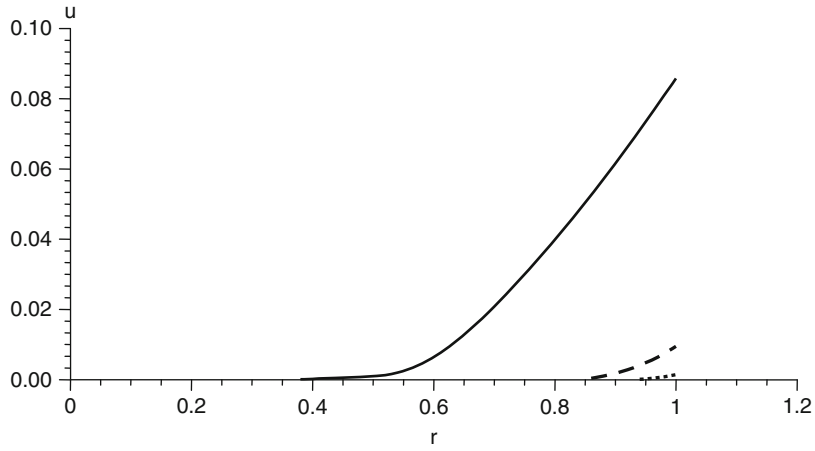

Axisymmetric Generalized Thermoelasticity Problems in Spherical Regions, Fig. 2 Displacement distribution against *r*

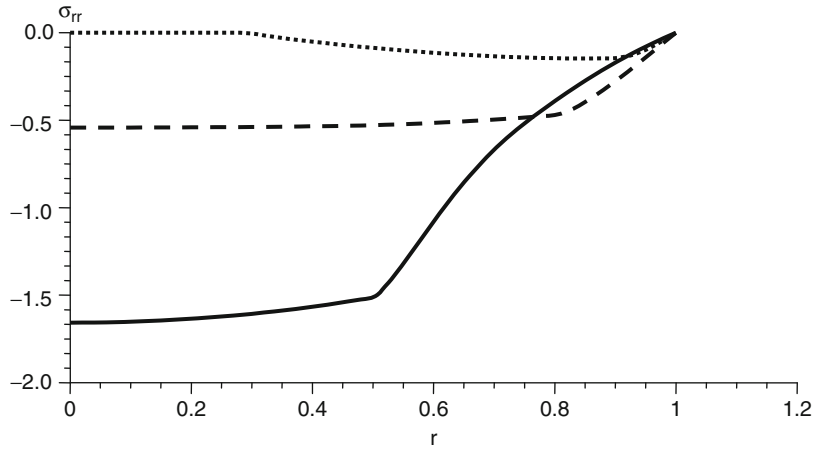

Axisymmetric Generalized Thermoelasticity Problems in Spherical Regions, Fig. 3 Stress distribution against *r*

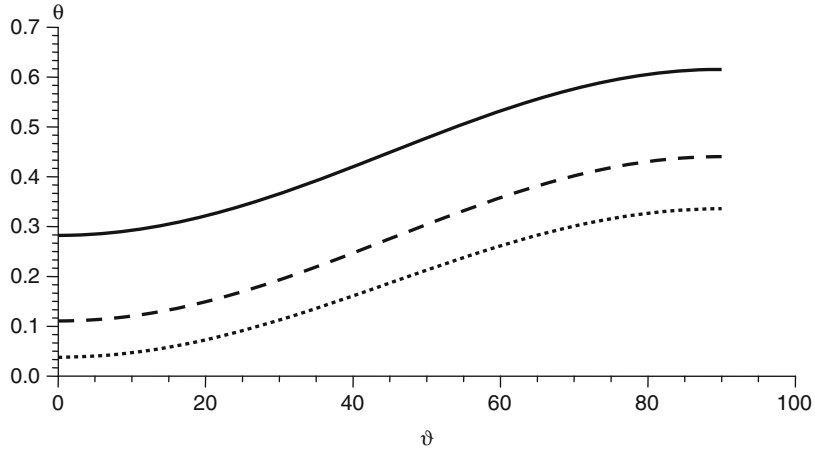

Axisymmetric Generalized Thermoelasticity Problems in Spherical Regions, Fig. 4 Temperature distribution on the surface

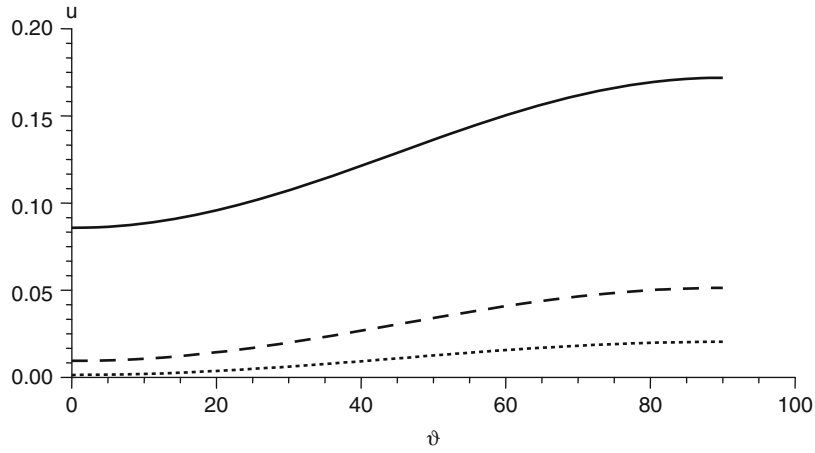

Axisymmetric Generalized Thermoelasticity Problems in Spherical Regions, Fig. 5 Radial displacement distribution on the surface

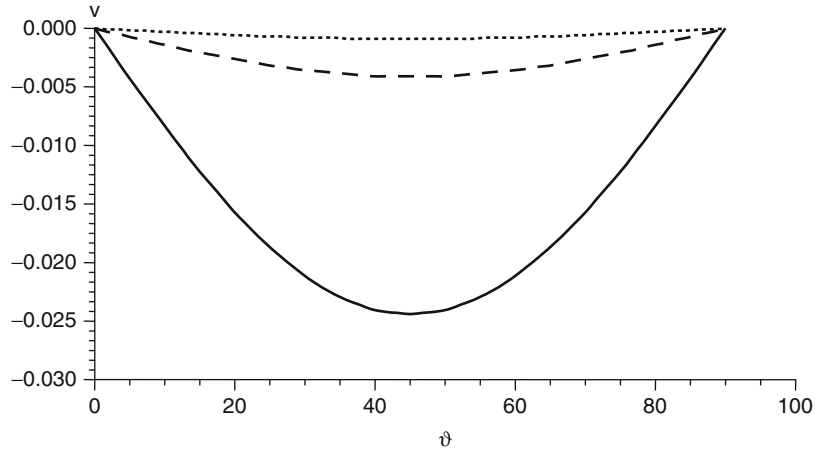

Axisymmetric Generalized Thermoelasticity Problems in Spherical Regions, Fig. 6 Transverse displacement distribution on the surface

predicts infinite speeds of wave propagation. This is evident from the fact that the temperature, say, is not identically zero for any value of time but fades gradually to very small values at points far removed from the surface [22]. The solution obtained using the equations of generalized thermoelasticity, however, exhibits the behavior of finite speeds of wave propagation. For small values of time, the solution is localized in a finite region of space surrounding the surface and is identically zero outside this region. This region grows with increasing time. Its edge is the location of the wave front. This region is determined only by the values of the time t and the relaxation time τ_0 and is the same for all functions considered. It is seen from Fig. 1, for example, that for $t = 0.1$, the temperature predicted by the generalized theory is identically zero for r less than 0.285.

References

1. Lord H, Shulman Y (1967) A generalized dynamical theory of thermoelasticity. J Mech Phys Solids 15:299–309
2. Biot M (1956) Thermoelasticity and irreversible thermo-dynamics. J Appl Phys 27:240–253
3. Dhaliwal R, Sherief H (1980) Generalized thermoelasticity for anisotropic media. Quart Appl Math 33:1–8

4. Ignaczak J (1982) A note on uniqueness in thermoelasticity with one relaxation time. J Therm Stress 5:257–263
5. Sherief H (1987) On uniqueness and stability in generalized thermoelasticity. Quart Appl Math 45:773–778
6. Anwar M, Sherief H (1988) State space approach to generalized thermoelasticity. J Therm Stress 11:353–365
7. Sherief H (1993) State space formulation for generalized thermoelasticity with one relaxation time including heat sources. J Therm Stress 16:163–180
8. Sherief H, Anwar M (1994) State space approach to two-dimensional generalized thermoelasticity problems. J Therm Stress 17:567–590
9. Anwar M, Sherief H (1988) Boundary integral equation formulation of generalized thermoelasticity in a laplace transform domain. Appl Math Model 12:161–166
10. Sherief H, Anwar M (1992) Generalized thermoelasticity problem for a plate subjected to moving heat source on both sides. J Therm Stress 15:489–505
11. Sherief H, Anwar M (1994) A two dimensional generalized thermoelasticity problem for an infinitely long cylinder. J Therm Stress 17:213–227
12. Sherief H, Hamza F (1994) A generalized thermoelastic problem of a thick plate under axisymmetric temperature distribution. J Therm Stress 17:435–452
13. Sternberg E, Chakravorty J (1959) Thermal shock in an elastic body with a spherical cavity. Quart Appl Math 17:205–218
14. Hata T (1991) Thermal shock in a hollow sphere caused by rapid uniform heating. J Appl Mech 58:63–69
15. Sherief H (1986) Fundamental solution of the generalized thermoelastic problem for short times. J Therm Stress 9:151–164
16. McDowell E, Sternberg E (1957) Axisymmetric thermal stresses in a spherical shell of arbitrary thickness. J Appl Mech 24:376–380
17. Ignaczak J (1960) The axially symmetric boundary value problem of thermoelasticity for a hemispherical shell of any thickness. Arch Mech Stos 12:415–435
18. Ignaczak J (1959) Dynamic thermoelastic problem of a spherical cavity. Arch Mech Stos 11:399–408
19. Piechocki W (1960) Axisymmetric dynamic problem of thermoelasticity for a solid sphere. Arch Mech Stos 12:553–561
20. Tanigawa Y, Kosako M (1986) Transient thermal stress analysis of an infinite medium with a spherical cavity due to a non-uniform heat supply. Int J Eng Sci 24:309–321
21. Tanigawa Y, Takeuti Y (1983) Three-dimensional thermoelastic treatment in spherical region and its application to solid sphere due to rotating heat source. ZAMM 63:317–324
22. Sherief H, Hamza F (1996) Generalized two-dimensional thermoelastic problems in spherical regions under axisymmetric distributions. J Therm Stress 19:55–76
23. Sherief H, Megahed F (1999) Two-dimensional problems for thermoelasticity with two relaxation times in spherical regions under axisymmetric distributions. Int J Eng Sci 37:299–314
24. Sherief H, Saleh H (1998) A problem for an infinite thermoelastic body with a spherical cavity. Int J Eng Sci 36:473–487
25. Sokolnikoff I (1956) Mathematical theory of elasticity, 2nd edn. McGraw-Hill, New York
26. Spiegel M (1968) Mathematical handbook. McGraw-Hill, New York
27. Honig G, Hirdes U (1984) A method for the numerical inversion of the Laplace transform. J Comp Appl Math 10:113–132

Axisymmetric Generalized Thermoelasticity Problems Using Cylindrical Coordinates

Farid A. Hamza
Department of Mathematics, Faculty of Science, University of Alexandria, Alexandria, Egypt

Overview

In 1967, the theory of generalized thermoelasticity with one relaxation time was introduced by Lord and Shulman [1]. The motivation behind the introduction of this theory was to deal with the apparent paradox of infinite speeds of propagation predicted by the coupled theory of thermoelasticity introduced by Biot [2] in 1956. The generalized equation of heat conduction is hyperbolic and hence automatically ensures finite speeds of wave propagation. This theory was extended by Dhaliwal and Sherief [3] to include the effects of anisotropy.

Among the contributions to this theory are the proofs of uniqueness theorems by Ignaczak [4] and by Sherief [5]. Anwar and Sherief [6] and Sherief [7] completed the state-space formulation for one-dimensional problems. Sherief and Anwar [8] conducted the state-space formulation for two-dimensional problems. The fundamental

solutions for the cylindrically symmetric spaces were obtained by Sherief and Anwar [9].

The importance of axisymmetric problems arises from the fact that they have many applications in industry. The most important one is in the fabrication of vehicle brakes and other machine components of cylindrical shapes. Sherief and Hamza [10] have obtained the complete solution to axisymmetric problems in generalized thermoelasticity with one relaxation time and studied wave propagation.

Two-Dimensional Axisymmetric Problems

We consider a homogenous isotropic thermoelastic region initially quiescent. The conditions of the problem are assumed to be axisymmetric. We shall take the axis of symmetry to be the z-axis. By denoting the cylindrical polar coordinates as (r, ψ, z) and the time variable by t, we can take the axisymmetric temperature distribution throughout the solid to be $T(r,z,t)$.

We shall use the following nondimensional variables:

$$r' = c_1\eta r,\ z' = c_1\eta z,\ u' = c_1\eta u,\ w' = c_1\eta w$$

$$t' = c_1^2\eta t,\ \tau_0' = c_1^2\eta\tau_0,\ \sigma_{ij}' = \frac{\sigma_{ij}}{\lambda+2\mu},\ \theta = \frac{\gamma(T-T_0)}{\lambda+2\mu}$$

In terms of these nondimensional variables, the governing equations take the form (dropping the primes for convenience) [10]:

$$\nabla^2\underline{\mathbf{u}} + \left(\beta^2-1\right) grad\, div\, \underline{\mathbf{u}} - \beta^2 grad\,\theta = \beta^2\ddot{\underline{\mathbf{u}}} \tag{1}$$

$$\nabla^2\theta = \left(\frac{\partial}{\partial t} + \tau_0\frac{\partial^2}{\partial t^2}\right)(\theta + \varepsilon e) \tag{2}$$

The constitutive equations have the form [10]:

$$\sigma_{rr} = \frac{2}{\beta^2}\frac{\partial u}{\partial r} + \frac{\left(\beta^2-2\right)}{\beta^2}e - \theta \tag{3a}$$

$$\sigma_{\psi\psi} = \frac{2}{\beta^2}\frac{u}{r} + \frac{\left(\beta^2-2\right)}{\beta^2}e - \theta \tag{3b}$$

$$\sigma_{zz} = \frac{2}{\beta^2}\frac{\partial w}{\partial z} + \frac{\left(\beta^2-2\right)}{\beta^2}e - \theta \tag{3c}$$

$$\sigma_{rz} = \frac{1}{\beta^2}\left(\frac{\partial u}{\partial z} + \frac{\partial w}{\partial r}\right) \tag{3d}$$

where e is the cubical dilatation given by:

$$e = div\,\underline{\mathbf{u}} = \frac{1}{r}\frac{\partial}{\partial r}(ru) + \frac{\partial w}{\partial z} \tag{4}$$

Solution in the Laplace-Hankel Transform Domain

Taking the Laplace transform of both sides of (1)–(4) and using the homogenous initial conditions, we get:

$$\overline{e} = \frac{1}{r}\frac{\partial}{\partial r}(r\overline{u}) + \frac{\partial\overline{w}}{\partial z} \tag{5}$$

$$\nabla^2\underline{\overline{\mathbf{u}}} + \left(\beta^2-1\right) grad\, div\,\underline{\overline{\mathbf{u}}} - \beta^2 grad\,\overline{\theta} = \beta^2 s^2\underline{\overline{\mathbf{u}}} \tag{6}$$

$$\left(\nabla^2 - s - \tau_0 s^2\right)\overline{\theta} = \varepsilon\left(s + \tau_0 s^2\right)\overline{e} \tag{7}$$

Equation of motion (6) takes the form:

$$\beta^2\, grad\, div\,\underline{\overline{\mathbf{u}}} - curl\, curl\,\underline{\overline{\mathbf{u}}} - \beta^2\, grad\,\overline{\theta} = \beta^2 s^2\underline{\overline{\mathbf{u}}} \tag{8}$$

Applying divergence operator to both sides of (8), we get:

$$\left(\nabla^2 - s^2\right)\overline{e} = \nabla^2\overline{\theta} \tag{9}$$

From (7) and (9), we obtain:

$$\left[\nabla^4 - \left\{s^2 + (1+\varepsilon)\left(s+\tau_0 s^2\right)\right\}\nabla^2 + s^3(1+\tau_0 s)\right]\begin{pmatrix}\overline{\theta}\\ \overline{e}\end{pmatrix} = 0 \tag{10}$$

Equation (10) can be factorized as:

$$\left(\nabla^2 - k_1^2\right)\left(\nabla^2 - k_2^2\right)\begin{pmatrix}\overline{\theta}\\ \overline{e}\end{pmatrix} = 0 \qquad (11)$$

where $k_i^2, i = 1, 2$ are the roots with positive real parts of the characteristic equation:

$$k^4 - \left[s^2 + (1+\varepsilon)\left(s + \tau_0 s^2\right)\right]k^2 + s^3(1 + \tau_0 s) = 0$$

The solution of (11) for $\bar{\theta}$ can be written in the form:

$$\overline{\theta} = \sum_1^2 \overline{\theta}_i$$

where $\overline{\theta}_i$ is the solution of the equation:

$$\left(\nabla^2 - k_i^2\right)\overline{\theta}_i = 0, \mathrm{i} = 1, 2 \qquad (12)$$

We shall use the Hankel transform defined by the relation [11]:

$$f^*(\alpha, z, s) = \mathrm{H}[f(r, z, s)] = \int_0^\infty f(r, z, s) r J_0(\alpha r) dr$$

where J_0 is the Bessel function of the first kind of order zero.

Applying the Hankel transform to both sides of (12), we obtain:

$$\left(\mathrm{D}^2 - \alpha^2 - k_i^2\right)\bar{\theta}_i{}^*(\alpha, z, s) = 0 \qquad (13)$$

where the operator D denotes partial differentiation with respect to z.

The solution of (13) has the form:

$$\bar{\theta}_i{}^*(\alpha, z, s) = \left(k_i^2 - s^2\right)\left(A_{1i}(\alpha, s)e^{\mu_i z} + A_{2i}(\alpha, s)e^{-\mu_i z}\right), \quad \mathrm{i} = 1, 2 \qquad (14)$$

where A_{1i}, A_{2i} are parameters that depend on α,s and μ_i is given by:

$$\mu_i = \sqrt{k_i^2 + \alpha^2}$$

Using (14) the solution of (11) can be written in the form:

$$\overline{\theta}^* = \sum_{i=1}^2 \left(k_i^2 - s^2\right)\left(A_{1i}e^{\mu_i z} + A_{2i}e^{-\mu_i z}\right) \qquad (15)$$

In a similar manner, we can show that the solution for $\overline{e}^*$ compatible with (14)–(15) is given by:

$$\overline{e}^* = \sum_{i=1}^2 k_i^2\left(A_{1i}e^{\mu_i z} + A_{2i}e^{-\mu_i z}\right) \qquad (16)$$

Applying the inversion formula of the Hankel transform to (15) and (16), we get:

$$\overline{\theta}(r, z, s) = \sum_{i=1}^2 \left(k_i^2 - s^2\right)\int_0^\infty \alpha J_0(\alpha r)\left(A_{1i}e^{\mu_i z} + A_{2i}e^{-\mu_i z}\right)d\alpha \qquad (17)$$

$$\overline{e}(r, z, s) = \sum_{i=1}^2 k_i^2 \int_0^\infty \alpha J_0(\alpha r)\left(A_{1i}e^{\mu_i z} + A_{2i}e^{-\mu_i z}\right)d\alpha. \qquad (18)$$

The components of (8) in the r- and z- directions, respectively, are:

$$\frac{\partial}{\partial z}\left(\frac{\partial \overline{w}}{\partial r} - \frac{\partial \overline{u}}{\partial z}\right) + \beta^2 s^2 \overline{u} = \beta^2 \frac{\partial}{\partial r}\left(\overline{e} - \overline{\theta}\right) \qquad (19)$$

$$\frac{1}{r}\frac{\partial}{\partial r}\left\{r\left(\frac{\partial \overline{u}}{\partial z} - \frac{\partial \overline{w}}{\partial r}\right)\right\} + \beta^2 s^2 \overline{w} = \beta^2 \frac{\partial}{\partial z}\left(\overline{e} - \overline{\theta}\right) \qquad (20)$$

Using (5) and (19), (20), we get:

$$\nabla^2 \overline{u} - \frac{\overline{u}}{r^2} - \beta^2 s^2 \overline{u} = \frac{\partial}{\partial r}\left(\left(1 - \beta^2\right)\overline{e} + \beta^2 \overline{\theta}\right) \qquad (21)$$

$$\nabla^2 \overline{w} - \beta^2 s^2 \overline{w} = \frac{\partial}{\partial z}\left(\left(1 - \beta^2\right)\overline{e} + \beta^2 \overline{\theta}\right) \qquad (22)$$

Introducing the function $\overline{\phi}$, defined by the relation,

$$\overline{u} = \frac{\partial \overline{\phi}}{\partial r} \qquad (23)$$

into (21), integrating the resultant equation with respect to r, we obtain:

$$\nabla^2\overline{\phi} - \beta^2 s^2\overline{\phi} = \left(1-\beta^2\right)\overline{e} + \beta^2\overline{\theta}$$

Taking the Hankel transform of both sides of the above equation, we get:

$$\left(\mathrm{D}^2 - \mu^2\right)\overline{\phi}^* = \left(1-\beta^2\right)\overline{e}^* + \beta^2\overline{\theta}^* \tag{24}$$

where $\mu^2 = \beta^2 s^2 + \alpha^2$.

Using (15) and (16), we get the following relation:

$$\left(\mathrm{D}^2 - \mu^2\right)\overline{\phi}^* = \sum_{i=1}^{2}\left(k_i^2 - \beta^2 s^2\right)\left(A_{1i}e^{\mu_i z} + A_{2i}e^{-\mu_i z}\right) \tag{25}$$

Thus, the general solution of (25) has the form:

$$\overline{\varphi}^* = A_1 e^{\mu z} + A_2 e^{-\mu z} + \sum_{i=1}^{2}\left(A_{1i}e^{\mu_i z} + A_{2i}e^{-\mu_i z}\right) \tag{26}$$

Applying the inversion formula of the Hankel transform, namely [11],

$$\begin{aligned} f(r,z,s) &= \mathrm{H}^{-1}[f^*(\alpha,z,s)] \\ &= \int_0^\infty f^*(\alpha,z,s) r J_0(\alpha r)\, d\alpha \end{aligned}$$

to the above equation, we obtain:

$$\begin{aligned} \overline{\varphi}(r,z,s) = \int_0^\infty \alpha J_0(\alpha r)\Bigg(A_1 e^{\mu z} + A_2 e^{-\mu z} \\ + \sum_{i=1}^{2}\left(A_{1i}e^{\mu_i z} + A_{2i}e^{-\mu_i z}\right)\Bigg) d\alpha \end{aligned} \tag{27}$$

Differentiating both sides of (27) with respect to r, we get upon using (23):

$$\begin{aligned} \overline{u}(r,z,s) = -\int_0^\infty \alpha^2 J_1(\alpha r)\Bigg(A_1 e^{\mu z} + A_2 e^{-\mu z} \\ + \sum_{i=1}^{2}\left(A_{1i}e^{\mu_i z} + A_{2i}e^{-\mu_i z}\right)\Bigg) d\alpha \end{aligned} \tag{28}$$

In a similar manner solving (22), we obtain:

$$\begin{aligned} \overline{w}(r,z,s) = \int_0^\infty \alpha J_0(\alpha r)\Bigg\{\frac{\alpha^2}{\mu}\left(A_1 e^{\mu z} - A_2 e^{-\mu z}\right) \\ + \sum_{i=1}^{2}\mu_i\left(A_{1i}e^{\mu_i z} - A_{2i}e^{-\mu_i z}\right)\Bigg\} d\alpha \end{aligned} \tag{29}$$

Finally, to obtain the Laplace transform of the stress components, we denote by F the quantity:

$$F(r,z,t) = \frac{\left(\beta^2 - 2\right)}{\beta^2} e - \theta \tag{30}$$

Taking the Laplace transform of both sides of the above equation and substituting from (15) and (16), we get:

$$\begin{aligned} \overline{F}(r,z,t) = \sum_{i=1}^{2}\left(s^2 - \frac{2k_i^2}{\beta^2}\right)\int_0^\infty \alpha J_0(\alpha r) \\ \times \left[\left\{A_{1i}e^{\mu_i z} + A_{2i}e^{-\mu_i z}\right\}\right] d\alpha \end{aligned} \tag{31}$$

Using the Laplace transform of (3a, c, d) and (30) together with (28) and (29), we obtain:

$$\begin{aligned} \overline{\sigma}_{rr} = \frac{2}{\beta^2}\int_0^\infty \alpha^3\left[\frac{1}{\alpha r}J_1(\alpha r) - J_0(\alpha r)\right]\Bigg\{A_1 e^{\mu z} + A_2 e^{-\mu z} \\ + \sum_{i=1}^{2}\left(A_{1i}e^{\mu_i z} + A_{2i}e^{-\mu_i z}\right)\Bigg\} d\alpha + \overline{F} \end{aligned} \tag{32a}$$

$$\begin{aligned} \overline{\sigma}_{zz} = \frac{2}{\beta^2}\int_0^\infty \alpha J_0(\alpha r)\left(\alpha^2\left[A_1 e^{\mu z} + A_2 e^{-\mu z}\right]\right. \\ \left. + \sum_{i=1}^{2}\mu_i^2\left(A_{1i}e^{\mu_i z} + A_{2i}e^{-\mu_i z}\right)\right) d\alpha + \overline{F} \end{aligned} \tag{32b}$$

$$\begin{aligned} \overline{\sigma}_{rz} = -\frac{1}{\beta^2}\int_0^\infty \alpha^2 J_1(\alpha r)\Bigg(\left(\frac{\mu^2 + \alpha^2}{\mu}\right)\left(A_1 e^{\mu z} - A_2 e^{-\mu z}\right) \\ + \sum_{i=1}^{2} 2\mu_i\left(A_{1i}e^{\mu_i z} - A_{2i}e^{-\mu_i z}\right)\Bigg) d\alpha \end{aligned} \tag{32c}$$

Example. We consider a thick plate composed of a homogenous isotropic thermoelastic material of infinite extent and finite thickness. The upper surface of the plate is subjected to an axisymmetric temperature distribution and is traction free. The lower surface of the plate is laid on a rigid foundation, which is thermally insulating. The region Ω of the plate is defined by:

$$\Omega = \{(r, \psi, z) : 0 \le r \le \infty, 0 \le \psi \le 2\pi, \text{ and } -\mathrm{h} < \mathrm{z} < \mathrm{h}$$

The boundary conditions in the Laplace transform domain are:

$$u = 0,\ w = 0,\ \frac{\partial \theta}{\partial z} = 0, \text{ for } z = -h \tag{33a}$$

$$\sigma_{zz} = 0,\ \sigma_{rz} = 0, \text{ for } z = h \tag{33b}$$

$$\theta = H(t) f(r), \text{ for } z = h \tag{33c}$$

where $f(r)$ is a known function of r.

From the boundary condition (33a, b, c) and (17), (28), (29), (31), and (32a, b, c), we get a system of six linear equations in the unknown parameters $A_1, A_2, A_{11}, A_{12}, A_{21}$ and A_{22}. Solving this system completes the solution in the transform domain.

Numerical Results

The copper material was chosen for purposes of numerical evaluations. The material constants of the problem are thus given by:

$$\beta^2 = 4,\ \rho = 8{,}954\,\mathrm{kg/m^3},\ \eta = 8886.73\,\mathrm{s/m^2},\ \tau_0 = 0.02\,\mathrm{s},\ \varepsilon = 0.0168,$$
$$c_E = 381\,\mathrm{J/kg/c},\ k = 386\,\mathrm{W/m/c},\ \lambda = 7.76(10)^{10}\,\mathrm{kg/m/s^2},\ \mu = 86(10)^{10}\,\mathrm{kg/m/s^2}$$

The half-thickness h of the plate was taken equal to 0.5. The computations were carried out for three values of time, namely, $t = 0.05$, $t = 0.1$, and $t = 0.15$.

The inversion of the Hankel transform was done using the inversion formula of the transform. The inversion of the Laplace transform was done using a numerical technique based on Fourier expansion [12].

The temperature of the surface of the upper plate is taken as:

$$f(r) = \begin{cases} \theta_0 & \text{if } r \le 1 \\ 0 & \text{otherwise} \end{cases}$$

where θ_0 is a constant. This means that starting at time $t = 0$, a circle of unit radius is suddenly raised to a temperature equal to θ_0 and kept at this temperature, while the rest of the upper surface is kept at zero temperature.

This can be written more concisely as:

$$f(r) = \theta_0 H(1 - r) \tag{34}$$

Taking the Hankel transform, we obtain:

$$f^*(\alpha) = \theta_0 \int_0^\infty H(1 - r) r J_0(\alpha r) dr$$
$$= \theta_0 \int_0^1 r J_0(\alpha r) dr = \frac{\theta_0}{\alpha} J_1(\alpha) \tag{35}$$

The constant θ_0 was taken equal to unity during computations.

We evaluated the different functions along the z-axis ($r = 0$) as functions of z. The results are shown in Fig. 1 for the temperature and Fig. 2 for the vertical displacement component w. The radial stress components σ_{rr} and the axial stress

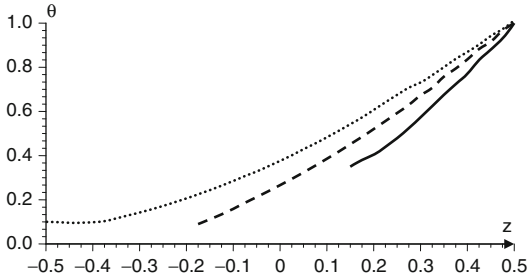

Axisymmetric Generalized Thermoelasticity Problems Using Cylindrical Coordinates, Fig. 1 Temperature distribution

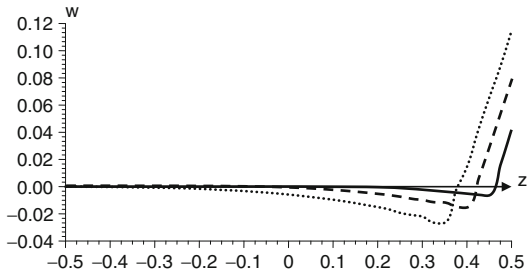

Axisymmetric Generalized Thermoelasticity Problems Using Cylindrical Coordinates, Fig. 2 Vertical displacement distribution

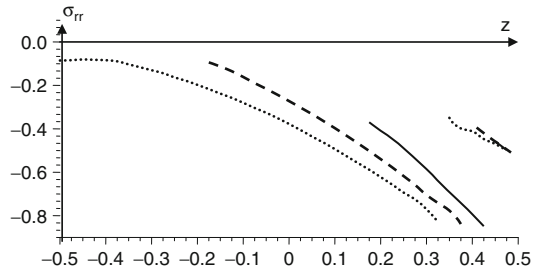

Axisymmetric Generalized Thermoelasticity Problems Using Cylindrical Coordinates, Fig. 3 Radial stress distribution

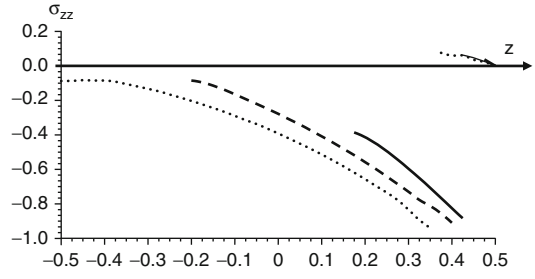

Axisymmetric Generalized Thermoelasticity Problems Using Cylindrical Coordinates, Fig. 4 Axial stress distribution

components σ_{zz} are shown in Figs. 3 and 4, respectively. The radial displacement component u is identically zero along the z-axis. Solid lines represent the case when $t = 0.05$, dashed lines represent the case when $t = 0.1$ while dotted lines represent the case when $t = 0.15$. The FORTRAN programming language was used. The accuracy maintained was five digits for the numerical program.

The finite speed of wave propagation manifests itself in all these figures. The upper surface is sending thermoelastic waves into the region of the plate. This is shown by the fact that the solution is not identically equal to zero for the value of time $t = 0.05$ when $0.12 < z < 0.5$ for all the functions considered. The solution is not equal to zero for the value of time $t = 0.1$ when $-0.18 < z < 0.5$. For $t = 0.15$, the solution fills the whole region of the plate.

We notice that the solution (for small values of time) is nonzero only in a region of space adjacent to the surface. This region expands with the passage of time to fill the whole region of the thick plate.

References

1. Lord H, Shulman Y (1967) A generalized dynamical theory of thermoelasticity. J Mech Phys Solid 15:299–309
2. Biot M (1956) Thermoelasticity and irreversible thermo-dynamics. J Appl Phys 27:240–253
3. Dhaliwal R, Sherief H (1980) Generalized thermoelasticity for anisotropic media. Quart Appl Math 33:1–8
4. Ignaczak J (1982) A note on uniqueness in thermoelasticity with one relaxation time. J Therm Stress 5:257–263
5. Sherief H (1987) On uniqueness and stability in generalized thermoelasticity. Q Appl Math 45:773–778
6. Anwar M, Sherief H (1988) State space approach to generalized thermoelasticity. J Therm Stress 11:353–365

7. Sherief H (1993) State space formulation for generalized thermoelasticity with one relaxation time including heat sources. J Therm Stress 16:163–180
8. Sherief H, Anwar M (1994) State space approach to two-dimensional generalized thermoelasticity problems. J Therm Stress 17:567–590
9. Sherief H, Anwar M (1986) Problem in generalized thermoelasticity. J Therm Stress 9:165–181
10. Sherief H, Hamza F (1994) Generalized thermoelastic problem of a thick plate under axisymmetric temperature distribution. J Therm Stress 17:435–452
11. Churchill R (1972) Operational mathematics, 3rd edn. McGraw-Hill, New York
12. Honig G, Hirdes U (1984) A Method for the numerical inversion of the Laplace transform. J Comp Appl Math 10:113–132

Axisymmetric Thermal Stresses in an Anisotropic Finite Hollow Cylinder

Peter Y. P. Chen
School of Electrical Engineering & Telecommunications, University of New South Wales, Sydney, Australia

Synonyms

Anisotropic

Overview

Based on the theory of linear elasticity, thermal stresses can be obtained from solutions of heat conduction and equilibrium displacement equations. If the equations involve only constant coefficients and the body of interest is simple, they can be solved by many well-established methods, both analytical and numerical [1]. Due to recent advances in technologies, a modern design may involve materials that have much more sophisticated properties that cannot simply be modeled by constants. Methods that could be used to solve for some of those complex mathematical models become more of a challenge. On the other hand, important system parameters in a heat generating body may be changed by thermal effects and stresses. A good design will need precise knowledge of the temperature and stress fields. A common example is in the design of miniaturized electronic device in which very small electrical current could induce large temperature changes. Many electronic properties are sensitive to both temperature and stress. All of these point to the importance of thermal stress analysis in modern system designs.

This entry is concerning with axisymmetric thermal stresses in a finite and hollow cylinder. Due to the axisymmetric assumption, both temperature and displacement equations are two-dimensional. Although within the framework of linear elasticity where strains are linearly proportional to stresses, nonconstant material properties could introduce complexity to the mathematical models such that the equations, even in two dimensions, cannot be solved analytically. Over the last 20–40 years or so, those problems are solved mostly by finite element methods [3, 5] that have been implemented in commercial computer packages for a large varieties of problems. The limitations of those methods are due to the fact that the approximation functions used have not been optimized such that many grid points are required in numerical simulations. In this entry, the pseudospectral methods [4] are suggested as preferred alternatives, as optimized series expansions are used such that at least an order fewer number of equations is required for the same level of solution accuracy. A pseudospectral method, known as the Lanczos-Chebyshev pseudospectral (LCPS) method [2] that uses an optimized power series, will be described in some details.

As a departure from common practice of deriving the equilibrium displacement equations for material with constant properties, a set of equations for materials with nonconstant properties will be given. However, numerical examples that may yield some insight into the importance of thermal stresses in a design will still be restricted to constant properties systems. An additional example will be given to show how a nonlinear problem could be solved by the LCPS method.

Formerly School of Mechanical and Manufacturing Engineering

Mathematical Formulation

A linear thermal stress problem shares the common mathematical formulation with linear elasticity in that a solid body is studied of how it would deform under prescribed loading internally or on the boundaries. In the case of thermal stresses, the internal loadings come from the thermal strains produced by the temperature field. Throughout this entry, we consider the plane problem of thermoelastics. For a circular hollow cylinder with finite length, cylindrical coordinates, r, θ, and z, are used in the analysis. With an axisymmetric problem, the formulation will not involve any θ-dependent terms resulting in sets of simpler governing equations as given below.

Geometric Equations (Strain–Displacement Relations)

$$\varepsilon_r = \frac{\partial u}{\partial r}, \quad \varepsilon_\theta = \frac{u}{r}, \quad \varepsilon_z = \frac{\partial w}{\partial z}, \quad \gamma_{rz} = \frac{\partial u}{\partial z} + \frac{\partial w}{\partial r} \tag{1}$$

where u and w are the radial and axial displacements. The above relations are based on so-called engineering notation. In mathematical notation, the strain–displacement equations are

$$\boldsymbol{\varepsilon} = \frac{1}{2}\left[\nabla \boldsymbol{u} + (\nabla \boldsymbol{u})^T\right] \tag{2}$$

where $\boldsymbol{\varepsilon}$ is the strain tensor and $\boldsymbol{u}$ is the displacement vector. Obviously, the separated use of these two notations will lead to a slightly different set of field equations.

Thermal Strains

Temperature changes could cause strains. In isotropic material, the induced thermal extensional strains are equal in all directions, and there are no shear strains. In the simplest cases, thermal strains can be treated as being proportional to temperature change in relative to a reference temperature. The proportional constant is called the coefficient of linear thermal expansion. For anisotropic material, the linear thermal expansion coefficient could have different values at different directions.

Generalized Hook's Law (The Stress–Strain Relations)

For anisotropic media, the symmetry of the stress tensor σ_{ij} means that there are at most six different elements of stress. Similarly, there are at most six different elements of the strain tensor ε_{ij}. For elastic materials, Hooke's law is

$$\boldsymbol{\sigma} = \boldsymbol{C} : \boldsymbol{\varepsilon} \tag{3}$$

where $\boldsymbol{\sigma}$ is the Cauchy stress tensor and $\boldsymbol{C}$ is the second-order stiffness tensor. The simplest anisotropic case that of cubic symmetry has three independent elements:

$$C_{\alpha\beta} = \begin{bmatrix} C_{11} & C_{12} & C_{12} & 0 & 0 & 0 \\ C_{12} & C_{11} & C_{12} & 0 & 0 & 0 \\ C_{12} & C_{12} & C_{11} & 0 & 0 & 0 \\ 0 & 0 & 0 & C_{44} & 0 & 0 \\ 0 & 0 & 0 & 0 & C_{44} & 0 \\ 0 & 0 & 0 & 0 & 0 & C_{44} \end{bmatrix} \tag{4}$$

The case of polar anisotropic (with 3-axis of symmetry) has five independent elements:

$$C_{\alpha\beta} = \begin{bmatrix} C_{11} & C_{11}-2C_{66} & C_{13} & 0 & 0 & 0 \\ C_{11}-C_{66} & C_{11} & C_{13} & 0 & 0 & 0 \\ C_{13} & C_{13} & C_{33} & 0 & 0 & 0 \\ 0 & 0 & 0 & C_{44} & 0 & 0 \\ 0 & 0 & 0 & 0 & C_{44} & 0 \\ 0 & 0 & 0 & 0 & 0 & C_{66} \end{bmatrix} \tag{5}$$

The case of orthotropic (the symmetry of a brick) has nine independent elements:

$$C_{\alpha\beta} = \begin{bmatrix} C_{11} & C_{12} & C_{13} & 0 & 0 & 0 \\ C_{12} & C_{22} & C_{23} & 0 & 0 & 0 \\ C_{13} & C_{22} & C_{33} & 0 & 0 & 0 \\ 0 & 0 & 0 & C_{44} & 0 & 0 \\ 0 & 0 & 0 & 0 & C_{55} & 0 \\ 0 & 0 & 0 & 0 & 0 & C_{66} \end{bmatrix} \tag{6}$$

The special isotropic case has elements involving two independent material properties K, the bulk modulus, and μ, the shear modulus:

$$C_{\alpha\beta} = \begin{bmatrix} K+4\mu/3 & K-2\mu/3 & K-2\mu/3 & 0 & 0 & 0 \\ K-2\mu/3 & K+4\mu/3 & K-2\mu/3 & 0 & 0 & 0 \\ K-2\mu/3 & K-2\mu/3 & K+4\mu/3 & 0 & 0 & 0 \\ 0 & 0 & 0 & \mu & 0 & 0 \\ 0 & 0 & 0 & 0 & \mu & 0 \\ 0 & 0 & 0 & 0 & 0 & \mu \end{bmatrix} \tag{7}$$

For an axisymmetric problem with anisotropic properties, there are only four nonzero stresses: applying Voigt notation for tensor indices, the four elements of stress in cylindrical coordinates are $\sigma_{11} = \sigma_r$, $\sigma_{22} = \sigma_\theta$, $\sigma_{33} = \sigma_z$, and $\sigma_{55} = \tau_{rz}$.

The Equilibrium Equations

The fundamental system of field equations for the time-independent behavior of a linearly elastic body consists of the strain–displacement relations, the stress–strain relations, and the equations of equilibrium. In the case of a plane axisymmetric problem, the equations of equilibrium in the absence of body forces are

$$\begin{aligned} \frac{\partial \sigma_r}{\partial r} + \frac{\partial \tau_{rz}}{\partial z} + \frac{\sigma_r - \sigma_\theta}{r} = 0 \\ \frac{\partial \tau_{rz}}{\partial r} + \frac{\partial \sigma_z}{\partial z} + \frac{\tau_{rz}}{r} = 0 \end{aligned} \tag{8}$$

Displacement Formulation for an Axisymmetric Problem

Altogether, the above equations involve four stresses, four strains, and two displacements with four stress–strain relations, four strain–displacement relations, and two equilibrium conditions. All these equations could be combined to give two displacement equations from which the stresses could be found. First, the strain–displacement (1) is substituted into (3) (Hooke's law) using as stiffness coefficients (5). The strains, excluding the thermal strains, are then eliminated to give:

$$\begin{aligned} \sigma_r &= C_{11}\frac{\partial u}{\partial r} + C_{12}\frac{u}{r} + C_{13}\frac{\partial w}{\partial z} - p_1 T \\ \sigma_\theta &= C_{12}\frac{\partial u}{\partial r} + C_{11}\frac{u}{r} + C_{13}\frac{\partial w}{\partial z} - p_1 T \\ \sigma_z &= C_{13}\frac{\partial u}{\partial r} + C_{13}\frac{u}{r} + C_{33}\frac{\partial w}{\partial z} - p_2 T \\ \tau_{rz} &= C_{44}\left(\frac{\partial u}{\partial z} + \frac{\partial w}{\partial r}\right) \end{aligned} \tag{9}$$

where $C_{12} = C_{11} - 2C_{66}$, $p_1 = (C_{11} + C_{12})\alpha_r + C_{13}\alpha_z$, $p_2 = 2C_{13} + C_{33}\alpha_z$, and α_r and α_z are the coefficient of linear thermal expansion along the radial and axial directions. Substituting (9) into (8) gives the displacement equations (i.e., the equilibrium equations in terms of the displacements):

$$\begin{aligned} &\left[\frac{\partial}{\partial r}\left(C_{11}\frac{\partial}{\partial r}\right) + \frac{C_{11}}{r}\frac{\partial}{\partial r} + \frac{1}{r}\frac{\partial C_{12}}{\partial r} - \frac{C_{11}}{r^2} + \frac{\partial}{\partial z}\left(C_{44}\frac{\partial}{\partial z}\right)\right] u(r,z) \\ &+ \left[\frac{\partial}{\partial r}\left(C_{13}\frac{\partial}{\partial z}\right) + \frac{\partial}{\partial r}\left(C_{44}\frac{\partial}{\partial z}\right)\right] w(r,z) = \frac{\partial}{\partial r}(p_1 T(r,z)) \\ &\left[\frac{\partial}{\partial z}\left(C_{13}\frac{\partial}{\partial r}\right) + \frac{\partial}{\partial r}\left(C_{44}\frac{\partial}{\partial z}\right) + \frac{1}{r}\frac{\partial C_{13}}{\partial z} + \frac{C_{44}}{r}\frac{\partial}{\partial z}\right] u(r,z) \\ &+ \left[\frac{\partial}{\partial r}\left(C_{44}\frac{\partial}{\partial r}\right) + \frac{C_{44}}{r}\frac{\partial}{\partial r} + \frac{\partial}{\partial z}\left(C_{33}\frac{\partial}{\partial z}\right)\right] w(r,z) = \frac{\partial}{\partial z}(p_2 T(r,z)) \end{aligned} \tag{10}$$

The equations above are applicable for cases in that the material properties are nonlinear and/or position dependent. For material with constant properties, these equations are simplified to

$$\begin{aligned} &\left[C_{11}\frac{\partial^2}{\partial r^2} + \frac{C_{11}}{r}\frac{\partial}{\partial r} - \frac{C_{11}}{r^2} + C_{44}\frac{\partial^2}{\partial z^2}\right] u(r,z) \\ &+ (C_{13} + C_{44})\frac{\partial^2}{\partial r \partial z} w(r,z) = p_1 \frac{\partial}{\partial r} T(r,z) \\ &\left[(C_{44} + C_{13})\frac{\partial^2}{\partial r \partial z} + \frac{C_{13} + C_{44}}{r}\frac{\partial}{\partial z}\right] u(r,z) \\ &+ \left[C_{44}\frac{\partial^2}{\partial r^2} + \frac{C_{44}}{r}\frac{\partial}{\partial r} + C_{33}\frac{\partial^2}{\partial z^2}\right] w(r,z) \\ &= p_2 \frac{\partial}{\partial z} T(r,z) \end{aligned} \tag{11}$$

For a finite and hollow cylinder of inner radius r_i and outer radius of r_o, and length of h, the boundary conditions associated with the displacement equations may involve specified stress components:

$$\begin{aligned}
\sigma_r|_{r_i,r_o} &= \left[\sigma_r^o(z)\right]_{r_i,r_o} \\
\tau_{rz}|_{r_i,r_o} &= \left[\tau_{rz}^o(z)\right]_{r_i,r_o} \\
\sigma_z|_{0,h} &= \left[\sigma_z^o\right]_{0,h} \\
\tau_{rz}|_{0,z} &= \left[\tau_{rz}^o\right]_{0,h}
\end{aligned} \tag{12}$$

Some of the stress conditions above could be replaced by specified displacements or displacement gradients.

Heat Conduction Equations

For isotropic bodies, the Fourier law states:

$$\mathrm{q} = -k\nabla T \tag{13}$$

The steady-state heat conduction equation then represents thermal energy balance:

$$\nabla \bullet \mathrm{q} + Q = 0 \tag{14}$$

where Q is the heat source. For an axisymmetric problem in cylindrical coordinates, the above becomes

$$\left[\frac{1}{r}\frac{\partial}{\partial r}\left(rk_r\frac{\partial}{\partial r}\right)+\frac{\partial}{\partial z}\left(k_z\frac{\partial}{\partial z}\right)\right]T(r,z)+Q(r,z)=0 \tag{15}$$

where k_r and k_z are the thermal conductivities in the radial and axial directions. The heat conduction for a system with constant properties (k_r and k_z are constant) is

$$\left[\frac{k_r}{r}\frac{\partial}{\partial r}\left(r\frac{\partial}{\partial r}\right)+k_z\frac{\partial^2}{\partial z^2}\right]T(r,z)+Q(r,z)=0 \tag{16}$$

Assume that the boundary conditions are given as follows:

$$\begin{aligned}
\left[k_r\frac{\partial T}{\partial r}+h_r(T-T_c)\right]_{r_i,r_o} &= 0 \\
\left[k_z\frac{\partial T}{\partial z}+h_z(T-T_c)\right]_{0,\ell} &= 0
\end{aligned} \tag{17}$$

where the parameters h, the heat transfer coefficient, and $T_{c,}$ the coolant temperature, are to be specified along the boundaries.

Solution Methods

In order to discuss solution methods in the simplest possible way, only equations for systems with constant properties are used here. The cases with nonconstant properties are deferred to a later section.

Conversion to Dimensionless Equations

For convenience in applications, it is useful to reduce all the equations to dimensionless forms. The following set of dimensionless variables will be used:

$$\begin{aligned}
&\bar{r} = \frac{r}{r_o}; \quad \bar{z} = \frac{z}{r_o} \\
&\bar{C}_{ij} = \frac{C_{ij}}{C_{11}}; \quad \bar{u} = \frac{u}{\alpha_o T_o r_o}; \quad \bar{w} = \frac{w}{\alpha_o T_o r_o} \\
&\bar{\sigma}_r = \frac{\sigma_r}{\alpha_o C_{11} T_o}; \quad \bar{\sigma}_\theta = \frac{\sigma_\theta}{\alpha_o C_{11} T_o}; \\
&\bar{\sigma}_z = \frac{\sigma_z}{\alpha_o C_{11} T_o}; \quad \bar{\tau}_{rz} = \frac{\tau_{rz}}{\alpha_o C_{11} T_o} \\
&\bar{T} = \frac{T}{T_o}; \quad \bar{k}_{r,z} = \frac{k_{r,z}}{k_o}; \quad \bar{Q} = \frac{Q r_o^2}{k_o T_o}; \\
&\bar{p}_{1,2} = \frac{p_{1,2}}{\alpha_o C_{11}}; \quad \bar{h} = \frac{h}{h_o}
\end{aligned} \tag{18}$$

where α_o, T_o, $k_{o,}$ and h_o are reference values of linear thermal expansion coefficient, temperature, thermal conductivity, and heat transfer coefficient. Substituting the above into all previous equations and canceling all the common factors will achieve the conversions. It should be noted that all equations have retained exactly their original forms and for simplicity all dimensionless quantities will be written without an overhead bar.

Pseudospectral Methods

Evolving from the well-known spectral methods over the last two decades, pseudospectral methods themselves have emerged as attractive alternatives to better known computational

procedures such as finite difference and finite element methods. The notable strength of the pseudospectral methods lies with their ability to solve differential equations with nonconstant coefficients such as in the particular displacement and heat conduction equations developed above.

The main idea behind all spectral approaches is to approximate the solution as a truncated series expansion in the most efficient way. For this reason, many versions of pseudospectral methods have been developed each with a set of different approximation functions, consisting mostly of orthogonal polynomials. The most widely used one is the Chebyshev polynomials. The use of orthogonal polynomials is a legacy inherited from the spectral methods in that orthogonal property of the approximating function is mandatory. It is quite different with the pseudospectral methods in that solutions are obtained by collocations at points specially selected to give least possible errors. The only conditions for the approximation functions to be suitable are that each function must be unique and the series is complete. With this freedom, users who are not prepared to work through the many complex mathematical properties of orthogonal polynomials may find that choices of non-orthogonal functions such as a power series are their preferred alternatives.

The Lanczos-Chebyshev Pseudospectral (LCPS) Method

The LCPS method uses power series as approximating functions and collocation at Chebyshev points so that the solutions obtained are as accurate as those based on the Chebyshev polynomial series when both expansions use the same number of terms. Implementation of this approach is best illustrated by showing how it can be used to solve the thermal stress problems as prescribed by the displacement and heat conduction equations.

Reduction to Algebraic Equations

The pseudospectral approach is used to reduce the governing differential equations to a set of algebraic equations that could be solved by well-established numerical techniques. In the case of a $\{r,z\}$ rectangular 2D problem as the one considered here, linear transformations are used to rescale the domain into a square $[-1,1] \times [-1, 1]$. Recalling that the finite and hollow cylinder considered has an inner radius of r_i, an outer radius of $r_{o,}$ and a length from 0 to l; the new coordinates $\{R,Z\}$ relate to $\{r,z\}$ through:

$$\begin{aligned} &r = a_r R + b_r;\ \ a_r = 0.5(r_o - r_i);\ \ b_r = 0.5(r_o + r_i) \\ &z = a_z Z + b_z;\ \ a_z = 0.5\ell;\ \ b_z = 0.5\ell \end{aligned} \tag{19}$$

Converting the displacement equations, (11), to the new coordinates to give:

$$\begin{aligned} &\left[\frac{C_{11}}{a_r^2}\frac{\partial^2}{\partial R^2} + \frac{C_{11}}{a_r(a_r R + b_r)}\frac{\partial}{\partial R}\right. \\ &\left. - \frac{C_{11}}{(a_r R + b_r)^2} + \frac{C_{44}}{a_z^2}\frac{\partial^2}{\partial Z^2}\right] u(R,Z) \\ &+ \frac{C_{13} + C_{44}}{a_r a_z}\frac{\partial^2}{\partial R \partial Z} w(R,Z) = \frac{p_1}{a_r}\frac{\partial}{\partial R} T(R,Z) \\ &\left[\frac{C_{44} + C_{13}}{a_r a_z}\frac{\partial^2}{\partial R \partial Z} + \frac{C_{13} + C_{44}}{a_z(a_r R + b_r)}\frac{\partial}{\partial Z}\right] u(R,Z) \\ &+ \left[\frac{C_{44}}{a_r^2}\frac{\partial^2}{\partial R^2} + \frac{C_{44}}{a_r(a_r R + b_z)}\frac{\partial}{\partial R} + \frac{C_{33}}{a_z^2}\frac{\partial^2}{\partial Z^2}\right] \\ &w(R,Z) = \frac{p_2}{a_z}\frac{\partial}{\partial Z} T(R,Z) \end{aligned} \tag{20}$$

Converting the heat conduction equation, (16), to the new coordinates to give:

$$\begin{aligned} &\left[\frac{k_r}{a_r^2}\frac{\partial^2}{\partial R^2} + \frac{k_r}{a_r(a_r R + b_r)}\frac{\partial}{\partial R} + \frac{k_z}{a_z^2}\frac{\partial^2}{\partial Z^2}\right] \\ &T(R,Z) + Q(R,Z) = 0 \end{aligned} \tag{21}$$

Similarly, all the associated boundary conditions can be converted. Also affected are the strain–displacement relations, (1), and the stress–strain relations, (9). Working with any equations, it is important to distinguish between $\{R,Z\}$ the computational coordinates and $\{r,z\}$ the physical coordinates. For example, solutions are to be worked out on the physical coordinates

while the computational coordinates are used in the numerical simulations.

Within the computational domain, the displacement and temperature fields may be approximated by

$$\begin{aligned} u(R,Z) &= \sum_{i,j}^{M,N} u_{ij} R^{i-1} Z^{j-1}; \\ w(R,Z) &= \sum_{i,j}^{M,N} w_{ij} R^{i-1} Z^{j-1} \\ T(R,Z) &= \sum_{i,j}^{M,N} t_{ij} R^{i-1} Z^{j-1} \end{aligned} \tag{22}$$

Terms used in the temperature approximation need not be the same as those for the displacements. Using the same number of terms as in (22) is purely for numerical convenience. The decision on the values for M and N are based on the smoothness of the solutions. It is often possible that 10–20 terms in each coordinate direction could give solutions with relative errors in the order of 10^{-4} or less.

Derivatives can be obtained from (20) using term-by-term differentiation. For example,

$$\begin{aligned} \frac{\partial u}{\partial R} &= \sum_{i,j}^{M,N} (i-1) u_{ij} R^{i-2} Z^{j-1}; \\ \frac{\partial^2 u}{\partial R^2} &= \sum_{i,j}^{M,N} (i-1)(i-2) u_{ij} R^{i-3} Z^{j-1} \\ \frac{\partial u}{\partial Z} &= \sum_{i,j}^{M,N} (j-1) u_{ij} R^{i-1} Z^{j-2}; \\ \frac{\partial^2 u}{\partial Z^2} &= \sum_{i,j}^{M,N} (j-1)(j-2) u_{ij} R^{i-1} Z^{j-2} \end{aligned} \tag{23}$$

The collocation points are chosen from the roots of the Chebyshev polynomials given by

$$\begin{aligned} R_m &= \cos\left(\frac{2m-1}{M-2}\frac{\pi}{2}\right), \quad m = 1, 2, \ldots M-2 \\ Z_n &= \cos\left(\frac{2n-1}{N-2}\frac{\pi}{2}\right), \quad n = 1, 2, \ldots N-2 \end{aligned} \tag{24}$$

Replacing at the collocation points all the variables and their derivatives by their series expansions, the differential equations are reduced to a set of simultaneous algebraic equations with the series expansion coefficients as the unknowns.

Treatment of Boundary Conditions

Differential equations cannot be completely solved by themselves without considering the boundary conditions. Having reduced the governing differential to a set of simultaneous algebraic equations, the collocation method is applied also to the boundary conditions. In the standard spectral approach, if the tau method is adopted, extra unknown variables, the tau's, are added to the series expansions to cater for the prescribed boundary conditions. It is the same with the power series approach. The order of the power series must be increased. In fact, these extra terms have already been built in when (24) is used. According to (24), the number of collocation points is $M - 2$ in the R-direction and $N - 2$ in the Z-direction, making up a total of $(M-2) \times (N-2)$ interior collocation points. As the series expansion has $M \times N$ coefficients, there are already excess numbers for the boundary conditions. For a boundary value problem-like thermal stresses, each governing 2nd-order partial-differential equation is associated with 4 boundary conditions, one each at the four sides of the computational domain. Applying the collocation method at the Chebyshev points on each of the boundaries will produce $2(M-2) + 2(N-2)$ equations. Considering also that there are 2 boundary conditions for each of the 4 corners will give a further 8 equations. The final total number of equations is $M \times N + 4$, that is, 4 more than the unknown coefficients. The fact that there are more equations than the unknowns is not a problem with the numerical solution procedures. A least-squares method could be employed to give a best set of solutions.

Discontinuous Boundary Conditions

For 2D or 3D problems, specified boundary conditions at the corners could be discontinuous and these could be a problem for some numerical

procedures. An example is in the case where the constant temperatures specified on the two sides of the corner are different. Physically, discontinuous conditions should not exist, although in some systems rapid temperature variations near the corners could be possible. If this is the actual situation, the preferred alternative is to consider a different model for the boundary condition. For the conduction problem with heat removing by a coolant, the preferred model is the conjugate boundary conditions in that both heat and heat flux are specified to be continuous across the boundary. A general boundary condition that includes of the function as well as the function derivative could also avoid discontinuity at the corner. Anyhow, it should be noted that the collocation approach outlined above is applicable even when conditions at the corners are modeled as discontinuous. This is possible because the equations are solved for their least-squares solutions including the least possible error at the discontinuous boundary point.

Implementation of the Reduction Procedures

Using the heat conduction equation, (21), as an illustrating example, the substitution of the power series for the temperature as well as its derivatives at the collocation points given by (24) leads to $(M-2)\times(N-2)$ algebraic equations as follows:

$$\sum_{i,j}^{M,N} t_{ij}\left[k_r\left(\frac{(i-1)(i-2)}{a_r^2R_m^2}+\frac{i-1}{a_r(a_rR_m+b_r)R_m}\right)+k_z\frac{(j-1)(j-2)}{a_z^2Z_n^2}\right]R_m^{i-1}Z_n^{j-1}+Q(R_m,Z_n)=0,\quad m=1,\ldots,M-2;\ n=1,\ldots,N-2 \tag{25}$$

It should be noted that the division by Rm and Zn in the equation above is just a convenient way of making up the loss of power index through differentiations. There is no other mathematical implication.

Now, applying collocation to the boundary conditions described by (17) and for $R=-1$ and $R=1$ (corresponding to $r=ri$ and $r=ro$) gives $2\times(N-2)$ equations:

$$\begin{aligned}&\sum_{i,j}^{M,N} t_{ij}\left[-\frac{k_r(i-1)}{a_r}+h_r(-1,Z_n)\right](-1)^{(i-1)}Z_n^{j-1}\\&=h_r(-1,Z_n)T_c,\quad n=1,\ldots N-2;\\&\sum_{i,j}^{M,N} t_{ij}\left[\frac{k_r(i-1)}{a_r}+h_r(1,Z_n)\right]Z_n^{j-1}\\&=h_r(1,Z_n)T_c,\quad n=1,\ldots N-2\end{aligned} \tag{26}$$

Similarly, for the boundary conditions at $Z=-1$ and $Z=1$ (corresponding to $z=0$ and $z=h$), there are $2\times(M-2)$ equations:

$$\begin{aligned}&\sum_{i,j}^{M,N} t_{ij}\left[-\frac{k_z(j-1)}{a_z}+h_z(-1,R_m)\right](-1)^{(j-1)}\\&R_m^{i-1}=h_z(-1,R_m)T_c,\quad m=1,\ldots,M-2;\\&\sum_{i,j}^{M,N} t_{ij}\left[\frac{k_z(j-1)}{a_z}+h_z(1,R_m)\right]\\&R_m^{i-1}=h_z(1,R_m)T_c,\quad m=1,\ldots,M-2\end{aligned} \tag{27}$$

There are eight equations from applying collocation to the four corner points:

$$\begin{aligned}&\sum_{i,j}^{M,N} t_{ij}\left[-\frac{k_r(i-1)}{a_r}+h_r(-1,-1)\right](-1)^{(i-1)}(-1)^{j-1}\\&=h_r(-1,-1)T_c;\\&\sum_{i,j}^{M,N} t_{ij}\left[-\frac{k_r(i-1)}{a_r}+h_r(-1,1)\right](-1)^{(i-1)}\\&=h_r(-1,1)T_c;\\&\sum_{i,j}^{M,N} t_{ij}\left[\frac{k_r(i-1)}{a_r}+h_r(1,-1)\right](-1)^{j-1}\\&=h_r(1,-1)T_c;\\&\sum_{i,j}^{M,N} t_{ij}\left[\frac{k_r(i-1)}{a_r}+h_r(1,1)\right]=h_r(1,1)T_c\end{aligned} \tag{28}$$

$$\sum_{i,j}^{M,N} t_{ij}\left[-\frac{k_z(j-1)}{a_z}+h_z(-1,-1)\right](-1)^{(j-1)}(-1)^{i-1} = h_z(-1,-1)T_c;$$

$$\sum_{i,j}^{M,N} t_{ij}\left[-\frac{k_z(j-1)}{a_z}+h_z(-1,1)\right](-1)^{(j-1)} = h_z(-1,1)T_c;$$

$$\sum_{i,j}^{M,N} t_{ij}\left[\frac{k_z(j-1)}{a_z}+h_z(1,-1)\right](-1)^{i-1} = h_z(1,-1)T_c;$$

$$\sum_{i,j}^{M,N} t_{ij}\left[\frac{k_z(j-1)}{a_z}+h_z(1,1)\right] = h_z(1,1)T_c \tag{29}$$

For the displacements, there are two variables, u and w, in (22). Applying the same collocation procedures will give twice as many equations as in the case of the conduction problem. Both sets of simultaneous equations, one for the temperatures and the other for the displacements, could be solved by routines for least-squares solutions. Having determined the coefficients, the power series in (22) could be used to find solutions at any positions in the computational space, while (19) could be used if conversion to the physical space is required.

Numerical Example 1

For this example, dimensionless quantities based on (18) are used. The chosen hollow and finite cylinder has $r_o = 1.0$, $r_i = 0.6$, and $\ell = 2.0$ with material constants 1.0, 0.25, 0.25, 1.0, and 0.25 for C_{11}, C_{12}, C_{13}, C_{33}, and C_{44}, respectively. The values for α_r and α_z are 1.0 and 0.95. For the stresses, the boundary conditions include zero stresses at the curved surfaces and $\sigma_z = 0$ and $\partial u/\partial z = 0$ at the $z = l$ plane. Assuming symmetry, the conditions at the $z = 0$ are $w = 0$ and $\partial w/\partial z = 0$.

For the heat conduction problem, the system parameters chosen are $k_r = k_z = 1.0$ and $Q = 1.0$. The boundary conditions are given in (24)–(27). It is chosen for this particular example that $T = 0$ at $r = r_i$ (i.e., $R = -1$, $k_r = 0$, $h_r = 1$ and $T_c = 0$); $\partial T/\partial R = 0$ at $r = r_o$ (i.e., $R = 1$, $k_r = 1$, $h_c = 0$ and $T_c = 0$); $\partial T/\partial R = 0$ at $z = 0$ (i.e., at $Z = -1$, $k_z = 1$, $h_z = 0$ and $T_c = 0$); $T = 0$ at $z = l$ (i.e., at $Z = 1$, $k_z = 0$, $h_z = 1$ and $T_c = 0$). Using $M = 10$ and $N = 20$, the stresses obtained are shown in Fig. 1.

Long Cylinder Solutions

From Fig. 1, it can be seen that the stresses over a distance more than three times of the wall thickness measured from the top end are no longer dependent of z. These stresses are known as long cylinder solutions as z-dependency could be discarded. Under an axially symmetric temperature field $T(r)$, axially independent boundary conditions, and assuming plane strain and $w = 0$, the radial displacement equation (The first of the two equations in (11) without the z-dependent terms) can be integrated analytically to give

$$u(r) = \frac{p_1}{c_{11}}\frac{1}{r}\int_{r_o}^{r} T(r)r\,dr + A_1 r + \frac{A_2}{r} \tag{30}$$

where A_1 and A_2 are integration constants that could be found from the given boundary conditions. The corresponding stresses for a displacement field given by (30) are

$$\sigma_r = -\frac{p_1}{c_{11}}\frac{c_{11}-c_{12}}{r^2}\int_{r_o}^{r} T(r)r\,dr + (c_{11}+c_{12})A_1 - (c_{11}-c_{12})A_2/r^2$$

$$\sigma_\theta = \frac{p_1}{c_{11}}\frac{c_{11}-c_{12}}{r^2}\int_{r_o}^{r} T(r)r\,dr + (c_{11}+c_{12})A_1 + (c_{11}-c_{12})A_2/r^2 + p_1\left(\frac{c_{12}}{c_{11}}-1\right)T(r) \tag{31}$$

There is also an axial stress,

$$\sigma_z = 2c_{13}A_1 + (c_{13}p_1/c_{11} - p_2)T + A_3 \tag{32}$$

where the constant A_3 is determined from the condition that the axial resultant force is zero. It is easy to obtain an analytical solution for the temperatures from the axially independent form

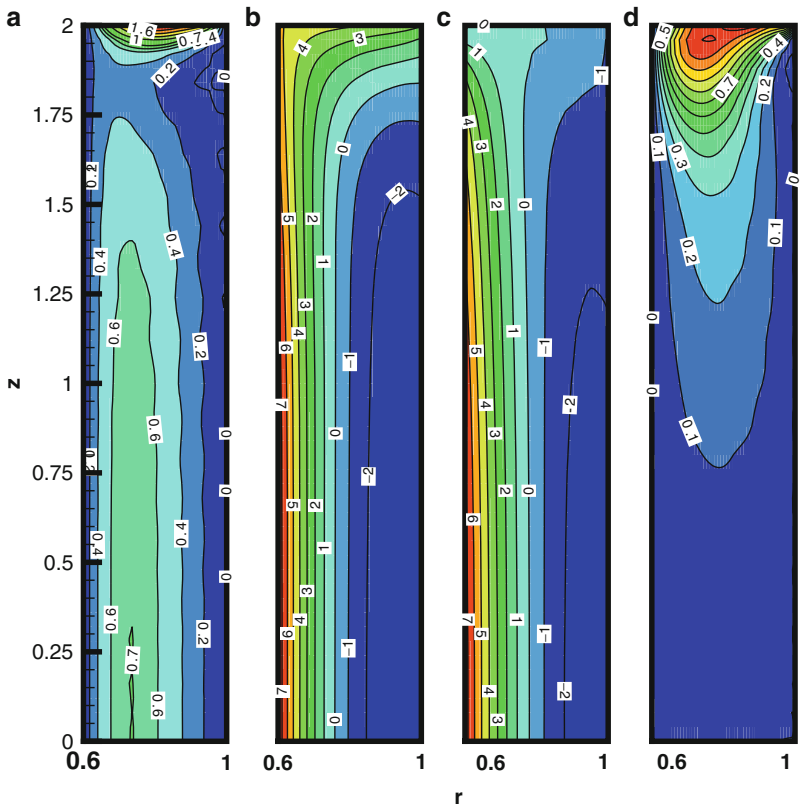

Axisymmetric Thermal Stresses in an Anisotropic Finite Hollow Cylinder,

Fig. 1 Contours of thermal stresses (× 100): (**a**) radial, (**b**) hoop, (**c**) axial, and (**d**) shear

of the heat conduction equation, (21). As it can be seen from results plotted in Fig. 2, the long cylinder solutions for the example used above are the same as the numerical results at the same locations. In fact, designs for long cylinders that require considerations of thermal stresses are often based on those analytical solutions. It is also convenience to use them to investigate various factors that could influence thermal stresses, as it is done in the examples given below.

Thermal Designs as a Stress Reduction Strategy

It is obvious that thermal stresses could be lowered by reducing temperature gradients. In the previously solved numerical example, the boundary condition at r_o was set at $\partial T/\partial r = 0$. (i.e., completely insulated). Simulation results shown in Table 1 indicate that if more and more heat is allowed to be removed from that boundary, the maximum stresses could be lowered.

Effects of Anisotropic Properties

Using the long cylinder solutions for the numerical example, results in Table 2 show that anisotropic properties only have relatively small influence on the stresses.

End Stresses

From Fig. 1, it could be seen that the stress fields near the top are quite different to those at the rest of the cylinder. As temperatures change rapidly from the main body to comply with the thermal boundary condition at the top end, the large temperature gradients are responsible for higher stresses in this end region. The effects on the temperature and displacement fields can be seen from the contour plots shown in Fig. 3a–b.

Designs of equipment involving heat transfers need to consider end stresses as they may be much higher than the long cylinder solutions. On the other hand, the thermal gradients could be changed by controlling the rate of heat leaving the top end (i.e., by changing the heat transfer

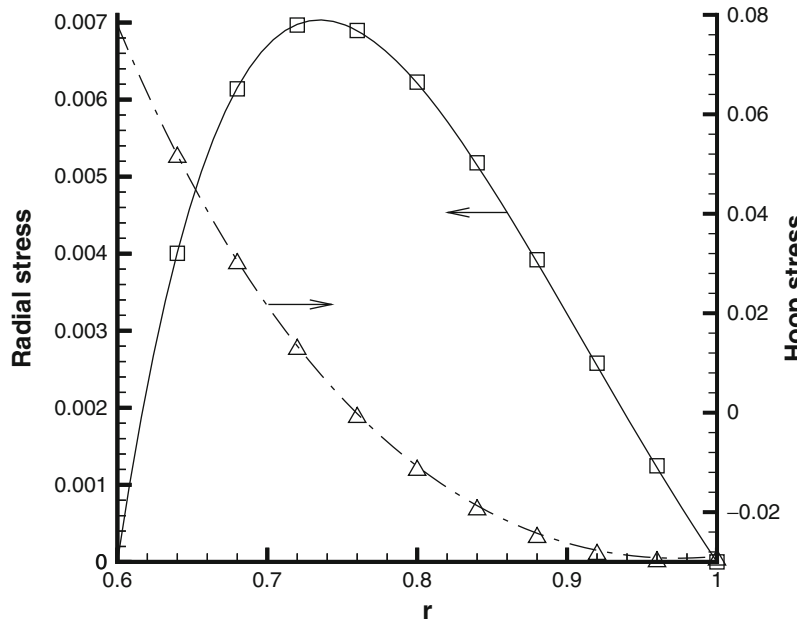

Axisymmetric Thermal Stresses in an Anisotropic Finite Hollow Cylinder, Fig. 2 Comparison of long cylinder analytical (points) and whole cylinder numerical (lines) stress solutions at z = 0

Axisymmetric Thermal Stresses in an Anisotropic Finite Hollow Cylinder, Table 1 Maximum stress reduction fractions due to thermal boundary condition changes at $r = r_o$ (The first case is used as the reference)

h_r	$\sigma_r/(\sigma_r)_{ref}$	$\sigma_\theta/(\sigma_\theta)_{ref}$	$\sigma_z/(\sigma_z)_{ref}$
0	1	1	1
0.5	0.811	0.836	0.836
1	0.686	0.722	0.722
5	0.333	0.421	0.421

Axisymmetric Thermal Stresses in an Anisotropic Finite Hollow Cylinder, Table 2 Maximum stress intensity comparisons for various combinations of anisotropic properties (The first case is used as the reference)

C_{11}	C_{12}	C_{13}	C_{33}	$\sigma_r/(\sigma_r)_{ref}$	$\sigma_\theta/(\sigma_\theta)_{ref}$	$\sigma_z/(\sigma_z)_{ref}$
1	0.25	0.25	1	1	1	1
1	0.25	0.25	0.9	1	1	0.911
1	0.25	0.25	1.1	1	1	1.089
1	0.25	0.3	1	1.033	1.033	1.009
1	0.25	0.2	1	0.967	0.967	0.987
1	0.3	0.25	1	0.964	0.964	0.989
1	0.2	0.25	1	1.031	1.031	1.011

coefficient). Table 3 shows how end stresses are reduced by lowering the heat transfer coefficient.

Systems with Nonlinear Material Properties

The displacement (10) has been derived from linear elasticity. Throughout the body under consideration, the linear stress–strain relations should hold everywhere. However, the stiffness coefficients or other material properties could be temperature or stress dependent, such that (10) is in fact a nonlinear problem. Numerically, the pseudospectral methods could still be used to reduce the differential equations into algebraic equations that are now nonlinear. Numerical procedures for nonlinear problems are then needed to solve the algebraic equations. There are many different methods available with various degree of efficiency. One method, the pseudo-transient approach, is chosen and described below because it is also being used for real transient problems. During a temperature transient, maximum stress level developed could be exceeding that of the steady state. Although this entry will not deal with transient stresses, it should be noted that given the temperature field at any time instant,

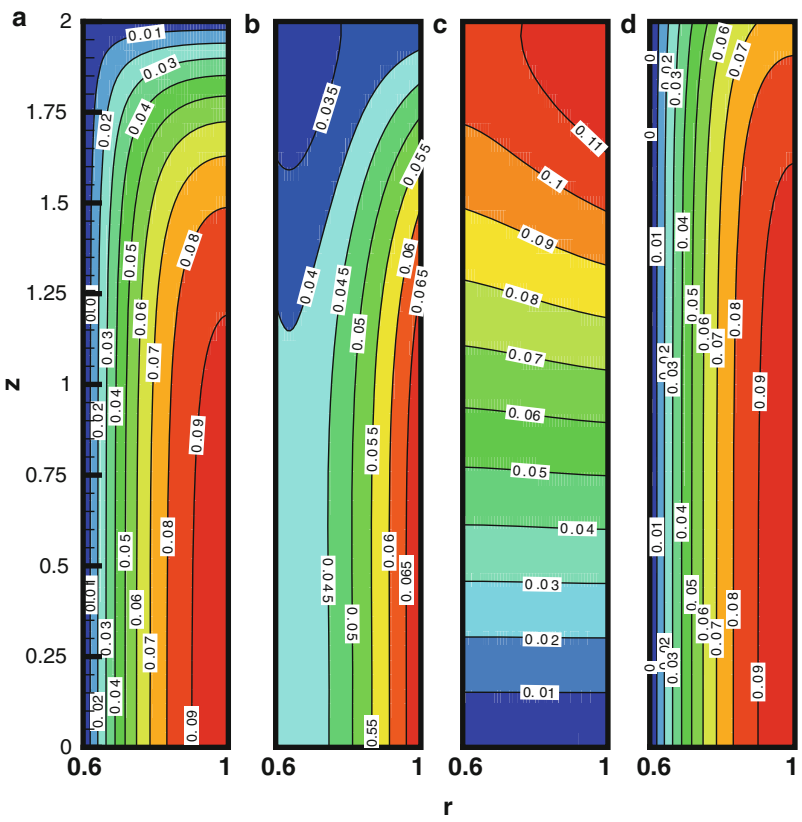

Axisymmetric Thermal Stresses in an Anisotropic Finite Hollow Cylinder, Fig. 3 Solution contours for the numerical example: (**a**) temperature, (**b**) radial displacement, (**c**) axial displacement, and (**d**) temperature with partial insulation at the top end

Axisymmetric Thermal Stresses in an Anisotropic Finite Hollow Cylinder, Table 3 Maximum end stress intensity factors for different heat transfer coefficients at the top end (The long cylinder solutions are used as references)

h_z	$\sigma_r/(\sigma_r)_{ref}$	$\sigma_\theta/(\sigma_\theta)_{ref}$	$\sigma_z/(\sigma_z)_{ref}$
100	2.777	0.909	0.781
10	2.164	0.948	0.828
5	1.771	0.976	0.867
1	1.026	1.086	0.943
100 (with temperature dependent conductivity)	2.127	0.875	0.757

the methodology of solving for the transient stresses is the same as those described in this entry. When the stress problems involve nonlinear properties, the same principles used in the temperature solutions, as described below, could be employed to obtain a set of nonlinear algebraic equations for the displacements.

The Pseudo-Transient Approach

Like many other boundary value problems, solutions of the heat conduction equation could be taken to be the stationary solutions of a transient equation which need not be exactly in the same form as the real transient heat conduction equation. This is the reason why the term pseudo-transient is used. After rearranging the differentiation terms, the heat conduction equation (15) could be written as a pseudo-transient problem where the variable t does not represent real time:

$$\begin{aligned}\frac{\partial T(r,z)}{\partial t} &= \left[k_r\left(\frac{\partial^2}{\partial r^2}+\frac{1}{r}\frac{\partial}{\partial r}\right)+\frac{\partial k_r}{\partial r}\frac{\partial}{\partial r}\right.\\ &\quad\left.+k_z\frac{\partial^2}{\partial z^2}+\frac{\partial k_z}{\partial z}\frac{\partial}{\partial z}\right]T(r,z)+Q(r,z)\\ &= L(r,z,t,T)T(r,z)+Q(r,z)\end{aligned} \tag{33}$$

where the operator L is written symbolically as dependent of t and T as thermal conductivity could be temperature dependent.

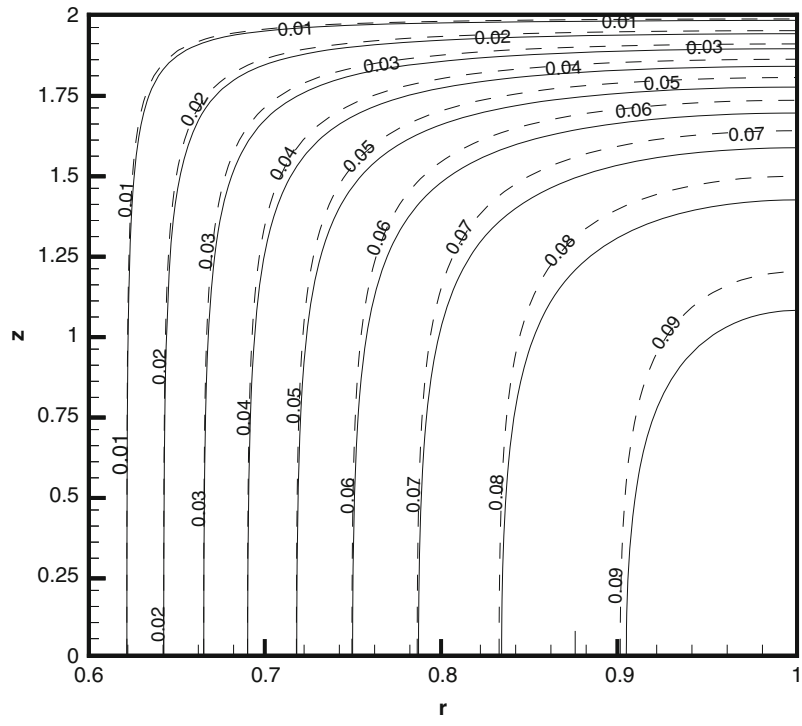

Axisymmetric Thermal Stresses in an Anisotropic Finite Hollow Cylinder, Fig. 4 Comparisons of temperature contours for temperature dependent (*solid lines*) and constant (*broken lines*) conductivities

When applying the Lanczos-Chebyshev pseudospectral spatial discretization formulation, it is necessary to approximate the coefficients in (33) by power series so that their values as well as their derivatives are available at the collocation points. For the pseudo-time term, the unconditionally stable Crank-Nicholson formulation could be used to reduce the equation to a discrete one:

$$\frac{T^{j+1}-T^{j}}{\Delta t} = \frac{1}{2}\left[L(r,z,t^{j+1},T^{j+1})T^{j+1}+L(r,z,t^{j},T^{j})T^{j}\right]+Q$$

where the superscript j refers to the pseudo-time step. With the temperature field represented by a power series and applying collocation method at the Chebyshev points, (24) is reduced to a set of nonlinear algebraic equations that could be solved by be a stepwise manner until the stationary solutions are reached. The step size Δt should be small enough to avoid the exponential growth of truncation errors.

Numerical Example 2

The previous numerical example under the same boundary conditions is chosen. All the system parameters are the same with the exception that the thermal conductivity is temperature dependent:

$$k_r = k_z = 1 + 0.1\,T(r,z) + 0.1\,T^2(r,z)$$

The temperature solutions compared with those of constant thermal conductivity are shown in Fig. 4. From the temperature contours, it can be seen that the higher conductivity introduced by the temperature dependency has decreased the temperature maxima and the temperature gradients. At the top end, stress intensities have also decreased as shown in Table 3 (last row).

Concluding Remarks

As in the example of a hollow cylinder of finite length and under a given axisymmetric

temperature field, the mathematical models to predict thermal stresses could be derived from basic geometrical relationships, heat, and force balances. The models are a set of partial differential equations that could be too complex to have analytical solutions. To overcome these difficulties, reduction techniques could be used to convert the governing equations to a set of algebraic equations. Some mathematical difficulties are still present in this set of equations such as how to deal with nonlinearity. However, procedures well established in numerical analysis are available and could be used to give solutions.

Areas within the theory of linear elasticity but not covered by this entry include bodies of nonrectangular shapes, layered structures, and three-dimensional problems. The possibilities of using domain subdivision to improve efficiency and flexibility have not been explored in this entry. However, the methodology described in this entry could be further developed to include these areas.

The potential to use the LCPS method for stress analysis has been demonstrated in examples used in this entry. There are clear evidences that solutions could be obtained with a far smaller number of grid points than both finite differences and finite element methods. Further research is needed to develop the LCPS method into a general purpose stress analysis tool.

References

1. Bower AF (2010) Applied mechanics of solids. CRC Press, Boca Raton
2. Chen PYP, Malomed BA (2011) Lanzos-Chebyshev pseudospectral methods for wave-propagation problems. Math Comput Simul. doi:10.1016/j.matcom.2011.05.013
3. Cook RD (1995) Finite element modeling for stress analysis. Wiley, New York
4. Gottlieb D, Orszag SA (1977) Numerical analysis of spectral methods: theory and applications. SIAM, Philadelphia
5. Krysl P (2006) A pragmatic introduction to the finite element method for thermal and stress analysis. World Scientific, Singapore

Axisymmetric Thermal Stresses in Disks

Naotake Noda
Shizuoka University, Hamamatsu, Japan

Overview

Mechanical and structural bodies are frequently subjected to both mechanical loads and temperature changes. The mechanical and structural elements are three-dimensional bodies such as rectangular bars, cylindrical bars, and spheres. The analysis of three-dimensional bodies typically relies on displacement potentials, such as Goodier's displacement function, Papkovich-Neuber functions, Michell's function, and Boussinesq's functions.

Two-dimensional axisymmetric thermal stresses in disks subjected to two-dimensional temperature changes are considered in the cylindrical coordinate system (r, z). Goodier's displacement function, Michell's function, and Boussinesq's function are introduced. The transient thermal stress in an infinite disk with thickness 2 h is discussed. Next, the transient thermal stress in a disk with radius a and thickness 2 h is explained. In this case, the analytical treatment is complex in order to satisfy the boundary conditions on both the circular and the flat surfaces.

Basic Equations in the Cylindrical Coordinate System (r, z)

The governing equations for axisymmetric thermoelastic problems in the cylindrical coordinate system (r, z) are summarized as follows [1]:

The equilibrium equations are

$$\begin{aligned} \frac{\partial \sigma_{rr}}{\partial r} + \frac{\partial \sigma_{zr}}{\partial z} + \frac{\sigma_{rr} - \sigma_{\theta\theta}}{r} + F_r = 0 \\ \frac{\partial \sigma_{rz}}{\partial r} + \frac{\partial \sigma_{zz}}{\partial z} + \frac{\sigma_{rz}}{r} + F_z = 0 \end{aligned} \quad (1)$$

where F_r and F_z denote the body forces in the r and z axes, respectively. The strains are defined by displacements u_r and u_z:

$$\begin{aligned}
&\varepsilon_{rr}=\frac{\partial u_r}{\partial r},\quad \varepsilon_{\theta\theta}=\frac{u_r}{r},\quad \varepsilon_{zz}=\frac{\partial u_z}{\partial z}\\
&\varepsilon_{zr}=\frac{1}{2}\left(\frac{\partial u_r}{\partial z}+\frac{\partial u_z}{\partial r}\right),\quad \varepsilon_{r\theta}=\varepsilon_{\theta z}=0\\
&e=\varepsilon_{rr}+\varepsilon_{\theta\theta}+\varepsilon_{zz}=\frac{\partial u_r}{\partial r}+\frac{u_r}{r}+\frac{\partial u_z}{\partial z}
\end{aligned}\tag{2}$$

Hooke's law is

$$\begin{aligned}
\varepsilon_{rr}&=\frac{1}{E}(\sigma_{rr}-\nu\sigma_{\theta\theta}-\nu\sigma_{zz})+\alpha\tau\\
\varepsilon_{\theta\theta}&=\frac{1}{E}(\sigma_{\theta\theta}-\nu\sigma_{zz}-\nu\sigma_{rr})+\alpha\tau\\
\varepsilon_{zz}&=\frac{1}{E}(\sigma_{zz}-\nu\sigma_{rr}-\nu\sigma_{\theta\theta})+\alpha\tau\\
\varepsilon_{rz}&=\frac{1}{2G}\sigma_{rz}
\end{aligned}\tag{3}$$

The alternative forms are

$$\begin{aligned}
\sigma_{rr}&=2\mu\varepsilon_{rr}+\lambda e-\beta\tau\\
\sigma_{\theta\theta}&=2\mu\varepsilon_{\theta\theta}+\lambda e-\beta\tau\\
\sigma_{zz}&=2\mu\varepsilon_{zz}+\lambda e-\beta\tau\\
\sigma_{rz}&=2\mu\varepsilon_{rz}
\end{aligned}\tag{3′}$$

in which E, G, ν, λ, μ, α and β are Young's modulus, the shear modulus, Poisson's ratio, Lame's constants, the coefficient of linear thermal expansion, and the thermoelastic constant $(\beta=\alpha(3\lambda+2\mu)=\alpha E/(1-2\nu))$, respectively.

Navier's equation is

$$\begin{aligned}
&(\lambda+2\mu)\frac{\partial e}{\partial r}-\mu\left(-\frac{\partial^2 u_r}{\partial z^2}+\frac{\partial^2 u_z}{\partial r\partial z}\right)-\beta\frac{\partial\tau}{\partial r}+F_r=0\\
&(\lambda+2\mu)\frac{\partial e}{\partial z}-\mu\left(\frac{1}{r}\frac{\partial u_r}{\partial z}+\frac{\partial^2 u_r}{\partial r\partial z}-\frac{\partial^2 u_z}{\partial r^2}-\frac{1}{r}\frac{\partial u_z}{\partial r}\right)\\
&\qquad-\beta\frac{\partial\tau}{\partial z}+F_z=0
\end{aligned}\tag{4}$$

Navier's equation, as expressed by (4), without body forces can be solved by Goodier's thermoelastic potential Φ and Boussinesq's harmonic functions φ and ψ:

$$\begin{aligned}
u_r&=\frac{\partial\Phi}{\partial r}+\frac{\partial\varphi}{\partial r}+z\frac{\partial\psi}{\partial r}\\
u_z&=\frac{\partial\Phi}{\partial r}+\frac{\partial\varphi}{\partial z}+z\frac{\partial\psi}{\partial z}-(3-4\nu)\psi
\end{aligned}\tag{5}$$

where the three functions satisfy:

$$\nabla^2\Phi=\frac{1+\nu}{1-\nu}\alpha\tau,\quad \nabla^2\varphi=\nabla^2\psi=0\tag{6}$$

and $\nabla^2=\frac{\partial^2}{\partial r^2}+\frac{1}{r}\frac{\partial}{\partial r}+\frac{\partial^2}{\partial z^2}$

The stress components are

$$\begin{aligned}
\sigma_{rr}&=2G\left[\frac{\partial^2\Phi}{\partial r^2}-\frac{1+\nu}{1-\nu}\alpha\tau+\frac{\partial^2\varphi}{\partial r^2}+z\frac{\partial^2\psi}{\partial r^2}-2\nu\frac{\partial\psi}{\partial z}\right]\\
\sigma_{\theta\theta}&=2G\left[\frac{1}{r}\frac{\partial\Phi}{\partial r}-\frac{1+\nu}{1-\nu}\alpha\tau+\frac{1}{r}\frac{\partial\varphi}{\partial r}+\frac{z}{r}\frac{\partial\psi}{\partial r}-2\nu\frac{\partial\psi}{\partial z}\right]\\
\sigma_{zz}&=2G\left[\frac{\partial^2\Phi}{\partial z^2}-\frac{1+\nu}{1-\nu}\alpha\tau+\frac{\partial^2\varphi}{\partial z^2}+z\frac{\partial^2\psi}{\partial z^2}-2(1-\nu)\frac{\partial\psi}{\partial z}\right]\\
\sigma_{rz}&=2G\left[\frac{\partial^2\Phi}{\partial r\partial z}+\frac{\partial^2\varphi}{\partial r\partial z}+z\frac{\partial^2\psi}{\partial r\partial z}-(1-2\nu)\frac{\partial\psi}{\partial z}\right]
\end{aligned}\tag{7}$$

The solutions of the Laplace equation (6) in the cylindrical coordinate system are

$$\begin{pmatrix}1\\ \ln r\end{pmatrix}\begin{pmatrix}1\\ z\end{pmatrix},\quad \begin{pmatrix}J_0(ar)\\ Y_0(ar)\end{pmatrix}\begin{pmatrix}\exp(az)\\ \exp(-az)\end{pmatrix}$$
$$\begin{pmatrix}J_0(ar)\\ Y_0(ar)\end{pmatrix}\begin{pmatrix}\cosh az\\ \sinh az\end{pmatrix},\quad \begin{pmatrix}I_0(ar)\\ K_0(ar)\end{pmatrix}\begin{pmatrix}\cos az\\ \sin az\end{pmatrix}\tag{8}$$

where $J_0(ar)$ and $Y_0(ar)$ are Bessel functions of the first and second kind, of order n, respectively, $I_0(ar)$ and $K_0(ar)$ are modified Bessel functions of the first and second kind, of order n, respectively, a is an arbitrary constant, and $\begin{pmatrix}1\\ \ln r\end{pmatrix}\begin{pmatrix}1\\ z\end{pmatrix}$ means $\begin{pmatrix}1\\ \ln r\\ z\\ z\ln r\end{pmatrix}$

Here, Michell's function M is related to Boussinesq's harmonic functions φ and ψ:

$$M=-\int(\varphi+z\psi)dz\tag{9}$$

Michell's function M must satisfy the equation:

$$\nabla^2\nabla^2 M = 0 \tag{10}$$

The displacements and the stresses are represented by

$$\begin{aligned} u_r &= \frac{\partial \Phi}{\partial r} - \frac{\partial^2 M}{\partial r \partial z} \\ u_z &= \frac{\partial \Phi}{\partial z} + 2(1-\nu)\nabla^2 M - \frac{\partial^2 M}{\partial z^2} \end{aligned} \tag{11}$$

$$\begin{aligned} \sigma_{rr} &= 2G\left[\frac{\partial^2 \Phi}{\partial r^2} - \frac{1+\nu}{1-\nu}\alpha\tau + \frac{\partial}{\partial z}\left(\nu\nabla^2 M - \frac{\partial^2 M}{\partial r^2}\right)\right] \\ \sigma_{\theta\theta} &= 2G\left[\frac{1}{r}\frac{\partial \Phi}{\partial r} - \frac{1+\nu}{1-\nu}\alpha\tau + \frac{\partial}{\partial z}\left(\nu\nabla^2 M - \frac{1}{r}\frac{\partial M}{\partial r}\right)\right] \\ \sigma_{zz} &= 2G\left\{\frac{\partial^2 \Phi}{\partial z^2} - \frac{1+\nu}{1-\nu}\alpha\tau + \frac{\partial}{\partial z}\left[(2-\nu)\nabla^2 M - \frac{\partial^2 M}{\partial z^2}\right]\right\} \\ \sigma_{rz} &= 2G\left\{\frac{\partial^2 \Phi}{\partial r \partial z} + \frac{\partial}{\partial r}\left[(1-\nu)\nabla^2 M - \frac{\partial^2 M}{\partial z^2}\right]\right\} \end{aligned} \tag{12}$$

The solutions of the bi-Laplace equation (10) in the cylindrical coordinate system are

$$\begin{pmatrix} 1 \\ \ln r \\ r^2 \\ r^2 \ln r \end{pmatrix}\begin{pmatrix} 1 \\ z \end{pmatrix}, \begin{pmatrix} J_0(ar) \\ Y_0(ar) \\ rJ_1(ar) \\ rY_1(ar) \end{pmatrix}\begin{pmatrix} \exp(az) \\ \exp(-az) \end{pmatrix}$$
$$\begin{pmatrix} J_0(ar) \\ Y_0(ar) \\ rJ_1(ar) \\ rY_1(ar) \end{pmatrix}\begin{pmatrix} \cosh az \\ \sinh az \end{pmatrix}, \begin{pmatrix} I_0(ar) \\ K_0(ar) \\ rI_1(ar) \\ rK_1(ar) \end{pmatrix}\begin{pmatrix} \cos az \\ \sin az \end{pmatrix}$$
$$\begin{pmatrix} 1 \\ \ln r \end{pmatrix}\begin{pmatrix} z^2 \\ z^3 \end{pmatrix}, \begin{pmatrix} J_0(ar) \\ Y_0(ar) \end{pmatrix}\begin{pmatrix} z\exp(az) \\ z\exp(-az) \end{pmatrix}$$
$$\begin{pmatrix} J_0(ar) \\ Y_0(ar) \end{pmatrix}\begin{pmatrix} z\cosh az \\ z\sinh az \end{pmatrix}, \begin{pmatrix} I_0(ar) \\ K_0(ar) \end{pmatrix}\begin{pmatrix} z\cos az \\ z\sin az \end{pmatrix} \tag{13}$$

We consider two problems:

[Case I] Transient thermal stress in an infinite disk with thickness 2 h.

[Case II] Transient thermal stress in a disk with radius a and thickness 2 h.

[Case I] Transient Thermal Stress in an Infinite Disk with Thickness 2 *h*

Consider transient temperature in an infinite circular disk with thickness 2 h. The governing equation for the transient temperature without internal heat generation is

$$\frac{1}{\kappa}\frac{\partial T}{\partial t} = \frac{\partial^2 T}{\partial r^2} + \frac{1}{r}\frac{\partial T}{\partial r} + \frac{\partial^2 T}{\partial z^2} \tag{14}$$

The boundary condition is

$$-\lambda\frac{\partial T}{\partial z} = \pm h_b[T - T_b(r)] \quad \text{on } z = \pm h \tag{15}$$

where $T_b(r)$ denotes the surrounding temperature, λ is the heat conductivity, and h_b denotes the heat transfer coefficient on the flat surfaces.

The initial condition is

$$T = T_i \text{ at } t = 0 \tag{16}$$

We introduce the temperature change $\tau\ (=T - T_i)$ from the constant initial temperature T_i. The governing equation, boundary conditions, and initial condition reduce to

$$\frac{1}{\kappa}\frac{\partial \tau}{\partial t} = \frac{\partial^2 \tau}{\partial r^2} + \frac{1}{r}\frac{\partial \tau}{\partial r} + \frac{\partial^2 \tau}{\partial z^2} \tag{14'}$$

$$-\lambda\frac{\partial \tau}{\partial z} = \pm h_b\{\tau - [T_b(r) - T_i]\} \quad \text{on } z = \pm h \tag{15'}$$

$$\tau = 0 \text{ at } t = 0 \tag{16'}$$

Here, we introduce the method of separation of variables to obtain the general solution of (14'). When the temperature is expressed as

$$\tau(r, z, t) = f(r)g(z)h(t) \tag{17}$$

three separation equations can be obtained by substitution of (17) into (14'):

$$\begin{aligned} \frac{dh(t)}{dt} + \kappa(s^2 + p^2)h(t) &= 0 \\ \frac{d^2 f(r)}{dr^2} + \frac{1}{r}\frac{df(r)}{dr} + s^2 f(r) &= 0 \\ \frac{d^2 g(z)}{dz^2} + p^2 g(z) &= 0 \end{aligned} \tag{18}$$

The solutions of (18) are

$$\begin{aligned}
&h(t) = 1, \quad f(r) = J_0(sr), \quad Y_0(sr)\\
&g(z) = \cosh sz, \quad \sinh sz \quad \text{for } p^2 = -s^2\\
&h(t) = 1, \quad f(r) = I_0(pr), \quad K_0(pr)\\
&g(z) = \cos pz, \quad \sin pz \quad \text{for } s^2 = -p^2\\
&h(t) = \exp[-\kappa(s^2+p^2)t] \quad \text{for } s^2+p^2 \neq 0\\
&f(r) = 1, \ \ln r \quad \text{for } s = 0\\
&f(r) = J_0(sr), \quad Y_0(sr) \quad \text{for } s \neq 0\\
&g(z) = 1, \ z \quad \text{for } p = 0\\
&g(z) = \cos pz, \quad \sin pz \quad \text{for } p \neq 0
\end{aligned} \tag{19}$$

The general solution of (14') for this problem is expressed by

$$\begin{aligned}
\tau(r,z) = &\int_0^\infty sJ_0(sr)\{A(s)\cosh sz\\
&+\sum_{m=1}^{\infty} A_m(s)\cos p_m z \exp[-\kappa(s+p_m^2)t]\}ds
\end{aligned} \tag{20}$$

First, we express the surrounding temperature $T_b(r) - T_i$ by the Bessel integral:

$$T_b(r) - T_i = \int_0^\infty T_{bs}(s)sJ_0(sr)ds \tag{21}$$

where

$$T_{bs}(s) = \int_0^\infty [T_b(r) - T_i]rJ_0(sr)dr \tag{22}$$

Taking into consideration the boundary conditions given by (15'), we can obtain that p_m are the eigenvalues of the equation:

$$(h_b h/\lambda)\cos p_m h - p_m h \sin p_m h = 0 \tag{23}$$

and

$$A(s) = \frac{(h_b h/\lambda)T_{bs}(s)}{(h_b h/\lambda)\cosh sh + sh\sinh sh} \tag{24}$$

The initial condition (16') gives

$$\sum_{m=1}^{\infty} A_m(s)\cos p_m z = -A(s)\cosh sz \tag{25}$$

Multiplying $\cos p_n z$ on both sides of (25) and integrating from 0 to h, we get

$$\begin{aligned}
&\sum_{m=1}^{\infty} A_m(s)\int_0^h \cos p_m z \cos p_n z dz\\
&= -A(s)\int_0^h \cosh sz \cos p_n z dz
\end{aligned} \tag{26}$$

Taking into consideration the integral results

$$\begin{aligned}
&\int_0^h \cos p_m z \cos p_n z dz\\
&= \begin{cases} 0 & m \neq n \\ (\cos p_n h \sin p_n h + p_n h)/(2p_n) & m = n \end{cases}\\
&\int \cosh sz \cos p_n z dz\\
&= \frac{1}{s^2+p_n^2}[p_n \cosh sz \sin p_n z + s\sinh sz \cos p_n z]
\end{aligned}$$

$A_n(s)$ can be determined as

$$A_n(s) = -\frac{2T_{bs}(s)p_n^2 h^2}{[\cos p_n h + p_n h/\sin p_n h](s^2h^2 + p_n^2 h^2)} \tag{27}$$

Then, the temperature change τ is determined by

$$\begin{aligned}
\tau(r,z) = &\int_0^\infty sJ_0(sr)T_{bs}(s)\\
&\times \left\{ \frac{h_b h/\lambda}{(h_b h/\lambda)\cosh sh + sh\sinh sh}\cosh sz \right.\\
&-2\sum_{m=1}^{\infty} \frac{p_m^2 h^2}{[\cos p_m h + p_m h/\sin p_m h](s^2h^2 + p_m^2 h^2)}\\
&\left.\times \cos p_m z \exp[-\kappa(s+p_m^2)t]\right\}ds
\end{aligned} \tag{28}$$

Next, we consider the thermal stresses under the boundary conditions

$$\sigma_{zz} = \sigma_{zr} = 0 \quad \text{at} \quad z = \pm h \tag{29}$$

Goodier's thermoelastic function Φ and Michell's functions M for this problem are:

$$\Phi(r,z,t) = \frac{1+v}{1-v}\alpha\int_0^\infty sJ_0(sr)\left\{\frac{A(s)}{2s}z\sinh sz - \sum_{m=1}^{\infty}\frac{A_m(s)}{s^2+p_m^2}\cos p_m z\exp[-\kappa(s^2+p_m^2)t]\right\}ds \tag{30}$$

$$M(r,z) = \int_0^\infty sJ_0(sr)[C_0(s)\sinh sz + D_0(s)z\cosh sz]ds \tag{31}$$

Substitution of (30) and (31) into (11) and (12) gives the displacements and thermal stresses as follows:

$$\begin{aligned} u_r = & \int_0^\infty s^2J_1(sr)\Bigg(sC_0(s)\cosh sz \\ & + D_0(s)(\cosh sz + sz\sinh sz) \\ & - \frac{1+v}{1-v}\alpha\Bigg\{\frac{A(s)}{2s}z\sinh sz - \sum_{m=1}^{\infty}\frac{A_m(s)}{s^2+p_m^2} \\ & \times\cos p_m z\exp[-\kappa(s^2+p_m^2)t]\Bigg\}\Bigg)ds \end{aligned} \tag{32}$$

$$\begin{aligned} u_z = & \int_0^\infty sJ_0(sr)\Bigg\{-C_0(s)s^2\sinh sz \\ & + D_0(s)s[2(1-2v)\sinh sz - sz\cosh sz] \\ & + \frac{1+v}{1-v}\alpha\Bigg\{\frac{A(s)}{2s}(\sinh sz + sz\cosh sz) \\ & + \sum_{m=1}^{\infty}\frac{p_mA_m(s)}{s^2+p_m^2}\sin p_m z\exp[-\kappa(s^2+p_m^2)t]\Bigg\}ds \end{aligned} \tag{33}$$

$$\begin{aligned} \frac{\sigma_{rr}}{2G} = & \int_0^\infty s\Bigg(C_0(s)s^3[J_0(sr) - \frac{1}{rs}J_1(sr)]\cosh sz \\ & + D_0(s)s^2\Bigg\{2vJ_0(sr)\cosh sz \\ & + [J_0(sr) - \frac{1}{sr}J_1(sr)](\cosh sz + sz\sinh sz)\Bigg\} \\ & - \frac{1+v}{1-v}\alpha\Bigg\{\frac{A(s)}{2}J_0(sr)(2\cosh sz + sz\sinh sz) \\ & - \frac{A(s)}{2}\frac{J_1(sr)}{sr}sz\sinh sz \\ & + \sum_{m=1}^{\infty}A_m(s)\frac{1}{s^2+p_m^2}[p_m^2J_0(sr) + \frac{s^2}{sr}J_1(sr)] \\ & \times\cos p_m z\exp[-\kappa(s^2+p_m^2)t]\Bigg\}\Bigg)ds \end{aligned} \tag{34}$$

$$\begin{aligned} \frac{\sigma_{\theta\theta}}{2G} = & \int_0^\infty s\Bigg(s^3C_0(s)\frac{1}{sr}J_1(sr)\cosh sz \\ & + s^2D_0(s)[2vJ_0(sr)\cosh sz \\ & + \frac{1}{rs}J_1(sr)(\cosh sz + sz\sinh sz)] \\ & - \frac{1+v}{1-v}\alpha\Bigg\{\frac{A(s)}{2}[2J_0(sr)\cosh sz \\ & + \frac{1}{sr}J_1(sr)sz\sinh sz] + \sum_{m=1}^{\infty}A_m(s) \\ & \times[J_0(sr) - \frac{s^2}{s^2+p_m^2}\frac{1}{sr}J_1(sr)] \\ & \times\cos p_m z\exp[-\kappa(s^2+p_m^2)t]\Bigg\}\Bigg)ds \end{aligned} \tag{35}$$

$$\begin{aligned} \frac{\sigma_{zz}}{2G} = & -\int_0^\infty sJ_0(sr)\Bigg(s^3C_0(s)\cosh sz \\ & - s^2D_0(s)[(1-2v)\cosh sz - sz \\ & \times\sinh sz] + \frac{1+v}{1-v}\alpha\{-\frac{A(s)}{2}sz \\ & \times\sinh sz + \sum_{m=1}^{\infty}\frac{s^2A_m(s)}{s^2+p_m^2}\cos p_m z \\ & \times\exp[-\kappa(s^2+p_m^2)t]\}\Bigg)ds \end{aligned} \tag{36}$$

$$\begin{aligned} \frac{\sigma_{rz}}{2G} = & \int_0^\infty s^2J_1(sr)\Bigg(s^2C_0(s)\sinh sz \\ & + sD_0(s)(2v\sinh sz + sz\cosh sz) \\ & - \frac{1+v}{1-v}\alpha\Bigg\{\frac{A(s)}{2s}(\sinh sz + sz\cosh sz) \\ & + \sum_{m=1}^{\infty}\frac{p_mA_m(s)}{s^2+p_m^2}\sin p_m z\exp[-\kappa(s^2+p_m^2)t]\Bigg\}\Bigg)ds \end{aligned} \tag{37}$$

The unknown coefficients C_0 and D_0 can be determined by the boundary conditions given by (29).

$$
\begin{aligned}
s^3 C_0(s) &= \frac{1+v}{1-v}\alpha\left\{\frac{A(s)}{2}(1-2v)\right. \\
&\quad sh[2v+(h_b h/\lambda)]\sinh sh \\
&\quad -sh\frac{[s^2h^2-(h_b h/\lambda)(1-2v)]\cosh sh}{\sinh sh\cosh sh+sh} \\
&\quad \left.\times\sum_{m=1}^{\infty}\frac{A_m(s)\cos p_m h}{s^2h^2+p_m^2h^2}\exp[-\kappa(s^2+p_m^2)t]\right\} \\
s^2 D_0(s) &= \frac{1+v}{1-v}\alpha\left\{\frac{A(s)}{2}\right. \\
&\quad +sh\frac{(h_a h/\lambda)\cosh sh+sh\sinh sh}{\cosh sh\sinh sh+sh} \\
&\quad \left.\times\sum_{m=1}^{\infty}\frac{A_m(s)\cos p_m h}{s^2h^2+p_m^2h^2}\exp[-\kappa(s^2+p_m^2)t]\right\}
\end{aligned}
\tag{38}
$$

[Case II] Transient Thermal Stress in a Disk with Radius *a* and Thickness 2*h*

The governing equation for transient temperature without internal heat generation is given by (14) [2]. The boundary conditions are

$$
\begin{aligned}
-\lambda\frac{\partial T}{\partial r} &= h_a(T-T_i) \quad \text{at } r=a \\
-\lambda\frac{\partial T}{\partial z} &= \pm h_b[T-T_b(r)] \quad \text{at } z=\pm h
\end{aligned}
\tag{39}
$$

where $T_b(r)$ denotes the surrounding temperature, λ is the heat conductivity, and h_a and h_b denote the heat transfer coefficients on the circular and flat surfaces, respectively.

The initial condition is

$$
T = T_i \text{ at } t=0 \tag{40}
$$

We introduce the temperature change τ ($=T-T_i$) from the constant initial temperature T_i. The governing equation, boundary conditions, and initial condition reduce to

$$
\frac{1}{\kappa}\frac{\partial\tau}{\partial t} = \frac{\partial^2\tau}{\partial r^2}+\frac{1}{r}\frac{\partial\tau}{\partial r}+\frac{\partial^2\tau}{\partial z^2} \tag{14'}
$$

$$
\begin{aligned}
-\lambda\frac{\partial\tau}{\partial r} &= h_a\tau \quad \text{on } r=a \\
-\lambda\frac{\partial\tau}{\partial z} &= \pm h_b\left\{\tau-[T_b(r)-T_i]\right\} \\
&\text{on } z=\pm h
\end{aligned}
\tag{39'}
$$

$$
\tau = 0 \text{ at } t=0 \tag{40'}
$$

Using the method of separation of variables, the general solution of (14') for this problem is expressed by

$$
\begin{aligned}
\tau(r,z) &= \sum_{n=1}^{\infty}J_0(s_n r)\left\{A_n\cosh s_n z\right. \\
&\quad \left.+\sum_{m=1}^{\infty}A_{nm}\cos p_m z\exp[-\kappa(s_n^2+p_m^2)t]\right\}
\end{aligned}
\tag{41}
$$

Taking into consideration the boundary condition given by the first equation (39'), s_n are the eigenvalues of the equation

$$
s_n a J_1(s_n a)-(h_a a/\lambda)J_0(s_n a)=0 \tag{42}
$$

We express the surrounding temperature $T_b(r)$ as the Bessel series:

$$
T_b(r)-T_i = \sum_{n=1}^{\infty}T_{bn}J_0(s_n r) \tag{43}
$$

where

$$
\begin{aligned}
T_{bn} &= \frac{2s_n^2}{J_0^2(s_n a)[s_n^2a^2+(h_a a/\lambda)^2]} \\
&\quad \times\int_0^a[T_b(r)-T_i]rJ_0(s_n r)dr
\end{aligned}
\tag{44}
$$

and p_m are the eigenvalues of the equation that satisfies the boundary condition (39'), i.e., $z=\pm h$

$$
(h_b h/\lambda)\cos p_m h - p_m h\sin p_m h = 0 \tag{45}
$$

and

$$A_n = \frac{T_{bn}(h_b h/\lambda)}{(h_b h/\lambda)\cosh s_n h + s_n h \sinh s_n h} \tag{46}$$

Taking into consideration the initial condition (40'), the unknown constants can be determined as

$$A_{nm} = -\frac{2p_m^2 h^2 T_{bn}}{[\cos p_m h + p_m h/\sin p_m h](s_n^2 h^2 + p_m^2 h^2)} \tag{47}$$

Then the temperature change τ is expressed by:

$$\begin{aligned}\tau(r,z) &= \sum_{n=1}^{\infty} J_0(s_n r)\left\{A_n \cosh s_n z + \sum_{m=1}^{\infty} A_{nm}\cos p_m z \exp[-\kappa(s_n^2+p_m^2)t]\right\} \\ &= \sum_{n=1}^{\infty} J_0(s_n r) T_{bn}\left\{\frac{(h_b h/\lambda)\cosh s_n z}{(h_b h/\lambda)\cosh s_n h + s_n h \sinh s_n h} - 2\sum_{m=1}^{\infty}\frac{p_m^2 h^2}{[\cos p_m h + p_m h/\sin p_m h](s_n^2 h^2 + p_m^2 h^2)} \times \cos p_m z \exp[-\kappa(s_n^2+p_m^2)t]\right\}\end{aligned} \tag{48}$$

Next, we consider thermal stresses under the following boundary conditions:

$$\sigma_{rr} = \sigma_{rz} = 0 \quad \text{on} \quad r = a \tag{49}$$

$$\sigma_{zz} = \sigma_{zr} = 0 \quad \text{on} \quad z = \pm h \tag{50}$$

Goodier's thermoelastic function Φ, and Michell's function M for this problem are:

$$\Phi(r,z,t) = \frac{1+v}{1-v}\alpha\sum_{n=1}^{\infty} J_0(s_n r)\left\{\frac{A_n}{2s_n} z \sinh s_n z - \sum_{m=1}^{\infty}\frac{A_{nm}}{s_n^2+p_m^2}\cos p_m z \exp[-\kappa(s_n^2+p_m^2)t]\right\} \tag{51}$$

$$\begin{aligned}M(r,z) &= E_0 r^2 z + E_0' z^3 \\ &+ \sum_{n=1}^{\infty} J_0(s_n r)[C_n(s_n)\sinh s_n z + D_n(s_n) z \cosh s_n z] \\ &+ \sum_{i=1}^{\infty} J_0(q_i r)[E_i \sinh q_i z + E_i' z \cosh q_i z] \\ &+ \sum_{j=1}^{\infty}[F_j I_0(v_j r) + F_j' r I_1(v_j r)]\sin v_j z\end{aligned} \tag{52}$$

where q_i and v_j are the eigenvalues for $J_0(q_i a) = 0$ and $\sin v_j h = 0$, respectively.

Substitution of (51) and (52) into (11) and (12) gives the displacements and thermal stresses:

$$\begin{aligned}u_r &= -2E_0 r + \sum_{n=1}^{\infty} s_n J_1(s_n r)\left(s_n C_n(s_n)\cosh s_n z + D_n(s_n)(\cosh s_n z + s_n z \sinh s_n z) - \frac{1+v}{1-v}\alpha\left\{\frac{A_n(s_n)}{2s_n} z \sinh s_n z - \sum_{m=1}^{\infty}\frac{A_{nm}}{s_n^2+p_m^2}\cos p_m z \exp[-\kappa(s_n^2+p_m^2)t]\right\}\right) \\ &+ \sum_{i=1}^{\infty} q_i J_1(q_i r)[q_i E_i \cosh q_i z + E_i'(\cosh q_i z + q_i z \sinh q_i z)] \\ &- \sum_{j=1}^{\infty}[v_j^2 F_j I_1(v_j r) + v_j^2 F_j' r I_0(v_j r)]\cos v_j z\end{aligned} \tag{53}$$

$$\begin{aligned}u_z &= 8(1-v)E_0 z + 6(1-2v)E_0' z \\ &+ \sum_{n=1}^{\infty} J_0(s_n r)\{-C_n(s_n)s_n^2 \sinh s_n z \\ &+ D_n(s_n)s_n[2(1-2v)\sinh s_n z - s_n z \cosh s_n z] \\ &+ \frac{1+v}{1-v}\alpha\left\{\frac{A_n(s_n)}{2s_n}(\sinh s_n z + s_n z \cosh s_n z) + \sum_{m=1}^{\infty}\frac{p_m A_{nm}}{s_n^2+p_m^2}\sin p_m z \exp[-\kappa(s_n^2+p_m^2)t]\right\} \\ &+ \sum_{i=1}^{\infty} J_0(q_i r)\{-E_i q_i^2 \sinh q_i z \\ &+ E_i' q_i[2(1-2v)\sinh q_i z - q_i z \cosh q_i z] \\ &+ \sum_{j=1}^{\infty}\{v_j^2 F_j I_0(v_j r) + v_j F_j'[4(1-v)I_0(v_j r) \\ &+ v_j r I_1(v_j r)]\}\sin v_j z\end{aligned} \tag{54}$$

$$\frac{\sigma_{rr}}{2G}=-2(1-2\nu)E_0+6\nu E_0^{'}$$
$$+\sum_{n=1}^{\infty}\Bigg(C_n(s_n)s_n^3[J_0(s_nr)-\frac{1}{rs_n}J_1(s_nr)]\cosh s_nz$$
$$+D_n(s_n)\{2\nu s_n^2J_0(s_nr)\cosh s_nz$$
$$+s_n^2[J_0(s_nr)-\frac{1}{s_nr}J_1(s_nr)](\cosh s_nz$$
$$+s_nz\sinh s_nz)\}$$
$$-\frac{1+\nu}{1-\nu}\alpha\Bigg\{\frac{A_n(s_n)}{2}J_0(s_nr)(2\cosh s_nz+s_nz\sinh s_nz)$$
$$-\frac{A_n(s_n)}{2}\frac{J_1(s_nr)}{s_nr}s_nz\sinh s_nz$$
$$+\sum_{m=1}^{\infty}A_{nm}\frac{1}{s_n^2+p_m^2}[p_m^2J_0(s_nr)$$
$$+\frac{s_n^2}{s_nr}J_1(s_nr)]\cos p_mz\exp[-\kappa(s_n^2+p_m^2)t]\Bigg\}\Bigg)$$
$$+\sum_{i=1}^{\infty}\Bigg(E_iq_i^3[J_0(q_ir)-\frac{1}{q_ir}J_1(q_ir)]\cosh q_iz$$
$$+E_i^{'}\Bigg\{2\nu q_i^2J_0(q_ir)\cosh q_iz$$
$$+q_i^2[J_0(q_ir)-\frac{1}{q_ir}J_1(q_ir)](\cosh q_iz+q_iz\sinh q_iz)\Bigg\}\Bigg)$$
$$-\sum_{m=1}^{\infty}\Bigg\{v_j^3F_j[I_0(v_jr)-\frac{1}{v_jr}I_1(v_jr)]$$
$$+v_j^2F_j^{'}[(1-2\nu))I_0(v_jr)+v_jrI_1(v_jr)]\Bigg\}\cos v_jz \tag{55}$$

$$\frac{\sigma_{\theta\theta}}{2G}=-2(1-2\nu)E_0+6\nu E_0^{'}$$
$$+\sum_{n=1}^{\infty}\Bigg(s_n^3C_n(s_n)\frac{1}{s_nr}J_1(s_nr)\cosh s_nz$$
$$+s_n^2D_n(s_n)[2\nu J_0(s_nr)\cosh s_nz$$
$$+\frac{1}{s_nr}J_1(s_nr)(\cosh s_nz+s_nz\sinh s_nz)]$$
$$-\frac{1+\nu}{1-\nu}\alpha\Bigg\{\frac{A_n(s_n)}{2}[2J_0(s_nr)\cosh s_nz$$
$$+\frac{1}{s_nr}J_1(s_nr)s_nz\sinh s_nz]$$
$$+\sum_{m=1}^{\infty}A_{nm}[J_0(s_nr)-\frac{s_n^2}{s_n^2+p_m^2}\frac{1}{s_nr}J_1(s_nr)]$$
$$\times\cos p_mz\exp[-\kappa(s_n^2+p_m^2)t]\Bigg\}\Bigg)$$
$$+\sum_{i=1}^{\infty}\Bigg(q_i^3E_i\frac{1}{q_ir}J_1(q_ir)\cosh q_iz$$
$$+q_i^2E_i^{'}[2\nu J_0(q_ir)\cosh q_iz$$
$$+\frac{1}{q_ir}J_1(q_ir)(\cosh q_iz+q_iz\sinh q_iz)]\Bigg)$$
$$-\sum_{j=1}^{\infty}[v_j^3F_j\frac{1}{v_jr}I_1(v_jr)$$
$$+(1-2\nu)v_j^2F_j^{'}I_0(v_jr)]\cos v_jz \tag{56}$$

$$\frac{\sigma_{zz}}{2G}=4(2-\nu)E_0+6(1-\nu)E_0^{'}$$
$$-\sum_{n=1}^{\infty}J_0(s_nr)\Bigg(s_n^3C_n(s_n)\cosh s_nz$$
$$-s_n^2D_n(s_n)[(1-2\nu)\cosh s_nz\ -s_nz\sinh s_nz]$$
$$+\frac{1+\nu}{1-\nu}\alpha\Bigg\{-\frac{A_n(s_n)}{2}s_nz\sinh s_nz$$
$$+\sum_{m=1}^{\infty}\frac{s_n^2A_{nm}}{s_n^2+p_m^2}\cos p_mz\exp[-\kappa(s_n^2+p_m^2)t]\Bigg\}\Bigg)$$
$$-\sum_{i=1}^{\infty}J_0(q_ir)\Bigg\{q_i^3E_i\cosh q_iz$$
$$-q_i^2E_i^{'}[-(1-2\nu)\cosh q_iz+q_iz\sinh q_iz]\Bigg\}$$
$$+\sum_{j=1}^{\infty}\Bigg\{v_j^3F_jI_0(v_jr)$$
$$+v_j^2F_j^{'}[2(2-\nu)I_0(v_jr)+v_jrI_1(v_jr)]\Bigg\}\cos v_jz \tag{57}$$

$$\frac{\sigma_{rz}}{2G}=\sum_{n=1}^{\infty}s_nJ_1(s_nr)\Bigg(s_n^2C_n(s_n)\sinh s_nz$$
$$+s_nD_n(s_n)(2\nu\sinh s_nz+s_nz\cosh s_nz)$$
$$-\frac{1+\nu}{1-\nu}\alpha\Bigg\{\frac{A_n(s_n)}{2s_n}(\sinh s_nz+s_nz\cosh s_nz)$$
$$+\sum_{m=1}^{\infty}\frac{p_mA_{nm}}{s_n^2+p_m^2}\sin p_mz\exp[-\kappa(s_n^2+p_m^2)t]\Bigg\}\Bigg)$$
$$+\sum_{i=1}^{\infty}q_iJ_1(q_ir)[q_i^2E_i\sinh q_iz$$
$$+qE_i^{'}(2\nu\sinh q_iz+q_iz\cosh q_iz)]$$

$$+\sum_{j=1}^{\infty}\left\{v_j^3F_jI_1(v_jr)+v_j^2F_j^{'}[2(1-v)I_1(v_jr)+v_jrI_0(v_jr)]\right\}\sin v_jz \tag{58}$$

The boundary conditions given by (50) give

$$\begin{aligned}&s_n^3C_n(s_n)\cosh s_nh-s_n^2D_n(s_n)[(1-2v)\cosh s_nh-s_nh\sinh s_nh]\\&=\frac{1+v}{1-v}\alpha\left\{\frac{A_n(s_n)}{2}s_nh\sinh s_nh-\sum_{m=1}^{\infty}\frac{s_n^2A_{nm}}{s_n^2+p_m^2}\cos p_mh\exp[-\kappa(s_n^2+p_m^2)t]\right\}\\&\times s_n^2C_n(s_n)\sinh s_nh+s_nD_n(s_n)(2v\sinh s_nh+s_nh\cosh s_nh)\\&=\frac{1+v}{1-v}\alpha\left\{\frac{A_n(s_n)}{2s_n}(\sinh s_nh+s_nh\cosh s_nh)+\sum_{m=1}^{\infty}\frac{p_mA_{nm}}{s_n^2+p_m^2}\sin p_mh\exp[-\kappa(s_n^2+p_m^2)t]\right\}\end{aligned} \tag{59}$$

$$\begin{aligned}&4(2-v)E_0+6(1-v)E_0^{'}-\sum_{i=1}^{\infty}J_0(q_ir)\{q_i^3E_i\cosh q_ih\\&-q_i^2E_i^{'}[-(1-2v)\cosh q_ih+q_iz\sinh q_ih]\}\\&+\sum_{j=1}^{\infty}(-1)^j\{v_j^3F_jI_0(v_jr)+v_j^2F_j^{'}\\&\times[2(2-v)I_0(v_jr)+v_jrI_1(v_jr)]\}=0\end{aligned} \tag{60}$$

$$q_i^3E_i\sinh q_ih+q_i^2E_i^{'}(2v\sinh q_ih+q_ih\cosh q_ih)=0 \tag{61}$$

The boundary conditions given by (49) give

$$\begin{aligned}&-2(2-v)E_0+6vE_0^{'}\\&+\sum_{n=1}^{\infty}\left(s_n^3[J_0(s_na)-\frac{1}{s_na}J_1(s_na)]C_n(s_n)\cosh s_nz\right.\\&+D_n(s_n)\{2vs_n^2J_0(s_na)\cosh s_nz+s_n^2[J_0(s_na)\\&-\frac{1}{s_na}J_1(s_na)](\cosh s_nz+s_nz\sinh s_nz)\}-\frac{1+v}{1-v}\\&\times\alpha\left\{\frac{A_n(s_n)}{2}J_0(s_na)(2\cosh s_nz+s_nz\sinh s_nz)\right.\\&-\frac{A_n(s_n)}{2}\frac{J_1(s_na)}{s_na}s_nz\sinh s_nz\\&+\sum_{m=1}^{\infty}A_{nm}\frac{1}{s_n^2+p_m^2}[p_m^2J_0(sa)+\frac{s_n^2}{s_na}J_1(sa)]\\&\left.\left.\cos p_mz\exp[-\kappa(s_n^2+p_m^2)t]\right\}\right)\\&-\sum_{i=1}^{\infty}\frac{1}{q_ia}J_1(q_ia)[q_i^3E_i\cosh q_iz\\&+E_i^{'}q_i^2(\cosh q_iz+q_iz\sinh q_iz)]\\&-\sum_{j=1}^{\infty}\{v_j^3F_j[I_0(v_ja)-\frac{1}{v_ja}I_1(v_ja)]\\&+v_j^2F_j^{'}[(1-2v))I_0(v_ja)+v_jrI_1(v_ja)]\}\cos v_jz=0\end{aligned} \tag{62}$$

$$\begin{aligned}&\sum_{n=1}^{\infty}s_nJ_1(s_na)\left(s_n^2C_n(s_n)\sinh s_nz\right.\\&+s_nD_n(s_n)(2v\sinh s_nz+s_nz\cosh s_nz)\\&-\frac{1+v}{1-v}\alpha\left\{\frac{A_n(s_n)}{2s_n}(\sinh s_nz+s_nz\cosh s_nz)\right.\\&\left.\left.+\sum_{m=1}^{\infty}\frac{p_mA_{nm}}{s_n^2+p_m^2}\sin p_mz\exp[-\kappa(s_n^2+p_m^2)t]\right\}\right)\\&+\sum_{i=1}^{\infty}J_1(q_ia)[q_i^3E_i\sinh q_iz\\&+q_i^2E_i^{'}(2v\sinh q_iz+q_iz\cosh q_iz)]\\&+\sum_{j=1}^{\infty}\left\{v_j^3F_jI_1(v_ja)\right.\\&\left.+v_j^2F_j^{'}[2(1-v)I_1(v_ja)+v_jrI_0(v_ja)]\right\}\sin v_jz=0\end{aligned} \tag{63}$$

The unknown coefficients C_n and D_n can be determined by (59). In order to determine the unknown coefficients E_0, $E_o^{'}$, E_i, $E_i^{'}$, F_j, and $F_j^{'}$ in (60)–(63), we expand the modified Bessel functions to a series of Bessel functions $J_0(q_ir)$ as follows:

$$\begin{aligned}I_0(v_jr)&=G_{j0}^{00}+\sum_{i=1}^{\infty}G_{ji}^{00}J_0(q_ir)\\rI_1(v_jr)&=G_{j0}^{10}+\sum_{i=1}^{\infty}G_{ji}^{10}J_0(q_ir)\end{aligned} \tag{64}$$

as well as expand the hyperbolic functions as a series of trigonometric functions as follows:

$$\begin{aligned}
\cosh(s_n z) &= H_{n0}^{cc} + \sum_{j=1}^{\infty} H_{nj}^{cc} \cos(v_j z) \\
z\sinh(s_n z) &= H_{n0}^{sc} + \sum_{j=1}^{\infty} H_{nj}^{sc} \cos(v_j z) \\
\sinh(s_n z) &= \sum_{j=1}^{\infty} H_{nj}^{ss} \sin(v_j z) \\
z\cosh(s_n z) &= \sum_{j=1}^{\infty} H_{nj}^{cs} \sin(v_j z) \\
\cosh(q_i z) &= Q_{n0}^{cc} + \sum_{j=1}^{\infty} Q_{ij}^{cc} \cos(v_j z) \\
z\sinh(q_i z) &= Q_{n0}^{sc} + \sum_{j=1}^{\infty} Q_{ij}^{sc} \cos(v_j z) \\
\sinh(q_i z) &= \sum_{j=1}^{\infty} Q_{ij}^{ss} \sin(v_j z) \\
z\cosh(q_i z) &= \sum_{j=1}^{\infty} Q_{ij}^{cs} \sin(v_j z) \\
\cos(p_m z) &= F_{m0}^{cc} + \sum_{j=1}^{\infty} F_{mj}^{cc} \cos(v_j z) \\
\sin(p_m z) &= \sum_{j=1}^{\infty} F_{mj}^{ss} \sin(v_j z)
\end{aligned} \tag{65}$$

Substitution of (64) and (65) into (60), (62), and (63) gives simultaneous linear equations to determine the unknown coefficients E_0, $E_0^{'}$, E_i, $E_i^{'}$, F_j, and $F_j^{'}$.

$$\begin{aligned}
&q_i^3 E_i \cosh q_i h - q_i^2 E_i^{'}[-(1-2v)\cosh q_i h \\
&+ q_i h \sinh q_i h] - \sum_{j=1}^{\infty} (-1)^j \{v_j^3 F_j G_{ji}^{00} \\
&+ v_j^2 F_j^{'}[2(2-v)G_{ji}^{00} + v_j G_{ji}^{10}]\} = 0
\end{aligned} \tag{66}$$

$$q_i^3 E_i \sinh q_i h + q_i^2 E_i^{'}(2v\sinh q_i h + q_i h \cosh q_i h) = 0 \tag{67}$$

$$\begin{aligned}
&[I_0(v_j a) - \frac{1}{v_j r} I_1(v_j a)] v_j^3 F_j \\
&+ [(1-2v) I_0(v_j a) + v_j r I_1(v_j a)] v_j^2 F_j^{'} \\
&- \sum_{n=1}^{\infty} \left(s_n^3 [J_0(s_n a) - \frac{1}{s_n a} J_1(s_n a)] C_n(s_n) H_{nj}^{cc} \right. \\
&+ D_n(s_n)\{2v s_n^2 J_0(s_n a) H_{nj}^{cc} \\
&+ s_n^2 [J_0(s_n a) - \frac{1}{s_n a} J_1(s_n a)](H_{nj}^{cc} + s_n H_{nj}^{sc})\} \\
&- \frac{1+v}{1-v}\alpha \left\{ \frac{A_n(s_n)}{2} J_0(s_n a)(2H_{nj}^{cc} + s_n H_{nj}^{sc}) \right. \\
&- \frac{A_n(s_n)}{2} \frac{J_1(s_n a)}{s_n a} s_n H_{nj}^{sc} \\
&+ \sum_{m=1}^{\infty} A_{nm} \frac{1}{s_n^2 + p_m^2} [p_m^2 J_0(s_n a) \\
&\left. \left. + \frac{s_n^2}{s_n a} J_1(s_n a)] F_{mj}^{cc} \exp[-\kappa(s_n^2 + p_m^2)t] \right\} \right) \\
&+ \sum_{i=1}^{\infty} \frac{1}{q_i a} J_1(q_i a)[q_i^3 E_i Q_{ij}^{cc} \\
&+ E_i^{'} q_i^2 (Q_{ij}^{cc} + q_i Q_{ij}^{cc})] = 0
\end{aligned} \tag{68}$$

$$\begin{aligned}
&v_j^3 F_j I_1(v_j a) + v_j^2 F_j^{'}[2(1-v) I_1(v_j a) + v_j r I_0(v_j a)] \\
&+ \sum_{n=1}^{\infty} s_n J_1(s_n a) \left(s_n^2 C_n(s_n) H_{nj}^{ss} \right. \\
&+ s_n D_n(s_n)(2v H_{nj}^{ss} + s_n H_{nj}^{cs}) \\
&- \frac{1+v}{1-v}\alpha \left\{ \frac{A_n(s_n)}{2s_n}(H_{nj}^{ss} + s_n H_{nj}^{cs}) \right. \\
&\left. \left. + \sum_{m=1}^{\infty} \frac{p_m A_{nm}}{s_n^2 + p_m^2} F_{mj}^{ss} \exp[-\kappa(s_n^2 + p_m^2)t] \right\} \right) \\
&+ \sum_{i=1}^{\infty} J_1(q_i a)[q_i^3 E_i Q_{ij}^{ss} + q_i^2 E_i^{'}(2v Q_{ij}^{ss} + q_i Q_{ij}^{cs})] = 0
\end{aligned} \tag{69}$$

Solving the simultaneous linear equations (66)–(69), we can obtain the unknown coefficients E_i, $E_i^{'}$, F_j, and $F_j^{'}$. Furthermore,

$$\begin{aligned}
&4(2-v)E_0 + 6(1-v)E_0^{'} \\
&= -\sum_{j=1}^{\infty} (-1)^j \{v_j^3 F_j G_{j0}^{00} + v_j^2 F_j^{'}[2(2-v) \\
&\times G_{j0}^{00} + v_j G_{j0}^{10}]\}
\end{aligned} \tag{70}$$

$$\begin{aligned}
&2(1-2v)E_0 - 6vE_0^{'} \\
&= \sum_{n=1}^{\infty} \left(s_n^3 [J_0(s_n a) - \frac{1}{s_n a} J_1(s_n a)] C_n(s_n) H_{n0}^{cc} \right.
\end{aligned}$$

$$+ D_n(s_n)\{2\nu s_n^2 J_0(s_n a)H_{n0}^{cc} + s_n^2[J_0(s_n a) - \frac{1}{s_n a}J_1(s_n a)](H_{n0}^{cc} + s_n H_{n0}^{sc})\} - \frac{1+\nu}{1-\nu}\alpha\left\{\frac{A_n(s_n)}{2}J_0(s_n a)(2H_{n0}^{cc} + s_n H_{n0}^{sc}) - \frac{A_n(s_n)}{2}\frac{J_1(s_n a)}{s_n a}s_n H_{n0}^{sc} + \sum_{m=1}^{\infty} A_{nm}\frac{1}{s_n^2 + p_m^2}[p_m^2 J_0(s_n a) + \frac{s_n^2}{s_n a}J_1(s_n a)]F_{m0}^{cc}\exp[-\kappa(s_n^2 + p_m^2)t]\right\}\Bigg) - \sum_{i=1}^{\infty}\frac{1}{q_i r}J_1(q_i a)[q_i^3 E_i Q_{i0}^{cc} + q_i^2 E_i'(Q_{i0}^{cc} + q_i Q_{i0}^{sc})] \quad (71)$$

Solving the simultaneous linear equations (70) and (71), we can obtain the unknown coefficients E_0 and E_o'.

We finally obtain the displacements and stresses by substituting these coefficients into (53)–(58).

References

1. Noda N, Hetnarski RB, Tanigawa Y (2003) Thermal stresses, 2nd edn. Taylor & Francis, New York/London
2. Takeuti Y, Noda N (1979) Thermal-stress problems in industry. 2: transient thermal stresses in a disk brake. J Therm Stress 2(1):61-72

Axisymmetric Thermal Stresses in Solid Cylinders

Naotake Noda
Shizuoka University, Hamamatsu, Japan

Overview

Mechanical and structural bodies are frequently subjected to both mechanical loads and temperature changes. The mechanical and structural elements are three-dimensional bodies such as rectangular bars, cylindrical bars, and spheres. The analysis of three-dimensional bodies typically relies on displacement potentials, such as Goodier's displacement function, the Papkovich-Neuber functions, Michell's function, and Boussinesq's functions.

Two-dimensional axisymmetric thermal stresses in solid cylinders subjected to two-dimensional temperature changes are considered in the cylindrical coordinate system (r, z). Goodier's displacement function, Michell's function, and Boussinesq's function are introduced. The transient thermal stress in an infinite solid circular cylinder with radius a is discussed. Next, the transient thermal stress in a finite solid circular cylinder with radius a and length $2l$ is explained. In this case, the analytical treatment is complex in order to satisfy the boundary conditions on both the circular and the flat surfaces.

Basic Equations in the Cylindrical Coordinate System (r, z)

The governing equations for axisymmetric thermoelastic problems in the cylindrical coordinate system (r, z) are summarized as follows [1]:

The equilibrium equations are:

$$\frac{\partial \sigma_{rr}}{\partial r} + \frac{\partial \sigma_{zr}}{\partial z} + \frac{\sigma_{rr} - \sigma_{\theta\theta}}{r} + F_r = 0$$
$$\frac{\partial \sigma_{rz}}{\partial r} + \frac{\partial \sigma_{zz}}{\partial z} + \frac{\sigma_{rz}}{r} + F_z = 0 \quad (1)$$

where F_r and F_z denote the body forces in the r and z axes, respectively. The strains are defined by displacements u_r and u_z:

$$\varepsilon_{rr} = \frac{\partial u_r}{\partial r}, \quad \varepsilon_{\theta\theta} = \frac{u_r}{r}, \quad \varepsilon_{zz} = \frac{\partial u_z}{\partial z}$$
$$\varepsilon_{zr} = \frac{1}{2}\left(\frac{\partial u_r}{\partial z} + \frac{\partial u_z}{\partial r}\right), \quad \varepsilon_{r\theta} = \varepsilon_{\theta z} = 0 \quad (2)$$
$$e = \varepsilon_{rr} + \varepsilon_{\theta\theta} + \varepsilon_{zz} = \frac{\partial u_r}{\partial r} + \frac{u_r}{r} + \frac{\partial u_z}{\partial z}$$

Hooke's law is:

$$\varepsilon_{rr} = \frac{1}{E}(\sigma_{rr} - \nu\sigma_{\theta\theta} - \nu\sigma_{zz}) + \alpha\tau$$
$$\varepsilon_{\theta\theta} = \frac{1}{E}(\sigma_{\theta\theta} - \nu\sigma_{zz} - \nu\sigma_{rr}) + \alpha\tau$$
$$\varepsilon_{zz} = \frac{1}{E}(\sigma_{zz} - \nu\sigma_{rr} - \nu\sigma_{\theta\theta}) + \alpha\tau \quad (3)$$
$$\varepsilon_{rz} = \frac{1}{2G}\sigma_{rz}$$

The alternative forms are:

$$\begin{aligned}\sigma_{rr} &= 2\mu\varepsilon_{rr} + \lambda e - \beta\tau \\ \sigma_{\theta\theta} &= 2\mu\varepsilon_{\theta\theta} + \lambda e - \beta\tau \\ \sigma_{zz} &= 2\mu\varepsilon_{zz} + \lambda e - \beta\tau \\ \sigma_{rz} &= 2\mu\varepsilon_{rz}\end{aligned} \tag{3'}$$

in which E, G, v, λ, μ, α and β are Young's modulus, the shear modulus, Poisson's ratio, Lame's constants, the coefficient of linear thermal expansion, and the thermoelastic constant ($\beta = \alpha(3\lambda + 2\mu) = \alpha E/(1-2v)$), respectively.

Navier's equation is:

$$\begin{aligned}&(\lambda+2\mu)\frac{\partial e}{\partial r} - \mu\Big(-\frac{\partial^2 u_r}{\partial z^2} + \frac{\partial^2 u_z}{\partial r \partial z}\Big) \\ &\quad - \beta\frac{\partial \tau}{\partial r} + F_r = 0 \\ &(\lambda+2\mu)\frac{\partial e}{\partial z} \\ &\quad - \mu\Big(\frac{1}{r}\frac{\partial u_r}{\partial z} + \frac{\partial^2 u_r}{\partial r \partial z} - \frac{\partial^2 u_z}{\partial r^2} - \frac{1}{r}\frac{\partial u_z}{\partial r}\Big) \\ &\quad - \beta\frac{\partial \tau}{\partial z} + F_z = 0\end{aligned} \tag{4}$$

Navier's equation, as expressed by (4), without body forces can be solved by Goodier's thermoelastic potential Φ and Boussinesq's harmonic functions φ and ψ:

$$\begin{aligned}u_r &= \frac{\partial \Phi}{\partial r} + \frac{\partial \varphi}{\partial r} + z\frac{\partial \psi}{\partial r} \\ u_z &= \frac{\partial \Phi}{\partial z} + \frac{\partial \varphi}{\partial z} + z\frac{\partial \psi}{\partial z} - (3-4v)\psi\end{aligned} \tag{5}$$

where the three functions satisfy:

$$\nabla^2\Phi = \frac{1+v}{1-v}\alpha\tau, \quad \nabla^2\varphi = \nabla^2\psi = 0 \tag{6}$$

and $\nabla^2 = \frac{\partial^2}{\partial r^2} + \frac{1}{r}\frac{\partial}{\partial r} + \frac{\partial^2}{\partial z^2}$.

The stress components are:

$$\begin{aligned}\sigma_{rr} &= 2G\Big[\frac{\partial^2\Phi}{\partial r^2} - \frac{1+v}{1-v}\alpha\tau + \frac{\partial^2\varphi}{\partial r^2} + z\frac{\partial^2\psi}{\partial r^2} - 2v\frac{\partial\psi}{\partial z}\Big] \\ \sigma_{\theta\theta} &= 2G\Big[\frac{1}{r}\frac{\partial\Phi}{\partial r} - \frac{1+v}{1-v}\alpha\tau + \frac{1}{r}\frac{\partial\varphi}{\partial r} + \frac{z}{r}\frac{\partial\psi}{\partial r} - 2v\frac{\partial\psi}{\partial z}\Big] \\ \sigma_{zz} &= 2G\Big[\frac{\partial^2\Phi}{\partial z^2} - \frac{1+v}{1-v}\alpha\tau + \frac{\partial^2\varphi}{\partial z^2} \\ &\qquad + z\frac{\partial^2\psi}{\partial z^2} - 2(1-v)\frac{\partial\psi}{\partial z}\Big] \\ \sigma_{rz} &= 2G\Big[\frac{\partial^2\Phi}{\partial r\partial z} + \frac{\partial^2\phi}{\partial r\partial z} + z\frac{\partial^2\psi}{\partial r\partial z} - (1-2v)\frac{\partial\psi}{\partial z}\Big]\end{aligned} \tag{7}$$

The solutions of the Laplace equation (6) in the cylindrical coordinate system are:

$$\begin{pmatrix}1\\ \ln r\end{pmatrix}\begin{pmatrix}1\\ z\end{pmatrix}, \quad \begin{pmatrix}J_0(ar)\\ Y_0(ar)\end{pmatrix}\begin{pmatrix}\exp(az)\\ \exp(-az)\end{pmatrix}$$
$$\begin{pmatrix}J_0(ar)\\ Y_0(ar)\end{pmatrix}\begin{pmatrix}\cosh az\\ \sinh az\end{pmatrix}, \quad \begin{pmatrix}I_0(ar)\\ K_0(ar)\end{pmatrix}\begin{pmatrix}\cos az\\ \sin az\end{pmatrix} \tag{8}$$

where $J_0(ar)$ and $Y_0(ar)$ are Bessel functions of the first and second kind, of order n, respectively, $I_0(ar)$ and $K_0(ar)$ are modified Bessel functions of the first and second kind, of order n, respectively, and a is an arbitrary constant.

Here, Michell's function M is related to Boussinesq's harmonic functions φ and ψ:

$$M = -\int(\varphi + z\psi)dz \tag{9}$$

Michell's function M must satisfy the equation:

$$\nabla^2\nabla^2 M = 0 \tag{10}$$

The displacements and the stresses are represented by:

$$\begin{aligned}u_r &= \frac{\partial\Phi}{\partial r} - \frac{\partial^2 M}{\partial r\partial z} \\ u_z &= \frac{\partial\Phi}{\partial z} + 2(1-v)\nabla^2 M - \frac{\partial^2 M}{\partial z^2}\end{aligned} \tag{11}$$

$$\sigma_{rr} = 2G\left[\frac{\partial^2\Phi}{\partial r^2} - \frac{1+v}{1-v}\alpha\tau + \frac{\partial}{\partial z}\left(v\nabla^2 M - \frac{\partial^2 M}{\partial r^2}\right)\right]$$
$$\sigma_{\theta\theta} = 2G\left[\frac{1}{r}\frac{\partial\Phi}{\partial r} - \frac{1+v}{1-v}\alpha\tau + \frac{\partial}{\partial z}\left(v\nabla^2 M - \frac{1}{r}\frac{\partial M}{\partial r}\right)\right]$$

$$\sigma_{zz} = 2G\left\{\frac{\partial^2\Phi}{\partial z^2} - \frac{1+\nu}{1-\nu}\alpha\tau + \frac{\partial}{\partial z}\left[(2-\nu)\nabla^2 M - \frac{\partial^2 M}{\partial z^2}\right]\right\}$$
$$\sigma_{rz} = 2G\left\{\frac{\partial^2\Phi}{\partial r\partial z} + \frac{\partial}{\partial r}\left[(1-\nu)\nabla^2 M - \frac{\partial^2 M}{\partial z^2}\right]\right\} \quad (12)$$

The solutions of the bi-Laplace equation (10) in the cylindrical coordinate system are:

$$\begin{pmatrix}1\\ \ln r\\ r^2\\ r^2\ln r\end{pmatrix}\begin{pmatrix}1\\ z\end{pmatrix}, \begin{pmatrix}J_0(ar)\\ Y_0(ar)\\ rJ_1(ar)\\ rY_1(ar)\end{pmatrix}\begin{pmatrix}\exp(az)\\ \exp(-az)\end{pmatrix}$$
$$\begin{pmatrix}J_0(ar)\\ Y_0(ar)\\ rJ_1(ar)\\ rY_1(ar)\end{pmatrix}\begin{pmatrix}\cosh az\\ \sinh az\end{pmatrix}, \begin{pmatrix}I_0(ar)\\ K_0(ar)\\ rI_1(ar)\\ rK_1(ar)\end{pmatrix}\begin{pmatrix}\cos az\\ \sin az\end{pmatrix}$$
$$\begin{pmatrix}1\\ \ln r\end{pmatrix}\begin{pmatrix}z^2\\ z^3\end{pmatrix}, \begin{pmatrix}J_0(ar)\\ Y_0(ar)\end{pmatrix}\begin{pmatrix}z\exp(az)\\ z\exp(-az)\end{pmatrix}$$
$$\begin{pmatrix}J_0(ar)\\ Y_0(ar)\end{pmatrix}\begin{pmatrix}z\cosh az\\ z\sinh az\end{pmatrix}, \begin{pmatrix}I_0(ar)\\ K_0(ar)\end{pmatrix}\begin{pmatrix}z\cos az\\ z\sin az\end{pmatrix} \quad (13)$$

Transient Thermal Stress in an Infinite Solid Circular Cylinder with Radius *a*

Consider transient temperature in an infinite solid circular cylinder with radius a. The governing equation for the transient temperature without internal heat generation is:

$$\frac{1}{\kappa}\frac{\partial T}{\partial t} = \frac{\partial^2 T}{\partial r^2} + \frac{1}{r}\frac{\partial T}{\partial r} + \frac{\partial^2 T}{\partial z^2} \quad (14)$$

The boundary condition is:

$$-\lambda\frac{\partial T}{\partial r} = h_b[T - T_b(z)] \quad \text{on r} = \text{a} \quad (15)$$

where $T_b(z)$ denotes the surrounding temperature, λ is the heat conductivity, h_b denotes the heat transfer coefficient on the circular surface, and $T_b(z) = T_b(-z)$ is assumed here.

The initial condition is:

$$T = T_i \quad \text{at} \quad \text{t} = 0 \quad (16)$$

We introduce the temperature change τ ($=T - T_i$) from the constant initial temperature T_i. The governing equation, boundary conditions, and an initial condition reduce to:

$$\frac{1}{\kappa}\frac{\partial\tau}{\partial t} = \frac{\partial^2\tau}{\partial r^2} + \frac{1}{r}\frac{\partial\tau}{\partial r} + \frac{\partial^2\tau}{\partial z^2} \quad (14')$$

$$-\lambda\frac{\partial\tau}{\partial r} = h_b\{\tau - [T_b(z) - T_i]\} \quad \text{on r} = \text{a} \quad (15')$$

$$\tau = 0 \quad \text{at} \quad \text{t} = 0 \quad (16')$$

Here, we introduce the method of separation of variables to obtain the solution of (14'). When the temperature change is expressed as:

$$\tau(r,z,t) = f(r)g(z)h(t) \quad (17)$$

Three equations can be obtained by substitution of (17) into (14'):

$$\frac{dh(t)}{dt} + \kappa(s^2+p^2)h(t) = 0$$
$$\frac{d^2f(r)}{dr^2} + \frac{1}{r}\frac{df(r)}{dr} + p^2 f(r) = 0 \quad (18)$$
$$\frac{d^2g(z)}{dz^2} + s^2 g(z) = 0$$

The solutions of (18) are:

$$h(t) = 1, \quad f(r) = J_0(pr), \quad Y_0(pr)$$
$$g(z) = \cosh pz, \quad \sinh pz \quad \text{for s}^2 = -\text{p}^2$$
$$h(t) = 1, \quad f(r) = I_0(sr), \quad K_0(sr)$$
$$g(z) = \cos sz, \quad \sin sz \quad \text{for p}^2 = -\text{s}^2$$
$$h(t) = \exp[-\kappa(s^2+p^2)t] \quad \text{for s}^2 + \text{p}^2 \neq 0$$
$$f(r) = 1, \ \ln r \quad \text{for p} = 0$$
$$f(r) = J_0(pr), \quad Y_0(pr) \quad \text{for p} \neq 0$$
$$g(z) = 1, \ z \quad \text{for s} = 0$$
$$g(z) = \cos sz, \quad \sin sz \quad \text{for } s \neq 0 \quad (19)$$

The general solution of (14') for this problem is expressed by:

$$\tau(r,z)=\int_0^\infty \cos sz\{A(s)I_0(sr)+\sum_{m=1}^{\infty}A_m(s)J_0(p_m r)\times\exp[-\kappa(s^2+p_m^2)t]\}ds \tag{20}$$

First, we express the surrounding temperature $T_b(z)$-T_i by the Fourier cosine integral:

$$T_b(z)-T_i=\int_0^\infty T_{bs}(s)\cos szds \tag{21}$$

where

$$T_{bs}(s)=\frac{2}{\pi}\int_0^\infty [T_b(z)-T_i]\cos szdz \tag{22}$$

Taking into consideration the boundary conditions given by (15'), we can obtain that p_m are eigen-values of the equation:

$$(h_b a/\lambda)J_0(p_m a)-p_m aJ_1(p_m a)=0 \tag{23}$$

and

$$A(s)=\frac{(h_b a/\lambda)T_{bs}(s)}{(h_b a/\lambda)I_0(sa)+saI_1(sa)} \tag{24}$$

The initial condition (16') gives:

$$\sum_{m=1}^{\infty}A_m(s)J_0(p_m r)=-A(s)I_0(sr) \tag{25}$$

Multiplying $rJ_0(p_n r)$ on both sides of (25) and integrating from 0 to a, we get:

$$\sum_{m=1}^{\infty}A_m(s)\int_0^a rJ_0(p_m r)J_0(p_n r)dr=-A(s)\int_0^a rJ_0(p_n r)I_0(sr)dr \tag{26}$$

Taking into consideration the integral results:

$$\int_0^r J_n(kr)J_n(mr)rdr=\begin{cases}\frac{r}{k^2-m^2}[kJ_n(mr)J_{n+1}(kr)-mJ_n(kr)J_{n+1}(mr)] & k\neq m\\ \frac{1}{2}r^2[J_n^2(kr)-J_{n-1}(kr)J_{n+1}(kr)] & k=m\end{cases}$$

$$\int_0^r I_n(kr)J_n(mr)rdr=\frac{r}{k^2+m^2}[kJ_n(mr)I_{n+1}(kr)+mI_n(kr)J_{n+1}(mr)]$$

$A_n(s)$ can be determined as:

$$A_n(s)=-\frac{2p_n^2a^2(h_b a/\lambda)T_{bs}(s)}{(p_n^2a^2+s^2a^2)[p_n^2a^2+(h_b a/\lambda)^2]J_0(p_n a)} \tag{27}$$

Then, the temperature change τ is determined by:

$$\tau(r,z)=\int_0^\infty \cos sz\Big\{\frac{(h_b a/\lambda)T_{bs}(s)}{(h_b a/\lambda)I_0(sa)+saI_1(sa)}I_0(sr)-2\sum_{m=1}^{\infty}\frac{p_m^2a^2(h_b a/\lambda)T_{bs}(s)}{(p_m^2a^2+s^2a^2)[p_m^2a^2+(h_b a/\lambda)^2]J_0(p_m a)}\times J_0(p_m r)\exp[-\kappa(s^2+p_m^2)t]\Big\}ds \tag{28}$$

Next, we consider the thermal stresses under the boundary conditions:

$$\sigma_{rr}=\sigma_{rz}=0 \quad \text{at} \quad r=a \tag{29}$$

Goodier's thermoelastic function Φ and Michell's functions M for this problem are:

$$\Phi(r,z,t)=\frac{1+v}{1-v}\alpha\int_0^\infty \cos sz\Big\{\frac{A(s)}{2s}rI_1(sr)-\sum_{m=1}^{\infty}\frac{A_m(s)}{s^2+p_m^2}J_0(p_m r)\times\exp[-\kappa(s^2+p_m^2)t]\Big\}ds \tag{30}$$

$$M(r,z)=\int_0^\infty [C_0(s)I_0(sr)+D_0(s)rI_1(sr)]\sin szds \tag{31}$$

Substitution of (30) and (31) into (11) and (12) gives the displacements and thermal stresses as follows:

$$u_r=\int_0^\infty \cos sz\Big(-s^2C_0(s)I_1(sr)-s^2D_0(s)rI_0(sr)+\frac{1+\nu}{1-\nu}\alpha\Big\{\frac{A(s)}{2}rI_0(sr)+\sum_{m=1}^{\infty}\frac{p_mA_m(s)}{s^2+p_m^2}J_1(p_mr)\times\exp[-\kappa(s^2+p_m^2)t]\Big\}\Big)ds \tag{32}$$

$$u_z=\int_0^\infty \sin sz\Big(s^2C_0(s)I_0(sr)+sD_0(s)[4(1-\nu)I_0(sr)+srI_1(sr)]-\frac{1+\nu}{1-\nu}\alpha\Big\{\frac{A(s)}{2}rI_1(sr)-\sum_{m=1}^{\infty}\frac{sA_m(s)}{s^2+p_m^2}J_0(p_mr)\exp[-\kappa(s^2+p_m^2)t]\Big\}\Big)ds \tag{33}$$

$$\frac{\sigma_{rr}}{2G}=\int_0^\infty \cos sz\Big(-s^3C_0(s)\Big[I_0(sr)-\frac{1}{sr}I_1(sr)\Big]-s^2D_0(s)[(1-2\nu)I_0(sr)+srI_1(sr)]-\frac{1+\nu}{1-\nu}\alpha\Big\{\frac{A(s)}{2}[I_0(sr)-srI_1(sr)]+\sum_{m=1}^{\infty}A_m(s)\frac{1}{s^2+p_m^2}\Big[s^2J_0(p_mr)+\frac{p_m^2}{p_mr}J_1(p_mr)\Big]\times\exp[-\kappa(s^2+p_m^2)t]\Big\}\Big)ds \tag{34}$$

$$\frac{\sigma_{\theta\theta}}{2G}=-\int_0^\infty \cos sz\Big(s^3C_0(s)\frac{1}{sr}I_1(sr)+s^2D_0(s)(1-2\nu)I_0(sr)+\frac{1+\nu}{1-\nu}\alpha\Big\{\frac{A(s)}{2}I_0(sr)+\sum_{m=1}^{\infty}A_m(s)\Big[J_0(p_mr)-\frac{p_m^2}{s^2+p_m^2}\frac{1}{p_mr}J_1(p_mr)\Big]\times\exp[-\kappa(s^2+p_m^2)t]\Big\}\Big)ds \tag{35}$$

$$\frac{\sigma_{zz}}{2G}=\int_0^\infty \cos sz\Big(s^3C_0(s)I_0(sr)+s^2D_0(s)[2(2-\nu)I_0(sr)+srI_1(sr)]-\frac{1+\nu}{1-\nu}\alpha\Big\{\frac{A(s)}{2}[2I_0(sr)+srI_1(sr)]+\sum_{m=1}^{\infty}\frac{p_m^2A_m(s)}{s^2+p_m^2}J_0(p_mr)\times\exp[-\kappa(s^2+p_m^2)t]\Big\}\Big)ds \tag{36}$$

$$\frac{\sigma_{rz}}{2G}=\int_0^\infty \sin sz\Big(s^3C_0(s)I_1(sr)+s^2D_0(s)[2(1-\nu)I_1(sr)+srI_0(sr)]-\frac{1+\nu}{1-\nu}\alpha\Big\{\frac{A(s)}{2}srI_0(sr)+\sum_{m=1}^{\infty}\frac{sp_mA_m(s)}{s^2+p_m^2}J_1(p_mr)\times\exp[-\kappa(s^2+p_m^2)t]\Big\}\Big)ds \tag{37}$$

The unknown coefficients C_0 and D_0 can be determined by the boundary conditions given by (29).

$$s^3C_0(s)=-\frac{1+\nu}{1-\nu}\alpha\frac{1}{E(s)}\frac{A(s)}{2}2(1-\nu)\times[I_1(sa)I_0(sa)-saI_1^2(sa)+saI_0^2(sa)]-\frac{1+\nu}{1-\nu}\alpha\frac{1}{E(s)}\Big\{\Big[2(1-\nu)(s^2a^2+\frac{h_ba}{\lambda})+s^2a^2\frac{h_ba}{\lambda}\Big]I_1(sa)+sa\Big[s^2a^2+2(1-\nu)\frac{h_ba}{\lambda}\Big]I_0(sa)\Big\}\times\sum_{m=1}^{\infty}\frac{A_m(s)J_0(p_ma)}{s^2+p_m^2}\exp[-\kappa(s^2+p_m^2)t]$$

$$s^2D_0(s)=\frac{1+\nu}{1-\nu}\alpha\frac{1}{E(s)}\frac{A(s)}{2}sa[I_0^2(sa)-I_1^2(sa)]+\frac{1+\nu}{1-\nu}\alpha\frac{sa}{E(s)}\Big[\frac{h_ba}{\lambda}I_0(sa)+saI_1(sa)\Big]\times\sum_{m=1}^{\infty}\frac{A_m(s)J_0(p_ma)}{s^2+p_m^2}\exp[-\kappa(s^2+p_m^2)t] \tag{38}$$

where

$$E(s) = \{s^2a^2I_0^2(sa) - [2(1-\nu) + s^2a^2]I_1^2(sa)]\}/sa$$

Transient Thermal Stress in a Finite Solid Circular Cylinder with Radius *a* and Length 2*l*

Consider transient temperature in a finite solid circular cylinder with radius a and length $2l$ [2]. The governing equation for transient temperature without internal heat generation is given by (14). The boundary conditions are:

$$\begin{aligned} -\lambda\frac{\partial T}{\partial r} &= h_b[T - T_b(z)] \quad \text{on r} = \text{a} \\ \lambda\frac{\partial T}{\partial z} &= 0 \qquad\qquad\quad \text{on z} = \pm\text{l} \end{aligned} \tag{39}$$

where $T_b(z)$ denotes the surrounding temperature on the circular surface, λ is the heat conductivity, and h_b denotes the heat transfer coefficient on the circular surface and $T_b(z) = T_b(-z)$ is assumed here.

The initial condition is:

$$T = T_i \quad \text{at} \quad \text{t} = 0 \tag{40}$$

We introduce the temperature change τ ($=T-T_i$) from the constant initial temperature T_i. The governing equation, boundary conditions, and initial condition reduce to:

$$\frac{1}{\kappa}\frac{\partial\tau}{\partial t} = \frac{\partial^2\tau}{\partial r^2} + \frac{1}{r}\frac{\partial\tau}{\partial r} + \frac{\partial^2\tau}{\partial z^2} \tag{14'}$$

$$\begin{aligned} -\lambda\frac{\partial\tau}{\partial r} &= h_b\{\tau - [T_b(z) - T_i]\} \quad \text{on r} = \text{a} \\ \lambda\frac{\partial\tau}{\partial z} &= 0 \qquad\qquad\quad \text{on z} = \pm\text{l} \end{aligned} \tag{39'}$$

$$\tau = 0 \quad \text{at} \quad \text{t} = 0 \tag{40'}$$

Using the method of separation of variables, the general solution of (14') for this problem is expressed by:

$$\begin{aligned} \tau(r,z) = &\sum_{n=0}^{\infty} \cos s_n z\{A_n I_0(s_n r) \\ &+ \sum_{m=1}^{\infty} A_{nm} J_0(p_m r)\exp[-\kappa(s_n^2 + p_m^2)t]\} \end{aligned} \tag{41}$$

Taking into consideration the boundary condition given by the second equation (39'), s_n are the eigen-values of the equation:

$$\sin s_n l = 0 \;\therefore\; s_n = n\pi/l \tag{42}$$

First, we express the surrounding temperature $T_b(z)-T_i$ by the Fourier series:

$$T_b(z) - T_i = T_{b0} + \sum_{n=1}^{\infty} T_{bn}\cos s_n z \tag{43}$$

where

$$\begin{aligned} T_{b0} &= \frac{1}{l}\int_0^l [T_b(r) - T_i]dz \\ T_{bn} &= \frac{2}{l}\int_0^l [T_b(r) - T_i]\cos s_n z dz \quad n = 1, 2, 3, .. \end{aligned} \tag{44}$$

Taking into consideration the first boundary condition given by (39'), we can obtain that p_m are eigen-values of the equation:

$$(h_b a/\lambda)J_0(p_m a) - p_m a J_1(p_m a) = 0 \tag{45}$$

and

$$A_0 = T_{b0},\; A_n = \frac{(h_b a/\lambda)T_{bn}}{(h_b a/\lambda)I_0(s_n a) + s_n a I_1(s_n a)} \tag{46}$$

Taking into consideration the initial condition (40'), the unknown constants can be determined as:

$$A_{nm} = -\frac{2p_m^2 a^2(h_b a/\lambda)T_{bn}}{(p_m^2a^2 + s_n^2a^2)[p_m^2a^2 + (h_b a/\lambda)^2]J_0(p_m a)} \tag{47}$$

where $s_0 = 0$. Then the temperature change τ is expressed by:

$$\begin{aligned}\tau(r,z) = &\sum_{n=0}^{\infty} \cos s_n z \Big\{ A_n I_0(s_n r) \\ &+ \sum_{m=1}^{\infty} A_{nm} J_0(p_m r) \exp[-\kappa(s_n^2 + p_m^2)t] \Big\} \\ = &\frac{h_b a}{\lambda} \sum_{n=0}^{\infty} T_{bn} \cos s_n z \Big\{ \frac{I_0(s_n r)}{(h_b a/\lambda) I_0(s_n a) + s_n a I_1(s_n a)} \\ &- \sum_{m=1}^{\infty} \frac{2 p_m^2 a^2 J_0(p_m r)}{(p_m^2 a^2 + s_n^2 a^2)[p_m^2 a^2 + (h_b a/\lambda)^2] J_0(p_m a)} \\ &\times \exp[-\kappa(s_n^2 + p_m^2)t] \Big\}\end{aligned} \tag{48}$$

Next, we consider thermal stresses under the following boundary conditions:

$$\sigma_{rr} = \sigma_{rz} = 0 \qquad \text{on} \quad \mathrm{r} = \mathrm{a} \tag{49}$$

$$\sigma_{zz} = \sigma_{zr} = 0 \qquad \text{on} \quad \mathrm{z} = \pm \mathrm{h} \tag{50}$$

Goodier's thermoelastic function Φ and Michell's function M for this problem are:

$$\begin{aligned}\Phi(r,z,t) = &\frac{1+\nu}{1-\nu} \alpha \sum_{n=0}^{\infty} \cos s_n z \Big\{ \frac{A_n}{2 s_n} r I_1(s_n r) \\ &- \sum_{m=1}^{\infty} \frac{A_{nm}}{s_n^2 + p_m^2} J_0(p_m r) \exp[-\kappa(s_n^2 + p_m^2)t] \Big\}\end{aligned} \tag{51}$$

$$\begin{aligned}M(r,z) = &E_0 r^2 z + E_0' z^3 \\ &+ \sum_{n=1}^{\infty} \sin(s_n z)[C_n I_0(s_n r) + D_n r I_1(s_n r)] \\ &+ \sum_{i=1}^{\infty} J_0(q_i r)[E_i \sinh q_i z + E_i' z \cosh q_i z] \\ &+ \sum_{j=1}^{\infty} [F_j I_0(v_j r) + F_i' r I_1(v_j r)] \sin v_j z\end{aligned} \tag{52}$$

where q_i and v_j are the eigen-values for $J_0(q_i a) = 0$ and $\sin v_j l = 0$, respectively.

Substitution of (51) and (52) into (11) and (12) gives the displacements and thermal stresses:

$$\begin{aligned}u_r = &-2E_0 r - \sum_{n=1}^{\infty} \cos s_n z [s_n^2 C_n I_1(s_n r) \\ &+ s_n^2 D_n r I_0(s_n r)] \\ &+ \frac{1+\nu}{1-\nu} \alpha \sum_{n=0}^{\infty} \cos s_n z \Big\{ \frac{A_n}{2} r I_0(s_n r) \\ &+ \sum_{m=1}^{\infty} \frac{p_m A_{nm}}{s_n^2 + p_m^2} J_1(p_m r) \exp[-\kappa(s^2 + p_m^2)t] \Big\} \\ &+ \sum_{i=1}^{\infty} q_i J_1(q_i r)[q_i E_i \cosh q_i z \\ &+ E_i'(\cosh q_i z + q_i z \sinh q_i z)] \\ &- \sum_{j=1}^{\infty} [v_j^2 F_j I_1(v_j r) + v_j^2 F_j' r I_0(v_j r)] \cos v_j z\end{aligned} \tag{53}$$

$$\begin{aligned}u_z = &8(1-\nu) E_0 z + 6(1-2\nu) E_0' z \\ &+ \sum_{n=1}^{\infty} \sin s_n z \{ s_n^2 C_n I_0(s_n r) \\ &+ s_n D_n [4(1-\nu) I_0(s_n r) + s_n r I_1(s_n r)] \} \\ &- \frac{1+\nu}{1-\nu} \alpha \sum_{n=1}^{\infty} \sin s_n z \Big\{ \frac{A_n}{2} r I_1(s_n r) \\ &- \sum_{m=1}^{\infty} \frac{s_n A_{nm}}{s_n^2 + p_m^2} J_0(p_m r) \exp[-\kappa(s_n^2 + p_m^2)t] \Big\} \\ &+ \sum_{i=1}^{\infty} J_0(q_i r) \Big\{ -E_i q_i^2 \sinh q_i z \\ &+ E_i' q_i [2(1-2\nu) \sinh q_i z - q_i z \cosh q_i z] \\ &+ \sum_{j=1}^{\infty} \{ v_j^2 F_j I_0(v_j r) + v_j F_j' [4(1-\nu) I_0(v_j r) \\ &+ v_j r I_1(v_j r)] \Big\} \sin v_j z\end{aligned} \tag{54}$$

$$\begin{aligned}\frac{\sigma_{rr}}{2G} = &-2(1-2\nu) E_0 + 6\nu E_0' \\ &- \sum_{n=1}^{\infty} \cos s_n z \{ s_n^3 C_n [I_0(s_n r) - \frac{1}{s_n r} I_1(s_n r)] \\ &+ s_n^2 D_n [(1-2\nu) I_0(s_n r) + s_n r I_1(s_n r)] \} \\ &- \frac{1+\nu}{1-\nu} \alpha \sum_{n=0}^{\infty} \cos s_n z \{ \frac{A_n}{2} [I_0(s_n r) - s_n r I_1(s_n r)] \\ &+ \sum_{m=1}^{\infty} \frac{A_{nm}}{s_n^2 + p_m^2} [s_n^2 J_0(p_m r)\end{aligned}$$

$$+\frac{p_m^2}{p_m r}J_1(p_m r)]\exp[-\kappa(s_n^2+p_m^2)t]\}$$
$$+\sum_{i=1}^{\infty}\Big(E_i q_i^3[J_0(q_i r)-\frac{1}{q_i r}J_1(q_i r)]\cosh q_i z$$
$$+E_i^{'}\Big\{2\nu q_i^2 J_0(q_i r)\cosh q_i z+q_i^2[J_0(q_i r)$$
$$-\frac{1}{q_i r}J_1(q_i r)](\cosh q_i z+q_i z\sinh q_i z)\Big\}\Big)$$
$$-\sum_{m=1}^{\infty}\Big\{v_j^3 F_j\Big[I_0(v_j r)-\frac{1}{v_j r}I_1(v_j r)\Big]$$
$$+v_j^2 F_j^{'}\Big[(1-2\nu)I_0(v_j r)+v_j r I_1(v_j r)\Big]\Big\}\cos v_j z \tag{55}$$

$$\frac{\sigma_{\theta\theta}}{2G}=-2(1-2\nu)E_0+6\nu E_0^{'}$$
$$-\sum_{n=1}^{\infty}\cos s_n z\Big[s_n^3 C_n\frac{1}{s_n r}I_1(s_n r)$$
$$+s_n^2 D_n(1-2\nu)I_0(s_n r)\Big]$$
$$+\frac{1+\nu}{1-\nu}\alpha\sum_{n=0}^{\infty}\cos s_n z\Big\{\frac{A_n}{2}I_0(s_n r)$$
$$+\sum_{m=1}^{\infty}A_{nm}\Big[J_0(p_m r)-\frac{p_m^2}{s_n^2+p_m^2}\frac{1}{p_m r}J_1(p_m r)\Big]$$
$$\times\exp[-\kappa(s_n^2+p_m^2)t]\Big\}$$
$$+\sum_{i=1}^{\infty}\Big\{q_i^3 E_i\frac{1}{q_i r}J_1(q_i r)\cosh q_i z$$
$$+q_i^2 E_i^{'}\Big[2\nu J_0(q_i r)\cosh q_i z$$
$$+\frac{1}{q_i r}J_1(q_i r)(\cosh q_i z+q_i z\sinh q_i z)\Big]\Big\}$$
$$-\sum_{j=1}^{\infty}\Big[v_j^3 F_j\frac{1}{v_j r}I_1(v_j r)$$
$$+(1-2\nu)v_j^2 F_j^{'}I_0(v_j r)\Big]\cos v_j z \tag{56}$$

$$\frac{\sigma_{zz}}{2G}=4(2-\nu)E_0+6(1-\nu)E_0^{'}$$
$$+\sum_{n=1}^{\infty}\cos s_n z\{s_n^3 C_n I_0(s_n r)$$
$$+s_n^2 D_n[2(2-\nu)I_0(s_n r)+s_n r I_1(s_n r)]\}$$
$$+\frac{1+\nu}{1-\nu}\alpha\sum_{n=0}^{\infty}\cos s_n z\Big\{-\frac{A_n}{2}[2I_0(s_n r)$$
$$+s_n r I_1(s_n r)]$$
$$-\sum_{m=1}^{\infty}\frac{p_m^2 A_{nm}}{s_n^2+p_m^2}J_0(p_m r)\exp[-\kappa(s_n^2+p_m^2)t]\Big\}$$
$$-\sum_{i=1}^{\infty}J_0(q_i r)\{q_i^3 E_i\cosh q_i z$$
$$-q_i^2 E_i^{'}[-(1-2\nu)\cosh q_i z+q_i z\sinh q_i z]\}$$
$$+\sum_{j=1}^{\infty}\{v_j^3 F_j I_0(v_j r)$$
$$+v_j^2 F_j^{'}[2(2-\nu)I_0(v_j r)+v_j r I_1(v_j r)]\}\cos v_j z \tag{57}$$

$$\frac{\sigma_{rz}}{2G}=\sum_{n=1}^{\infty}\sin s_n z\{s_n^3 C_n I_1(s_n r)$$
$$+s_n^2 D_n[2(1-\nu)I_1(s_n r)+s_n r I_0(s_n r)]\}$$
$$-\frac{1+\nu}{1-\nu}\alpha\sum_{n=1}^{\infty}\sin s_n z\Big\{\frac{A_n}{2}s_n r I_0(s_n r)$$
$$+\sum_{m=1}^{\infty}\frac{s_n p_m A_{nm}}{s_n^2+p_m^2}J_1(p_m r)\exp[-\kappa(s_n^2+p_m^2)t]\Big\}$$
$$+\sum_{i=1}^{\infty}q_i J_1(q_i r)[q_i^2 E_i\sinh q_i z$$
$$+q_i E_i^{'}(2\nu\sinh q_i z+q_i z\cosh q_i z)]$$
$$+\sum_{j=1}^{\infty}\{v_j^3 F_j I_1(v_j r)$$
$$+v_j^2 F_j^{'}[2(1-\nu)I_1(v_j r)+v_j r I_0(v_j r)]\}\sin v_j z \tag{58}$$

The boundary conditions given by (49) give:

$$s_n^3 C_n\Big[I_0(s_n a)-\frac{1}{s_n a}I_1(s_n a)\Big]$$
$$+s_n^2 D_n[(1-2\nu)I_0(s_n a)+s_n a I_1(s_n a)]$$
$$=-\frac{1+\nu}{1-\nu}\alpha\Big\{\frac{A_n}{2}[I_0(s_n a)-s_n a I_1(s_n a)]$$
$$+\sum_{m=1}^{\infty}\frac{A_{nm}}{s_n^2+p_m^2}\Big[s_n^2 J_0(p_m a)$$
$$+\frac{p_m^2}{p_m a}J_1(p_m a)\Big]\exp[-\kappa(s_n^2+p_m^2)t]\Big\} \tag{59}$$

$$
\begin{aligned}
&s_n^3 C_n I_1(s_n a)+s_n^2 D_n[2(1-\nu)I_1(s_n a)+s_n a I_0(s_n a)]\\
&\quad=\frac{1+\nu}{1-\nu}\alpha\Big\{\frac{A_n}{2}s_n a I_0(s_n a)\\
&\qquad+\sum_{m=1}^{\infty}\frac{s_n p_m A_{nm}}{s_n^2+p_m^2}J_1(p_m a)\\
&\qquad\times\exp[-\kappa(s_n^2+p_m^2)t]\Big\}
\end{aligned}
\tag{60}
$$

$$
\begin{aligned}
&-2(1-2\nu)E_0+6\nu E_0^{'}\\
&-\frac{1+\nu}{1-\nu}\alpha\Big[\frac{A_0}{2}+\sum_{m=1}^{\infty}\frac{A_{0m}}{p_m a}J_1(p_m a)\exp(-\kappa p_m^2 t)\Big]\\
&-\sum_{i=1}^{\infty}\frac{J_1(q_i a)}{q_i a}[E_i q_i^3\cosh q_i z\\
&+E_i^{'}q_i^2(\cosh q_i z+q_i z\sinh q_i z)]\\
&-\sum_{j=1}^{\infty}\Big\{v_j^3 F_j\Big[I_0(v_j a)-\frac{1}{v_j a}I_1(v_j a)\Big]\\
&+v_j^2 F_j^{'}[(1-2\nu))I_0(v_j a)\\
&+v_j a I_1(v_j a)]\Big\}\cos v_j z=0
\end{aligned}
\tag{61}
$$

$$
\begin{aligned}
&\sum_{i=1}^{\infty}q_i J_1(q_i a)[q_i^2 E_i\sinh q_i z\\
&+qE_i^{'}(2\nu\sinh q_i z+q_i z\cosh q_i z)]\\
&+\sum_{j=1}^{\infty}\{v_j^3 F_j I_1(v_j a)\\
&+v_j^2 F_j^{'}[2(1-\nu)I_1(v_j a)\\
&+v_j a I_0(v_j a)]\}\sin v_j z=0
\end{aligned}
\tag{62}
$$

The boundary conditions given by (50) give:

$$
\begin{aligned}
&4(2-\nu)E_0+6(1-\nu)E_0^{'}\\
&+\sum_{n=1}^{\infty}\cos s_n l\{s_n^3 C_n I_0(s_n r)\\
&+s_n^2 D_n[2(2-\nu)I_0(s_n r)+s_n r I_1(s_n r)]\}\\
&+\frac{1+\nu}{1-\nu}\alpha\sum_{n=0}^{\infty}\cos s_n l\Big\{-\frac{A_n}{2}[2I_0(s_n r)+s_n r I_1(s_n r)]\\
&-\sum_{m=1}^{\infty}\frac{p_m^2 A_{nm}}{s_n^2+p_m^2}J_0(p_m r)\exp[-\kappa(s_n^2+p_m^2)t]\Big\}\\
&-\sum_{i=1}^{\infty}J_0(q_i r)\{q_i^3 E_i\cosh q_i l-q_i^2 E_i^{'}[-(1\\
&-2\nu)\cosh q_i l+q_i z\sinh q_i l]\}\\
&+\sum_{j=1}^{\infty}\{v_j^3 F_j I_0(v_j r)+v_j^2 F_j^{'}[2(2\\
&-\nu)I_0(v_j r)+v_j r I_1(v_j r)]\}\cos v_j l\\
&=0
\end{aligned}
\tag{63}
$$

$$
q_i^2 E_i\sinh q_i l+q_i E_i^{'}(2\nu\sinh q_i l+q_i l\cosh q_i l)=0
\tag{64}
$$

The unknown coefficients C_n and D_n can be determined by (59) and (60). In order to determine the unknown coefficients E_0, $E_o{}'$, E_i, E_i', F_j, and F_j' in (61)–(64), we expand both the Bessel function and the modified Bessel functions to a series of Bessel functions $J_0(q_i r)$ and $J_1(q_i r)$ as follows:

$$
\begin{aligned}
I_0(v_j r)&=G_{j0}^{00}+\sum_{i=1}^{\infty}G_{ji}^{00}J_0(q_i r)\\
rI_1(v_j r)&=G_{j0}^{10}+\sum_{i=1}^{\infty}G_{ji}^{10}J_0(q_i r)\\
I_0(s_n r)&=H_{n0}^{00}+\sum_{i=1}^{\infty}H_{ni}^{00}J_0(q_i r)\\
rI_1(s_n r)&=H_{n0}^{10}+\sum_{i=1}^{\infty}H_{ni}^{10}J_0(q_i r)
\end{aligned}
$$

$$
\begin{aligned}
rI_0(s_n r)&=\sum_{i=1}^{\infty}F_{ni}^{01}J_1(q_i r)\\
I_1(s_n r)&=\sum_{i=1}^{\infty}F_{ni}^{11}J_1(q_i r)\\
J_0(p_m r)&=E_{m0}^{00}+\sum_{i=1}^{\infty}E_{mi}^{00}J_0(q_i r)\\
J_1(p_m r)&=\sum_{i=1}^{\infty}E_{mi}^{11}J_1(q_i r)
\end{aligned}
\tag{65}
$$

as well as expand the hyperbolic functions as a series of trigonometric functions as follows:

$$\begin{aligned}\cosh(q_i z) &= Q_{i0}^{cc} + \sum_{j=1}^{\infty} Q_{ij}^{cc} \cos(v_j z)\\ z\,\sinh(q_i z) &= Q_{i0}^{sc} + \sum_{j=1}^{\infty} Q_{ij}^{sc} \cos(v_j z)\\ \sinh(q_i z) &= \sum_{j=1}^{\infty} Q_{ij}^{ss} \sin(v_j z)\\ z\,\cosh(q_i z) &= \sum_{j=1}^{\infty} Q_{ij}^{cs} \sin(v_j z)\end{aligned} \tag{66}$$

Substitution of (65) and (66) into (61), (62) and (63) gives

$$\begin{aligned}&-2(1-2\nu)E_0 + 6\nu E_0'\\ &= \frac{1+\nu}{1-\nu}\alpha\left[\frac{A_0}{2} + \sum_{m=1}^{\infty}\frac{A_{0m}}{p_m a} J_1(p_m a)\exp(-\kappa p_m^2 t)\right]\\ &\quad + \sum_{i=1}^{\infty}\frac{J_1(q_i a)}{q_i a}[E_i q_i^3 Q_{i0}^{cc} + E_i' q_i^2 (Q_{i0}^{cc} + q_i Q_{i0}^{sc})]\end{aligned} \tag{67}$$

$$\begin{aligned}&\sum_{i=1}^{\infty}\frac{J_1(q_i a)}{q_i a}[E_i q_i^3 Q_{ij}^{cc} + E_i' q_i^2 (Q_{ij}^{cc} + q_i Q_{ij}^{sc})]\\ &+ v_j^3 F_j\left[I_0(v_j a) - \frac{1}{v_j a} I_1(v_j a)\right]\\ &+ v_j^2 F_j'[(1-2\nu) I_0(v_j a) + v_j a I_1(v_j a)] = 0\end{aligned} \tag{68}$$

$$\begin{aligned}&\sum_{i=1}^{\infty} q_i J_1(q_i a)[q_i^2 E_i Q_{ij}^{ss} + q E_i'(2\nu Q_{ij}^{ss} + q_i Q_{ij}^{cs})]\\ &+ v_j^3 F_j I_1(v_j a) + v_j^2 F_j'[2(1-\nu) I_1(v_j a)\\ &+ v_j a I_0(v_j a)] = 0\end{aligned} \tag{69}$$

$$\begin{aligned}&4(2-\nu)E_0 + 6(1-\nu)E_0'\\ &+ \sum_{j=1}^{\infty}(-1)^j\left\{v_j^3 F_j G_{j0}^{00}\right.\\ &\left.+ v_j^2 F_j'[2(2-\nu)G_{j0}^{00} + v_j G_{j0}^{10}]\right\}\\ &= -\sum_{n=1}^{\infty}(-1)^n\left\{s_n^3 C_n H_{n0}^{00}\right.\\ &\quad\left.+ s_n^2 D_n[2(2-\nu)H_{n0}^{00} + s_n H_{n0}^{10}]\right\}\\ &\quad - \frac{1+\nu}{1-\nu}\alpha\sum_{n=0}^{\infty}(-1)^n\left\{-\frac{A_n}{2}[2H_{n0}^{00} + s_n H_{n0}^{10}]\right.\\ &\quad\left.- \sum_{m=1}^{\infty}\frac{p_m^2 A_{nm}}{s_n^2 + p_m^2} E_{m0}^{00}\exp[-\kappa(s_n^2 + p_m^2)t]\right\}\end{aligned} \tag{70}$$

$$\begin{aligned}&-q_i^3 E_i \cosh q_i l + q_i^2 E_i'[-(1-2\nu)\cosh q_i l\\ &+ q_i l \sinh q_i l] + \sum_{j=1}^{\infty}(-1)^j\{v_j^3 F_j G_{ji}^{00}\\ &+ v_j^2 F_j'[2(2-\nu)G_{ji}^{00} + v_j G_{ji}^{10}]\}\\ &= -\sum_{n=0}^{\infty}(-1)^n\left\{s_n^3 C_n H_{ni}^{00}\right.\\ &\quad + s_n^2 D_n[2(2-\nu)H_{ni}^{00} + s_n H_{ni}^{10}]\left.\right\}\\ &\quad - \frac{1+\nu}{1-\nu}\alpha\sum_{n=0}^{\infty}(-1)^n\left\{-\frac{A_n}{2}[2H_{ni}^{00} + s_n H_{ni}^{10}]\right.\\ &\quad\left.- \sum_{m=1}^{\infty}\frac{p_m^2 A_{nm}}{s_n^2 + p_m^2} E_{mi}^{00}\exp[-\kappa(s_n^2 + p_m^2)t]\right\}\end{aligned} \tag{71}$$

Solving the simultaneous linear equations (64), (68), (69), and (71), we can obtain the unknown coefficients E_i, E_i', F_j, and F_j'. Furthermore, we can obtain the unknown coefficients E_0 and E_o' solving the simultaneous linear equations (67) and (70). We finally obtain the displacements and stresses by substituting these coefficients into (53)–(58).

References

1. Noda N, Hetnarski RB, Tanigawa Y (2003) Thermal stresses, 2nd edn. Taylor & Francis, New York/London
2. Noda N, Takeuti Y (1977) Unsteady thermal stresses in a finite circular cylinder under non-symmetric heating in axial direction. Theor Appl Mech Japan 25:637–644

Axisymmetric Thermal Stresses in Spheres

Yoshinobu Tanigawa[1] and Naotake Noda[2]
[1]Osaka Prefecture University, Osaka, Japan
[2]Shizuoka University, Hamamatsu, Japan

Overview

Mechanical and structural bodies are frequently subjected to both mechanical loads and temperature changes. The sphere is one of the important

mechanical and structure elements. The thermal stress analysis of three-dimensional bodies typically relies on displacement potentials, such as Goodier's displacement function and Boussinesq's function.

Axisymmetric thermal stresses in spheres subjected to axisymmetric temperature changes are considered in the spherical coordinate system (r, θ, ϕ). The steady thermal stress problems in a hollow sphere and an infinite body with a spherical cavity and the transient thermal stress problem in a solid sphere are discussed. Goodier's displacement function and Boussinesq's function are introduced in analytical treatment.

Basic Equations in the Spherical Coordinate System (r, θ, ϕ)

The governing equations for three-dimensional thermoelastic problems in the spherical coordinate system (r, θ, ϕ) are summarized as follows [1]:

The equilibrium equations are

$$\begin{aligned}
&\frac{\partial \sigma_{rr}}{\partial r}+\frac{1}{r}\frac{\partial \sigma_{\theta r}}{\partial \theta}+\frac{1}{r\sin\theta}\frac{\partial \sigma_{\phi r}}{\partial \phi}\\
&\quad+\frac{1}{r}(2\sigma_{rr}-\sigma_{\theta\theta}-\sigma_{\phi\phi}+\sigma_{\theta r}\cot\theta)+F_r=0\\
&\frac{\partial \sigma_{r\theta}}{\partial r}+\frac{1}{r}\frac{\partial \sigma_{\theta\theta}}{\partial \theta}+\frac{1}{r\sin\theta}\frac{\partial \sigma_{\phi\theta}}{\partial \phi}\\
&\quad+\frac{1}{r}[(\sigma_{\theta\theta}-\sigma_{\phi\phi})\cot\theta+3\sigma_{r\theta}]+F_\theta=0\\
&\frac{\partial \sigma_{r\phi}}{\partial r}+\frac{1}{r}\frac{\partial \sigma_{\theta\phi}}{\partial \theta}+\frac{1}{r\sin\theta}\frac{\partial \sigma_{\phi\phi}}{\partial \phi}\\
&\quad+\frac{1}{r}(3\sigma_{r\phi}+2\sigma_{\theta\phi}\cot\theta)+F_\phi=0
\end{aligned} \tag{1}$$

where F_r, F_θ, and F_ϕ denote the body forces in the r, θ, and ϕ axes, respectively. The strains are defined by displacements u_r, u_θ, and u_ϕ:

$$\begin{aligned}
\varepsilon_{rr}&=\frac{\partial u_r}{\partial r},\quad \varepsilon_{\theta\theta}=\frac{u_r}{r}+\frac{1}{r}\frac{\partial u_\theta}{\partial \theta}\\
\varepsilon_{\phi\phi}&=\frac{u_r}{r}+\cot\theta\frac{u_\theta}{r}+\frac{1}{r\sin\theta}\frac{\partial u_\phi}{\partial \phi}\\
\varepsilon_{r\theta}&=\frac{1}{2}\left(\frac{1}{r}\frac{\partial u_r}{\partial \theta}+\frac{\partial u_\theta}{\partial r}-\frac{u_\theta}{r}\right)\\
\varepsilon_{\theta\phi}&=\frac{1}{2}\left(\frac{1}{r}\frac{\partial u_\phi}{\partial \theta}-\cot\theta\frac{u_\phi}{r}+\frac{1}{r\sin\theta}\frac{\partial u_\theta}{\partial \phi}\right)\\
\varepsilon_{\phi r}&=\frac{1}{2}\left(\frac{1}{r\sin\theta}\frac{\partial u_r}{\partial \phi}+\frac{\partial u_\phi}{\partial r}-\frac{u_\phi}{r}\right)\\
e&=\varepsilon_{rr}+\varepsilon_{\theta\theta}+\varepsilon_{zz}\\
&=\frac{\partial u_r}{\partial r}+2\frac{u_r}{r}+\frac{1}{r}\frac{\partial u_\theta}{\partial \theta}+\cot\theta\frac{u_\theta}{r}+\frac{1}{r\sin\theta}\frac{\partial u_\phi}{\partial \phi}
\end{aligned} \tag{2}$$

Hooke's law is

$$\begin{aligned}
\varepsilon_{rr}&=\frac{1}{E}(\sigma_{rr}-\nu\sigma_{\theta\theta}-\nu\sigma_{\phi\phi})+\alpha\tau\\
\varepsilon_{\theta\theta}&=\frac{1}{E}(\sigma_{\theta\theta}-\nu\sigma_{\phi\phi}-\nu\sigma_{rr})+\alpha\tau\\
\varepsilon_{\phi\phi}&=\frac{1}{E}(\sigma_{\phi\phi}-\nu\sigma_{rr}-\nu\sigma_{\theta\theta})+\alpha\tau\\
\varepsilon_{r\theta}&=\frac{1}{2G}\sigma_{r\theta},\ \varepsilon_{\theta\phi}=\frac{1}{2G}\sigma_{\theta\phi},\ \varepsilon_{\phi r}=\frac{1}{2G}\sigma_{\phi r}
\end{aligned} \tag{3}$$

The alternative forms are

$$\begin{aligned}
\sigma_{rr}&=2\mu\varepsilon_{rr}+\lambda e-\beta\tau\\
\sigma_{\theta\theta}&=2\mu\varepsilon_{\theta\theta}+\lambda e-\beta\tau\\
\sigma_{\phi\phi}&=2\mu\varepsilon_{\phi\phi}+\lambda e-\beta\tau\\
\sigma_{r\theta}&=2\mu\varepsilon_{r\theta},\ \ \sigma_{\theta\phi}=2\mu\varepsilon_{\theta\phi},\ \ \sigma_{\phi r}=2\mu\varepsilon_{\phi r}
\end{aligned} \tag{4}$$

where E, G, ν, λ, μ, α, and β are Young's modulus, the shear modulus, Poisson's ratio, Lamé's constant, the coefficient of linear thermal expansion, and the thermoelastic constant ($\beta=\alpha(3\lambda+2\mu)=\alpha E/(1-2\nu)$), respectively.

Navier's equations are

$$\begin{aligned}
&(\lambda+2\mu)\frac{\partial e}{\partial r}-\frac{2\mu}{r\sin\theta}\left[\frac{\partial(\omega_\phi\sin\theta)}{\partial\theta}-\frac{\partial\omega_\theta}{\partial\phi}\right]\\
&\quad-\beta\frac{\partial\tau}{\partial r}+F_r=0\\
&(\lambda+2\mu)\frac{1}{r}\frac{\partial e}{\partial\theta}-\frac{2\mu}{r\sin\theta}\left[\frac{\partial\omega_r}{\partial\phi}-\sin\theta\frac{\partial(r\omega_\phi)}{\partial r}\right]\\
&\quad-\beta\frac{1}{r}\frac{\partial\tau}{\partial\theta}+F_\theta=0\\
&(\lambda+2\mu)\frac{1}{r\sin\theta}\frac{\partial e}{\partial\phi}-\frac{2\mu}{r}\left[\frac{\partial(r\omega_\theta)}{\partial r}-\frac{\partial\omega_r}{\partial\theta}\right]\\
&\quad-\beta\frac{1}{r\sin\theta}\frac{\partial\tau}{\partial\phi}+F_\phi=0
\end{aligned} \tag{5}$$

where

$$\begin{aligned}\omega_r &= \frac{1}{2r\sin\theta}\left[\frac{\partial(u_\phi \sin\theta)}{\partial\theta} - \frac{\partial u_\theta}{\partial\phi}\right]\\ \omega_\theta &= \frac{1}{2r\sin\theta}\left[\frac{\partial u_r}{\partial\phi} - \sin\theta\frac{\partial(ru_\phi)}{\partial r}\right]\\ \omega_\phi &= \frac{1}{2r}\left[\frac{\partial(ru_\theta)}{\partial r} - \frac{\partial u_r}{\partial\theta}\right]\end{aligned} \tag{6}$$

When the body forces do not act on the body, Navier's equations, as given by (5) can be solved by Goodier's thermoelastic potential Φ and Boussinesq's harmonic functions ϕ, ϑ, and ψ:

$$\begin{aligned}u_r &= \frac{\partial\Phi}{\partial r} + \frac{\partial\varphi}{\partial r} + \frac{2}{r}\frac{\partial\vartheta}{\partial\theta} + r\cos\theta\frac{\partial\psi}{\partial r}\\ &\quad - (3-4\nu)\psi\cos\theta\\ u_\theta &= \frac{1}{r}\frac{\partial\Phi}{\partial\theta} + \frac{1}{r}\frac{\partial\phi}{\partial\theta} + \frac{2}{r\tan\theta}\frac{\partial\vartheta}{\partial\phi}\\ &\quad + \cos\theta\frac{\partial\psi}{\partial\theta} + (3-4\nu)\psi\sin\theta\\ u_\phi &= \frac{1}{r\sin\theta}\frac{\partial\Phi}{\partial\phi} + \frac{1}{r\sin\theta}\frac{\partial\varphi}{\partial\phi} - 2\sin\theta\frac{\partial\vartheta}{\partial r}\\ &\quad - 2\frac{\cos\theta}{r}\frac{\partial\vartheta}{\partial\theta} + \frac{1}{\tan\theta}\frac{\partial\psi}{\partial\phi}\end{aligned} \tag{7}$$

where Goodier's thermoelastic potential Φ is the particular solution of the equation:

$$\nabla^2\Phi = \frac{1+\nu}{1-\nu}\alpha\tau \tag{8}$$

$$\begin{aligned}\nabla^2 = &\frac{\partial^2}{\partial r^2} + \frac{2}{r}\frac{\partial}{\partial r} + \frac{1}{r^2}\frac{\partial^2}{\partial\theta^2} + \frac{1}{r^2\tan\theta}\frac{\partial}{\partial\theta}\\ &+ \frac{1}{r^2\sin^2\theta}\frac{\partial^2}{\partial\phi^2}\end{aligned} \tag{9}$$

and the three functions φ, ϑ, and ψ must satisfy the Laplace equation:

$$\nabla^2\varphi = \nabla^2\vartheta = \nabla^2\psi = 0 \tag{10}$$

Basic Equations for Axisymmetric Problems

When the spherical bodies are deformed symmetrically with respect to the coordinate axis z, the basic equations (1) to (10) reduce to

$$\begin{aligned}&\frac{\partial\sigma_{rr}}{\partial r} + \frac{1}{r}\frac{\partial\sigma_{\theta r}}{\partial\theta}\\ &+ \frac{1}{r}(2\sigma_{rr} - \sigma_{\theta\theta} - \sigma_{\phi\phi} + \sigma_{\theta r}\cot\theta) + F_r = 0\\ &\frac{\partial\sigma_{r\theta}}{\partial r} + \frac{1}{r}\frac{\partial\sigma_{\theta\theta}}{\partial\theta}\\ &+ \frac{1}{r}[(\sigma_{\theta\theta} - \sigma_{\phi\phi})\cot\theta + 3\sigma_{r\theta}] + F_\theta = 0\end{aligned} \tag{11}$$

The strains are

$$\begin{aligned}&\varepsilon_{rr} = \frac{\partial u_r}{\partial r},\quad \varepsilon_{\theta\theta} = \frac{u_r}{r} + \frac{1}{r}\frac{\partial u_\theta}{\partial\theta},\\ &\varepsilon_{\phi\phi} = \frac{u_r}{r} + \cot\theta\frac{u_\theta}{r}\\ &\varepsilon_{r\theta} = \frac{1}{2}\left(\frac{1}{r}\frac{\partial u_r}{\partial\theta} + \frac{\partial u_\theta}{\partial r} - \frac{u_\theta}{r}\right)\\ &e = \varepsilon_{rr} + \varepsilon_{\theta\theta} + \varepsilon_{zz} = \frac{\partial u_r}{\partial r} + 2\frac{u_r}{r}\\ &\qquad + \cot\theta\frac{u_\theta}{r} + \frac{1}{r}\frac{\partial u_\theta}{\partial\theta}\end{aligned} \tag{12}$$

Hooke's law is

$$\begin{aligned}\varepsilon_{rr} &= \frac{1}{E}(\sigma_{rr} - \nu\sigma_{\theta\theta} - \nu\sigma_{\phi\phi}) + \alpha\tau\\ \varepsilon_{\theta\theta} &= \frac{1}{E}(\sigma_{\theta\theta} - \nu\sigma_{\phi\phi} - \nu\sigma_{rr}) + \alpha\tau\\ \varepsilon_{\phi\phi} &= \frac{1}{E}(\sigma_{\phi\phi} - \nu\sigma_{rr} - \nu\sigma_{\theta\theta}) + \alpha\tau\\ \varepsilon_{r\theta} &= \frac{1}{2G}\sigma_{r\theta}\end{aligned} \tag{13}$$

The alternative forms are

$$\begin{aligned}\sigma_{rr} &= 2\mu\varepsilon_{rr} + \lambda e - \beta\tau\\ \sigma_{\theta\theta} &= 2\mu\varepsilon_{\theta\theta} + \lambda e - \beta\tau\\ \sigma_{\phi\phi} &= 2\mu\varepsilon_{\phi\phi} + \lambda e - \beta\tau\\ \sigma_{r\theta} &= 2\mu\varepsilon_{r\theta}\end{aligned} \tag{14}$$

Navier's equations are

$$\begin{aligned}&(\lambda+2\mu)\frac{\partial e}{\partial r} - \frac{2\mu}{r\sin\theta}\frac{\partial(\omega_\phi\sin\theta)}{\partial\theta} - \beta\frac{\partial\tau}{\partial r} + F_r = 0\\ &(\lambda+2\mu)\frac{1}{r}\frac{\partial e}{\partial\theta} + \frac{2\mu}{r}\frac{\partial(r\omega_\phi)}{\partial r} - \beta\frac{1}{r}\frac{\partial\tau}{\partial\theta} + F_\theta = 0\end{aligned} \tag{15}$$

where

$$\omega_\phi = \frac{1}{2r}\left[\frac{\partial(ru_\theta)}{\partial r} - \frac{\partial u_r}{\partial \theta}\right] \tag{16}$$

When the body forces do not act on the body, Navier's equations, as given by (15) can be solved by Goodier's thermoelastic potential Φ and Boussinesq's harmonic functions φ and ψ:

$$\begin{aligned} u_r &= \frac{\partial \Phi}{\partial r} + \frac{\partial \varphi}{\partial r} + r\cos\theta\frac{\partial \psi}{\partial r} - (3-4v)\psi\cos\theta \\ u_\theta &= \frac{1}{r}\frac{\partial \Phi}{\partial \theta} + \frac{1}{r}\frac{\partial \varphi}{\partial \theta} + \cos\theta\frac{\partial \psi}{\partial \theta} + (3-4v)\psi\sin\theta \end{aligned} \tag{17}$$

where Goodier's thermoelastic potential Φ is the particular solution of the equation:

$$\nabla^2\Phi = \frac{1+v}{1-v}\alpha\tau \tag{18}$$

$$\nabla^2 = \frac{\partial^2}{\partial r^2} + \frac{2}{r}\frac{\partial}{\partial r} + \frac{1}{r^2}\frac{\partial^2}{\partial \theta^2} + \frac{1}{r^2\tan\theta}\frac{\partial}{\partial \theta} \tag{19}$$

and the two functions φ and ψ must satisfy the Laplace equation:

$$\nabla^2\varphi = \nabla^2\psi = 0 \tag{20}$$

The stress comportments are

$$\begin{aligned} \sigma_{rr} &= 2G\left[\frac{\partial^2\Phi}{\partial r^2} - \frac{1+v}{1-v}\alpha\tau + \frac{\partial^2\varphi}{\partial r^2} + r\cos\theta\frac{\partial^2\psi}{\partial r^2}\right. \\ &\quad \left. - 2(1-v)\cos\theta\frac{\partial\psi}{\partial r} + 2v\frac{\sin\theta}{r}\frac{\partial\psi}{\partial\theta}\right] \\ \sigma_{\theta\theta} &= 2G\left[\frac{1}{r}\frac{\partial\Phi}{\partial r} + \frac{1}{r^2}\frac{\partial^2\Phi}{\partial\theta^2} - \frac{1+v}{1-v}\alpha\tau\right. \\ &\quad + \frac{1}{r}\frac{\partial\varphi}{\partial r} + \frac{1}{r^2}\frac{\partial^2\varphi}{\partial\theta^2} + (1-2v)\cos\theta\frac{\partial\psi}{\partial r} \\ &\quad \left. + \frac{\cos\theta}{r}\frac{\partial^2\psi}{\partial\theta^2} + 2(1-v)\frac{\sin\theta}{r}\frac{\partial\psi}{\partial\theta}\right] \\ \sigma_{\phi\phi} &= 2G\left[\frac{1}{r}\frac{\partial\Phi}{\partial r} + \frac{\cot\theta}{r^2}\frac{\partial\Phi}{\partial\theta} - \frac{1+v}{1-v}\alpha\tau\right. \\ &\quad + \frac{1}{r}\frac{\partial\varphi}{\partial r} + \frac{\cot\theta}{r^2}\frac{\partial\varphi}{\partial\theta} + (1-2v)\cos\theta\frac{\partial\psi}{\partial r} \\ &\quad \left. + (\cos\theta\cot\theta + 2v\sin\theta)\frac{1}{r}\frac{\partial\psi}{\partial\theta}\right] \\ \sigma_{r\theta} &= 2G\left[\frac{\partial^2}{\partial r\partial\theta}\left(\frac{\Phi}{r}\right) + \frac{\partial^2}{\partial r\partial\theta}\left(\frac{\varphi}{r}\right)\right. \\ &\quad + (1-2v)\sin\theta\frac{\partial\psi}{\partial r} + \cos\theta\frac{\partial^2\psi}{\partial r\partial\theta} \\ &\quad \left. - 2(1-v)\frac{\cos\theta}{r}\frac{\partial\psi}{\partial\theta}\right] \end{aligned} \tag{21}$$

Let us consider the general solutions of the Laplace equation (20) in the spherical coordinate system. Introducing a new variable defined by

$$\mu = \cos\theta \tag{22}$$

Laplace equation (20) reduces to

$$\frac{\partial^2\varphi}{\partial r^2} + \frac{2}{r}\frac{\partial\varphi}{\partial r} + \frac{1}{r^2}\frac{\partial}{\partial\mu}\left[(1-\mu^2)\frac{\partial\varphi}{\partial\mu}\right] = 0 \tag{23}$$

We assume that the potential function ϕ can be expressed by a product of two functions.

$$\varphi(r,\mu) = f(r)g(\mu) \tag{24}$$

Substitution of (24) into (23) gives

$$\begin{aligned} &\frac{r^2}{f(r)}\left(\frac{d^2}{dr^2} + \frac{2}{r}\frac{d}{dr}\right)f(r) \\ &= -\frac{1}{g(\mu)}\frac{d}{d\mu}\left[(1-\mu^2)\frac{dg(\mu)}{d\mu}\right] \equiv v(v+1) \end{aligned} \tag{25}$$

where v is an arbitrary constant. Equation (25) yields to

$$\begin{aligned} &\frac{d^2f(r)}{dr^2} + \frac{2}{r}\frac{df(r)}{dr} - \frac{v(v+1)}{r^2}f(r) = 0 \\ &\frac{d}{d\mu}\left[(1-\mu^2)\frac{dg(\mu)}{d\mu}\right] + v(v+1)g(\mu) = 0 \end{aligned} \tag{26}$$

Second equation of (26) is called Legendre's differential equation. The general solution of (26) is

$$f(r) = \begin{pmatrix} r^{v} \\ r^{-v-1} \end{pmatrix}, \; g(\mu) = \begin{pmatrix} P_v(\mu) \\ Q_v(\mu) \end{pmatrix} \tag{27}$$

where $P_v(\mu)$ and $Q_v(\mu)$ denote the Legendre's function of the first kind and second kind of order v, respectively. The general solutions of the two functions φ and ψ are

$$\begin{pmatrix} \varphi \\ \psi \end{pmatrix} = \begin{pmatrix} r^{v} \\ r^{-v-1} \end{pmatrix} \begin{pmatrix} P_v(\cos\theta) \\ Q_v(\cos\theta) \end{pmatrix} \tag{28}$$

Since axisymmetric problems are considered, the arbitrary constant v reduces to integer n. The Legendre's function of the second kind $Q_n(\cos\theta)$ has a singular value when $\cos\theta = 1$ $(\theta = 0)$. Then, the general solutions of the two functions for axisymmetric problems in the spherical coordinate reduce to

$$\begin{pmatrix} \varphi \\ \psi \end{pmatrix} = \begin{pmatrix} r^{n} \\ r^{-n-1} \end{pmatrix} P_n(\cos\theta) \; (n = 0, 1, 2, \ldots) \tag{29}$$

Steady Thermal Stress in a Hollow Sphere

Consider a steady thermal stress in a hollow sphere with inner radius a and outer radius b, when the hollow sphere is subjected to the steady temperature change.

The heat conduction equation is

$$\frac{\partial^2 T}{\partial r^2} + \frac{2}{r}\frac{\partial T}{\partial r} + \frac{1}{r^2}\frac{\partial^2 T}{\partial \theta^2} + \frac{1}{r^2 \tan\theta}\frac{\partial T}{\partial \theta} = 0 \tag{30}$$

The boundary and initial conditions are

$$\begin{aligned} T &= T_a(\theta) \;\text{ on }\; r = a \\ T &= T_b(\theta) \;\text{ on }\; r = b \end{aligned} \tag{31}$$

$$T = T_i \qquad \text{at} \quad t = 0 \tag{32}$$

The steady temperature T is

$$T = A_0 + B_0 r^{-1} + \sum_{n=1}^{\infty} (A_n r^n + B_n r^{-n-1}) P_n(\mu) \tag{33}$$

where $\mu = \cos\theta$. We expand both the boundary temperatures $T_a(\theta)$ and $T_b(\theta)$ into the series of Legendre polynomials

$$\begin{aligned} \begin{pmatrix} T_a(\theta) \\ T_b(\theta) \end{pmatrix} &= \begin{pmatrix} T_{a0} \\ T_{b0} \end{pmatrix} + \sum_{n=1}^{\infty} \begin{pmatrix} T_{an} \\ T_{bn} \end{pmatrix} P_n(\mu) \\ \begin{pmatrix} T_{an} \\ T_{bn} \end{pmatrix} &= \frac{2n+1}{2} \int_{-1}^{1} \begin{pmatrix} T_a(\theta) \\ T_b(\theta) \end{pmatrix} P_n(\mu) d\mu \end{aligned} \tag{34}$$

Substitution of (33) into (31) gives

$$\begin{aligned} A_n &= (T_{bn} b^{n+1} - T_{an} a^{n+1})/(b^{2n+1} - a^{2n+1}) \\ B_n &= a^{n+1} b^{n+1} (T_{an} b^n - T_{bn} a^n)/(b^{2n+1} - a^{2n+1}) \\ &\qquad (n = 0, 1, 2, \ldots) \end{aligned} \tag{35}$$

Therefore, the temperature change τ $(= T - T_i)$ is

$$\tau = A_0 - T_i + B_0 r^{-1} + \sum_{n=1}^{\infty} (A_n r^n + B_n r^{-n-1}) P_n(\mu) \tag{36}$$

When the temperature change τ is given by (36), the particular solution of Goodier's thermoelastic potential Φ in (18) is

$$\begin{aligned} \Phi = \frac{1+v}{1-v}\alpha \{ &(A_0 - T_i)\frac{r^2}{6} + B_0 \frac{r}{2} \\ &+ \sum_{n=1}^{\infty} [\frac{1}{2(2n+3)} A_n r^{n+2} \\ &- \frac{1}{2(2n-1)} B_n r^{-n+1}] P_n(\mu) \} \end{aligned} \tag{37}$$

The general solutions of the Boussinesq's harmonic functions φ and ψ are

$$\begin{aligned} \varphi &= C_0' + D_0' r^{-1} + \sum_{n=1}^{\infty} (C_n' r^n + D_n' r^{-n-1}) P_n(\mu) \\ \psi &= E_0' + F_0' r^{-1} + \sum_{n=1}^{\infty} (E_n' r^n + F_n' r^{-n-1}) P_n(\mu) \end{aligned} \tag{38}$$

Substitution of (38) into (17) gives the radial displacement $\bar{u}_r$ in terms of φ and ψ.

$$\begin{aligned}\bar{u}_r &= \frac{\partial\varphi}{\partial r} + r\cos\theta\frac{\partial\psi}{\partial r} - (3-4\nu)\psi\cos\theta \\ &= -D_0' r^{-2} + \sum_{n=1}^{\infty}[nC_n' r^{n-1} - (n+1)D_n' r^{-n-2}]P_n(\mu) \\ &\quad - (3-4\nu)\mu E_0' - 4(1-\nu)\mu F_0' r^{-1} \\ &\quad + \sum_{n=1}^{\infty}\left[(n-3+4\nu)E_n' r^n - (n+4-4\nu)F_n' r^{-n-1}\right] \\ &\quad \times \frac{1}{2n+1}[(n+1)P_{n+1}(\mu) + nP_{n-1}(\mu)]\end{aligned} \tag{39}$$

Equation (39) is not suitable to satisfy the boundary conditions because it contains three kinds of Legendre's functions with different orders $n-1$, n, and $n+1$ under the summation signs. Therefore, we introduce new unknown constants given by

$$\begin{aligned} C_n' &= C_n - (n-4+4\nu)E_{n-2} \\ D_n' &= D_n - (n+5-4\nu)F_{n+2} \\ E_n' &= (2n+1)E_{n-1}, \quad F_n' = (2n+1)F_{n+1}\end{aligned} \tag{40}$$

The radial displacement $\bar{u}_r$ in terms of φ and ψ reduces to

$$\begin{aligned}\bar{u}_r = &- D_0 r^{-2} - 2(1-2\nu)E_0 r \\ &+ \sum_{n=1}^{\infty}\Big\{nC_n r^{n-1} - (n+1)D_n r^{-n-2} \\ &+ (n+1)(n-2+4\nu)E_n r^{n+1} \\ &- n(n+3-4\nu)F_n r^{-n}\Big\}P_n(\mu)\end{aligned} \tag{41}$$

Then, we can get the displacements and thermal stresses

$$\begin{aligned}u_r = &\frac{1+\nu}{1-\nu}\alpha\Big\{(A_0 - T_i)\frac{r}{3} + \frac{1}{2}B_0 \\ &+ \sum_{n=1}^{\infty}\left[\frac{n+2}{2(2n+3)}A_n r^{n+1} + \frac{n-1}{2(2n-1)}B_n r^{-n}\right]P_n(\mu)\Big\} \\ &- D_0 r^{-2} - 2(1-2\nu)E_0 r \\ &+ \sum_{n=1}^{\infty}\Big[nC_n r^{n-1} - (n+1)D_n r^{-n-2} \\ &+ (n+1)(n-2+4\nu)E_n r^{n+1} \\ &- n(n+3-4\nu)F_n r^{-n}\Big]P_n(\mu)\end{aligned} \tag{42}$$

$$\begin{aligned}u_\theta = &-\frac{1+\nu}{1-\nu}\alpha\frac{1}{\sqrt{1-\mu^2}}\sum_{n=1}^{\infty}\Big[\frac{1}{2(2n+3)}A_n r^{n+1} \\ &- \frac{1}{2(2n-1)}B_n r^{-n}\Big](n+1)[\mu P_n(\mu) \\ &- P_{n+1}(\mu)] \\ &- \frac{1}{\sqrt{1-\mu^2}}\sum_{n=1}^{\infty}\Big[C_n r^{n-1} + D_n r^{-n-2} \\ &+ (n+5-4\nu)E_n r^{n+1} \\ &+ (n-4+4\nu)F_n r^{-n}\Big] \\ &(n+1)[\mu P_n(\mu) - P_{n+1}(\mu)]\end{aligned} \tag{43}$$

$$\begin{aligned}\frac{\sigma_{rr}}{2G} = &\frac{1+\nu}{1-\nu}\alpha\Big\{-\frac{2}{3}(A_0 - T_i) - B_0 r^{-1} \\ &+ \sum_{n=1}^{\infty}\Big[\frac{n^2-n-4}{2(2n+3)}A_n r^n \\ &- \frac{n^2+3n-2}{2(2n-1)}B_n r^{-n-1}\Big]P_n(\mu)\Big\} \\ &+ 2D_0 r^{-3} - 2(1+\nu)E_0 \\ &+ \sum_{n=1}^{\infty}[n(n-1)C_n r^{n-2} + (n+1)(n+2)D_n r^{-n-3} \\ &+ (n+1)(n^2-n-2-2\nu)E_n r^n \\ &+ n(n^2+3n-2\nu)F_n r^{-n-1}]P_n(\mu)\end{aligned} \tag{44}$$

$$\begin{aligned}\frac{\sigma_{\theta\theta}}{2G} = &\frac{1+\nu}{1-\nu}\alpha\Big\{-\frac{2}{3}(A_0 - T_i) - \frac{1}{2}B_0 r^{-1} \\ &+ \sum_{n=1}^{\infty}\Big\{\frac{(n+1)}{2(2n+3)}A_n r^n\Big[\frac{\mu}{1-\mu^2} \\ &\times(\mu P_n(\mu) - P_{n+1}(\mu)) - (n+1)P_n(\mu)\Big] \\ &+ \frac{1}{2(2n-1)}B_n r^{-n-1}\times\Big[-\frac{(n+1)\mu}{1-\mu^2}(\mu P_n(\mu) \\ &- P_{n+1}(\mu)) + (n-1)^2 P_n(\mu)\Big]\Big\}\Big\} \\ &- D_0 r^{-3} - 2(1+\nu)E_0 + \sum_{n=1}^{\infty}\Big\{C_n r^{n-2} \\ &\times\Big[(n+1)\frac{\mu}{1-\mu^2}(\mu P_n(\mu) - P_{n+1}(\mu)) - n^2 P_n(\mu)\Big]\end{aligned}$$

$$
\begin{aligned}
&+(n+1)D_n r^{-n-3}\times\left[\frac{\mu}{1-\mu^2}(\mu P_n(\mu)-P_{n+1}(\mu))\right.\\
&\left.-(n+1)P_n(\mu)\right]+(n+1)E_n r^n\\
&\times\left[(n+5-4\nu)\frac{\mu}{1-\mu^2}(\mu P_n(\mu)-P_{n+1}(\mu))\right.\\
&\left.-(n^2+4n+2+2\nu)P_n(\mu)\right]+F_n r^{-n-1}\\
&\times\left[(n+1)(n-4+4\nu)\frac{\mu}{1-\mu^2}\right.\\
&(\mu P_n(\mu)-P_{n+1}(\mu))\\
&\left.-n(n^2-2n-1+2\nu)P_n(\mu)\right]\Bigg\}
\end{aligned}
\tag{45}
$$

$$
\begin{aligned}
\frac{\sigma_{\phi\phi}}{2G}=\frac{1+\nu}{1-\nu}\alpha\Bigg\{&-\frac{2}{3}(A_0-T_i)-\frac{1}{2}B_0 r^{-1}\\
&+\sum_{n=1}^{\infty}\Bigg\{\frac{1}{2(2n+3)}A_n r^n\Big[-(n+1)\\
&\frac{\mu}{1-\mu^2}(\mu P_n(\mu)-P_{n+1}(\mu))-(3n+4)P_n(\mu)\Big]\\
&+\frac{1}{2(2n-1)}B_n r^{-n-1}\Big[(n+1)\frac{\mu}{1-\mu^2}(\mu P_n(\mu)\\
&-P_{n+1}(\mu))-(3n-1)P_n(\mu)\Big]\\
&-D_0 r^{-3}-2(1+\nu)E_0\\
&-\sum_{n=1}^{\infty}\Bigg\{C_n r^{n-2}\times\Big[(n+1)\frac{\mu}{1-\mu^2}(\mu P_n(\mu)\\
&-P_{n+1}(\mu))-nP_n(\mu)\Big]\\
&+(n+1)D_n r^{-n-3}\times\Big[\frac{\mu}{1-\mu^2}(\mu P_n(\mu)\\
&-P_{n+1}(\mu))+P_n(\mu)\Big]+(n+1)E_n r^n\\
&\times\Big[(n+5-4\nu)\frac{\mu}{1-\mu^2}(\mu P_n(\mu)\\
&-P_{n+1}(\mu))-(n-2-4\nu n-2\nu)P_n(\mu)\Big]\\
&+F_n r^{-n-1}\times\Big[(n+1)(n-4+4\nu)\frac{\mu}{1-\mu^2}(\mu P_n(\mu)\\
&-P_{n+1}(\mu))+n(n+3-4\nu n-2\nu)P_n(\mu)\Big]\Bigg\}
\end{aligned}
\tag{46}
$$

$$
\begin{aligned}
\frac{\sigma_{r\theta}}{2G}=&-\frac{1+\nu}{1-\nu}\alpha\frac{1}{\sqrt{1-\mu^2}}\sum_{n=1}^{\infty}(n+1)\Big[\frac{n+1}{2(2n+3)}A_n r^n\\
&+\frac{n}{2(2n-1)}B_n r^{-n-1}\Big][\mu P_n(\mu)-P_{n+1}(\mu)]\\
&-\frac{1}{\sqrt{1-\mu^2}}\sum_{n=1}^{\infty}(n+1)[(n-1)C_n r^{n-2}-(n+2)\\
&D_n r^{-n-3}+(n^2+2n-1+2\nu)E_n r^n-(n^2-2+2\nu)\\
&F_n r^{-n-1}]\times[\mu P_n(\mu)-P_{n+1}(\mu)]
\end{aligned}
\tag{47}
$$

The boundary conditions are

$$
\begin{aligned}
\sigma_{rr}=\sigma_{r\theta}=0\quad&\text{on}\quad r=a\\
\sigma_{rr}=\sigma_{r\theta}=0\quad&\text{on}\quad r=b
\end{aligned}
\tag{48}
$$

Substitution of (44) and (47) into the boundary condition (48) gives

$$
\begin{aligned}
2D_0a^{-3}-2(1+\nu)E_0&=\frac{1+\nu}{1-\nu}\alpha\Big[\frac{2}{3}(A_0-T_i)+B_0a^{-1}\Big]\\
2D_0b^{-3}-2(1+\nu)E_0&=\frac{1+\nu}{1-\nu}\alpha\Big[\frac{2}{3}(A_0-T_i)+B_0b^{-1}\Big]
\end{aligned}
\tag{49}
$$

$$
\begin{aligned}
&n(n-1)C_n a^{n-2}+(n+1)(n+2)D_n a^{-n-3}\\
&+(n+1)(n^2-n-2-2\nu)E_n a^n\\
&+n(n^2+3n-2\nu)F_n a^{-n-1}]=-\frac{1+\nu}{1-\nu}\\
&\alpha\Big[\frac{n^2-n-4}{2(2n+3)}A_n a^n-\frac{n^2+3n-2}{2(2n-1)}B_n a^{-n-1}\Big]\\
&n(n-1)C_n b^{n-2}+(n+1)(n+2)D_n b^{-n-3}\\
&+(n+1)(n^2-n-2-2\nu)E_n b^n\\
&+n(n^2+3n-2\nu)F_n b^{-n-1}]\\
&=-\frac{1+\nu}{1-\nu}\alpha\Big[\frac{n^2-n-4}{2(2n+3)}A_n b^n-\frac{n^2+3n-2}{2(2n-1)}B_n b^{-n-1}\Big]\\
&(n-1)C_n a^{n-2}-(n+2)D_n a^{-n-3}\\
&+(n^2+2n-1+2\nu)E_n a^n-(n^2-2+2\nu)F_n a^{-n-1}\\
&=-\frac{1+\nu}{1-\nu}\alpha\Big[\frac{n+1}{2(2n+3)}A_n a^n+\frac{n}{2(2n-1)}B_n a^{-n-1}\Big]\\
&(n-1)C_n b^{n-2}-(n+2)D_n b^{-n-3}\\
&+(n^2+2n-1+2\nu)E_n b^n-(n^2-2+2\nu)F_n b^{-n-1}\\
&=-\frac{1+\nu}{1-\nu}\alpha\Big[\frac{n+1}{2(2n+3)}A_n b^n+\frac{n}{2(2n-1)}B_n b^{-n-1}\Big]
\end{aligned}
\tag{50}
$$

The unknown coefficients can be determined by solving simultaneous equations (49) and (50). Substitution of the coefficients determined by (49) and (50) into (42)–(47) gives the displacements and thermal stresses.

Steady Thermal Stress in an Infinite Body with a Spherical Cavity

Consider a steady thermal stress in an infinite body with a spherical cavity with radius a, when the body is subjected to the steady temperature change. The hollow sphere reduces to the infinite body with a spherical cavity, when the ratio a/b in the hollow sphere tends to be zero. Then, the temperature in the infinite body is from (36)

$$\tau = -T_i + B_0 r^{-1} + \sum_{n=1}^{\infty} B_n r^{-n-1} P_n(\mu) \tag{51}$$

where $B_n = T_{an} a^{n+1}$.

The corresponding displacements and thermal stresses are given from (42) to (47)

$$\begin{aligned} u_r = &- D_0 r^{-2} - \frac{1+\nu}{1-\nu}\alpha\left(T_i \frac{r}{3} - \frac{1}{2}B_0\right) \\ &- \sum_{n=1}^{\infty}\left[(n+1)D_n r^{-n-2} + n(n+3-4\nu)F_n r^{-n}\right. \\ &\left. - \frac{1+\nu}{1-\nu}\alpha\frac{n-1}{2(2n-1)}B_n r^{-n}\right]P_n(\mu) \end{aligned} \tag{52}$$

$$\begin{aligned} u_\theta = &- \frac{1}{\sqrt{1-\mu^2}}\sum_{n=1}^{\infty}\left[D_n r^{-n-2} + (n-4+4\nu)F_n r^{-n}\right. \\ &\left. - \frac{1+\nu}{1-\nu}\alpha\frac{1}{2(2n-1)}B_n r^{-n}\right](n+1)[\mu P_n(\mu) \\ &- P_{n+1}(\mu)] \end{aligned} \tag{53}$$

$$\begin{aligned} \frac{\sigma_{rr}}{2G} = &\, 2D_0 r^{-3} + \frac{1+\nu}{1-\nu}\alpha\left(\frac{2}{3}T_i - B_0 r^{-1}\right) \\ &+ \sum_{n=1}^{\infty}\left[(n+1)(n+2)D_n r^{-n-3}\right. \\ &+ n(n^2+3n-2\nu)F_n r^{-n-1} \\ &\left. - \frac{1+\nu}{1-\nu}\alpha\frac{n^2+3n-2}{2(2n-1)}B_n r^{-n-1}\right]P_n(\mu) \end{aligned} \tag{54}$$

$$\begin{aligned} \frac{\sigma_{\theta\theta}}{2G} = &- D_0 r^{-3} + \frac{1+\nu}{1-\nu}\alpha\left(\frac{2}{3}T_i - \frac{1}{2}B_0 r^{-1}\right) \\ &+ \sum_{n=1}^{\infty}\left\{(n+1)D_n r^{-n-3}\left[\frac{\mu}{1-\mu^2}(\mu P_n(\mu)\right.\right. \\ &\left. - P_{n+1}(\mu)) - (n+1)P_n(\mu)\right] + F_n r^{-n-1}[(n+1) \\ &(n-4+4\nu)\frac{\mu}{1-\mu^2}(\mu P_n(\mu) - P_{n+1}(\mu)) \\ &- n(n^2-2n-1+2\nu)P_n(\mu)] \\ &- \frac{1+\nu}{1-\nu}\alpha\frac{1}{2(2n-1)}B_n r^{-n-1} \\ &\left.\times\left[\frac{(n+1)\mu}{1-\mu^2}(\mu P_n(\mu) - P_{n+1}(\mu)) - (n-1)^2 P_n(\mu)\right]\right\} \end{aligned} \tag{55}$$

$$\begin{aligned} \frac{\sigma_{\phi\phi}}{2G} = &- D_0 r^{-3} + \frac{1+\nu}{1-\nu}\alpha\left(\frac{2}{3}T_i - \frac{1}{2}B_0 r^{-1}\right) \\ &- \sum_{n=1}^{\infty}\left\{(n+1)D_n r^{-n-3}\left[\frac{\mu}{1-\mu^2}(\mu P_n(\mu) - P_{n+1}(\mu))\right.\right. \\ &\left. + P_n(\mu)\right] + F_n r^{-n-1}[(n+1)(n-4+4\nu) \\ &\times\frac{\mu}{1-\mu^2}(\mu P_n(\mu) - P_{n+1}(\mu)) \\ &+ n(n+3-4\nu n-2\nu)P_n(\mu)] \\ &- \frac{1+\nu}{1-\nu}\alpha\frac{1}{2(2n-1)}B_n r^{-n-1}[(n+1)\frac{\mu}{1-\mu^2} \\ &\left.\times(\mu P_n(\mu) - P_{n+1}(\mu)) - (3n-1)P_n(\mu)]\right\} \end{aligned} \tag{56}$$

$$\begin{aligned} \frac{\sigma_{r\theta}}{2G} = &\frac{1}{\sqrt{1-\mu^2}}\sum_{n=1}^{\infty}(n+1)[(n+2)D_n r^{-n-3} \\ &+ (n^2-2+2\nu)F_n r^{-n-1} \\ &- \frac{1+\nu}{1-\nu}\alpha\frac{n}{2(2n-1)}B_n r^{-n-1}] \\ &\times[\mu P_n(\mu) - P_{n+1}(\mu)] \end{aligned} \tag{57}$$

The boundary conditions are

$$\sigma_{rr} = \sigma_{r\theta} = 0 \quad \text{on} \quad r = a \tag{58}$$

The unknown coefficients can be determined as

$$\begin{aligned} D_0 &= -\frac{1+\nu}{1-\nu}\alpha\left(\frac{1}{3}T_i a^3 - \frac{1}{2}B_0 a^2\right) \\ D_n &= (1+\nu)\alpha\frac{a^2}{2(n^2+n+1-2\nu n-\nu)}B_n \\ F_n &= \frac{1+\nu}{1-\nu}\alpha\frac{n-1}{2(2n-1)(n^2+n+1-2\nu n-\nu)}B_n \end{aligned} \tag{59}$$

Transient Thermal Stress in a Solid Sphere

Consider transient thermal stress in a solid sphere with a radius a, when the solid sphere is subjected to the transient temperature change. The heat conduction equation is

$$\frac{\partial^2 T}{\partial r^2}+\frac{2}{r}\frac{\partial T}{\partial r}+\frac{1}{r^2}\frac{\partial^2 T}{\partial \theta^2}+\frac{1}{r^2\tan\theta}\frac{\partial T}{\partial \theta}=\frac{1}{\kappa}\frac{\partial^2 T}{\partial t^2} \tag{60}$$

where t and κ denote time and the thermal diffusivity, respectively. The boundary condition and initial condition are

$$T = T_a(\theta) \quad \text{on} \quad r = a \tag{61}$$

$$T = T_i \qquad \text{at} \quad t = 0 \tag{62}$$

Then, the heat conduction equation and the boundary and initial conditions for the temperature change τ $(=T - T_i)$ reduce to

$$\frac{\partial^2 \tau}{\partial r^2}+\frac{2}{r}\frac{\partial \tau}{\partial r}+\frac{1}{r^2}\frac{\partial}{\partial \mu}\left[(1-\mu^2)\frac{\partial \tau}{\partial \mu}\right]=\frac{1}{\kappa}\frac{\partial^2 \tau}{\partial t^2} \tag{63}$$

$$\tau = T_a(\theta) - T_i \quad \text{on} \quad r = a \tag{64}$$

$$\tau = 0 \qquad \text{at} \quad t = 0 \tag{65}$$

where $\mu = \cos\theta$. Here, we introduce the method of separation of variables to obtain the general solution of (63). When the temperature change is expressed as

$$\tau(r, z, t) = f(r)g(\mu)h(t) \tag{66}$$

three separation equations can be obtained by substitution of (66) into (63):

$$\begin{aligned}
&\frac{d}{d\mu}\left[(1-\mu^2)\frac{dg(\mu)}{d\mu}\right]+n(n+1)g(\mu)=0\\
&\frac{d^2 f(r)}{dr^2}+\frac{2}{r}\frac{df(r)}{dr}+\left(s^2-\frac{n(n+1)}{r^2}\right)f(r)=0\\
&\frac{dh(t)}{dt}+\kappa s^2 h(t)=0
\end{aligned} \tag{67}$$

where the second equation in (67) is called the spherical Bessel's equation. The general solutions of (61) are

$$g(\mu)=\begin{pmatrix}P_v(\mu)\\ Q_v(\mu)\end{pmatrix} \tag{68}$$

$$f(r)=\begin{pmatrix}r^n\\ r^{-n-1}\end{pmatrix},\ h(t)=1 \text{ for } s=0 \tag{69}$$

$$f(r)=\begin{pmatrix}j_n(sr)\\ y_n(sr)\end{pmatrix},\ h(t)=\exp(-\kappa s^2 t) \text{ for } s\neq 0 \tag{70}$$

where $j_n(r)$ and $y_n(r)$ are the spherical Bessel functions of the first and second kind of order n, respectively.

The general solution of (63) for this problem is expressed by

$$\begin{aligned}
\tau=&\sum_{n=0}^{\infty}A_n r^n P_n(\mu)\\
&+\sum_{n=0}^{\infty}\sum_{i=1}^{\infty}A_{ni}j_n(s_{ni}r)P_n(\mu)\exp(-\kappa s_{ni}^2 t)
\end{aligned} \tag{71}$$

Taking into consideration the boundary conditions given by (64), we can obtain that s_{ni} are the eigenvalues of the equation:

$$j_n(s_{ni}a)=0 \tag{72}$$

and

$$A_0=T_{a0}-T_i,\ \ A_n=T_{an}/a^n\ \ (n=1,2,....) \tag{73}$$

where

$$T_a(\theta)=\sum_{n=0}^{\infty}T_{an}P_n(\mu) \tag{74}$$

The initial condition (65) gives

$$\sum_{i=1}^{\infty}A_{ni}j_n(s_{ni}r)=-A_n r^n \tag{75}$$

Multiplying $r^2 j_n(s_{nj}r)$ on both sides of (75) and integrating from 0 to a, we get

$$A_{nj} = -2A_n \frac{a^n}{s_{nj} a j_{n+1}(s_{nj}a)} = -2T_{an} \frac{1}{s_{nj} a j_{n+1}(s_{nj}a)} \tag{76}$$

Then, the temperature change τ is determined by

$$\tau = T_{a0} - T_i + \sum_{n=1}^{\infty} T_{an} \left(\frac{r}{a}\right)^n P_n(\mu) - 2\sum_{n=0}^{\infty}\sum_{i=1}^{\infty} T_{an} \frac{j_n(s_{ni}r)}{s_{ni} a j_{n+1}(s_{ni}a)} P_n(\mu) \exp(-\kappa s_{ni}^2 t) \tag{77}$$

Next, we consider the thermal stresses under the boundary conditions

$$\sigma_{rr} = \sigma_{r\theta} = 0 \qquad \text{at} \quad r = a \tag{78}$$

Goodier's thermoelastic function Φ and the Boussinesq's harmonic functions φ and ψ are for this problem:

$$\Phi = \frac{1+\nu}{1-\nu}\alpha \left[\sum_{n=0}^{\infty} \frac{1}{2(2n+3)} A_n r^{n+2} P_n(\mu) - \sum_{n=0}^{\infty}\sum_{i=1}^{\infty} \frac{A_{ni}}{s_{ni}^2} j_n(s_{ni}r) P_n(\mu) \exp(-\kappa s_{ni}^2 t) \right] \tag{79}$$

$$\varphi = \sum_{n=0}^{\infty} [C_n - (n-4+4\nu)E_{n-2}] r^n P_n(\mu) \qquad \psi = \sum_{n=0}^{\infty} (2n+1) E_{n-1} r^n P_n(\mu) \tag{80}$$

Then, we can get the displacements and thermal stresses:

$$u_r = \frac{1+\nu}{1-\nu}\alpha \left\{ \sum_{n=0}^{\infty} \frac{n+2}{2(2n+3)} A_n r^{n+1} P_n(\mu) \right\} - \sum_{n=0}^{\infty}\sum_{i=1}^{\infty} \frac{A_{ni}}{s_{ni}^2} \left[\frac{n}{r} j_n(s_{ni}r) - s_{ni} j_{n+1}(s_{ni}r) \right] \times P_n(\mu) \exp(-\kappa s_{ni}^2 t) + \sum_{n=0}^{\infty} [nC_n r^{n-1} + (n+1)(n-2+4\nu)E_n r^{n+1}] P_n(\mu) \tag{81}$$

$$u_\theta = -\frac{1+\nu}{1-\nu}\alpha \frac{1}{\sqrt{1-\mu^2}} \times \left\{ \sum_{n=1}^{\infty} \frac{1}{2(2n+3)} A_n r^{n+1} \times (n+1) \times [\mu P_n(\mu) - P_{n+1}(\mu)] - \sum_{n=1}^{\infty}\sum_{i=1}^{\infty} \frac{A_{ni}}{s_{ni}^2} \frac{1}{r} j_n(s_{ni}r) \times (n+1) \times [\mu P_n(\mu) - P_{n+1}(\mu)] \exp(-\kappa s_{ni}^2 t) \right\} - \frac{1}{\sqrt{1-\mu^2}} \sum_{n=1}^{\infty} [C_n r^{n-1} + (n+5-4\nu)E_n r^{n+1}] \times (n+1)[\mu P_n(\mu) - P_{n+1}(\mu)] \tag{82}$$

$$\frac{\sigma_{rr}}{2G} = \frac{1+\nu}{1-\nu}\alpha \left\{ \sum_{n=0}^{\infty} \frac{n^2-n-4}{2(2n+3)} A_n r^n P_n(\mu) \right\} - \sum_{n=0}^{\infty}\sum_{i=1}^{\infty} \frac{A_{ni}}{s_{ni}^2} \left[\frac{n(n-1)}{r^2} j_n(s_{ni}r) + 2\frac{s_{ni}}{r} j_{n+1}(s_{ni}r) \right] P_n(\mu) \exp(-\kappa s_{ni}^2 t) \right\} + \sum_{n=1}^{\infty} [n(n-1)C_n r^{n-2} + (n+1)(n^2-n-2-2\nu)E_n r^n] P_n(\mu) \tag{83}$$

$$\frac{\sigma_{\theta\theta}}{2G} = \frac{1+\nu}{1-\nu}\alpha \left\{ \sum_{n=0}^{\infty} \frac{1}{2(2n+3)} A_n r^n \left[\frac{(n+1)\mu}{1-\mu^2} (\mu P_n(\mu) - P_{n+1}(\mu)) - (n+2)^2 P_n(\mu) \right] - \sum_{n=0}^{\infty}\sum_{i=1}^{\infty} \frac{A_{ni}}{s_{ni}^2} \left\{ [(s_{ni}^2 - \frac{n^2}{r^2}) j_n(s_{ni}r) - \frac{s_{ni}}{r} j_{n+1}(s_{ni}r)] P_n(\mu) + \frac{1}{r^2} j_n(s_{ni}r)(n+1) \times \frac{\mu}{1-\mu^2} [\mu P_n(\mu) - P_{n+1}(\mu)] \right\} \exp(-\kappa s_{ni}^2 t) \right\} + \sum_{n=1}^{\infty} \{ C_n r^{n-2} [(n+1)\frac{\mu}{1-\mu^2}(\mu P_n(\mu) - P_{n+1}(\mu)) - n^2 P_n(\mu)] + (n+1) E_n r^n \times [(n+5-4\nu)\frac{\mu}{1-\mu^2}(\mu P_n(\mu) - P_{n+1}(\mu)) - (n^2+4n+2+2\nu)P_n(\mu)] \} \} \tag{84}$$

$$\frac{\sigma_{\phi\phi}}{2G}=\frac{1+\nu}{1-\nu}\alpha\Bigg\{\sum_{n=0}^{\infty}\frac{1}{2(2n+3)}A_n r^n$$
$$[-(n+1)\frac{\mu}{1-\mu^2}(\mu P_n(\mu)-P_{n+1}(\mu))$$
$$-(3n+4)P_n(\mu)]$$
$$-\sum_{n=0}^{\infty}\sum_{i=1}^{\infty}\frac{A_{ni}}{s_{ni}^2}\Bigg\{[(s_{ni}^2+\frac{n}{r^2})j_n(s_{ni}r)$$
$$-\frac{s_{ni}}{r}j_{n+1}(s_{ni}r)]P_n(\mu)-\frac{1}{r^2}j_n(s_{ni}r)(n+1)$$
$$\times\frac{\mu}{1-\mu^2}[\mu P_n(\mu)-P_{n+1}(\mu)]\Bigg\}\exp(-\kappa s_{ni}^2 t)\Bigg\}$$
$$-\sum_{n=1}^{\infty}\{C_n r^{n-2}[(n+1)$$
$$\frac{\mu}{1-\mu^2}(\mu P_n(\mu)-P_{n+1}(\mu))$$
$$-nP_n(\mu)]+(n+1)E_n r^n[(n+5-4\nu)$$
$$\frac{\mu}{1-\mu^2}(\mu P_n(\mu)-P_{n+1}(\mu))$$
$$-(n-2-4\nu n-2\nu)P_n(\mu)]\} \tag{85}$$

$$\frac{\sigma_{r\theta}}{2G}=-\frac{1+\nu}{1-\nu}\alpha\frac{1}{\sqrt{1-\mu^2}}$$
$$\times\Bigg\{\sum_{n=1}^{\infty}\frac{(n+1)^2}{2(2n+3)}A_n r^n[\mu P_n(\mu)-P_{n+1}(\mu)]$$
$$-\sum_{n=0}^{\infty}\sum_{i=1}^{\infty}\frac{A_{ni}}{s_{ni}^2}\left[\frac{n-1}{r^2}j_n(s_{ni}r)-\frac{s_{ni}}{r}j_{n+1}(s_{ni}r)\right]$$
$$\times(n+1)[\mu P_n(\mu)-P_{n+1}(\mu)]\exp(-\kappa s_{ni}^2 t)\Bigg\}$$
$$-\frac{1}{\sqrt{1-\mu^2}}\sum_{n=1}^{\infty}(n+1)[(n-1)C_n r^{n-2}$$
$$+(n^2+2n-1+2\nu)E_n r^n][\mu P_n(\mu)-P_{n+1}(\mu)] \tag{86}$$

The unknown coefficients can be determined from the boundary condition (78).

References

1. Noda N, Hetnarski RB, Tanigawa Y (2003) Thermal stresses, 2nd edn. Taylor & Francis, New York/London